

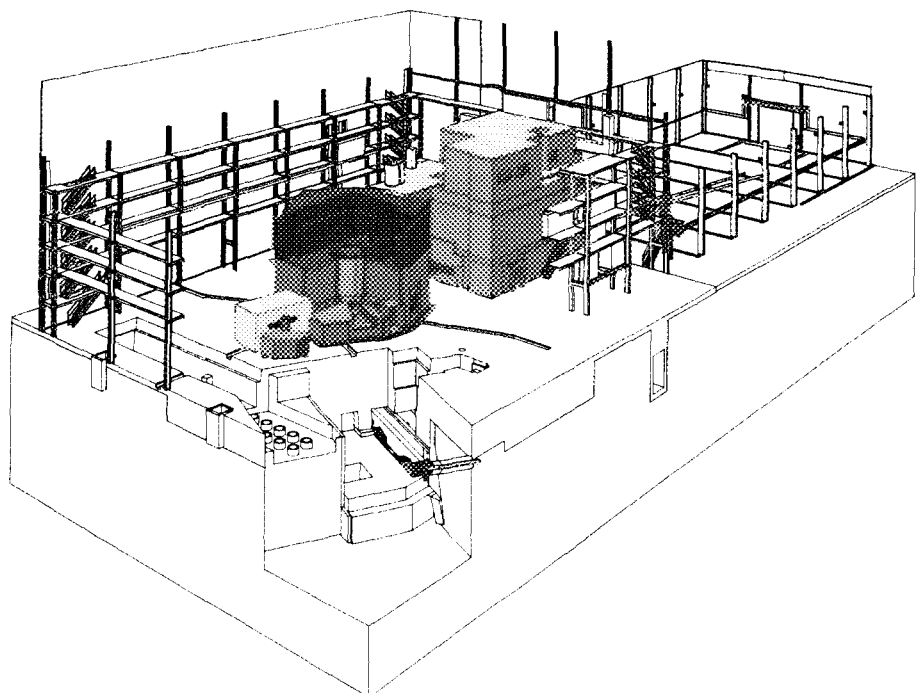
PAUL SCHERRER INSTITUT



PSI Proceedings 96-02
November 1996
ISSN 1019-6447



CH9700028



New Instruments and Science around SINQ

Lecture Notes of the 4th Summer School
on Neutron Scattering

Zuoz, Switzerland
August 18-24, 1996

PSI-Proceedings 96-02
November 1996
ISSN 1019-6447

New Instruments and Science around SINQ

**Lecture Notes of the
4th Summer School on Neutron Scattering**

**Zuoz, Switzerland
August 18-24, 1996**

**edited by
Albert Furrer**

**Paul Scherrer Institut, 1996
Villigen, Switzerland**

Organization of the School

Chairman

W.E. Fischer, Paul Scherrer Institut

Secretary

R. Bercher, Paul Scherrer Institut

Programme Committee

Chairman: A. Furrer, ETH Zürich & PSI

Members: G. Bauer, PSI

P. Böni, PSI

W. Bührer, ETH Zürich & PSI

D. Clemens, PSI

P. Fischer, ETH Zürich & PSI

S. Janssen, Univ. Saarbrücken & PSI

J. Mesot, PSI

J. Schefer, PSI

W. Wagner, PSI

Sponsored by

Paul Scherrer Institut (PSI)

Schweizerische Gesellschaft für Neutronenstreuung

Program of the
4th Summer School on Neutron Scattering, 18-24 August 1996, Zuoz, Switzerland

	18 August	19 August	20 August	21 August	22 August	23 August	24 August
08.00		BREAKFAST	BREAKFAST	BREAKFAST	BREAKFAST	BREAKFAST	BREAKFAST
09.00		W. FISCHER Opening Introduction to neutron scattering (NS)	W. PETRY Martensitic phase transitions W. WAGNER SANS	J. KERN Prompt gamma analysis H.W. GÄGGERL Activation Analysis	Excursions	D. MADEN Data acquisition J. SCHEFER Four-circle diffractometer SC3	Departure
10.00		COFFEE BREAK	COFFEE BREAK	COFFEE BREAK		COFFEE BREAK	
10.30		P. FISCHER Powder diffractometers HRPT and DMC S. DECURTINS Supramolecular magnets	P.SCHURTERBERGER Polymers and colloids M.W. LONG Magnetic diffuse scattering	D. CLEMENS Reflectometer H. ZABEL Layered magnets		W. STEURER Quasicrystals Th. WOIKE Optical storage systems	
12.15		LUNCH Free Afternoon	LUNCH Free Afternoon	LUNCH Free Afternoon		LUNCH Free Afternoon	
16.00		COFFEE	COFFEE	COFFEE	COFFEE	COFFEE	
16.30	Arrival	M. MEDARDE Metal-insulator transitions POSTER SESSION	S. JANSSEN Time-of-flight spectrometer FOCUS U. BUCHENAU Dynamics of polymers B.D. RAINFORD Magnetic excitations	M. STAMM Polymer surfaces H. STUHRMANN Dynamic nuclear polarization J. MESOT Extreme conditions (p,T,H)	P. BÖNI Polarized triple-axis spectrometer TASP B. DORNER Polarization analysis P.J. BROWN The INVAR problem	G.A. WEBSTER Residual stress G. BAUER Summary Instruments S.W. LOVESEY Summary Science A. FURRER CLOSING	
19.15		DINNER	DINNER	DINNER	DINNER	DINNER	
20.15		W. BÜHRER Triple-axis spectrometer Drüchal R. CURRAT Incommensurate phase transitions	E. LEHMANN Non-diffractive methods G. BAYON Neutron radiography	Free Evening		BANQUET	
21.45							

FOREWORD

The spallation neutron source at PSI will be commissioned towards the end of this year together with a set of first generation instruments. This facility should then be available for the initial scientific work after spring next year. One of the main goals of this year's summer school for neutron scattering was therefore the preparation of the potential customers at this facility for its scientific exploitation. In order to give them the - so to speak - last finish, we have dedicated the school to the discussion of the instruments at SINQ and their scientific potential. While the second and third school emphasized a particular physical topic (-like hydrogen in matter and magnetism) this school was hence more similar to the first one which covered the general applications of the experimental technique of neutron scattering. In view of the immediate future we believed this to be the last opportunity to give the users of the facility a chance to become familiar with the principles and the experimental possibilities at SINQ.

Thanks to the spirit of good cooperation of the invited lecturers the write up's of the lectures could be made available to the participants at the very start of the school. It is our experience from previous events that this occasion for pre-study (at least some individually selected lectures) is highly appreciated. This the more, since the school was kept on a relatively high professional standard.

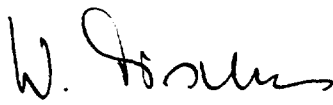
ACKNOWLEDGMENTS

First of all I am grateful for the great effort of all the lectures. Apart from the presentation of their excellent courses, they have again provided considerable stimulation to the scientific atmosphere.

I believe that I am allowed to express in the name of all participants our appreciation for the excellent service and help provided by the administration and its staff of the Lyceum Alpinum. Accommodation and meals (or rather dishes) of the best - we became used to it.

Finally I am pleased to thank our school secretary, Mrs. Renate Bercher. With her competence and help, deal with such a school just means easy going - for the chairman.

Villigen, August 1996



W.E. Fischer
 Head of Department
 Condensed Matter Research at Large Facilities

Editorial

Ninety participants and lecturers assembled at the Lyceum Alpinum at Zuoz (Switzerland), a small village in the upper Engadine valley, from August 18-24, 1996, for the 4th Summer School on Neutron Scattering organized by the Paul Scherrer Institute (PSI) to discuss "New Instruments and Science Around SINQ". The aim of the School was twofold:

- To introduce the first-generation instruments installed at the spallation neutron source SINQ at PSI;
- To get acquainted with typical experiments at the forefront of science and technology which can be performed on these instruments.

In order to achieve these goals the instruments and subjects discussed were:

- Introduction to neutron scattering (*W.E. Fischer*);
- Single-crystal diffractometer (*J. Schefer*), quasicrystals (*W. Steurer*), optical information storage systems (*Th. Woike*), residual stress (*G.A. Webster*);
- Powder diffractometers (*P. Fischer*), supramolecular magnetism (*S. Decurtins*), metal-insulator transitions (*M. Medarde*);
- Three-axis spectrometer (*W. Bührer*), incommensurate phase transitions (*R. Currat*), martensitic phase transitions (*W. Petry*);
- Polarized three-axis spectrometer (*P. Böni*), identification of magnetic modes by polarization analysis (*B. Dorner*), INVAR (*P.J. Brown*);
- Time-of-flight spectrometer (*S. Janssen*), dynamics of polymers (*U. Buchenau*), magnetic excitations (*B.D. Rainford*);
- Small-angle diffractometer (*W. Wagner*), polymers and colloids (*P. Schurtenberger*);
- Reflectometer (*D. Clemens*), layered magnets (*H. Zabel*), polymer surfaces, interfaces and thin films (*M. Stamm*);
- Non-diffractive methods (*E. Lehmann*), neutron radiography (*G. Bayon*), prompt gamma analysis (*J. Kern*), neutron activation analysis (*H.W. Gäggeler*);
- Sample environment: dynamic nuclear polarization (*H. Stuhrmann*), extreme conditions (*J. Mesot*);
- Data acquisition (*D. Maden*).

Some of the participants presented the results of their own activities in neutron scattering as posters which throughout touched interesting topics in condensed matter research and neutron applications. These presentations are not included in the Proceedings which are divided into two parts:

- Part A gives a complete description of the first-generation instruments and sample environment at SINQ. For all the instruments the relevant parameters for planning experiments are listed. Part A is completed by *Günter Bauers* summary on experimental facilities and future developments at SINQ.
- Part B presents the lecture notes dealing with relevant applications of neutron based techniques in science and technology. The summary lecture by *S.W. Lovesey* is also included.

The programme of the School was very dense and on a high level, particularly for those participants with little or no prior knowledge in the field of neutron scattering. The present Proceedings will certainly help to digest all the presentations in more detail as well as to be a useful compendium when transforming ideas and concepts into neutron experiments.

The major load in the School was on the invited lecturers. I would like to thank them all for their excellent presentations as well as their excellently written lecture notes. I thank all the participants for their interest, their presentations and votes during the discussions. I thank my colleagues of the Programme Committee for their advice in setting up the programme of the School. Finally I thank Walter Fischer for accepting to be the chairman of the School. Last but not least I acknowledge the invaluable efforts of the secretary, Renate Bercher, for all her efforts that everything went so smoothly.



September 1996

Albert Furrer

Contents

Organization of the School	3
Program of the School	5
Foreword <i>W.E. Fischer</i>	7
Editorial <i>A. Furrer</i>	9
Table of Contents	11
A. Instruments and Sample Environment	
1. Powder Neutron Diffractometers HRPT and DMCG <i>Peter Fischer, Andreas Dönni, Urs Staub and Markus Zolliker</i>	15
2. The New Single Crystal Diffractometer SC3 <i>J. Schefer, M. Koch, P. Keller, S. Fischer and R. Thut</i>	23
3. Triple-Axis Spectrometer DrüchaL <i>Willi Bührer and Peter Keller</i>	29
4. Polarized Triple-Axis Spectrometer TASP <i>Peter Böni and Peter Keller</i>	35
5. FOCUS: Time-of-Flight Spectrometer for Cold Neutrons at SINQ <i>Stefan Janssen, Joël Mesot and Rolf Hempelmann</i>	45
6. The Small Angle Diffractometer SANS at PSI <i>W. Wagner</i>	55
7. The Neutron Reflectometer at SINQ <i>Daniel Clemens</i>	65
8. Extreme Conditions (p,T,H) <i>Joël Mesot</i>	79
9. Dynamic Nuclear Spin Polarization <i>H.B. Stuhrmann</i>	87
10. Nondiffractive Applications of Neutrons at the Spallation Source SINQ <i>E. Lehmann</i>	101

11.	Prompt Gamma-Ray Activation Analysis <i>Jean Kern</i>	115
12.	Neutron Activation Analysis (NAA), Radioisotope Production via Neutron Activation (PNA), and Fission Product Gas-Jet (GJA) <i>Heinz W. Gäggeler</i>	125
13.	The SINQ Data Acquisition System <i>David Maden</i>	133
14.	Summary on Experimental Facilities and Future Developments at SINQ <i>Günter S. Bauer</i>	143
B. Scientific Applications		
15.	Introduction to Neutron Scattering <i>W.E. Fischer</i>	155
16.	Quasicrystals <i>Walter Steurer</i>	187
17.	Optical Information Storage <i>Th. Woike</i>	199
18.	Principles of the Measurement of Residual Stress by Neutron Diffraction <i>G.A. Webster and A.N. Ezeilo</i>	217
19.	Magnetism: A Supramolecular Function <i>S. Decurtins, R. Pellaux, H.W. Schmalle and P. Fischer</i>	235
20.	The Metal-Insulator Transition of $R\text{NiO}_3$ Perovskites <i>Maria Luisa Medarde</i>	249
21.	Incommensurate Phase Transitions <i>R. Currat</i>	265
22.	Martensitic Phase Transitions <i>Winfried Petry and Jürgen Neuhaus</i>	293
24.	Identification of Different Magnetic Modes in CsFeCl_3 by Polarization Analysis <i>Bruno Dorner, Boris Toperverg, Markus Bahr and Daniel Petitgrand</i>	317

25.	Spin-Lattice Interactions Studied by Polarized and Unpolarized Inelastic Scattering: Application to the INVAR Problem <i>P.J. Brown</i>	329
26.	Magnetic Diffuse Scattering: A Theorists Perspective <i>M.W. Long</i>	347
27.	Magnetic Excitations Studied with Time-of-Flight Spectroscopy <i>Brian Rainford</i>	361
28.	Dynamics of Polymers <i>U. Buchenau</i>	379
29.	Polymers and Colloids <i>Peter Schurtenberger</i>	397
30.	Polymer Surfaces, Interfaces and Thin Films <i>Manfred Stamm</i>	413
31.	Layered Magnets: Polarized Neutron Reflection Studies <i>Hartmut Zabel and Andreas Schreyer</i>	427
31.	Review on Use of Neutron Radiography at Saclay Nuclear Research Centre <i>Guy Bayon</i>	439
32.	Summary Science <i>Stephen W. Lovesey and Ewald Balcar</i>	447
	List of Participants	450



POWDER NEUTRON DIFFRACTOMETERS HRPT AND DMCG

PETER FISCHER

*Laboratory for Neutron Scattering ETH Zurich & Paul Scherrer Institute
CH-5232 Villigen PSI, Switzerland*

and

ANDREAS DÖNNI, URS STAUB and MARKUS ZOLLIKER

*Laboratory for Neutron Scattering ETH Zurich & Paul Scherrer Institute
CH-5232 Villigen PSI, Switzerland*

ABSTRACT

Basic properties and applications of SINQ powder neutron diffractometers are described. For optimum use of the continuous neutron beams these instruments are equipped with position sensitive detectors, and both high-intensity and high-resolution modes of operation are possible. HRPT attaining resolutions $\delta d/d \leq 10^{-3}$, d = lattice spacing, at a thermal neutron channel of the target station and DMCG at a cold neutron guide coated with $m = 2$ supermirrors, are complementary concerning the applications: The former will be mainly used for structural studies and the latter to investigate magnetic ordering phenomena.

1. Introduction

1.1 Why powder neutron diffraction ?

New materials are generally at first only available in polycrystalline, quasi crystalline or amorphous form. Here powder neutron diffraction yields complementary to powder X-ray diffraction on an atomic scale important first informations on average static properties such as crystal structure and on magnetic ordering phenomena. Due to the special features of thermal neutron waves (cf. table I) this technique represents a versatile, interdisciplinary research tool in many fields of applications such as crystallography, solid state physics, chemistry, materials science, geology and biology, which range from basic science to technical applications. In particular the generally weak absorption of neutrons facilitates essentially experiments as a function of external parameters such as high or very low temperatures.

Therefore, two complementary powder neutron diffractometers will be installed at SINQ: HRPT for thermal neutrons and DMCG at a cold neutron guide.

1.2. Optimum powder neutron diffractometers for continuous neutron sources of medium intensity ?

Compared to the generally very high intensity of X-ray synchrotron radiation the present neutron sources are rather limited in flux. Obvious ways to make efficient use of a continuous neutron source for powder neutron diffraction are to maximise the number of detectors and to use large vertical divergences. Presently the best such instrument is D2B [1] at the high-flux reactor of ILL, Grenoble. It is based on 64 5' mylar-Gd-O collimators of Soller type (20 cm high) and 64 He³ detectors, spaced at 2.5° intervals and uses the

high take-off angle 135° for a vertically focusing Ge wafer monochromator. With a primary mylar-Gd-O Soller collimator of $5'$ highest resolution $\delta d/d \approx 5 \times 10^{-4}$ may be obtained. To get a complete diffraction pattern in the scattering angle range of 160° with angular step 0.025° 99 steps are necessary. This requires with a measurement time of ≈ 20 sec per point half an hour. Advantages of such an instrument are the now standard technology and the fact that the resolution does not depend on the sample diameter. However, to obtain the same counting statistics at the continuous spallation neutron source SINQ with about an order of magnitude lower thermal neutron flux would require about 5 hours. Therefore, at SINQ an instrument design to get this value down to the order of minutes, has been chosen.

Table I: Basic neutron properties and resulting applications.

neutron properties	consequences	applications
wavelength comparable to interatomic distances	interference effects on an atomic scale	investigation of crystal, quasi crystalline, amorphous and liquid structures
electric neutrality	generally weak absorption, mainly information on volume properties	phase analysis, average over large sample volumes, ease of performing investigations as a function of external parameters such as temperature, pressure etc.
nuclear particle/wave	nuclear scattering isotropic, constant amplitude not depending on scattering angle, irregular dependence on the atomic number, isotope dependent	precise location of light and/or similar atoms, ions, isotopes such as deuterium precise determination of average thermal motions such as isotropic, anisotropic and anharmonic temperature factors
low energy	almost no radiation damage	non-destructive investigations of internal strains (residual stresses) or in biological experiments
'limited' neutron source intensity	weak scattering intensities	compensation by sample size and by multidetectors
magnetic moment	magnetic neutron scattering, depending on scattering angle	investigation of magnetic ordering phenomena in condensed matter on an atomic scale

2. Design, Properties and Applications of the High-Resolution Powder Neutron Diffractometer HRPT for Thermal Neutrons

At the 10 MW reactor Saphir of Paul Scherrer Institute we got very good experience with the DMC [2] 'banana' type detector (BF_3 , 400 wires at 0.2° intervals at a radius of 1.5 m). Therefore, and in view of the as a function of time compared to a reactor certainly considerably less stable neutron flux at SINQ, it was decided to use a large position-sensitive (PSD) He^3 detector system consisting of $25 \times 64 = 1600$ detectors at 0.1° intervals at a radius of 1.5 m, similar to D20 of ILL. It has been shown by Popovici et al. [3] that such a PSD system has particular advantages for smaller sample sizes (diameter < 15 mm, best figure of merit for sample diameter of 5 mm), which is frequently needed in case of new materials available only in smaller quantities. Compared to D2B the 25 times larger number of detectors compensates the lower source flux.

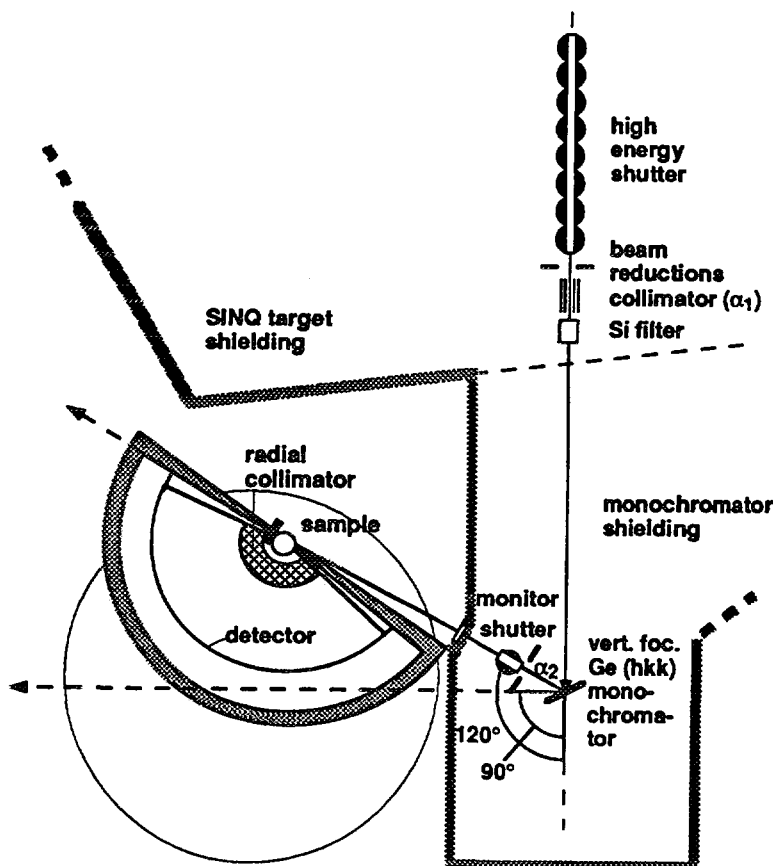


Fig. 1: Schematic view of the high-resolution powder diffractometer HRPT for thermal neutrons.

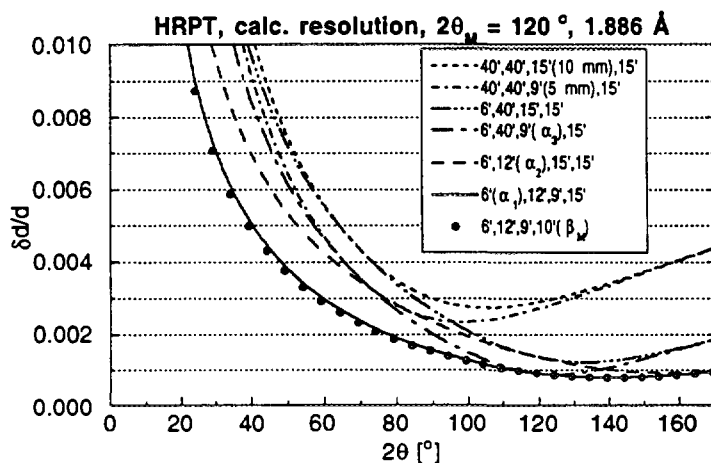


Fig. 2: Calculated resolution functions of HRPT for $2\theta_M = 120^\circ$.

The new multidetector powder neutron diffractometer HRPT, illustrated in figure 1, will allow real-time experiments in a scattering angle range of 160° with a single position

Table II: Characteristics of HRPT.

SINQ target hall, thermal neutron beam =1RNS41 (H_2O scatterer)			
Primary beam width: 55, 44 or 29 mm (+ beam closed), height 150 mm			
Primary collimation:			
Al alloy-Gd-O Soller collimators with $\alpha_1 = 6'$, 12' (high resolution), - (high intensity)			
Liquid N_2 cooled Si filter of 20 cm length			
Monochromator:			
Ge (hkk), wafer type, vertically focusing			
Ge (hkk) ω_M^{100} wavelength $\lambda [\text{\AA}]$			
[°] $2\theta_M = 90^\circ$ $2\theta_M = 120^\circ$			
111 54.74 4.620 5.658			
311 25.24 2.413* 2.955			
400 0.00 2.000 2.450*			
511 15.79 1.540 1.886			
533 40.32 1.220 1.494			
711 11.42 1.120 1.372			
733 31.22 0.978 1.197			
755 45.29 0.804 0.985			
* PG(C) filter			
α_2 : concerning horizontal width variable slit system			
$2\theta \approx 5^\circ \div 165^\circ$, $\delta 2\theta: \pm 0.001^\circ$			
radial (1°) mylar-Gd-O collimator			
PSD detector:			
He ³ (3 bars) + CF ₄ (1 bar)			
25x64 = 1600 (150 mm high Au plated W wires of $\varnothing \approx 25 \mu$), angular spacing 0.1°			
Sample temperature: 7 mK \div 2100 K			
zero matrix pressure cell			

between monochromator and sample allows further optimisation of resolution and background. Compared to D20 a unique feature of HRPT should be the large radial mylar-Gd-O collimator suppressing Bragg peaks from the sample environment. A similar device has been successfully used on DMC [2].

Applications of HRPT will be high-resolution determination and refinement of chemical and magnetic structures including detection of structural defects such as stacking faults and internal strains. In particular measurements as a function of external parameters such as temperature will be possible on e. g. high-temperature superconducting materials (HTSC) and related systems, nickelates with metal-insulator transitions, other ceramics, ionic and proton conductors, zeolites, sodalites, metal deuterides and other hydrogen-bond systems, supramolecular and other magnetic compounds, intercalates, fullerenes and quasi crystals etc.. A particular feature should be real-time investigations of structural and magnetic phase transitions as well as the study of slow chemical reactions. Moreover phase analysis of novel materials, e.g. of composite systems and in situ investigations of hydrogen storage systems will become possible.

of the detector bank. It will be positioned with an accuracy of $\pm 0.001^\circ$ by means of air cushions moving on a granite floor of high-precision flatness, thus permitting to measure e. g. at well-defined intermediate positions.

The instrument is situated at a tangential beam tube for thermal neutrons of the target station of SINQ, as it will be important to reach small lattice spacings in case of high-resolution structural studies (large Q range). To obtain high resolution the large take-off angle of the monochromator $2\theta_M = 120^\circ$ as well as primary collimation of 6' may be used. On the other hand without primary collimator and with $2\theta_M = 90^\circ$ high-intensity modes of operation are possible. Corresponding calculated resolution functions are shown in figure 2. Further characteristics of HRPT are summarised in table II.

Because of the high energetic spallation neutrons a 'high energy shutter' system and a liquid nitrogen cooled Si filter are installed in the plug. Different primary collimations may be chosen by means of collimator drums in this plug. A massive prototype monochromator shielding should absorb unwanted radiation. The vertically focusing wafer type Ge monochromator [4] with mosaic spread $\approx 10' \div 15'$ will be 28 cm high, consisting of 11 slabs of 57 mm width, 25 mm height, 10 mm thickness and primary orientation (511).

Similar to D2B the horizontal slit system (α_2)

3. Properties and Applications of the Double-Axis Multi-Counter Powder Neutron Diffractometer DMCG at a Cold Neutron Guide

As the highest neutron flux will be attained at SINQ for cold neutrons, and as the background conditions should be best on a neutron guide, the successful PSD neutron diffractometer DMC [2] will be re-installed as DMCG (figure 3) at such a guide of SINQ coated with $m = 2$ supermirrors. Due to a flexible monochromator shielding this

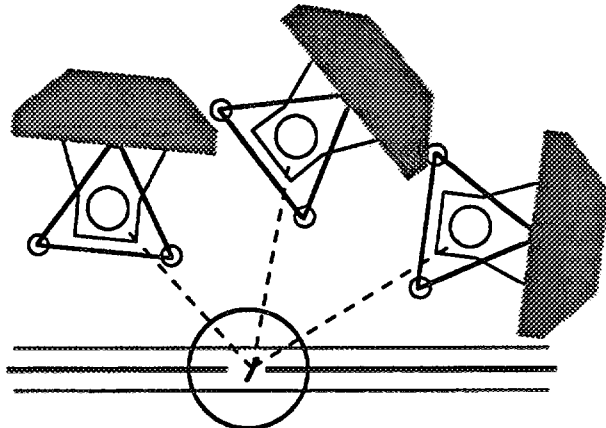


Fig. 3: Schematic view of the double-axis multi-counter powder diffractometer at a SINQ cold guide.

Table III: Characteristics of DMCG.

SINQ guide hall, cold neutron guide =1RNR12	
Optional primary collimation: mylar-Gd-O Soller collimator $\alpha_1 = 10'$	
Monochromators:	
Ge (hkk) or PG(C) (0 0 2), vertically focusing	
Ge (hkk)	ω_M^{100} [$^\circ$] λ [\AA] ($2\theta_M = 128.4^\circ$)
111	54.74 5.882
311	25.24 3.072
400	0.00 2.547*
511	15.79 1.961
PG002	$2\theta_M$ [$^\circ$] λ [\AA]
	40.8 2.338*
	77.5 4.200**
* PG(C) filter, ** Be filter	
PSD detector:	
BF ₃ (1 bar), 400 wires with 0.2° angular spacing	
Sample temperature: 7 mK \pm 2100 K	
zero matrix pressure cell	
Future option: Polarised neutrons	

instrument will provide either high-intensity (vertically focusing PG(C) monochromator and PG(C) filter for 2.5 \AA neutrons, Be filter for $\approx 4.2 \text{\AA}$ neutrons) or high-resolution options similar to D1A at ILL, Grenoble and at LLB, Saclay [5] (focusing Ge '(311)' monochromator, ≈ 2 and 2.5 \AA neutrons with large monochromator take-off angles, see table III). For highest resolution also the option of a primary mylar-Gd-O collimator ($\alpha_1 = 10'$) will exist. Without this collimator the primary collimation will be defined by total reflection from the guide, being proportional to the neutron wavelength λ with a factor of 24' (for $m = 2$, λ in \AA [5]). Corresponding calculated resolution functions are shown in figure 4. The best values are approximately a factor of four smaller than those of DMC at reactor Saphir with a monochromator take-off angle $2\theta_M = 60^\circ$. An interesting option will be the use of polarised neutrons to separate ferromagnetic and nuclear neutron intensities, e. g. to study undercooled ferromagnetic melts. Thus DMCG with 400 detectors (BF₃, angular separation 0.2°) is expected to become a versatile SINQ powder

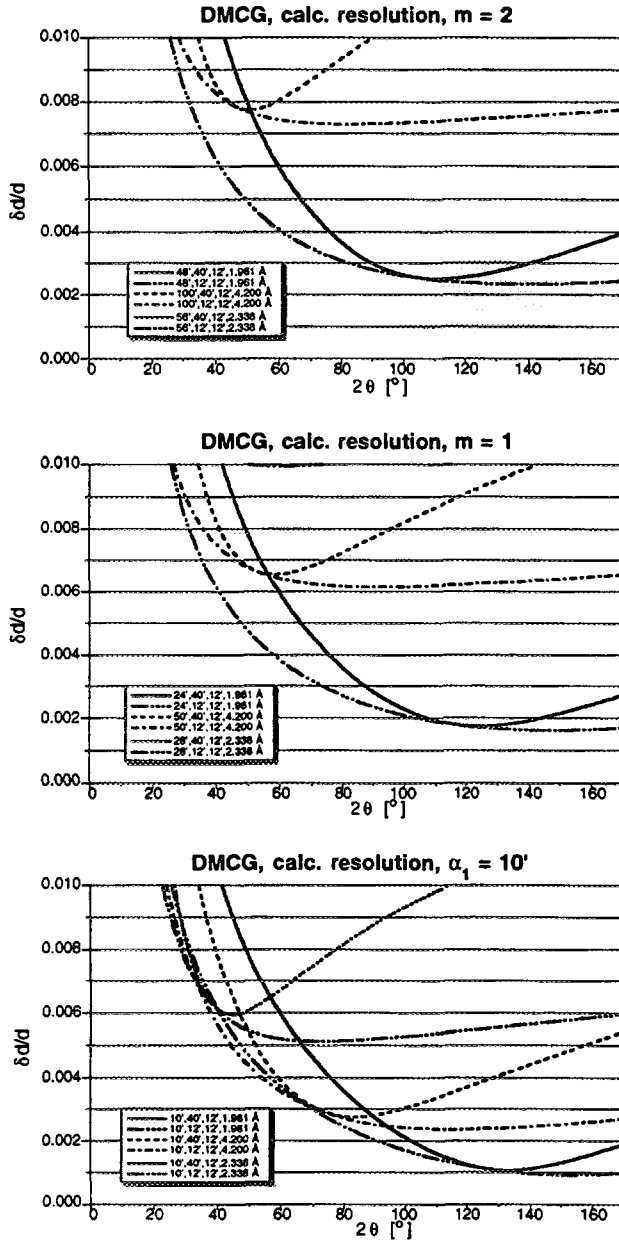


Fig. 4: Calculated resolution functions of DMCG.

diffractometer which will be to a large extent complementary to HRPT. Also in case of DMCG a well working radial collimator [2] will suppress Bragg peaks from the sample environment such as of dilution refrigerators, other cryostats and furnaces.

The applications of DMCG will focus on the investigation of magnetic ordering phenomena with high-intensity (2.5 Å neutrons) and high-resolution options, in particular very low temperature experiments. Thus the temperature dependencies of structural and magnetic phase transitions may be measured. Examples are e. g. antiferromagnetic rare-earth ordering in HTSC compounds and related materials, magnetic ordering in nickelates with metal-insulator transitions, in Kondo and heavy Fermion systems and in supramolecular magnets (with e. g. 4.5 Å neutrons because of large lattice parameters). Other possibilities of DMCG will be Bragg peak indexing in case of unknown chemical structures or analysis of complex magnetic ordering by means of well-resolved long-wavelength neutron diffraction patterns. Similar to DIA refinement of chemical structures as a function of temperature (with ≤ 2 Å neutrons) should be possible. Moreover one may perform in situ phase analysis, e. g. of hydrogen storage systems as well as real-time experiments of slow chemical reactions with 2.5 Å neutrons.

4. Acknowledgements

The realisation of the powder neutron diffractometers at SINQ including essential new components such as supermirrors (P. Böni et al.), the big monochromator shielding, focusing wafer type germanium monochromators (J. Schefer et al., mechanics by R. Thut [4]) is only possible due to a good team work of many members of LNS and of the workshop and electronics divisions of LNS and PSI (in particular department B8). Concerning HRPT initial financial support of M. Zolliker by Prof. K. Yvon, University of Geneva, the mechanical construction by M. Koch as well as electronics developments by N. Schlumpf should be particularly mentioned. The PSD He³ neutron detector is in production at CERCA, Romans, France (E. Berruyer et al.). The radial collimator based on a new design will be fabricated by J. Linderholm, JJ X-Ray, Risø, Denmark. Essential contributions to the installation of DMCG were also made by P. Keller and M. Koch et al. (monochromator shielding, mechanical adaptions). For test measurements and for valuable advice we are indebted to ILL, in particular to A. Oed, I. Anderson, A. Magerl and A. W. Hewat et al..

5. References

1. A. W. Hewat, *High Resolution Powder Diffraction* (Ed. C. R. A. Catlow), *Materials Science Forum, Volume 9* (Trans Tech Publ. Ltd., Switzerland, 1986) p. 69.
2. J. Schefer, P. Fischer, H. Heer, A. Isacson, M. Koch, and R. Thut, *Nucl. Instr. and Meth. A* **288** (1990) 477.
3. M. Popovici, W. B. Yelon, R. Berliner, A. D. Stoica, I. Ionita, and R. Law, *Nucl. Instr. and Meth. A* **338** (1994) 99.
4. J. Schefer, M. Medarde, S. Fischer, R. Thut, M. Koch, P. Fischer, U. Staub, M. Horisberger, G. Böttger, and A. Dönni, *Nucl. Instr. Meth. A* **372** (1996) 229.
5. J. Rodriguez-Carvajal, *PSI-Proceedings 93-01, ISSN 1019-6447* (Lecture Notes of the First Summer School on Neutron Scattering, Zuoz, 1993) p. 73.



THE NEW SINGLE CRYSTAL DIFFRACTOMETER SC3

J. SCHEFER, M. KOCH, P. KELLER, S. FISCHER AND R. THUT

Laboratory for Neutron Scattering ETH Zurich and Paul Scherrer Institute
CH-5232 Villigen PSI, Switzerland

ABSTRACT

Single crystal diffraction is a powerful method for the determination of precise structure parameters, superlattices, stress. Neutron single crystal diffraction gives additionally to X-rays information on magnetic structures, both commensurate and incommensurate, hydrogen positions, hydrogen bonding behavior and accurate bondlengths, e.g. important in cuprates. The method is therefore especially powerful if combined with X-ray diffraction results. The new instrument at SINQ has been designed for inorganic materials and is positioned at a thermal beam tube, pointing on an water scatterer. This scatterer is presently operating with H₂O at ambient temperature, but a change to another medium at different temperature is possible. The instrument will be equipped with three area detectors, moving at fixed difference in 2θ. Each detector may be individually moved around a vertical circle (tilting angle γ), allowing to use not only 4-circle geometry in the temperature range from 1.5 to 380K, but also any equipment from a dilution refrigerator (7 mK) to a heavy magnet. A high temperature furnace for 4-circle geometry is foreseen as a future option.

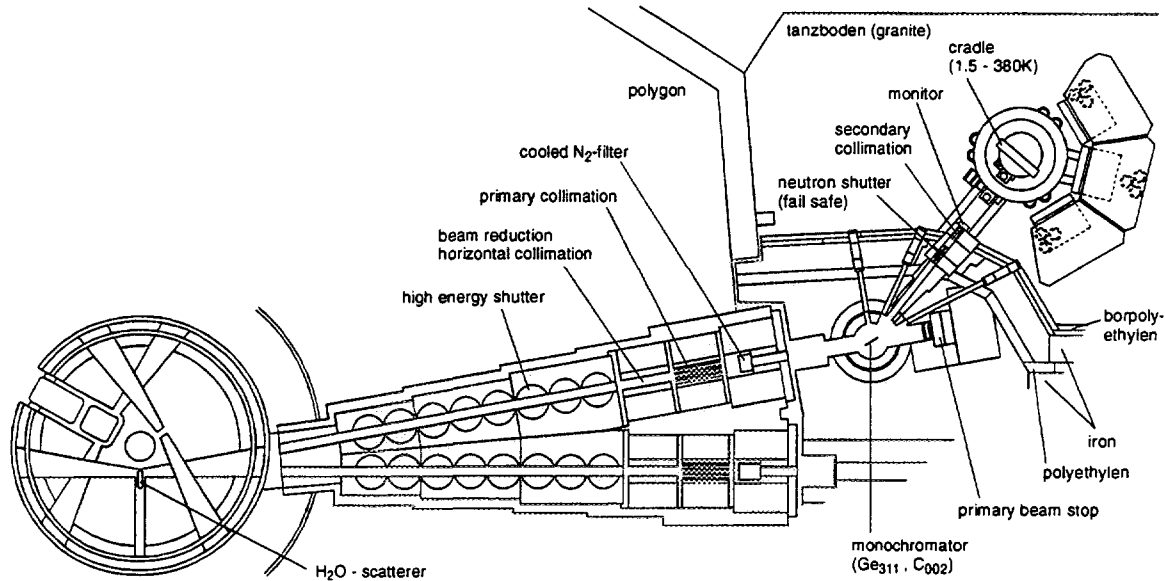
1. Introduction

An ideal four circle diffractometer can be defined by three points: Source, sample position and the detector, defining the diffraction plane normally to be horizontal for neutron diffraction. Four angles are used to position the sample: The angle ω, which is vertical rotation axis, the angle χ defined as the rotation around a perpendicular axis and the angle φ, perpendicular to the rotation axis of χ. The last angle used for four circle geometry is the detector angle 2θ. As this geometry is over determining the system, a fifth pseudo-angle ψ may be defined as the rotation angle around the scattering vector τ. ψ is defined to be zero if τ is measured in bisection mode. Therefore we can measure a reflection *hkl* at any desired ψ, which allows us to avoid shadowed regions, e.g. caused by the massive mechanics of the cradle and allows to perform Renninger-scans [1] to determine anisotropic extinction and absorption. However, if the cradle cannot support the weight of the sample environment or the equipment is not supposed to be tilted such as a very low temperature dilution cryostat, our spectrometer allows out-of-plane measurements by tilting the detectors (angle γ) individually out of plane instead of tilting τ into the plane by the help of the cradle.

The SC3 gives all the possibilities mentioned above. In addition it is equipped with three area detectors allowing the simultaneous measurement of 10 to 20 reflections, depending on both crystal symmetry and lattice spacing. This is particularly important for medium thermal neutron flux as the case of the continuos neutron source SINQ.

Fig. 1:

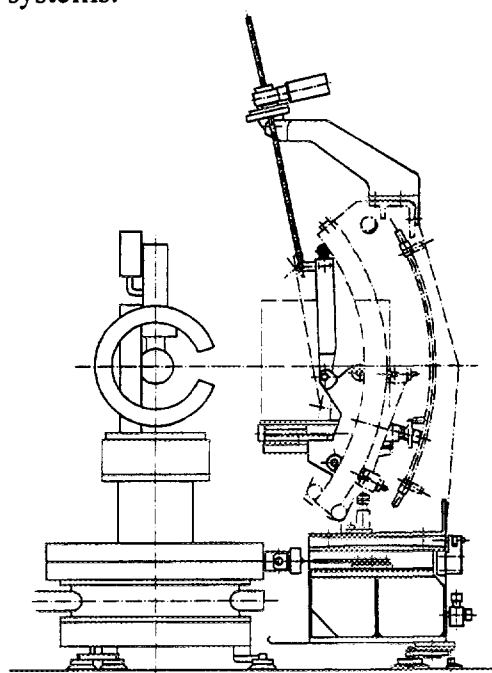
Geometry of the four-circle diffractometer showing the situation at beam port 41 pointing onto the H_2O scatterer presently installed in a T-shaped beam tube.



2. Why neutron single crystal diffraction?

Fig. 2:

Vertical cut through one of the detector systems.



As pointed out by the contribution of P. Fischer et al [2] on neutron powder diffraction, neutrons are a versatile tool especially due to the fact, that the neutron is a neutral particle, not interacting strongly with the sample. This avoids surface scattering, giving real information on the whole crystal. Another important fact is, that the scattering potential is located at the very small nucleus, which causes the form factor to be practically constant as a function of $\sin(\Theta)/\lambda$. This is expressed by the following two functions (e.g. [3]):

$$V(\mathbf{r}) = \frac{2\pi\hbar^2}{m} b \cdot \delta(\mathbf{r} - \mathbf{R})$$

$$\langle \mathbf{k}'|V|\mathbf{k} \rangle = \frac{m}{2\pi \cdot \hbar^2} \frac{2\pi \cdot \hbar^2}{m} b \int d\mathbf{r} \cdot \exp(-i\mathbf{k}'\cdot\mathbf{r}) \delta(\mathbf{r}) \exp(i\mathbf{k}\cdot\mathbf{r}) = b = \text{const},$$

where \mathbf{k} is the wave vector of the incoming beam, \mathbf{k}' the outgoing wave vector, \mathbf{R} the locations of the nucleus, V the scattering potential and b the nuclear scattering amplitude. Therefore, b shows no dependence on the momentum transfer. The absolute value of \mathbf{k} and \mathbf{k}' is identical as we are assuming elastic scattering. This is in contrast to X-rays, where the scattering occurs at the electron shells, forcing a fall-off of this value at high scattering angles as the scattering potential may not be described anymore as a δ -function located at the nucleus as done for neutrons. Neutrons yield therefore more accurate information on thermal motions. In addition the neutron has a magnetic moment. As neutron diffraction can be done on our instrument down to 7 mK, this opens a wide field of applications. The advantage of single crystal diffraction to powder diffraction is obvious: Reflections are separated in reciprocal space, allowing a much better and less model-based interpretation of the data.

3. Instrument Layout

The SC3 is built as a good resolution single crystal diffraction instrument, covering the most often asked area between D9 and D19 at ILL. The operating mode is close to D19, the resolution between D9 and D19.

3.1 Specialties of the SC3

The SC3 is equipped with three area detectors of extended size. This allows the simultaneous measurement of 10 to 20 reflections. The number strongly depends on symmetry (lower symmetry = more simultaneous reflections) and size of the unit cell (small unit cell = more simultaneous reflections). Therefore the longer the expected measurement time, the more the instrument compensates by simultaneous measurement of reflections on the detectors. This is essential, as SINQ yields a thermal flux of a medium size reactor, and SINQ is not equipped with a hot source. However, the resolution will limit this compensation to the point where reflections start to overlap.

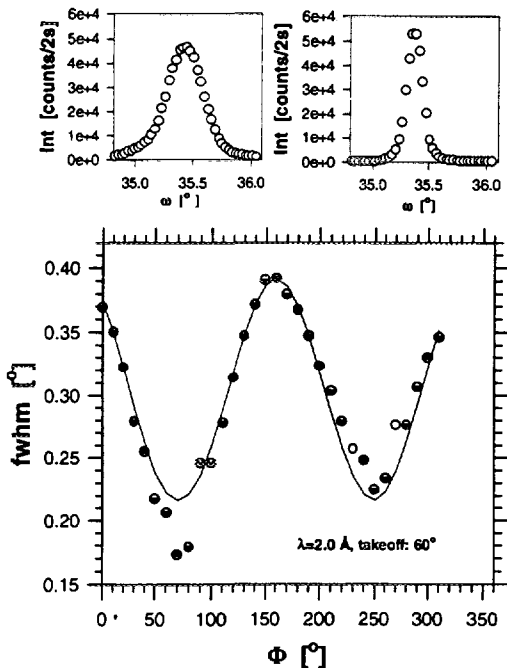
The second specialty is the tilting possibility, which allows to install almost any equipment on the instrument. However, by tilting the detectors one is leaving the horizontal scattering plane and therefore loses resolution [4]. The instrument has flexible supports for the detectors, allowing to follow expected future development of detectors.

3.2 The monochromator

A focusing composite germanium monochromator (figure 5) using the reflection 311 presently under completion [5] will be installed as the primary monochromator. Anisotropic mosaic (c.f. figure 4) is used to gain additional intensity without losing resolution. Firstly, we will use a take-off angle $2\Theta_M$ of 40.2° yielding a wavelength of $\lambda=1.15$ Å. The second monochromator mounted on the lift system is pyrolytic graphite $C_{\alpha\beta\gamma}$, giving access to $\lambda=2.3$ Å at high intensity/low resolution, ideal for many magnetic structure problems and also alignment of the crystals. The germanium $Ge_{\alpha\beta\gamma}$ monochromator has a width of 55 mm and a height of 115 mm.

Fig. 4:

Ge_{311} -wafer package No.3, consisting of 24 wafers after 6 bending cycles [6] all flattened with a ceramic plate and glued together using tin (measured at T13C, ILL Grenoble, M.Böhm). The figures show the highly anisotropic mosaic useful for diffraction.



Possible monochromator take-off-angles are 17.5° , $38.4 \pm 4.0^\circ$, 54.6° and 90° . This allows a limited adaptation to future developments of monochromators. A full flexibility has been abandoned due to a lack of experience for shielding high energy neutrons and as shielding calculations are limited in the accuracy. The massive inner part of the shielding is shown in figure 6. It is surrounded by polyethylene, additional steel and boropolyethylene as shown in figure 1.

Fig. 5:

Mechanical layout of the focusing monochromator including the tilting, transition and rotation axis.

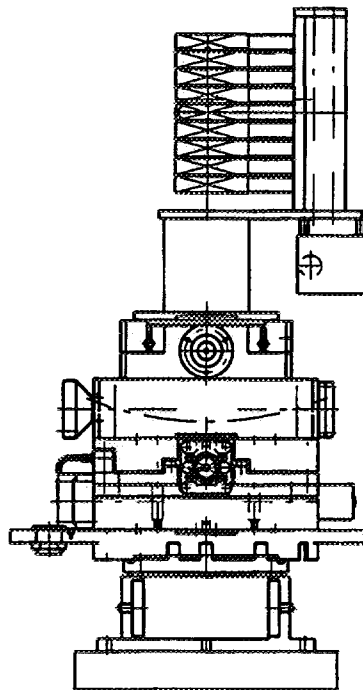
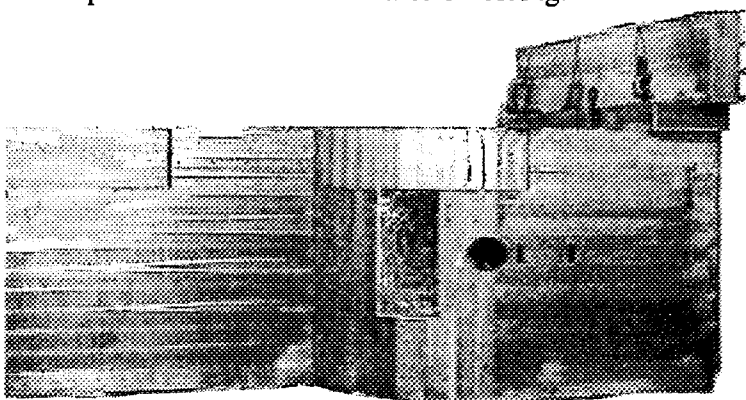


Fig. 6:

Inner part of the monochromator shielding.



3.3 The detector

We are presently mounting a two dimensional He³-gas detector [7] based on an extended microstrip plate, similar to the original design of Oed et al. [6]. The detector is using charge division with 2 readouts on front and back side and a energy readout on the front side. This electronic could be replaced in the future by a single-'wire'-readout system. Microstrip detectors are relatively simple in as the stripes are manufactured by photographic methods. Compared to present scintillation plates, gas detectors allow a single event read-out, allowing a better peak-to-background separation.

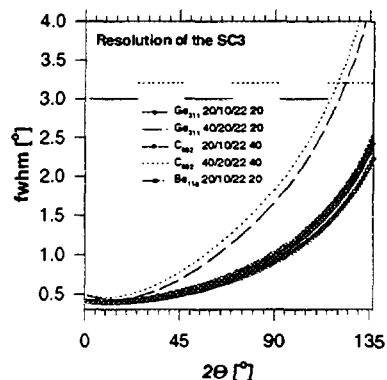
Table 1:

Parameters of the He³ based microstrip detector system used for the SC3.

detector size	203/203mm ² (8 by 8 ")	
glass type	Schott S 8900, 0.5 mm thick	
substrate	chromium	200nm, twice sputtered
active area	176/186	mm
anode thickness (front)	12	
number of anodes	190	μm
cathode thickness	500	μm
delay line thickness	40	μm
distance anode/anode	1000	μm
resolution	1.5-2	mm
R anode	≈14	kΩ
R cathode (energy)	40	μm
cathode width (back)	960	
number of cathodes	172	μm
gap	40	μm
resolution	2-2.5	mm
R cathode	≈13	kΩ
³ Helium (detection)	4.5	bar
CF ₄ (stopping gas)	1.5	pixels
readout:	256x256	max.
Voltage:	1.3-1.5	kV

Fig. 7:

Resolution of the SC3 using different monochromators and different collimations. Beryllium is presently not available. D1-D3 and D1'-D3' show two positions of the detectors covering the full 2θ-range.



4. Applications

The use of the SC3 is the determination of nuclear and magnetic structures of single and quasi crystals of size >5 mm³ with unit cells in the range of $\approx 15\text{-}20$ Å (depending the symmetry), investigations of structural and magnetic phase transitions, oxygen positions, hydrogen bonding and ordering, quasi-crystals, texture, pole figure-measurements, magnetic and nuclear superstructures, determination of unknown magnetic modulations. The temperature range available is 7 mK to 450 K in the beginning and could be extended up to 2000K. Above 1.5K we can use the Eulerian cradle, below 1.5K and with ‘strange’ auxiliary equipment, we have to use the (from the point of resolution) less favorable tilting mode.

5. Acknowledgments

The instrument has been realized by an extended collaboration inside and outside of our institute such as Dr. Thomas Vogt/ILL&BNL, Dr. A. Oed and P. Geltenbort/ILL, Dr. C. Wilkinson/EMBL, J.Allibon/ILL, Prof. G. Heger/Aachen&CENS and all not mentioned here personally. There help with numerous discussions is acknowledged here. We thank PSI and the University of Constance (BMFT) for their financial support. We thank also the different construction groups and workshops at PSI/LNS ETHZ&PSI for their excellent work. Specially I would like to thank Walter Bucher for the help in the beginning and H.Oschwald and Peter Keller in the realization phase and Mrs. I. Kusar for the graphics. The detector mechanics has been designed and manufactured by IRELEC, the monochromator shielding is designed by SUW Thun, and manufactured by VOEST, von Roll, Röchling and DELU.

6. References

1. R.M. Moon and C.G. Shull, *Acta Cryst.* **17** (1964) 805-812
2. P. Fischer et al., this summer school
3. S.W. Lowsey, *Theory of Neutron Scattering from Condensed Matter*, Vol. I, (Clarendon Press, Oxford, 1987) p.11
4. B. Schoenborn, J. Schefer and D.K. Schneider D.K., *Nucl.Instr. Methods* **A252** (1986) 180-187
5. J.Schefer et al., *Nuclear Instrument and Methods* **A372** (1996) 229-232
6. A. Oed ,P. Convert M. Berneron and H. Junk, *Nucl. Instr. Methods* **A284** (1989) 223-226
7. J. Schefer, M.Koch, A. Isacson, N. Schlumpf and R. Thut,in *Proceedings of the International Workshop on Microstrip Gas Chambers*, Lyon 1995, ed. D. Contardo and F. Sauli (Medcom Lyon, ISBN 2-9510204-0-6, 1995) 81-83



TRIPLE-AXIS SPECTROMETER DrüchaL

Willi Bührer and Peter Keller
Laboratory for Neutron Scattering
ETH Zürich & Paul Scherrer Institute
CH-5232 Villigen PSI, Switzerland

Abstract

DrüchaL is a triple-axis spectrometer located at a cold guide. The characteristics of guide and instrument allow the use of a broad spectral range of neutrons. The resolution in momentum and energy transfer ($\hbar\vec{Q}$, $\hbar\omega$) can be tuned to match the experimental requirements by using either collimators or focusing systems (monochromator, anti-trumpet, analyser).

1. Introduction

The triple-axis spectrometer DrüchaL ("Drü-achsigs am chalte Leiter", Swiss dialect for "triple-axis at cold guide") is a sister instrument of TASP [1]. Both spectrometers are identically constructed as far as possible, the main difference being the positions at the guide: DrüchaL is located in an intermediate position close to the source whereas TASP is in an end position.

The triple-axis spectrometer (TAS) was invented 40 years ago by Brockhouse [2], and the basic design has not been changed since then: the reason is that a TAS is the most versatile instrument for inelastic neutron scattering experiments on single crystals. From the experimentalist's viewpoint, it offers the unique possibility of measuring intensities at well-defined points in (\vec{Q}, ω) space, e.g. points of high symmetry in reciprocal space, where theory predicts an unusual behaviour, e.g. as function of temperature (structural transition), etc.. However one has to be aware that such a selective measurement might not make a very efficient use of all the scattered neutrons and that a TAS has a low data acquisition rate.

2. Fundamentals

Scattering process

The central quantity of interest is the scattering function $S(\vec{Q}, \omega)$:

$$\frac{d^2\sigma}{d\Omega dE'} = \frac{k}{k_0} S(\vec{Q}, \omega)$$

The basic task of the theorist is to calculate this quantity with the help of an appropriate microscopic model. The task of the experimenter is to extract this function from the experiment and to assess the precision of the data in the sense of statistics and resolution.

The 'instrument' is the 'technical vehicle' that allows the scientist to have experimental access to the cross-section.

Kinematic range

The vector sum $\bar{Q} = \bar{k} - \bar{k}'$ can be represented as a triangle ('scattering triangle')

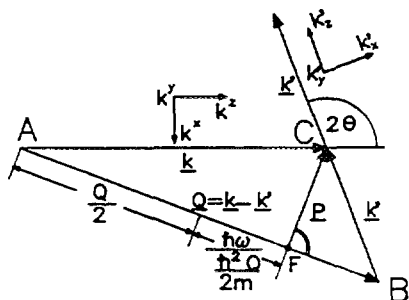


Figure 1:

The scattering triangle $\bar{Q} = \bar{k} - \bar{k}'$ for inelastic scattering with energy transfer $\hbar\omega$

In order to see what region in (\bar{Q}, ω) -space is accessible in an experiment at a given \bar{k} , we can plot the 3-dim loci of point B (Fig. 1) as a function of the co-ordinates Q_1 (parallel to \bar{k}), Q_2 (perpendicular to \bar{k}) and $\hbar\omega$. This results in the surface of a paraboloid with apex $(k, 0, E)$ whose locus is the dispersion relation for the free neutron $E = (\hbar^2 k^2 / 2m)$.

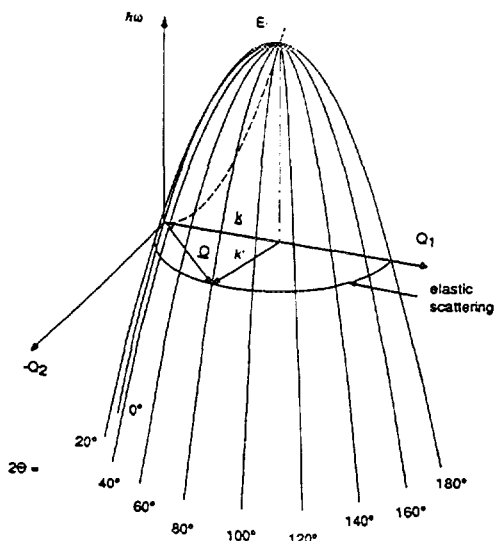


Figure 2:

The locus for all allowed \bar{Q}, ω -combinations in a neutron scattering process is a paraboloid with apex $(k, 0, E)$; parabolae are shown for different scattering angles 2θ

In order for scattering to be possible, the scattering law must intersect this paraboloid whose size depends on \vec{k} of the incident energy only.

The experimental determination of the scattering function $S(\vec{Q}, \omega)$ in the variables \vec{Q} and ω is therefore restricted by these kinematical limits (i.e. small \vec{Q} and large $\hbar\omega$ are not easily accessible).

Further restrictions are given by the mechanical construction of the instrument (monochromator and analyser 2θ -angles, scattering angle, shielding, etc.), by special sample environment (cryostat, furnace, pressure cell, etc.), and by neutron background problems (e.g. scattering at very small angles).

Resolution - Intensity

The goal of the measurement is to determine $S(\vec{Q}, \omega)$ with the maximum possible precision, and hence it would be desirable to have \vec{k} or \vec{k}' defined as precisely as possible. Apart from this being impossible due to the way in which available phase space operators work, this would also result in an almost complete loss of intensity and hence poor statistics. It is therefore necessary, to retain a finite, but optimised volume $\delta\vec{k}$ and $\delta\vec{k}'$ around \vec{k} and \vec{k}' , resulting in an uncertainty of the value of \vec{Q} , $\delta\vec{Q}$ and, of course, also of ω , $\delta\omega$.

Neutron scattering is a 'signal limited' technique, a consequence of both the low phase space density of neutron sources and of the weak interaction between neutrons and matter. Therefore it is generally not possible (although desirable) to measure cross-sections with best resolution in momentum transfer and energy transfer.

There are in principle several possibilities to improve the situation:

- i) increase the source flux: *restricted (power density, costs)*
- ii) increase the counting time: *limited (number of facilities)*
- iii) increase the sample size: *limited (new materials, absorption, etc.)*
- iv) decrease the resolution of the spectrometer:

"dedicated" spectrometers.

In other words, it is necessary to make a selection. But in order to do this, the cross-section has to be known (\vec{Q} -dependence, ω -dependence): one has to know which quantity can be 'relaxed', or over which quantity can (experimentally) be integrated.

However the physics to be investigated in the future is not known! The problem that arises in constructing a new spectrometer is that it must be dedicated and versatile, or in other words, one has to solve the problem of the 'squared circle'.

3. DrüchaL

The dedication of DrüchaL starts with the choice of the incoming energies to be used: **cold neutrons** got the priority. Because the spallation process produces very high energy neutrons, the primary shielding of the source is rather thick and therefore the use of **neutron guides** is mandatory. This has the advantage of a lower neutron background because the spectrometer can be placed away from the source. The drawback of a reduced intensity due to the good angular resolution (critical angle of total reflection) can be overcome by a **supermirror coating** with an m -value of ~ 2 [1].

The SINQ 'day 1' target will produce a moderate neutron flux, and therefore 'day 1' **monochromator** and **analyser** are equipped with **pyrolytic graphite** crystals. Options of **vertical focusing** and **horizontal focusing** on the monochromator and analyser respectively will give an enhanced neutron flux (at the expense of resolution). A further increase for small samples can be obtained by inserting a **converging guide** ('anti-trumpet') between monochromator and sample.

A vertical section through the instrument is shown in Fig. 3, the main components can easily be identified. The 'Tanzboden' is made of granite, with an (expected) better durability than marble. Air cushions, rotatory modules and length modules are commercial products. The monochromator shielding with blocks moving on a two-level system ('high' in the direction of the monochromatic beam, 'low' in order to pass below the guide) is completely mechanically controlled with a 2 stage lift-system (i.e. no pneumatic pistons, no electric switches). Goniometers for monochromator, sample and analyser alignments respectively are again standard products. The analyser shielding blocks are pneumatically lifted by a single piston (between analyser and detector). The neutron shielding is 'home-made', a mixture of polyurethane and boron carbide, poured in corresponding moulds. Only non-magnetic material has been used for all mechanical components near the neutron beam path in order to allow polarised neutron experiments.

The electronics (hardware) is PSI standard, the software is an upgraded version of MAD-TAS. Instrument control can be made either by a laptop near by the instrument, or from a cabin.

Planning and realisation of a new neutron source with appropriate instrumentation are tedious processes. Decisions have sometimes to be made at early stages without knowing all the future details. DrüchaL has been constructed with the premise 'not to loose any good neutron, and not to pick-up any bad neutron', and we expect that DrüchaL will satisfy the user's demands of the coming years.

[1] P. Böni and P. Keller, this Summer School

[2] B.N. Brockhouse and A.T. Stewart, Trans. Roy. Soc. Can. III, 50 (1956), and Rev. Mod. Phys. 30, 236 (1958)

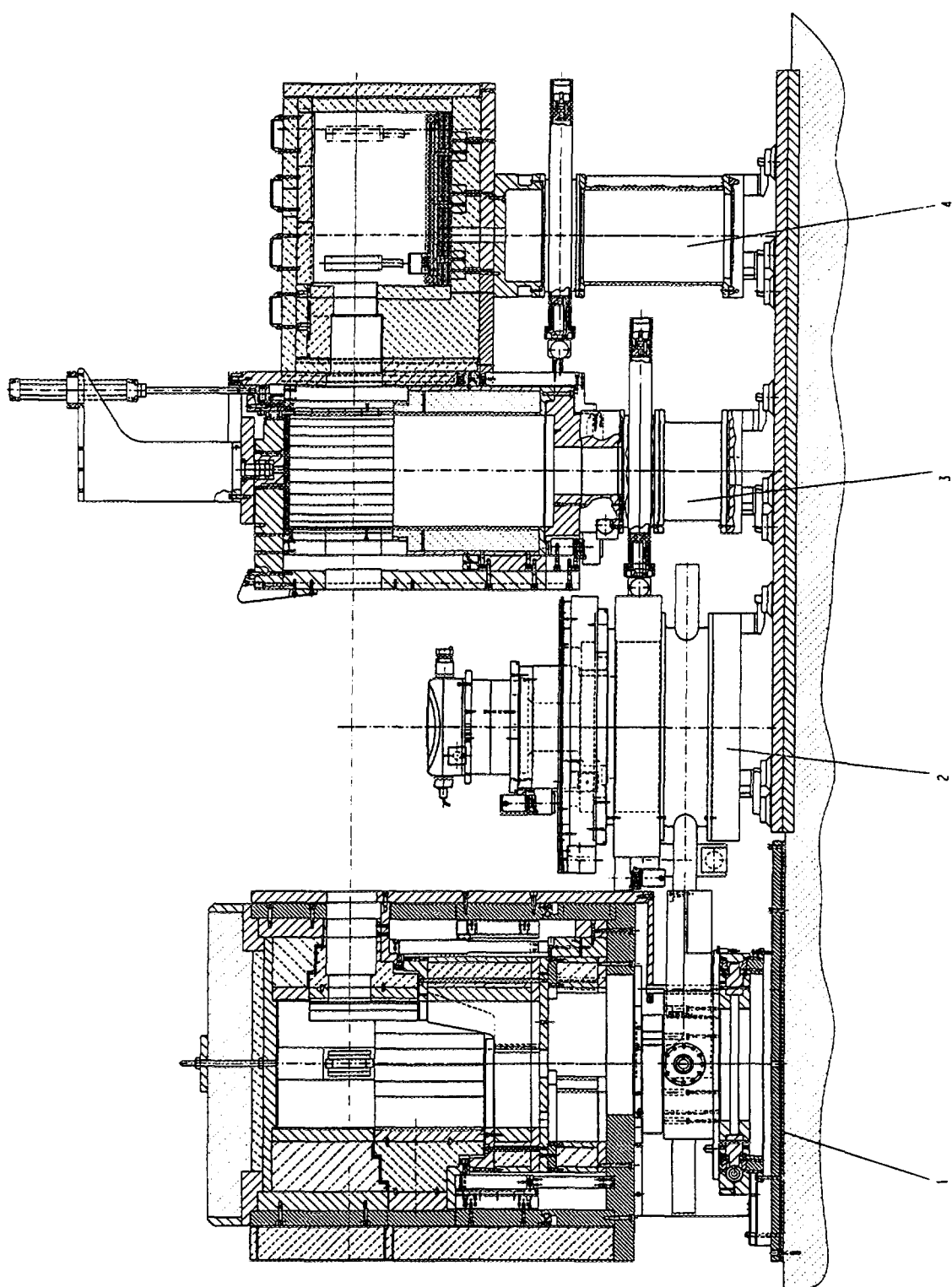


Figure 3: Vertical section through Drüchäl (for a horizontal view, see Fig. 2 in [1].)

Technical Specification of DrüchAL

Guide hall, neutron guide 1RN13 (30 x 120 mm), 37 m from the cold source

<i>monochromator</i>	scattering angle $29^\circ \leq 2\theta_M \leq 145^\circ$ PG (002) ($d=3.355 \text{ \AA}$), vertically focusing $2 \text{ meV} \leq E_M \leq 30 \text{ meV}$
<i>focusing anti-trumpet</i>	$L=1160 \text{ mm}$, supermirror $m \sim 4$
<i>sample</i>	scattering angle $-155^\circ < 2\theta_S < 155^\circ$ table: max. load 500 kg
<i>collimation</i>	α_0 (supermirror guide) = $120 / k_M (\text{min}/\text{\AA}^{-1})$ $\alpha_1, \alpha_2, \alpha_3 = 20', 40', 80'$, open
<i>analyser</i>	PG (002), option for horizontal focusing scattering angle $-145^\circ \leq 2\theta_A \leq 145^\circ$
<i>detectors</i>	2 monitors (incident and monochromatic beam, ^3He detector (50 mm \varnothing , 170 mm L))
<i>typical resolution</i>	$\Delta E \sim 0.01 \text{ meV}$ ($E_M = 2 \text{ meV}$) $\Delta E \sim 0.46 \text{ meV}$ ($E_M = 14.7 \text{ meV}$)
<i>lengths</i>	variable (monochromator-sample, sample-analyser, and analyser-detector)
<i>filters</i>	graphite (40 x 130 x 50 mm), beryllium (cooled, 40 x 130 x 170 mm)
<i>instrument responsible</i>	Willi Bührer

POLARIZED TRIPLE-AXIS SPECTROMETER TASP

PETER BÖNI AND PETER KELLER

*Laboratory for Neutron Scattering
 ETH-Zürich & Paul Scherrer Institute
 CH-5232 Villigen PSI, Switzerland*

ABSTRACT

The polarized triple-axis spectrometer TASP at SINQ has been optimized for measuring magnetic cross sections in condensed matter. The neutrons are polarized or analyzed either by means of benders or Heusler monochromators. The beam divergence, i.e. the intensity, and the spectral range of the neutrons is rather large because of the supermirror coatings of the feeding neutron guide. The intensity can be further increased at the sample position by means of a focussing monochromator and a focussing anti-trumpet. The end position of TASP allows the tailoring of the neutron beam already before the monochromator and to scatter neutrons over very wide ranges of angles.

1. Introduction

The Triple Axis Spectrometer for Polarized neutrons, TASP, is a sister instrument of Drüchal [1]. Both spectrometers are built in an almost identical way. The main difference being that TASP is located further away from the cold source and has the option of using polarized neutrons. Therefore TASP will be particularly useful for the investigation of magnetic scattering and/or the differentiation between coherent und incoherent scattering contributions, for example in hydrogen containing materials.

The triple-axis spectrometer was invented almost 40 years ago by Brockhouse and the basic design has not changed since then. The first and the third axis, i.e. monochromator and analyzer, define the energy of the incident and the scattered neutrons, E_i and E_f , respectively, and the second axis defines the orientation of the reciprocal lattice of the sample with respect to the scattering vector $\mathbf{Q} = \mathbf{k}_i - \mathbf{k}_f$ (Fig. 1). The energy transfer from the neutron to the sample is given by $E = E_i - E_f$, where $E_\alpha = (\hbar k_\alpha)^2 / 2m_n$. m_n is the mass of the neutron. A so called constant- \mathbf{Q} scan is performed by, for example, varying k_i , keeping k_f fixed, and by rotating the sample in such a way that \mathbf{Q} remains constant with respect to the reciprocal lattice. The measured intensity $I(E)$ is then directly proportional to the scattering function $S(\mathbf{Q}, \omega)$, i.e. the Fourier transform of the pair correlation function.

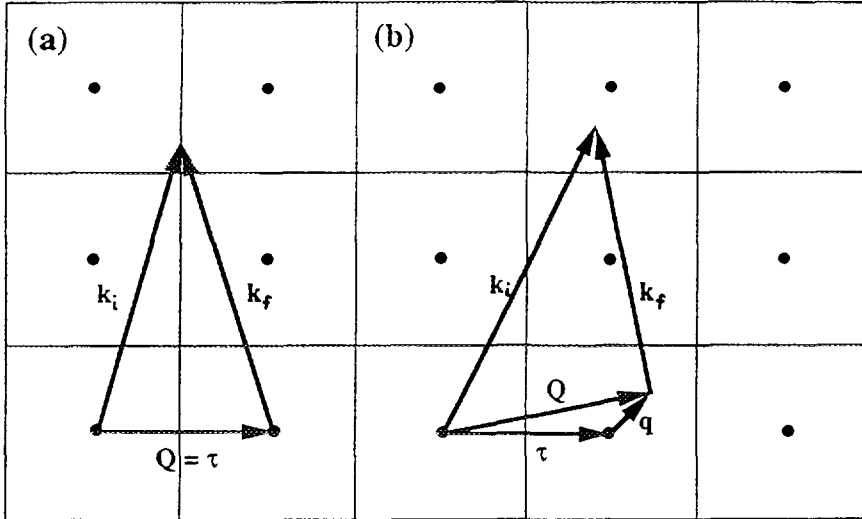


Fig. 1: Visualization of a quadratic lattice in reciprocal space for elastic (a) and inelastic (b) scattering. The lines indicate the Brillouin zone boundaries and the filled circles denote the zone centers.

In 1969, polarization analysis was introduced by Moon, Riste, and Koehler [2]. They polarized and analyzed the neutrons by means of appropriate, magnetized single crystals. Spin flippers before and after the sample were used to select the spin eigenstate of the neutrons (see Fig. 2). A measurement of the four different cross sections σ_{++} , σ_{-+} , σ_{+-} , and σ_{--} allows an almost unambiguous determination of the magnetic and nuclear scattering cross sections. For example, if \mathbf{Q} is chosen to be parallel to the polarization of the neutrons, then all magnetic scattering is spin flip scattering (Table 1). Moreover, the difference intensity $|I_{HF} - I_{VF}|$ for spin flip (or non spin flip) scattering is purely magnetic, i.e. even nuclear spin incoherent scattering and (constant) room background scattering cancel.

Table 1: Magnetic, σ_M , nuclear (coherent), σ_{nuc} , and nuclear spin incoherent, σ_{NSI} , cross sections for the polarization analysis setup. σ_{BG} designates the background.

field	spin flip scattering (-+)(+-)	non spin flip scattering (++)(--)
horizontal: $\mathbf{B}_h \parallel \mathbf{Q}$	$\sigma_M + \frac{2}{3}\sigma_{NSI} + \sigma_{BG}$	$\sigma_{nuc} + 0\sigma_M + \frac{1}{3}\sigma_{NSI} + \sigma_{BG}$
vertical: $\mathbf{B}_v \perp \mathbf{Q}$	$\frac{1}{2}\sigma_M + \frac{2}{3}\sigma_{NSI} + \sigma_{BG}$	$\sigma_{nuc} + \frac{1}{2}\sigma_M + \frac{1}{3}\sigma_{NSI} + \sigma_{BG}$
difference intensity	$\frac{1}{2}\sigma_M$	$\frac{1}{2}\sigma_M$

Presently, most (cold) triple-axis spectrometers occupy intermediate positions at cold neutron guides, thus the angular range of the scattering angles at all three axis are often restricted in such a way that the so called "W" configuration cannot be used [3], thus yielding a resolution function that has a rather complicated orientation in the 4-dimensional momentum-energy space. Moreover, the intensity of incident neutrons with E_i larger than 20 meV is low because of the small divergence of the

Ni coatings of the (bent) guides. Therefore neutron energy loss spectroscopy is restricted to small energy transfers.

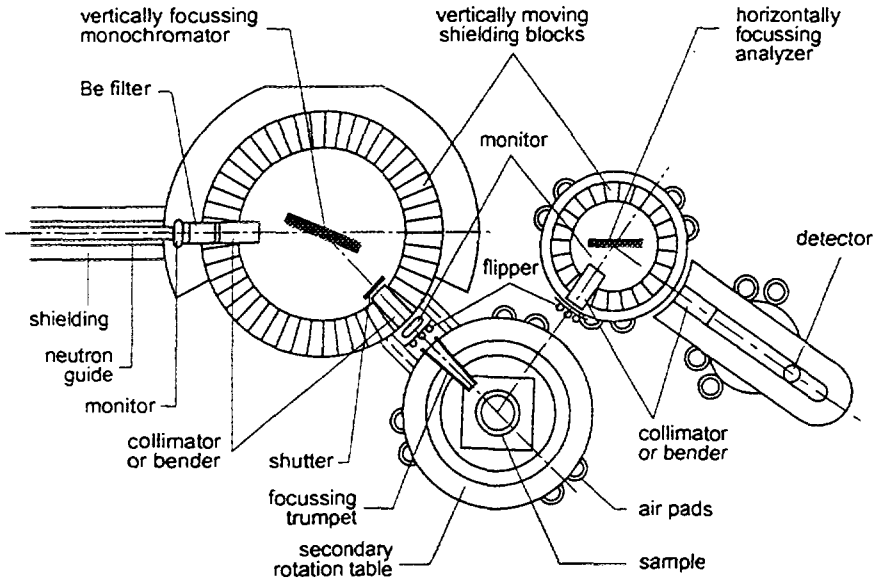


Fig. 2: Schematics of the polarized beam, triple-axis spectrometer TASP at SINQ. The instrument moves on air cushions.

Because all spectrometers at SINQ are fed by supermirror-coated neutron guides, the energy range of the incident neutrons is significantly enlarged (Fig. 3) [4]. In addition, the end position of TASP allows to insert filters and collimators before the monochromator and to use polarizing Heusler monochromators. Thus the dynamic range and the resolution conditions can be varied over a very wide range. In the following we describe some of the basic features of TASP. The technical specifications are given at the end of the paper. For details on the mechanical part see the contribution by W. Bührer [1].

2. Monochromator stage

The TASP monochromator stage occupies the end position of a 54 m long neutron guide that is fed by a D₂ cold source ($T = 28$ K). Due to the bending, γ and fast neutron background are significantly reduced. Moreover, the phase space and the polarization of the beam can be selected in the primary beam path without impeding the performance of any other instrument (Fig. 2). The flux at the monochromator is increased by more than a factor of three for neutrons with a wavelength of $\lambda \simeq 4$ Å, because of the supermirror coating of the neutron guide (Fig. 3). The increase of the divergence of the neutron beam allows measurements with reasonable flux even at $E_i = 30$ meV.

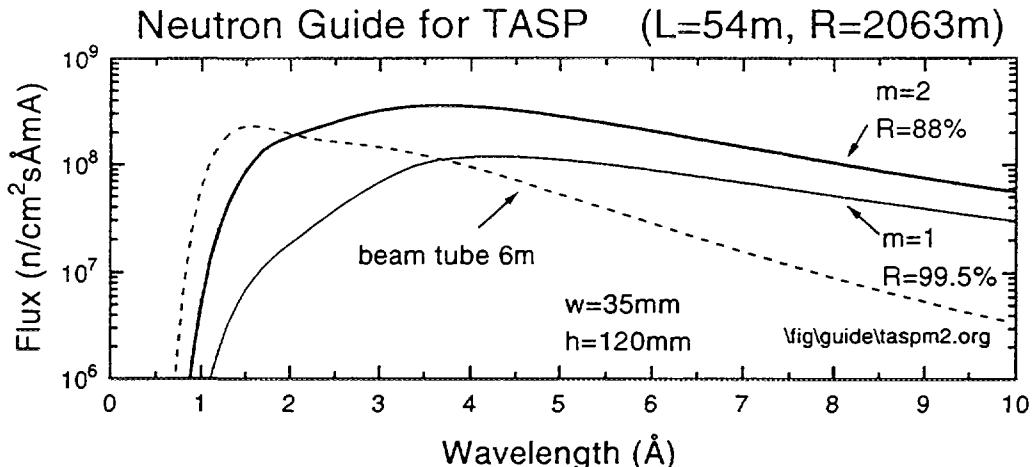


Fig. 3: Calculated neutron flux at the monochromator position of TASP. It is 54 m away from the cold source. Also shown is the flux for a "normal" neutron guide, coated with Ni ($m = 1$) and the flux at the end of a 6 m long beam tube.

The Be filter is located directly after the exit of the guide, i.e. within the monochromator shielding. The Be is therefore well shielded from the detector. A collimation stage before the monochromator allows to operate TASP under optimum conditions with respect to the conflicting requirements of resolution and intensity. The collimations can be varied between 5'-5'-5'-5' and open-focussing-open-open. A lift allows a choice between vertically focussing graphite or Heusler monochromators. Moreover, a (111) reflection of perfect Si can be used, because the graphite is mounted on Si single crystal with the (111) reflection in the scattering plane, 7° off the (00L) reflection of graphite. Fig. 4 shows the reflectivities of graphite (002) and of one of the best Heusler (111) monochromators measured with unpolarized neutrons. The peak intensity of Heusler is 28% of graphite. In a saturating magnetic field, the ratio increases to $\simeq 34\%$.

The monochromated beam leaves the shielding via a beam plug that contains either permanent magnets or electromagnets that provide a vertical magnetic guide field or a field for remanent supermirror benders that can be used as spin selecting devices. Then no flippers are necessary [5]. The plug can accommodate either a collimator, a bender, or a doubly focussing anti-trumpet. Clearly, a bender is only used in conjunction with a graphite monochromator. The range of monochromator scattering angles is $29^\circ < 2\theta_M < 145^\circ$.

The benders contain glass sheets that are coated with polarizing, remanent supermirror having more than three times the critical angle of bulk Ni ($m > 3$). For geometrical details see Table 2. The transmission of the two types of benders is plotted in Fig. 5. The inset shows a reflectivity profile of a glass sheet of the bender. The number of layers of the coating has been reduced from ideally 450 (see Ref. [5]) to 343 layers in order to achieve a higher production yield for the fabrication of supermirrors.

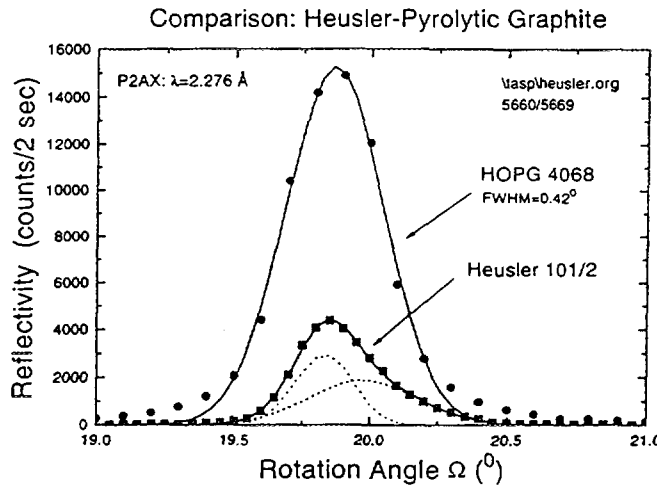


Fig. 4: Reflectivity of graphite (002) (circles) and Heusler (111) (squares). The solid and broken lines indicate Gaussian fits. The monochromator size is $25 \times 50 \text{ mm}^2$.

The bending geometry is such that the polarized neutrons leave the polarizer along the optical axis of the instrument. Therefore, the monochromator must be translated and rotated in such a way that the beam enters the bender properly. These corrections can easily be taken care of by the spectrometer program. Thus the change from unpolarized to polarized beam is trivial: It involves simply the exchange of the exit collimator by a polarizing bender. Moreover, because the bender is positioned inside the monochromator shielding there is little cross talk between external fields at the sample and the spin selecting device.

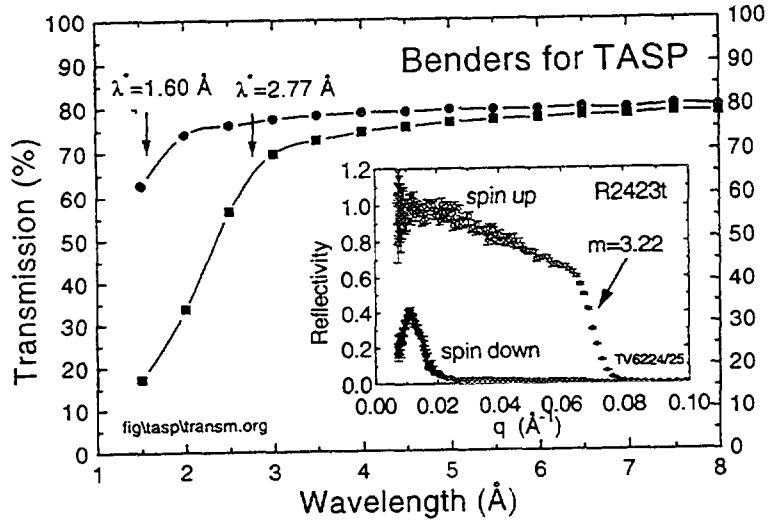


Fig. 5: Transmission of the short (squares) and long (circles) benders. The inset shows the reflectivity profile of an $m = 3$ supermirror.

The doubly focussing trumpet is 1160 mm long and contains supermirror coatings

with $m \simeq 4$. It reduces the horizontal beam size from initially 35 mm to 17.5 mm at the sample position (Fig. 6). The vertical focussing is provided by the monochromator and the vertical section of the trumpet. Experiments at ILL [6] and LLB [7] show that intensity gains $1.5 < G < 7$ can be obtained, depending on the sample geometry, the neutron wavelength and the requirements on the beam divergence.

Table 2: Parameters of the guide and the polarizing benders of TASP. λ^* is the critical wavelength of the bending section.

	neutron guide	short bender	long bender
length (mm)	54 000	290	580
radius of curvature (m)	2063	9.22	31.9
gap (mm)	35	0.95	1.10
m (units of θ_c^{Ni})	2	3	3
λ^* (\AA)	1.68	2.77	1.60
Al in the beam (mm)	> 0	3	6

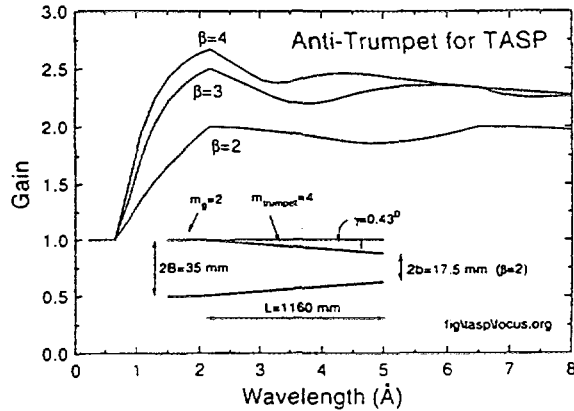


Fig. 6: Calculated flux gains [8] for the horizontally focussing trumpet with $R = 1$ at $m = 4$. β is the ratio B/b . The insert shows a schematics of the part that provides the horizontal focussing.

3. Sample Position

The sample table is equipped with two rotation stages. The primary one determines the orientation of the sample with respect to the incident beam. The second one has been foreseen for two purposes:

- Support for a horizontal field magnet, thus \mathbf{B}_h can always be kept parallel to the scattering vector \mathbf{Q} , even during inelastic measurements.

- Support for a microstrip detector, thus TASP can be used as a polarized single crystal diffractometer. This option is particularly interesting for investigating incommensurate magnets.

In addition, motorized linear tables for adjusting the sample in the ($x - y$)-plane and two goniometers for tilting the sample are provided.

4. Analyzer and Detector

The shielding of the analyzer housing is composed of shielding blocks that are operated by means of a single compressed air piston. The change between the different horizontally focussing analyzers, graphite and Heusler, is done manually. The inserts have similar dimensions as those in the monochromator shielding, therefore allowing a simple interchange between collimators and polarizing benders. In fact, polarization analysis is most conveniently done by inserting a bender before the detector because i) no corrections for the deviation of the beam have to be made and ii) the cross talk between fields at the sample position and the bender is minimized.

The ^3He detector has a diameter of 50 mm and a length of 170 mm. Therefore the "vertical focussing" is accomplished by integrating the neutron counts along the vertical dimension of the tube. The detector can be moved inside the detector shielding in order to provide the proper matching sample-analyzer and analyzer-detector distance.

5. Polarization Equipment

In addition to the polarizing and analyzing equipment described above, additional devices are needed to perform a polarized beam experiment. In order to define the quantisation axis for the polarized neutrons, permanent and/or electromagnetic guide fields between monochromator and sample and sample-analyzer-detector are provided. At the sample position Helmholtz coils ($\mathbf{B}_v^{\max} = 30 \text{ mT}$, and $\mathbf{B}_h^{\max} = 2 \text{ mT}$) produce a magnetic guide field that can be oriented in any arbitrary direction with respect to the sample without moving the coils. In particular, the angular access to the sample is larger than 180° , therefore there are no "dark spots" in the beam. This magnet is particularly useful for studying paramagnetic or spin-incoherent scattering.

In addition, for magnetic measurements below the ordering temperature, an asymmetric, superconducting magnet will be available that provides a horizontal field $\mathbf{B}_h = 2 \text{ T}$ and a vertical field $\mathbf{B}_v = 6 \text{ T}$. The opening angle of the large windows are 150° at the front side and 140° at the back side. The magnet is equipped with a room temperature bore having a diameter of 100 mm. Due to mechanical limitations it is not allowed to operate both fields together.

The polarization of the neutron beams can be changed before and after the sample by means of flat coil spin flippers if no (white beam) spin selective devices are used, thus allowing the measurement of four cross sections σ_{++} , σ_{-+} , σ_{+-} , and σ_{--} [2]. The horizontally wound flipper coil compensates the external guide field and the vertically wound coil (\rightarrow horizontal field) rotates the neutron spin by 180°.

6. Concluding Remarks

TASP is a modern, flexible and compact cold triple-axis spectrometer at the spallation source SINQ. It takes advantage of recent developments in neutron optics, in particular supermirror guides, focussing units as well as remanent spin selective devices. The goal is to provide a very user-friendly polarised beam environment for the investigation of spin dependent cross sections, in particular in the field of magnetism. Special attention has been paid to provide an adequate sample environment.

7. Acknowledgements

We are grateful to the technical and electronics personnel at LNS and PSI that made invaluable contributions for the spectrometers TASP and Drüchal. I thank I. S. Anderson for supplying the program for calculating the gains for a focussing trumpet.

References

- [1] W. Bührer, this summer school
- [2] R. Moon, T. Riste, and W. C. Koehler, *Phys. Rev.* **181** (1969) 920 .
- [3] Either the sample table, analyzer shielding, or the detector touch the shielding of the ongoing neutron guide.
- [4] The neutron energy $E(\text{meV})$ is related to the wavelength $\lambda(\text{\AA})$ by $E = 81.81/\lambda^2$.
- [5] P. Böni, J. Neutron Research, (1996) in print.
- [6] J. Mesot, W. Bührer, M. Zolliker, P. Böni, M. Koch, and P. Decarpentries, *Annual Progress Report 1995*, Laboratory for Neutron Scattering, 59 (1996).
- [7] I. N. Goncharenko, I. Mirebeau, P. Molina, and P. Böni, subm. to *Physica B*.
- [8] I. S. Anderson, *SPIE* **983**, 84 (1988).

Appendix: Technical Specifications of TASP

Monochromator scattering angle	$29^\circ < 2\theta_M < 145^\circ$
Analyzer scattering angle	$29^\circ < 2\theta_A < 145^\circ$
Neutron energy (PG 002)	$2 \text{ meV} < E_N < 30 \text{ meV}$
	$6.40 \text{ \AA} > \lambda > 1.65 \text{ \AA}$
	$0.98 \text{ \AA}^{-1} < k_N < 3.81 \text{ \AA}^{-1}$
Sample scattering angle	$ 2\theta_S < 150^\circ$
Monochromator size, graphite	$150 \times 125 \text{ mm}^2 (w \times h)$ ♠
Monochromator size, Heusler	$100 \times 125 \text{ mm}^2 (w \times h)$
Monochromator, perfect Si(111)	5 pc. $150 \times 25 \text{ mm}^2 (w \times h)$
Beam size at sample (approx.)	$20 \times 30 \text{ mm}^2 (w \times h)$
Monochromator drum diameter	$d = 1.15 \text{ m}$
Monochromator to sample distance	$1.18 \text{ m} < L_s < 2.93 \text{ m}$
Sample to analyzer distance	$0.82 \text{ m} < L_a < 1.43 \text{ m}$
Analyzer to detector	$0.74 \text{ m} < L_d < 2.55 \text{ m}$
Inpile collimation	$5', 10', 20', 40', 80', \text{open}$
External collimation	$5', 10', 20', 40', 80', \text{open}$
Polarizing benders	$\lambda^* = 1.60 \text{ \AA} \text{ or } \lambda^* = 2.77 \text{ \AA}$
Focussing anti-trumpet	$l = 1160 \text{ mm, supermirror } m \simeq 4$
Detector	${}^3\text{He}$ ($d = 50 \text{ mm, } l = 170 \text{ mm}$)
Typical spectrometer res.	$\Delta E = 7 \mu\text{eV}$ ($E_N \simeq 2 \text{ meV}$)
(for $20'-20'-20'-20'-20'$)	$\Delta E = 0.46 \text{ meV}$ ($E_N = 14.7 \text{ meV}$)
(Vanadium width)	$\Delta E = 1.71 \text{ meV}$ ($E_N = 30 \text{ meV}$)
pyrolytic graphite filter	$40 \times 130 \times 50 \text{ (w} \times \text{h} \times \text{l)}$
cooled Be-filter	$40 \times 130 \times 170$, before monochromator
Magnetic fields	2 T horizontal, 6 T vertical
Temperature	$5 \text{ mK} < T < 2000 \text{ K}$

♠ w : width, h : height, d : diameter, l : length

**FOCUS: TIME-OF-FLIGHT SPECTROMETER
FOR COLD NEUTRONS AT SINQ**

STEFAN JANSSEN^{1,2}, JOEL MESOT¹

¹*Laboratory for Neutron Scattering
ETH Zürich & Paul Scherrer Institute
CH-5232 Villigen PSI, Switzerland*

ROLF HEMPELMANN²

²*Physical Chemistry, University of Saarbrücken
Im Stadtwald - Bldg. 9.2
D-66123 Saarbrücken, Germany*

ABSTRACT

The physical layout of the Time-Of-Flight spectrometer at the new spallation source SINQ is presented. The concept shows up a hybrid-TOF combining a Fermi-chopper with a crystal monochromator. The demand of a versatile and flexible instrument for several applications is taken into account by the option of switching from time-focusing to monochromatic focusing mode such that the spectrometer can be optimised for both quasielastic and inelastic scattering applications.

1. Introduction

Neutron Time-of-Flight (TOF) spectroscopy is a powerful tool for the study of several dynamic processes, e.g. diffusion, molecular spectroscopy, glass transitions, polymer dynamics, or magnetic excitations. Differently from a triple-axis spectrometer a TOF-experiment simultaneously detects several points in the (Q, ω) -phase space by a time resolved neutron detection within a large solid angle by the use of typically several hundreds of detectors. The TOF-spectroscopy uses the correlation between the wavelength λ of the neutron and its velocity v that reads

$$\lambda = h/mv \Rightarrow \lambda [\text{\AA}] = 3956 \text{\AA} \text{ms}^{-1} / v [\text{ms}^{-1}] \quad (1)$$

Typical neutron velocities used in a scattering experiment range from 200 - 3000 m/s. Therefore the flight times for experimentally relevant distances of several meters are in the order of milliseconds being conveniently accessible. By measuring the time the neutrons need to pass a known distance one can calculate the wavelength that directly yields the energy E . Thus in a TOF-experiment a facility is needed to give an electronic signal starting the clock that counts the neutrons' necessary time to the detectors. This time marker chops up (therefore called chopper) the beam into several bunches by opening and closing in defined intervals. Thus usually more than 98% of the beam is lost due to the closed chopper. The loss in intensity might be compensated in a TOF-experiment by the simultaneous detection of various points in the (Q, ω) -space.

2. General Principles

2.1 Direct and Inverted TOF-Geometry

TOF-experiments can either have direct or inverted geometry. Direct geometry means that the sample is illuminated by a monochromatic neutron beam. After the scattering process the final energies E' of the detected neutrons are calculated from the flight time they need to pass the known distance from the sample to the detectors. From the known incident neutron energy E one is able to calculate the energy transfer $\hbar\omega$ at the sample, the quantity one is essentially interested in. Inverted TOF-spectrometers operate in the opposite way. Here a polychromatic neutron beam hits the sample. After the scattering process crystal analysers reflect only neutrons with a certain final energy E' into the detectors. From the measured time of flight one is able to calculate the initial energy E and thus again the energy transfer. Figure 1 shows up the respective space-time diagrams for both geometries.

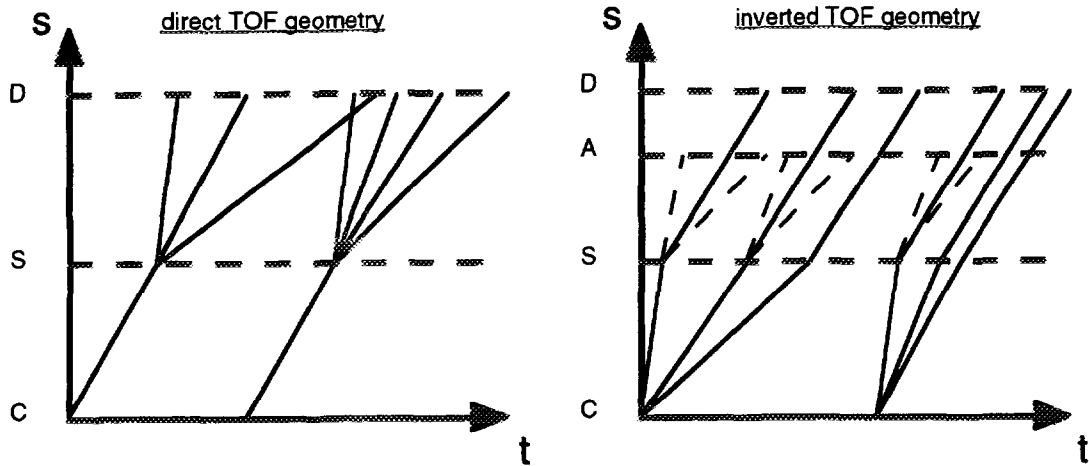


Fig. 1: Space-time diagrams of direct (left) and inverted (right) TOF-techniques with the components chopper (C), sample (S), analyser (A), and detectors (D). For the inverted geometry the neutrons following the flight paths indicated with dashed lines hit the analyser but are not transported to the detectors.

The main advantage of the inverted TOF-method compared to a direct geometry crystal monochromator (Hybrid-) TOF such as FOCUS (see next section) is the fixed geometry for every experiment. On the other hand direct geometry experiments usually provide lower background signals due to the fact that only a monochromatic and not a white beam illuminates the sample. In the following we will focus on direct TOF-geometry only.

2.2 Chopper and Hybrid TOF

There are two different philosophies of monochromatizing the beam for a direct geometry TOF-experiment. The first method uses two or more choppers (usually disc-choppers) separated from each other. The frequency determines the repetition rate of the pulses, whereas the phase shift yields the initial energy.

Figure 2 presents a four-disc chopper system as it is used on the IN5 spectrometer at the ILL [1]. Basically the pulse production and the monochromatization works with only two disc-choppers. As one can see from the left part of Figure 1, it might happen that the fast neutrons of a later pulse overtake the slow neutrons from the preceding one (frame overlap). Therefore one uses a third chopper rotating with a lower frequency to enlarge the temporal distance between the pulses. The fourth chopper is then used to suppress neutrons that travel with integer multiples or $1/2$, $1/3$, $1/4$, etc. of the desired velocity that would pass a two-or three chopper system.

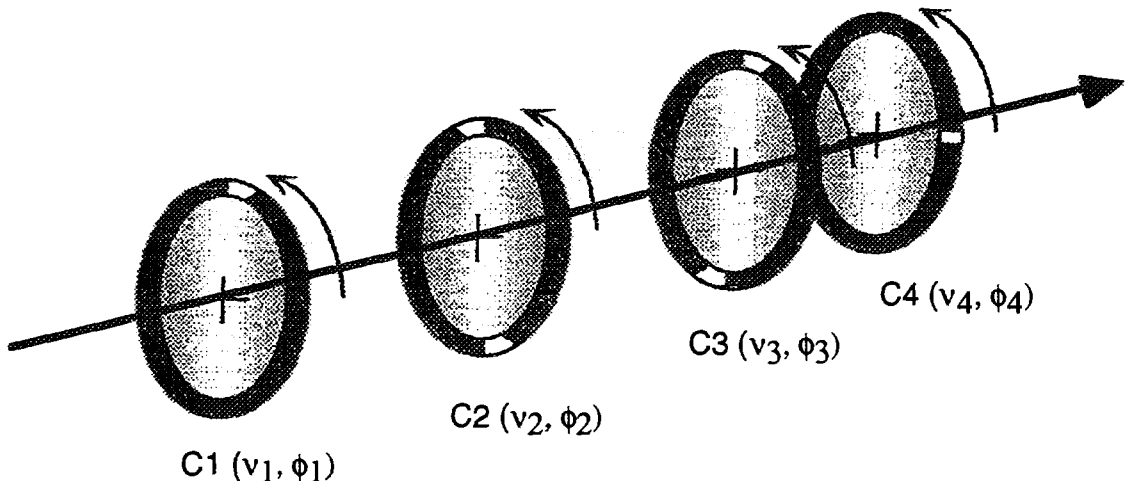


Fig.2: Chopper system consisting of four disc-choppers as it is used e.g. on IN5. C1 and C4 determine wavelength and pulse width. C2 suppresses unwanted harmonics and C3 works as anti-overlap chopper rotating with a lower frequency. v and ϕ denote the chopper frequency and phase angle, respectively.

The other possibility to monochromatize and pulse a neutron beam is the use of a crystal monochromator in combination with a Fermi-chopper (hybrid solution). A Fermi-chopper is a rotating collimator of typically a few degrees collimation. A second chopper (either Fermi or disc) serves as anti-overlap chopper. The obtainable energy resolution for a certain initial energy is not that narrow and ideal shaped as for a multi-chopper TOF, but the large intensity on the sample in case of using a focusing monochromator combined with the flexibility of the instrument provides the possibility to investigate a broad spectrum of applications. The prototype for this kind of TOF-spectrometers is the time-focusing IN6 at the ILL [2,3].

For the first years FOCUS will be the only TOF-spectrometer at SINQ. Therefore it exists the essential demand to have a versatile instrument to be suited for a lot of different applications. Thus the physical concept foresees a hybrid-TOF with two interchangeable monochromators (pyrolytic graphite and MICA) that cover continuously a range of initial energies from $0.27\text{meV} < E < 20\text{meV}$ [4-6]. The demand of being highly flexible is answered by the option to operate either in time- or monochromatic focusing mode (see section 5). FOCUS will be located at the end of a curved neutron guide viewing the cold D₂ source.

3. Layout of the Spectrometer

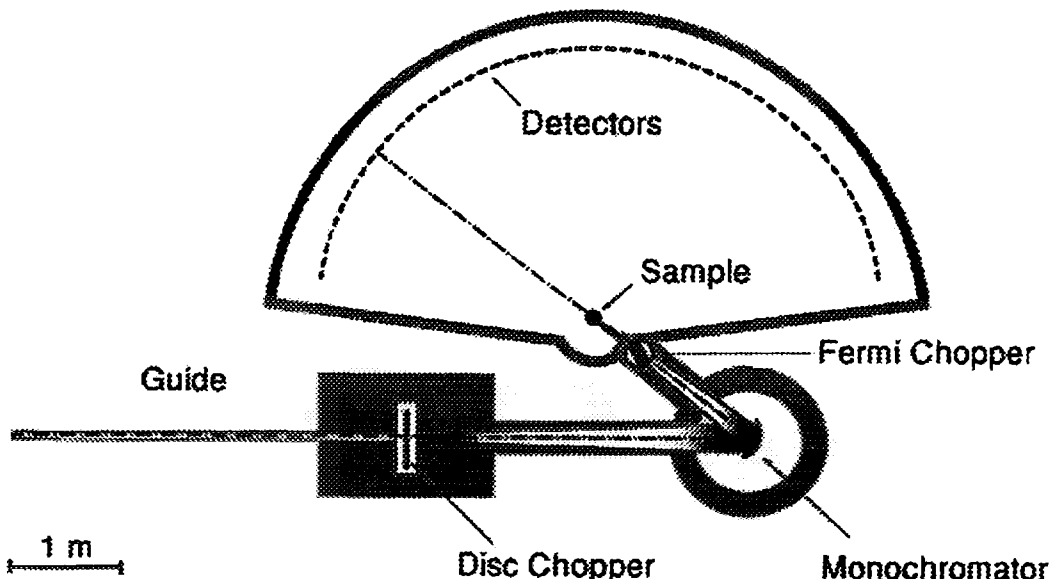


Fig. 3: Horizontal cut through the SINQ-TOF FOCUS. The sample-detector distance amounts 2.5m.

In Figure 3 a schematic horizontal cut through the spectrometer and its main components is given. A vertically converging neutron guide reduces the beam size from 12 x 5 cm² to 10 x 5 cm² (vert. x hor.). At the end of this guide a disc-chopper is located that acts as anti-overlap chopper. At a distance of 3m from the end of the guide the crystal monochromator is located. By means of variable curvatures it focuses the beam as well horizontally as vertically on the sample. The principles of the focusing device have been described elsewhere in detail [7]. The standard monochromator will be a pyrolythic graphite one giving access to the initial wavelength range from $\sim 1.5\text{\AA} < \lambda < 6\text{\AA}$. The lower limit is given by the spectrum provided from the cold source and is based on a Monte Carlo simulation [8]. Depending on the flux measurements for the high wavelength tail of the initial white spectrum it is foreseen to equip the spectrometer with a complementary second monochromator (MICA, d-spacing $\sim 10\text{\AA}$) interchangeable with the first one. Such access is provided to wavelengths ranging from $6\text{\AA} < \lambda < 17\text{\AA}$. For initial wavelengths above 4\AA a cooled Be-filter can be inserted into the beam to remove unwanted higher order reflections.

The main TOF-chopper is a Fermi-chopper with a collimation angle β of 2.4° for the day-1 operation. Later it is envisaged to have two or three interchangeable rotors with different Fermi-packages such that one can vary the Fermi-chopper collimation. As will be seen below intensity and energy resolution are strongly dependent on β . The Fermi-chopper is located behind the monochromator at a distance of 0.5m from the sample. After the scattering process the neutrons pass a 2.5m ⁴He-filled flight box in front of the detectors to reduce background. On day-1 FOCUS will be provided with one bank made of 200 ³He-counter tubes with rectangular cross section (3 x 1.2 x 40 cm³ (w x d x h), 6 bar He-pressure). Space is reserved for two additional detector banks such that FOCUS can be equipped with 600 detectors in its final version.

As has been mentioned above the spectrometer can be operated either in time- or monochromatic focusing mode. This is achieved by a variable distance between monochromator and sample (1.5m and 3.0m) as well as by inserting an additional neutron guide in between the end of the converging guide and the monochromator. Such the position of the neutron source is shifted with respect to the monochromator that changes the neutron optical conditions. Table I collects the relevant spectrometer parameters.

Table I: Physical parameters of the FOCUS-components:

Component		Dimension	
guide	horizontal	5 cm	
	vertical	12 cm	
	converg. guide vertical	12 cm → 10 cm	
end of guide -> disc-chopper end of guide -> monochromator monochromator -> Fermi-chopper Fermi-chopper -> sample sample -> detectors		0.2 m	
		1.5 m and 3 m	
		1.5 m and 3 m	
		0.5 m	
		2.5 m	
monochromator	horizontal	18 cm	
	vertical	18 cm	
	mosaicity (PG)	(0.8±0.1)°	
	Take-Off Angle	35° < 2θ < 130°	
	initial energy (total accessible range)	0.25 meV < E < 20 meV	
chopper: Fermi: Disc:	frequency	≤ 20000 rpm	
	window	6 cm	
		10 cm	
	collimation	(1-3)°, day-1 operation: 2.3°	
	diameter	70 cm	
	frequency	≤ 10000 rpm	
	windows (2)	9.2 cm (outside), 8.0 cm (inside)	
		10 cm	

4. Doubly Focusing Monochromator

The crystal monochromator used on FOCUS will be curved both horizontally and vertically. The ideal focusing monochromator surface is approximated by small rectangular crystal pieces forming a polygon surface [9]. It is interesting to consider the local divergencies α_o and α_i per crystal piece as they are given in Figure 4. The contribution of a flat monochromator piece to the energy resolution is given by:

$$(d\lambda/\lambda)_{loc} = \cot(\theta)d\theta \quad (2)$$

$d\theta$ is the uncertainty of the Bragg angle. For a single crystal piece with mosaicity η it is related to the local divergencies per crystal piece by [10,11]:

$$d\theta = \sqrt{\frac{\alpha_o^2 \eta^2 + \alpha_i^2 \eta^2 + \alpha_o^2 \alpha_i^2}{\alpha_o^2 + \alpha_i^2 + 4\eta^2}} \quad (3)$$

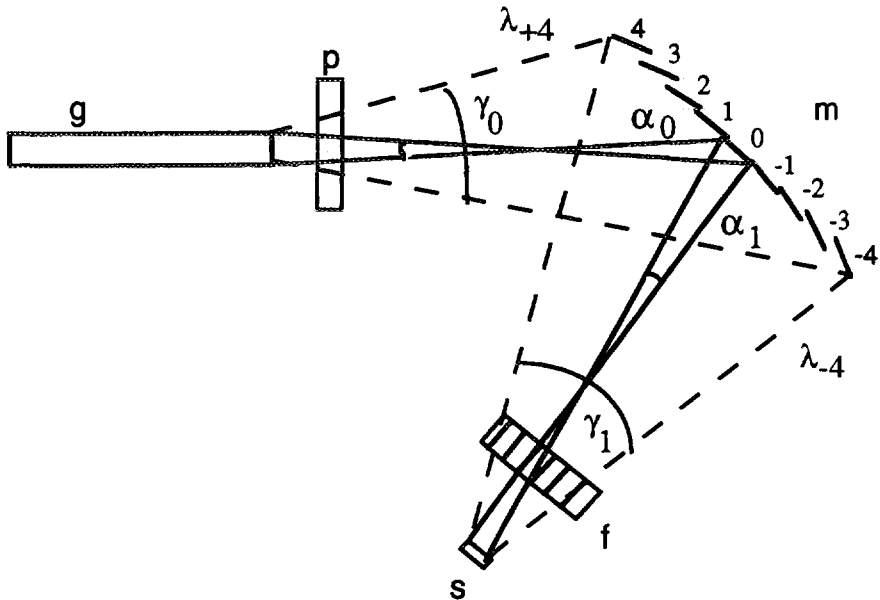


Fig. 4: Horizontal cut through the spectrometer components. g denotes the guide, p the anti-overlap chopper, m the monochromator, f the Fermi-chopper, and s the sample. Relevant for the energy resolution are the local divergencies α and not the total beam divergencies γ . Indices '0' and '1' denote before and after Bragg reflection at the monochromator, respectively.

Due to the enlarged total beam divergence emerging from the SINQ supermirror guide system it is advantageous to enlarge the distance guide-monochromator so that the local divergencies become minimised. For the FOCUS geometry with $\eta = 0.8^\circ$ and α , being below 1° one gains approximately a factor 2 in $d\theta$ by moving the monochromator from the direct end of the guide to a distance of 3m. Of course, an increase of the distance guide-monochromator causes an increase of the monochromator's dimensions. By focusing the beam horizontally and vertically it is then possible to gain the mentioned better resolution without loss in intensity.

The basic principles of focusing crystal monochromators are well known, see e.g. [10,12-14]. Focusing in real space always has the intention to increase the flux, whereas focusing in \mathbf{k} -space for a TOF-experiment strongly affects the energy resolution. Vertical focusing (perpendicular to the Bragg plane) has been used at several neutron scattering instruments. Horizontal focusing (within the Bragg plane) applications are more rare [15]. The first TOF-spectrometer using both horizontal and vertical focusing setup of the monochromator was the IN6 at the ILL [2,3], a hybrid-TOF on a cold guide.

The vertical and horizontal radii of curvature for focusing the beam are given by [14]:

$$R_v = 2f \sin(\theta) \quad \text{and} \quad R_h = 2f / \sin(\theta) \quad (4)$$

with the the focal distance f . Focusing in the vertical direction is easily achieved due to the large beam height. There is no effect on the monochromatic properties by vertical focusing because it takes place perpendicular to the scattering plane. Contrary, horizontal focusing within the scattering plane additionally images in \mathbf{k} -space (i.e. focusing of $|\mathbf{k}|$) as will be discussed in the next chapter.

5. Time- and Monochromatic Focusing

A curved monochromator delivers a wavelength band approximately given by [15]:

$$(d\lambda/\lambda)_{tot} = 0.5 \cdot \cot(\theta) |\gamma_i - \gamma_o| \quad (6)$$

Here the total beam divergencies γ are important and thus eq. 6 yields the total wavelength uncertainty of the monochromator. There are two possibilities to reduce the influence of this effect on the energy resolution.

5.1 Time-Focusing

The principle of time-focusing takes into account the fact that the neutrons emerging from different sites of the monochromator have slightly different wavelengths with $(d\lambda/\lambda)_{tot}$ being at most 5% over the entire FOCUS monochromator. Now the Fermi-chopper scans the monochromator in such a way that it allows the 'slow' neutrons of each pulse to pass earlier than the 'fast' ones. Neutrons having a wavelength distribution around a certain λ_o then simultaneously arrive at the detectors within a sharp pulse. For a certain initial and final wavelength λ and λ' , respectively, one obtains the following focal condition for the Fermi-chopper frequency v [15]:

$$v = \left(\left(1 - \frac{\overline{MS}}{\overline{GM}} \right) \left(\overline{CS} + \overline{SD} (\lambda'/\lambda)^3 \right) \cdot \pi \cdot C \cdot \lambda \cdot \cot \theta \right)^{-1} \quad (5)$$

with $C = 252.78 \mu\text{s}/\text{\AA}/\text{m}$ and the respective distances between the components, e.g. \overline{MS} : monochromator-sample (G: guide, C: Fermi-chopper, D: detectors). The time-focusing mode is well suited for applications which are interested either in a single inelastic excitation at a certain energy transfer or for quasielastic scattering (around energy transfer $\hbar\omega = 0$), because the energy resolution gets rather poor out of the focal condition. If one is interested in a good resolution over a wide range of energy transfers it is advantageous to focus monochromatically.

5.2 Monochromatic-Focusing

For equal distances \overline{GM} and \overline{MS} one has no wavelength distribution besides the one arising from the local divergencies α . This is the case of a triple-axis spectrometer. For the use on FOCUS this configuration is very attractive since it provides a high flexibility. Due to the two envisaged monochromatic configurations $\overline{GM} = \overline{MS} = 3.0\text{m}$ or 1.5m one can choose between high resolution and high intensity mode, respectively. To obtain the best possible resolution the Fermi-chopper has to rotate at its maximum frequency to minimise the delay time between the first and the last neutrons to pass through it.

It should be remarked that monochromatic focusing geometry would also be possible for non equal distances \overline{GM} and \overline{MS} in case of the perfect Johannson-geometry [16] with $R_L = 2R_h$, R_L being the radius of curvature of the monochromator lattice planes. Due to practical reasons this geometry is not achievable on the proposed spectrometer.

6. Performance of the Spectrometer

Intensities and energy resolutions for FOCUS have been calculated as well analytically [4] as based on a modified version of a Monte Carlo program developed by Mutka [15]. As has been shown elsewhere both results agree well [6].

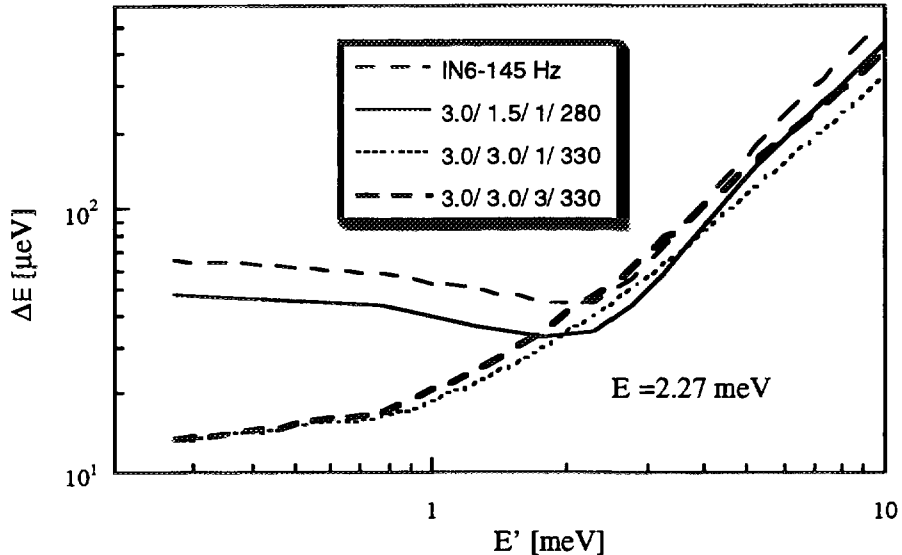


Fig. 5: Energy resolution ΔE as a function of final energy E' for an incoming energy of $E=2.27\text{ meV}$ ($\lambda=6\text{\AA}$). The calculation has been performed for several settings of FOCUS. The numbers given in the legend mean (distances GM , MS , chopper-collimation, frequency). For comparison the respective resolution curve of the IN6/ILL is also included.

Figure 5 presents the calculated energy resolutions ΔE as a function of the final neutron energy E' . An initial energy $E=2.27\text{ meV}$ has been chosen. The calculations have been done for three different configurations of FOCUS. The solid line represents a standard configuration of the spectrometer focusing in time on the elastic line. As one can see ΔE is low at the elastic position and gets worse off the focal condition. For a better comparison also the respective time-focused resolution of the IN6/ILL is included. Contrary, the monochromatic focusing configurations (dotted and bold dashed lines) with Fermi-chopper collimations of 1° and 3° , respectively, reveal a good resolution over a wide range of E' , especially on the neutron energy loss side.

Table II collects the calculated energy resolutions for $E=2.27\text{ meV}$ at three energy transfers as well as the expected intensity for FOCUS and the IN6. The given intensities are normalised to the respective neutron fluxes of the sources. For Fermi-chopper frequencies being higher than 160Hz an anti-overlap condition has been included in our intensity calculations. As one can see especially the monochromatic configurations of the instrument are quite attractive since they provide a high flexibility in the variation of intensity and resolution by changing the spectrometer distances and the Fermi-chopper frequency. On the other hand the best resolution at the elastic position is obtained from the time-focusing geometry.

Table II: Calculated performance for FOCUS compared to the IN6/ILL for E= 2.27meV

	$\lambda=6 \text{ \AA}$	Intensity	Resol. (μeV)	Resol. (μeV)	Resol. (μeV)	Comments
	Instr. Configur.	$I/(d\sigma/d\lambda)$	$\Delta E = -2 \text{ meV}$	$\Delta E = 0 \text{ meV}$	$\Delta E = 10 \text{ meV}$	
				PG002		
	IN6-ILL					
1	145 Hz	1.00	66	45	850	Time-foc.
	FOCUS					
	<i>GM/MS/β / v</i>					
2	3.0/ 1.5/ 1/ 260	0.26	47	35	690	Time-foc.
3	3.0/ 1.5/ 1/ 160	0.67	46	54	1140	
4	1.5/ 1.5/ 3/ 160	1.82	26	85	1060	Monochr.
5	3.0/ 3.0/ 3/ 330	0.42	13	46	580	Monochr.

To summarise FOCUS will complement the SINQ-instrumentation with a flexible and versatile high resolution TOF-spectrometer. Due to the option of changing the optical conditions from a monochromatic to a time-focusing configuration intensity and energy resolution can be optimised for both quasielastic and inelastic scattering applications.

7. Acknowledgements

Fruitful and stimulating discussions with H. Mutka, B. Dorner (both ILL), D. Richter, M. Prager (both KFA Jülich), as well as A. Furrer and W. Bührer (both PSI) are gratefully acknowledged. Furthermore, we thank L. Holitzner (PSI and University of Saarbrücken) for his technical assistance and the German 'Bundesministerium für Bildung und Forschung' (BMBF-project nr. 03-HE4SA2-2) for generous financial support.

8. References

1. F. Douchin, R. E. Lechner, Y. Blanc, "The Multichopper IN5" *73D26T* (ILL, 1973).
2. Y. Blanc, "Le Spectrometre a temps de vol IN6" *ILL 83BL21G* (ILL, 1983).
3. R. Scherm, C. Carlile, J. Dianoux, J. Suck, J. White, "Another Time-of-Flight Spectrometer" *ILL report 76S235* (ILL, 1976).
4. J. Mesot, "A Time-of-Flight Spectrometer at the SINQ" *895/MJ33-401* (PSI, 1994).
5. J. Mesot, S. Janßen et al., FOCUS: A New Time-of-Flight Spectrometer at the Neutron Spallation Source SINQ/CH, G. S. Bauer, R. Bercher, Eds., ICANS-XIII, Paul Scherrer Institute (PSI, 1995).
6. J. Mesot, S. Janßen, L. Holitzner, R. Hempelmann, *Journ. Neutr. Res.* in press (1996).

7. W. Bührer, R. Bührer, A. Isacson, M. Koch, R. Thut, *Nucl. Instr. Meth.* **179**, 259 (1981).
8. F. Atchison, P. Böni, "Intensities at the SINQ Guide System" 816/AF30-404 (PSI, 1994).
9. W. Bührer, *Nucl. Instr. and Meth. in Phys. Res. A* **338**, 44 (1994).
10. J. Kalus, B. Dorner, *Acta Cryst. A* **29**, 526 (1973).
11. B. Dorner, *Nucl. Instr. and Meth. in Phys. Res. A* **338**, 33 (1994).
12. H. M. Leibnitz, *Ann. Acad. Sci. Fenn. Ser. A VI*, 267 (1967).
13. J. Kalus, G. Gobert, E. Schedler, *J. Phys. E: Sci. Instr.* **6**, 147 (1973).
14. R. H. Scherm, E. Krüger, *Nucl. Instr. and Meth. in Phys. Res. A* **338**, 1 (1994).
15. H. Mutka, *Nucl. Instr. and Meth. in Phys. Res. A* **338**, 144 (1994).
16. T. Johannson, *Z. Phys.* **82**, 507 (1933).

THE SMALL ANGLE DIFFRACTOMETER SANS AT PSI

W. Wagner

Paul Scherrer Institut, 5232 Villigen PSI, Switzerland

ABSTRACT

With the start-up of SINQ an instrument for small angle neutron scattering will be operational which compares well with the world's largest and most powerful facilities of this kind. Following the classical principle of the D11-instrument of ILL, it is equipped with state-of-the-art components as are nowadays available, including options for further upgrading. Great emphasis was laid upon providing a flexible, universal multi-user facility which guarantees a comfortable and reliable operation.

In the present paper, the principle layout of the instrument is presented, and the individual components are described in detail. The paper concludes with a model application of small angle scattering to a system of dilute CuCo alloys which undergo a phase separation under thermal treatment, forming spherical Co-precipitates dispersed in a Cu-rich matrix.

1. Introduction

Small Angle Neutron Scattering (SANS) generally serves to characterize structures on a size scale in the nanometer range, typically between 1 and 100 nm. With this capability it serves a variety of disciplines in materials science and structural research, ranging from metal physics and metallurgy to polymer science and structural biology. It further has several industrial applications, like characterizing the porosity of minerals or catalytic converter materials, or following the microstructural fatiguing of structural parts under load. This broad spectrum of different applications, combined with a high turn-round rate, requires that a modern instrument fulfills three primary conditions:

- i. high flexibility
- ii. reliability in operation
- iii. comfortable and highly standardized operation control

The required **flexibility** combines the ability to cover a wide range in momentum transfer Q and Q -resolution with an easy operational mode to adjust the desired instrument configuration. It further refers to an easy adaptation of the various kinds of specimens in different environments, i.e. high or low temperatures, magnetic field, high pressure, vacuum or special gas atmospheres. In addition, options for special applications must be provided, adapted in a way, however, that they do not imply drawbacks to the instrument performance in the basic configuration.

Reliability is primarily a matter of a solid technical layout and careful manufacturing and maintenance. Comfortable **operation control** includes a self-explaining menu-guided user software, but also, in view of the many users expected from different disciplines, a conceptual design which allows a straight-forward and uncomplicated optimization of the instrument configuration for a dedicated problem to

be investigated. The SANS-instrument at SINQ aims to fulfill these requirements, involving state of the art components and options for future upgrading.

2. Principle layout

The conceptual design of the SINQ-SANS instrument follows the classical concept of the D11-instrument of ILL Grenoble [1]. The principle layout is illustrated schematically in Fig. 1. Installed at a cold neutron guide, it uses in basic configuration a mechanical velocity selector for monochromatization, and a straight pin-hole collimation system for the primary beam tailoring. Behind the sample, in the secondary flight path, a two-dimensional position sensitive detector is used to register the neutrons scattered around the primary beam. In this concept, the covered Q-range is a linear function of the selected average neutron wavelength and sample-detector distance; further, the resolution is a linear function of the wavelength spread, the collimation angle and the size of the detection elements. These simple relations fulfill the condition of a straight-forward choice of the appropriate instrument configuration.

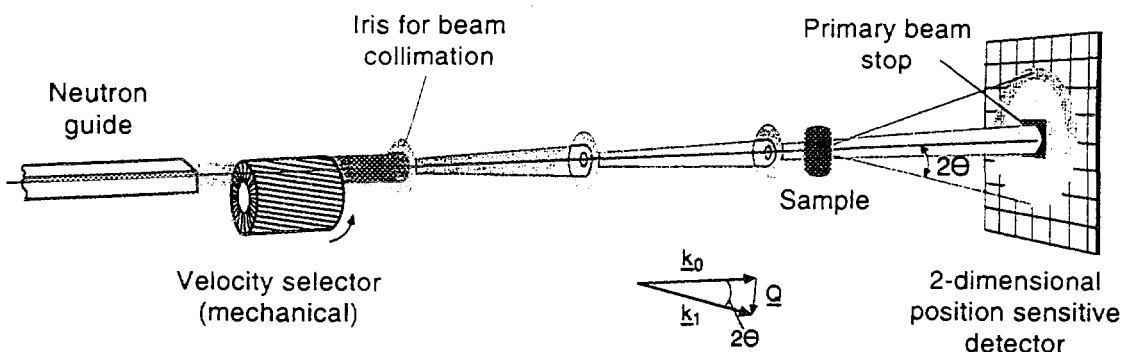


Fig. 1: Principle of a small angle scattering facility. A beam carefully shaped (collimated) by irises at various positions and limited in wavelength spread by a mechanical velocity selector, hits the specimen. A two-dimensional position sensitive detector records the radiation which was deflected from the forward direction.

The main components of the instrument and their position in the overall layout are shown in Fig. 2. Aside from the velocity selector (which is placed inside the bunker), the instrument is assembled in the guide hall of SINQ, stretching to a total length of about 40 m to allow for a secondary flight path of up to 20 m.

3. The individual components

3.1 Neutron beam and wavelength selection

The neutron guide, facing the cold D₂-moderator at its entrance, is curved to filter epithermal and higher energy neutrons. Coated with isotopically enriched ⁵⁸Ni in the curved section, its lower cut-off wavelength ("characteristic wavelength") is at 4.2 Å. The cross-section is a square of 50 mm x 50 mm.

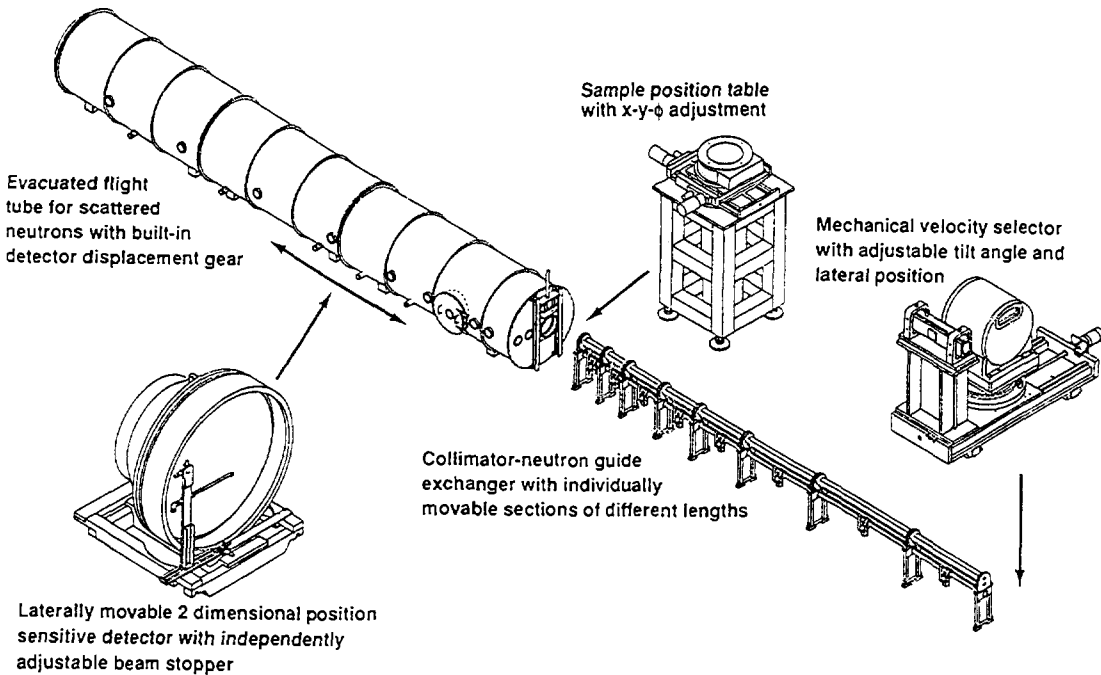


Fig. 2: The main components of the SINQ small angle neutron scattering facility

Still inside the bunker, the guide has a gap of 43 cm in which a primary beam monitor and mechanical velocity selector are placed. We have chosen the Dornier high-tech velocity selector, turning at a maximum speed of 28300 rpm for neutrons of 4.5 Å with a rotor length of only 25 cm. The standard wavelength spread is 10% (FWHM); by tilting the selector relative to the neutron beam direction this value can be decreased to 8% (tilting -10°) or increased up to 20.6% (tilting +10°). More details on the performance can be found in Ref. [2].

3.2 Collimation

The collimation device allows to adjust the collimation length, i.e. the distance between the two extreme pinholes at the guide exit and at the specimen position, in discrete steps between 1 m and 18 m to match the Q-resolution chosen by the sample-detector distance. Mechanically, this flexibility is achieved by a system of eight collimator segments of lengths between 1 m and 4 m, mounted in sequence with vacuum-tight connections, each of them having a revolving device with three tubes. One of the tubes is always filled with a neutron guide, the second one, lined with shielding material, carries apertures for beam tailoring and absorption of parasitic radiation. The third one either carries special elements or is empty. The lengths of the segments are such that the exit of the closest neutron guide can be placed at 1m, 1.4m, 2m, 3m, 4.5m, 6m, 8m, 11m, 15m and 18m from the sample.

For the 1m distance, a focusing neutron guide in the last collimator segment allows an increase the neutron flux on the specimen in the high Q - low resolution configuration.

3.3 Detection

In the secondary flight path a steel-made vacuum tube with a diameter of 2.5 m houses the detector, a two-dimensional ^3He proportional counter with a sensitive area of 96 cm x 96 cm and 128x128 detection elements of 7.5 mm x 7.5 mm each. The detector

is mounted inside the vacuum tank on a rail-guided trolley such that it may be positioned at any distance between 1.20 m and 20 m from the sample. Further, an increase of the Q-range covered at any detector distance can be achieved by an optional lateral displacement of the detector of up to 50 cm, combined with a rotation around the central vertical axis of the detector to minimize parallax effects.

The detector electronics (preamplifier, amplifier, logic units etc.) is entirely mounted on its rear in a volume which is at atmospheric pressure and connected to the outside by a series of flexible tubes in which run cables and a cooling air flow. Immediately in front of the detector, a beamstop of B_4C -Cd-plates is mounted on a thin-walled aluminium tube, moveable in vertical and horizontal direction. Four beamstops of dimensions 40 mm x 40 mm, 70 mm x 70 mm, 85 mm x 85 mm and 100 mm x 100 mm are available and may be exchanged by remote control in the vacuum.

3.4 Available Q-range

The momentum transfer $Q (=4\pi(\sin \theta)/\lambda$, where 2θ is the full scattering angle and λ the neutron wavelength) at a given point on the detector is given by

$$Q(r) = 4\pi \left[\sin \left[\frac{1}{2} \operatorname{arctg}(r/D) \right] \right] / \lambda \quad (1)$$

where r is the radial distance of the point on the detector from the beam axis, and D the sample-to-detector distance. If we assume that the closest distance to the beam center at which reliable data may be recorded is 4 cm, then the minimum in Q-range to be covered at $D=20$ m and for $\lambda = 20$ Å is

$$Q_{\min} = 6 \times 10^{-3} \text{ nm}^{-1}$$

The maximum Q to be reached at $D = 1.20$ m and $\lambda = 4.5$ Å with the detector centered to the beam axis ($r_{\max} = 48$ cm) is

$$Q_{\max} = 5.4 \text{ nm}^{-1}$$

or, for a 50 cm lateral detector displacement ($r_{\max} = 98$ cm)

$$Q^*_{\max} = 10.5 \text{ nm}^{-1}$$

3.5 Sample environment

The sample area has all flexibility for the installation of specimen supports or environmental equipment according to the user's requirements. Two basic configurations are provided

- i. A sample table with a load capacity of up to 400 kg, with a vertical lift to adjust the position of the top plate between 530 mm and 680 mm below the beam axis. On this, equipment may be mounted directly or via precision X and Y tables for translation and an ω table for rotation around the central vertical axis. It can support an automatic sample changer or other devices like cryostat, furnace, magnet, pressure cell or a shielding box for radioactive samples. In this configuration, the exit of the collimator and the entrance of the secondary flight path are covered by neutron-transparent vacuum windows.
- ii. A vacuum chamber, connected directly to the gate valves mounted to the collimator tube and the detector vessel, which allows to connect all three chambers together to one common vacuum recipient without any window between collimator entrance and detector. The specimen chamber is sufficiently large to house most of the usual specimen environments or supports.

3.6 Alignment System

The alignment of the sample in the beam is carried out via an optical system. A silicon wafer, permanently in the beam, oriented with its surface at 45° to the beam axis is situated about 0.8 m before the sample position and acts as a mirror for a light beam from either a halogen lamp or a laser fixed outside the evacuated collimation tube and shining through a quartz window. This light beam is adjusted such that its axis is coincident with that of the neutron beam and hence the sample may be accurately aligned without breaking the collimator vacuum.

The main components of the instrument together with the characteristic performance data are collated in Table 1.

Table 1: Main instrument components and characteristic performance data of the SANS at SINQ

Beam tube	cold neutron guide =1RNR16, 50 mm x 50 mm
Monochromator	helical slot velocity selector
Incident wavelength	$4.5 \text{ \AA} < \lambda < 20 \text{ \AA}$
Wavelength resolution	$\Delta\lambda/\lambda = 10\% \text{ FWHM}$
Detector	2-dim ^3He -detector with 128 x 128 elements, each 7.5 mm x 7.5 mm, active area 96 cm x 96 cm
Sample to detector distances	$1.2 \text{ m} \leq D \leq 20 \text{ m}$
lateral detector displacement	$0 \leq L \leq 50 \text{ cm}$
collimation lengths	1m, 1.4m, 2m, 3m, 4.5m, 6m, 8m, 11m, 15m, 18m
Q-range detector in central position 50 cm laterally displaced	$6 \times 10^{-3} \leq Q (\text{nm}^{-1}) \leq 5.4$ $Q (\text{nm}^{-1}) \leq 10.5$

4. Options

4.1 Polarization

In the first segment of the collimator (seen from the source), the third tube of the revolving device will be furnished with a polarizer combined with a spin-flipper. The polarizer itself is a combination of a neutron guide and supermirror-based polarizing plates [3,4]. This "polarizing cavity" operates in transmission and thus does not deflect the neutrons or spread the beam. A length of 280 cm is foreseen for this device, plus 20 cm for the spin-flippers.

When the polarizer is switched into the beam line (which can be done by just pushing a button), the instrument is supplied at the entrance with polarized neutrons, and else can be operated as usual, except that the longest available collimation distance is reduced from 18 m to 15 m.

To maintain the polarization of the neutrons up to the specimen area, coils will be wrapped around the collimator tubes for a magnetic guide field. To avoid magnetic disturbances in the primary flight path, all parts of the collimator, as far as possible, were made of aluminium or other nonmagnetic materials.

4.2 Double-crystal monochromator

The design of the collimator with its revolving drums gives further the possibility to have a second beam axis, shifted vertically downwards by 20 cm with respect to the main beam. This allows to insert a double crystal monochromator instead of or in combination with the velocity selector. The wavelength resolution then would be significantly improved to typically $\Delta\lambda/\lambda \approx 2\%$ (on the expense of intensity, of course). This would be an interesting option for high-resolution experiment, e.g. diffraction from crystals of large unit cell.

4.3 TOF-Mode

With a chopper or a sequence of choppers installed in the primary beam, replacing the velocity selector, the instrument could well operate in time-of-flight (TOF) mode, using the most intense part of the white beam. In TOF-mode, changing the wavelength resolution would be very flexible, and the simultaneously covered Q-range would be increased for any given instrument setup.

In the data acquisition system a TOF mode is foreseen in any case to be used for the calibration of wavelength and wavelength resolution, and for cyclic or dynamic experiments with characteristic time constants in the millisecond to seconds range.

5. Illustrating application

5.1 Microstructural model and scattering formulae

In a specimen of usually several mm³ or even cm³ in volume, the number of structural features which contribute to small angle scattering is typically between 10¹³ and 10¹⁷, and they are not necessarily all of the same type. Therefore in many cases it is essential for a conclusive interpretation of the data to have a microstructural model. This model can either be gained from assumptions based on theoretical considerations, from experience and/or from additional informations obtained from complementary techniques, like electron microscopy.

A quite general and frequently used microstructural model for the analysis and interpretation of small angle scattering data is represented by a polydisperse array of scattering objects, i.e. particles of a specific shape and size, dispersed in a homogeneous matrix of solid, liquid or gaseous material with a scattering length density which is different from that of the particles. Assuming only nuclear scattering contrast (contributions of additional magnetic scattering are outlined in Ref [5]), the differential scattering cross section is given by

$$\left(\frac{d\sigma}{d\Omega} \right)_N = (\Delta b)^2 |F_N(Q, R)|^2 \quad (2)$$

where $(\Delta b)^2$ is the contrast for nuclear scattering between particles and matrix, given by

$$(\Delta b)^2 = (\bar{b}_m - \bar{b}_p)^2 \quad (3)$$

with \bar{b}_m and \bar{b}_p the mean scattering length of matrix and of particles, respectively.

In the small angle regime, atomic form factor and Debye-Waller-factor can well be neglected. Then, the structure function of our particles, $|F(Q, R)|$, which comprises all information on shape, size, size distribution and density, can be described by the general ansatz

$$|F(Q, R)|^2 = \frac{1}{\Omega} \int S^2(Q, R) V(R) N(R) dR \quad (4)$$

where Ω is the atomic volume, $S(Q, R)$ the single particle scattering function, $V(R)$ the particle volume, and $N(R)dR$ the incremental volume fraction of particles in the size interval between R and $R+dR$. If specific informations on the shape of the particles are available, one uses the corresponding specific shape function as given for example in Ref. [6]. If not, it is convenient and in most cases not a general restriction to approximate the single particle scattering functions $S(Q, R)$ by the structure function for spheres of radius R ,

$$S(QR) = \frac{3}{(QR)^3} (\sin QR - QR \cos QR) \quad (5)$$

Now, provided the model assumptions are correct, the measured scattering data can be fitted using the combined eqs. (2) to (5). The fit yields the incremental volume fraction $N(R)dR$ which contains the informations on the size distribution and hence, the size average (volume weighted and number weighted). Further, provided the scattering data were measured in absolute units and the contrast (eq (3)) was known, the volume fraction f_p of the particles is obtained by integration

$$f_p (1-f_p) = \int_R N(R) dR \quad (6)$$

One of the problems not mentioned so-far is the parameterization of the size distribution function when the size distribution of the scattering particles is not explicitly known. It could be a Gaussean or, in extreme cases, a δ -function. In practice, one frequently finds that a log-normal function, or a linear combination of several log-normal functions, adequately describes the underlying distribution in size. In this case,

$$N(R) = \sum_i A_i \exp - \frac{(\log R / R_i)^2}{2\sigma_i^2} \quad (7)$$

where A_i is the relative amplitude of the i -th distribution function.

5.2 Selected examples: Precipitation in dilute CuCo alloys

Cu rich alloys of the system CuCo were frequently recognized as a model system for a solid-solid phase transformation reaction: The solubility of Co in Cu is very small (less than 0.4% below 800 K), and the microstructure of the precipitating Co-rich α -phase is strikingly simple, characterized by spherical shape of the precipitates, coherency between precipitates and matrix and a moderate lattice mismatch. Therefore, several experimental studies of nucleation and early stage decomposition are reported in literature, e.g. [7-13], some of them using SANS as the major experimental tool [10-13]. For our purpose here, selected SANS results from these studies may illustrate the data evaluation by the application of the formulae given above.

Fig. 3 presents a sequence of SANS data measured from a Cu-0.8% Co alloy. The original data on the 2-dimensional detector were found isotropic around the incoming beam, the intensity was therefore averaged azimuthally at each value of Q . Before plotting Fig. 3, the raw intensity data were properly corrected for background, specimen transmission, detector efficiency and geometric effects, and normalized by a standard water specimen to obtain the differential scattering cross section in absolute units. The different scattering pattern shown in Fig. 3 represents the alloy after quenching from the solution treatment temperature and subsequent annealing at 833 K which is inside the

miscibility gap. The quenched reference specimen (WQ), although being a homogeneous mixture of Cu and Co, shows two obvious scattering contributions:

- i. the constant isotope-incoherent scattering determined to

$$\left(\frac{d\sigma}{d\Omega} \right)_{inc} = (0.035 \pm 0.005) b / (\text{sr at.})$$

- ii. a Q^4 -dependent contribution at low Q , fitted by Porod's law $S(Q)=P \cdot Q^4$ [14]

The Porod-constant P has determined to $1.0 \times 10^{-4} \text{ b nm}^4$. This contribution is attributed to geometric sample heterogeneities on a size scale $> 100 \text{ nm}$ like grains, grain boundaries and surface roughness. Both contributions of the WQ specimen are part of the scattering curves of all other specimens as well, and obviously unchanged by the annealing treatment.

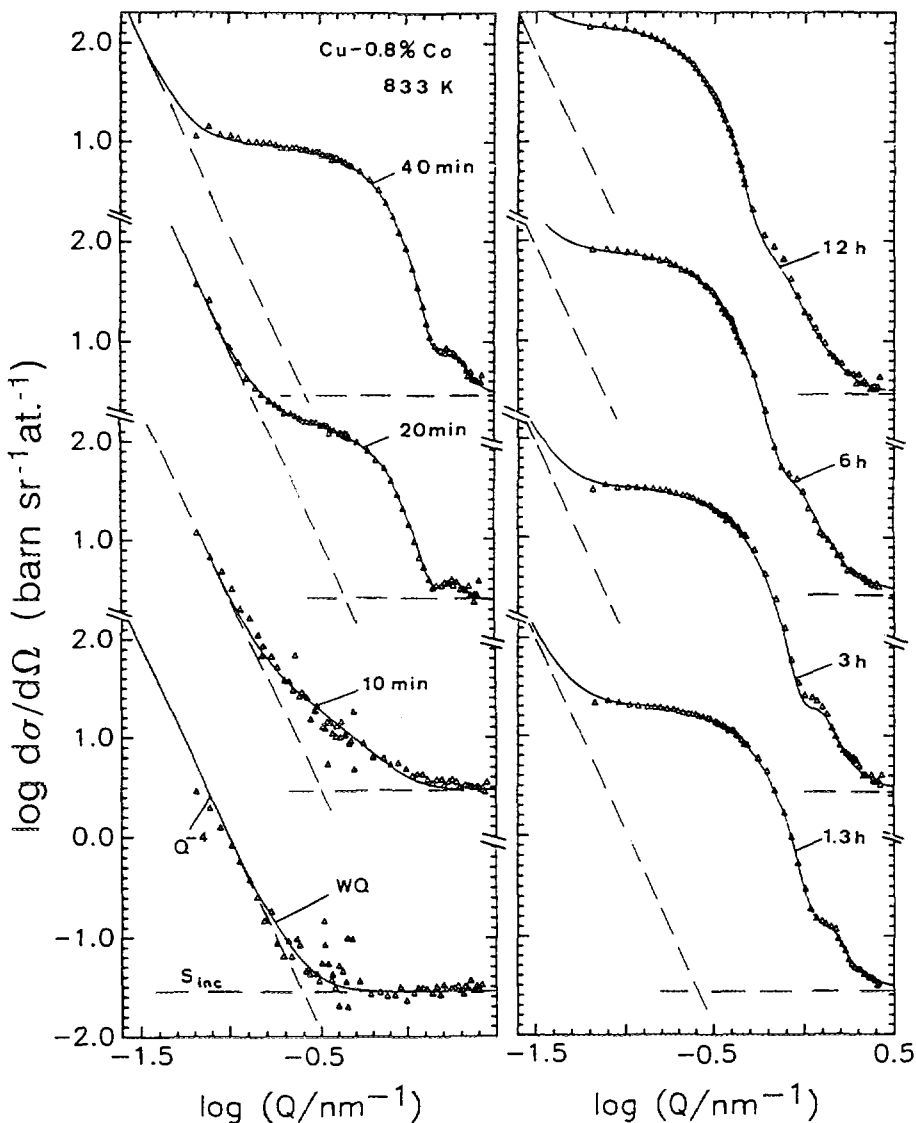


Fig. 3: SANS results for Cu-0.8 at.% Co after solution treatment (WQ) and subsequent annealing at 833 K. The solid curves are calculated structure functions fitted to the data, which model the scattering due to the phase transformation in addition to the isotope incoherent scattering S_{inc} and a Q^4 dependent scattering of geometric sample inhomogeneities (both latter contributions are extrapolated by dashed lines).

After annealing a further scattering contribution is supposed, originated by the undergoing phase transformation (Fig. 3). For the short reaction period of 10 min at 833 K this contribution shows an approximately straight Q-dependence in the log-log presentation with slope -1.4. For longer periods the scattering curves show the characteristic structure for spherical α -Co precipitates as described by eqs. (2) - (5). A remarkable and for alloy systems rather rare observation is the second order maximum in the structure function, resolved from 20 min of annealing at a position of $\log(Q/\text{nm}^{-1})$ around 0.2. It indicates a distinctly narrow distribution in size of the precipitates.

The quantitative evaluation of the scattering curves by fitting the model structure function to the data reveals the precipitate size distributions and the results for average size, volume fraction and number density as a function of the annealing time. These data were used to critically scrutinize the theoretical predictions of nucleation, growth and coarsening of the precipitates in CuCo. In particular, the SANS study revealed spatially extended precursor fluctuations which crucially influence the reaction kinetics and open a path to overcome prohibiting energy barriers for nucleation in this alloy system [13].

6. Concluding remarks

Not by chance but as a product of a fruitful collaboration between HMI Berlin, ILL Grenoble and PSI the SINQ-SANS was designed as a "sister instrument" of the D22-instrument of ILL, with only some dimensions modified. The D22 itself has copied some parts of the Berlin SANS, in particular the collimator system. For universal multi-user facilities as SANS instruments are, the coordinated design certainly helps to facilitate the operation for the users and to explore more efficiently the capabilities of the technique.

7. References

1. Ibel, J. *Appl. Crystallogr.* **9** /1976) 296
2. H. Friedrich, V. Wagner, P. Wille, *Physica B* **156 & 157** (1989), 547 and *Physica B* **180 & 181** (1992), 938
3. F. Mezei, *Atomkernenergie-Kerntechnik*, Suppl. to Vol. **44** (1984) 735
4. T. Krist, C. Lartigue and F. Mezei, *Physica B* **180 & 181** (1992) 1005
5. W. Wagner, A. Wiedenmann, W. Petry, A. Geibel and H. Gleiter, *J. Mater. Res.* **6** (1991) 2305
6. A. Guinier and G. Fournet, in "Small-Angle Scattering of X-rays", John Wiley & Sons, New York (1955)
7. I.S. Servi and D. Turnbull, *Acta metall.* **14**, (1966) 161
8. L.E. Tanner and I.S. Servi, *Acta metall.* **14**, (1966) 231
9. F.K. LeGoues and H. I. Aaronson, *Acta metall.* **32**, (1984) 1855
10. W. Wagner, *J. Phys F* **16**, (1986) L239
11. M.F. Chisholm and D.E. Laughlin, in Phase Transformations (edited by G.W. Lorimer). Inst. of Metals, London (1988)
12. W. Wagner, *Z. Metallk.* **80**, (1989) 873
13. W. Wagner, *Acta metall. mater.* **38**, (1990) 2711
14. G. Porod, *Kolloid Z.* **124** (1951) 83



THE NEUTRON REFLECTOMETER AT "SINQ"

DANIEL CLEMENS

*Laboratorium für Neutronenstreuung,
ETH Zürich & Paul Scherrer Institut,
CH - 5232 Villigen PSI, Switzerland*

ABSTRACT

SINQ's dedicated reflectometer will be a flexible instrument in many respect. A 'white beam time of flight' as well as a 'constant wavelength' setup are possible for reflectometric experiments in a vertical scattering geometry. The phase controlled double chopper at the beginning of the instrument together with properly chosen time channels at the detector allow for the variation of the temporal resolution. Collimation slits serve to determine the angular resolution. In combination, the resolution can be tailored to the experimental needs. Additionally, one can adjust the illumination of the sample by setting the sample table and the detector to an appropriate distance. A mounting for exchangeable mirrors can be used to supply polarized neutrons by a multilayer polarizer or monochromatic neutrons by a multilayer monochromator. When it is equipped with a supermirror as a deflecting unit one can maintain a horizontal sample position which makes reflectometry on liquid samples practicable. Remanent polarizers are assigned for the changing over of the neutron polarization. A 1 T electromagnet installed on the sample manipulation table and polarization analyzers complete the polarized reflectometry setup. Alternatively, an x-y-detector and single detectors will be available. By 1997/1998 the neutron reflectometer will be operational as a users' instrument.

1. Introduction

The physics and properties in thin films and multilayers as well as the processes in and along lipid membranes cannot be understood without a deep insight into the structure and dynamics of surfaces and interfaces. In the past years, X-ray and neutron reflectometry [1.] have been established as nondestructive microscopic probes for the investigation of stratified structures and hidden interfaces. Reflectometric measurements using X-ray can be traced back to 1931 [2.]. Neutrons were introduced to the technique by the first observation of the total reflection of neutrons from a surface up to a critical angle ϑ_c by Zinn and Fermi in 1944 [3. - 5.]. In the following, the measurement of ϑ_c developed to one of the first methods to determine the scattering length b of the elements. Nevertheless, only with the advent of sophisticated deposition apparatuses and techniques to produce two dimensional and isotope labeled soft matter films, together with the development of complementary characterization methods, like SIMS, RBS, Möbbauer spectroscopy, AES, XPS, ICP, TEM, AFM, etc., the method 'boomed' not

earlier than in the last two decades. Consequently, the scheduled beam-time at neutron scattering centers providing reflectometers to a user community is heavily overbooked. The unique interaction of the neutron with matter allows in the case of this measurement technique to determine quantitatively layer thicknesses, roughness at interfaces and surfaces, interdiffusion parameters, and magnetic moments in thin films and multilayers, within the film and at the interfaces. Reflectometry can contribute to research on phenomena like growth, wetting, absorption, adhesion, (inter-)diffusion, corrosion, nanocrystalline materials, magnetism, and thin film superconductivity. Many of these are relevant for industrial applications. The contrast variation method can be exploited to enhance the signal obtained from the sample. Polarized neutrons are of excellent value for investigations of magnetic materials.

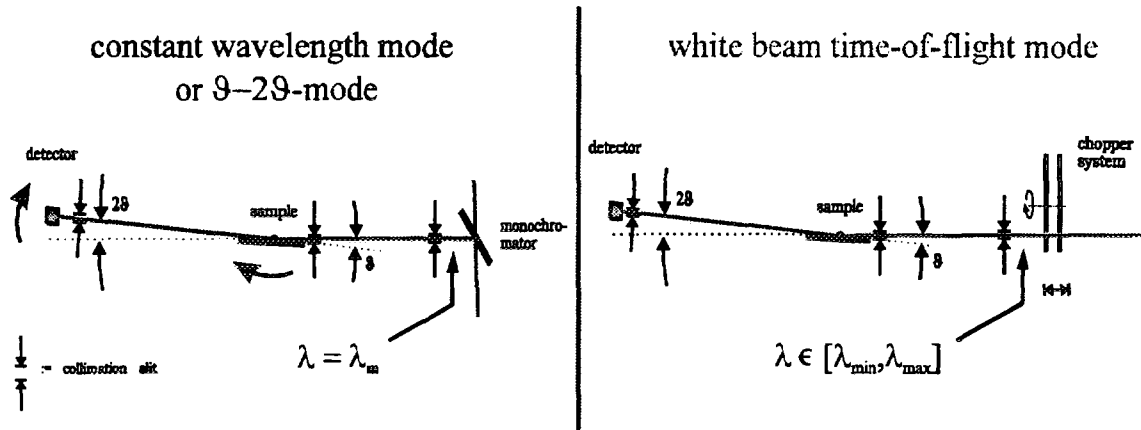


Fig. 1. Principal setup of a fixed wavelength and a white beam time-of-flight reflectometer

In principle, reflectometry can be performed using monochromatic radiation as got by reflection from a monochromator and scanning the sample in angles, i.e. for specular reflectivity, a ϑ - 2ϑ -scan giving $R = R(\vartheta)$, or in the white beam time of flight (TOF) mode. In the TOF mode, the time neutrons take from a pulsed origin to the detector is measured in a fixed geometry (Fig. 1). With it one measures R as a function of time of flight which can be translated to a function of velocity $R = R(v)$ or wavelength $R = R(\lambda)$, respectively. The TOF mode is usually implemented in reflectometers at spallation sources [6. - 8.], whereas the constant wavelength (CW) mode is typical for instruments at continuous neutron sources [9., 10.].

Considering an interface between vacuum and a medium (Fig. 2) total reflection occurs because no wave field can propagate in the medium for $\vartheta < \vartheta_c$. Only an evanescent wave exists near to the boundary.

Taken

$$n = \frac{k_{\text{med}}}{k_{\text{vac}}} = \sqrt{\frac{\frac{2m}{\hbar^2}(E - V_{\text{opt}})}{\frac{2m}{\hbar^2}E}} = \sqrt{1 - \frac{V_{\text{opt}}}{E}} \cong 1 - \frac{V_{\text{opt}}}{2E} = 1 - \frac{\frac{2\pi\hbar^2}{m}\rho_{\text{sc}}}{2\frac{\hbar^2k^2}{2m}} = 1 - \frac{\lambda^2}{2\pi}\rho_{\text{sc}} \quad (1),$$

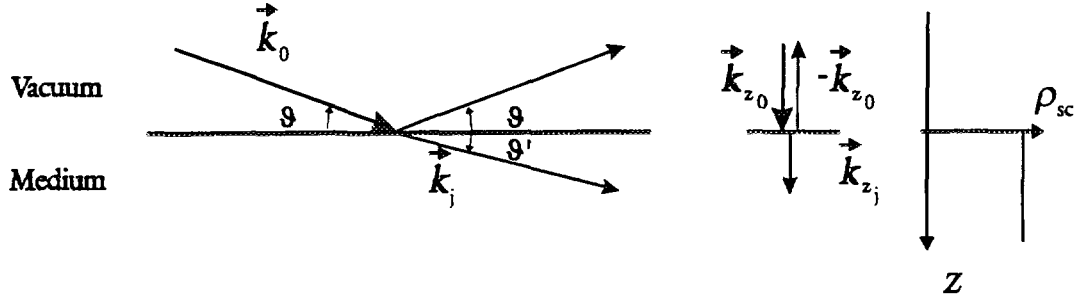


Fig. 2. Refraction of a wave at the interface to a medium j : geometry, normal components of the vectors, and scattering length density profile (from left to right)

as the refractive index, where V_{opt} is the optical potential, i.e., the average over the Fermi pseudo potential:

$$V_{\text{opt}}^\pm(\vec{r}) = \frac{2\pi\hbar^2}{m} \left\langle \sum_i (b_i \pm p_i) \cdot \delta(\vec{r} - \vec{r}_i) \right\rangle = \frac{2\pi\hbar^2}{m} \rho_{sc}^\pm(\vec{r}) \quad (2)$$

where

$$\rho_{sc}^\pm = \rho_{at} \cdot (b \pm p) \quad (3)$$

is the scattering length density for neutrons polarized parallel (+) or antiparallel to the quantization axis (ρ_{at} atom density, b : complex scattering length with σ_a and σ_i in the imaginary part, and p : magnetic scattering length). Herein, a Zeeman term has to be added to the purely nuclear potential if the scattering is also by the magnetic moments in the medium. This is expressed by

$$p = \frac{2m}{\hbar^2} \vec{\mu}_n \cdot \vec{B}_\perp \quad (4),$$

where \vec{B}_\perp denotes the field component in the magnetic medium perpendicular to \vec{Q} . In reflectometry \vec{B}_\perp lies in a plane parallel to the surface of the sample. And, if the polarization of the beam is realized through reflection from a magnetized mirror, the direction of $\vec{B}_{\perp,\text{pol}}$ at that polarizer determines the quantization axis for the experiment.

The optical laws also hold for the neutron wave [11.]. Taking Snell's law

$$n = k_j/k_0 = \cos \vartheta / \cos \vartheta' \quad (5)$$

at the limit where $\cos \vartheta' = 0$, with the expansion $\cos \vartheta \approx 1 - \vartheta^2/2$, and using Eq. 1, one finds an expression for the critical angle ϑ_c :

$$\vartheta_c = \lambda \sqrt{\frac{\rho_{sc}}{\pi}} \quad (6).$$

For $\vartheta > \vartheta_c$ the wave field of the reflected beam is governed by the Fresnel equations which gives a specular reflectivity R_0 according to Porod's law:

$$R_0(Q) \propto Q^{-4} \quad (7)$$

Actually, $R(Q)$ is the Fourier transform of the scattering length density. The effect of interface roughness at a planar boundary between media i and j on $R(Q)$ can be taken into account by a static, Debye-Waller like factor in the form [12.]

$$R(Q) = R_0(Q) e^{-4k_{z_i} k_{z_j} \langle \sigma^2 \rangle}, \quad k_{z_{i,j}} = k \sin \vartheta_{i,j} \quad (8).$$

In the exponential of Eq. 8 σ denotes a root mean square (rms) value or the variance of a Gaussian roughness profile. The situation for multiple parallel interfaces involves refraction and (multiple) reflection at every boundary between materials with different ρ_{sc} , as well as the absorption for propagating partial waves within the layers. It can be calculated in the frame of a matrix formalism that provides one matrix for every interface. The product of these matrices describes the scattering of the whole sample and can be used to simulate the spectrum of its specular reflectivity [13. - 15.]. Roughness can be taken into account for every interface following the concepts in Ref. [16.]. Equivalently, recursion formulae can be used to calculate the theoretical reflectivity [1.]. For a spin-dependent matrix formalism see [17.]. For the analysis of the off-specular reflectivity theories on the basis of the distorted wave born approximation have been developed [18. — 21.] that give information about the in-plane structure of the interface.

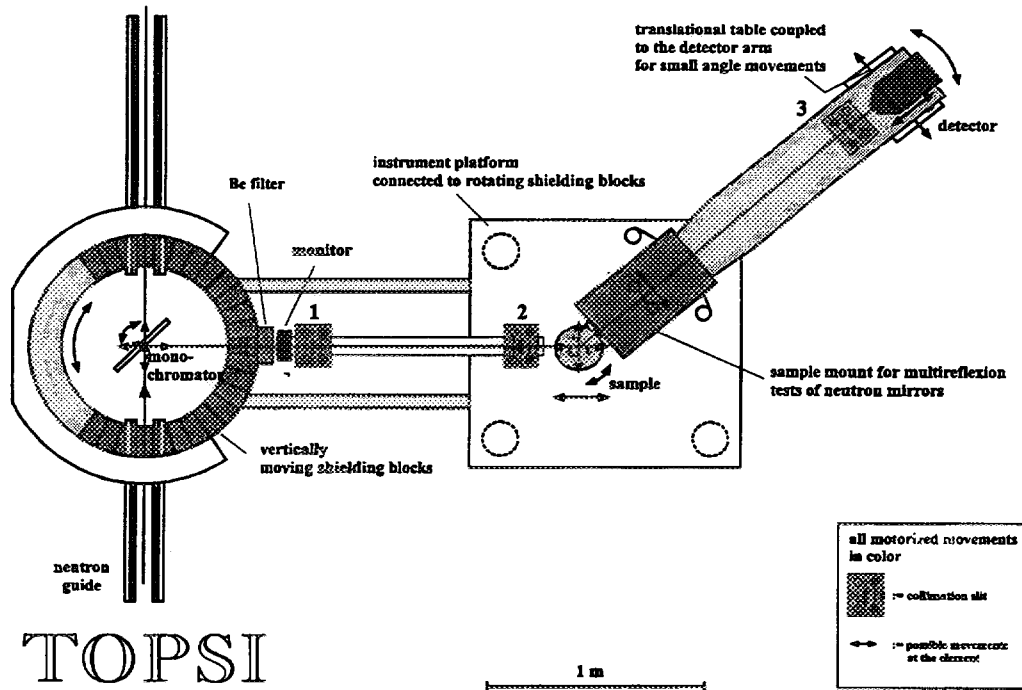


Fig. 3. Sketch of the TOPSI two axis spectrometer on a cold neutron guide

At SINQ two instruments will serve the interested user for reflectometry with neutrons. A two axis/neutron optics spectrometer (TOPSI, Fig. 3) working with cold neutrons in constant wavelength mode in a horizontal scattering geometry has been moved from the decommissioned SAPHIR reactor to the new source. At SAPHIR it has been vastly used to characterize the neutron mirrors that now build up the SINQ neutron guides. For its position at SINQ it has been extended to a multi-purpose instrument.

There are restrictions to the possible reflectometric measurements on TOPSI, especially as its partly running with other two axis experiments. Therefore, a concept for a dedicated reflectometer for SINQ has been worked out which is meant to supply users from Switzerland and abroad with a modern and precise facility, that is flexible enough to meet most of the requirements that are connected with their specific experiment.

2. Instrumental Considerations

The end position of one guide (1RNR17) is solely assigned to the neutron reflectometer which will be constructed as part of the first instrumentation program. The guide has a cross section of 50 mm * 50 mm. The supermirror coated walls reflect up to two times the critical angle of natural nickel ($\vartheta_m = m \cdot \vartheta_c(Ni)$, $m = 2$) with a reflectivity of 86% and more. The guide geometry leads to a nominal cut off wavelength $\lambda_c = 0.19$ nm. A ray tracing calculation which takes into account the geometry of the cold source as well as the guide [22.] shows that the cold flux (per mA proton current) at 1RNR17 will be rather high. A comparison to values measured for H15 at the I.L.L. in Grenoble is given in Fig. 5.

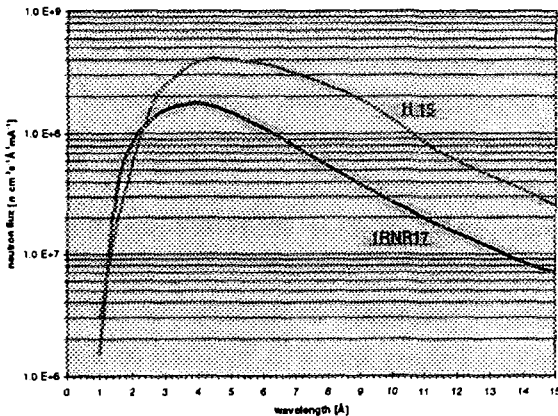


Fig. 4. Comparison of the flux at the cold neutron guides H15 (ILL) and at 1RNR17 (for a proton current of 1 mA impinging on a Pb target, calculated by P.Allenspach)

The fixed geometry in the white beam TOF mode offers advantages over the fixed wavelength mode. They are closely connected to the resolution terms. The resolution in Q for a TOF reflectometric experiment is given by

$$\frac{(\Delta Q)^2}{Q^2} = \frac{(\Delta t_{tch})^2 + (\Delta t_{pul})^2}{t^2} + \frac{(\Delta \vartheta)^2}{\vartheta_i^2} \quad (9),$$

where $\Delta \vartheta$ is the geometrical resolution for the incident beam direction, Δt_{pul} is the pulse width, and Δt_{tch} is the time channel window for neutrons passing the distance L from the pulse source (spallation target or chopper) to the detector in a time t . Each of the contributions can be chosen to give almost equal values. The difference in $\Delta t_{pul}/t$ for neutrons of different velocity can be balanced by adjusting the time channels

appropriately, in order to get a constant $\Delta t/t$. $\Delta\vartheta/\vartheta$ is constant, due to the fixed geometry. In the two-axis mode the resolution for specular reflection is given by

$$\frac{(\Delta Q)^2}{Q^2} = \frac{(\Delta\lambda)^2}{\lambda^2} + \frac{(\Delta\vartheta)^2}{\vartheta_i^2}. \quad (10),$$

where $\Delta\lambda$ is dominated by the mosaicity of the monochromator, and $\Delta\vartheta/\vartheta_i$, again, depends on the geometry. Hence, for fixed collimation slit widths the relative angular resolution changes during the experiment, but can be held constant using programmable slits. This gives a constant 'footprint' on the sample as it is guaranteed in the TOF mode in any case. For TOF the resolution terms do not change during the scan. They are easy to match, independently. In the fixed wavelength mode the matching of the resolution terms depends on the mosaicity of the monochromator. This is coupled to the beam collimation and therefore the flexibility in the adjustment of the instrumental resolution is restricted [6.]. It is pleasing that preliminary results can be acquired in the TOF mode due to the fact that every measured burst contains information about $R(Q)$.

For a chosen resolution the instrument can be adapted to the area of interest on the sample by changing the length of the primary and secondary arm. In most cases, this is not possible for very low angles of incidence ϑ_i . TOF reflectometry usually operates at $\vartheta_i \sim 0.5^\circ$ or higher. Therefore, and contrary to the fixed wavelength mode, its geometry is fully adaptable to the experimental needs. Predetermined by the measurement principle there are no or only few sample movements required except for the initial orientation. This minimizes possible positioning errors.

Despite the conveniences of TOF reflectometry, the substantial drawback of the lacking beam brightness for an instrument installed on a continuous source has to be considered. Nevertheless, practical experience at existing instruments [23.] and theoretical calculations [24.] show that it is justified to install a TOF reflectometers at a reactor.

Fig. 5 shows the principal setup of the reflectometer. To keep a high degree of flexibility the main elements are mounted on tables riding on an optical bench, where they

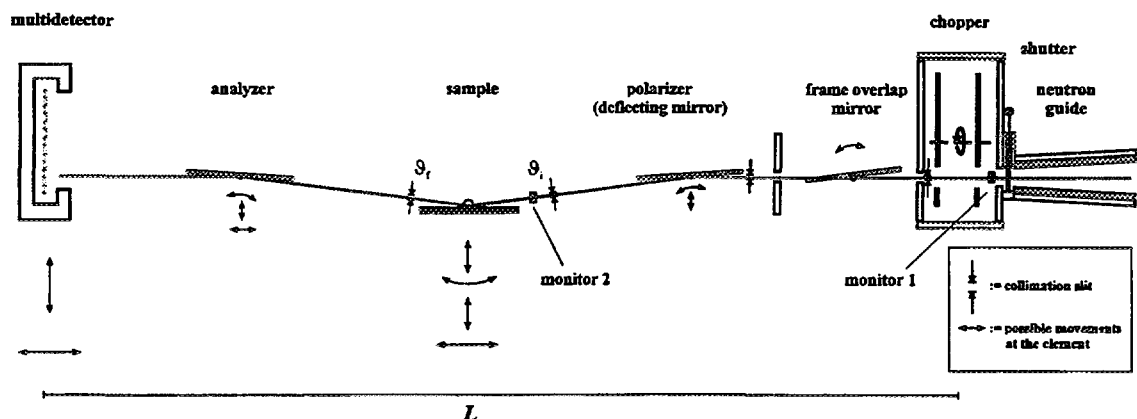


Fig. 5. Sketch of the overall instrumental layout of the proposed SINQ reflectometer. Components for the generation of magnetic fields and positioning aids are omitted.

can be moved by hand along the beam direction. The precision rotations and translations indicated for each table are made by motorized units. By the use of a deflecting mirror in this position one can achieve a horizontal sample geometry. This is an important option for measurements on liquids and can be helpful in the operation of sample environments that have a low flexibility or a large mass. Optionally, a spin analyzer can be installed on the secondary arm of the instrument for spin polarized reflectometry. In the primary arm a guidance of vertical supermirror segments reduce the losses due to the horizontal divergence of the beam.

Exceeding the requirements for a TOF reflectometer with a wide application field, the flexibility of the setup can be exploited to take advantage of the $\vartheta-2\vartheta$ -mode. It is possible to move the chopper out of the beam and to replace the deflecting mirrors by a multilayer monochromator. The layer sequence of it has to be specially designed to reflect a wavelength band according to the resolution requirements. Prototype monochromators of this type have been recently produced and tested by our group. The original concept [25.] that envisaged two beam paths guided onto the same spot of the sample has been abandoned in order to simplify the mechanical layout.

3. Description of the instrument components

3.1. Chopper

On our continuous source the chopper defines the origin of a white beam neutron burst. To afford for the flexibility of the instrument one can adjust the rotation frequency

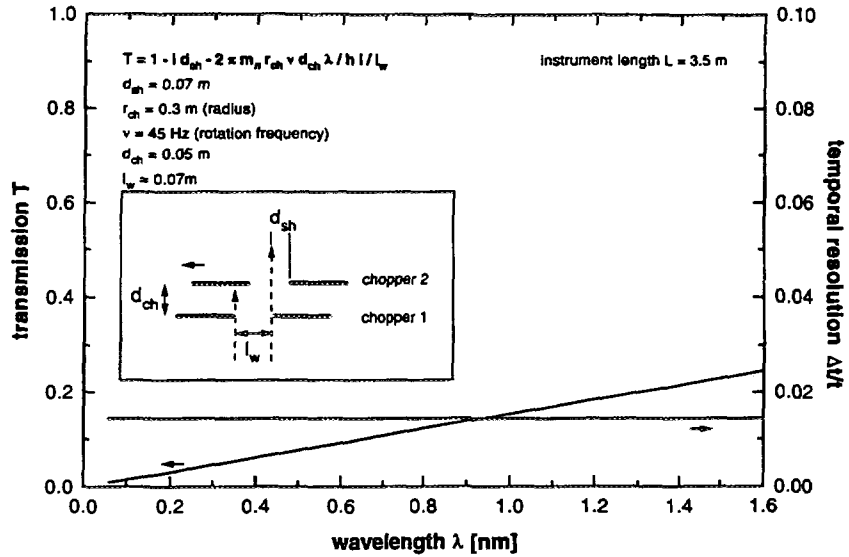


Fig. 6: Transmission function and temporal resolution, optimized for a $\Delta t_{pu}/t = 0.014$ at a constant value

v and the width of the gating window. The frequency of the chopper has to be adapted to the length of the flight path, which can be varied in order to illuminate the sample optimally at a chosen resolution and take-off angle. Thus, to prevent a second neutron

burst from interference with the foregoing, the chopper frequency can be chosen between $v = 20$ Hz and $v = 100$ Hz. Depending on the length L of the instrument, i.e. the distance chopper to detector, and on the wanted time resolution, opening times t_{pul} of tens to hundreds of microseconds have to be realized. The width d_{sh} of the chopper window which is situated at a radius r_{ch} to the axis of the chopper disk shall be variable in the range of 1 mm to 20 mm to get an optimal adaption of $\Delta t_{\text{pul}}/t$ to the other resolution terms. A method to provide the desired variable chopper window is to rotate two identical chopper disks with an adjustable phase delay and adjustable distance d_{ch} to one another. The concept of having a constant, wavelength independent $\Delta t_{\text{pul}}/t$ has been worked out in Ref. [26.]. A corresponding setup is displayed in Fig. 6.

3.2. Frame overlap mirrors

Frame overlap mirrors are put into the primary arm in order to remove the slowest portion of the neutrons in the burst which might be reached by neutrons of the succeeding burst at the locus of the detector. Undesired neutrons with $\lambda > 1.3$ nm can easily be eliminated from the beam when they are reflected from a supermirror. The supermirrors can be coated on the two faces of a silicon wafer, so that the device transmits only 0.5% at ϑ_m . As the frame overlap mirrors shall cover a maximum beam height of 20 mm their length would exceed up to 0.5 m.

3.3. Deflecting mirrors / polarizers

An important part for the desired flexibility of the instrument is the cradle that holds the deflecting mirrors. High performance Ni-Ti-supermirrors [27.], reaching cut-off angles $\vartheta_c = m \cdot \vartheta_c(\text{Ni})$ from $m = 2$ up to $m = 4$, will be used to reflect neutrons onto the sample under the chosen angle of inclination. A single segment with a total length of 1 m has to be used to accept the beam even for a relaxed angular resolution. Because the total extension L of the reflectometer can be varied and with it the sample position.

Tab. I: Characteristics of the deflection units

	deflection unit
number of segments	1
length of supermirror per segment [mm]	1'000
width of supermirror per segment [mm]	70
tilting angle of a segment	$\pm 5^\circ$
accuracy in angle better than	0.01°
range for vertical placement [mm]	50
min. accuracy in vertical placement [mm]	0.01

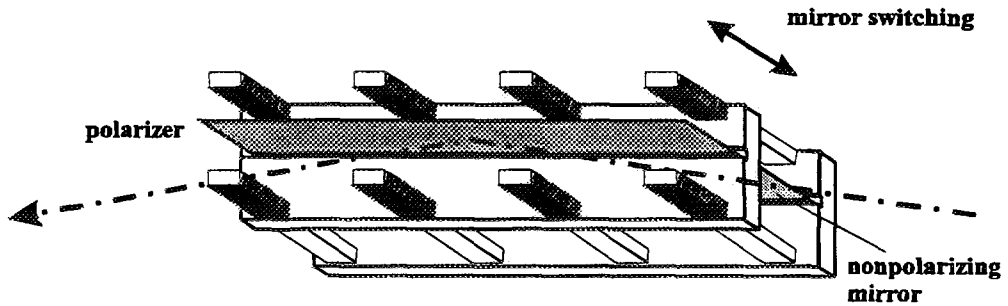


Fig. 7. Model for the principal arrangement of a polarizer and a second mirror in the deflecting unit

Parallel to a first mirror each cradle holds a second one. This can be inserted into the beam by a simple shift perpendicular to the scattering plane. With this device a deflecting mirror can be substituted by a multilayer monochromator or a polarizing mirror. Fig. 8 shows an extended reflection spectrum of a multilayer monochromator with $\Delta\lambda/\lambda = 4\%$, now in dependence of $k_z = 2\pi \sin \vartheta_i / \lambda$. The first order peak reflects neutrons with $R = 50\%$. This has been measured in a high resolution TOF mode.

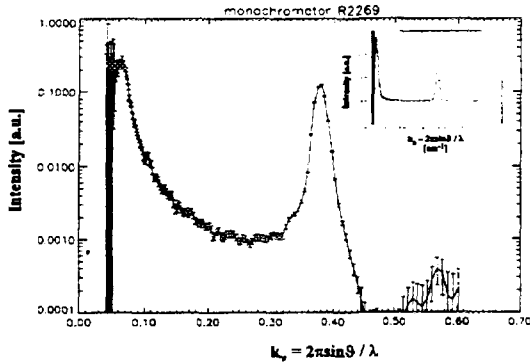


Fig. 8: Reflection from a Ni-Ti multilayer monochromator as measured in TOF mode on ROG [24.]

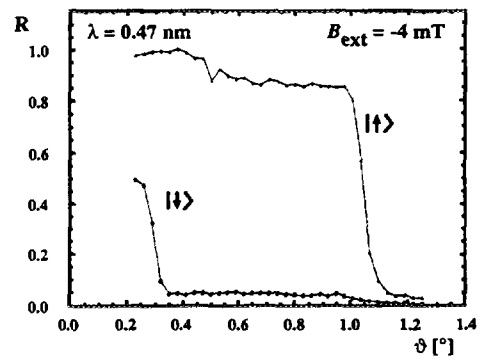


Fig. 9: Polarized neutron reflection from a 150 layer $\text{Ti}_{1-u}\text{N}_u\text{-Fe}_{0.50}\text{Co}_{0.48}\text{V}_{0.02}$ supermirrors in the remanent state [28.]

Polarizers consisting of a combination of $\text{Fe}_{0.50}\text{Co}_{0.48}\text{V}_{0.02}$ with Ti:N [28.] exhibit saturation in $B_{\text{ext}} \approx 20 \text{ mT}$. Furthermore, their magnetization stays remanent even in small oppositely oriented magnetic fields ($\sim 5 \text{ mT}$). At this stage, they perform with a flipping ratio $R_{\text{flip}} \geq 40$. Consequently, there is no need for a flipper coil in the polarized neutron option. The other spin eigenstate can be reflected just by saturating the polarizer in the opposite direction and setting the field back to the value of the guide field. The needed saturation field can be provided with a simple yoke equipped with electromagnet coils. A device similar to the described deflection unit serves as a mount for an analyzer mirror.

3.4. Collimation slits

Also running on the optical benches, precision apertures are used for the angular collimation. Vertically, they shall cover a range of 0.05 mm to 20 mm with an accuracy of 0.01 mm. Each blade is directly controlled with incremental encoders. ^6Li is the first

choice as absorber material on the blades because it gives less contribution to the radiative background.

3.5. Sample table and sample environment

An active damping system will be placed on the positioning drives of the sample manipulation table in order to disconnect the specimen from any vibration transported through the instrument. Easy handling and exchange of the specimen can be afforded for by using special mounting plates that may be inserted onto a basis support. Proposed exchange plates are: (i) A simple flat plane with some bore-holes to fix solid samples with clamps, etc. (ii) A variable sample holder for glasses, wafers, etc., where the sample is pressed against the bottom side of a clamp. It also shall allow transmission measurements. Therefore 10 mm space has to be left open underneath the body of the sample. (iii) A plate, onto which samples can be suck by exhausting the air underneath it. Similar mounts are used in the semiconductor industry. (iv) A sample exchanger of one of these types or a combination of them. Its construction shall be made in a way, that a number of samples of a maximum size of 70 mm * 120 mm can be mounted and can be automatically brought into a position, that was previously stored as a result of the alignment procedure, and (v) a trough for the reception of liquids (70 mm * 200 mm * 5 mm). Additional sample holders and compact sample environments can be produced later according to the demands of the users. Parallel to the rotation axis of the ω -circle a maximum magnetic field of $B = 1$ T shall be applicable. Additionally a superconducting magnet is purchased by our laboratory, reaching $B = 2$ T homogeneously over 25 mm. The alignment of the sample will be facilitated by a laser beam, fed in parallel to the neutron beam path at a position in front of the deflection mirrors. Furthermore, the tilting angle at the sample can be controlled by a precision inclinometer that the experimenter may attach to the sample holder.

3.6. Detectors

Two kinds of detectors are considered for the reflectometer. A position sensitive x-y-detector and alternatively a set of two single detectors. The single detectors serve as standard detectors for routine specular reflectometric measurements. If we can provide an analyzer mirror that divides the beam into two analyzed shares by reflecting one spin state and transmitting the other ($\text{Fe}_{0.89}\text{Co}_{0.11}$ -Si-supermirror [29.]) both signals can be measured simultaneously. For neutron detection in reflectometry a low background and a high thermal neutron sensitivity, combined with a good localization of the detection event is essential. In cooperation with a research group at the ILL our lab is developing ^3He microstrip detectors. With its sensitive area of 172 mm * 190 mm it can cover the reflected beam under almost all measurement conditions [30.]. A comparable but smaller device on the basis of a CCD camera coupled to a neutron sensitive luminescence film is commercially available but may cause problems with the accessible dynamic range and the

readout time. The concept of the ILL/PSI x-y-detector is the ideal solution to guarantee for alignment control with neutrons, accumulating data coming from diffuse reflectivity, reasonable spacial resolution (~2 mm), spacial separation but simultaneous acquisition of signals coming from two beams, low detector costs, high detection efficiency, high signal to noise ratio, and a large dynamic range. Suitable electronics are under development at PSI.

3.7. Optical bench

As the backbone for the intended flexibility of the reflectometer and basis for a high stability of the installation this part has to fulfil certain requirements. It shall have a very accurate slide track and effectively suppress vibrations. Blocks of synthetic granite are considered to match these items. The optical bench extends to a length of ~10 m beginning at the first collimation slits.

3.8. Software

The software requirements for this instrument are somewhat different from those useful for other instruments at SINQ. For the control of the instrument and the data treatment new software must be developed or existing software from other centers (e.g., IRI Delft) may be adapted, the agreement of the authors provided.

4. Conclusion

The concept of a new SINQ reflectometer promises to provide a modern instrument flexible enough to meet the needs of a large spectrum of polarized and nonpolarized neutron reflectometry experiments. It will be available to Swiss and international users. The operation is in time-of-flight mode but it offers an option to be converted into a monochromatic beam reflectometer using thin film multilayers as monochromators. The flexibility is achieved by means of an optical bench on which the sample manipulation table, the detector, the apertures and mirrors can be set independently. Experimental requirements to resolution and sample illumination can be matched. Recent improvements in the field of polarizing mirrors and multilayers have been implemented. The spin flipper becomes superfluous due to the magnetic hysteresis of the PSI polarizer mirrors. The installation of an ILL/PSI x-y-microstrip detector promises to fit well with the needs of diffuse neutron reflectometry. Further instrumental developments at the SINQ reflectometer should preferably flow into the enlargement of available sample environments, i.e. a cryostat, a furnace, a deposition chamber for in-situ studies of growing metallic films.

Tab. II: Main characteristics of the SINQ reflectometer

neutron guide		
cold source	D_2	
λ_{peak}	0.4 nm	
simulated peak flux	$1.8 * 10^8 \text{ ns}^{-1} \text{cm}^{-2} \text{mA}^{-1}$, for Pb target	
coating	Ni-Ti-supermirrors, $\vartheta_c = 2\vartheta_c(\text{Ni})$	
cross section	50 mm * 50 mm	
λ_c from simulation	0.1 nm	
chopper		
disks	2, side by side, phase coupled	
gating frequency	20 ... 100 Hz	
window	1 ... 20 mm	
relative distance d_{ch}	50 ... 350 mm	
frame overlap mirrors		
type	double side supermirror on Si wafer	
length	0.5 m	
cut off wavelength	~ 1.3 nm	
deflecting mirrors / polarizers		
	1 unit (see Tab. I)	supermirrors, polarizer, monochromator
collimation slits		
	slit dimensions	(0.05 ... 20 mm) * (5 ... 55 mm)
sample manipulation table		
	rotations	2 circles (ω, χ), $\pm 10^\circ$
	translations	2 directions
sample holder / exchanger		
	4 exchangeable plates &	1 automatic exchanger
sample environment		
	electromagnet	$B_{max} = 1$ T
alignment aids		
	optical	laser
	electronical	inclinometer
analyzer		
		FeCo-Si (or Ti)-supermirrors
	length	60 cm
detectors		
	^3He x-y-microstrip	172 mm * 190 mm
	^3He single detectors	2, "squashed" type
maximum sample size		150 mm * 500 mm
resolution		1.5% ... 10%
total length chopper - detector L		2.5 ... 10 m

5. References

1. See for example T.P. Russell, *Materials Science Reports* **5** (1990) 171
2. H. Kiessig, *Ann. Phys.* **10** (1931) 769
3. E. Fermi, *Collected Papers*, ed. E.Segrè (University of Chicago Press, 1962), Paper no. 217
4. E. Fermi and W.H. Zinn, *Phys. Rev.* **70** (1946) 103
5. E. Fermi and W.H. Zinn, Cambridge Conference 1947, in ref. [3], Paper No. 220
6. G.P. Felcher, R.O. Hilleke, R.K. Crawford, J. Haumann, R. Kleb, and G. Ostrowski, *Rev. Sci. Instrum.* **58** (1987) 609
7. J. Penfold, R.C. Ward, and W.G. Williams, *J. Phys. E* **20** (1987) 1411
8. A. Karim, B.H. Arendt, R. Goyette, Y.Y. Huang, R. Kleb, and G.P. Felcher, *Physica B* **173** (1991) 17
9. M. Stamm, S. Hüttenbach, and G. Reiter, *Physica B* **173** (1991) 11
10. H. Toews, *Ph.D. Thesis* (German), Techn. Univ. Berlin (1993); T. Robertson (ed.): *HMI Report* (BENSC) HMI-B 493, Hahn-Meitner-Institut Berlin (1993)
11. A.G. Klein and S.A. Werner, *Rep. Prog. Phys.* **46** (1983) 259
12. L. Nérot and P. Croce, *J. Appl. Cryst.* **7** (1974) 125
13. J. Schelten and K. Mika, *Nucl. Instrum. Meth.* **160** (1979) 287
14. O. Schärf, *Physica B* **156 & 157** (1989) 631; **174** (1991) 514
15. D. Clemens, *Ph.D. Thesis* (German), Techn. Univ. Berlin (1993)
16. T. Megademi and B. Pardo, *J. Optics* **16** (1985) 289
17. G.P. Felcher, R.O. Hilleke, R.K. Crawford, J. Haumann, R. Kleb, and G. Ostrowski, *Rev. Sci. Instrum.* **58** (1987) 609
18. S.K. Sinha, E.B. Sirota, S. Garoff and H.B. Stanley, *Phys Rev. B* **38** (1988) 2297
19. R. Pynn, *Phys Rev. B* **45** (1992) 602
20. V. Holý, J. Kubena, I. Ohlidal, K. Lischka and W. Plotz, *Phys Rev. B* **47** (1993) 15896
21. V. Holý and T. Baumbach, *Phys Rev. B* **49** (1994) 10668
22. P. Allenspach, Labor für Neutronenstreuung ETH Zürich & Paul Scherrer Institut, CH-5232 Villigen PSI
23. C. Fermon, *ILL Reflectometry Workshop*, oral presentation, Grenoble (1995)
24. V.O. de Haan, *Ph.D. Thesis*, Techn. Univ. Delft (1995), ISBN 90-73861-23-3
25. D. Clemens, *Physica B* **221** (1996) 507
26. A.A. van Well, *Physica B* **180 & 181** (1992) 959
27. P. Böni, D. Clemens, H.P. Friedli, H. Grimmer and H. Van Swygenhoven, *Lab. für Neutronenstreuung Annual Progress Report LNS-175* (1994)
28. D. Clemens, P. Böni, H.P. Friedli, R. Göttel, C. Fermon, H. Grimmer, H. Van Swygenhoven, J. Archer, F. Klose, Th. Krist, F. Mezei, P. Thomas, and H. Toews, *Physica B* **213 & 214** (1995) 942
29. T. Krist, C. Pappas, T. Keller, and F. Mezei, *Physica B* **213 & 214** (1995) 939
30. J. Schefer, P. Geltenbort, A. Oed, M. Koch, A. Isacson, N. Schlumpf and R. Thut; *Proc. Int. Workshop on Microstrip Detectors*, Legnaro, Italy, (1994)



EXTREME CONDITIONS (p, T, H)

JOEL MESOT

*Laboratory for Neutron Scattering
ETH Zürich & Paul Scherrer Institute
CH-5232 Villigen PSI, Switzerland*

ABSTRACT

The aim of this paper is to summarize the sample environment which will be accessible at the SINQ. In order to illustrate the type of experiments which will be feasible under extreme conditions of temperature, magnetic field and pressure at the SINQ a few selected examples are also given.

1. Introduction

Only about one third of the neutron scattering experiments performed at the Saphir reactor of the Paul Scherrer Institut were realised at ambient conditions. Mainly low temperature ($T < 10$ K) was needed for magnetic studies and accurate structural studies.

Variation of temperature, pressure or magnetic field may strongly affect the interatomic or magnetic interactions. The modification of the corresponding potentials can lead either to simple changes like rotation of atomic groups or magnetic moments, or to drastic changes like phase transitions to energetically more favourable (nuclear or magnetic) structures. The structural changes may also affect electronic interactions which might induce electronic transitions, particularly when competing interactions are involved.

It is therefore extremely desirable to determine the (magnetic) structures and their corresponding excitations in the whole (p, T, H) diagram. Of course some practical limitations define the area accessible experimentally. On one hand the deeply penetrating characteristics of the neutrons render transparent most of the sample environments. On the other hand rather large sample volumes ($\approx \text{cm}^3$) are needed for neutron scattering experiments, which imposes severe constraints on, e.g., the highest pressure achievable or the magnetic field and temperature homogeneities.

2. Temperature

3.1 Low Temperature

The study of magnetic systems usually requires measurements on a wide temperature range since the strength of the magnetic interactions covers many decades, e.g.:

Nuclear dipole-dipole coupling	$\approx n\text{K}$	
Hyperfine coupling	$\approx m\text{K}$	($1 \text{ meV} \approx 11.6 \text{ K}$)
electronic dipole-dipole coupling	$\approx \text{K}$	
electronic exchange coupling	$1 - 1000 \text{ K}$	

While only very few exotic experiments have been performed in the nK temperature range [1], the demand is much larger for mK temperatures, which can be routinely achieved

with ^3He - ^4He dilution refrigerators (Fig.1). Above 1.2 K liquid ^4He cryostats can be used, while above 10K closed cycle ^4He gas compressors (Displex) are sufficient.

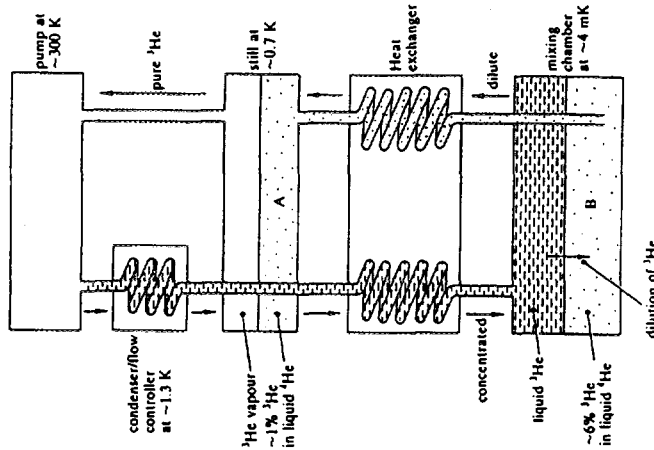


Fig.1: Layout of components in conventional dilution refrigerator (for more details see ref [2])

A good example of how several competing magnetic-interactions develop as a function of temperature is given by the NdNiO_3 perovskite. The temperature dependence of the magnetic Bragg peaks have been measured between 300 K and 10 mK. First the Ni moments order at about 250 K, as shown by the appearance of the 111 reflection. The intensity increases until the magnetic moment has saturated. Around 20 K additional intensity is observed (Fig. 2) due to the polarisation of the Nd atoms by the Ni atoms [3]. Finally, a third increase of the intensity has been observed below 200 mK (see insert of Fig. 2), because of the polarisation of the Nd-nuclei through the hyperfine interaction [3]. A similar behaviour has also been observed in NdGaO_3 [4].

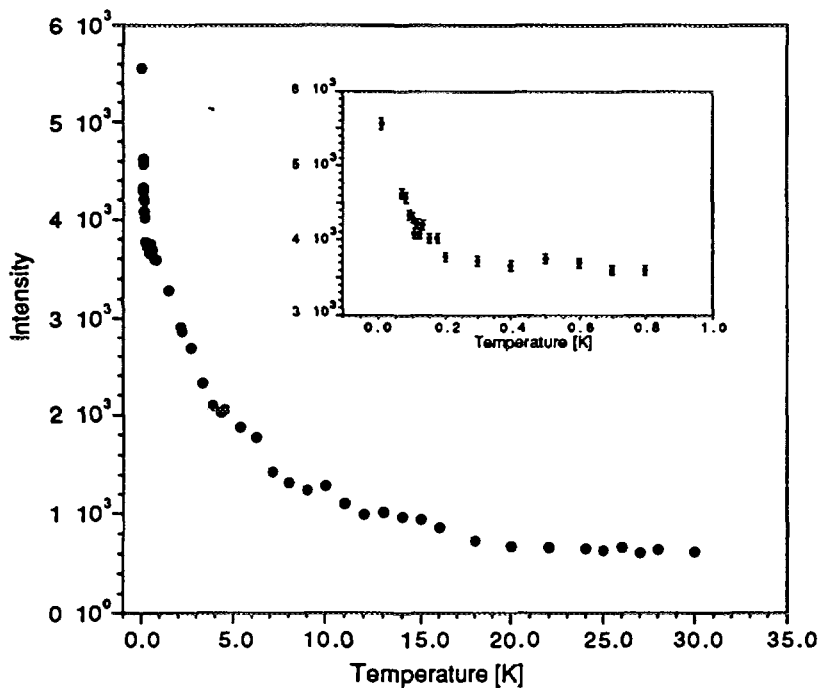


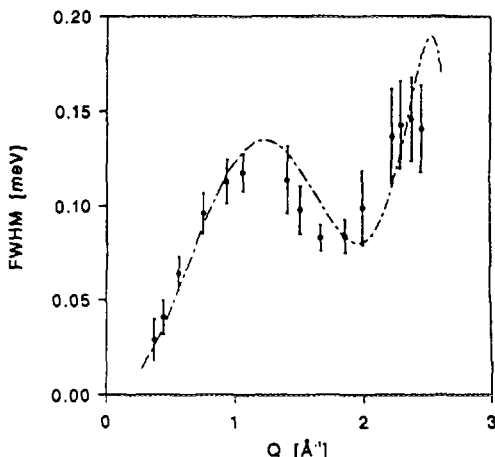
Fig.2: Thermal evolution of the integrated intensity of the 111 magnetic reflection in NdNiO_3 .

3.2 High Temperature

Since most metals have an appreciable neutron absorption, the heater element and heat shields have to be carefully chosen with respect to their absorption and their finite lifetime due to evaporation at the highest temperatures. Furthermore a large number of heat shields are necessary to reduce radiation losses. Care must also be taken to avoid reactivity between sample and container materials at high temperatures. Most metals soften well below their melting points, and some have the tendency to recrystallise at high temperatures (e.g. tantalum). Niobium is the best candidate for furnace components subject to the highest temperatures.

Interesting systems for high temperature studies are the ionic conductors. Li_2S for example shows a sudden increase of conductivity above 800 K, due to an increasing mobility of the Li ions. The temperature dependence of the diffusion process has been investigated by quasielastic incoherent neutron scattering [5]. The Q dependence of the halfwidth of the quasielastic line (Fig.3) enabled the authors to determine the jump vectors and the jump rates of the Li ions.

Fig.3: Experimentally determined halfwidths for Li_2S as a function of Q at 1170 K fitted with one Lorentzian. The dashed line is a calculation using the Chudley and Elliott model [5]. The data have been taken on the D7-spectrometer (ILL) using a single crystal.



3. Pressure

It is obviously clear that a high pressure cell for neutron scattering must be a compromise between highest attainable pressure P_{\max} and largest sample volume V_{\max} . This is due to the limited energy product $P_{\max} \cdot V_{\max}$ which can be supported by the pressure cell. This compromise must be worked out individually for each pressure cell. For pressure lower than 10 kbar a cylindrical pressure cell and helium gas as the pressure transmitting medium can be used (Fig. 4a). The pressure remains hydrostatic down to very low temperatures. Such a cell allows also an *in situ* change of both pressure and temperature. Above 10 kbar the only successful type of pressure cell for reasonable sample volume ($> 0.5 \text{ cm}^3$) turns out to be the supported piston cylinder cell (Fig. 4b). Fluorinert has to be used as a transmitting medium. Although fluorinert solidifies very rapidly with increasing pressure, it remains amorphous in the solid state. Such a cell does not allow changes of pressure *in situ*, however it can be designed to have a 2π access in the horizontal plane [6].

An additional problem occurs for high pressure experiments on powder diffractometers equipped with multidetectors since, with conventional materials like steel or aluminum, the diffraction data contain Bragg scattering from the cell itself. These unwanted reflections can be order of magnitudes larger than the reflections from the sample, thus rendering impossible a precise structure refinement. In order to avoid this problem, one can use a

zero-matrix pressure cell made of an alloy of Ti and Zr. Having coherent scattering lengths of opposite sign, it is possible to prepare a material whose averaged coherent scattering length is equal to zero [7]. No Bragg reflections from the pressure cell will then contribute to the diffraction pattern. The price to pay is an increase of the background due to incoherent scattering. Very high pressure diffraction experiments (> 100 kbar) on powders can only be achieved either at pulsed neutron sources or on Fourier diffractometers. In both cases the 90° scattering geometry can be used to perfectly collimate the beam in such a way that any scattering from the pressure cell can be excluded [8].

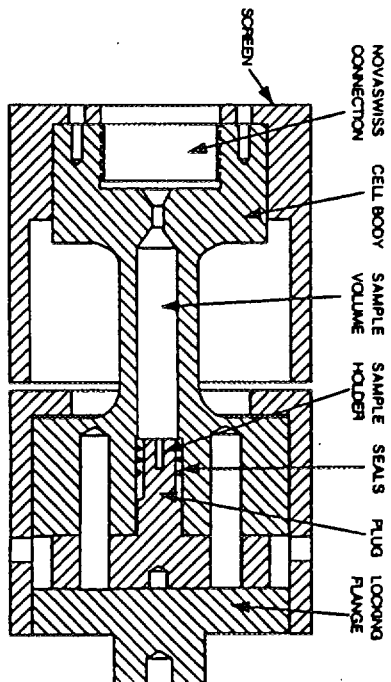


Fig.4a: Helium gas cell

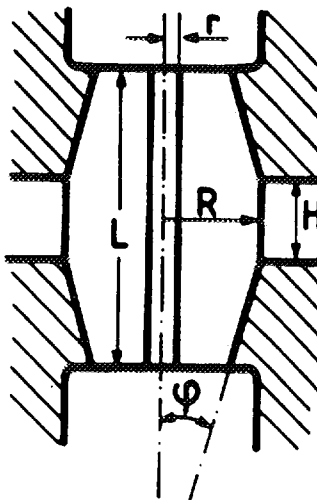


Fig.4b: Characteristic shape of the supported piston cylinder cell

The feasibility of high pressure experiments at medium neutron fluxes is demonstrated by the structural study of PrNiO_3 up to 5 kbar and down to 5 K. These perovskites (see paper by Medarde in these proceedings) show a strong decrease of the metal-insulator transition temperature T_{MI} under external pressure ($dT_{MI}/dp \approx -4$ K/kbar). A diffractogram measured on the DMC diffractometer at the Saphir reactor is shown in Fig. 5. The data analysis reveals that the superexchange angle Ni-O-Ni increases with pressure [9]. This flattening of the Ni-O-Ni bond may indeed induce a broadening of the O-2p band and thus stabilizes the metallic state. In addition the measurements performed at 5 kbar and 5 K strongly suggest that the Ni-magnetic structure remains unchanged at 4.7 kbar (insert in Fig. 5). This result is very difficult to reconcile with the reentrant metallic behaviour reported in the resistance measurements [10]. Actually, very few high pressure studies on magnetic materials have been reported so far.

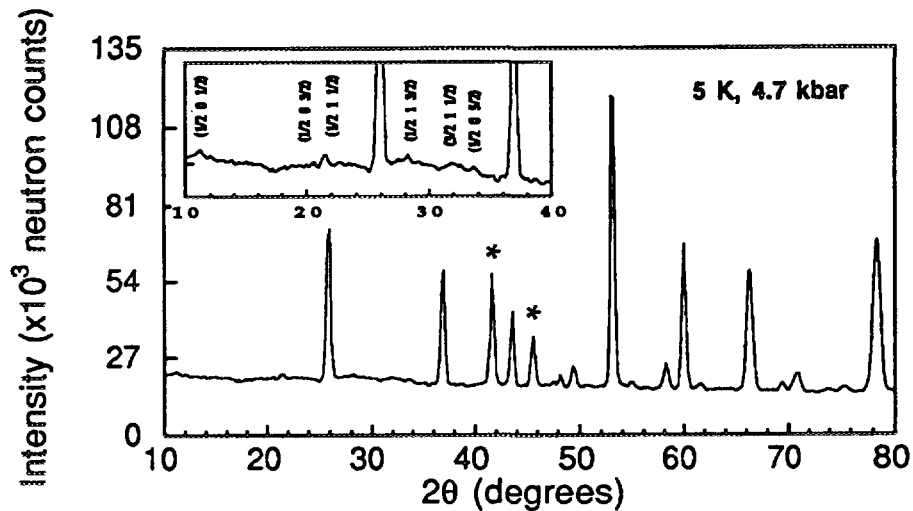


Fig.5: Neutron powder-diffraction pattern of PrNiO₃ taken on the DMC (Saphir-PSI). The peaks marked with an asterisk are the (100) and (101) reflections of solid helium.

4. Magnetic field

The use of magnetic fields in neutron scattering experiments can be divided into two, not necessarily mutually exclusive, areas. In one area, a field interacts directly with the neutron. The most prominent examples are the polarisation analysis and neutron spin-echo technique. In the other area, which we shall discuss in more detail, a field is applied to modify the properties of the scattering sample. This modification may manifest itself in a variety of ways. Magnetically ordered compounds are often in a multidomain state. By application of an external magnetic field a single domain state can be created which is highly advantageous for a rigorous data interpretation (see Fig. 6) [11]. Magnetic fields can also be used to induce magnetic phase transitions as observed, e.g. in holmium phosphide [12]. In the area of inelastic scattering the application of a magnetic field is for instance indispensable for the observation of solitons [13].

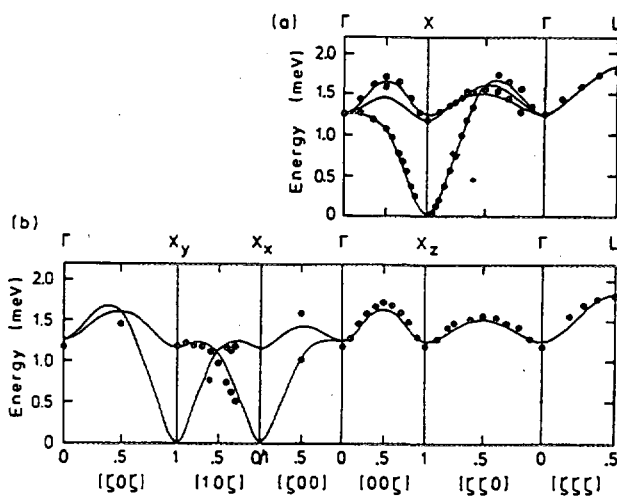


Fig.6: Dispersion curves of the spin-wave excitations in CeAs at T=4.2 K:
a) in the multidomain state (H=0); b) in the z-domain state (H_z = 4 Tesla).

For fields lower than 1 Tesla, electromagnets can be used, while at higher fields superconducting magnets are necessary. In most cases superconducting magnets are fabricated with multifilamentary NbTi wires. This alloy has a critical field of about 10 T at 4.2 K. The experimentalist usually requires access to the horizontal plane for incident and scattered neutron beams, together with vertical access for the sample. This can be achieved by means of the split pair configuration shown in Fig.7. In addition, an asymmetric geometry can be designed in order to prevent the neutron beam to pass through any field nodes. The bore diameter must be on the one side sufficiently large to accommodate for cryostats or furnaces, and on the other side small enough to fulfil the field homogeneity requirements. In order to support the extremely large forces generated by superconducting magnets a set of wedges are required, however, the "dark angles" have to be carefully minimized.

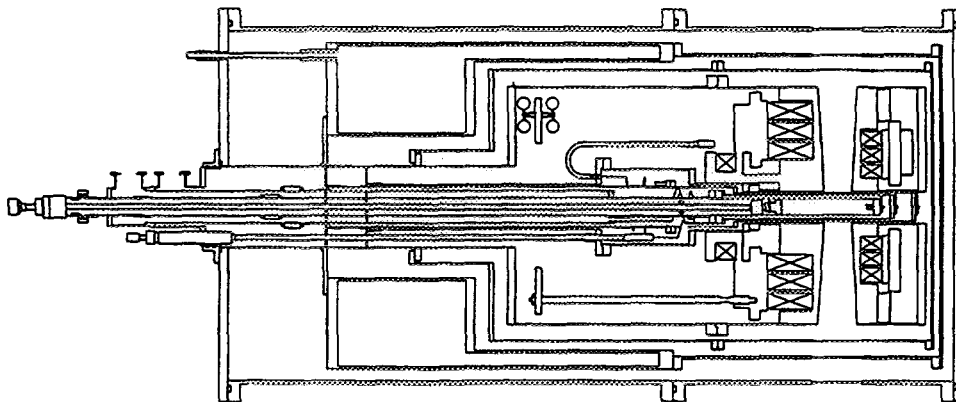


Fig.7: 6 Tesla asymmetric split pair superconducting magnets for neutron scattering (taken from Ref. 14).

5. Ancillary equipment at SINQ

	Description	Range	Availability
a) <u>Temperature</u>			
	Displex helium refrigerator (4)	10 K $\leq T \leq$ 300 K	now
	^4He cryostat (2)	1.5 K $\leq T \leq$ 300 K	now
	Dilution cryostat	7 mK $\leq T \leq$ 1.4 K	now
	Dilution insert	50 mK $\leq T \leq$ 300 K	1998
	Cryo-furnace	1.5 K $\leq T \leq$ 600 K	1997
	Furnace	300 K $\leq T \leq$ 800 K	now
	Furnace	300 K $\leq T \leq$ 1400 K	now
	Furnace	300 K $\leq T \leq$ 2100 K	now
b) <u>Pressure</u>			
	Uniaxial pressure device	$F \leq$ 1 ton	now
	Ti-Zr cell (He gas)	$P \leq$ 10 kbar	1998
	Al_2O_3 cell (He gas)	$P \leq$ 10 kbar	1998
	Clamp / liquid cell (fluorinert)	$P \leq$ 20 - 30 kbar	1998

c) Magnetic fields

Superconducting magnet	$H \leq 5$ Tesla vertical or 5 Tesla horizontal $1.5 K \leq T \leq 300 K$	now
Superconducting magnet	$H \leq 6$ Tesla vertical and 2 Tesla horizontal ($50 mK \leq T \leq 800 K$)	1997

6. Acknowledgements

The author thanks Dr Medarde and Prof. Furrer for the careful reading of the manuscript.

7. References

- 1 M. Steiner, Int. J. Mod. Phys., **B7** (1993) 2909.
- 2 D. S. Betts, *An introduction to the millikelvin technology* (Cambridge University Press, Cambridge, 1989).
- 3 S. Rosenkranz, private communication.
- 4 W. Marti, M. Medarde, S. Rosenkranz, P. Fischer and A. Furrer, Phys. Rev. B **52** (1995) 4275.
- 5 F. Altorfer, W. Bührer, I. Anderson, O. Schärf, H. Bill, P. L. Carron and H. G. Smith, Physica B **180 & 181** (1992) 795.
- 6 D. B. McWhan, C. Vettier, R. Youngblood and G. Shirane, Phys. Rev. B **47** (1979) 296.
- 7 J. Mesot, M. Medarde, S. Rosenkranz, P. Fischer, P. Lacorre and K. Gobrecht, High Pressure Research **14** (1995) 35.
- 8 J. M. Besson, S. Klotz, G. Hamel, I. Makarenko, R. J. Nelmes, J. S. Loveday, R. M. Wilson and W. G. Marshall, High Pressure Research **14** (1995) 1.
- 9 M. Medarde, J. Mesot, P. Lacorre, S. Rosenkranz, P. Fischer and K. Gobrecht, Phys. Rev. B **52** (1995) 9248.
- 10 X. Obradors, L. M. Paulius, M. B. Maple, J. B. Torrance, A. I. Nazzal, J. Fontcuberta and X. Granados, Phys. Rev. B **47** (1993) 12353.
- 11 B. Hälg, A. Furrer, J. K. Kjems and O. Vogt, Phys. Rev. Lett., **50** (1983) 1085.
- 12 P. Fischer, A. Furrer, E. Kaldis, D. Kim, J. K. Kjems and P. M. Levy, Phys. Rev. B **31** (1985) 456.
- 13 J. K. Kjems and M. Steiner, Phys. Rev. Lett. **41** (1978) 1137.
- 14 T. E. Wood, Revue Phys. Appl. **19** (1984) 685



DYNAMIC NUCLEAR SPIN POLARIZATION

H.B. STUHRMANN

GKSS Forschungszentrum, D-21502 Geesthacht, Germany

ABSTRACT

Polarized neutron scattering from dynamic polarized targets has been applied to various hydrogenous materials at different laboratories. In situ structures of macromolecular components have been determined by nuclear spin contrast variation with an unprecedented precision. The experiments of selective nuclear spin depolarisation not only opened a new dimension to structural studies but also revealed phenomena related to propagation of nuclear spin polarization and the interplay of nuclear polarisation with the electronic spin system. The observation of electron spin label dependent nuclear spin polarisation domains by NMR and polarized neutron scattering opens a way to generalize the method of nuclear spin contrast variation and most importantly it avoids precontrasting by specific deuteration. It also likely might tell us more about the mechanism of dynamic nuclear spin polarisation.

1. The Importance of Scattering Lengths

The interaction of thermal neutrons with hydrogen nuclei shows several peculiarities which give rise to numerous applications in biological structure research. In the case of neutron scattering by protons the scattering length strongly depends on the spin (S) of the compound nucleus formed: $b_{(+)}$ with $S = 1/2 + 1/2$ is 1.08×10^{-12} cm whereas a negative scattering length $b_{(-)}$ of -4.7×10^{-12} cm is observed with $S=1/2-1/2$. Spin dependent scattering is nothing unusual. The difference is that the effect is very large and most importantly about half of the atoms in biological samples are hydrogens. The heavier isotope of hydrogen, ^2H (Deuterium) with its spin 1 changes the scattering length much less and in this respect it hardly differs from other non-spinless nuclei (Glättli & Goldman).

The large difference between $b_{(+)}$ and $b_{(-)}$ of protons is the reason for a large cross section of incoherent scattering of 80 barns ($= 3\pi/4 (b_{(+)} - b_{(-)})^2$) when both the incident neutron beam and the proton spins of the sample are unpolarized. The cross section varies with the mutual polarisation of the interacting particles. There is no incoherent scattering when both the incident neutron beam and the proton spins of the sample are completely polarized in the same direction with respect to an external magnetic field. There is an even increased cross section of incoherent scattering of 105 barns when the completely polarized neutrons encounter proton spins in opposite direction. This is the reason why proton spin targets are efficient neutron spin

filters (or neutron spin 'polarizers') (Koghi, Ishida, Ishikawa, Ishimoto, Kanno, Masaike, Masuda & Morimoto, 1987).

In biological and polymer structure research it is the scattering amplitude of coherent scattering b_{coh} which is interest. b_{coh} is the weighted average of $b_{(+)}$ and $b_{(-)}$. For protons, it amounts to -0.374×10^{-12} cm. It shares its negative value with rather few of other nuclei, none of them being of biological importance. Hence the scattering length of protons is rather unique among the other nuclei occurring in living matter. b_{coh} of the latter varies between 0.58 (oxygen) and 0.95×10^{-12} cm (nitrogen). Carbon just falls between these two values as does deuterium. The substitution of protons by deuterons changes b_{coh} of hydrogen by 0.69×10^{-12} cm. This is the most frequently used method of isotopic substitution in biological structure research. Moreover, b_{coh} of polarized neutron scattering varies with the polarization of the proton spins from $(-0.374 + 1.456) \times 10^{-12}$ cm = 1.08×10^{-12} cm ($= b_{(+)}$) to $(-0.374 - 1.456) \times 10^{-12}$ cm = -1.87×10^{-12} cm (NOT equal to $b_{(-)}$). The change of b_{coh} induced by proton spin polarization is about three times more efficient than with isotopic substitution. This is the basis of nuclear spin contrast variation.

2. Contrast Variation

The properties of coherent scattering from protons look very attractive whereas the large incoherent scattering is a nuisance in structural studies. This is one of the reasons why biological samples for neutron scattering are always deuterated to some extent, since ^2H has a relatively small cross section of incoherent scattering of 2 barn only. Another reason is the creation of contrast. This is done by specific exchange of protons by deuterons (H/D exchange).

The easiest and mostly used method is the exchange of light water (H_2O) by heavy water (D_2O). Samples with different D_2O content are measured by neutron scattering. The intensity of scattered neutrons changes with the D_2O content. At low momentum transfer, i.e. at low structural resolution, it may appear that there is no coherent neutron scattering at some $\text{H}_2\text{O}/\text{D}_2\text{O}$ ratio. At this point the scattering density of the solute is equal to that of the solvent. There is no contrast and hence there is no small-angle scattering. This happens with proteins in 40% D_2O and ribonucleic acids loose their contrast in 70% D_2O , for instance. In this way the components of complex composite particles like nucleoproteins (viruses, ribosomes, chromatin), lipoproteins or glycoproteins can be analyzed. This method is called EXTERNAL contrast variation. It leads to models with a modest structural resolution comparable to the particle

radius. This is so, as the change in contrast is uniform in the whole particle volume, i.e. the volume of the particle is acting as a label.

INTERNAL contrast variation starts from labels which are much smaller than the total particle. They provide a better starting point for a more detailed structural analysis. The preparation particles with selectively deuterated components is less wide-spread as it is more difficult. It may start from cells which grow in heavy water (Vanatalu, Paalme, Vilu, Diedrich, Jünemann, May, Rühl, Wadzack & Nierhaus, 1993). The relevant deuterated components are isolated. Similarly the protonated components are obtained from cell grown in normal media. The reconstitution of complex particles starts from an ensemble of carefully chosen deuterated and protonated components(Nierhaus, Lietzke, May, Nowotny, Schulze, Simpson & Wurmbach, 1983). The magic of self-assembly does the rest. The result is a specifically deuterated particle, e.g. a deuterated functional complex of the ribosome with two protonated transferRNAs.

The advantage of a small labelled region in a complex structure is considerable. The neutron scattering data are most sensitive to the structure of the label. The influence of the total structure on the intensity of neutron scattering is kept small or it may be eliminated completely by some clever strategy. This is the starting point of various methods to determine the *in situ* structure of labelled regions in large biomolecules.

3. The *in situ* structure

Let M be the amplitude of the total unlabelled particle and L be the amplitude of the label, the IN SITU structure of which is to be determined. Then the intensity of coherent scattering is given by

$$|M + L|^2 = |M|^2 + 2 \operatorname{Re}\{ML^*\} + |L|^2 \quad (1)$$

The direct approach is eliminate the contrast which gives rise to the amplitude M . If the scattering density distribution of the particle is uniform contrast variation in H_2O/D_2O will do. When the particle is consisting of chemically different components, like proteins and nucleic acids then there is no way to match the scattering density of proteins and RNA simultaneously. There are two ways to proceed: either the scattering densities of proteins and RNA are made equal by restricted deuteration - the glassy ribosome is an example [2] - or one varies the contrast of the labels by stepwise deuteration (x):

$$|M + xL|^2 = |M|^2 + 2x \operatorname{Re}\{ML^*\} + x^2 |L|^2 \quad (2)$$

The scattering intensity of the label $|L|^2$ can be obtained by collecting data at three different x . A variant of this method is better known as TIS which stands for triple isotopic substitution (Serdyuk & Pavlov, 1988)

Small deuterated labels became popular with label triangulation. A solution of particles containing two labels (amplitudes L_1 and L_2) at distance d give rise side to a neutron scattering profile $I(Q)$ described by:

$$I(Q) \approx 2 + \sin(dQ) / dQ \quad (3)$$

Q = is the momentum transfer. To obtain the second term in (3) four samples differing in the deuteration of the labels had to be prepared. The cross term $L_1 L_2$ resulting from $|L_1 + L_2 + M|^2 - |L_1 + M|^2 - |L_2 + M|^2$ reflects the use of one undeuterated and three specifically deuterated samples. At small Q , $L_1 L_2$ is well approximated by $\sin(dQ) / dQ$, where d is the distance between the labels L_1 and L_2 . From a sufficient number of inter-label distances $d_{L_i-L_j}$ the spatial arrangement of the labels inside the total particle can be obtained. The determination of the location of all 21 ribosomal proteins of the small subunit of E.coli ribosomes is the best known result of the triangulation method (Capel, Engelman, Freeborn, Kjeldgaard, Langer, Ramakrishnan, Schindler, Schneider, Schoenborn, Sillers, Yabuki, & Moore, 1988).

TIS and the label triangulation method eliminate the crossterm $2\operatorname{Re}\{ML^*\}$ in (2). The structure of the total particle does not need to be known. On the other side, the total structure is a reality. Its mere existence means that it has a center of mass. Hence, the distance between the center mass of the label and that of the total structure may be derived from the product of the amplitudes ML^* . At this stage, no information about the structure of the total particle is required. In many cases the shape of large biomolecules is known from electron microscopy at admittedly modest resolution. This structural information defines the amplitude M , which is considered as known. The amplitude L is the unknown to be determined from the neutron scattering data. As L is defined in the coordinate system of the total particle, the knowledge of L provides both the location and the shape of the labelled component.

4. An Example: The functional Complex of the Ribosome.

The correlation between the label and the total particle is most easily obtained from nuclear spin contrast variation. This will demonstrated for the functional complex of the deuterated ribosome with two bound protonated transfer ribonucleic acids (tRNA) (Nierhaus, Wadzack, Burkhardt, Jünemann, Frank, Meerwinck, Schmitt & Stuhrmann, 1996). The amplitude of the unpolarized sample is

$$U = C_M M + C_L L \quad (4a)$$

As the ribosome is dissolved in a mixture if deuterated glycerol and heavy water the contrast C_M is small, whereas that of the protonated label C_L is strongly negative as can be deduced from the scattering lengths given above. When the proton spins are polarized an additional amplitude V_H develops

$$V_H = {}^H C_M M + {}^H C_L L \quad (4b)$$

Again the contrast ${}^H C_M$ is weak as there are only few protons in the deuterated particle and deuterated solvent left, whereas ${}^H C_L$ is very large and positive as the label is protonated. ${}^H C_M$ and ${}^H C_L$ refer to completely polarized targets. As the volume of the label is 3% of that of the total particle the amplitudes are comparable at small Q . Similarly holds for for the deuteron spin target of the same sample:

$$V_D = {}^D C_M M + {}^D C_L L \quad (4c)$$

The intensity of polarized neutron scattering varies with the polarization of the neutron spins and the nuclear spins, P (Abragam & Goldman, 1982):

$$I = |U|^2 \pm 2P \operatorname{Re}\{UV^*\} + P^2 |V|^2 \quad (5)$$

V may be V_H or V_D when one of the isotopes is selectively depolarized or $V_H + V_D$ in the case of the dynamic polarized target. The polarization direction of the completely polarized neutron beam is assumed to be either parallel (+) or antiparallel (-) to the external magnetic field. From the difference of the neutron scattering intensities measured at different polarizations of the neutron spins one obtains the crossterm $\operatorname{Re}\{UV^*\}$. The sum of the same

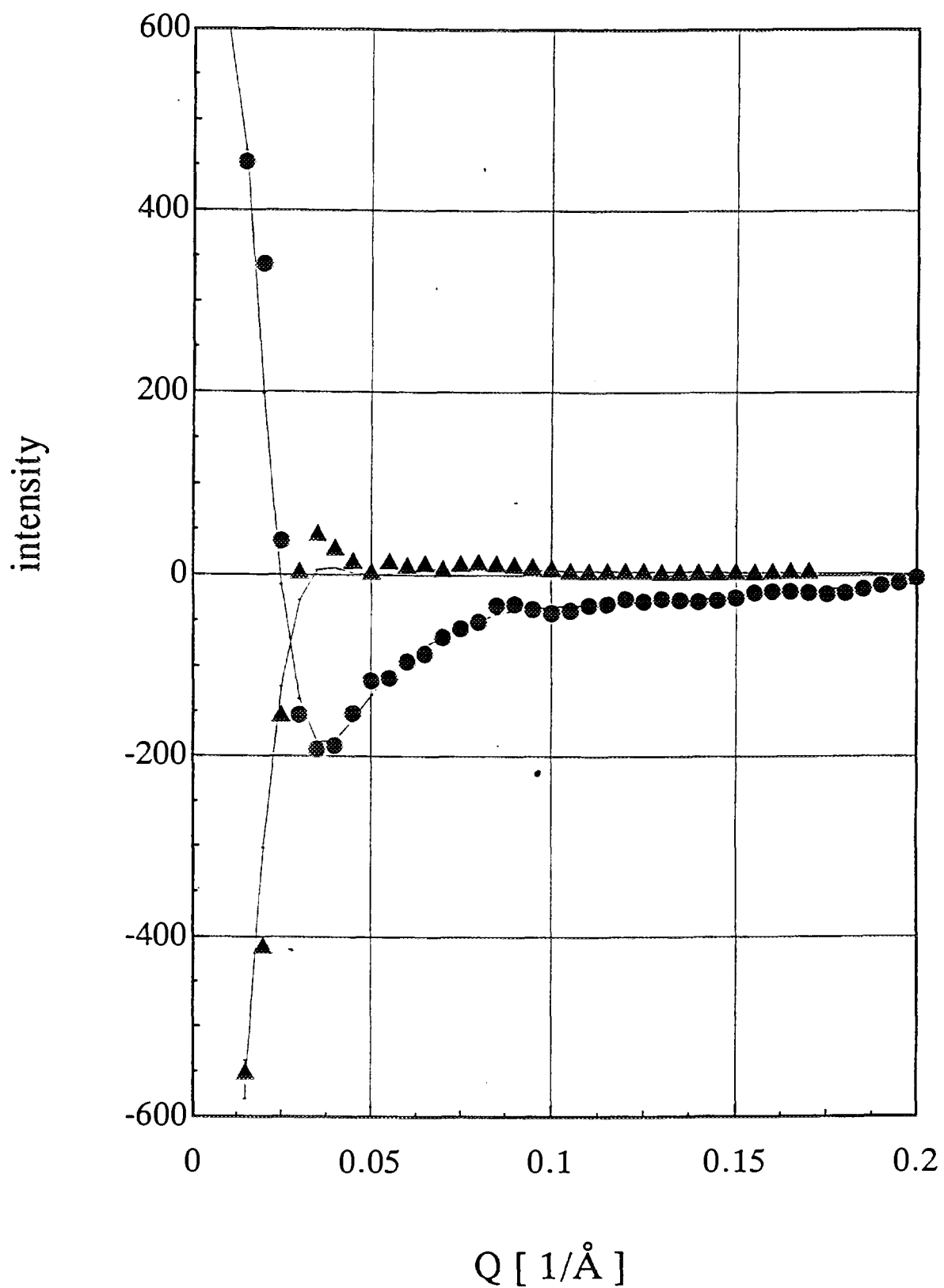


Fig. 1 The cross terms $2 \operatorname{Re}[\text{UVH}^*]$ of proton spin contrast variation (●) and $2\operatorname{Re}[\text{UVD}^*]$ of deuteron spin contrast variation (▲).

two sets of data yields $|V|^2$ as $|U|^2$ is observed at $P=0$. Fig.1 shows the basic scattering function $2\text{Re}[\text{UV}_H^*]$ of proton spin contrast variation and the corresponding function $2\text{Re}[\text{UV}_D^*]$ of deuteron spin contrast variation obtained from the specifically deuterated functional complex of the ribosome.

The striking difference between these functions needs some considerations. Both functions are cross terms and therefore they are not directly measurable but obtained as differences. As such they may be positive or negative at any momentum transfer Q . $\text{UV}_D(0)$ is negative. Hence, either $U(0)$ and $V_D(0)$ must have opposite signs. It can be shown that the number density of deuterons in perdeuterated proteins and perdeuterated nucleic acids is always lower than in heavy water. i.e. the deuteron spin contrast is negative. Hence $V_D(0) < 0$ and $U(0) > 0$. The average scattering density of the ribosome in the unpolarized state is higher than that of the deuterated solvent and even hides the negative contrast of the unpolarized protonated tRNA. As $\text{UV}_H(0)$ is positive $V_H(0)$ must have the same sign. This means that the number density of protons in the deuterated ribosome is (slightly) higher than that of the deuterated solvent. Also the profile of these cross terms looks very different: There is a sharp decrease of the intensity to almost zero which is typical of shape scattering of the ribosome. The weak deuteron polarization dependent contrast ${}^D\text{C}_L$ of the label is due to the very low deuteron concentration on the protonated label. This is different for $2\text{Re}[\text{UV}_H^*]$ where the polarized proton spins of the protonated tRNA give rise to a significant contribution the cross term which is well visible at $Q > 0.04 \text{ \AA}^{-1}$.

The analysis of the basic scattering functions starts from the known shape of the ribosome which enters into M (e.g from electron microscopy: Frank, Penczek, Grasucci & Srivastava, 1991). The contrast of both the deuterated ribosome and the protonated label are known from the chemical composition and the degree of deuteration of the ribosome and of its label respectively. The structure of the label giving rise to L is represented by a simple model, usually as a sphere to start with. In a first step, the coordinates of the center of the label with respect to the ribosome will have to be determined. This done by systematic search in the whole volume of the ribosomal particle which may require a long computing time. The criterium is given by the agreement of the calculated scattering intensity (5) with the basic scattering functions deduced from the experimental data.

There are two tRNAs bound to the ribosome, the center of mass of which is now known. The structure of tRNA is known to atomic resolution (Sussman, Holbrook, Warrant, Church & Kim, 1978). Moreover, the mutual arrangement of the tRNAs is to some extent restricted by functional aspects (Lim, Venclovas, Spirin, Brimacombe, Mitchell & Müller, 1992): Both the anticodons and the opposite ends of the tRNAs must be close to each other. The definition

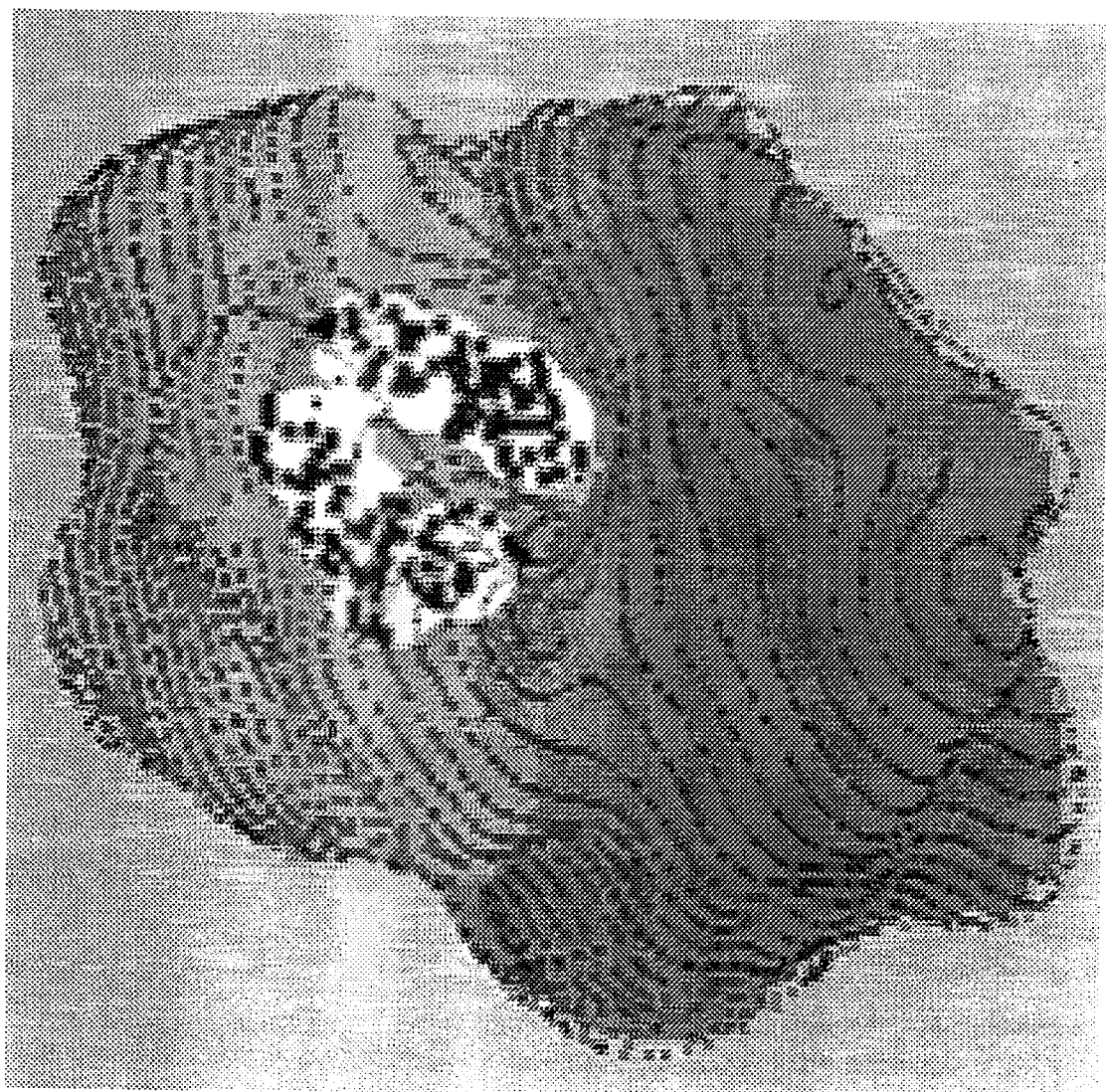


Fig. 2

The binding site of the complex of the 2 tRNAs inside the ribosome. The analysis of the polarized neutron small-angle scattering data is restricted to the determination of the coordinates (x, y, z) of the center of mass of the 2 tRNAs with respect to the ribosome, the Euler angles (α, β, γ) defining the orientation of the 2 tRNAs and the angle of mutual orientation of the tRNAs. All other structural details of the model are taken from other sources.

of these two quasi-connections still allows for different mutual orientations of the tRNAs which is intimately correlated with the function the ribosome, the biosynthesis of proteins. The orientation of the tRNAs with respect to the ribosome given by three Eulerian angles and the mutual of the tRNA (one angle) are determined from a further minimization of the difference of the calculated scattering intensity (5) from the measured ones. In order to speed of this procedure the amplitudes in (4) are developed as spherical harmonics (Stuhrmann, 1993; Stuhrmann, Burkhardt, Diedrich, Jünemann, Meerwinck, Schmitt, Wadzack, Willumeit, Zhao & Nierhaus, 1995). The result of this approach is shown in Fig. (2).

5. Spin Label Bound Nuclear Polarization Domains

Although the method of nuclear spin contrast variation is extremely powerful and highly beneficial to structural studies on macromolecules its use is limited to those cases where specifically deuterated samples are available and the additional structural information from neutron scattering is really needed. The field of applications could probably be enlarged considerably if the obligatory deuteration could be avoided. The way to do this has been discovered accidentally during the attempt to depolarize proton spins by NMR saturation, when it turned out that proton spins near paramagnetic centers behave differently (Stuhrmann et al., 1995)

To explain this phenomenon it is important to remember that the method of dynamic nuclear polarization (DNP) is used. In the presence of paramagnetic centers (e.g. EHBA-Cr(V), for the synthesis see: Krumpolc, de Boer & Rocek, 1978), at $B = 2.5$ T and $T < 1$ K the irradiation of 4 mm microwaves polarizes all non-spinless nuclei to a degree which is related to the nuclear magnetic momentum. Solutions of biological material are best prepared in mixtures of glycerol and water (11:9) which solidify as a glass when shockfrozen in a liquid nitrogen cooled copper mold (Douzou, 1977). For polymers ortho terphenyl is a convenient solvent (Glättli, Fermon & Eisenkremer, 1989).

The polarization of proton spins in biological targets reaches about 70% to 80% while the polarization of deuterons stays at 20% and that of the nitrogen nuclei at 10% the nuclear spin temperature being equal in all spin systems.

In a further step - when the microwaves are switched off and the temperature of the sample has dropped to about 0.1 K an rf-sweep of 200 kHz width across the NMR profile of the polarized proton spins at 106.4 MHz erases the NMR profile. The effect is also observed with polarized neutron scattering which quite unexpectedly shows only half the expected change. Prolonged

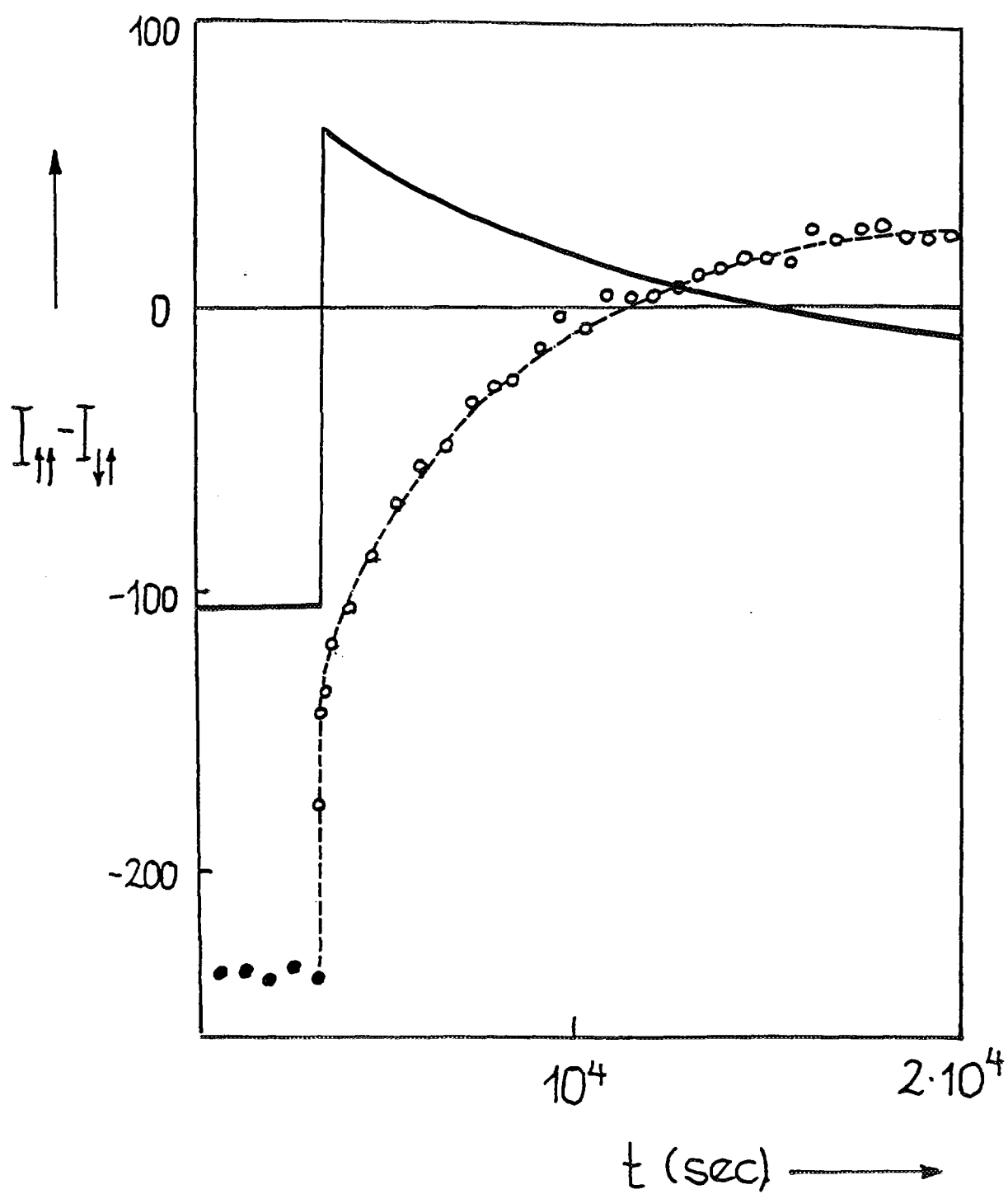


Fig. 3.

Time dependence of proton spin polarization as observed by proton NMR (—) and by neutron polarisation dependent scattering ($I_{\uparrow\uparrow} - I_{\downarrow\downarrow}$) (-o-o-). AFP is applied at $t = 3 \times 10^3$ s. The proton spin polarization then jumped from -0.56 to +0.34. The degree of deuteration of the sample was 98%.

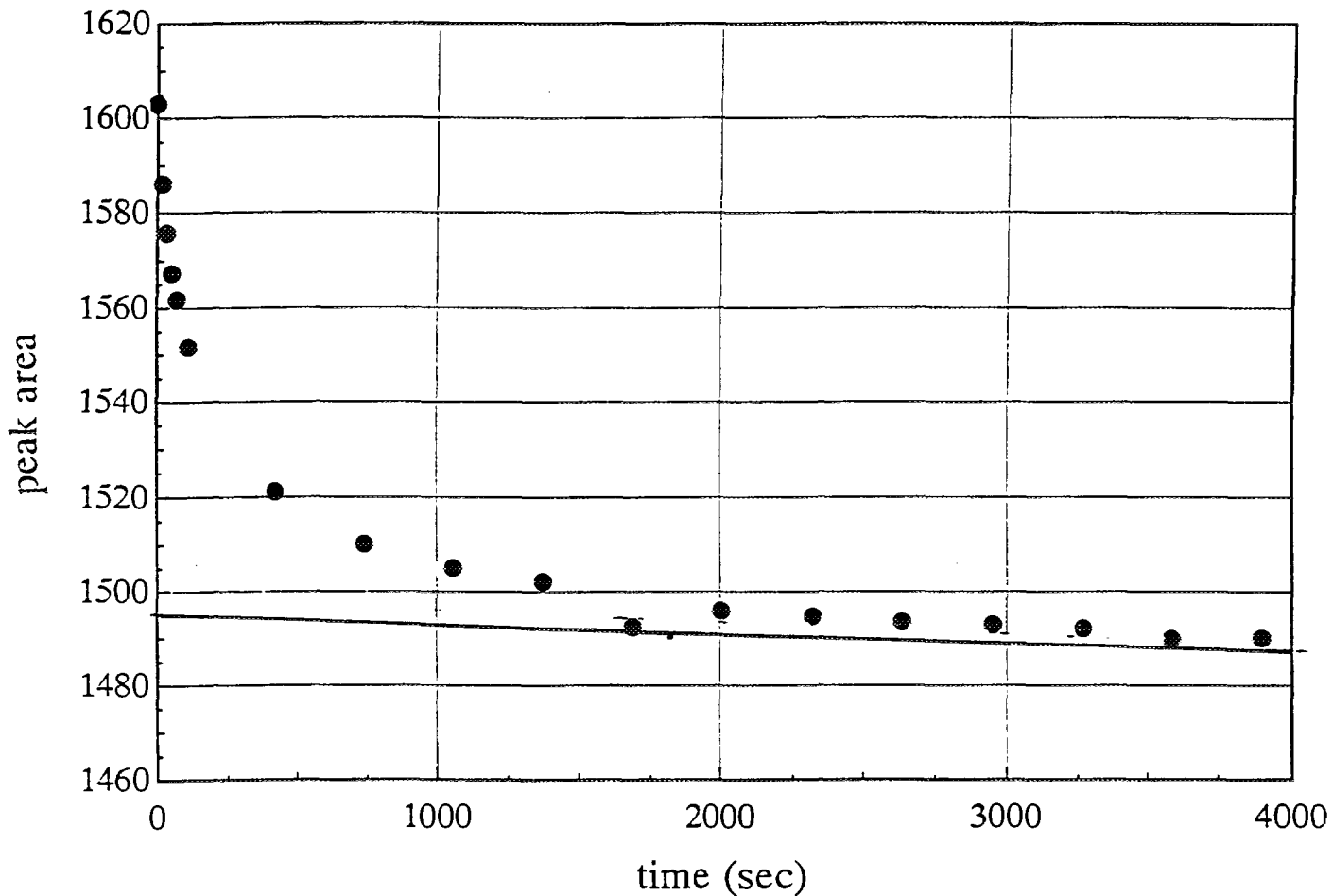


Fig 4.

Decay of proton spin polarization (●) after polarization reversal by the method of adiabatic fast passage (AFP). The sample was a 0.8 wt.% solution of EHBA-Cr(V) in a mixture of glycerol and water (11:9). The degree of deuteration of the sample was 87%.

rf-irradiation has little influence on the slow depolarization of proton spins at a half time of about 4 hours. Increasing the width of the rf-sweep from 0.2 MHz to 1.5 MHz leads to almost complete depolarization of the proton spins as it has been verified by polarized neutron scattering. As the 20 proton spins of each paramagnetic center EHBA-Cr(V) give rise to a very broad NMR signal which is not easily recognized on the screen they largely escaped to depolarization by the rf-sweep of 200 kHz width. They remained polarized whereas those few protons in the deuterated solvent became depolarized.

The half time of the clusters polarized proton spins depends on the proton density in the deuterated bulk material. If the degree of protonation is increased from about 1.5% to 12% the half time of the polarized spin domains associated with EHBA-Cr(V) decreases to about 5 minutes. Proton spin diffusion is facilitated. A relaxation time of not more than 1 minute is expected in fully protonated media.

Similar results are obtained after reversal of nuclear spins by the method of adiabatic fast passage (Hautle, 1993). With EHBA-Cr(V) in a deuterated solvent the polarization of the proton spins of the paramagnetic center remain polarized for hours in an environment of proton spins of opposite polarisation direction and low concentration (Fig.3). Again the increase of the proton density of the solvent favours a more rapid establishment of the equilibrium (Fig. 4).

Proton spin domains associated with paramagnetic centers are small. From the analysis of neutron small-angle scattering it appears that there are hardly more than 20 to 50 proton spins significantly influenced by the magnetic field of the electronic spin. The Q-dependence of polarized neutron scattering is very weak and not easily separated from incoherent scattering. Polarized proton spin clusters of that size are likely to be of use in crystallographic studies when they are associated with spin labels at chemically well-defined sites of a macromolecule. The large dimension of the unit cell mean distances between spin labels large enough for their treatment as independent entities. The first experiment of polarized neutron scattering from dynamic polarized proton spins in a single crystal of lanthanum magnesium nitrate (LMN) is an early example (Hayter, Jenkin, White, 1974; Leslie, Jenkin, Hayter, White, Cox & Warner, 1980). These authors were the first to observe spatial fluctuations of the proton spin polarisation.

The short life time of polarized proton spin clusters necessitates measurements in time slices of the order of seconds. Neutron scattering experiments will have to be repeated many times in order to accumulate data of sufficient resolution in time and momentum transfer. In view of the light which can be shed on the mechanism of DNP, selective depolarization and

nuclear spin diffusion this is a rewarding task, not to mention the increase of the potential of polarized neutron diffraction in macromolecular structure research.

6. Acknowledgement

Neutron scattering experiments with this degree of complexity needed the help of many people. The polarized target station (Niinikoski & Udo, 1976) has been developed and adapted to the requirements of neutron scattering by CERN, Geneva. The neutron spin polarizer is that of Otto Schärf (ILL, Grenoble)(Schärf, 1989). The specifically deuterated ribosomes were prepared at the MPI for Molecular Genetics (Berlin). The experiments of polarized neutron scattering from the nuclear spin polarized samples were done at the research reactor FRG1 of GKSS (Geesthacht).

7. References

- Abragam A. & Goldman M. (1982) Nuclear Magnetism: Order and Disorder, Oxford University Press
- Douzou P. (1977) Cryobiochemistry, In Introduction, London: Academic Press
- Capel M.S., Engelman D.M., Freeborn B.R., Kjeldgard M., Langer J.A., Ramakrishnan V., Schindler D.G., Schneider D.K., Schoenborn B.P., Sillers I.-Y., Yakuki S. & Moore P.B. (1988) Makromol. Chem., Macromol. Symp. 15, 123-130
- Frank J., Penczek P., Grasucci R. & Srivastava S. (1991) J. Cell Biology, 155 597-
- Glättli H. & Goldman M. (1987) Methods of Experimental Physics 23C 241-286
- Glättli H., Fermon C. and Eisenkremer M (1989) J. Phys. 50 2 375
- Hautle, P. (1993) Polarization Reversal by Adiabatic Fast Passage in Deuterated Alcohols, Dissertation ETH No. 10068, Zürich
- Hayter J.B., Jenkin & White J.W. (1974) Phys. Rev. Lett. 33, 696

Knop W., Nierhaus K.H., Nowotny V., Niinikoski T.O., Krumpolc M., Rieubland M., Rijllart A., Schärf O., Schink H.-J., Stuhrmann H.B. & Wagner R. (1986) *Helv. Phys. Acta* 50, 741

Koghi M., Ishida M., Ishikawa Y., Ishimoto S., Kanno Y., Masaike A., Masuda Y. & Morimoto K. (1987) *J. Phys. Soc. Jpn* 56, 2681

Krumpolc M., de Boer B.G. & Rocek J. (1978) *J. Am. Chem. Soc.* 100, 145

Leslie M., Jenkin G.T., Hayter J.B., White J.W., Cox S. & Warner G. (1980) *Phil. Trans. R. Soc. London B* 290, 497

Lim V., Venclovas C., Spirin A., Brimacombe R., Mitchell P., & Müller F. (1992) *Nucleic Acids Research* 20 2627

Nierhaus K.H., Lietzke R., May R.P., Nowotny V., Schulze H., Simpson K. & Wurmbach P. (1983) *Proc. Nat. Acad. Sci. USA*, 80 2889-2893

Nierhaus K.-H. Wadzack J., Burkhardt N. Jünemann R., Frank J., Meerwinck W., Schmitt M. & Stuhrmann H.B. (1996) *J. Mol. Biol.* (submitted)

Serdyuk I.N. & Pavlov M.Yu. (1988) *Makromol. Chem., Macromol. Symp.* 15, 167- 190

Stuhrmann H.B. (1993) *Phys. Scripta T* 49, 644

Stuhrmann H.B., van den Brandt, B., Hautle,P., Konter J.A., Nierhaus K.H., Niinikoski, T.O., Schmitt. M., Willumeit M., Zhao J., Mango S. (1996) to be submitted to *J. Appl. Cryst.*

Sussman J., Holbrook S.R., Warrant R.W., Church G.M. & Kim S.-H. (1978) *J. Mol. Biol.* 123, 607

Stuhrmann H.B., Burkhardt N., Diedrich G., Jünemann R., Meerwinck W., Schmitt M., Wadzack J., Willumeit R., Zhao J. & Nierhaus K.H. (1995) *Nuclear Instr. Methods in Physics Research A*356 124-132

Vanatalu K., Paalme T., Vilu R., Burckhardt N., Jünemann R., May R., Rühl M., Wadzack J. & Nierhaus K.H. (1993) *Eur. J. Biochem.* 216, 315



NONDIFFRACTIVE APPLICATIONS OF NEUTRONS AT THE SPALLATION SOURCE SINQ

E. LEHMANN

*Department Spallation Source, Paul-Scherrer-Institute,
CH-5231 Villigen PSI, Switzerland*

ABSTRACT

The paper delivers an overview about experiments with neutrons from the spallation source SINQ which are not especially devoted to neutron scattering. A total of six experimental facilities are under construction using thermal as well as cold neutrons. Starting with some general considerations about the interaction of neutrons with matter, the principles, boundary conditions and the experimental set up of these experiments are described briefly. Some more details are given for the neutron radiography facility NEUTRA as the author's special interest and research field.

1. Behaviour of neutrons in interaction with matter

If a beam of free neutrons meets a material sample there will be interactions and changes of the properties of the sample and the neutron beam as well. The different kinds of interactions are very dependent on the sample material, but also on the energy of the neutrons. In very rough terms the interactions can be categorized as:

- absorption
- scattering
- fission
- spallation

The probabilities for interactions are described by cross-sections σ_x , where the index may describe the special kind of interaction. Whereas this meeting's topic is mainly devoted to neutron scattering, some important experimental arrangements at the spallation source SINQ will also use some other types of neutron interactions.

The scattering process represents only a weak sustainable influence on the sample properties, but the scattered neutrons provide information on the inner structure and distributions of the nuclei of the sample. Therefore, neutron diffraction is a very helpful tool for basic research in condensed matter physics.

On the other hand, neutron absorption leads to modifications of the nuclei of the irradiated sample. Prompt reactions have to be distinguished from processes which excite nuclides (activation), followed by an deexcitation by the emission of particles or gamma radiation. As result of the absorption process other nuclides are generated (stable or radioactive).

Fission by neutrons can be caused in a few materials only. Only some special isotopes with atomic weights above and including uranium can be split up into fission product nuclides with thermal neutrons. With fast neutrons some more isotopes are fissionable, but with lower efficiency compared to slow neutrons.

To illustrate the behaviour of nuclides in interaction with neutrons the cross-sections of zirconium are shown in fig. 1 for the different kinds of interactions in dependency on the neutron energy.

Whereas hydrogen has a dominating scattering cross-section compared to its absorption behaviour, the nuclides with higher atom mass show an increasing number of reaction types with increasing neutron energies. This behaviour is especially valid for the higher actinide materials. A very interesting effect is the occurrence of resonances in the keV region which is important for nuclear reactor physics, but also for the understanding of the inner structure of the nuclei.

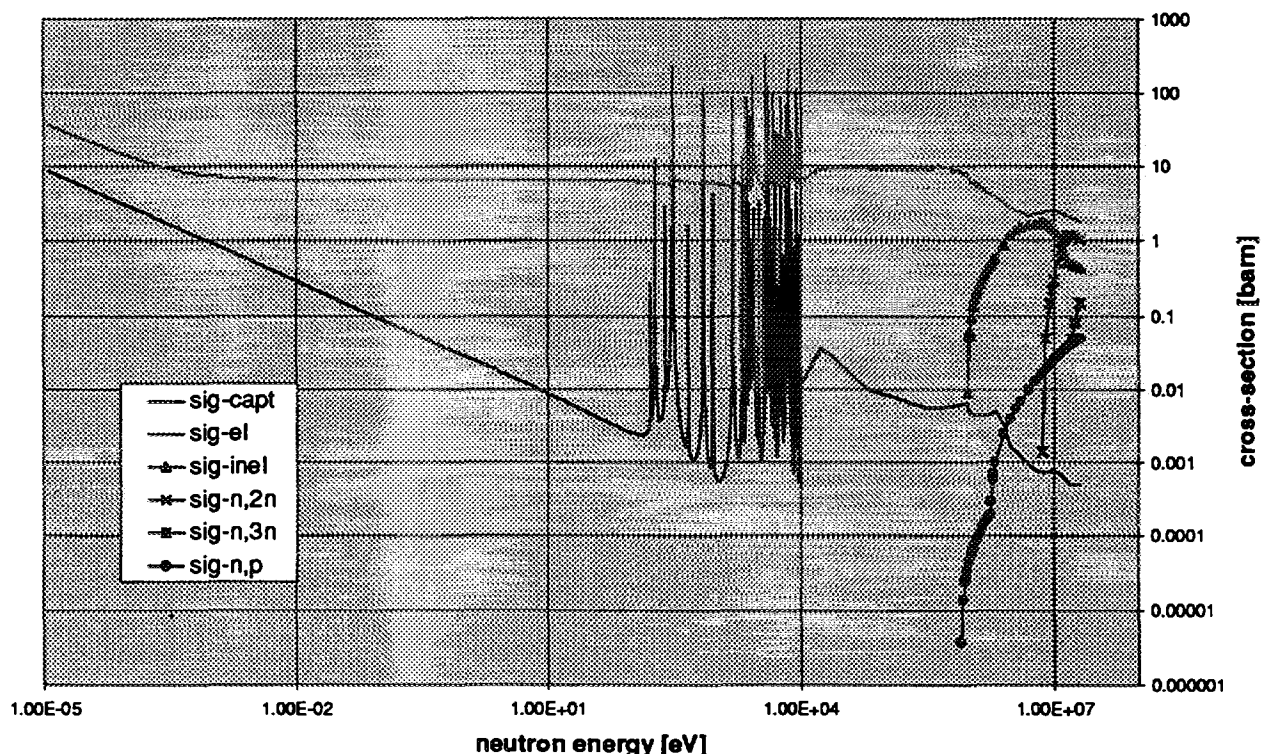


Fig. 1: Comparison of neutron reaction cross-sections of zirconium for different reaction types in dependency on the neutron energy

Spallation of nuclei can be obtained only with high energy neutrons (above 20 MeV). The processes during these interactions become very complex and can be simulated with statistical nuclear models. At these high energies neutrons and protons show about the same behaviour in interactions. The bombardment of a heavy material target with high energy particles is one possibility to generate free neutrons, as practically intended with spallation sources.

2. Applications and utilisation of neutrons from reactors

For the last decades since the discovery of nuclear fission research reactors have been used as the most important neutron sources for research, nuclear technology and industrial applications. Compared to nuclear power plants which are optimised to produce electricity in the order of several hundreds of MW, research reactors are designed for a maximum gain of free neutrons per generated heat (which has to be removed useless). Typical research reactors providing thermal fluxes of about 10^{14} neutrons $\text{cm}^{-2} \text{s}^{-1}$ are operating at 5 to 10 MW power.

The applications of neutrons from research reactors can be roughly divided into three categories: (1) research (2) industrial applications (3) medical irradiations. The priorities among these applications have been changed over the years, also depending on the properties of the specific reactor type.

In the beginning the research on reactors was mainly focused on the understanding of the reactor itself and the development of reactor technology for electrical power stations. For this reason numerous test irradiations of nuclear components (fuel elements, cladding, structural materials) were performed.

In parallel to these practically motivated investigations neutron diffraction, radiochemistry and activation analysis became very interested clients of the research reactors neutrons. Up to now, these investigations remain very helpful tools of the understanding and analysis of matter, utilising very sophisticated methods and devices.

As industrial applications silicon doping for the generation of very homogeneous semiconductor raw material and the production of isotopes for medical applications are the most important. Gemstone colouring is an interesting possibility of material modification, but limited by the problem of residual activity after the irradiation.

The irradiation of patients with neutron (and gamma radiation) from research reactors is established at a few stations only. Because of their limited penetration through the tissue thermal neutrons can only be applied at the surface of the body. For deeper penetration into the tissue fast neutrons generated by converter elements are used.

3. New options developed during the last years

Despite or because of the tendency of reducing the number of research reactors very dramatically during the last years, some important developments and new techniques were established at research reactors [1].

The extension of the wavelength range of neutrons into the subthermal region is a very important possibility for neutron scattering investigations. This can be done by means of cold neutron sources consist of moderators with very low temperatures. For the extraction of these slow neutrons with highest efficiency (avoiding the background of faster neutrons and gamma radiation) neutron guiding systems were developed. By means of mirrors (for instance ^{58}Ni) or sheets of different layers of mirrors cold neutrons can be transmitted from the source to experimental devices over dozens of meters without large losses.

The methods for neutron detection were improved by the development of imaging plates, multiwire counters and the application of camera systems. The application of these devices is associated with the rapid development of the performance of personal computers which are needed to handle the very large amounts of data generated by the new systems. This is especially valid for neutron tomography as a new feature of neutron radiography.

As tool for the treatment of cancer in brains boron neutron capture therapy (BNCT) is under development. Although the first ideas for this method are decades old, new methods and special developments were needed to raise the acceptance for such treatments. The development of special boron containing substances absorbed by the cancerous tissue is one of the main problems for this method.

Beside the usual activation analysis which is using the decay of activated nuclides for the estimation of very small amounts of material in samples the prompt gamma activation analysis (PGAA) was developed during the last recent years. It is possible with this method to investigate and analyse those nuclides which have no delayed but prompt emission of radiation. Compared to traditional activation analysis, other nuclides with changed sensitivities can be studied.

4. Possibilities of experiments and facilities for nondiffractive applications at SINQ

After the final shut down of the research reactor SAPHIR (10 MW_{th}, MTR-type) the spallation source SINQ will play the role of the strongest neutron source for research purposes in Switzerland.

Compared to a research reactor some special features have to be considered:

- During the spallation process initiated by protons with 590 MeV high energy neutrons are generated. Not all of them can be slowed down to thermal energies. Therefore, a massive shielding is necessary around the source. Between the target region were the peak of neutron distribution is located and the „outer world“ shielding of about 6 m thickness is arranged (mainly iron, borated concrete).
- The space in the neighbourhood of the target is very limited and difficult to access. Compared to pool reactors there is no possibility to arrange irradiation facilities with large volumes.
- If the shielding is penetrated to extract neutrons or to place material samples inside, an urgent demand for shielding occurs, especially against the high energy neutrons.

Under these circumstances and boundary conditions a total of six independent experimental facilities are under development and installation (see fig. 2). They will be described succinctly in the following chapters.

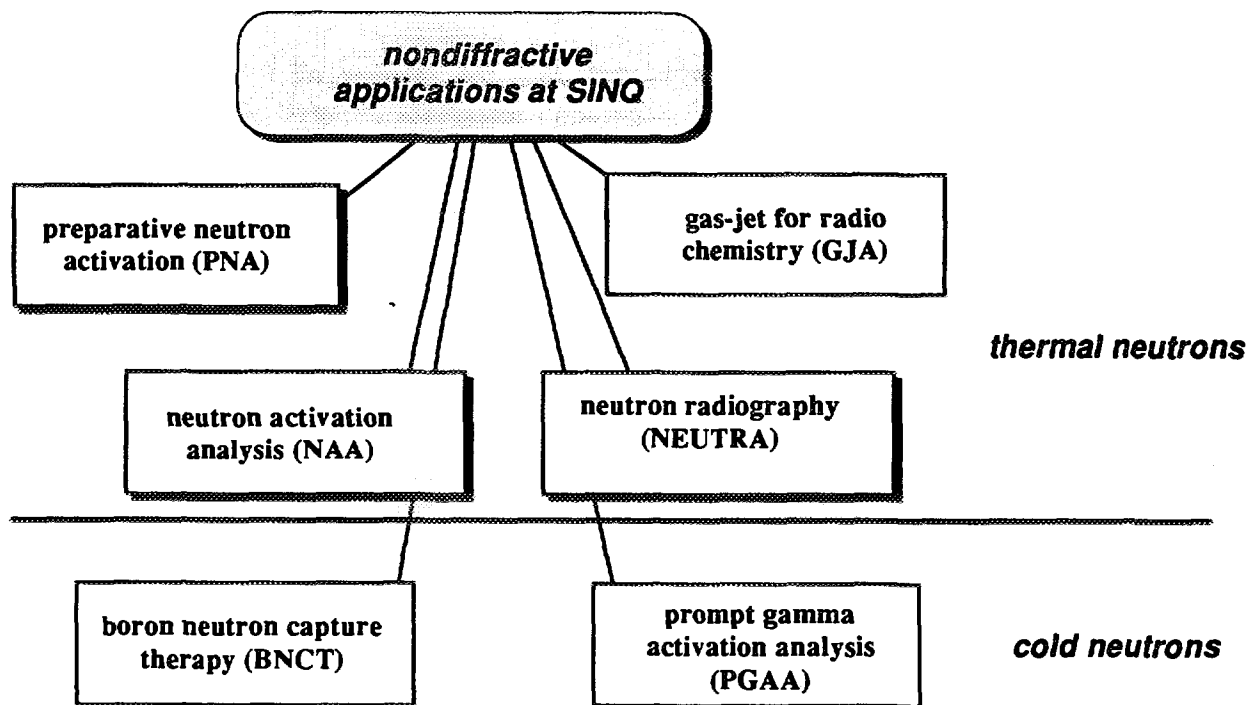


Fig. 2: Experiments for nondiffractive applications at SINQ (shadowed: operated mainly by department ASQ)

4.1. Irradiation facilities

In order to irradiate material samples with neutrons two independent rabbit systems are installed. The samples are enclosed in capsules which are driven to the end position in the moderator tank by helium gas flow. The neutron spectrum at the irradiation positions is mainly given by the

properties of the moderator, which is heavy water in the case of SINQ. A comparison to the neutron spectrum of a light water moderated research reactor is given in fig. 3. The ratio of thermal to fast neutrons is larger for SINQ, however the component of high energy neutrons might cause some problems.

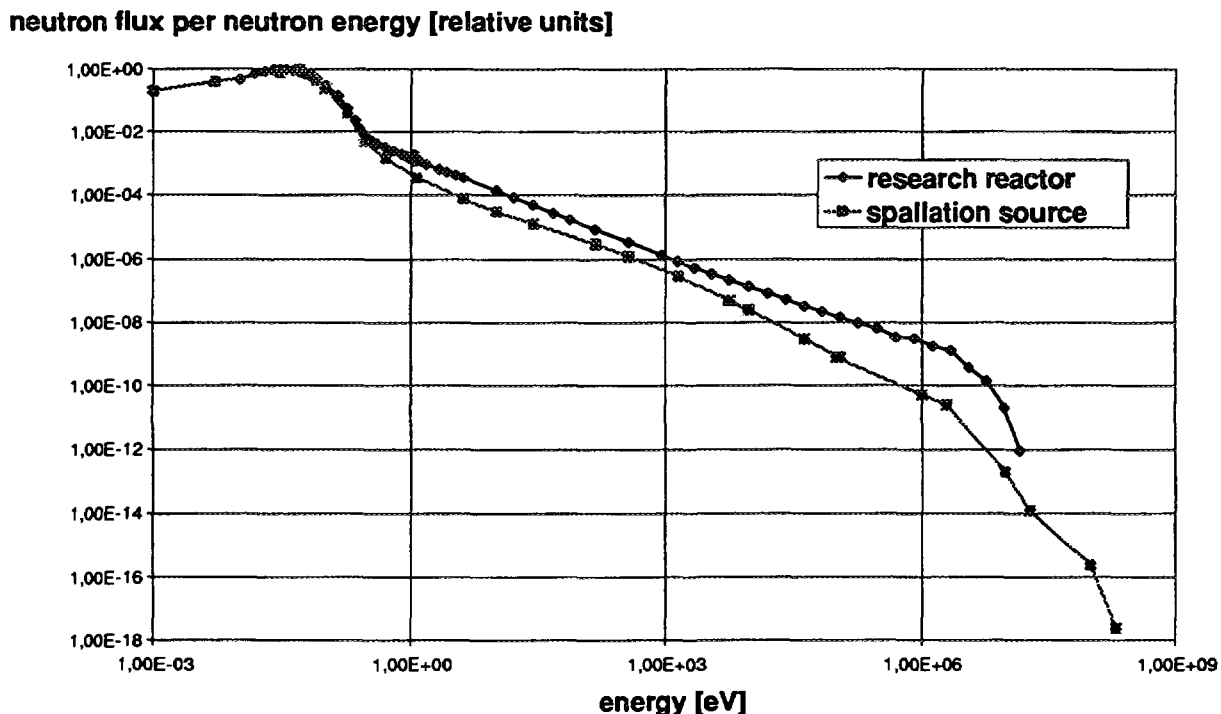


Fig. 3: Neutron spectrum inside the moderator tank of SINQ, compared to that in a light water moderated research reactor

4.1.1 Facility for preparative neutron activation (PNA)

The aim of the irradiation is the generation of nuclides for use in medical applications. Especially, the research and development for chemical substances applied for cancer treatment needs the production of nuclides which guarantee the following requirements:

- ⇒ emitters of beta-radiation with half-life between 2 and 5 days
- ⇒ the maximum of the energy of the radiation should be only about 1 MeV
- ⇒ accompanying gamma radiation should be only weak with energies below 200 keV
- ⇒ high efficiency for applications by the use of pure nuclides

Among different candidates for nuclides with those properties ^{111}Ag , ^{186}Re , ^{166}Ho , ^{159}Gd , ^{153}Sm , ^{165}Dy are interesting in this order of priority. For the generation of these nuclides the properties of the raw material as well as the irradiation conditions are important. Because of the low cross-sections of the target materials the thermal flux level should be as high as possible. The irradiation will need several days of irradiation time at $3 \times 10^{13} \text{ cm}^{-2} \text{ s}^{-1}$.

The rabbit system for PNA has its end position inside the moderator tank near the maximum of the thermalized neutron flux. The target material is enclosed in welded aluminium capsules which are driven and cooled by helium. For reloading and handling of the irradiated capsules a shielded transfer station is located near the outlet of the rabbit line. Figure 4 gives an overview of the inner installation of the irradiation devices in SINQ.

4.1.2. Facility for neutron activation analysis (NAA)

This analysis methods is well established at PSI and has a good tradition for the estimation of very small concentrations of material inside small samples. The methods has some important advantages compared to other analytical procedures:

- the physical state of the sample material is unimportant (solid preferred)
- different isotopes can be simultaneously considered
- very high sensitivity with small sample amounts
- the samples remain essentially undisturbed

During the last years the method was mainly applied to the estimations of environmental poisons and rare earth elements concentrations. The irradiation times are in the order of seconds to minutes only at thermal fluxes of about $10^{13} \text{ cm}^{-2} \text{ s}^{-1}$. The samples are enclosed in polyethylene capsules which are driven by helium (inside the shielding) and compressed air (over the long distance to the chemistry lab).

4.2. Radiochemical experiments - gas jet

This device is an arrangement of thin uranium foils where fission product nuclides are generated by the neutron irradiation. These emitted (mainly radioactive) particles can be extracted and transported within a gas flow to a chemistry lab. Therefore, the gas-jet system represents a very important and flexible tool for radiochemical investigations [2].

4.3. Neutron radiography

This method represents an important tool for non-destructive inspections of macroscopic components and material samples. Compared to X-ray radiography the sensitivity of detection with neutrons differs very much regarding the observed materials. Especially for light materials with high cross-sections the contrasts with neutron radiography are much higher than with X-rays. An example is given in fig. 4 by comparison of the images of a diskette obtained with both methods.

Detailed methodical explanations are given in chapter 5.

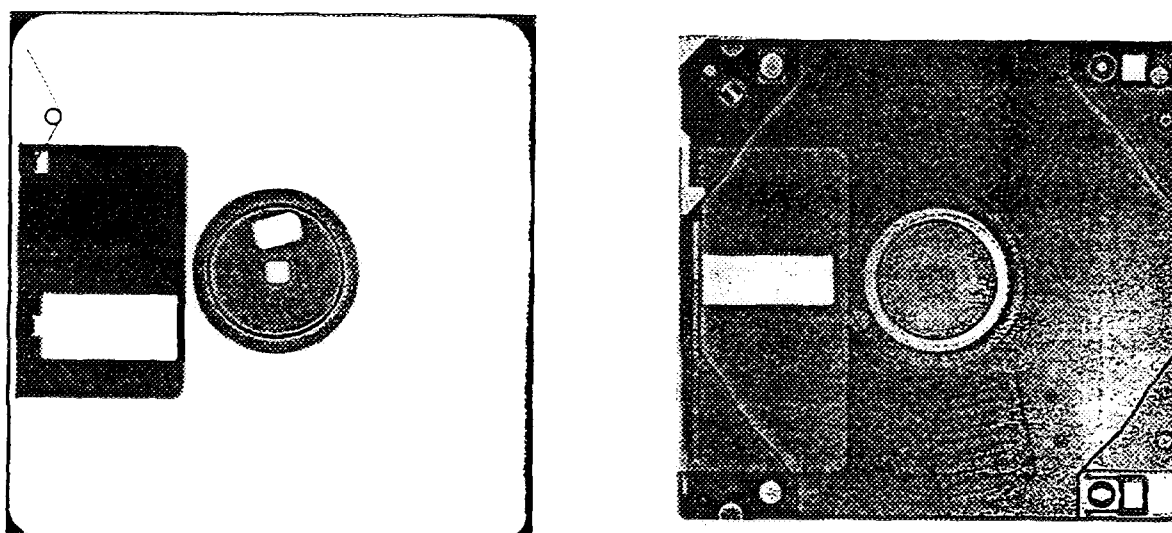


Fig. 4: Radiographic images of a diskette with X-rays (left) and thermal neutrons (right)

4.4. Prompt gamma activation analysis

By means of gamma spectrometry it is also possible to investigate nuclides which are not activated by neutrons, but emitting prompt gamma radiation when neutron capture occurs. In this manner, some very important materials like hydrogen, carbon, nitrogen, phosphor, sulphur, cadmium and mercury can be analysed concerning their distribution and concentration, especially at the sample's surface. Methodical improvements are possible using cold neutrons, neutron concentrators and different spectrometer options. A new facility with these new features will be installed at SINQ [3].

4.5. Investigations for boron neutron capture therapy (BNCT)

The basic principle of BNCT is the interaction of the isotope ^{10}B with neutrons, where alpha particles and ^7Li nuclei are produced. Because of their high biological impact the tissue in the neighbourhood can be destroyed. One of the research fields for BNCT is the development of substances which are well absorbed by the cancerous tissue. For the estimation of the boron distribution after application of these substances in experiments with animals a method with track etch detectors was developed [4]. Using the neutron guide line 1RNR13 for cold neutrons these investigations will be continued and improved by raising the spatial resolution to $1\text{-}2 \mu\text{m}$. For minimising the background from recoil protons the contribution of neutrons above 0.4 eV should be very small (about 0.2%).

5. NEUTRA - The neutron radiography facility at SINQ

At the thermal beamline in sector 30 a new neutron radiography facility will be installed using the practical experiences of devices at research reactors [5,6]. For the design of the facility, the special properties of a spallation source to be considered. The layout should be as universal as possible to supply a wide range of applications. Although SINQ can provide thermal as well as cold neutrons, it was decided to use thermal neutrons for radiography because of their deeper penetration through macroscopic samples.

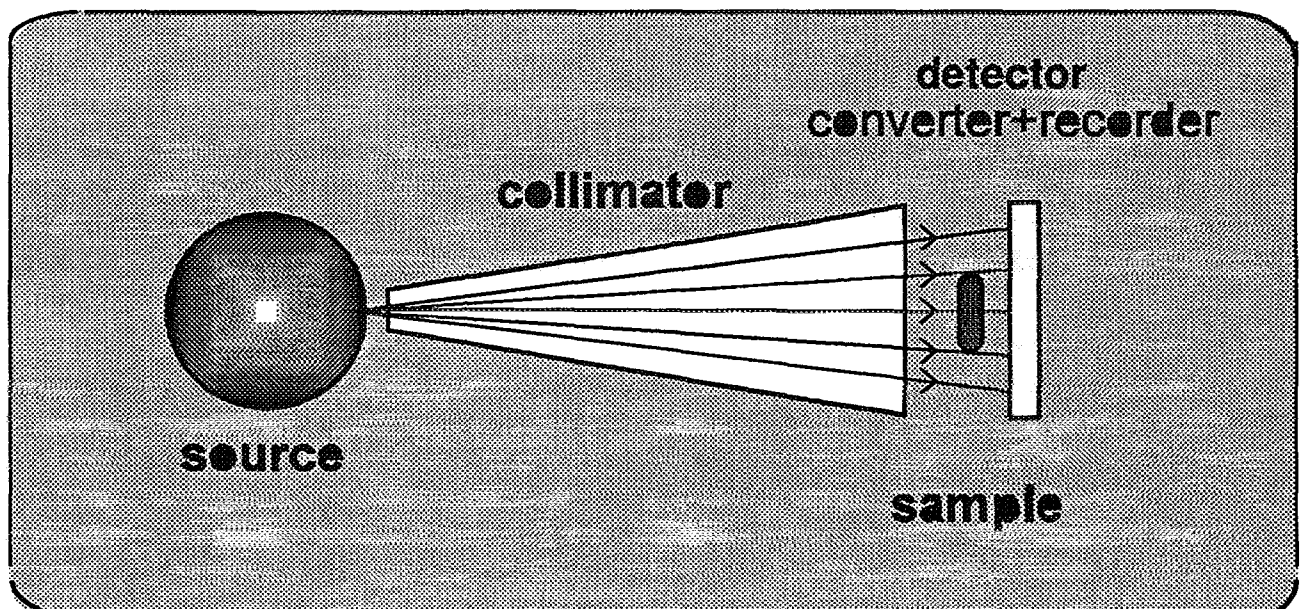


Fig. 5: Basic set up of a neutron radiography system

5.1. Principle of neutron radiography

In Fig. 5 the set up of a neutron radiography facility is given with the neutron source, the collimator, the sample and the detector system. The arrangement is usually completed by filter systems and shutter devices. In this manner, the detector is producing an image of the neutrons transmitted through the sample (collided or uncollided). The performance of the radiography system and quality of the produced images are mainly given by the quality of neutron source and the sensitivity of the detector system.

5.2. Neutron Source

Different sources for neutron radiography purposes exist. The most powerful stations are installed at reactors because of their high flux level. Mostly the thermal flux is used for radiography, but there are also devices operating with fast or cold neutrons.

The disadvantage of reactor stations is their loss of mobility. For in-situ investigations there are some other possibilities using accelerator driven systems or radioactive sources with special moderator assemblies. However, the portable sources can never reach the flux performance of reactors. Therefore, very long exposition times or lack in the image quality is the consequence.

At SINQ the first neutron radiography station working at a spallation source will be installed. Some special consideration were done to optimize the system concerning flux level, spatial resolution and radiation protection demands.

5.3. Detector types

As neutron detector for radiography a layer of neutron absorbing material is needed to produce a latent image on a recorder with high efficiency. As suited absorber material Gd, Dy, ^{10}B and ^6Li were found.

Traditionally X-ray films and track etch foils are used as recorder materials. With film it is possible to achieve a resolution up to 10 μm depending on the film quality. With track etch foils nearly each interaction of neutrons with the detector material can be microscopically analysed.

New techniques are available now with CCD-camera systems with scintillator screens, neutron sensitive imaging plates and intensifier tubes reducing the recording time. Static and dynamic investigation are now possible by on line recording and storing of the images.

5.3.1. Direct methods

If the neutron sensitive detector is in contact with the recorder of the produced image it is called a „direct“ system. The advantage is the very high sensitivity and the possibility to get the image simultaneously to or nearly immediately after the exposition. However, some of the recorders are sensitive to γ -radiation too and the neutronic image might be disturbed.

5.3.2. Transfer methods

If the beam from the neutron source has very high contributions of γ -radiation or the sample is radioactive or it is producing additional radiation by neutron interactions, clear images can only be obtained by transfer methods. In this case, the converter is activated by the transmitted neutron beam but not influenced by other radiation fields. Short time after the exposure this converter is put together with the recorder (film or imaging plate) for a time which is corresponding to the half-life of the detector material. As detector/converter material natural dysprosium is mainly used. The decay of two nuclides can be used for the generation of the recorded image (^{165}Dy - $T_{1/2}=2.35\text{h}$, $^{165\text{m}}\text{Dy}$ - $T_{1/2}=1.3\text{ min}$).

This procedure is especially important for investigations of spent fuel elements and other highly radioactive components of nuclear power plants.

5.3.3. Neutron tomography

If the investigated object is observed with radiographic methods and about 100 images are produced during the rotation around the vertical axis, this amount of data about the sample can be used for the tomographic reconstruction. Compared to other tomographic techniques the effect of scattered neutrons has to be considered very carefully because of their more random interactions with the sample [7].

Although neutron tomography has high requirements concerning computer performance (especially storage capacity), the developments for computers will help to push neutron tomography to a useful completion of standard radiography.

5.4 Layout of the SINQ facility

In Fig. 6 some details of the neutron radiography facility NEUTRA at SINQ (sector 30) are shown. Whereas all components inside the target block are installed and ready for operation, the outer beam line and the shielded working room cannot be placed before all SINQ components have found their right place during the installation work.

The most important characteristics of the facility are summarized in table I. Beside the thermal neutron flux level at the detector position the performance of the facility is mainly given by the ratio of the diameter of the first aperture D and the distance between this aperture and the detector L. In the case of NEUTRA L/D is in the order of 550, indicating that the geometric unsharpness of the beam will be in the same order or better than the resolution of most sensitive detector systems.

NEUTRA : Neutron Radiography Station at SINQ

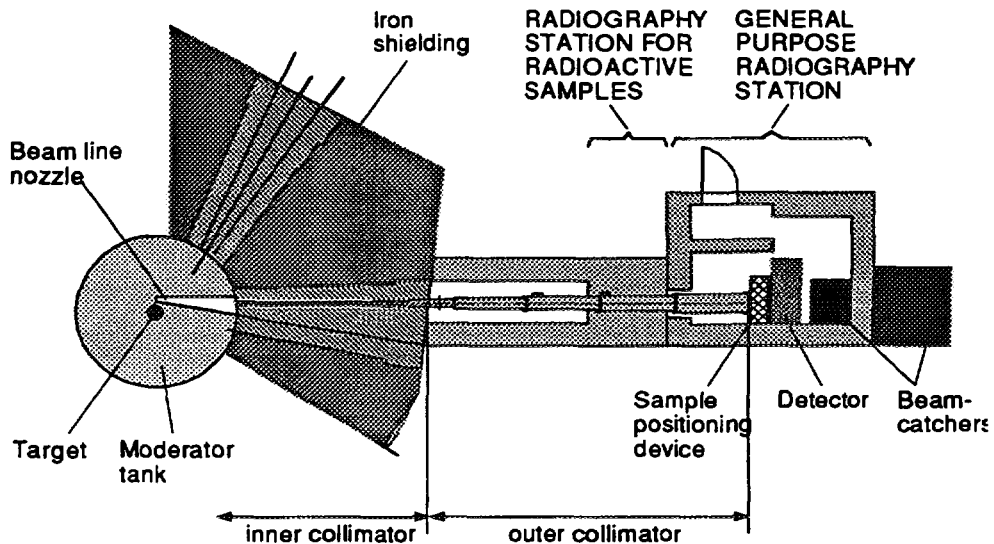


Fig. 6: Layout of the neutron radiography station NEUTRA at a thermal beam line of SINQ

A new CCD-camera based detector system was developed, installed and successfully tested at the thermal column of the test facility PROTEUS at PSI. In Fig. 7 the basic design of the detector box is illustrated.

Table I: Design parameters of the neutron radiography facility NEUTRA

neutron generator	spallation source SINQ	
structure of the source	target	Zircaloy pins
	proton beam	1 mA on the target
	moderator	D ₂ O , diameter 2 m
structure of beam formatting assemblies	beam tube nozzles inside the moderator tank	opening angle 10°, minimum distance from target centre 24 cm
	cooled shielding plug with window	iron with an Al-window
	convergent collimator	iron wall
	first aperture	boron carbide filled plate
	divergent collimator with beam shutter	iron wall, partial cladded with Cd
	outer collimation tube	
additive structures for beam quality enhancement and operation	filter	Bi, thickness 5 cm, diameter 8 cm
	additional apertures	2 inside the shielding, 3 in the outer collimator tube
	shutter	6 iron drums, driven electrically
characteristics of the produced neutron beam	flux (thermal)	5 * 10 ⁶ cm ⁻² s ⁻¹
	L	11 m
	D	2 cm circular
	L/D	
	shape and size of the irradiation area	circular ; diameter 40 cm

Table II: Practical applications of neutron radiography

NEUTRON RADIOGRAPHY APPLICATIONS

Field of application	Basic research	Industrial application	Examples
Aerospace	X	X	Inspection of honeycomb structures* , detection of moisture and corrosion, assembly control
Archaeology	X		Examination of composite metal objects*
Art	X		Investigation of paintings
Automobile industry & research	X	X	Study of fluid flow in combustion engine, quality control of gas pile, quality control of airbag
Biology	X		Root growth
Ceramics		X	Inspection for cracks*
Chemical & petrochemical industry	X	X	Hydrating of steel, visualisation of two phases, quality control of sealings
Civil engineering	X		Water transport in porous building materials* , behaviour of steel in reinforced concrete
Defence		X	Quality control of explosive charges*
Dentistry	X		R&D on filling techniques* , quality control of metal components for crowns*
Forensic utilisation			Determination of authenticity or integrity of documents
Geology	X		Porosity of rock*, layers in sediment soils*
Heat transfer	X	X	Visualisation of two phases behaviour
Material sciences	X	X	Alloy distribution
Medical research	X		Determination of gallstone structure, study of compounds for BNCT (Boron Neutron Capture Therapy)
Nuclear	X	X	Inspection of irradiated fuel cladding* , quality control of fuel elements*
Turbine manufacturing		X	quality control of turbine blades

* performed as program or as feasibility test in the framework of the PSI neutron radiography activities

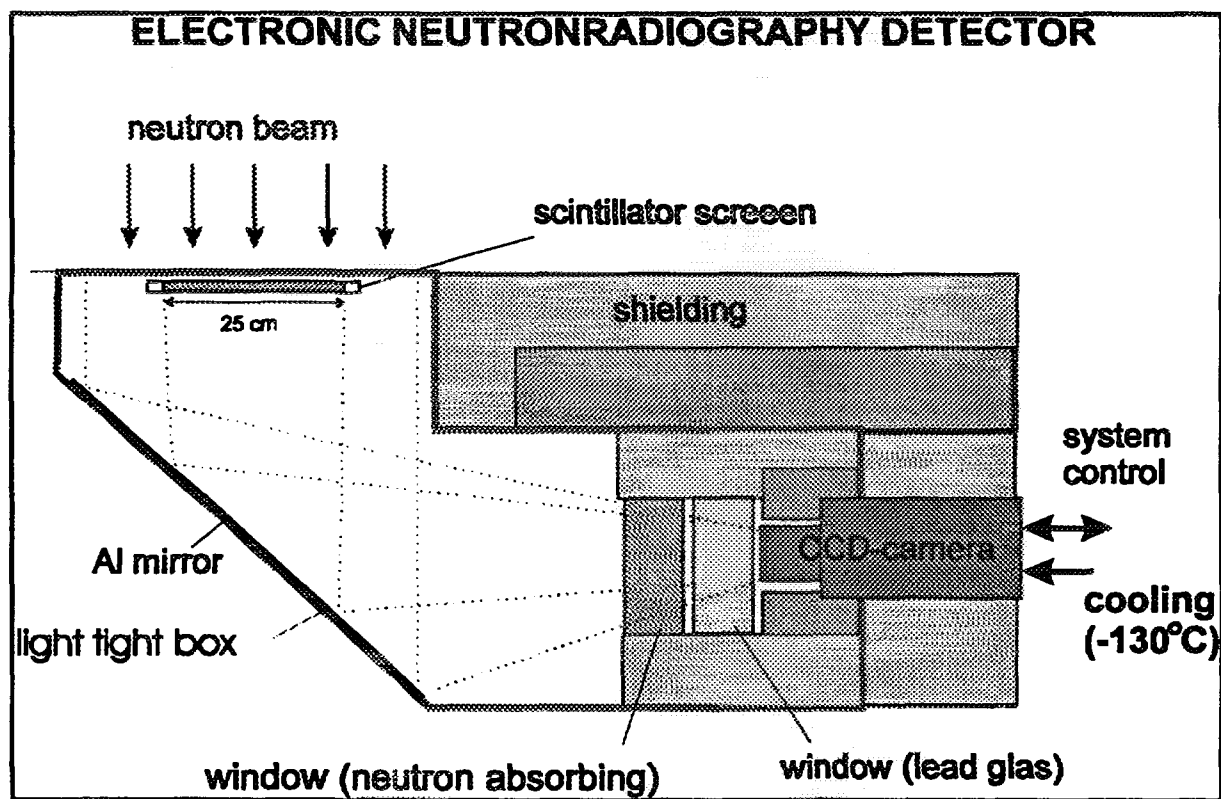


Fig. 7: Design of a camera based neutron radiography detector system

5.5. Practical applications

Becoming the only powerful neutron radiography facility in Switzerland, different applications are foreseen in continuation of the reactor tradition at SAPHIR and the TRIGA of the Atominstitut in Vienna [8,9].

Table II summarizes the applications and research fields for neutron radiography. Own practical experiences are written in boldface. The extension of applications to other fields is depending on the user's demands and the manpower available.

6. Summary - Status of the installations at SINQ

This paper has attempted to illustrate the properties of the different experiments at SINQ, summarised under the global term „nondiffractive“. Using the different properties of neutrons in interaction with matter (absorption, scattering, fission,...), a wide range of applications and research tools will be available at SINQ.

From the six mentioned facilities about 2 will be in operation during the SINQ start with the first proton beam on the spallation target. Nevertheless, the completion of the remaining facilities will be performed during the first half in 1997, than reaching the level of routine operation.

Acknowledgements

The author is obliged to the operators of the reactor facility PROTEUS for their helpful support with thermal neutrons for detectors tests. I am also thanking my colleague H. Pleinert for her helpful discussions and many activities in neutron radiography.

References

1. T. Riste, *Neutron beam sources in the OECD countries*, Neutron News **6** (1995), Nr. 4, 32
2. H. Gäggeler, *Isotope production facility, neutron activation analysis and gas jet at SINQ*, contribution H₃ o this meeting
3. J. Kern, *Prompt gamma activation analysis*, contributuin H₂ to this meeting
4. B. Larson, D. Gabel, H. Börner, *Boron-loaded macromolecules in experimental physiology: tracing by neutron capture radiography*, Phy. Med. Biol. **29** (1984), 361
5. H. Pleinert, E. Lehmann, J. Hammer, *Neutron Radiography at the Paul Scherrer Institute*, Neutron News **7** (1996), Nr. 2, 17
6. J. Hammer, E. Lehmann, H. Pleinert, *Proc. 5th World Conf. on Neutron Radiography 1996*, in preparation
7. B. Schillinger, C. Rausch, *High Performance neutron detector for radiography and small angle scattering*, SPIE Vol. 2198, (1994), 974
8. E. Lehmann, H.Pleinert, L.Wiezel, *Status of the Installation of a new Neutron Radiography Facility at the Spallation Neutron Source SINQ*, Proc. 5th World Conf. on Neutron Radiography 1996, in preparation
9. H. Pleinert, C. Degueldre, *Neutron radiographic measurement of porosity of crystalline rock samples: a feasibility study*, Jour. of Cont. Hydrology. **19** (1995), 29-46

Prompt Gamma-ray Activation Analysis (PGAA)

Jean Kern

*Physics Department, University, CH-1700 Fribourg,
Switzerland*

1. Introduction

There are in principle two ways to use neutrons for elemental and isotopic abundance analysis in samples. One is the "neutron activation analysis", a method presented here by Prof. Gäggeler. I will label it as "off-line", since the neutron-induced radioactivity is observed after the end of the irradiation. The other method, which I will call "on-line", consists in observing the capture gamma-ray during neutron bombardment. This will be the subject of the present lecture.

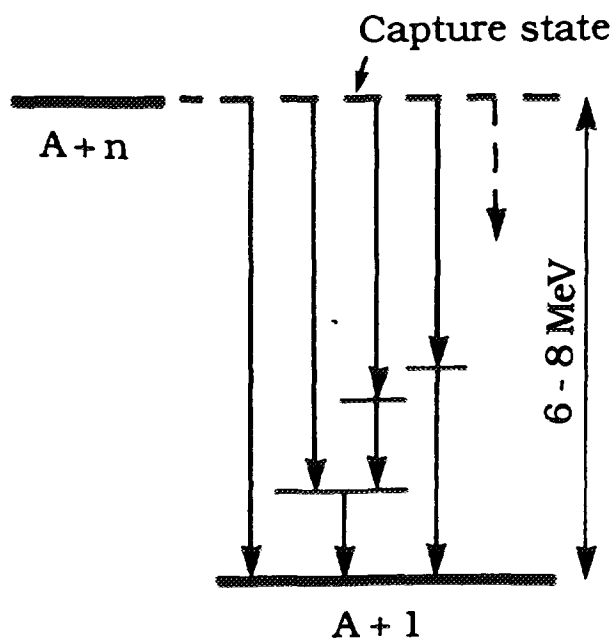


Fig. 1 :
Slow neutron capture. Primary transitions are issued from the capture state.

As shown in Fig. 1, if a nucleus A captures a slow (thermal or cold neutron), it will form a nucleus A+1 in an excited (so-called **capture**) state with an energy of about 6-8 MeV above the ground state (except for hydrogen for which it is only 2.2 MeV). This energy is, of course, the same as would be needed to take out

the least bound neutron out of the nucleus A+1. The capture state decays first by the emission of **primary** transitions to low-lying excited states, which in turn decay by one or more transitions, called **secondary** transitions, to the ground state. All these transitions, primary and secondary, are characteristic for the capturing isotope and their observation provides therefore **fingerprints** for assessing the presence of particular elements in the sample. Thus the PGAA method consists in observing the primary and/or secondary γ -ray transitions with

the proper instruments. The transition energies and intensity ratios are used for identifying the isotopes (elements) contained in the sample, the intensities for the determination of isotopic (elemental) abundances.

The method is most useful for assessing the presence of low Z elements, presenting a sizable neutron cross section, and which do not produce measurable radioactive products. The interest for low Z elements is because they are not easily observable by X-ray methods (low cross sections, low transition energies). Among the most important applications is the detection of **hydrogen** and of **boron**. As you know well, hydrogen has a high scattering cross section and hence its presence is unwanted in the scattering targets. Since the method is **non-destructive** and has a good sensitivity (see sect. 4), neutrons scatterers are good "customers" of PGAA facilities. Boron has a large neutron capture cross section and can therefore be detected with a very high sensitivity. The PGAA can be used successfully to determine the amount of H and B in metals: this is interesting because even small amounts of these elements can strongly modify their mechanical properties [1]. Let us also mention the importance of boron in the semiconductor industry. PGAA's find also useful applications in nuclear physics (see e.g. [2]).

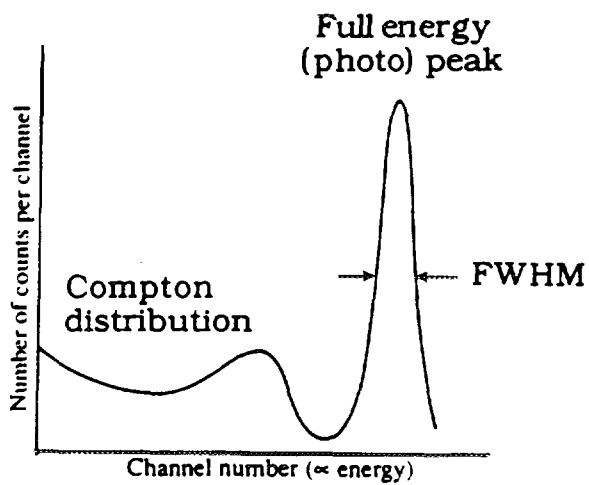
2. Detection of gamma-rays

The gamma-rays interact with matter by either the photoelectric, the Compton or the pair effect. In the photo-process, the whole incoming photon energy is deposited into the detector. The Compton effect is an inelastic process. The energy released in the detector depends on the scattering angle. It is negligible close to 0° and maximum at 180° . In the pair process an electron-positron pair is created. The kinetic energy of these particles is generally deposited in the detector. As the positron reaches a low energy, it annihilates with an electron, creating a pair of 511 keV photons (annihilation radiation). Each of these photons can either escape or interact with the detector.

The detectors which will enter in the construction of the PGAA are:

- scintillators
- semiconductors.

Among the mostly used scintillators are NaI(Tl) and BGO. Sodium iodide, activated with thallium has the highest sensitivity, i.e. the average deposited energy needed to produce a low energy photon is the smallest (see table 1). Consequently this scintillator presents better energy resolution. The schematical response to a monoenergetic gamma radiation is shown in

**Fig. 2 :**

Schematic response of a scintillator to a monoenergetic γ -radiation of energy smaller than the pair-production threshold (1022 keV).

Fig. 2. It is usual to give the resolution for the 662 keV line emitted in the decay of ^{137}Cs . It is of the order of 7 to 12 % for NaI(Tl), depending, in particular, on the detector geometry.

The chemical formula of BGO is $\text{Bi}_4\text{Ge}_3\text{O}_{12}$. Its advantages with respect to NaI(Tl) are its higher density (see table 1) and the high Z elements entering in its composition. The probability of a Compton effect is proportional to the density, favouring a multiprocess leading to a full absorption. The photo-effect cross section is proportional to Z^5 and the pair formation cross section increases with Z^2 . The inconvenience, however, is its relatively low sensitivity, i.e. the low energy threshold is as high as about 60 keV. This results also in a poorer energy resolution, about 2 times as large as that obtained with NaI(Tl). Further problems with BGO are that it is very brittle (difficult to machine) and its high cost.

	BGO	CsI(Tl)	NaI(Tl)
Density [g/cm ³]	7.13	4.51	3.67
Linear absorption coefficient [cm ⁻¹] at 150 keV	9.98	3.5	2.22
Relat. pulse height (with respect to NaI(Tl)) %	8.10	45	100
Disintegration constant [μs]	0.3	1.0	0.25

Table 1 : Characteristics of a few widely used γ -ray scintillators.

Germanium is practically always used in semiconductor γ -ray detectors. Because of its higher density (see table 2) and higher Z it is much superior to silicon, except at very low energies (<50 keV). Because the energy gap is small, Ge detectors have to be used at low temperatures, for practical reasons at liquid N₂ temperature. Germanium detectors have a much better resolution than the best scintillators. It is about 1 keV at ^{137}Cs . It is therefore possible to resolve relatively complicated spectra, as are those observed in on-line spectroscopy.

	Si	Ge
Atomic number	14	32
Density [g/cm ³]	2.42	5.46
Energy gap [eV]	1.10	0.75
Average energy to create an electron-hole pair [eV]	3.6	2.975

Table 2 : Some characteristics of semiconductor detectors.

There is, however, one problem: the low energy lines "ride" on top of the Compton distribution produced by the interaction of higher energy transitions in the detector. When the number of lines is large, this Compton background gets large, so that small intensity peaks are not anymore detectable. In addition, the fit of the spectra is then quite difficult because of an

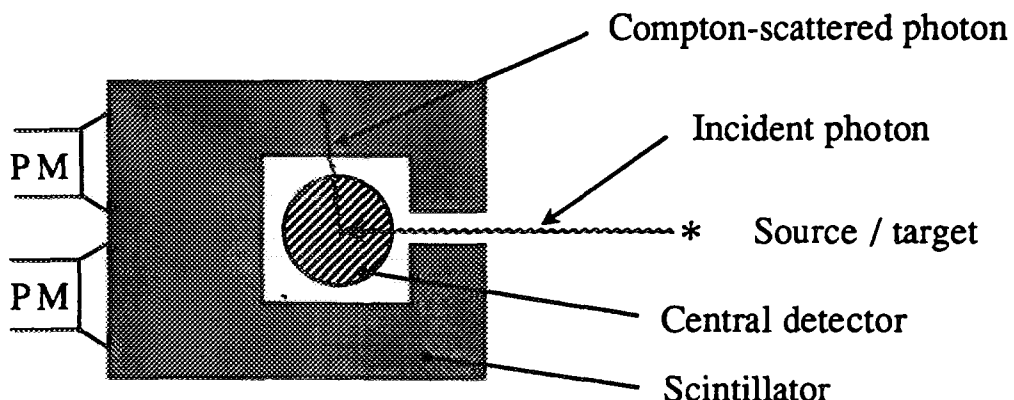


Fig. 3 : Cut of a Compton-Suppression Spectrometer (CSS) to show its principle of operation.

undulating background. Fig. 3 shows, in principle, how the background can be reduced by placing the germanium detector inside a scintillator. Suppose that a gamma-ray, emitted by a radioactive source or a target, impinges on the central Ge-detector and produces a Compton interaction. A scattered photon will in general escape (the probability depends on the size of the Ge detector). If it is detected by the scintillator, an electronic circuit will reject the electrical pulse produced by the central detector. Photoelectric events are not rejected and the peak-to-background ratio can be improved up to a factor 10.

Fig. 4 presents part of the γ -ray spectrum emitted following neutron capture in ^{159}Tb observed with a CSS. Without the Compton rejection the background would be much larger, especially at low energy. It must be noted that the spectrum in Fig. 4 presents results from neutron capture in a mono-isotopic target. When several elements (isotopes) are present, the spectra become more complicated. Isotopes with small capture cross section are then difficult to detect and the analysis may involve only the identification of the strongest lines.

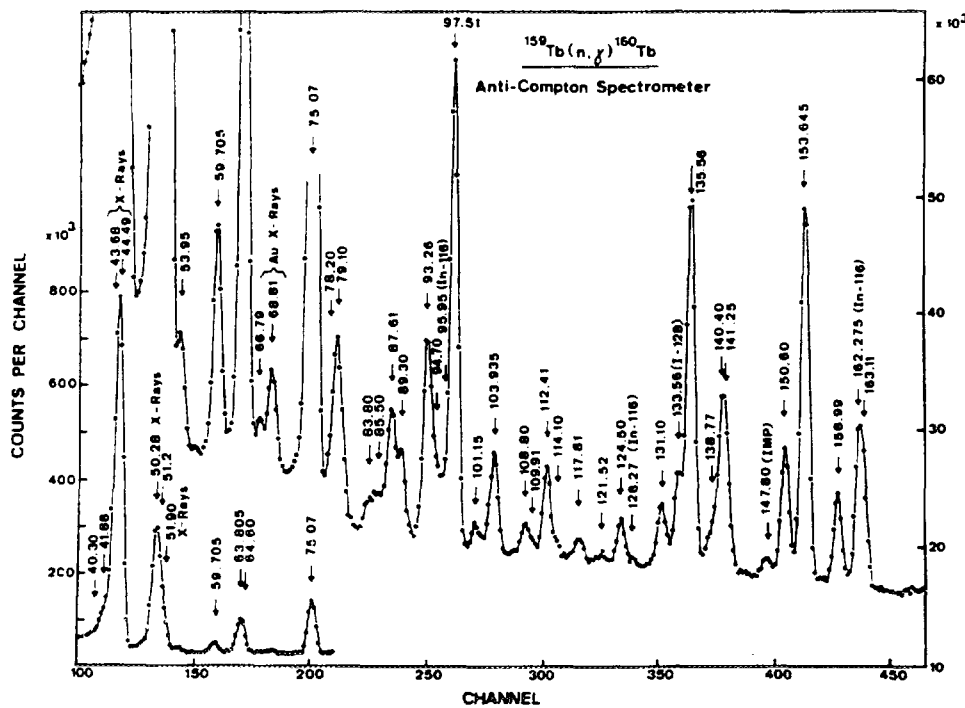


Fig. 4 : Portion of the low-energy part of $^{159}\text{Tb}(n, \gamma)$ spectrum observed with a Compton-suppression spectrometer [3]. The final nucleus being doubly odd, heavy and deformed, the spectrum is particularly dense.

When high-energy ($\gtrsim 2$ MeV) γ -rays impinge on a detector, the most probable interaction is the pair formation. The full photon energy can be released in the detector if the annihilation radiation is reabsorbed. If only one of the annihilation photon is reabsorbed, a "single-escape peak" will appear 511 keV lower in energy than the full energy peak. If both annihilation photons escape, a "double-escape peak" will appear in the spectrum 1022 keV below the full energy peak (Fig. 5). A monoenergetic transition will therefore produce 3 peaks in the spectrum, in addition to a Compton continuum. This leads to a complicated situation while

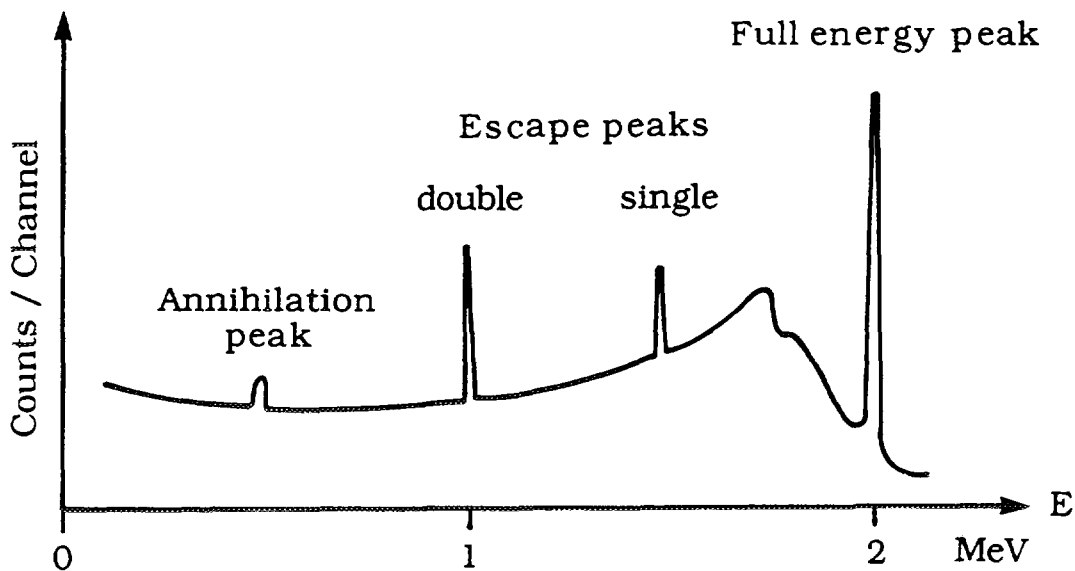


Fig. 5 : Response of a semiconductor detector to a monoenergetic radiation of energy $E_\gamma = 2 \text{ MeV}$. The (broader) annihilation peak is due to interaction of the radiation with matter in the neighbourhood of the detector. The relative intensities of the full energy and of the escape peaks depend on the detector volume and geometry.

observing simultaneously a larger number of transitions. To alleviate this situation a **pair spectrometer** has been devised to select the double-escape peak. The principle is shown in Fig. 6.

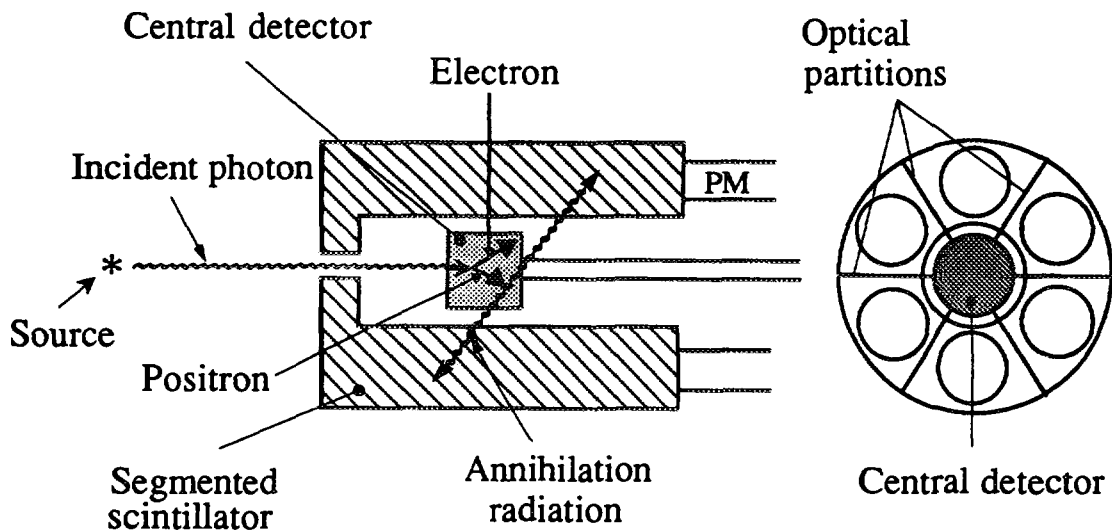


Fig. 6 : Principle of the pair spectrometer.

The germanium detector is placed in the axis of a large, cylindrical scintillator divided optically in six slices, each viewed by a photomultiplier (PM). The selection of a pair event is

performed by requiring a triple coincidence condition between the central detector signal and the 511 keV signals from two opposite slices of the scintillator. This system is very effective.

More detailed information on radiation detectors can be found in refs. [4-6].

3. The PGAA project at SINQ

A horizontal cut of the PGAA project is shown in Fig. 7. The facility will be placed at the end of a half guide. The cold neutron will be focused by a **neutron lens** on a target viewed by a pair and a Compton-suppression spectrometer. The scintillator of the pair spectrometer is made of NaI(Tl) which provides a relatively good selection of the 511 keV annihilation photons. The CSS scintillator will have a part in NaI(Tl) in the rear direction (towards the target) and a part of BGO in the front direction (close to the PM), because the Compton radiation is hard around the 0° (front) and soft in the rear direction (180°).

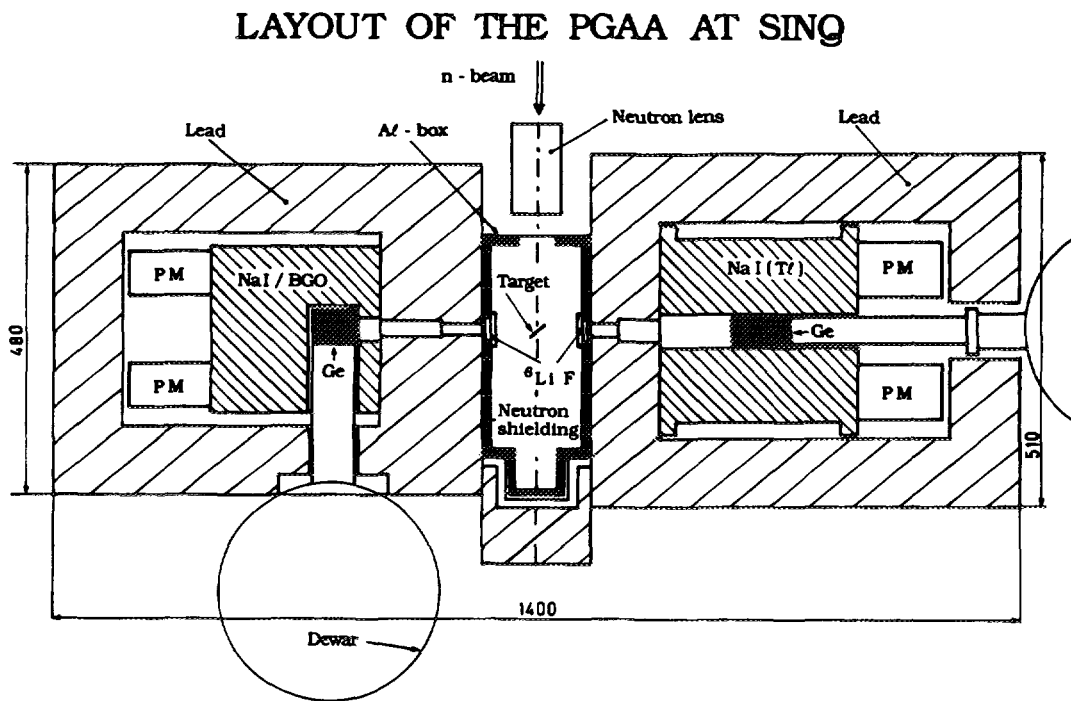


Fig. 7: Schematic plan of the PGAA facility at SINQ

One of the most interesting features is the neutron lens [7]. The principle is shown in Fig. 8. The neutrons are lead through a large number of capillaries just as light in optical fibers. The

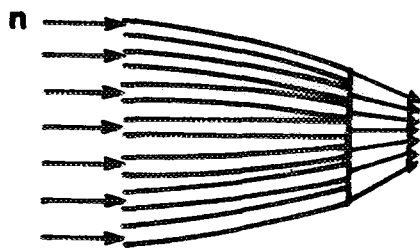


Fig. 8:
Principle of the neutron lens.

capillaries are converging toward a focus. The lens at PSI will produce a neutron spot of less than 1 mm diameter. The flux enhancement will be larger than 30. The use of the lens will provide the following advantages with respect to existing facilities (see e.g. [8,9]):

- increased sensitivity; very small sample of rare material can be analysed
- two-dimensional scanning of samples
- spectroscopy of isotopes with small capture cross sections.

4. Expected performances

Since the PGAA at PSI is not yet operational, we compare in Table 3 a few estimated sensitivity limits with effective numbers measured [2,10] at a facility in Japan [8]. We expect that we will be able to decrease the experimental limits, taking advantage of better conditions and of several experimental improvements.

Element	Predicted [µg]	Observed [µg]	Element	Predicted [µg]	Observed [µg]
H	0.1	1	Mn	0.1	2.2
B	0.0001	0.0023	As	2	9.1
Na	1	4.2	Cd	0.0005	0.007
Al	2	12	In	0.1	0.43
Cl	0.1	0.5	Nd	0.05	0.36
Ti	0.2	0.66	Sm	0.0002	0.003
Va	0.2	1.1	Gd	0.0001	0.0047

Table 3 : Observed [2,10] detection limits for cold-neutron PGAA compared with predictions.

Acknowledgments:

The author acknowledges the support of the Swiss National Science Foundation and of the Paul Scherrer Institut.

REFERENCES

- [1] D.A. Meyn, Metall. Trans. **5** (1974) 2505.
- [2] R.M. Lindstrom et al., Proc. 8th Int. Symp. on Capture Gamma-Ray Spectroscopy and Related Topics, Fribourg 1993, ed. J. Kern (World scientific, Singapore 1994) p. 955.
- [3] J. Kern et al., Nucl. Phys. **A221** (1974) 333.
- [4] W.R. Leo, Techniques for Nuclear and Particle Physics Experiments (Springer, Berlin Heidelberg 1987).
- [5] K. Debertin and R.G. Helmer, Gamma- and X-Ray Spectrometry with Semiconductor Detectors (North Holland, Amsterdam 1988).
- [6] C.F.G. Delaney and E.C. Finch, Radiation Detectors (Clarendon Press, Oxford 1992).
- [7] M.A. Kumakhov and V.A. Sharov, nature **357** (1992) 390; H. Chen et al. Nature **357** (1992) 391.
- [8] C. Yonezawa et al., Nucl. Instr. Meth. **A329** (1993) 207.
- [9] G. Molnár et al., J. Radioanal. Nucl. Chem. **167** (1993) 133.
- [10] C. Yonezawa, Anal. Sci. **9** (1993) 185.



Neutron Activation Analysis (NAA), Radioisotope Production via Neutron Activation (PNA) and Fission Product Gas-Jet (GJA)

Heinz W. Gäggeler

*Labor für Radio- und Umweltchemie, Universität Bern, Freiestrasse 3, CH-3012 Bern
and*

Labor für Radio- und Umweltchemie, Paul Scherrer Institut, CH-5232 Villigen PSI

ABSTRACT

Three different non-diffractive applications of neutrons are outlined: neutron activation analysis, production of radionuclides, mostly for medical applications, and production of short-lived fission nuclides with a so-called gas-jet. It is shown that all three devices may be incorporated into one single insert at SINQ due to their different requests with respect to thermal neutron flux. Some applications of these three facilities are summarized.

1. Introduction

Neutron activation analysis (NAA) is a powerful technique in analytical chemistry. It bases on the well known fact that via neutron capture stable nuclides transform to neighbouring, mostly radioactive isotopes. A measurement of the nuclear decay of these isotopes, usually via γ -spectroscopy, can then be used for a quantitative mass determination of the corresponding element. For NAA without any chemical separation the acronym INAA (Instrumental-NAA) is used, and if chemical separations are required after irradiation but prior to a measurement of the radioactive species the label RNAA (Radiochemical-NAA) is applied.

A clear advantage of NAA is the fact that it is a non-destructive method. This strongly reduces contamination problems. NAA is therefore a reference technique in analytical chemistry and often the preferred method in ultra-trace analysis. Most of the alternative techniques such as inductively coupled plasma - mass spectrometry (ICP-MS) and - optical emission spectrometry (ICP-OES) as well as atomic absorption spectrometry (AAS) and others require dissolution of the sample prior to injection into the corresponding device.

Formation of radioactive nuclides via neutron-capture (PNA) is also frequently applied for production of radiotracers for widespread applications. Examples are optimizations in chemical synthesis or developments of chemical analytical separations. Important is also the production of radioisotopes for radio-pharmaceutical and nuclear medical applications. In this case, relatively long-lived radionuclides (half-lives \geq hours) are needed since production facility and application site (i.e. hospital) are usually not within short distance. Moreover, for therapy applications highly radioactive compounds are needed. The irradiation facility has then to fulfill some special requirements to safely handle such a production site.

Another application of thermal neutrons in radiochemistry are the so-called gas-jet facilities for fission products [1]. Here, a thin ^{235}U target is placed in a closed chamber exposed to neutrons. This chamber is continuously flushed with a carrier gas containing aerosol particles. From the target recoiling fission fragments are thermalized in the gas and then attached to the aerosol particles. With high efficiency such particles can then be swept out of the production chamber and continuously transported along thin capillaries to a laboratory. With this technique short-lived nuclides with half-lives down to about one second are available for further applications such as e.g. chemical studies. Typical examples are modeling experiments for heaviest elements or studies of surface chemical interactions in an aerosol. A special option is to use the nuclear decay time as a clock to measure a time of a chemical reaction [2].

2. The concept of „Insert 60“ at SINQ

All three different techniques described above have been included into one single insert (see [3]). This was possible due to their different requests with respect to thermal neutron flux. The position of RPN is closest to the core, with the highest beam intensity, followed by the position of NAA, and, finally, by the gas-jet facility. Expected thermal neutron fluxes are $4 \cdot 10^{13}$, 10^{13} and $10^9 \text{ cm}^{-2}\text{s}^{-1}$ at the positions of PNA, NAA and GJA, respectively.

3. Neutron activation analysis (NAA)

Neutron activation analysis is especially attractive if short-lived isotopes are formed by the neutron capture process. This requires a fast transportation of the samples, mounted in a suitable container, from a laboratory to the irradiation position and back again. Usually the containers are moved via pneumatic transport („rabbit“ systems). Such a device was operational for many years at the SAPHIR reactor („BLASIUS“ system). With this system the samples were irradiated between 20 s and 1 h at a flux of $2.2 \cdot 10^{13} \text{ cm}^{-2}\text{s}^{-1}$ and then transported along a 100 m pneumatic transfer tube to the radiochemistry laboratory in a neighbouring building.

Generally, the production of an isotope via NAA may be described by the following equation:

$$A = N\sigma\phi[1-\exp(-\lambda t_b)]\exp(-\lambda\Delta t)[\lambda t_m/\{1-\exp(-\lambda t_m)\}] \quad (1),$$

with

A: Activity of the produced isotope at the beginning of the counting time, in Becquerel (Bq)
N: Number of target atoms, in cm^{-2}

σ : Thermal neutron capture cross section, in cm^2 (see e.g. [4])

λ : Decay constant of the produced isotope, in s^{-1} (see e.g. [4])

t_b : Irradiation time, in s

Δt : Time difference between end of bombardment and start counting, in s

t_m : Measuring time, in s

ϕ : Neutron flux, in $\text{cm}^{-2} \text{s}^{-1}$

As a general rule, an activity of 10 Bq can be defined as detection limit.

In reality NAA is mostly used as a relative method since the neutron flux at the irradiation position is not known with sufficient accuracy and usually not constant along the irradiation tube. This has the consequence that standards have to be irradiated simultaneously with the real samples.

Detection limits which may be reached with NAA for a 10 min irradiation with 10^{13} n/cm² s are summarized in Table I. They base on an activity of 10 Bq after a Δt of 20 s (a typical minimum time expected for transportation and mounting of the samples in front of a detector at the new device NAA/SINQ). However, it has to be kept in mind that the detection limit might be higher if no convenient γ -line is available for detection. Moreover, if less than 1g of material is used, the detection limit has to be corrected accordingly.

Table I: Detection limits for several elements in a *1g sample* under typical SINQ conditions and an irradiation time of 10 min (see text).

Element	Detection limit in ppb	Element	Detection limit in ppb
Mg	20	Rh	0.002
Al	0.2	Ag	0.01
Cl	3	Cd	100
Ca	70	In	0.03
Sc	0.02	Sn	50
Ti	20	I	0.2
V	0.02	Ba	10
Cr	10	Pr	0.2
Co	0.01	Nd	7
Cu	0.2	Sm	0.2
Ge	3	Gd	2
Se	0.2	Dy	0.001
Br	0.2	Hf	0.04
Rb	15	Re	1
Nb	2	Pt	5
Mo	20	Hg	10

$$1 \text{ ppb} = 1 \text{ part per billion} = 10^{-9} \text{ g/g}$$

At BLASIUS typical applications of NAA were

- trace analysis of heavy metals in the system atmosphere-biosphere(forest)-soil,
- determinations of several essential elements in food,
- Se concentrations in blood plasma or Cu in liver tissues (Wilson disease),
- absolute mass determinations of silver aerosols,
- studies of halogen profiles in meteorites,

- irradiations of single crystals doped with ^{235}U for diffusion studies of fission products,
- La determinations for industry (EMS company) etc.

With the new NAA/SINQ facility the samples will be transported within less than 10 s to the radiochemistry laboratory at PSI West (WBGA/C41). There the tubes (polyethylene, dia. 25 mm, length 48 mm) containing the samples will be collected in a shielded container placed inside a hood. After dismounting, the samples will be measured with HPGe detectors placed at a distance of a few meter from the hood. For informations on γ -spectroscopy see [5]. Nuclides with half-lives as short as about 10 s may be determined.

With this new facility similar applications are scheduled as for the previous BLASIUS device. The emphasis will most probably lie on aerosol studies, since NAA as a non-destructive multi-element detection method is especially powerful as a „finger print“ technique to investigate source regions of such particles. Other fields of future interest may be heavy metal trace analysis in samples from solid state chemistry or from environmental samples as well as rare earth determinations in e.g. meteorites. It's also planned to increase NAA applications for external users, both for research (e.g. earth sciences or materials sciences at universities and research centres) as well as for industry. Last but not least applications of this facility for educational purposes should be mentioned.

4. Radioisotope Production via Neutron Activation (PNA)

This chapter bases on informations made available to the author by P. Bläuenstein [6]. Production of labelled radiopharmaceuticals requires access to radionuclides with high specific activity, in some cases of carrier-free species. Of great interest are nuclides which can be incorporated into molecules with high tumor affinity. Optimum are nuclides with half-lives of similar values as the time periods these molecules are biologically active, usually about 0.5 to 5 days. For therapy applications weak $\beta-$, Auger electron or even α -emitters are used due to their high local energy deposition. For monitoring purpose it is useful if these nuclides emit γ -rays, however with low probability, to reduce whole body irradiation. Total activities of up to 20 GBq may be applied to a single patient (e.g. of ^{131}I -meta-iodbenzylguanidin for neuroblastom therapy).

In case of diagnostic applications much lower activities are used, typically on the order of 10 to 100 MBq per patient.

Typical radionuclides used at PSI and to be produced with SINQ/PNA are ^{131}I ($T_{1/2} = 8.0$ d) from nuclear fission of ^{235}U , and ^{111}Ag ($T_{1/2} = 7.45$ d), produced via neutron activation of ^{110}Pd and subsequent β -decay and ^{186}Re ($T_{1/2} = 3.8$ d) from neutron activation of ^{185}Re .

5. Fission product gas-jet system (GJA)

Thermal neutron induced fission of ^{235}U produces a well known double-humped distribution of fission nuclides (Fig. 1). The so-called light fission fragments are centered around mass numbers (isobars) $A = 95$ and the heavy ones around $A = 138.5$ (the difference of about 2.5 mass units between the sum of both values and the mass of the fissioning nucleus, ^{236}U , is caused by evaporation of prompt neutrons). The corresponding second

moments of both mass peaks are rather high with 15 and 22 mass units for the light and heavy mass peak, respectively, which leads to a broad range of elements being produced as primary fission fragments. They are, at a level of $\geq 1\%$ independent fission yield [4], Se, Br, Kr, Rb, Sr, Y, Zr, Nb, Mo and Tc in the light peak and Sb, Te, I, Xe, Cs, Ba, La, Ce, Pr and Nd in the heavy peak. The primary products are neutron rich isotopes of the corresponding elements which have short half-lives of typically a few seconds to minutes. Via β -decay chains long lived secondary fission products are formed. Well known examples of such secondary products are ^{137}Cs , ^{90}Sr or ^{131}I .

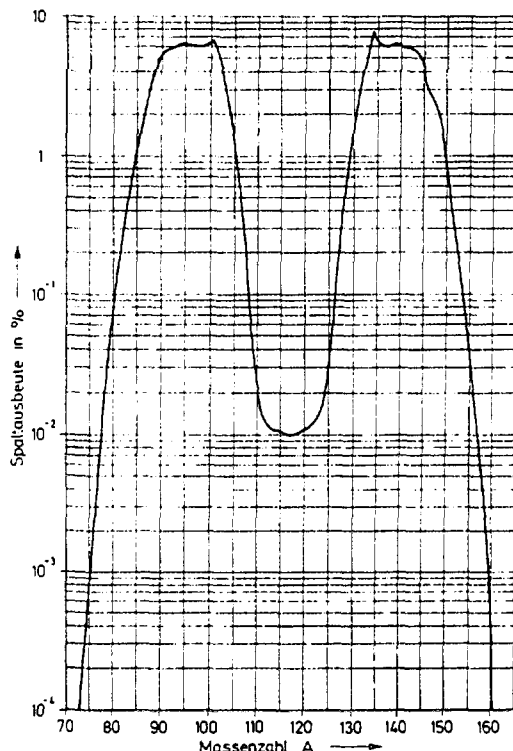


Fig. 1: Mass distribution from thermal neutron induced fission of ^{235}U [7].

The average total kinetic energy (TKE) released to both fission fragments is, for thermal neutron induced fission of ^{235}U , 168.3 ± 1.7 MeV. Due to moment conservation, this TKE is divided to the fragments indirectly proportional to the fragment masses, i.e. the light fission fragments have average kinetic energies of about 100 MeV and the heavy ones of about 69 MeV. This has the consequence that fission products from the light mass peak have higher recoil ranges in a material than those of the heavy mass peak.

Fission product gas-jet facilities use ^{235}U targets of $\leq 1 \text{ mg/cm}^2$ thickness. In this case most of the fission products escape from the target. They can then be thermalized in a gas volume. Typical ranges for fission products in gases - under NTP condition - are about 1 to 2 cm in Ar and N_2 and about 15 cm in He. To design a device which should make available fission products from the light mass peak only the target has to be covered by a degrader foil of appropriate thickness.

Usually, the primary products attach via diffusional processes and adsorption to aerosol particles contained in the gas. Mostly salt or graphite particles of about 20 to 100 nm size are used for this purpose. If the carrier gas containing the aerosol particles is continuously flushed through such a collection chamber, the fission products can be continuously transported from

the production site along thin capillaries (typically with 1 - 2 mm diameter) over long distances to a laboratory. The relatively large aerosol particles have low diffusion coefficients which prevents losses caused by surface interactions with the wall of the capillary. On the other hand, gravitational sedimentation velocities are still small, preventing losses due to this effect.

At SINQ a set of three different production chambers will be installed (Fig. 2). All three chambers contain two ^{235}U targets, one at the front side and one at the rear side. Each target contains 2.5 to 3 mg ^{235}U . This yields a fission rate of about 10^7 s^{-1} in each chamber, assuming a thermal neutron flux of 10^9 s^{-1} and a fission cross section of 584 barn. To adjust the real fission rate to the needs of the experiment, a tunable mechanical shutter will be placed in front of the chamber array which will allow to vary the neutron beam impinging onto the targets between 0 and 100 %.

The sizes of the chambers are adjusted to the following applications:

Chamber 1 : All fission products in Ar or N₂. No cover foil.

Chamber 2 : All fission products in He. Target covered by a 3 μm thick Ni cover foil to pre-degrade fission fragment energy. This is required to reduce the total recoil range in He to the dimensions of the chamber.

Chamber 3: Light fission products in Ar or N₂. Target covered by a 6 μm thick Ni cover foil to stop entirely the fission fragments from the heavy mass peak.

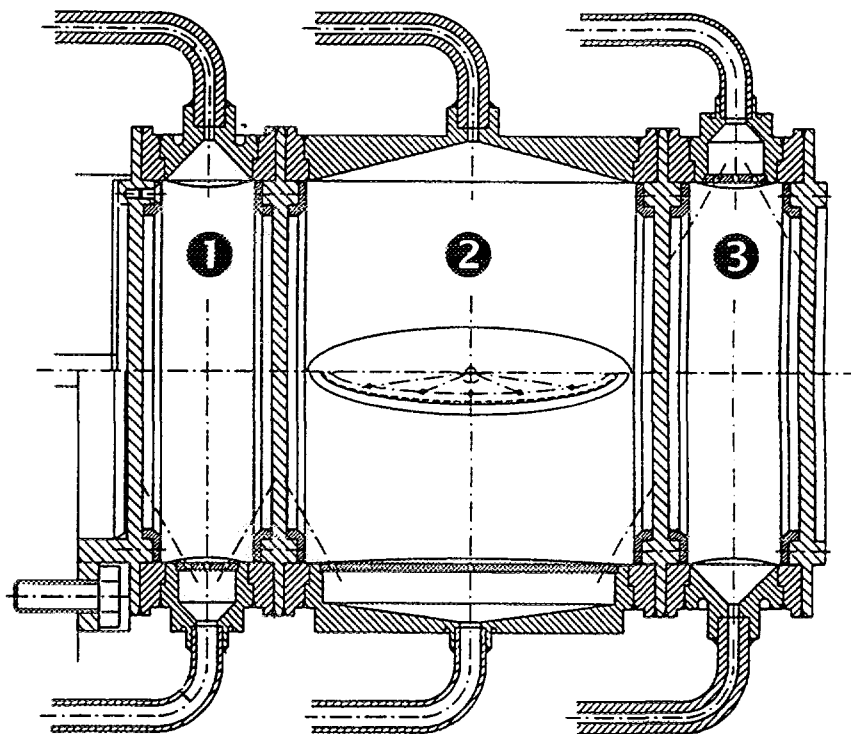


Fig. 2: Layout of the array of the 3 SINQ gas-jet chambers (see text)

The reason for including chamber 3 is initiated by the fact that some fission products from the heavy mass peak have very complicated γ -spectra. This may hamper detection of some nuclides from the light mass peak. An example of a γ -spectrum measured in a gas-jet device with degrader foil is depicted in Fig. 3 [8].

In a first series of experiments it is planned to run modeling experiments with the nuclides ^{105}Mo ($T_{1/2} = 37$ s) and ^{106}Tc ($T_{1/2} = 36$ s) to develop a fast separation device for studying the chemistry of element 106 (Seaborgium, Sg) and, for the first time, of element 107 (Nielsbohrium, Ns). Mo and Tc belong to the same groups in the periodic table as Sg and Ns, respectively.

Another planned application intends to produce brominated organic molecules, labelled e.g. with ^{87}Br ($T_{1/2} = 56$ s), to investigate heterogeneous surface interactions with supercooled droplets, a topic of great current interest in the context of the ozon depletion problem in the stratosphere.

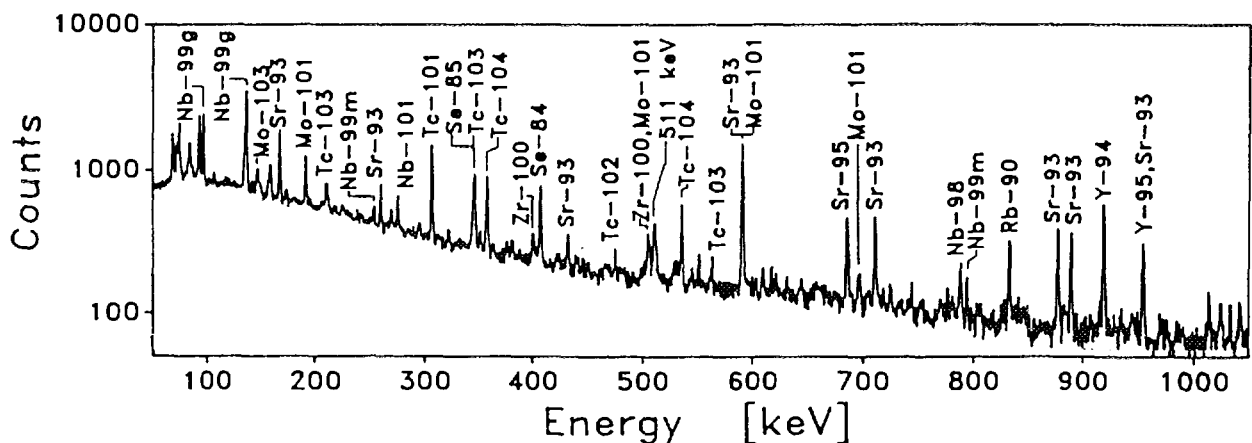


Fig 3: γ -spectra of fission products from a gas-jet device containing a target covered by a 12 μm thick Al foil (from ref. 8). Only fission products from the light mass peak are visible.

References

- [1] see e.g.: G. Herrmann, N. Trautmann, *Ann. Rev. Nucl. Part. Sci.* (1982) **32**
- [2] H.W. Gäggeler, D.T. Jost, U. Baltensperger, A. Weber, A. Kovacs, D. Vermeulen, A. Türler, *Nucl. Instr. Meth.* **A309** (1991) 201
- [3] E. Lehmann, *these Proceedings* (1996)
- [4] Karlsruher Nuklidkarte, 5th Edition (1996)
- [5] J. Kern, *these Proceedings* (1996)
- [6] P. Bläuenstein, *priv. communication* (1996)
- [7] see e.g. R. Vandenbosch, J.R. Huizenga, in *Nuclear Fission*, (Academic Press, New York and London, 1973)
- [8] Ya Nai-Qi, D.T. Jost, U. Baltensperger, H.W. Gäggeler, *Radiochim. Acta* (1989) **47,1**



The SINQ Data Acquisition Environment

David Maden

*Paul Scherrer Institut
CH-5232 Villigen PSI, Switzerland*

ABSTRACT

The data acquisition environment for the neutron scattering instruments supported by LNS at SINQ is described. The intention is to provide future users with the necessary background to the computing facilities on site rather than to present a user manual for the on-line system.

1. Introduction

A user's view of the data acquisition system (DAQ) of a neutron scattering instrument is typically as shown in Fig. 1. Commands to the system are entered via the key-

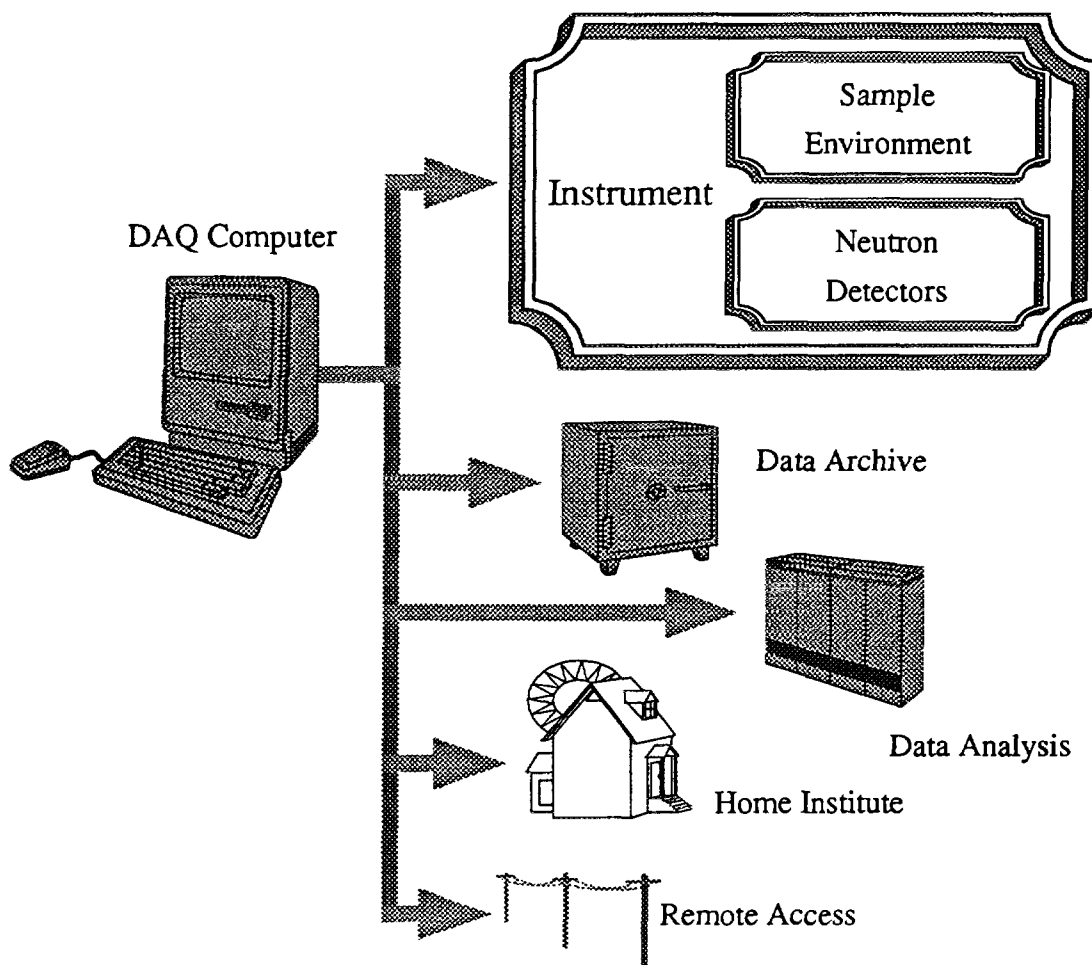


Fig. 1 : User View of a Neutron Scattering Data Acquisition System

board and mouse of the DAQ computer and the feedback to the user is via the display. This is particularly the case if one is working in a counting room, remote from the instrument.

The user requires the means of setting the environment of his sample and, once these settings have been realised, to perform a measurement. The results of the measurements must be archived for later analysis.

The DAQ system should:

- provide the user with an ergonomic, physics oriented interface to the instrument;
- provide the user with sufficient feedback to satisfy him that his measurement is proceeding correctly;
- continually monitor the sample's environment, generating alarms and taking appropriate action if parameters such as temperature go out of tolerance;
- automate routine procedures wherever feasible, allowing the user to initiate measurement sequences which may last for several hours;
- allow remote access, possibly via modem, so that the user may monitor the progress of a measurement sequence and, if necessary, take corrective action.

Access to the user's home institute (e.g. for e-mail or for the transfer of measured data) and access to data analysis engines (e.g. for on-line analysis in real-time of the measured data) should also be available.

2. Data Acquisition Configuration

A block diagram of a SINQ instrument is shown in Fig. 2. Most of the "slow" devices associated with the instrument geometry and sample environment are controlled via RS-232-C devices connected to a terminal server. The various types of multi-detector are connected via a fibre optic link to a histogramming memory. More details of the interfacing of these devices is given in Section 6.

A very early decision was made in the design of the SINQ data acquisition system [1] to use an Ethernet based network for interconnecting the components of the system. The resulting configuration is shown in Fig. 3. The use of a network interconnection strategy has provided great freedom in the physical location of the various devices. The location of devices as shown in the diagram is therefore subject to change. In the early design stages, it was assumed that most activity, and hence most of the electronics, would be situated in the counting rooms, as is normal with experiments at particle accelerators. With the passage of time, the expected centre of gravity of activity seems to be drifting towards the vicinity of the instrument, more in keeping with the practice at reactor centres.

For routine operation, however, it is still expected that the data acquisition computer will be used directly and will be located in the counting room. For setting up opera-

tions, an X-terminal, located near to the instrument, will be available for running tests by means of a remote-login to the data acquisition computer.

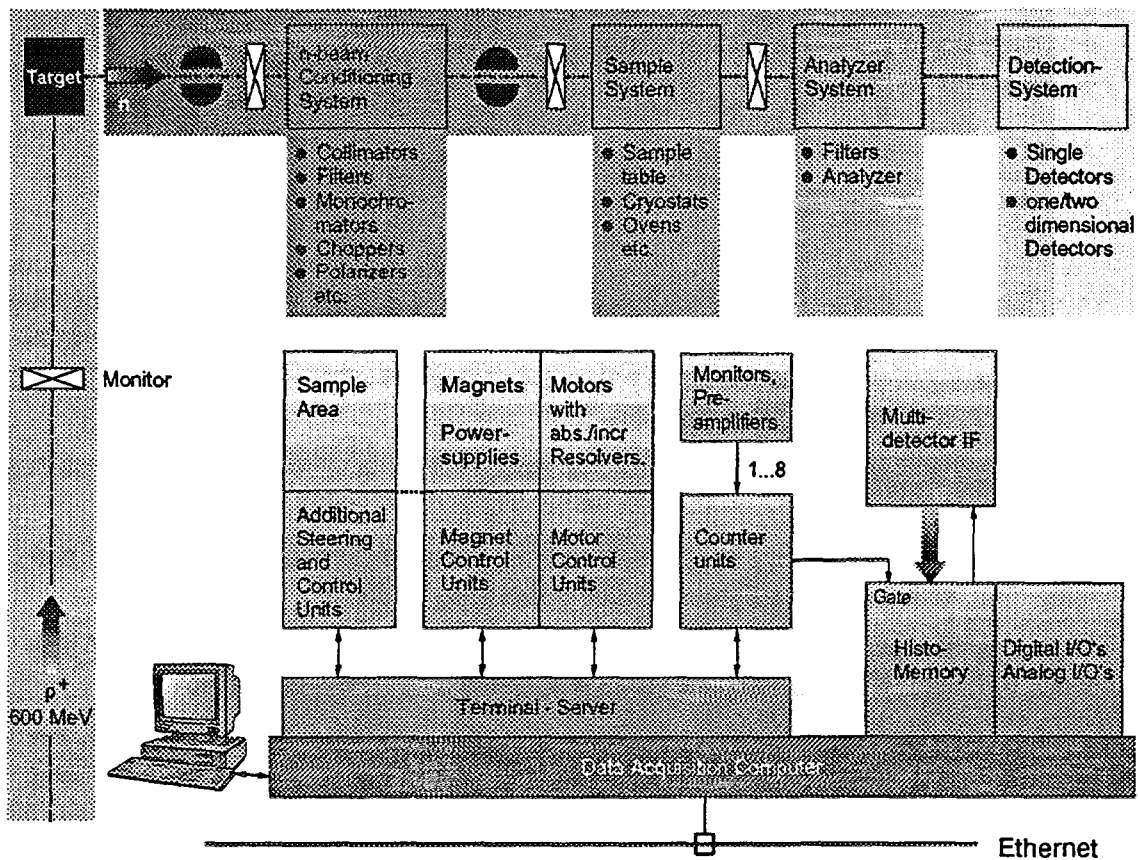


Fig. 2 : Block Diagram of a SINQ Instrument

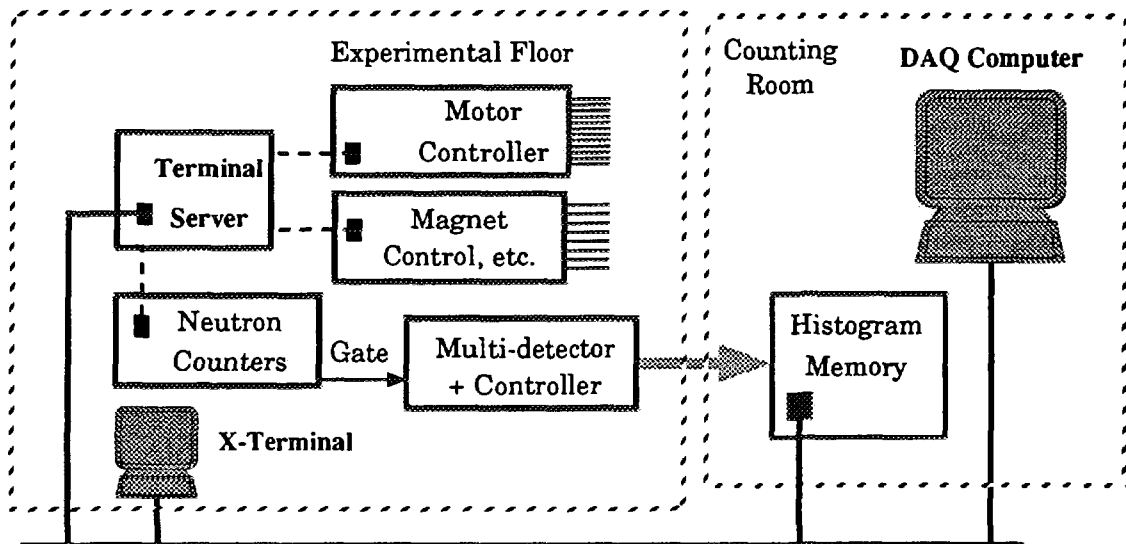
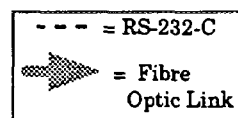


Fig. 3 : Typical SINQ Instrument Layout.

The Ethernet connections are only schematic. See Sect. 3 for more detailed information. The Terminal Server may also handle GPIB devices.



For low-level debugging of the RS-232-C devices, the “terminal server”, which is also located in the vicinity of the instrument, can be used in stand-alone mode. For large instruments such as SANS, it may be advantageous to install a second terminal server with its relatively reliable network cable rather than attempting to drive RS-232-C connections over long distances.

3. Computer Networking

The main advantage and motivation for using the Ethernet for interconnecting the various components of the data acquisition system is the increased geographical flexibility in locating the various devices of the system without the necessity of designing and installing complicated cabling systems.

There are, of course, potential disadvantages to this approach which must be considered:

- a failure in one of the, normally transparent, network components can block data acquisition and be difficult to locate;
- the network must be configured so that there is sufficient isolation between the various instruments to avoid mutual interference;
- certain experiments may saturate the network. In general, though, the Ethernet bandwidth is more than adequate for most neutron scattering experiments and can, if necessary, be expanded further;
- there is the possibility of destructive hacking.

Experience at PSI has shown that the advantages outweigh the disadvantages. Medium energy particle physics and μ SR experiments on the PSI cyclotron use Ethernet connections to transfer data between front-end data acquisition computers and back-end monitoring/data-archiving computers [2]. The network is realised via thin-wire Ethernet cable segments and failures due to the network have proven to be minimal.

In the SINQ halls, the network capability is much higher. The network cabling is concentrated through three network “hubs”. From these hubs, there is a fibre optic link to the vicinity of each instrument and several 10baseT (twisted-pair Ethernet) connections to each counting room. The fibre optic links are terminated in distribution boxes with 8 10baseT connections per instrument. The network connection hierarchy is shown in Fig. 4. Each experiment has its own independent Ethernet for devices in the vicinity of the instrument and for devices in the counting room. Transfers between the counting room and the experimental floor, however, go via the hub and could be subject to interference from other experiments. The comparatively high bandwidth of the hub is expected to render this interference insignificant. If it proves to be a problem, extra isolation can be installed in the hub.

Since there is likely to be a relatively high data traffic between the histogram memory module (see Sect. 6.3) and the host computer, it is intended to locate both of these in the counting rooms so that the data transfers do not go via the hub. A separate fibre optic link between the instrument and its counting room will be installed to enable this.

4. Data Acquisition Software

So far, effort has been concentrated on software for the triple-axis and diffraction experiments. In this respect, we are very grateful to ILL and, in particular, Alain Barthélémy and John Allibon, for allowing us to adopt and adapt their MAD/TASMAD software to the SINQ environment. The main work on our side has been:

- to replace the sections of code associated with the driving of motors and neutron counters to use PSI equivalents;
- to modify the *PLOT* command so that it provides a better quality plot of the current measurement by means of the PGPlot package;
- to enhance the MSPY program, a utility which provides an updating display of the status of TASMAD, so that a plot of the current scan is presented and
- to modify the data format of the archived data to follow the recommendations of the SOFTNESS working group.

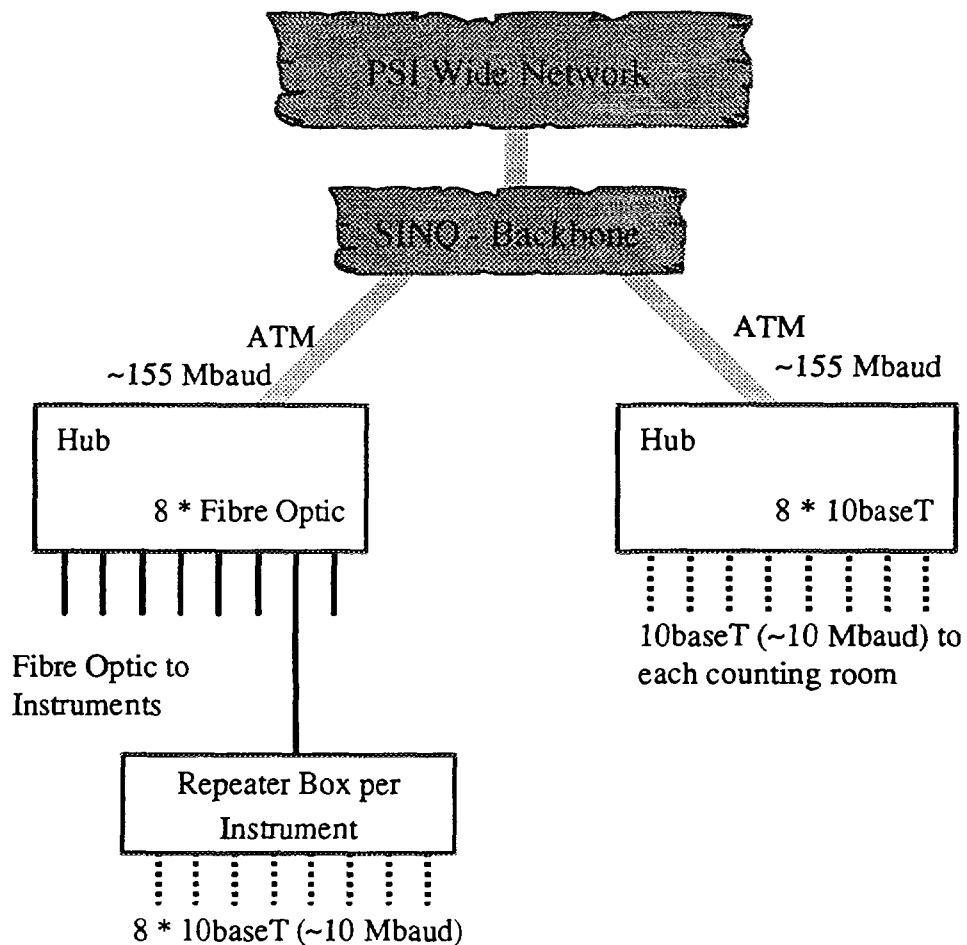


Fig. 4 : Network Hierarchy in the SINQ Halls

The development of code to handle the histogram memory with associated multi-detectors and to handle a temperature controller is still in development.

MAD, in its various forms, is a command-line oriented system running under the OpenVMS operating system on VAX or AXP computers. The possibility of porting the software to a Unix environment prior to the startup of SINQ is still open. An alternative route, which is being explored and which may prove to be more user friendly and portable, is to use the Tcl/Tk scripting language as a means of implementing the MAD capabilities.

For details of using MAD, reference should be made to the user documentation [3]. The following two examples are provided simply to give a flavour of what is available:

```
MAD > lt
```

TARGETS AND POSITIONS

```
*****
```

	POSN	TARG		POSN	TARG
A1	80.00	-1.65	A2	163.76	163.76
etc.					

```
MAD > scan en 16 den 2 np 15 mn 10000
```

The first command, lt, is the “List Targets” command. The actual and requested (target) motor positions are displayed. The second command, scan, is the command to perform a scan. This may be either a scan of simple physical quantities such as motor positions or temperature or, as in the above example, something much more complex. In the example, a 15 point (np) scan of the neutron energy transfer (en) about a central value of 16 meV is performed. The step size (den) is 2 meV and, at each position, a measurement is performed until the incident neutron monitor (mn) has accumulated a count of 10000.

5. Data Archiving and Data Transfer Facilities

In October 1994, the first workshop on Software Development at Neutron Scattering Sources, SOFTNESS, took place at ANL, Argonne. A small group of software specialists, mainly from neutron and X-ray sources in the USA, met to discuss the common problems in software development and support at the various sites. A follow-up meeting took place at NIST, Gaithersburg, in September, 1995. The most fruitful result of these meetings to date has been the specification of a common data format, NEXUS [4].

A description of NEXUS would exceed the scope of this report. Suffice it to say that it is based on the Hierarchical Data Format, HDF [5]. This was originally designed as a platform independent data format for the exchange of scientific data at the NCSA, Illinois. The HDF library is available for a wide range of computer architectures and operating systems and HDF files are portable between these various systems. Scalar and vector data items can be created within an HDF file and grouped together into a self-describing hierarchy. This is ideal for saving neutron scattering data.

The triple-axis software has been enhanced to provide a command for writing data files following the current NEXUS proposals. The existing ILL ASCII format is, of course, also available. Conversion programs from NEXUS to other data formats will be provided as required.

The simplest place to store one's measured data is on the disk of the data acquisition computer. Disk space here is, however, limited. It is intended to set up a procedure so that acquired data files are transferred automatically to the central PSI file archive. There is also the possibility of transferring data to one's home institute via the Internet or of writing it to various types of tape or diskette.

6. Instrument Interfacing

This section should not be relevant to the average user of SINQ since it is the purpose of the data acquisition software to conceal such details from him. However, on those hopefully rare occasions where there are hardware or software problems with the system, such details may be helpful in resolving the problem.

6.1 RS-232-C Devices

As can be seen from Figures 2 and 3, most interfacing with an instrument's hardware is via asynchronous serial RS-232-C connections. For those devices developed at PSI, there is a simple command/response protocol over the serial line. There is also an interrupt mechanism provided in the protocol but the use of this has been avoided in the software in the interests of reliability and with a view to transferring the software to other operating systems in the future.

The serial devices are connected to a *terminal server*. The server software has been developed using LabVIEW. It operates as a classical TCP/IP server providing a service to its clients, in this case, the MAD software running on the host computer. Up to 8 clients may be active concurrently on any given server, MAD establishes connections to the server on a per device basis and is therefore able to communicate with several servers concurrently.

6.2 GPIB Devices

At present, there are no devices foreseen which require interfacing via the GPIB (IEEE-488) bus. Should the requirement for GPIB devices arise, a GPIB interface will be added to the terminal server. LabVIEW, the subsystem used to implement the server, provides good GPIB support. It should therefore be straightforward to extend the TCP/IP protocol of the terminal server to cover GPIB devices and to enhance the terminal server software accordingly.

6.3 Multi-detectors and Position Sensitive Detectors

The interfacing of multi-detectors and position sensitive detectors is currently being developed. A block diagram of the electronics is shown in Fig. 5. The multi-detector interface can be configured to suit the various types of detector and will convert signals from the detector into a data stream via a fibre optic link to the histogram memory.

The histogram memory is realised as a PowerPC single board computer housed in a VME module. In its first version, at least, it will act as a TCP/IP server to the data acquisition software in a similar way to that which has been employed successfully in the μ SR experiments at PSI [6]. The data acquisition software will be able to configure the histogram memory, instruct it to acquire data and to read out the compiled histograms via the network link.

7. Conclusion

This report has attempted to provide prospective users with an overview of what they might expect to be available on the various SINQ instruments. At the time of writing (July 1996), there was still no complete spectrometer available on which realistic testing could be performed. Some changes are therefore to be expected before the first

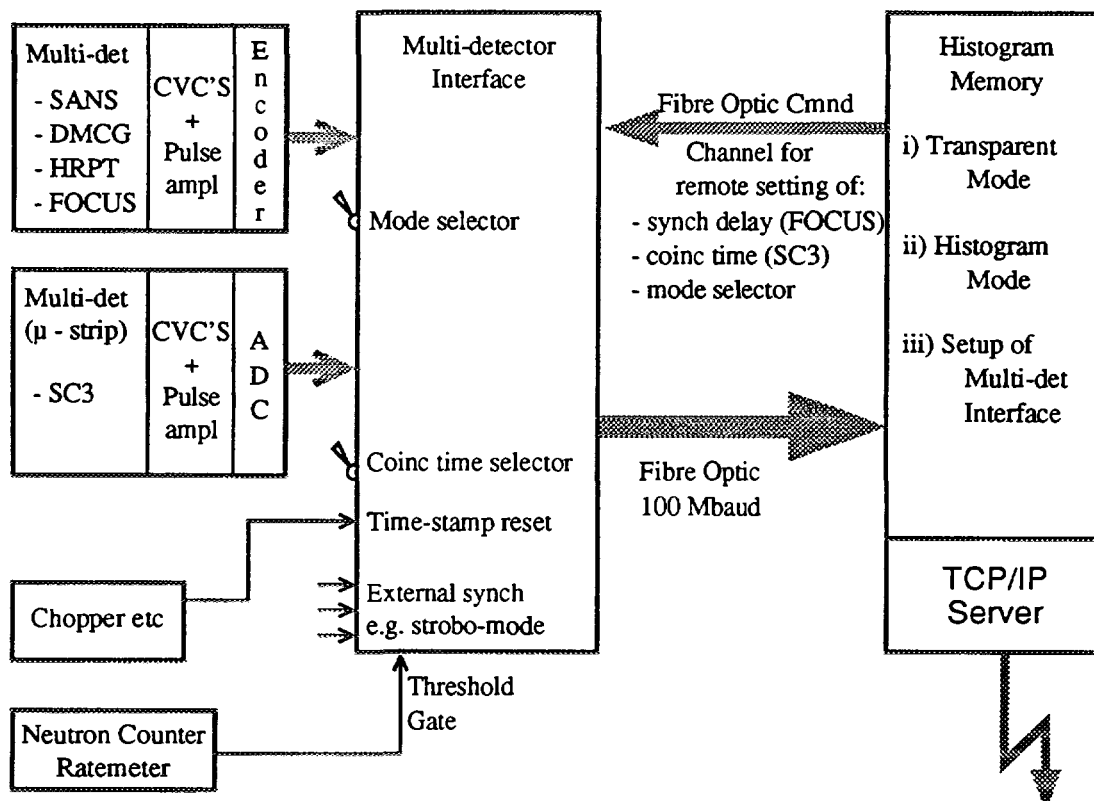


Fig. 5 : Block Diagram of Detector Electronics

neutron will be measured. It is hoped that these changes will be more of a cosmetic nature and that the fundamental structures described here will remain valid.

8. Acknowledgements

Apart from the indebtedness to ILL already mentioned in the text, I should like to thank my co-workers, Heinz Heer, Mark Könnecke, Marc Pepin and Markus Zolliker for their valuable contributions. We are also very grateful for the efforts of many groups at PSI, in particular the Networking Group under Hermann Kneis and the Electronics Group under Nik Schlumpf.

9. References

1. H.Heer, *Computer Concept for SINQ Experiments*. PSI Internal Report, SINQ/891/HH33-401, February 1994 (in German).
2. F.W.Schlepütz, *TANDEM, the new Data Acquisition System at PSI*. IEEE Transactions on Nuclear Science, NS-36(5):1630-1634, October 1989.
3. P. Blanchard et A. Barthélemy, *TASMAD User's Manual, Version 1.2*, I.L.L.,Grenoble, France, 1994.
4. Reports on the SOFTNESS meetings and information on the NEXUS proposals can be found at the WWW site, <http://www.neutron.anl.gov/>.
5. HDF is available via anonymous FTP from <ftp.ncsa.uiuc.edu>. Documentation will be found in directory /Documentation/HDF/HDF3.3/Ref_Manual.
6. D.Maden, *The μSR Histogram Memory Server*, PSI Internal Report CTN-94-005, Oct 1994.



SUMMARY ON EXPERIMENTAL FACILITIES AND FUTURE DEVELOPMENTS AT SINQ

GÜNTER S. BAUER

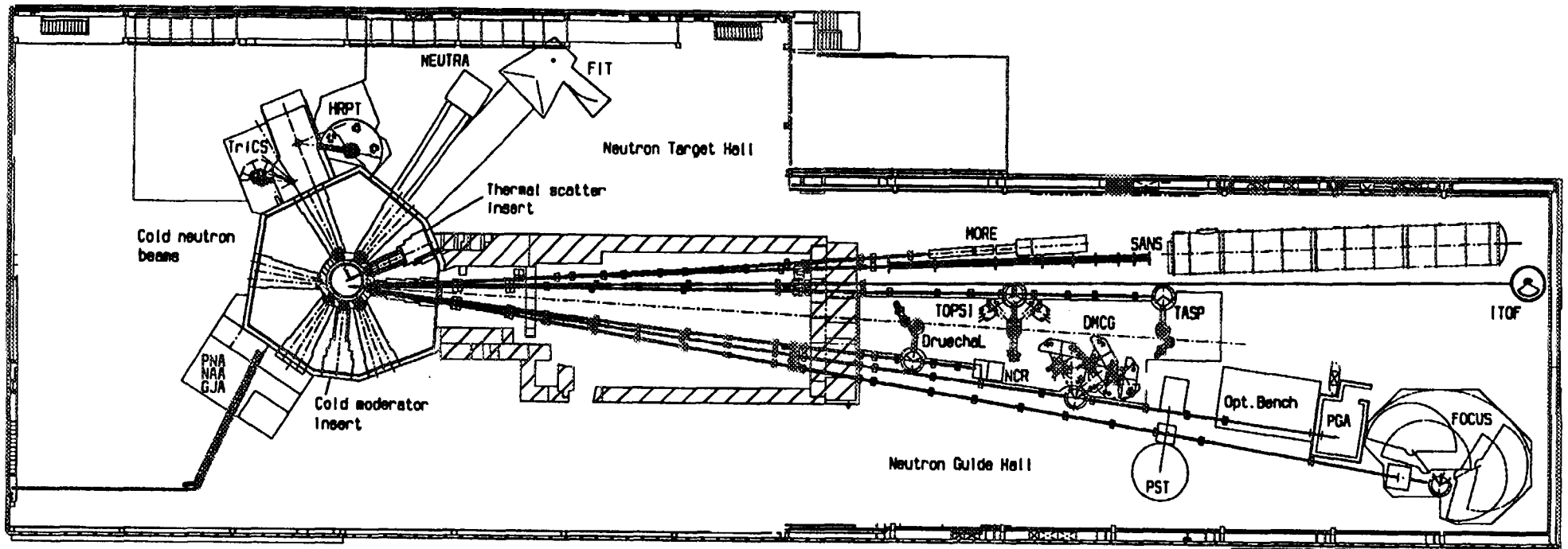
*Spallation Source Division, Paul Scherrer Institut,
Villigen PSI, Switzerland*

ABSTRACT

With 13 experimental facilities under construction to become available during the first year of SINQ operation, a nearly complete suite of options for users will be made available to carry out research with neutrons at PSI. Three more facilities are under design and will come on line somewhat later. To complete the suite, three more specialized instruments are being evaluated. SINQ being a novel neutron source concept, significant scope for improvement is also seen on the source side. It is a major goal of PSI to exploit these opportunities and to make - among others - use of neutron instruments to carry out the necessary research.

1. SINQ as a neutron source with a wide range of applications

The present Zuoz Neutron School being the last one before SINQ is expected to go into operation, this was a timely opportunity to present the activities going on in the field of future exploitation of the source. It became obvious that SINQ will not only provide opportunities for neutron scattering but will also be a strong focus for non diffractive uses of neutrons. Out of the thirteen facilities listed in Fig. 1, eight are in fact instruments to measure elastically or inelastically scattered neutrons, whereas five make use of neutrons in different ways. This clearly shows that the significance of SINQ goes beyond pure neutron scattering, as did that of the research reactors it is meant to replace. This is a noteworthy feature because pulsed spallation neutron sources developed elsewhere are predominantly used for neutron scattering techniques, which are the only class of experimental techniques that can take advantage of a time structure on the neutron flux to compensate for a low average flux level. By contrast, SINQ being a continuous neutron source by default, due to the existing accelerator used to drive it, is designed to resemble (from the user's point of view) a medium flux research reactor as closely as possible. The large volume of D₂O moderator and reflector around the target made it possible to install facilities for isotope production and neutron activation analysis in a region of reasonably high thermal neutron flux and to include a radioisotope extraction facility without undue constraints to the planned neutron scattering activities. As can be seen from the floor plan shown in Fig. 1, these facilities occupy one of the four sectors around the target block which allow access to the thermal neutron flux in the reflector. Out of the remaining three, one is occupied by the four circle single crystal diffractometer TriCS (renamed from SC3, lecture Fr-28) and the high resolution powder diffractometer HRPT (lecture Mo-2) which share a common monochromator shielding. This shielding has been designed as a very massive one to allow for a possible contamination of the beam by high energy neutrons from the spallation process in the target. Practical experience after the commissioning of the source will show whether this is adequate and will help to decide on the future use of the remaining thermal neutron beam holes. One pair has, however, been dedicated already to another pair of instruments, both of which will limit the beam cross section to a small size deep inside the target block and are therefore expected to pose less of a shielding problem against high energy neutrons: The neutron transmission radiography facility described in paper Tu-14 and the Fourier-inverted time of flight diffractometer (see below).



Under Construction:

High Res. Powder Diffractom. for Therm. Neutr.	HRPT	P. Fischer
Diffractometer with Multicounter on a Guide	DMCG	L. Keller
Triple-Axis Spectrometer on a Cold Guide	Drüchel	W. Bührer
Small Angle Diffractometer	SANS	W. Wagner
Time of Flight Spectrometer for Cold Neutrons	FOCUS	S. Janssen
Neutron Transmission Radiography Facility	NEUTRA	H. Pleinert
Prompt Gamma Activation Analysis	PGA	M. Crittin
Neutron Activation Analysis	NAA	L. Tobler
Isotope-Production by Neutron Activation	PNA	P. Bläuerstein
Gas Jet Radioisotope Extraction Facility	GJA	B. Eichler
Two Axis Neutron-Optics Instrument	TOPSI	D. Clemens
Polarized Triple Axis Spectrometer	TASP	P. Böni
Single Crystal Diffractometer	TriCS	J. Schefer

Under Design:

Multi-Option Neutron Reflectometer	(MORE)	D. Clemens
Neutron-Optical Bench on a Guide	(NOBL)	?
Neutron Capture Radiography	NCR	G. Kühne

Under Evaluation:

Fourier Inverse Time of Flight Diffractometer	FIT	U. Stuhr
High Resolution Crystal Analyser Spectrometer	ITOF	P. Allenspach
Phase Space Transform. Monochrom. Spectrom.	(PST)	?

Fig. 1: Floor plan of the SINQ neutron target hall and neutron guide hall, showing the location of the various experimental facilities

The majority of instruments on SINQ clusters around the (seven) neutron guides viewing the cold D₂-moderator. Due to the fact that SINQ is a medium flux neutron source only and the comparatively low level of γ -radiation on a spallation source, the cold moderator could be placed in an optimum flux position close to the target (Fig. 2).

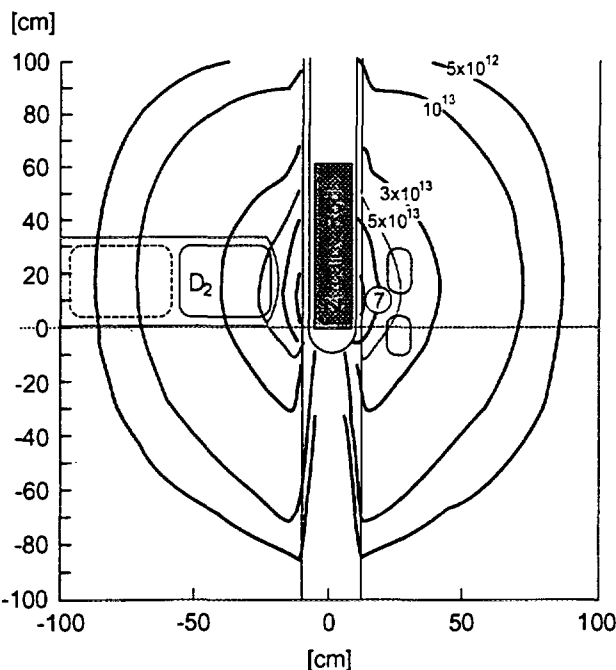


Fig. 2: Calculated unperturbed distribution of the thermal neutron flux of SINQ when running with the zircaloy target. The positions of the cold moderator and beam tube noses are indicated.

Together with the use of supermirror-coated neutron guides [1], this will make the SINQ-cold neutron beams competitive on an international level, once the source has reached its full expected level of performance (see chapter 3). The spectral distribution expected for the different beam tubes and guides in this situation are shown in Fig. 3.

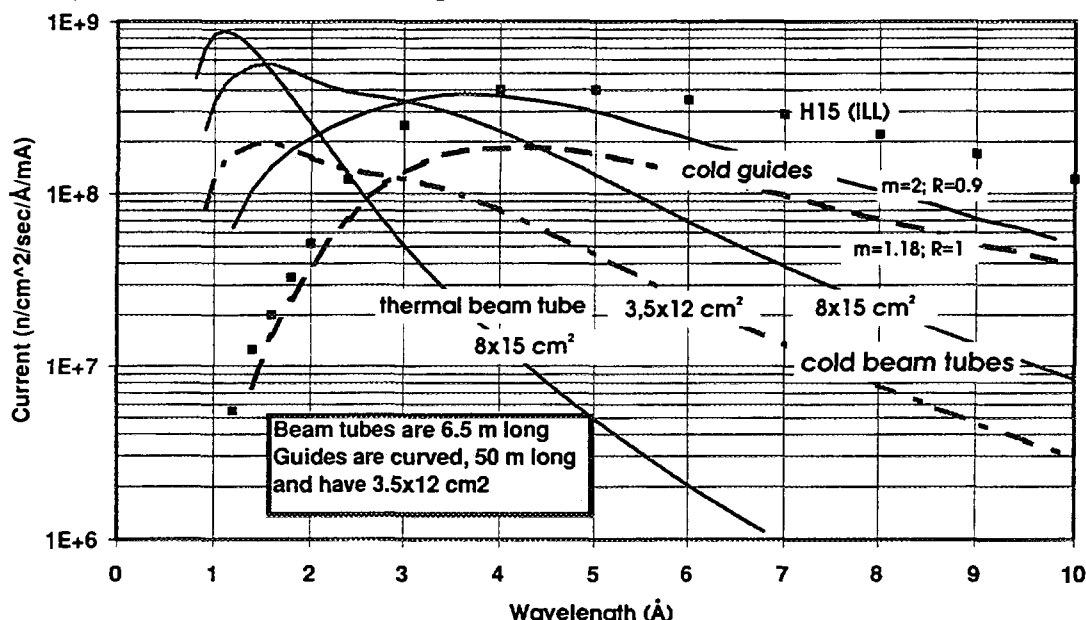


Fig. 3: Neutron spectra anticipated for SINQ on its beam tubes and neutron guides of different cross sections when operating with an optimized Lead or Lead-Bismuth target in a low absorption container [1]. m gives the angle of total reflection of a guide relative to that of natural Nickel and R is the reflectivity of the coating. For comparison, values are also given for the H15 guide at the ILL-reactor.

For comparison the spectral intensity available at the H-15 guide at the ILL-reactor is also given. While this preference for cold neutrons at SINQ, together with the limited space available for the cold neutron guide hall, lead to a rather crowded situation already with the first generation of instruments, there is still some space left to install a few more in the future.

2. Experimental facilities under construction and under study

2.1 *The present situation*

The experimental facilities under construction and expected to become available for users during the first year of SINQ operation were presented in detail in the individual lectures and will not be described any more. They are listed in Fig. 1 together with the responsible scientist. Remarkably, out of the eight neutron scattering instruments, three (DrüchAL, TASP and FOCUS) are clearly devoted to inelastic neutron scattering. Considering the relatively modest flux SINQ will be delivering during the first years of its operation (cf. chapter 3) this seems like a courageous decision. However, based on the use of the most highly developed experimental techniques throughout, in particular focusing monochromators and supermirrors, together with the experience gained from the instruments that had been in use on the SAPHIR-reactor for many years, performance estimates for these instruments are still quite encouraging.

Of course, modern developments, especially on the detector side with regards to position sensitive detectors are also incorporated in the other instruments in order to make them as efficient and user-friendly as possible. This holds for the diffractometers (HRPT and DMCG and TriCS) as well as for the small angle scattering facility (SANS) and the neutron radiography station (NEUTRA). The prompt gamma activation analysis facility will use a "neutron lens" [2] to generate a small focus of intense beam. In order to be able to handle the large data arrays from position sensitive detector systems properly and efficiently, a state of the art data acquisition and data handling system will be implemented for each facility (lecture Fr-27). Since the radiation protection code in effect at PSI will limit access to the instruments while the beam is on, a control cabin is provided for each instrument where electronic equipment that need not be close to the spectrometers can be located and from where the measurements can be surveyed and controlled.

2.2 *Looking ahead*

Considering the fact that experience with working on a continuous spallation neutron source has yet to be gained, the early instrumentation provided for SINQ is a fairly comprehensive one, covering most aspects of the use one can make of a modern neutron source. There remain, however, a few gaps, especially in the field of high resolution techniques, which should be closed in order to exploit the full potential of modern research with neutrons. Instruments under design or study are listed in Fig. 1.

2.2.1 Neutron capture radiography

In addition to the neutron transmission radiography station in which neutrons not scattered or absorbed in the specimen are used to create an image, SINQ will also feature a neutron capture radiography facility, in which a special reaction, mainly ^{10}B (n, α), is used to generate an image of the distribution of the parent nucleus of the reaction in the test sample. The charged particle generated in the capture reaction is recorded on a nuclear track detector plate brought in close contact with the sample. After processing, this track detector allows to produce an overall image or to carry out quantitative analysis with very high spatial resolution. The current main interest in this facility is in the medical field to investigate the efficiency of special cell-seeking agents developed to transport specific isotopes to certain kinds of tissue. If successful, this technique will allow to label certain types of tissue with isotopes either for diagnostic or clinical purposes.

2.2.2 Reflectometry and the future of TOPSI

One complement to the present suite was presented in detail in lecture We-18, namely a multi-option reflectometer which will significantly increase the capabilities in reflectometry work relative to what TOPSI has to offer. Once this new instrument is operational, ideas to fit TOPSI with zero field spin echo equipment and make it a highly performing quasielastic spectrometer can be pursued further.

2.2.3 Neutron optics and high resolution small angle scattering

Another important asset will be the construction of a neutron-optical bench with several pairs of perfect crystal systems. This will not only allow to do neutron optics and interferometry but also to perform double crystal small angle scattering experiments at Q-values much smaller than the ones accessible on the SANS-instrument. Although this technique is plagued with several difficulties compared to the traditional method, it allows to investigate much larger structures and forms an important link to optical methods.

2.2.4 Diffraction under special conditions

The two dedicated "powder" diffractometers presently under construction at SINQ (HRPT and DMCG) both use monochromated beams and a wide range of scattering angles to measure several reflexes simultaneously. In certain cases, in particular when specialized sample environment such as high pressure cells or tight shielding for radioactive samples is to be used, this is a severe limitation because generally only a small angular range can be allowed for the outgoing beam. Another case where one would like to have only one well defined direction for the outgoing beam is the measurement of internal stresses and texture in order to have the gauge volume clearly defined by the intersection of the incoming and outgoing beam (cf. lecture Fr-31) and have it constant for a whole set of measurements. This condition can be best fulfilled if a "white" beam is allowed to impinge on the specimen and time of flight is used to identify the wavelength of the neutrons scattered into a given solid angle. For a cw-source such as SINQ this requires a chopper in the incident beam. If the emphasis is on the investigation of the position and intensity of certain prominent diffraction lines (as is the case in most of the experiments mentioned above), a Fourier-chopper can be used [3] [4], which allows a significantly higher intensity on the sample than a standard periodic chopper.

Since an instrument using this technique is still under evaluation for SINQ, only a sketch of principle is given in Fig. 4. The distance between the chopper and the sample will be either covered by a curved guide or by a neutron mirror to bring the sample out of the line of direct sight of the beam path. While a 90°-scattering angle is best suited to define a small gauge volume in the sample, it is foreseen to have a detector bank also in near backward scattering for true high resolution work.

2.2.5 High resolution inelastic and quasielastic spectrometer (ITOF)

An instrument for high resolution inelastic measurements with an energy resolution of $3+4 \cdot 10^{-3}$ is being studied to complement the triple axis and time of flight spectrometers presently under construction.

The instrument is planned to use Mica analysers in back scattering geometry. This yields final energies of 0.208, 0.832 and 1.872 meV for the 002, 004 and 006 reflexes respectively. In order to cover a reasonably large range of incident energies ($0.1 \leq E_i \leq 10$ meV) a time-of-flight energy selection is studied with a chopper to sample distance of 35 m and pulse-shaping and frame overlap choppers in between. A rough sketch is shown in Fig. 5.

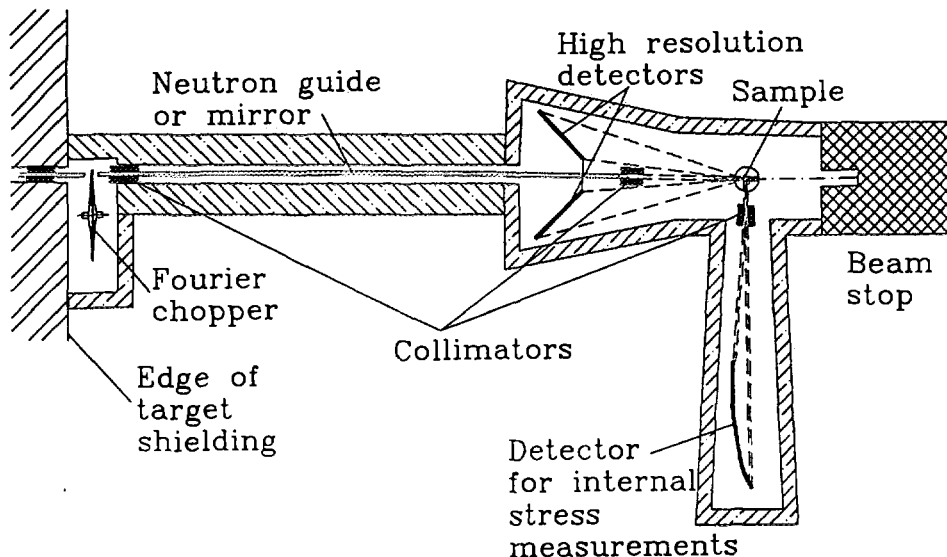


Fig. 4: Sketch of the principle of a Fourier diffractometer as studied for installation at SINQ.

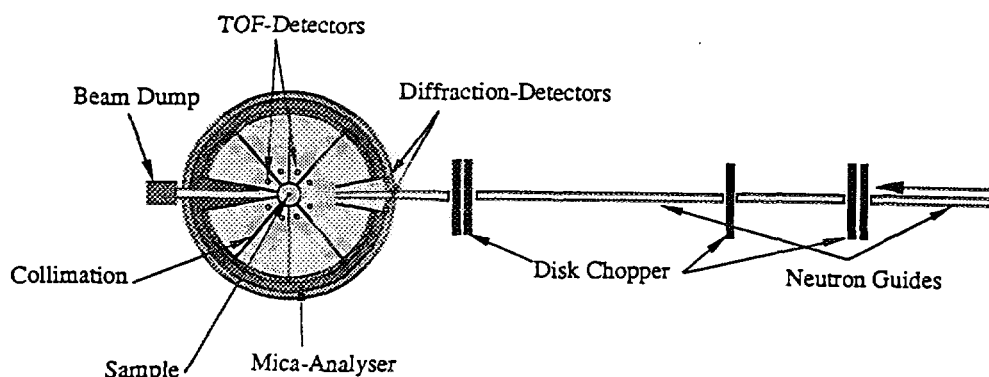


Fig. 5: Schematic layout of the inverted-time-of-flight high resolution inelastic spectrometer "ITOF".

2.2.6 Doppler-Crystal Phase Space Transformation Instrument

The fact that there is a potential problem with the use of thermal beam tubes at SINQ for background reasons on the one hand and the relatively high performance expected for the cold source on the other, makes an attractive old idea to transform cold neutrons into thermal ones at constant phase space density even more attractive. The proposal goes back to a paper by Maier-Leibnitz [5] and was first worked out for the SNQ-project by B. Alefeld [6].

The idea is to take advantage of the high phase space density at a cold neutron source and coherently transform the neutrons by reflection from a fast moving crystal back to near-thermal energies. In this way substantial gains are expected, at least theoretically, as can be seen from Fig. 6, which shows the phase space density on a neutron guide for four different moderator temperatures and the gain (relative to the room temperature moderator or the cold moderator, which ever is appropriate) that can be obtained, if the wave number is shifted by 1.59 \AA^{-1} corresponding to a velocity of the Doppler crystal of 500 m/s.

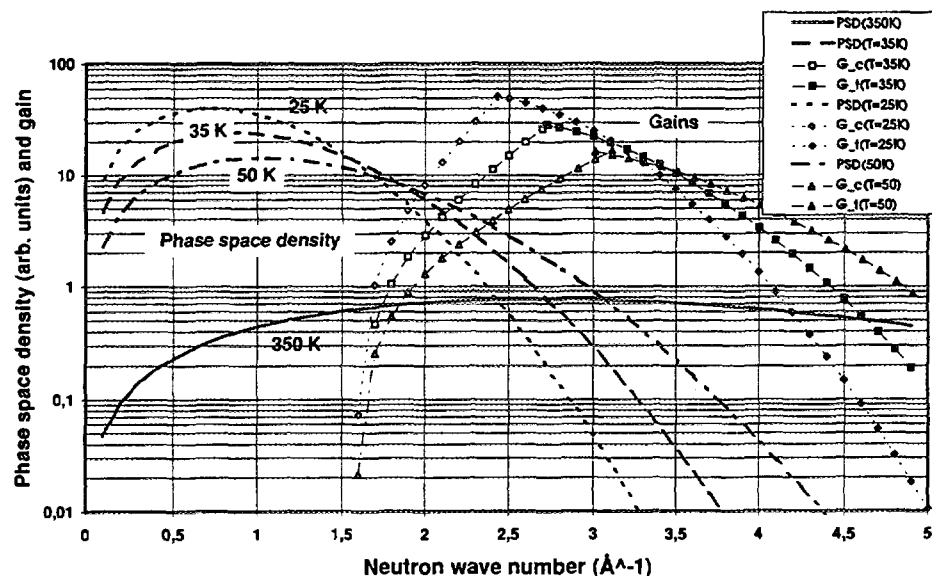


Fig. 6: Phase space density at a neutron guide for moderators of different effective (Maxwell-) temperatures and gains that can theoretically be obtained by coherently transforming the spectra through a wave number of 1.59 \AA^{-1} (corresponding to the reflection from a Doppler crystal moving with 500 m/s). The gains are shown with respect to the cold (open symbols) or room temperature moderator (full symbols), whichever has the higher intrinsic at the corresponding wave number.

While the original proposal by Alefeld had the fast moving Doppler crystal facing the end of the neutron guide and the energy-shifted beam was deflected to the sample, it is proposed for the instrument under study for SINQ to deflect the cold neutrons out of the beam first and have the Doppler drive and the analyser part of the instrument on different sides of the neutron guide, as shown in Fig. 7. This not only has the advantage of being able to utilize the guide for other instruments further downstream, it also provides extra flexibility in choosing the energy of the neutrons before transformation. Some examples are given in Table 1.

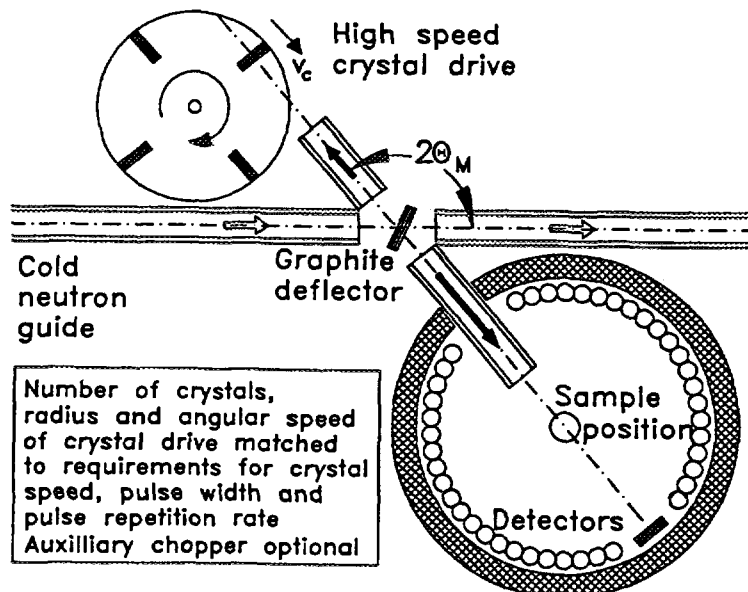


Fig. 7: Sketch of a phase space transformation time-of-flight instrument with deflection of the neutrons from the guide before transformation.

Table 1: Examples for reflected wavelengths λ_r , deflection angles $2 \cdot \theta_m$ at the graphite crystal and approximate optimum gain factors G (35 K) for different lattice spacings Δd of the Doppler crystals at 500 m/s.

Doppler crystal drive: v = 500 m/s final				Deflector crystal (C-002, d = 3.348 Å)		G (35 K) appr. gain	
λ_r	k_f	λ_o	d _{Doppler}	reflex	sin (θ_m)	$2 \cdot \theta_m$	
2.38	2.64	5.99	1.705	Ge311	0.90	127.04	22
2.32	2.71	5.60	1.64	Si311	0.84	113.61	27
2.08	3.02	4.38	1.41	Ge400	0.65	81.75	21
1.96	3.21	3.87	1.3	Ge331	0.58	70.67	16
1.78	3.53	3.24	1.15	Ge422	0.48	57.93	12
1.73	3.64	3.06	1.104	Si422	0.46	54.44	8
1.60	3.94	2.68	1.0	Ge440	0.40	47.13	4

While there is no doubt that the practical realization of this technique poses a severe challenge and many details need yet to be worked out concerning realistic gain figures to be expected, there is no doubt either that, if the technique can be made to work, it is a significant step in increasing the performance of neutron spectrometers. While, at a first glance, the technique seems to lend itself to time-of-flight spectrometers because of the chopping action of each Doppler crystal, it is also conceivable that a sufficiently large number of crystal could be placed on the drive to make the transformed beam quasi-continuous again.

3. SINQ-target development efforts

It was recognized from the very beginning [7], [8] that, for a continuous spallation neutron source, such as SINQ, a liquid Lead-Bismuth target was the ideal solution, in terms of neutron flux as well as for other reasons. This is clearly confirmed by the numbers given in Table 2. However, a liquid metal target had never been operated or built before and it was decided at some point during the project to start with a heavy water cooled target made from zircaloy rods in order to be able to test the concept of an outer safety hull [9] and to carry out research on the effect of the spallation source radiation environment on potential structural materials. Very little is known on this problem [10], [11] and the data base is clearly not good enough to make reliable predictions on the anticipated life time of a liquid metal target shell.

Table 2: Calculated Flux levels per mA of 570 MeV protons for different target concepts for SINQ (unperturbed)

Target system	Maximum thermal flux (cm ⁻² s ⁻¹)	Useable flux at 25 cm (cm ⁻² s ⁻¹)	Relative flux at 25 cm radius
Pb or Pb-Bi with weakly absorbing container	2×10^{14}	1.3×10^{14}	1
Pb-Bi with steel container	0.9×10^{14}	0.85×10^{14}	0.65
W-plates in Al-container	0.8×10^{14}	0.6×10^{14}	0.46
Ta-plates in Al container	0.55×10^{14}	0.45×10^{14}	0.35
Pb-rods in zircaloy tubes	1.5×10^{14}	1×10^{14}	0.70
Zircaloy rods	0.8×10^{14}	0.5×10^{14}	0.38

However, as can bee seen from Table 2, there is a potential to double, or even triple, the neutron flux in the target and every effort will be made to take advantage of this improvement which would profit all of the roughly 20 experimental facilities.

Fig. 8 shows a rough sketch of the present solid rod target and a possible future liquid metal target. The common feature between the two is a separately cooled double walled safety container. In the case of the liquid metal target an additional container will be provided to hold the liquid metal. It is this container for which most research work is required. One of the main issues in this context is the effect of the high Hydrogen and Helium generation rate in the material. In order to investigate this problem, individual target rods of the zircaloy target will be designed as irradiation test capsules containing test material in an outer zircaloy tube. Two kinds of specimens will be provided:

- "bulk" specimens to invesitgate the role of temperature gradients and stress
- "miniaturized" test spciemens (Fig. 9) to use conventional destructive (tensile testing, fatigue testing etc.) and non-destructive methods for post irradiation examinations in the hot cells.

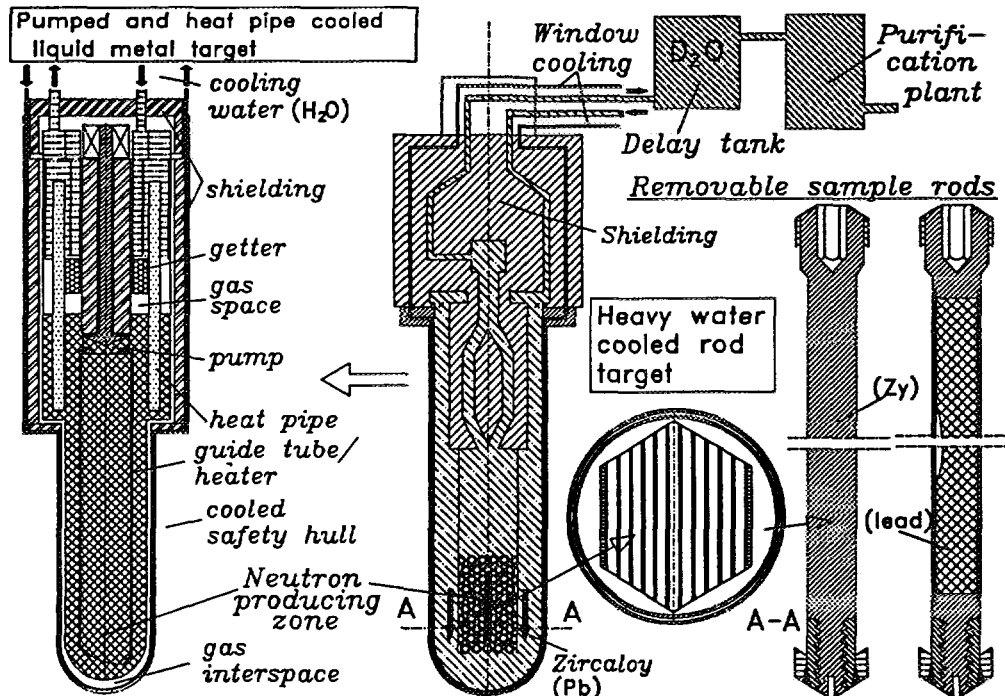


Fig. 8: Schematic representation of the SINQ-targets. Shown to the left is the liquid metal target as presently under study. The zircaloy rod target as planned for initial use is shown at the right, together with examples of removable target rods which can be examined on selected SINQ-instruments.

The "bulk" specimens will be examined mainly for the distribution of Hydrogen, for precipitations, internal stresses and segregation to grain boundaries. Much of this work can be done in a non-destructive way by using neutrons from SINQ. In order to enable this, it is planned to equip three instruments with well shielded sample environment such that radioactive specimens can be investigated:

- the small angle scattering facility for investigation of precipitation, pores, small gas agglomerations and segregation to grain boundaries

- the transmission radiography facility to measure the distribution of hydrogen
- and the Fourier-Diffractometer for investigation of internal stresses and potentially new phases in the material.

It is anticipated that, in this way, using SINQ instruments as an analytic tool, significant contributions can be made to improving the source's performance and availability.

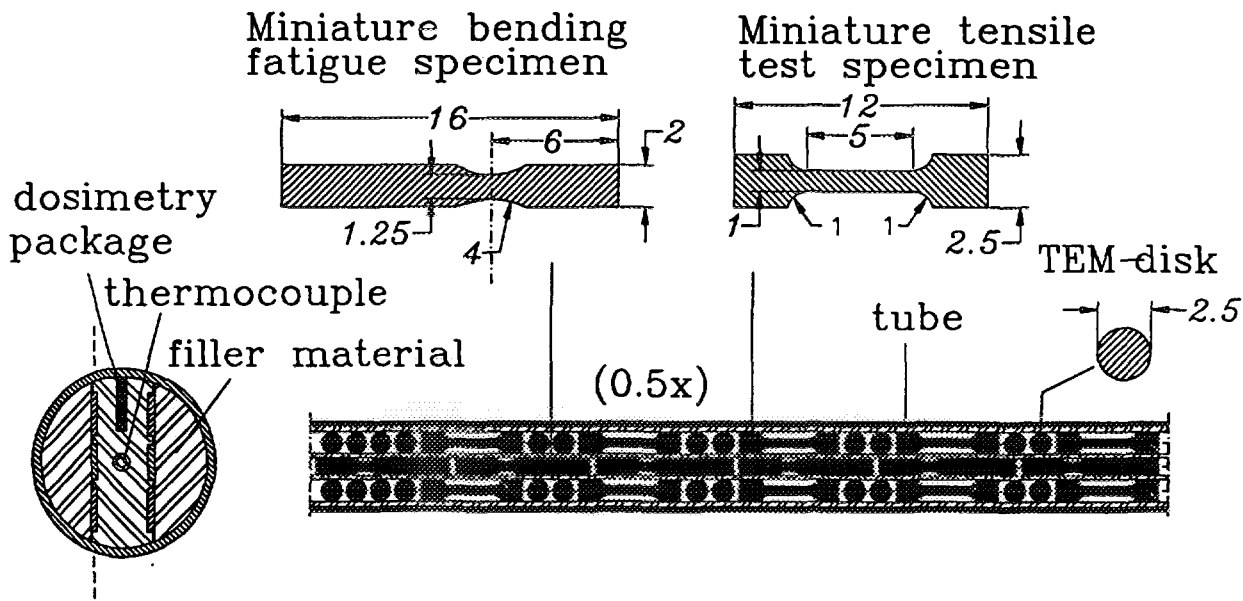


Fig. 9: Examples of miniaturized test specimens for irradiation in SINQ to be post irradiation examined in the hot cells at PSI.

4. References

- [1] F. Atchison and P. Böni, SINQ-report SINQ/816/AF30-404, Paul Scherrer Institut (1994) and Swiss Neutron News 6 (1994) 25-28
- [2] see e.g. H.J. Plask, Neutron News 6 #4 (1995) 39
- [3] J. Schröder, V.A. Kudryashev, J.M. Kreuter, H.G. Priesmeyer, J. Larsen and A. Tiitta "FSS-A Novel RTOF-Diffractometer Optimized for Residual Stress Investigationd" J. Neutr. Res. Vol 2,4 (1994) pp 129-141
- [4] V.A. Kudryashev, H.G. Priesmeyer, J.M. kreuter, J. Schröder, R. Wagner V.A. Tunov "Optimization of detectors in time-focusing geometry for RTOF neutron diffractometers" Nucl. Inst. Meth. Phys. Res. B93 (1994) 355-361
- [5] H. Maier-Leibnitz in Inelastic Neutron Scattering (Proc. Symp. Grenoble) IAEA Vienna,(1972)
- [6] R. Scherm, B. Alefeld "Instruments for High Flux Sources with Time Structure of Neutron Flux" paper IAEA-CN-46/80 in "Neutron Scattering in the 'Nineties", IAEA conference proceedings, Vienna, (1985) p. 247-259

- [7] G.A. Bartholomew and P.R. Tunnicliffe (eds), "The AECL-Study for an Intense Neutron Generator"; rep. AECL-2600 (1966)
- [8] C. Tschalär "Spallation Neutron Source at SIN" Proc. ICANS IV, KENS-report II, Tsukuba (1981) pp 56-76
- [9] G. Heidenreich and G.S. Bauer, "The PSI-SINQ Target Development Programme"; in PSI-Proceedings 92-03 (1992) p. C1
- [10] H. Ullmaier and F. Carsughi "Radiation damage problems in high power spallation neutron sources" Nucl. Inst. Meth. in Phys. Res. B101 (1995) 406-421
- [11] G.S. Bauer "Research and Development for Molten Heavy Metal Targets" To be publ. in Proc 2nd Int. Conf. on Accelerator-Driven Transmutation Technologies and Applications, Kalmar (1996)



INTRODUCTION TO NEUTRON SCATTERING (The theoretical principles)

W.E. FISCHER

Paul Scherrer Institut

CH-5232 Villigen PSI

ABSTRACT

We give here an introduction to the theoretical principles of neutron scattering. The relationship between scattering - and correlation-functions is particularly emphasized. Within the framework of linear response theory (justified by the weakness of the basic interaction) the relation between fluctuation and dissipation is discussed. This general framework explains the particular power of neutron scattering as an experimental method.

1. Introduction

The notion of complementarity is often used in the context of different information about structure and dynamics of condensed matter which can be obtained by scattering experiments with different probing particles. To be more specific we propose to use this notion in two different ways - namely kinematical - and dynamical - complementarity.

i) kinematical complementarity

Due to the different relationship between energy and wave length of various probes (de Broglie), their range of access in reciprocal space of the sample is different.

For example - the photons used in optical spectroscopy and energetically well matched to investigate excitations, have too low momentum to range the whole Brioullin zone. On the other hand X-rays possessing this momentum have to high an energy in order to scan properly the lower lying excitations in a solid. Thermal neutrons are nearly ideal concerning this purpose.

ii) dynamical complementarity

The nature of the coupling of the probe to the various degrees of freedom in the sample is different.

While the neutrons - coupling to the nuclear scattering density - probe the

fluctuations of the mass density, X-rays (via their coupling to the electric charge) probe the charge density fluctuations.

Although both - X-rays and neutrons - couple to the magnetization density (albeit it is much weaker for X-rays) the two probes are again complementary, since their elementary coupling laws differ.

Furthermore there is an other important property of the various probes which is of major concern. This is the **coupling strength** to the sample.

For weakly coupling probes - (like neutrons and X-rays, at least in the Thomson regime) - Born approximation and linear response theory is valid. Perturbation of the sample in the presence of the probe is marginal. Straightforward interpretation of the data in terms of a scattering function, characterizing the unperturbed sample is possible. Kinematical approximation, neglecting all multiscattering effects, is valid.

Probes with strong coupling (usually charged particles) perturb (e.g. polarize) the sample up to the extent that Born approximation and in particular the linear response approach break down. A model input to describe the scattering process is generally necessary to interpret the data. Furthermore corrections for multiple scattering effects have often to be applied.

In the following we deal with weakly interacting probes only. In this case the whole information of the experiment about the sample is contained in the scattering function. The double differential cross section is directly proportional to this scattering function which depends on two kinematical variables of the scattering process: The **energy - transfer** and the **momentum - transfer** from the probe to the sample, respectively, are given by

$$\hbar\omega = E_0 - E_1, \quad (1.1)$$

$$\vec{\kappa} = \vec{k}_0 - \vec{k}_1. \quad (1.2)$$

(E_0, \vec{k}_0) and (E_1, \vec{k}_1) are the energy and the wave vector of the incident and escaping particle, respectively. For neutrons we have

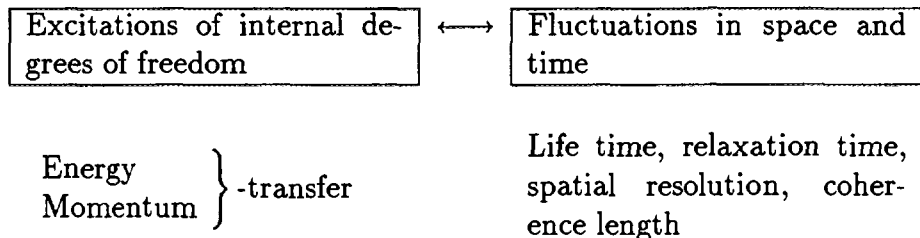
$$\lambda = \frac{2\pi}{|\vec{k}|} = \frac{h}{mv}, \quad (1.3)$$

and

$$E = \frac{\hbar^2 k^2}{2m} = \frac{h^2}{2m} \cdot \frac{1}{\lambda^2}, \quad (1.4)$$

where λ is the de Broglie wave length and v the velocity of the neutron. m is the mass of the neutron.

As will be discussed further on, the scattering function is the spatial and temporal Fourier transform of a correlation function in space and time [1]. This leads to the following correspondence:



As already mentioned above, the nature of the fluctuations investigated depends on the particular coupling of the probe to the sample. This correspondence between **momentum transfer and correlation lengths** on the one hand and **energy transfer and relaxation times** on the other hand, is indicated by the two scales on the axes of Fig. 1. Various experimental methods are placed into the kinematical field which they can cover. Various experimental methods are placed into the kinematical field which they can cover. This demonstrates their kinematical complementarity. The methods indicated along the left (energy-correl. time) axis are restricted to low momentum and hence probe a small region around the center of the Brillouin zone. These are particularly powerful methods to investigate the temporal correlations and therefore the energetic scale of the excitation spectrum of the sample.

The momentum, carried by neutrons and X-rays as probes allows the exploration of essentially the whole relevant region of \vec{k} -space in the sample. This corresponds to spatial correlations within $10^{-5} - 10^{-8}$ cm. Simultaneously — by means of inelastic scattering experiments — it is possible to investigate the energy scale of the excitations of internal degrees of freedom. This is particularly true for the use of neutrons as probes. As a matter of fact with neutrons the investigation of the whole first Brillouin-zone of almost all practical materials is possible. As a guide to the eye we have drawn schematically into this field the dispersive behaviour of the acoustic and optical branches of phonon excitations in a lattice. We recognize from Fig. 1 that the region for hard phonon branches is within reach of hot neutrons as well as of soft X-rays as probe. A spectrometer with extremely high resolution at a synchrotron light source with high brilliance is however needed for the latter method.

Fig. 2 shows the principle set up of a spectrometer for inelastic neutron scattering with a monochromatic beam and an analyzer crystal for the determination of the

final neutron energy of the scattering process (triple axis spectrometer). If appropriate, either of the two crystal selectors may be replaced by a time-of-flight configuration at a pulsed neutron beam. The energy - and momentum-transfer variable ($\omega, \vec{\kappa}$) are the kinematical variables of the scattering function $S(\omega, \vec{\kappa})$. Accordingly Fig. 3 shows the kinematical domain of $(\omega, \vec{\kappa})$, which can be reached with an incident beam energy E_0 of the incident neutron. The lower field - indicated with "Anti-Stokes" - corresponds to a positive energy transfer from the sample to the neutron and is therefore only populated for a sample at higher temperature.

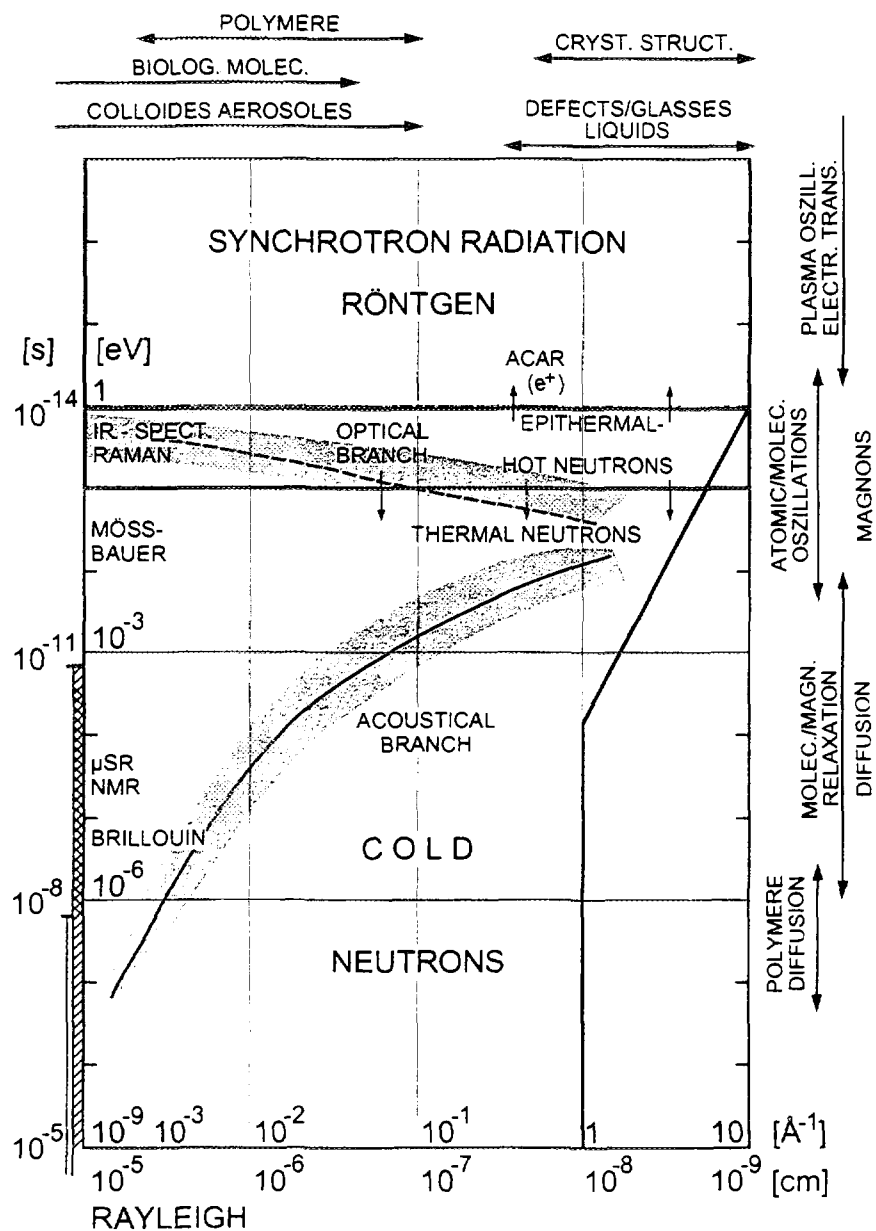


Fig. 1: Range of access in energy and momentum by various experimental methods. Correspondence to correlation-time and -length is also indicated.

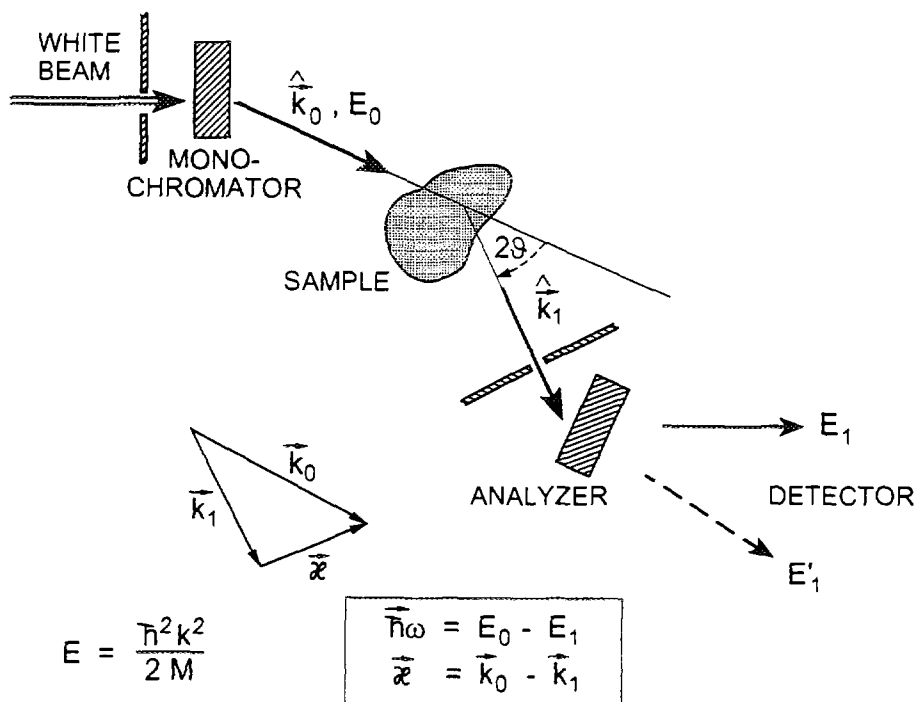


Fig. 2: Principle of a set up for inelastic neutron scattering

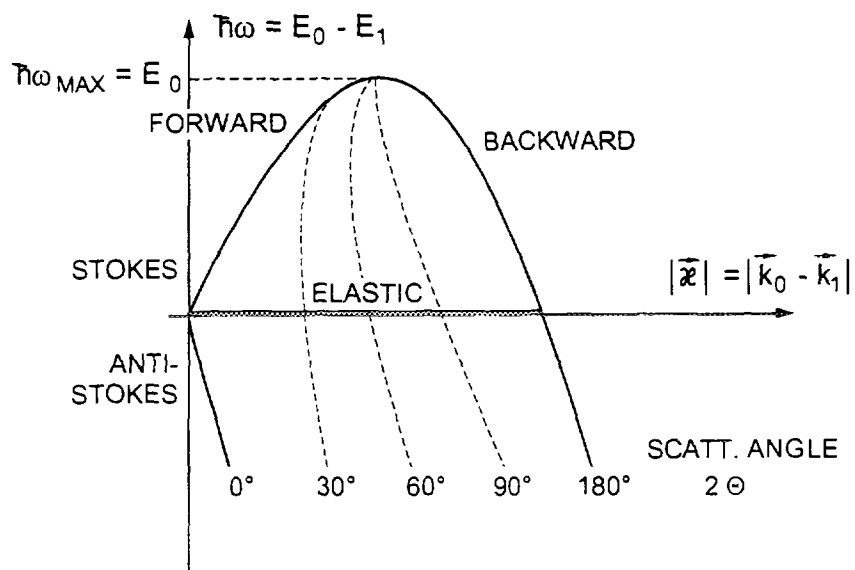


Fig. 3: Kinematical domain in energy- and momentum transfer for inelastic neutron scattering with incident beam energy E_0 .

2. Elementary Interactions

2.1 Nuclear Interaction of Neutrons

If we do not express the isospin dependence of the nuclear interaction of neutrons on nuclei explicitly, we can write for the phenomenological amplitude of neutron-nucleus scattering at very low energies

$$A + B\vec{s}_n \cdot \vec{I}, \quad (2.1)$$

where $\vec{s}_n = \frac{1}{2}(\vec{\sigma}_x, \vec{\sigma}_y, \vec{\sigma}_z)$ is the neutron spin operator expressed by Pauli spin-matrices and \vec{I} the spin operator for the nucleus. The restriction to the simple form (2.1) is a consequence of the invariance of strong interaction under

- i) rotational transformation (conservation of angular momentum),
- ii) parity transformation and (conservation of parity),
- iii) time reversal.

A and B are determined by the strong interaction between the neutron and the nucleus and can - at very low energy - usually be represented by a pseudo-potential (scattering length). Let us consider the partial wave expansion of the spin independent scattering amplitude of (2.1)

$$A(\vartheta) = \frac{1}{2ik} \sum_l (2l+1)(e^{2i\delta_l} - 1) P_l(\cos \vartheta). \quad (2.2)$$

Apart from exceptional resonance conditions the phase shifts δ_l behave as

$$\operatorname{tg}\delta_l \longrightarrow \text{const.} k^{2l+1} \quad \text{as} \quad k \rightarrow 0,$$

k being the wave number of the neutron. For very low energies we can restrict (2.2) to the contribution from the s-wave only. (There are exceptions like nuclei with high absorption at threshold).

$$A(\vartheta) \sim \frac{1}{2ik} (e^{2i\delta_0} - 1) \sim \left(\frac{1}{k} \left(\delta_0 - 2 \frac{\delta_0^2}{i} \right) \right) \quad (2.3)$$

If the interaction potential falls off sufficiently fast we have

$$\lim_{k \rightarrow 0} \operatorname{ctg}\delta_0 = -a, \quad (2.4)$$

and therefore a total cross section of

$$\sigma = 4\pi a^2. \quad (2.5)$$

$A(0)$ fulfills the optical theorem

$$\sigma = \frac{4\pi}{k} A(0). \quad (2.6)$$

For the application of neutron scattering in the investigation of structure and dynamics of condensed matter, the neutrons are scattered at nuclei bound in molecules or in a lattice. The amplitude of their thermal motion (e.g. vibrations) is very large compared to the range of the strong interaction. Therefore an impulse approximation is by far sufficient to describe the scattering amplitude of the neutron with a bound nucleus and its excitation into the n^{th} -state in the lattice, that is

$$-\frac{M+m}{M} a \int \psi_n^*(\vec{x}) \psi_0(\vec{x}) e^{i\vec{k}\vec{x}} d^3x. \quad (2.7)$$

Here m and M are the masses of the neutron and the nucleus respectively. $\hbar\vec{k}$ is the momentum transfer to the target. We can write the same amplitude formally in Born approximation as:

$$-\frac{2\pi m}{\hbar^2} \int V(\vec{x}') e^{i\vec{k}\vec{x}'} d^3x' \int \psi_n^*(\vec{x}) \psi_0(\vec{x}) e^{i\vec{k}\vec{x}} d^3x. \quad (2.8)$$

Eqs. (2.7) and (2.8) become identical if we chose for the potential

$$V(\vec{x}) = 2\pi\hbar^2 \frac{M+m}{Mm} a \delta(\vec{x}) = 2\pi\hbar^2 b \delta(\vec{x}).$$

(2.9)

This is the *pseudopotential* used as “elementary” interaction in the description of scattering processes of low energy (thermal) neutrons in condensed matter.

A few remarks are in order:

- i) The scattering length b has a specific value for every isotope of the nucleus of the particular element. This is due to the isospin dependence of strong interaction which has not been particularly expressed in the formula above.
- ii) The strong interaction being spin dependent (2.1) leads to different scattering lengths for the two amplitudes A and B .
- iii) Since amplitudes of different origin according to i) and ii) do not interfere with each other they lead to a contribution of incoherent scattering at a many body system consisting of nuclei with $I_n \neq 0$ and their isotopes with different isospins T .
- iv) Due to the local nature of the interaction potential ($\sim \delta(\vec{x})$), there appears no form factor for the elementary scattering, that is the differential cross section does not decrease for large momentum transfer (large scattering angles).

2.2 Electromagnetic Interaction of Neutrons

The neutron is a baryon with vanishing electrical charge. Therefore no magnetic moment is generated via minimal coupling as in the Dirac equation for the electron. The observed magnetic moment μ of the neutron is exclusively due to mesonic field fluctuations. This “anomalous” magnetic moment can be described phenomenologically within a Dirac equation via an additional interaction of the Zeeman type, $-\mu\vec{\sigma}\cdot\vec{B}$. In relativistically invariant form, this modified Dirac equation then reads

$$\left[i\hbar\gamma^\mu\partial_\mu - \frac{\mu}{2c}\sigma_{\mu\nu}F^{\mu\nu} - mc \right] \psi = 0, \quad (2.10)$$

where $F^{\mu\nu}$ is the electromagnetic field tensor and $\sigma_{\mu\nu} = \frac{i}{2}[\gamma_\mu, \gamma_\nu]$. Note that $\sigma_{\mu\nu}F^{\mu\nu}$ is the *only* scalar under Lorentz transformations which is linear in $F^{\mu\nu}$. The wave function of a free neutron is conveniently written as $\psi = (\chi, \varphi)e^{-imc^2t/\hbar}$ where χ, φ are 2-component Pauli spinors. The Dirac equation (2.10) then takes the form

$$(i\hbar\partial_t + \mu\vec{\sigma}\cdot\vec{B})\varphi = c\vec{\sigma}\cdot(\vec{p} - \frac{i\mu}{c}\vec{E})\chi, \quad (2.11a)$$

$$(i\hbar\partial_t - \mu\vec{\sigma}\cdot\vec{B} + 2mc^2)\chi = c\vec{\sigma}\cdot(\vec{p} + \frac{i\mu}{c}\vec{E})\varphi. \quad (2.11b)$$

For neutrons with a kinetic energy which is small compared to the energy of the rest mass, the third term in the second equation dominates and suggests the following approximation

$$\chi = \frac{1}{2mc}\vec{\sigma}\cdot(\vec{p} + \frac{i\mu}{c}\vec{E})\varphi. \quad (2.12)$$

With (2.11a) we then obtain for φ the Schrödinger equation

$$i\hbar\partial_t\varphi = H\varphi, \quad (2.13)$$

with the Hamiltonian:

$$H = \frac{\vec{p}^2}{2m} - \mu\vec{\sigma}\cdot\vec{B} - \frac{\mu}{2mc}\vec{\nabla}\cdot\vec{E} + \frac{\mu}{2mc}\vec{\sigma}\cdot(\vec{p}\wedge\vec{E} - \vec{E}\wedge\vec{p}) + \frac{\mu^2 E^2}{2mc^2}. \quad (2.14)$$

If we set the magnetic field \vec{B} to zero and neglect the “Darwin”-term prop. to $\vec{\nabla}\cdot\vec{E}$ (which has its origin in the position fluctuations of the neutron), the Hamiltonian becomes:

$$H = \frac{1}{2m}(\vec{p} + \frac{\vec{\mu}}{c}\wedge\vec{E})^2 - \frac{\mu^2 E^2}{2mc^2}, \quad (2.15)$$

with

$$\vec{\mu} = \mu\vec{\sigma}. \quad (2.16)$$

This suggests that the canonical momentum of the neutron in an electrical field is given by the substitution

$$\vec{p} \longrightarrow \vec{p} + \frac{\vec{\mu}}{c}\wedge\vec{E}. \quad (2.17)$$

Let us now shortly discuss (2.14) term by term:

- i) $\frac{\vec{p}^2}{2m}$: This is the term for the kinetic energy of the free neutron
- ii) $\vec{\mu} \cdot \vec{B}$: Zeeman term - responsible for magnetic scattering of the neutron at magnetic moments of nuclei (nuclear magnetism) or much more important at the electronic magnetisation density in a many body system.
- iii) $\frac{\mu}{2mc} \vec{\nabla} \cdot \vec{E}$: Darwin term – a very small contribution to electron-neutron scattering, usually neglected in work on condensed matter physics.
- iv) $\frac{\mu}{2mc} \vec{\sigma} \cdot (\vec{p} \wedge \vec{E} - \vec{E} \wedge \vec{p})$: spin orbit interaction associated to the magnetic moment of the neutron. Neutron motion induces an electric moment which interacts with the external field \vec{E} .

The spin-orbit term (iv) vanishes as $|\vec{p}| \rightarrow 0$ for very low neutron energies.

The dominant and (today) practically useful term of electromagnetic interaction is the Zeeman term (ii). It leads to two contributions with an electron at position \vec{x}_e

- i) dipole-dipole interaction with a magnetic moment of an electron
- ii) interaction with a current density

The corresponding Hamiltonians are

- i) Dipole-dipole interaction with a magnetic moment of an electron

$$H = -\vec{\mu} \cdot \vec{B}_e = -\gamma \mu_N \vec{\sigma} \cdot \vec{B}_e = 2\gamma \mu_N \mu_B \vec{\sigma} \cdot \vec{\nabla}_e \wedge \frac{\vec{S}_e \wedge \vec{x}_e}{|\vec{x}_e|^3}, \quad (2.18)$$

where \vec{S}_e is the spin operator for the electron and μ_B the Bohr magneton

$$\mu_B = \frac{e\hbar}{2m_e c}. \quad (2.19)$$

- ii) Interaction with a current density

$$\vec{J} = \frac{e}{m_e} \delta(\vec{x} - \vec{x}_e) \vec{p}_e. \quad (2.20)$$

The Hamiltonian for the interaction of the neutron with this current is

$$H = -\gamma \mu_N \frac{e}{2m_e c} \left(\vec{p}_e \cdot \frac{\vec{\sigma} \wedge \vec{x}_e}{|\vec{x}_e|^3} + \frac{\vec{\sigma} \wedge \vec{x}_e}{|\vec{x}_e|^3} \cdot \vec{p}_e \right); \quad \vec{p}_e = -i\hbar \vec{\nabla}_e. \quad (2.21)$$

The relative strength of the nuclear - and magnetic-interaction is approximately the same for small momentum. We have to compare b^2 for typical isotopes with $(-1.19 r_e)^2$, where r_e is the classical electron radius.

3. Cross Section and Scattering Function

3.1 Coherence and Incoherence

The measured cross section of the inelastic scattering process is defined as the ratio of the number of scattered particles with momentum \vec{k}_1 within the solid angle $d\Omega$ and an energy resolution ΔE , to the incident flux with momentum \vec{k}_0 . Note that \vec{k}_1 determines the direction Ω and the energy E_1 of the scattered particles.

$$\vec{\kappa} = \vec{k}_0 - \vec{k}_1, \quad \hbar\omega = E_0 - E_1, \quad (3.1)$$

are the momentum and the energy transfer in the scattering process, respectively. The partial differential cross section is then

$$\frac{d^2\sigma}{d\Omega dE} = \frac{k_1}{k_0} x_1^2 d\Omega \sum_{\Delta E} |\psi_s|^2, \quad (3.2)$$

where x_1 is the distance from the sample to the detector; it has to be large compared to the dimensions of the sample. It then finally drops from the final expression since $|\psi_s|^2$ turns out to be proportional to x_1^{-2} . The sum runs over the number of terms in the resolution range ΔE .

Hence, all we have to do is to calculate $|\psi_s|^2$ — the scattered wave — in the appropriate approximations. We have

- i) Born approximation: $T \simeq V$
- ii) Kinematical approximation with

$$V(t) = \sum_j \frac{2\pi\hbar^2}{m} b_j \delta(\vec{x} - \vec{X}_j(t)) \quad (3.3)$$

for neutron scattering, where $\vec{X}_j(t)$ are the positions of the scattering centers in the sample.

For the incident wave (channel state) we take

$$\langle \vec{x} | \vec{k} \rangle = e^{i(\vec{k}_0 \vec{x} - \omega_0 t)}. \quad (3.4)$$

The time-dependent version of the scattered wave written out explicitly is,

$$\psi_s(\vec{x}', t) = \int d^3x \int dt' G(\vec{x} - \vec{x}'; t - t') \cdot \sum_j b_j \delta(\vec{x} - \vec{X}_j(t')) \cdot e^{i(\vec{k}_0 \vec{x} - \omega_0 t')}, \quad (3.5)$$

where the Green's function G satisfies

$$\left(\Delta + \frac{2mi}{\hbar} \partial_t \right) G(\vec{x} - \vec{x}'; t - t') = 4\pi \delta(\vec{x} - \vec{x}', t - t'). \quad (3.6)$$

We do not have the time here to go through the full procedure to obtain $|\psi_s|^2$. Although the job is somewhat tedious, every student should however have seen it once. I shall therefore distribute a hand-written version of this calculation – including (hopefully) every i and π . The final result is (where the integration variable τ has the dimension of time).

$$\boxed{\frac{d^2\sigma}{d\Omega dE} = \frac{k_1}{k_0} \frac{1}{2\pi\hbar} \int_{-\infty}^{+\infty} d\tau e^{-i\omega\tau} \sum_{ij} b_i^* b_j \overline{e^{i\vec{\kappa}\vec{X}_i(\tau)} e^{-i\vec{\kappa}\vec{X}_j(0)}}}. \quad (3.7)$$

The bar over the exponentials indicates a time average of the type

$$\lim_{T \rightarrow \infty} \frac{1}{T} \int_0^T dt'. \quad (3.8)$$

The scattering lengths b_i are assumed to be (exclude compound nuclear states) constant in time; we may pull them in front of the integral. On the other hand they may be different for different indices (e.g. different isotopes as scattering centers). For the average over the sample we write

$$\overline{b_i^* b_j} = \bar{b}_i^* \bar{b}_j = |\bar{b}|^2 \quad \text{for } i \neq j, \quad (3.9)$$

assuming random distribution of isotopes (hence no correlation between $i \neq j$). Furthermore

$$\overline{b_i^* b_i} = \overline{|b_i|^2} = \overline{|b|^2} \quad \text{for } i = j. \quad (3.10)$$

For the double sum we get then

$$\sum_{i \neq j} \overline{b_i^* b_j} = N(N-1)|\bar{b}|^2, \quad (3.11)$$

$$\sum_{i=j} \overline{b_i^* b_j} = N \overline{|b|^2}. \quad (3.12)$$

All together,

$$\begin{aligned} \sum_{ij} \overline{b_i^* b_j} &= N^2 |\bar{b}|^2 + N (\overline{|b|^2} - |\bar{b}|^2) \\ &= N^2 |\bar{b}|^2 + N \overline{(\delta b)^2}. \end{aligned}$$

The second term is the average of the squared fluctuation. It is proportional to the number of scattering centers ($\sim N$) and describes therefore incoherent scattering

$$\overline{(\delta b)^2} = b_{inc}^2 \quad (3.13)$$

The first term — proportional to N^2 — describes the coherent scattering; in the absolute sense for elastic ($\tau \rightarrow \infty$), in the relative sense for inelastic scattering.

$$|\bar{b}|^2 = b_c^2. \quad (3.14)$$

The exponentials in (3.7) form a time correlation function, whose variables are the position operators of the scattering centers. Assuming the ergodic principle (in the sense of Birkhoff) for the sample, we may replace the time average by an average over a canonical statistical ensemble

$$\langle e^{i\vec{\kappa}\vec{X}_i(\tau)} e^{-i\vec{\kappa}\vec{X}_j(0)} \rangle_T = \text{Sp} (\rho e^{i\vec{\kappa}\vec{X}_i(\tau)} e^{-i\vec{\kappa}\vec{X}_j(0)}) , \quad (3.15)$$

where ρ is the density operator of the canonical ensemble,

$$\rho = \frac{e^{-\beta H_0^{(s)}}}{\text{Sp} (e^{-\beta H_0^{(s)}})} , \quad (3.16)$$

for the temperature $T(\beta = \frac{1}{k_B T})$ of the sample. Note that $H_0^{(s)}$ is the Hamiltonian of the sample to be investigated.

The partition function

$$Z = \text{Sp} (e^{-\beta H}) = e^{-\beta F} , \quad (3.17)$$

where

$$F = -k_B T \ln Z , \quad (3.18)$$

is the free energy of the sample. (We write from now on H instead of $H_0^{(s)}$ for its Hamiltonian). The expectation value of an operator \hat{O} which represents an observable of the sample in thermal equilibrium at temperature T is

$$\langle \hat{O} \rangle_T = \text{Sp} (\rho \hat{O}) = \frac{\text{Sp} (e^{-\beta H} \hat{O})}{\text{Sp} (e^{-\beta H})} = \frac{\text{Sp} (e^{-\beta H} \hat{O})}{Z} , \quad (3.19)$$

and explicitly in terms of energy eigenvalues and eigenvectors,

$$\langle \hat{O} \rangle_T = \sum_i \frac{e^{-\beta E_i}}{Z} \langle i | \hat{O} | i \rangle . \quad (3.20)$$

We now use this development to define the coherent and incoherent differential cross section and write

$$\left. \frac{d^2 \sigma}{d\Omega dE} \right|_{coh} = \frac{k_1}{k_0} \frac{\sigma_c}{4\pi} \frac{1}{2\pi\hbar} \int_{-\infty}^{+\infty} d\tau e^{-i\omega\tau} \sum_{ij} \langle e^{i\vec{\kappa}\vec{X}_i(\tau)} e^{-i\vec{\kappa}\vec{X}_j(0)} \rangle_T , \quad (3.21)$$

$$\left. \frac{d^2 \sigma}{d\Omega dE} \right|_{incoh} = \frac{k_1}{k_0} \frac{\sigma_i}{4\pi} \frac{1}{2\pi\hbar} \int_{-\infty}^{+\infty} d\tau e^{-i\omega\tau} \sum_j \langle e^{i\vec{\kappa}\vec{X}_j(\tau)} e^{-i\vec{\kappa}\vec{X}_j(0)} \rangle_T , \quad (3.22)$$

where we have introduced,

$$\sigma_c = 4\pi |\bar{b}|^2 , \quad \sigma_i = 4\pi |\delta b|^2 . \quad (3.23)$$

Coherent and incoherent cross sections are then time-Fourier transforms of a correlation function

$$Y_{ij}(\kappa, \tau) = \langle e^{+i\vec{\kappa}\vec{X}_i(\tau)} e^{-i\vec{\kappa}\vec{X}_j(0)} \rangle_T. \quad (3.24)$$

We now show that this corresponds to a density correlation function in space and time

$$C_{ij}(\vec{x}, \tau) = \left(\frac{1}{2\pi}\right)^3 \int d^3\kappa e^{-i\vec{\kappa}\vec{x}} Y_{ij}(\kappa\tau). \quad (3.25)$$

With the exponential representation of the δ -function, i.e.,

$$\left(\frac{1}{2\pi}\right)^3 \int d^3\kappa e^{-i\vec{\kappa}(\vec{x}-\vec{x}'+\vec{X}_j(0))} = \delta^{(3)}(\vec{x} - \vec{x}' + \vec{X}_j(0)), \quad (3.26)$$

we obtain

$$C_{ij}(\vec{x}, \tau) = \int d^3x' \langle \delta(\vec{x}' - \vec{X}_i(\tau)) \delta(\vec{x} - \vec{x}' + \vec{X}_j(0)) \rangle_T. \quad (3.27)$$

For the double sum

$$C(\vec{x}, \tau) = \sum_{ij} C_{ij}(\vec{x}, \tau) = \frac{1}{N} \int d^3x' \langle \rho(\vec{x}', \tau) \rho(\vec{x} - \vec{x}', 0) \rangle_T \quad (3.28)$$

with

$$\rho(\vec{x}, \tau) = \sum_j \delta(\vec{x} - \vec{X}_j(\tau)). \quad (3.29)$$

According to (3.21) and (3.22) we define two different correlation functions, depending on the summation procedure over the scattering centers, namely the

- i) sum over all i and j gives the general coherent correlation function $C(\vec{x}, \tau)$. It defines pair correlation in space and time.
- ii) the sum over $i = j$ only, gives the correlation function which determines the incoherent scattering $C_S(\vec{x}, \tau)$. It defines a one particle (self)-correlation in space and time.

This point of view to interpret such scattering experiment has been introduced by Leon van Hove [1]. In a somewhat popular language these experiments answer the question:

"Where are the positions of the atoms and how do they move."

It is evident that the correlation function $C(\vec{x}, \tau)$ contains information about collective excitations in dependence of the temperature of the sample. The incoherent correlation function $C_s(\vec{x}, \tau)$ (among others) describes diffusion processes in the sample.

Note that in principle a similar approach is also possible for magnetic neutron scattering and also for X-ray and electron-scattering experiments. Due to the different coupling of these probes to the scattering centers, the information obtained is complementary. The various probes are sensitive to different kind of correlations (fluctuations) in the sample; namely:

Neutrons	$\begin{cases} \text{nuclear} & \text{mass-density} \\ \text{magnetic} & \text{density of magnetization} \end{cases}$
X-rays	electric charge density and to order $(\frac{v}{c})$ also den- sity of spin and orbital magnetizations
Electrons	(like x-rays)

Following van Hove, let us define here the scattering function:

$$S(\vec{\kappa}, \omega) = \frac{1}{N} \frac{1}{2\pi\hbar} \int_{-\infty}^{+\infty} d\tau e^{-i\omega\tau} \sum_{ij} Y_{ij}(\vec{\kappa}, \tau), \quad (3.30)$$

which has the dimension of (energy⁻¹). For the cross sections we then have

$$\boxed{\left. \frac{d^2\sigma}{d\Omega dE} \right|_{coh} = N \frac{k_1}{k_0} \frac{\sigma_c}{4\pi} S(\vec{\kappa}, \omega),} \quad (3.31)$$

$$\boxed{\left. \frac{d^2\sigma}{d\Omega dE} \right|_{incoh} = N \frac{k_1}{k_0} \frac{\sigma_{in}}{4\pi} S_i(\vec{\kappa}, \omega),} \quad (3.32)$$

where S_i contains only the sum of the diagonal terms of Y_{ij} . The structure function is the spatial and temporal Fourier transform of the correlation function $C(\vec{x}, \tau)$.

3.2 Elastic- and Inelastic Scattering [2]

From (3.54) we write for the microscopic particle density, which has dimension (1/volume),

$$\rho(\vec{x}, \tau) = \sum_j \delta(\vec{x} - \vec{X}_j(\tau)) = \frac{1}{V} \sum_{\vec{\kappa}} \rho_{\vec{\kappa}} e^{i\vec{\kappa}\vec{x}}, \quad (3.33)$$

with the Fourier components,

$$\rho_{\vec{\kappa}} = \sum_j e^{-i\vec{\kappa}\vec{X}_j(\tau)}, \quad (3.34)$$

and then for the scattering function according to (3.24) and (3.30)

$$S(\vec{\kappa}, \omega) = \frac{1}{2\pi\hbar} \frac{1}{N} \int_{-\infty}^{+\infty} d\tau e^{-i\omega\tau} \langle \rho_{\vec{\kappa}}(\tau) \rho_{\vec{\kappa}}^\dagger(0) \rangle_T. \quad (3.35)$$

For very large times $\rho_{\vec{\kappa}}(\tau)$ and $\rho_{\vec{\kappa}}^\dagger(0)$ can be considered as uncorrelated, hence

$$\lim_{\tau \rightarrow \infty} \langle \rho_{\vec{\kappa}}(\tau) \rho_{\vec{\kappa}}^\dagger(0) \rangle_T = \langle \rho_{\vec{\kappa}}(\tau) \rangle \langle \rho_{\vec{\kappa}}^\dagger(0) \rangle. \quad (3.36)$$

Accordingly we split the correlation function (the coherent as well as the incoherent) into two parts

$$C(\vec{x}, \tau) = C(\vec{x}, \infty) + C'(\vec{x}, \tau), \quad (3.37)$$

with

$$\lim_{\tau \rightarrow \infty} C'(\vec{x}, \tau) = 0. \quad (3.38)$$

The first term describes the persistent part of the structure (e.g. crystal structure), the second part is given by the actual fluctuations. We now show, that the first term is described by elastic scattering and the second by inelastic scattering phenomena.

The cross section related to $C(x, \infty)$ is

$$\begin{aligned} \frac{d^2\sigma}{d\Omega dE} &= N \frac{\sigma_c}{4\pi} \delta(\hbar\omega) \int d^3x e^{i\vec{\kappa}\vec{x}} C(\vec{x}, \infty) \\ &= \frac{\sigma_c}{4\pi} \delta(\hbar\omega) \left| \int d^3x e^{i\vec{\kappa}\vec{x}} \langle \rho(\vec{x}) \rangle \right|^2. \end{aligned} \quad (3.39)$$

For a *static* (rigid) Bravais lattice defined by vectors $\{\vec{l}\}$,

$$\rho(\vec{x}) = \sum_l \delta(\vec{x} - \vec{l}), \quad (3.40)$$

we have

$$\left(\frac{d\sigma}{d\Omega} \right)_{coh} = \frac{\sigma_c}{4\pi} \left| \sum_l e^{i\vec{\kappa}\vec{l}} \right|^2. \quad (3.41)$$

There is no inelastic scattering from a static lattice. Similarly, for the self-correlation $C_S(\vec{x}, \infty)$ we obtain

$$\left(\frac{d\sigma}{d\Omega} \right)_{inc} = \frac{\sigma_i}{4\pi} \sum_j \left| e^{i\vec{\kappa}\vec{x}_j} \right|^2 = N \frac{\sigma_i}{4\pi}, \quad (3.42)$$

an isotropic diffuse scattering.

Note in (3.41) we can use the identity

$$\left| \sum_l e^{i\vec{\kappa}\vec{l}} \right|^2 = N \frac{(2\pi)^3}{V_0} \sum_\tau \delta(\vec{\kappa} - \vec{\tau}), \quad (3.43)$$

where V_0 is the volume of the unit cell, and $\{\vec{\tau}\}$ the lattice vectors of the reciprocal lattice defined from $\{\vec{l}\}$. (3.43) shows the Bragg peaks i.e. the elastic scattering is zero at all wave vectors except $\vec{k} = \vec{\tau}$.

For a *non rigid* lattice we assume the positions of the scattering centers to be given by

$$\vec{X}_j = \vec{l}_j + \vec{u}_j(\vec{l}_j). \quad (3.44)$$

This represents a Bravais lattice with average positions \vec{l}_j and (time dependent) deviations from these positions $\vec{u}_j(\vec{l}_j)$ (e.g. due to thermal motion).

$$\langle u_j(\vec{l}_j) \rangle_T = 0. \quad (3.45)$$

With (3.44) we can write for the average particle density

$$\begin{aligned} \langle \rho(\vec{x}) \rangle &= \sum_j \langle \delta(\vec{x} - \vec{X}_j) \rangle_T = \\ &= \left(\frac{1}{2\pi} \right)^3 \int d^3 \kappa \sum_j e^{i\vec{\kappa}(\vec{x} - \vec{l}_j)} \langle e^{-i\vec{\kappa}\vec{u}(\vec{l}_j)} \rangle_T. \end{aligned} \quad (3.46)$$

By means of the Bloch relation, valid for harmonic vibrations,

$$\langle e^{\hat{Q}} \rangle = e^{\frac{1}{2}\langle \hat{Q}^2 \rangle}, \quad (3.47)$$

we rewrite the last term under the integral (3.46) as

$$\langle e^{-i\vec{\kappa}\vec{u}(\vec{l}_j)} \rangle = e^{-\frac{1}{2}\langle (\vec{\kappa}\vec{u}(\vec{l}_j))^2 \rangle_T} = e^{-W(\vec{\kappa})}. \quad (3.48)$$

In (3.48),

$$2W(\vec{\kappa}) = \langle (\vec{\kappa}\vec{u}(\vec{l}))^2 \rangle_T \quad (3.49)$$

is the famous Debye-Waller factor. Note that (3.47) is an identity for a quantum mechanical observable which is a linear combination of annihilation and creation phonon operators. We have to deal with $\vec{u}(\vec{l})$ accordingly.

We do not give here the proof of Bloch's relation; it can be found in the literature [2]. It contains basically the quantum mechanical treatment of the degrees of freedom of the sample. Accordingly, due to zero point motions the Debye-Waller factor does not vanish at $T = 0$.

For the special case of the three cubic Bravais lattices we can write

$$W(\vec{\kappa}) = \frac{1}{2} \langle (\vec{\kappa}\vec{u})^2 \rangle = \frac{1}{6} \kappa^2 \langle \vec{u}^2 \rangle, \quad (3.50)$$

and according to (3.46)

$$\langle \rho(\vec{\kappa}) \rangle = \left(\frac{3}{2\pi \langle \vec{u}^2 \rangle} \right)^{\frac{3}{2}} \sum_l e^{-\frac{|\vec{x}-\vec{l}|^2}{2\langle \vec{u}^2 \rangle}}, \quad (3.51)$$

is a Gaussian form-factor centered at the equilibrium position of the scattering centers. The elastic cross sections are now

$$\left(\frac{d\sigma}{d\Omega} \right)_{coh}^{el} = \frac{N\sigma_c}{4\pi} \frac{(2\pi)^3}{V_0} \sum_{\vec{\tau}} \delta(\vec{\kappa} - \vec{\tau}) e^{-2W(\vec{\kappa})}, \quad (3.52)$$

and,

$$\left(\frac{d\sigma}{d\Omega} \right)_{incoh}^{el} = \frac{N\sigma_i}{4\pi} e^{-2W(\vec{\kappa})}. \quad (3.53)$$

We recognize that the Debye-Waller factor diminishes the intensity of elastic processes. Indeed, it is a measure of the probability for the reaction being elastic. Furthermore, the incoherent scattering — due to the $\vec{\kappa}$ -dependence of the Debye-Waller factor — in general, is not isotropic anymore.

The correlations in the sample described by $C'(\vec{x}, \tau)$ in a nonrigid lattice are responsible for inelastic scattering processes. Energy carried by the internal degrees of freedom can be transferred to the probe. The reversed process is also possible. The probability of these two processes are intimately related with each other, as we shall see.

We do not intend in this lecture to discuss the inelastic cross sections in detail. I just would like to emphasize a few points, which will turn out to be of importance for the discussion of general properties of the correlation function and the "linear response" concept.

We start according to (3.37) with

$$C'(\vec{x}, \tau) = C(\vec{x}, \tau) - C(\vec{x}, \infty). \quad (3.54)$$

With (3.44) and a similar procedure as above we obtain

$$\begin{aligned} C'(\vec{x}, \tau) &= \left(\frac{1}{2\pi} \right)^3 \sum_{ik} \int d^3 \kappa e^{-i\vec{\kappa}\vec{x}} e^{-i\vec{\kappa}(\vec{l}_j - \vec{l}_k)} e^{-2W(\vec{\kappa})} \\ &\times \left\{ \exp [\langle \vec{\kappa} \vec{u}(\vec{l}_j) \cdot \vec{\kappa} \vec{u}(\vec{l}_k, \tau) \rangle_T] - 1 \right\}. \end{aligned} \quad (3.55)$$

The deviation of the position of an atom from its equilibrium position can be represented as a linear combination of the eigenmodes of the crystal oscillations,

$$\vec{u}(\vec{l}) = \sum_{j, \vec{q}} \left(\frac{\hbar}{3NM\omega_j(\vec{q})} \right)^{1/2} \left[\vec{\alpha}^{(j)}(\vec{q}) e^{i\vec{q}\vec{l}} a_j(\vec{q}, t) + \vec{\alpha}^{(j)*}(\vec{q}) e^{-i\vec{q}\vec{l}} a_j^\dagger \right]. \quad (3.56)$$

The dynamics of the oscillations is governed by the equation

$$i\hbar \partial_t a_j = [a_j, \mathcal{H}], \quad (3.57)$$

where \mathcal{H} is the Hamiltonian of the lattice oscillations. In the harmonic approximation (3.57) reduces to $i\hbar \partial_t a_j = \hbar \omega_j a_j$ and describes $3N$ independent harmonic oscillations

$$a_j(\vec{q}, t) = a_j(\vec{q})e^{-i\omega_j(\vec{q})t}, \quad (3.58a)$$

$$a_j^\dagger(\vec{q}, t) = a_j^\dagger(\vec{q})e^{i\omega_j(\vec{q})t}. \quad (3.58b)$$

The a_j and a_j^\dagger are the usual annihilation and creation operators, fulfilling the well-known commutation relations of the linear oscillator. Furthermore the following averages over the canonical partition are obtained

$$\langle a_j^\dagger(\vec{q})a_k(\vec{q}') \rangle_T = \delta_{jk}\delta_{qq'}n_j(\vec{q}), \quad (3.59a)$$

$$\langle a_j(\vec{q})a_k^\dagger(\vec{q}') \rangle_T = \delta_{jk}\delta_{qq'}(n_j(\vec{q}) + 1), \quad (3.59b)$$

in which $n_j(\vec{q})$ describes the population of the mode j

$$n_j(\vec{q}) = (e^{\beta\hbar\omega_j(\vec{q})} - 1)^{-1}. \quad (3.60)$$

The exponent in the Debye-Waller factor then becomes

$$\langle [\vec{\kappa}\vec{u}(\vec{l})]^2 \rangle_T \sim \sum_{j,\vec{q}} \frac{|\vec{\kappa}\vec{a}^j(\vec{q})|^2}{\omega_j(\vec{q})} (2n_j(\vec{q}) + 1). \quad (3.61)$$

This demonstrates explicitly how this factor depends on the population of the lattice excitations.

For the time-dependent exponent in (3.55) we get

$$\begin{aligned} \langle \vec{\kappa}\vec{u}(\vec{l}_i) \cdot \vec{\kappa}\vec{u}(\vec{l}_k, \tau) \rangle_T = \\ \sum_{j,\vec{q}} \frac{|\vec{\kappa}\vec{a}^j(\vec{q})|^2}{\omega_j(\vec{q})} [e^{i\vec{q}(\vec{l}_k - \vec{l}_i)} e^{i\omega_j(\vec{q})\tau} (1 + n_j(\vec{q})) + e^{-i\vec{q}(\vec{l}_k - \vec{l}_i)} e^{-i\omega_j(\vec{q})\tau} \cdot n_j(\vec{q})] \end{aligned} \quad (3.62)$$

Expansion of $\exp[\langle \quad \rangle_T]$ in (3.55) and keeping the linear term only, leads with (3.62) to a scattering function and hence an inelastic coherent cross-section which contains typical terms proportional to

$$1) \quad n_j(\vec{q})\delta(\omega + \omega_j(\vec{q}))\delta(\vec{\kappa} + \vec{q} - \vec{\tau}), \quad (3.63)$$

$$2) \quad (n_j(\vec{q}) + 1)\delta(\omega - \omega_j(\vec{q}))\delta(\vec{\kappa} - \vec{q} - \vec{\tau}). \quad (3.64)$$

The first term represents a process of phonon annihilation (absorption) ($\omega_j(\vec{q}), \vec{q}$) by the probing incident particle. The second term is the corresponding phonon creation term. Energy- and momentum conservation for these inelastic processes are,

$$E' = E \pm \hbar\omega_j(\vec{q}), \quad (3.65)$$

$$\vec{k}' = \vec{k} \pm \vec{q} - \vec{\tau}, \quad (3.66)$$

where $\vec{\tau}$ is a reciprocal lattice vector.

4. Properties of the Scattering - and the Correlation-Function

With the help of (3.33) and (3.34) we write the scattering function in the following form

$$S(\vec{\kappa}, \omega) = \frac{1}{2\pi\hbar} \int_{-\infty}^{+\infty} dt e^{-i\omega t} \langle \rho_{\vec{\kappa}}(0) \rho_{-\vec{\kappa}}(t) \rangle_T. \quad (4.1)$$

Since the position- and momentum operators are self-adjoint (observables), the Fourier-component of the density operator has the property

$$\rho_{-\vec{\kappa}} = \rho_{\vec{\kappa}}^\dagger \quad (4.2)$$

where \dagger stands for Hermitian conjugation.

$\rho_{-\vec{\kappa}}(t)$ with $t \neq 0$ and $\rho_{\vec{\kappa}}(0)$ do not usually commute - therefore, instead of the relation

$$e^A \cdot e^B = e^{A+B} \quad (4.3)$$

which is only valid for classical numbers A and B; when A and B are quantum operators we have to use,

$$e^A \cdot e^B = e^{A+B+C} \quad (4.4)$$

where the operator C can be expressed as an expansion of nested commutators,

$$C = \frac{1}{2}[A, B] + \frac{1}{12}[[A, B], B] + \frac{1}{12}[[B, A], A] + \dots \quad (4.5)$$

This is easily verified by expanding the exponents. Here A and B are

$$A = -i\vec{\kappa}\vec{X}_i(0), \quad B = i\vec{\kappa}\vec{X}_j(t). \quad (4.6)$$

Returning to (4.2) we can show that

$$\boxed{\langle \rho_{\vec{\kappa}}(0) \rho_{\vec{\kappa}}^\dagger(t) \rangle_T^* = \langle \rho_{\vec{\kappa}}(t) \rho_{\vec{\kappa}}^\dagger(0) \rangle_T} \quad (4.7)$$

where * stands for the complex conjugate.

The average $\langle \dots \rangle_T$ describes the many-body system in thermal equilibrium. In this stationary state, it is therefore invariant under a translation operation in time, and

$$\boxed{\langle \rho_{\vec{\kappa}}(-t) \rho_{\vec{\kappa}}^\dagger(0) \rangle_T = \langle \rho_{\vec{\kappa}}(0) \rho_{\vec{\kappa}}^\dagger(t) \rangle_T} \quad (4.8)$$

Note that these relations are generally only true for the thermal average and not as proper operator relations.

These two symmetry relations guarantee that the Fourier transform (4.1) is a purely real function. The scattering function $S(\vec{\kappa}, \omega)$ is therefore real - as it has to be the case for an experimentally accessible cross section.

The correlation function $C(\vec{x}, t)$ is generally not purely real. Under the conditions mentioned above, the following relationship is obtained

$$\boxed{C(\vec{x}, t) = C^*(-\vec{x}, -t)} \quad (4.9)$$

Let us express $\Re e C$ and $\Im m C$ in the form of anticommutator and commutator

$$\Re e C(\vec{x}, t) = \frac{1}{2} \int d^3x' \langle \{\rho(\vec{x}', t), \rho(\vec{x}' - \vec{x}, 0)\} \rangle_T, \quad (4.10)$$

and

$$\Im m C(\vec{x}, t) = \frac{i}{2} \int d^3x' \langle [\rho(\vec{x}', t), \rho(\vec{x}' - \vec{x}, 0)] \rangle_T. \quad (4.11)$$

Since the density operators do not commute for $t \neq 0$ the imaginary part of C (4.11) does not vanish. This condition - not valid generally - would be equivalent to

$$\langle \rho_{\vec{\kappa}}(t) \rho_{\vec{\kappa}}^\dagger(0) \rangle_T = \langle \rho_{\vec{\kappa}}^\dagger(0) \rho_{\vec{\kappa}}(t) \rangle_T. \quad (4.12)$$

That (4.12) is not valid can be demonstrated by an analytical extension to imaginary time.

$$\begin{aligned} \langle \rho_{\vec{\kappa}}(t) \rho_{\vec{\kappa}}^\dagger(0) \rangle_T &= \frac{1}{Z} \text{Sp} [e^{-\beta H} e^{i/\hbar H t} \rho_{\vec{\kappa}} e^{-i/\hbar H t} \rho_{\vec{\kappa}}^\dagger] \\ &= \frac{1}{Z} \text{Sp} [e^{-\beta H} \rho_{\vec{\kappa}}^\dagger e^{-\beta H + i/\hbar H t} \rho_{\vec{\kappa}} e^{\beta H - i/\hbar H t}] \\ &= \frac{1}{Z} \text{Sp} [e^{-\beta H} \rho_{\vec{\kappa}}^\dagger \rho_{\vec{\kappa}}(t + i\hbar\beta)] \\ &= \langle \rho_{\vec{\kappa}}^\dagger(0) \rho_{\vec{\kappa}}(t + i\hbar\beta) \rangle_T. \end{aligned} \quad (4.13)$$

As a reminder, we have made use of cyclic exchange of noncommuting operators, which is allowed under the trace operation. We recognize from (4.13) that (4.12) becomes valid in the limit $\hbar \rightarrow 0$. Hence, the classical correlation function is real, and $\Im m C \neq 0$ is a quantum mechanical effect. Particularly for fluids (however not “quantum” fluids like liquid He) the classical, real correlation function is normally sufficient for the description of its structure. The same is obviously true for gaseous systems.

5. Linear Response

In this chapter we investigate the scattering process of a probe on the target sample from the point of view of a perturbative response. The incident particle acts to the target as a perturbation to which the latter responds. The response function - a generalized susceptibility - is related to the correlation function discussed in the

last chapter and contains the information about the scatterer.

5.1 The perturbative interaction

A scattering process corresponds to a change in the condition of the beam of radiation incident on the sample to a possibly different condition of the secondary beam, e.g. the incident beam is deflected by the scattering event. The change in condition of the beam is related to changes induced in the sample, which is the information to be extracted.

We summarize the perturbative part of the Hamiltonians causing the scattering process. Generally the perturbative Hamiltonian has the form

$$H_1(t) = B(t)h(t), \quad (5.1)$$

where $h(t)$ describes the perturbing external field induced by the probe. $B(t)$ expresses the coupling of this external field to the dynamical degrees of freedom of the sample.

We assume that for $t \rightarrow -\infty$ the sample is undisturbed and is described by a Hamiltonian H_0 . Any time dependent perturbation is in its Fourier transform described by a set of monochromatic components and is hence proportional to $e^{i\omega t}$. In its explicit expression H_1 is switched on adiabatically, that is the sample stays always very close to thermal equilibrium. This can be accomplished by the choice

$$h(t) \sim e^{i\omega t + \epsilon t} \quad \text{with } \epsilon \rightarrow 0^+. \quad (5.2)$$

Normally H_1 contains the sum of couplings to individual particles in the system, usually expressed by a space-integration. Guided by the representation of the various interactions we therefore write for H_1

- i) Electromagnetic interaction (e.g. X-rays)

$$H_1 = \frac{e}{c} \int d^3x \vec{A}(\vec{x}, t) \cdot \vec{j}(\vec{x}), \quad (5.3)$$

with the current densities of the charge carriers

$$\vec{j}(\vec{x}) = \sum_i \frac{1}{2m} (\vec{p}_i \delta(\vec{x} - \vec{x}_i) + \delta(\vec{x} - \vec{x}_i) \vec{p}_i),$$

and $\vec{A}(\vec{x}, t)$ the electromagnetic potential of the incident field and m is the mass of an electron with charge $-e$.

- ii) Magnetic interaction of neutrons

$$H_1 = \int d^3x \vec{A}(\vec{x}, t) \cdot \vec{m}(\vec{x}) \quad (5.4)$$

with the magnetization density either given by magnetic moments of the electrons in the sample

$$\vec{m} = 2\mu_B \sum_j \int d^3x \vec{\sigma}_e \delta(\vec{x} - \vec{x}_j), \quad (5.5)$$

or by their orbital currents

$$\vec{M} = \frac{e}{m} \sum_j \int d^3x (\vec{p}_j \delta(\vec{x} - \vec{x}_j) + \delta(\vec{x} - \vec{x}_j) \vec{p}_j). \quad (5.6)$$

$\vec{A}(\vec{x}, t)$ is here the electromagnetic potential due to the magnetic moment of the neutron

$$\vec{A}(\vec{x}, t) = \mu_N \vec{\sigma}_N \wedge \vec{\nabla} \frac{1}{|\vec{x}|}. \quad (5.7)$$

iii) Nuclear interaction with neutrons

$$H_1 = \int d^3x e^{i(\omega t - \vec{k}\vec{x})} \rho(\vec{x}), \quad (5.8)$$

with a weighted nuclear scattering density

$$\rho(\vec{x}) = \sum_j b_j \delta(\vec{x} - \vec{x}_j). \quad (5.9)$$

5.2 The Dynamics of the Density Operator

We define the Hamiltonian, split into two parts

H_0 this part describes the unperturbed sample to be investigated

$H_1(t)$ describes the time-dependent perturbation produced by an external probe interacting with the sample.

Hence the composite system of the radiation and sample is described by the Hamiltonian,

$$H = H_0 - H_1(t). \quad (5.10)$$

The expectation value of an operator \hat{O} of the system is

$$\langle \hat{O} \rangle = Sp(\hat{O}\rho(t)), \quad (5.11)$$

where $\rho(t)$ is the density operator of the system, governed by the equation of motion

$$i\hbar \partial_t \rho = [H, \rho]. \quad (5.12)$$

We now work in the interaction-picture (Dirac) where the time development of operators is governed by the unperturbed Hamiltonian H_0

$$\hat{O}(t) = e^{(i/\hbar)H_0 t} \hat{O} e^{-(i/\hbar)H_0 t}. \quad (5.13)$$

The dynamics of the system is then described by

$$i\hbar\partial_t\rho_I = [H_1^I(t), \rho_I(t)], \quad (5.14)$$

with

$$H_1^I(t) = e^{(i/\hbar)H_0 t} H_1(t) e^{-(i/\hbar)H_0 t}. \quad (5.15)$$

A formal solution of (5.14) can be represented by the series

$$\rho_I(t) = \rho(0) - \frac{i}{\hbar} \int_{-\infty}^t d\tau [H_1^I(\tau), \rho_0] - \frac{1}{\hbar^2} \int_{-\infty}^t d\tau \int_{-\infty}^\tau d\tau' [H_1^I(\tau'), [H_1^I(\tau), \rho_0]] + \dots \quad (5.16)$$

If we are allowed to neglect the higher order terms in (5.16) we can express the expectation value of any observable by means of (5.11) as

$$\langle \hat{O} \rangle = \text{Sp}(O_I(t)\rho_0) - \frac{i}{\hbar} \int_{-\infty}^t d\tau \text{Sp}(O_I(t)[H_1^I(\tau), \rho_0]), \quad (5.17)$$

where ρ_0 is the equilibrium density operator. The traces in (5.17) give the average over the canonical ensemble of the enclosed quantities and we may write for the expected response of the observable

$$\langle \delta \hat{O} \rangle_T = \langle \hat{O} \rangle - \text{Sp}(O_I(t)\rho_0) = -\frac{i}{\hbar} \int_{-\infty}^t d\tau \langle [\hat{O}_I(t), H_1^I(\tau)] \rangle_T. \quad (5.18)$$

We now introduce the perturbation Hamiltonian in its general form. For elegance and convenience - after all, electromagnetic fields are relativistic objects - we chose the relativistic covariant form (see appendix A).

$$H_1^I(\tau) = \int d^3x J_\mu(x) \mathcal{A}^\mu(x) \quad (5.19)$$

where \mathcal{A}^μ is the four-vector potential of the external field. Using (5.19) we obtain for the response of the current operator according to (5.18)

$$\begin{aligned} \langle \delta J_\beta \rangle_T &= -\frac{i}{\hbar} \int_{-\infty}^t d\tau \langle [J_p^\dagger(\vec{x}, \tau) \int d^3x' J_\mu(x') \mathcal{A}^\mu(x')] \rangle_T \\ &= -\frac{i}{\hbar} \int d^4x' \theta(x_0 - x'_0) \langle [J_\beta(x'), J_\mu(x')] \rangle_T \mathcal{A}^\mu(x'). \end{aligned} \quad (5.20)$$

We write this in the following form

$$\langle \delta J_\beta \rangle_T = \int d^4x' K_{\beta\mu}(x - x') \mathcal{A}^\mu(x') \quad (5.21)$$

with a kernel

$$K_{\beta\mu}(x - x') = -\frac{i}{\hbar}\theta(x_0 - x'_0)\langle [J_\beta^\dagger(x), J_\mu(x')] \rangle_T \quad (5.22)$$

The tensor K admits an interpretation as a generalized susceptibility. In the following it will be one of our tasks to establish the relationship of K with the scattering function or the correlation function.

From now on we call K the response function or the response kernel. (5.21) and (5.22) may serve as a starting point for a field theoretical approach for treatment of many-body problems since K is closely related to the polarization tensor and to the field-theoretical four-point functions.

5.3 The Response Kernel and the Kramers-Kronig Relations

Assuming translational invariance in space-time coordinates we can write (5.22)

$$K_{\alpha\beta}(x) = -\frac{i}{\hbar}\theta(x_0)\langle [J_\alpha^\dagger(x)J_\beta(0)] \rangle_T, \quad (5.23)$$

where

$$J_\alpha^\dagger(x) = e^{(i/\hbar)px}J_\alpha^\dagger(0)e^{-(i/\hbar)px}. \quad (5.24)$$

We now calculate the Fourier-transform of (5.23)

$$\tilde{K}_{\alpha\beta} = \tilde{K}_{\alpha\beta}(\omega, \vec{k}) = \left(\frac{\hbar}{2\pi}\right)^2 \int d^4x e^{i\vec{k}x} K_{\alpha\beta}(x).$$

Analogous to (4.13) we rewrite the second term of the commutator (5.23) by cyclic interchange of the operators under the trace

$$\text{Sp}(e^{-\beta H} J_\beta(0) e^{(i/\hbar)Ht} J_\alpha^\dagger(0) e^{-(i/\hbar)Ht}) = \text{Sp}(e^{-\beta H} J_\alpha(t - i\hbar\beta) J_\beta(0)). \quad (5.25)$$

We then use the integral representation (B1) for the θ -function and interchange the two integrations. By means of (B8) we separate off the imaginary part of \tilde{K} and obtain

$$\begin{aligned} \Im m \tilde{K}_{\alpha\beta} &= \left(\frac{1}{2\pi}\right)^2 \frac{1}{2\hbar} \sum_n e^{-\beta(\hbar\omega_n - F)} \cdot \langle n | J_\alpha^\dagger(\omega, \vec{k}) J_\beta(0) | n \rangle (1 - e^{-\beta\hbar\omega}) \\ &= \left(\frac{1}{2\pi}\right)^2 \frac{1}{2\hbar} \text{Sp}(\rho J_\alpha^\dagger(\omega, \vec{k}) J_\beta(0)) (1 - e^{-\beta\hbar\omega}). \end{aligned} \quad (5.26)$$

We now specify again for nuclear neutron scattering, replacing the currents by the density operators. Comparison between the scattering function (4.1) with the right side of (5.26) leads to the relation (for this case a scalar relation).

$$4\pi(1 + n(\omega)) \Im m \tilde{K}(\omega, \vec{k}) = S(\omega, \vec{k}) \quad (5.27)$$

with

$$n(\omega) = \frac{1}{e^{\beta\hbar\omega} - 1}. \quad (5.28)$$

This relationship expresses the so-called **dissipation-fluctuation theorem** [3]. We shall come back to this point later on.

I first would like, however, to emphasize that according to (5.27) the cross section (scattering function) seems to determine only the imaginary part of the response function. However, we can show that due to the analyticity properties of the response function its real part is determined by the imaginary part. To show this, let us define

$$\Phi(\tau) = \langle [J^\dagger(\tau)J(0)] \rangle_T = \Im m \langle J^\dagger(\tau)J(0) \rangle_T. \quad (5.29)$$

(We suppress here the momentum dependence of the operators for simplicity of writing).

$\Phi(\tau)$ is antisymmetric in τ as can be shown using (4.7) and (4.8).

$$\Phi(\tau) = -\Phi(-\tau). \quad (5.30)$$

The response function is then

$$\tilde{K}^R(\omega) = \int_{-\infty}^{+\infty} d\tau e^{-i\omega\tau} \theta(\tau) \Phi(\tau). \quad (5.31)$$

The presence of the θ -function in (5.31) takes care of the causality condition for the scattering process and reduces (5.31) to an actual Laplace transform. Hence $\tilde{K}^R(\omega)$ is an analytic function in the upper half-plane $\omega \geq 0$.

We rewrite (5.31) by using the integral representation of the θ -function (B1)

$$\tilde{K}^R(\omega) = -\frac{1}{2\pi i} \int_{-\infty}^{+\infty} d\tau \int_{-\infty}^{+\infty} d\xi \frac{e^{-i\xi\tau}}{\omega - \xi - i\epsilon} \Phi(\tau). \quad (5.32)$$

We now use (5.30) to write for the integral over τ

$$2i \int_0^\infty d\tau \sin(\xi\tau) \Phi(\tau) = 2i \Im m \tilde{K}^R(\xi). \quad (5.33)$$

In view of the analyticity properties of $\tilde{K}^R(\omega)$ we are allowed to use (B8) and obtain

$$\begin{aligned} \tilde{K}^R(\omega) &= \frac{1}{\pi} \int_{-\infty}^{+\infty} \frac{\Im m \tilde{K}^R(\xi)}{\omega - \xi - i\epsilon} d\xi \\ &= i \int_{-\infty}^{+\infty} d\xi \delta(\omega - \xi) \Im m \tilde{K}^R(\xi) + \frac{P}{\pi} \int_{-\infty}^{+\infty} \frac{\Im m \tilde{K}^R(\xi)}{\omega - \xi} d\xi. \end{aligned} \quad (5.34)$$

where P means the principal value of the integral. Separating real- and imaginary-part of \tilde{K}^R

$$\tilde{K}^R(\omega) = \chi'(\omega) + i\chi''(\omega), \quad (5.35)$$

we can read off from (5.34) the famous Kramers-Kronig (or dispersion-) relations

$$\begin{aligned} \chi'(\omega) &= \frac{P}{\pi} \int_{-\infty}^{+\infty} \frac{\chi''(\omega)}{\omega - \xi} d\xi \\ \chi''(\omega) &= -\frac{P}{\pi} \int_{-\infty}^{+\infty} \frac{\chi'(\omega)}{\omega - \xi} d\xi \end{aligned} \quad (5.36)$$

By these relations which are the consequence of the causality condition, the response function is fully determined by the scattering function $S(\omega)$ - hence, by the differential cross section.

From the dispersion relation and (5.32) we can find a general representation of the response function $\tilde{K}^R(\omega)$

$$\tilde{K}^R(\omega) = \frac{1}{\pi} \int_{-\infty}^{+\infty} \frac{\rho(\omega')}{(\omega' - \omega) - i\epsilon} d\omega' \quad (5.38)$$

with the spectral function $\rho(\omega)$

$$\rho(\omega) = \sum_{n,m} e^{-\beta(\hbar\omega_n - F)} A_{nm} \delta(\omega - \omega_{mn}) (1 - e^{\beta\hbar\omega_{mn}}). \quad (5.39)$$

Here

$$\omega_{mn} = \omega_m - \omega_n, \quad (5.40)$$

and

$$A_{nm} = \begin{cases} \langle n | \rho_{\vec{\kappa}} | m \rangle \langle m | \rho_{\vec{\kappa}}^\dagger | n \rangle \\ \langle n | J_\alpha(\vec{\kappa}) | m \rangle \langle m | J_\beta^\dagger(\vec{\kappa}) | n \rangle \end{cases}, \quad (5.41)$$

where the first expression is for neutron - the second for light scattering. (5.38) is called the Lehmann representation.

Let us now look a bit closer to the spectral function $\rho(\omega)$. The term

$$e^{-\beta(\hbar\omega_n - F)}$$

is the population probability P_n of the state $|n\rangle$. The expression

$$e^{-\beta(\hbar\omega_n - F)} e^{-\beta\hbar\omega_{mn}}$$

with (5.40) stands for the probability of populating state $|m\rangle$. The product of matrix elements A_{nm} expresses the transition probability $\omega_{n \rightarrow m}$ between the states $|n\rangle$ and $|m\rangle$. Therefore the sum

$$\sum_m (P_n - P_m) w_{n \rightarrow m}, \quad (5.42)$$

is to be interpreted as the transition rate from state $|n\rangle$ into any other (excited) state of the system during the scattering process. The total rate of energy dissipated into the sample is then given by the following master equation

$$\partial_t E = \sum_{n,m} \hbar \omega_{nm} (P_n - P_m) w_{n \rightarrow m}. \quad (5.43)$$

Considering (5.27) this relationship is intimately related to the time derivative at $\tau = 0$ of $\Phi_\kappa(\tau)$ at $\tau = 0$

$$\int_{-\infty}^{+\infty} d\omega \omega (1 - e^{-\hbar\omega\beta}) S(\vec{r}, \omega) = \partial_\tau \Phi_\kappa(\tau) |_{\tau=0}, \quad (5.44)$$

with

$$\Phi_\kappa(t) = \langle [\rho_\kappa(\tau) \rho_\kappa^\dagger(0)] \rangle_T.$$

The relationship (5.43) shows that the spectral function $\rho(\omega)$ acquires its contributions from the excited states (dynamical degrees of freedom) of the system and hence from the variety of possibilities of energy transfer from the neutron to the sample.

Due to the detailed balance factor in (5.43) the range of integration contributing to the integral of (5.38) is restricted to the positive ω -axis for $T = 0$ ($\beta \rightarrow \infty$). For higher temperatures this range extends into the negative axis. Using (B8) it can be shown that $\tilde{K}^R(\omega)$ is holomorphic (regular) in the cut complex ω -plane - the cut being along the real axis, starting at some $\omega < 0$ which depends on the temperature of the sample (Fig. 4). The discontinuity between the lower and the upper bord of the cut is

$$\tilde{K}^R(\omega + i\epsilon) - \tilde{K}^R(\omega - i\epsilon) = 2i\rho(\omega) = 2i\Im m \tilde{K}^R(\omega). \quad (5.45)$$

According to (5.39) the contribution to (5.45) are the residues of a sequence of poles at ω_{nm} .

It is now evident that $\Im m \tilde{K}^R(\omega)$ is intimately related to the power, which has to be dissipated in the sample, in order to keep up its thermal equilibrium.

We now define the temporal correlation function for the fluctuations in a stationary case

$$\langle J^\dagger(t) J(t') \rangle = \varphi(t - t') = \varphi(\tau). \quad (5.46)$$

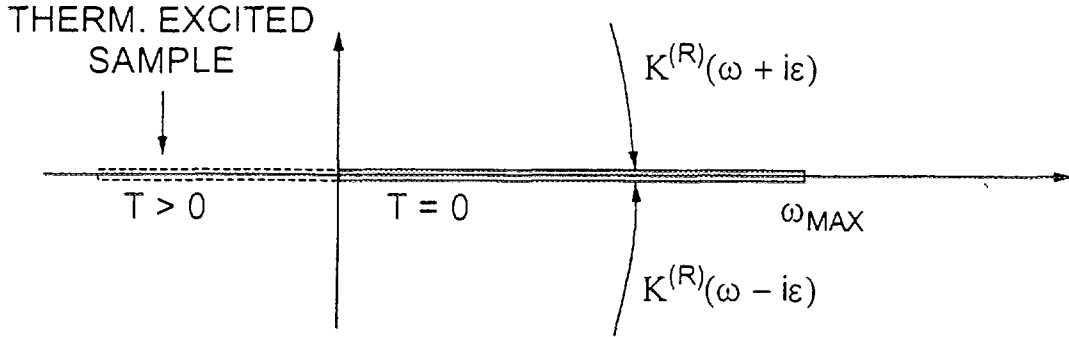


Fig. 4: Cut in the complex energy plan as an illustration to the Lehmann representation of the retarded response function.

The power spectrum of the fluctuations is then [3]

$$\begin{aligned} \langle \tilde{J}^\dagger(\omega)\tilde{J}(\omega') \rangle &= \frac{1}{2\pi} \int_{-\infty}^{+\infty} dt' \int_{-\infty}^{+\infty} dt e^{i(\omega t + \omega' t')} \langle J^\dagger(t)J(t') \rangle \\ &= \delta(\omega + \omega') \int_{-\infty}^{+\infty} d\tau e^{i\omega\tau} \varphi(\tau). \end{aligned} \quad (5.47)$$

We write (5.47) as

$$\langle \tilde{J}(\omega)\tilde{J}^\dagger(\omega') \rangle = \delta(\omega + \omega') \langle \tilde{J}^2(\omega) \rangle. \quad (5.48)$$

The $\tilde{J}'s$ are quantum mechanical operators which generally do not commute – hence we prefer to write the left hand side of (5.48) as an anticommutator. With a similar procedure as in (5.25) and (5.26) we compare

$$\int_{-\infty}^{+\infty} d\tau e^{i\omega\tau} \langle [J^\dagger(\tau)J(0)] \rangle_T, \quad (5.49)$$

with

$$\int_{-\infty}^{+\infty} d\tau e^{i\omega\tau} \langle \{J^\dagger(\tau)J(0)\} \rangle_T. \quad (5.50)$$

With the help of (5.27) we obtain

$$\langle \tilde{J}^2(\omega) \rangle = \hbar \Im m \tilde{K}(\omega) \operatorname{Cth} \left(\frac{\beta}{2} \hbar \omega \right) = 2\hbar \Im m \tilde{K}(\omega) \left\{ \frac{1}{2} + \frac{1}{e^{\beta \hbar \omega} - 1} \right\} \quad (5.51)$$

Note that for very low temperatures ($kT \ll \hbar\omega$) the hyperbolic cotangens function approaches one. The term $\frac{1}{2}$ in (5.51) obviously represents the zero-energy of the sample.

For high temperature ($kT \gg \hbar\omega$) the function rises beyond any limits. Hence, so do the fluctuations in spite of finite energy dissipation, represented by $\Im m \tilde{K}$.

This relation shows now the connection between fluctuations (represented by $\langle \tilde{J}^2(\omega) \rangle$) and dissipation ($\Im m \tilde{K}(\omega)$) [4]. The fluctuations in an unperturbed system in thermal equilibrium at temperature T is therefore related and determined by the linear response function of the sample to an external perturbation. Note that this is true in adiabatic approximation – that is, for an isentropic scattering process.

Furthermore I would like to emphasize, that – the conditions just mentioned fulfilled – these relationships are a consequence of the validity of the general principles discussed in this lecture. They do not depend on the particular interaction of the probe with the sample (be it electromagnetic or nuclear) – it has just to be weak, as has been discussed. In this sense these relations express the general theoretical framework and explain the particular power of this experimental method.

6. Acknowledgements

I thank H.B. Braun and E. Balcar for their effort to clean up the manuscript.

A Appendix

For four-dimensioned covariant notation we choose the following convention. The metric tensor is given by the matrix

$$g_{\mu\nu} = g^{\mu\nu} = \begin{pmatrix} 1 & & & \\ & -1 & & \\ & & -1 & \\ & & & -1 \end{pmatrix}, \quad (A.1)$$

and the scalar product is defined by

$$x \cdot x = x_\mu x^\mu = g^{\mu\nu} x_\mu x_\nu.$$

In particular we have for the product of a four-momentum with a space-time vector

$$p \cdot x = p_\mu x^\mu = p_0 x_0 - \vec{p} \cdot \vec{x}, \quad (A.2)$$

where

$$x^\mu = (x_0, \vec{x}) = (ct, \vec{x}), \quad (A.3)$$

and

$$p^\mu = (p_0, \vec{p}) = (E/c, \vec{p}). \quad (A.4)$$

The energy and the momentum for a massless particle can be expressed in wave numbers

$$E = \hbar\omega, \quad \vec{p} = \hbar\vec{k}, \quad (A.5)$$

such that

$$e^{ip \cdot x / \hbar} = e^{i(\omega t - \vec{k} \cdot \vec{x})}. \quad (A.6)$$

B Appendix

In this appendix we summarize some expressions on generalized functions, which are useful in the mathematical developments of scattering theory.

With the theorem of residues, the step function can be shown to have the following integral representation

$$\theta(\tau) = \frac{-1}{2\pi i} \lim_{\epsilon \rightarrow 0} \int_{-\infty}^{+\infty} d\xi \frac{e^{i\xi\tau}}{\xi - i\epsilon} = \frac{1}{2\pi i} \lim_{\epsilon \rightarrow 0} \int_{-\infty}^{+\infty} d\xi \frac{e^{-i\xi\tau}}{\xi + i\epsilon}. \quad (B.1)$$

The formal derivative of (B.1) leads to the δ -function

$$\theta'(\tau) = \frac{1}{2\pi i} \int_{-\infty}^{+\infty} d\xi \frac{i\xi}{\xi - i\epsilon} e^{i\xi\tau} \xrightarrow{\epsilon \rightarrow 0} \frac{1}{2\pi} \int_{-\infty}^{+\infty} e^{i\xi\tau} d\xi = \delta(\tau). \quad (B.2)$$

By means of (B.1) the δ -function can also be represented differently. Consider

$$\begin{aligned} \int_0^{+\infty} e^{ikx} dk &= \int_{-\infty}^{+\infty} \theta(k) e^{ikx} dk = \\ &= \frac{1}{2\pi i} \int_{-\infty}^{+\infty} d\xi \int_{-\infty}^{+\infty} dk \frac{e^{ik(\xi+x)}}{\xi - i\epsilon} = -i \int_{-\infty}^{+\infty} d\xi \frac{\delta(x + \xi)}{\xi - i\epsilon}, \end{aligned}$$

and similarly

$$\int_{-\infty}^0 e^{ikx} dk = -i \int_{-\infty}^{+\infty} d\xi \frac{\delta(x - \xi)}{\xi + i\epsilon}$$

Summing up gives

$$\frac{1}{2\pi} \int_{-\infty}^{+\infty} e^{ikx} dk = \delta(x) = \frac{1}{2\pi i} \left[\frac{1}{x - i\epsilon} - \frac{1}{x + i\epsilon} \right] \quad (B.3)$$

and therefore

$$\pi\delta(x) = \lim_{\epsilon \rightarrow 0} \frac{\epsilon}{x^2 + \epsilon^2}. \quad (B.4)$$

Let $f(\zeta)$ be a regular function in the complex ζ -plane. We assume $f(\zeta)$ to decrease sufficiently fast for large arguments $|\zeta| \rightarrow \infty$. The value of the function f at a point ω within a certain region R is then given by the values on the boundary δR , that is

$$f(\omega) = \frac{1}{2\pi i} \oint \frac{f(\zeta)}{\zeta - \omega} d\zeta \quad (B.5)$$

If ω_1 real and $f(\zeta) \rightarrow 0$ for $|\zeta| \rightarrow \infty$ we can write for (B.5)

$$\lim_{\omega \rightarrow \omega_1 + i\epsilon} f(\omega_1) = \frac{1}{2\pi i} \int_{-\infty}^{+\infty} \frac{f(\zeta)}{\zeta - \omega_1 - i\epsilon} d\zeta = \frac{1}{2\pi i} \lim_{\epsilon \rightarrow 0} \left[\int_{-\infty}^{\omega_1 - \epsilon} \frac{f(\zeta)}{\zeta - \omega_1} d\zeta + \int_{\omega_1 + \epsilon}^{\infty} \frac{f(\zeta)}{\zeta - \omega_1} d\zeta \right], \quad (B.6)$$

where the third term stems from the integration around the ($\epsilon \rightarrow 0$) semi-circle around the pole on the real axis. The integral in brackets is by definition the Cauchy-principal value. Hence

$$\lim_{\omega \rightarrow \omega_1} 2\pi i f(\omega) = P \int_{-\infty}^{+\infty} \frac{f(\zeta)}{\zeta - \omega_1} d\zeta + \pi f(\omega_1). \quad (B.7)$$

From (B.6) and (B.7) we can read off the formal relationship (Plemelij)

$$\lim_{\epsilon \rightarrow 0} \frac{1}{\zeta - \zeta_0 \pm i\epsilon} = P \frac{1}{\zeta - \zeta_0} \mp i\pi\delta(\zeta - \zeta_0). \quad (B.8)$$

Looking at (B.7) as

$$f(\omega) = \frac{1}{i\pi} P \int_{-\infty}^{+\infty} \frac{f(\zeta)}{\zeta - \omega} d\zeta, \quad (B.9)$$

we obtain by separation of real and imaginary parts the relationships

$$\Re f(\omega) = \frac{1}{\pi} P \int \frac{\Im m f(\zeta)}{\zeta - \omega} d\zeta \quad (B.10a)$$

$$\Im m f(\omega) = -\frac{1}{\pi} P \int \frac{\Re e f(\zeta)}{\zeta - \omega} d\zeta \quad (B.10b)$$

that is, a relation between real and imaginary part of the function f as a consequence of its analyticity properties.

We must emphasize that the derivations in this appendix should be considered as formal heuristic procedures at best - proper mathematical proofs need the concept of distributions.

7. References

1. L. van Hove, Phys.Rev. 95, 249, ibid 1374 (1954).
2. St. W. Lovesey, Theory of Neutron Scattering from Condensed Matter, Vol.1, Clarendon Press, Oxford, 1987.
3. L.D. Landau, E.M. Lifschitz, Statistische Physik, Teil 1, Band V, Akademie Verlag Berlin, 1987, English language version Pergamon Press, Oxford.
4. H.B. Callen, Th. A. Welton, Phys. Rev. 83, 34 (1951)

QUASICRYSTALS

WALTER STEURER

*Laboratory of Crystallography, ETH Zurich,
CH-8092 Zurich, Switzerland*

ABSTRACT

Quasicrystals are new materials with strictly defined quasiperiodic atomic long-range order. One of their most striking features is their scaling symmetry (self-similarity) in direct and reciprocal space. The quasiperiodic order gives rise to a new type of low-energy excitations, the so-called phason modes which are related to well-defined atomic jumps. The open problems connected with the research on quasicrystals and the role of neutron scattering in their solution is discussed.

1. What are Quasicrystals?

1.1. Introduction

The discovery of an Al-Mn phase with icosahedral diffraction symmetry in 1984 [1] (Fig. 1) opened a new and exciting field for crystallographers and solid state physicists. It was a big surprise and hardly believable that a material could crystallize with "non-crystalline" symmetry despite the fact that quasiperiodic tilings with fivefold orientational symmetry had already been studied by Roger Penrose ten years before [2,3]. Even the optical diffraction pattern of such a "Penrose tiling" had been published by Alan Mackay in 1982 proving that sharp Bragg reflections and lack of translational symmetry are compatible with each other [4].

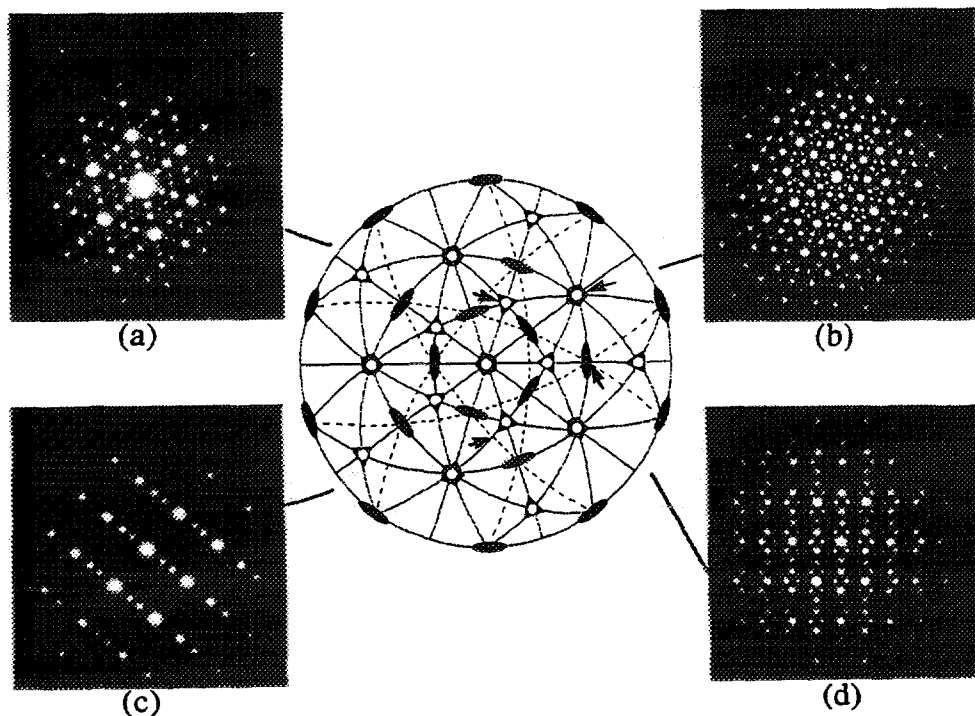


Fig. 1. Selected area electron diffraction (SAED) patterns of icosahedral Al-Mn taken in the characteristic orientations marked by arrows in the stereographic projection [5].

The first years of quasicrystal structure analysis were marked by the investigation of badly characterized samples with non-crystallographic diffraction symmetry, shortly called "quasicrystals", with spectroscopical and powder diffraction techniques. It was all but clear whether these samples were homogenous and quasiperiodically ordered, whether they were twinned approximants (i.e. closely related structures with huge unit cells), or had rather a kind of complicated crystalline nanodomain structure. The generalization of models basing on singular experimental results caused confusion in many cases until one learnt that the experimental findings were strongly dependent on chemical composition, thermal history and growth conditions of the samples. The turning point came with the discovery of an increasing number of stable quasicrystals with icosahedral or decagonal diffraction symmetry. It turned out that most stable quasicrystals transform to crystalline phases at lower temperature or higher pressure running through intermediate states with sometimes complicated modulated and/or nanodomain structures. The stable quasicrystals can be grown to dimensions suited at least for single crystal X-ray diffraction studies and in several cases also for neutron scattering experiments (Fig. 2).

What do we know today about quasicrystals, twelve years and approximately 3500 publications later? Some structural principles of quasicrystals and their relationships to approximants are now fairly understood: both the quasiperiodic and periodic related structures are built from the same clusters. Whether the structural units order periodically or quasiperiodically can be influenced by slight changes in composition for stable samples and also by the annealing conditions for metastable ones. The physical properties of quasicrystals have also been studied by several groups. Most of them, e.g. the mechanical properties, change only gradually going from the quasiperiodic to a low order approximant phase. Others, like the electronic transport properties which are more sensitive to changes in the global ordering of atoms, change drastically even by decreasing the quality of a quasicrystal. Characteristic for quasiperiodic structures are also new low-energy excitations, the phason modes. Contrary to phonon modes which are propagating and associated with the physical space, the phason modes are diffusive and associated with the complementary space (see next paragraph). The existence of phason modes give also rise to new mechanisms of diffusion and movement of dislocations in quasicrystals (for reviews see, e.g., [5,7,8].

1.2 Definitions

Regular crystal structures can be characterized by the dimensions of the unit cell, the space group, and the information what atoms occupy which Wyckoff position. The space group includes the information about the crystal system, the Bravais lattice type, atomic coordinates and site symmetries. A comparable description for quasiperiodic structures is possible in terms of the higher-dimensional approach [9]. Another way is the structure description by a quasilattice (quasiperiodic tiling) with two or more different unit cells, its symmetry and decoration with atomic clusters.

The classical example of a quasiperiodic tiling with five-fold orientational symmetry is the Penrose tiling (PT) (Fig. 3). It can be constructed using two types of unit cells, a fat (72° and 108° angles) and a skinny rhomb (36° and 144° angles) with edge lengths all equal to a_F , and areas in the ratio $\tau:1$, like their frequencies in the tiling. The irrational number τ , related to the golden mean, is the solution of the algebraic equation $\tau^2 - \tau - 1 = 0$, and has the value $\tau = \frac{1 + \sqrt{5}}{2} = 2\cos 36^\circ = 1.6180\dots$. Since the unit tiles can also be arranged periodically or randomly, local matching rules are

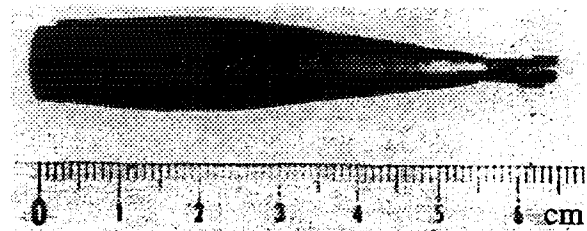


Fig. 2. Icosahedral Al-Mn-Pd single crystal grown by the Czochralski method [6].

1.3 Higher-dimensional approach

Quasiperiodic structures can always be described as sections of higher-dimensional periodic structures [9]. Five-fold rotational symmetry, for instance, which is incompatible with three-dimensional translational order can be a symmetry operation of a four-dimensional lattice. Thus, non-crystallographic symmetries in the three-dimensional space \mathbb{R}^3 can become crystallographic in the \mathbb{R}^n . It is quite natural, consequently, to describe quasiperiodic structures with their non-crystallographic symmetries as periodic structures in the \mathbb{R}^n . For axial quasicrystals, which are quasiperiodic in two dimensions and periodic in the third one, the five-dimensional embedding space \mathbb{R}^5 is necessary. The icosahedral phases can be embedded in the \mathbb{R}^6 , and one-dimensional quasicrystals in the \mathbb{R}^4 .

The principles of the higher-dimensional embedding method are demonstrated on the simple example of the one-dimensional quasiperiodic Fibonacci sequence, which can be described as a quasiperiodic section of a two-dimensional periodic lattice. The Fibonacci sequence may be obtained from the substitution rule

$$\begin{pmatrix} L \\ S \end{pmatrix} \rightarrow \begin{pmatrix} 1 & 1 \\ 1 & 0 \end{pmatrix} \begin{pmatrix} L \\ S \end{pmatrix} = \begin{pmatrix} L + S \\ L \end{pmatrix} \quad (1)$$

Starting with L one obtains the sequences

sequence	number of	
	L	S
L	1	0
LS	1	1
LSL	2	1
LSLLS	3	2
LSLLSLSL	5	3
LSLLSLSLLSLLS	8	5
LSLLSLSLLSLLSLLSLLS	13	8
.	.	.
.	.	.
.	.	.
	F_{n+1}	F_n

where $F_n = F_{n-1} + F_{n-2}$ are the Fibonacci numbers with $\lim_{n \rightarrow \infty} \frac{F_{n+1}}{F_n} = \tau$.

One finds that the substitution rule always leaves the existing sequence invariant. Thus, it corresponds to a self-similarity operation in the case of an infinite Fibonacci sequence. Replacing the letters L and S by intervals of length τ and 1 one gets due to

$$\frac{L}{S} = \frac{L+S}{L} = \tau \quad (2)$$

a structure being invariant under the scaling by a factor τ^n , with n an integer number. Assigning atomic distances to the letters L and S, a 1D quasiperiodic structure is obtained.

necessary to obtain a quasiperiodic tiling. The PT has the following characteristic properties [10,11]:

- *Quasiperiodic translational order:*
there is no nontrivial translation leaving the tiling invariant. The mass density function is quasiperiodic, i.e. it can be expressed as a finite sum of periodic functions with periods being incommensurate to each other. For example, the function $f(x) = \cos x + \cos ax$ is quasiperiodic if a is an irrational algebraic number (i.e. an irrational solution of the equation $a_n x^n + a_{n-1} x^{n-1} + \dots + a_0 = 0$).
- *Orientational order:*
each edge of each unit tile is oriented along one of the set of orientational star axes. Except in singular cases, there is no rotational or mirror symmetry in a quasiperiodic tiling.
- *Indeterminacy of the construction process:*
the infinite pattern is not determined by a finite region. Starting from a finite region allows an uncountable infinity of ways to continue the construction. All resulting tilings belong to the same local isomorphism class and are homometric structures (i.e., they have the same diffraction patterns).
- *Local isomorphism:*
any region, however large it might be, belonging to a given infinite tiling, can be found in any other different (i.e. non superposable) tiling.
- *Self-similarity:*
to any PT a different PT can be associated whose tiles are smaller by a factor τ and which includes all the vertices of the former tiling (deflation). The local matching rules can be obtained from the deflation operation.

The Penrose tiling may be used as quasilattice for structures with two-dimensional quasiperiodicity and five-fold orientational order (decagonal phases). A three-dimensional variation of the PT, with prolate and oblate rhombohedra for unit cells, their volumes are in the ratio $\tau:1$ like their frequencies, may represent a quasilattice for the icosahedral quasicrystals.

In the course of regular structure analysis, the determination of the correct crystal lattice, which has to be one of the 14 Bravais lattices, does never make any problems. In the case of quasicrystal structure analysis, however, for a given diffraction symmetry an infinite number of different quasilattices are possible. Thus, the selection of the quasilattice cannot be separated from the determination of the quasicrystal structure itself. So helpful the tiling approach might be for the understanding of the geometrical principles of a quasicrystal structure, it is not suited for performing *ab initio* structure analyses of quasicrystals. This has to be done by means of the higher-dimensional approach.

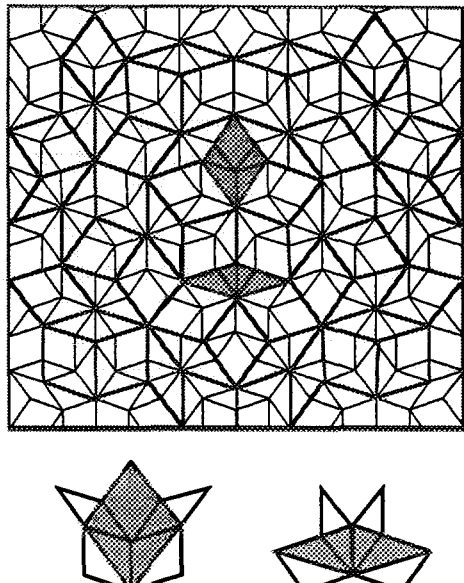


Fig. 3. A section of a Penrose tiling (thin lines) superposed by its τ -deflated tiling (thick grey lines). The inflation rule of the Penrose tiling is illustrated for both the fat and the skinny unit rhomb (shadowed). Deflation (inflation) means that the number of tiles is deflated (inflated) and their size is inflated (deflated).

The same 1D quasiperiodic structure results from an irrational cut of a 2D square lattice decorated with appropriate atomic surfaces (Fig. 4).

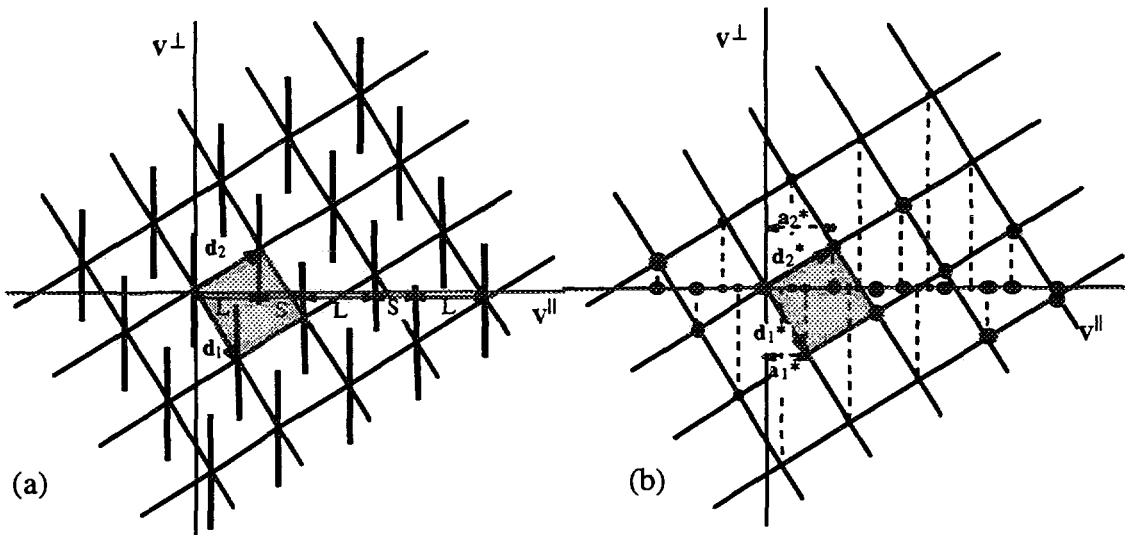


Fig. 4. (a) 2D embedding of the Fibonacci chain: the short and long distances S and L are generated by the intersection of the atomic surfaces with the physical space V^{\parallel} . The lengths of the atomic surfaces correspond to the projection of one unit cell (shadowed) upon V^{\perp} . (b) Schematic representation of the reciprocal space of the embedded Fibonacci chain depicted in (a). The physical space reciprocal basis a_1^* and a_2^* is marked. The actual 1D diffraction pattern of the 1D Fibonacci chain results from a projection of the 2D reciprocal space onto the parallel space.

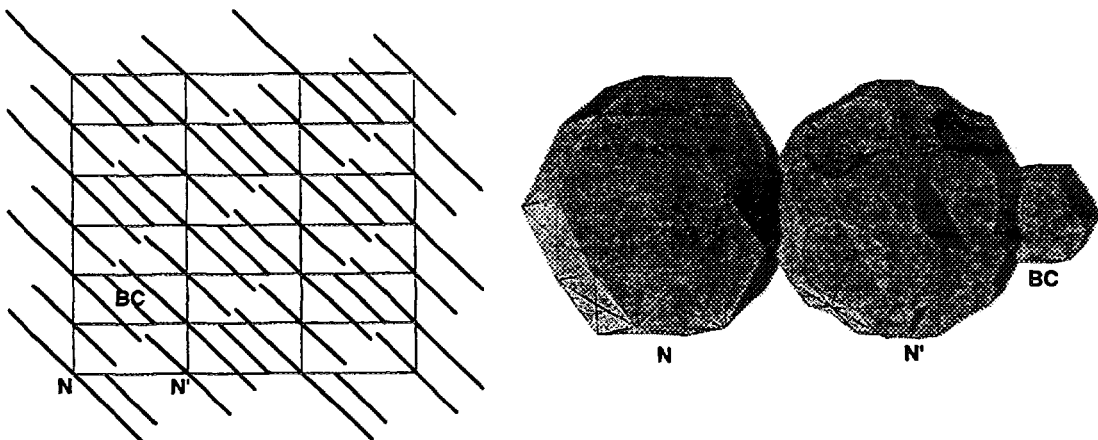


Fig. 5. Realistic 3D atomic surfaces, connected along their fivefold axis, for the icosahedral phase Al-Cu-Fe (left picture). The atomic surfaces located on the 6D lattice nodes N (000000), N' (100000) and the body center BC 1/2(111111) are shown in a section with the 6D rational fivefold plane passing through the 6D body centers [12].

One big advantage of the higher-dimensional approach is that the structural information can be given in closed form. It is mainly contained in the position and shape of the hyperatoms (Fig. 5). In terms of the tiling-decoration method, it would not be sufficient to define the type of tiling (what needs not always be possible in closed form) and the decoration of the unit tiles since, generally, the decoration can be context dependent.

2. Interesting Problems

Quasicrystals can exhibit perfect structural order, i.e. they can reach the same degree of structural perfection as silicon. This has been demonstrated by dynamical X-ray diffraction effects on an icosahedral Al-Mn-Pd crystal indicating coherent scattering (correlation) lengths over several tens of μm [13]. Nevertheless, it is still an open question whether the structure of "quasicrystals" is strictly or only on average quasiperiodic (random-tiling model) (Fig. 6).

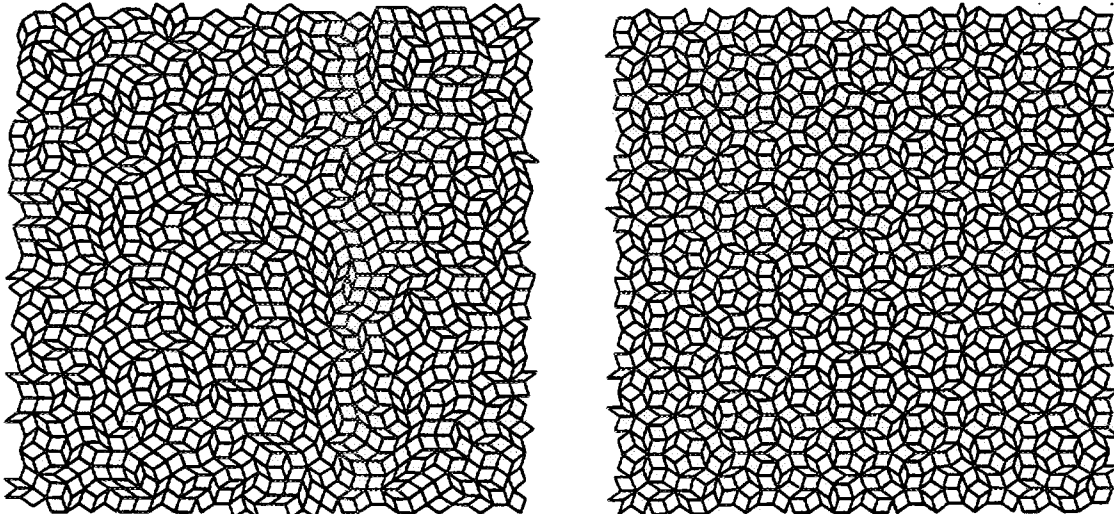


Fig. 6. Random tiling (at left) and perfect quasiperiodic tiling (at right). Note that the ratio of skinny and thick unit rhombs and the orientational symmetry is equal in both cases [14].

A random tiling can be obtained from a Penrose tiling by the introduction of special random point defects. These result from a vertex rearrangement ("phason flip") inside of two types of hexagons. Thereby, the local matching rules are violated (Fig. 7). In a real quasicrystal, phason flips refer to discrete atomic jumps. The static disorder caused by such a mechanism is called "phason-like". In the higher-dimensional approach, it can be described by shifts of the atomic surfaces parallel to the perpendicular space. Continuous displacements of atoms along the parallel space, on the contrary, are called "phonon-like".

There has also been suggested a self-diffusion mechanism basing on phason flips [15]. The generation and movement of defects (point defects and dislocations) show also specific features not known from regular crystalline phases [16].

In summary, interesting open questions are:

- Quasiperiodic ordering - is it strictly quasiperiodic or only on average (random tiling)?

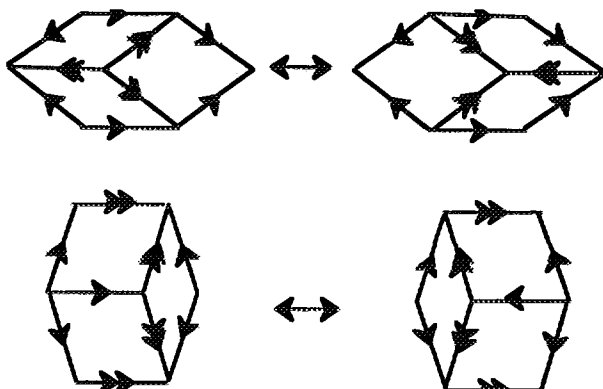


Fig. 7. Phason flips in the Penrose tiling. The two possible, different cases of hexagon-flips are shown. The violation of the matching rules (indicated by arrows and double arrows) can be seen by comparing the flipped hexagons (at right) with the original ones (at left).

- Chemical ordering - what is the role of the different atomic species in the formation of order/disorder (Fig. 8)?
- Low-energy excitations - how does the phason dynamics look like?
- Self-diffusion - move atoms by phason flips through the quasicrystal?
- Defects - how are dislocations generated and how to they move?

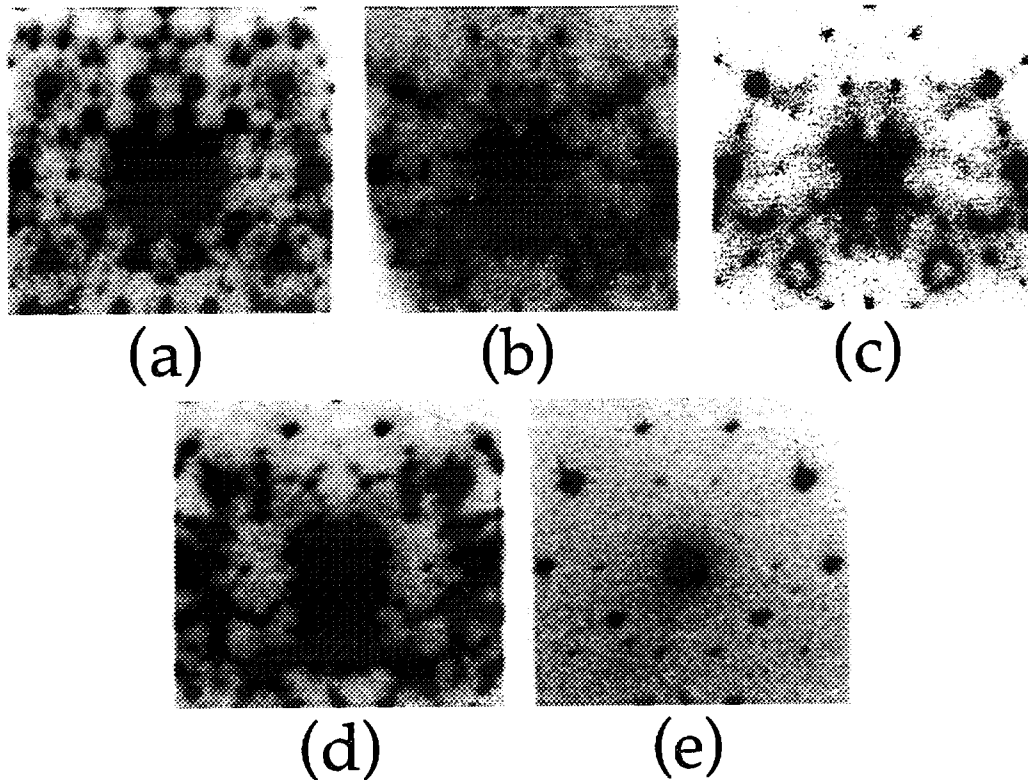


Fig. 8. Order/disorder phenomena: series of X-ray precession photographs of ternary phases in the system Al-Co-Ni showing the same small reciprocal space section around the $100\bar{1}0$ reflection: (a) “Twinned approximant”, (b) and (c) modulated nanodomain phases, (d) quasiperiodic superstructure, (e) basic decagonal phase. The Co/Ni ratio changes gradually from 4/1 in (a) to 1/4 in (e) for a constant Al component of $\approx 70\%$.

The methods of choice to answer the above mentioned questions are:

- Electron microscopy - lattice imaging elucidates the intermediate range ordering of the projected structure, whether the sample shows a nanodomain structure or is in agreement with quasiperiodic ordering of clusters.
- Contrast variation in diffraction experiments - it allows the solution of the average structure and to study the contribution of the different atomic species to static and dynamic order/disorder processes.
- High-resolution single-crystal diffraction - profile analysis indicates the degree and kind of structural long-range order (Fig. 9).
- *In situ* high-temperature single-crystal diffraction - the intensity increase of particular Bragg reflections indicates random-tiling-like behavior.
- Quasi-elastic and inelastic neutron diffraction - it allows the study of phason and phonon dynamics.

In the following paragraphs, two examples for the application of neutron scattering in the study of quasicrystal structure and phason dynamics, respectively, are given.

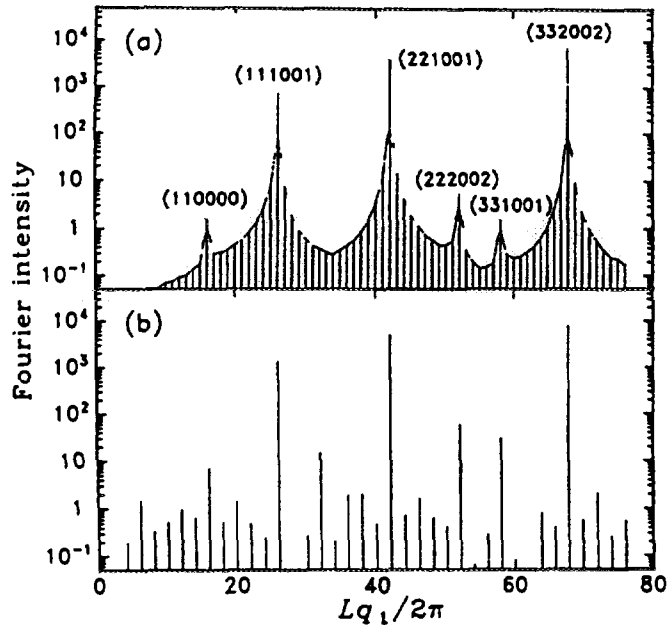


Fig. 9. Fourier Spectrum of a (a) random and (b) ideal 3D Penrose tiling. In (a) diffuse scattering intensity is clearly visible in between sharp Bragg reflections [17].

3. Structure Solution by Neutron Contrast Variation Techniques

Neutron contrast variation for the determination of partial structure factors and phasing of total structure factors has successfully been used for the icosahedral phases in the systems Al-Cu-Li [18], Al-Mn-Si [19], Al-Cu-Fe [20] and Al-Mn-Pd [21]. One of the next problems to be solved with contrast variation is that of the Co/Ni-ordering in decagonal Al-Co-Ni (Fig. 8). For the highly-symmetric icosahedral quasicrystals, powder diffraction can be sufficient. In the case of decagonal phases, singl crystal diffraction is essential.

Al-Mn-Pd [21]:

An equiatomic FeCr-mixture (σ -phase) has been found to substitute Mn randomly. Four icosahedral $\text{Al}_{71}(\text{Mn}_{1-c}\sigma_c)_{21}\text{Pd}_{19}$ samples ($c=0, 0.362, 0.696, 1$) have been measured by neutron powder diffraction (ILL, D2B two-axis diffractometer, $\lambda=1.5947$ Å) (Fig. 10). The corresponding average coherent neutron scattering lengths of the mixtures $\text{Mn}_{1-c}\sigma_c$ are -0.373 (pure Mn), 0 (only Al, Pd "visible"), $+0.3445$ (equal to b_{Al}) and $+0.0658$ (pure b_{FeCr}) in units of 10^{-12}cm . For Al and Pd the scattering lengths are $+0.3449$ and $+0.591 \times 10^{-12}\text{cm}$. For comparison, the scattering power for X-ray diffraction is proportional to the atomic numbers: $Z_{\text{Al}}=13$, $Z_{\text{Mn}}=25$ and $Z_{\text{Pd}}=46$.

The intensities can be separated into the contributions from Al and transition metal (TM) atoms $\text{Mn}_{1-c}\sigma_c$

$$I(\mathbf{H}) = \left| b_{\text{Al}} F_{\text{Al}}(\mathbf{H}) + b_{\text{TM}} F_{\text{TM}}(\mathbf{H}) \right|^2 \quad (3)$$

with the partial structure factors

$$\begin{aligned} F_{Al}(\mathbf{H}) &= |F_{Al}(\mathbf{H})| \exp(i\varphi_{Al}) = \sum_{Al} \exp(2\pi i \mathbf{H} \cdot \mathbf{r}_{Al}), \\ F_{TM}(\mathbf{H}) &= |F_{TM}(\mathbf{H})| \exp(i\varphi_{TM}) = \sum_{TM} \exp(2\pi i \mathbf{H} \cdot \mathbf{r}_{TM}) \end{aligned} \quad (4)$$

and written explicitly

$$I(\mathbf{H}) = b_{Al}^2 |F_{Al}(\mathbf{H})|^2 + b_{TM}^2 |F_{TM}(\mathbf{H})|^2 + 2b_{Al} b_{TM} |F_{Al}(\mathbf{H})| |F_{TM}(\mathbf{H})| \cos \Delta\varphi \quad (5)$$

with the phase difference $\Delta\varphi = \varphi_{Al} - \varphi_{TM}$ between the partial structure factors for the Al and the TM substructures. The unknown magnitudes $|F_{Al}(\mathbf{H})|$, $|F_{TM}(\mathbf{H})|$ and $|\Delta\varphi|$ can be determined for each Bragg reflection by measuring at least three independent intensities $I(\mathbf{H}, b_{TM})$. Since icosahedral Al-Mn-Pd crystallizes in the centrosymmetric 6D space group $Fm\bar{3}\bar{5}$ the values of $|\Delta\varphi|$ can only be 0 or π . Fourier transformation of the partial structure factors gives the partial electron density distributions (Fig. 11)

$$\begin{aligned} \rho_{Al}(\mathbf{r}) &= \sum_{\mathbf{H}} F_{Al}(\mathbf{H}) \exp(2\pi i \mathbf{H} \cdot \mathbf{r}), \\ \rho_{TM}(\mathbf{r}) &= \sum_{\mathbf{H}} F_{TM}(\mathbf{H}) \exp(2\pi i \mathbf{H} \cdot \mathbf{r}) \end{aligned} \quad (6)$$

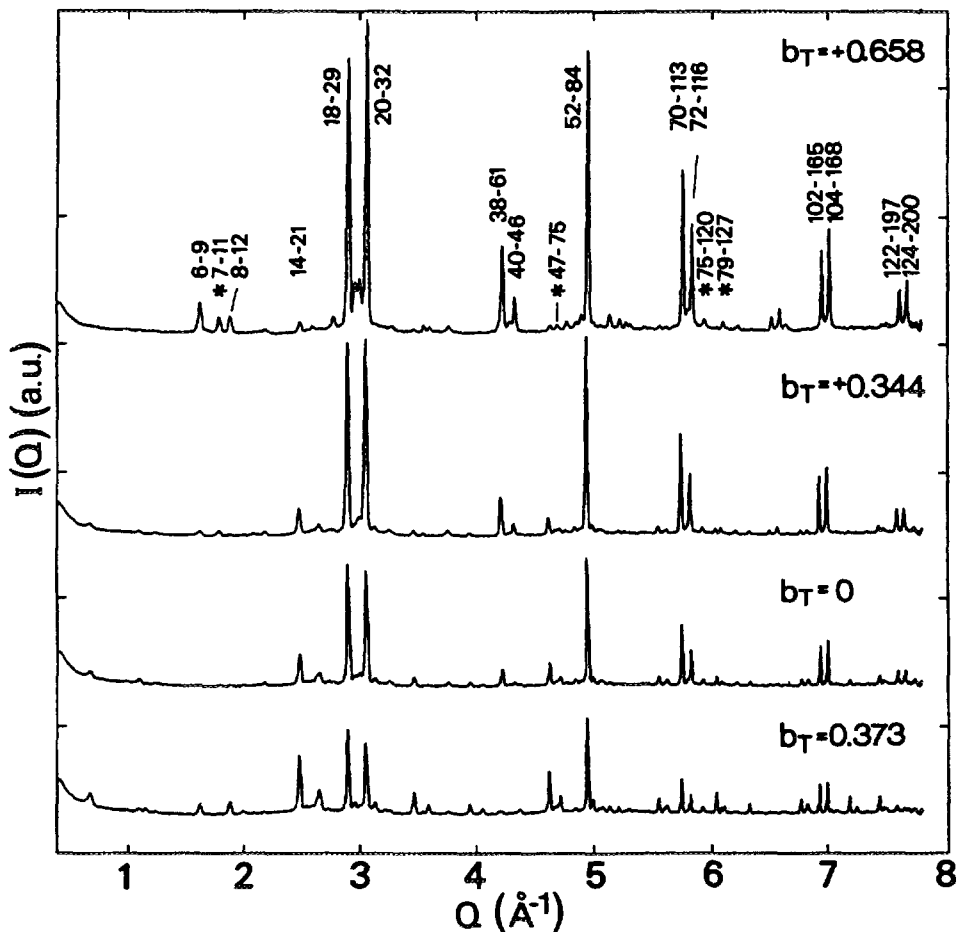


Fig. 10. Neutron powder diffractograms of icosahedral $Al_{71}(Mn_{1-c}\sigma_c)_{21}Pd_{19}$ phases. The scattering length b_T ($\times 10^{-12} \text{ cm}$) of the $Mn_{1-c}\sigma_c$ mixture indicates the contrast changes with changing the value of c [21].

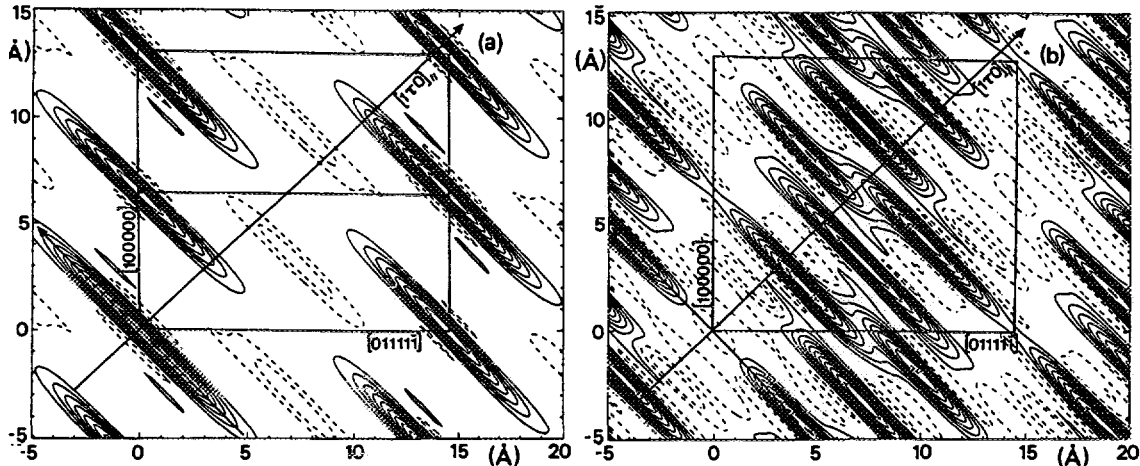


Fig. 11. Partial density maps in characteristic fivefold sections for (a) the transition metals $Mn_{1-c}C_c$ and (b) Al-Pd atomic surfaces. TM atoms are mainly located at the two different node positions (even and odd). Al-Pd atomic surfaces surround the TM surfaces and are also located at the body centers [21].

4. Phason Dynamics

The phason dynamics of quasicrystals, i.e. the atomic hopping between particular double well potentials, plays a crucial role for the understanding of:

- the global structure (ideal quasiperiodicity or only on average, i.e. quasiperiodic tiling or random tiling approach),
- local structure (atomic decoration),
- self diffusion,
- phase transformations.

In the following, the power of quasi-elastic neutron scattering for the study of phason dynamics is demonstrated on results of the groups collaborating with Gerrit Coddens [22-24].

The first example deals with quasi-elastic neutron scattering on powder samples of icosahedral $Al_{62}Cu_{25.5}Fe_{12.5}$ (TOF spectrometer MIBEMOL, Saclay, $\lambda=7.5$ Å, elastic resolution $50\mu eV$) (Fig. 12). By this experiment, the existence of phason modes in the temperature range $500^{\circ}C \leq T \leq 800^{\circ}C$ was proved. Near the melting point, nearly 20% of the Cu atoms are involved in atomic hopping with a characteristic

distance of $3.9(3)$ Å and a "depinning energy" of 0.75 eV as derived from an Arrhenius plot [22].

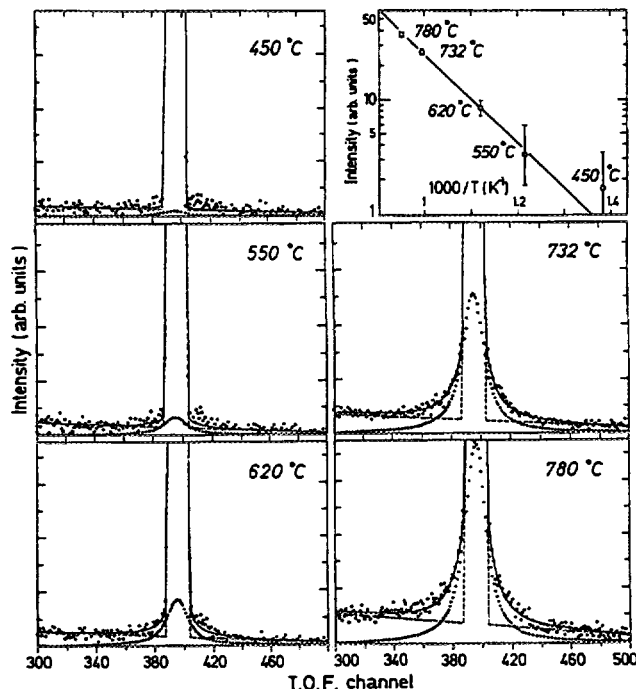


Fig. 12 Temperature dependence of the quasi-elastic scattering (Lorentzian component at the foot of the elastic peak). An Arrhenius plot is shown at upper right [22].

In an other experiment, the anisotropy of the atomic jumps in icosahedral Al-Mn-Pd could be demonstrated by quasi-elastic scattering on a huge single crystal on a triple-axis-spectrometer (4F2 Saclay, $k_f = 1.64 \text{ \AA}^{-1}$, constant Q-scans, graphite double monochromator) [24] (Fig. 13). The results indicate a preferred direction of the atomic hopping parallel to the two-fold directions.

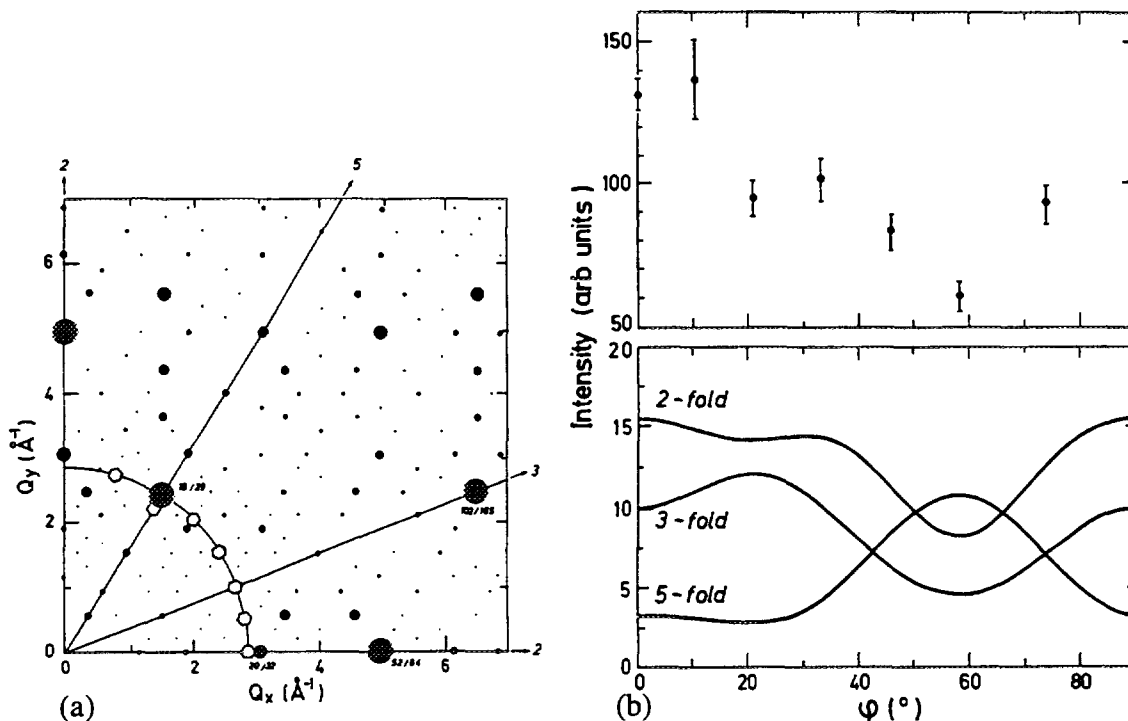


Fig. 13. (a) Scattering geometry of the experiment. Bragg peaks are marked by ●. Positions of constant Q-scans are indicated by open hexagons. (b) Anisotropy of the intensity obtained from the fits as a function of the polar coordinate angle φ , compared with results of a simplified calculation [24].

5. References

1. D. Shechtman, I. Blech, D. Gratias, J.W. Cahn, *Phys. Rev. Lett.* **53** (1984) 1951.
2. R. Penrose, *Bull. Math. Appl.* **10** (1974) 266.
3. R. Penrose, *Math. Intelligencer* **2** (1979) 32.
4. A.L. Mackay, *Physica* **A114** (1982) 609.
5. K.F. Kelton, in *Intermetallic Compounds*, ed. J.H. Westbrook and R.L. Fleischer (John Wiley & Sons, Chichester, 1995) Vol. I, p. 453.
6. M. Boudard, E. Bourgeat-Lami, M. de Boissieu, C. Janot, M. Durand-Charret, H. Klein, M. Audier and B. Hennion, *Phil. Mag. Lett.* **71** (1995) 11.
7. W. Steurer, in *Physical Metallurgy*, ed. R.W. Cahn & P. Haasen (Elsevier Science North Holland, Amsterdam, 1996) Vol. I, p. 371.
8. J.-M. Dubois, *Phys. Scripta* **T49** (1993) 17.
9. T. Janssen, *Acta Crystallogr.* **A42** (1986) 261.
10. A. Pavlovitch and M. Kléman, *J. Phys. A: Math. Gen.* **20** (1987) 687.

11. D. Levine, and P.J. Steinhardt, *Phys.Rev.* **B34** (1986) 596.
12. A. Le Lann and J. Devaud, *J. Phys. France* **5** (1995) 129.
13. S.W. Kycia, A.I. Goldman, T.A. Lograsso, D.W. Delaney, D. Black, M. Sutton, E. Dufresne, R. Brüning and B. Rodricks, *Phys. rev.* **B48** (1993) 3544.
14. T.R. Welberry, *J. Appl. Crystallogr.* **24** (1991) 203.
15. P.A. Kalugin and A. Katz, *Europhysics Lett.* **21** (1993) 921.
16. J. Bohsung and H.-R. Trebin, in *Aperiodicity and Order*, ed. M.V. Jaric (Academic Press, San Diego, 1989) Vol 2, p 184.
17. L.H. Tang, *Phys. Rev. Lett.* **64** (1990) 2390.
18. M. de Boissieu, C. Janot, J.M. Dubois, M. Audier and B. Dubost, *J. Phys. :Cond. Matter* **3** (1991) 1.
19. C. Janot, M. de Boissieu, J.M. Dubois and J. Pannetier, *J. Phys. :Cond. Matter* **1** (1989) 1029.
20. M. Cornier-Quiquandon, R. Bellissent, Y. Calvayrac, J.W. Cahn, D. Gratias and B. Mozer, *J. Non-Cryst. Solids* **153 & 154** (1993) 10.
21. M. Boudard, M. de Boissieu, C. Janot, J.M. Dubois and C. Dong, *Phil. Mag. Lett.* **64** (1991) 197.
22. G. Coddens, *Ann. Chim.: Sci. Mater. France* **18** (1993) 513.
23. G. Coddens, C. Soustelle, R. Bellissent and Y. Calvayrac, *Europhys. Lett.* **23** (1993) 33.
24. S. Lyonnard, G. Coddens, B. Hennion, R. Bellissent and Y. Calvayrac, *Physica* **B219 & 220** (1996) 342.

Optical information storage

Th. Woike, Institut für Kristallographie, Universität zu Köln

Introduction

IN ORDER TO INCREASE STORAGE CAPACITY AND DATA TRANSFER VELOCITY BY ABOUT THREE ORDERS OF MAGNITUDE COMPARED TO CD OR MAGNETIC DISC IT IS NECESSARY TO WORK WITH OPTICAL TECHNICS, ESPECIALLY WITH HOLOGRAPHY.

ABOUT 100 TBYTE CAN BE STORED IN A WAVER OF AN AREA OF 50 cm^2 VIA HOLOGRAMS WHICH CORRESPONDS TO A DENSITY OF $2 \cdot 10^9 \text{ BYTE/mm}^2$. EVERY HOLOGRAM CONTAINS DATA OF 1 MBYTE, SO THAT A PARALLEL-PROCESSING IS POSSIBLE FOR READ-OUT. USING HIGH-SPEED CCD-ARRAYS A READ-OUT VELOCITY OF 1 MBYTE/ μsek CAN BE REACHED.

FURTHER, HOLOGRAPHIC TECHNICS ARE VERY IMPORTANT IN SOLID STATE PHYSICS. WE WILL DISCUSS THE EXISTANCE OF A SPACE CHARGE FIELD IN $\text{Sr}_{1-x}\text{Ba}_x\text{Nb}_2\text{O}_6$ DOPED WITH CERIUM AND THE PHYSICAL PROPERTIES OF METASTABLE STATES, WHICH ARE SUITED FOR INFORMATION STORAGE.

Holographic storage in photorefractive materials

The basic principle of holography is the generation of a modulation of the index of refraction Δn or absorption $\Delta\alpha$ by interference pattern.

As shown in figure 1, the laser beam is devided by a beam-splitter BS into two beams, R and S, which are reflected by the mirrors M1 and M2 onto the crystal.

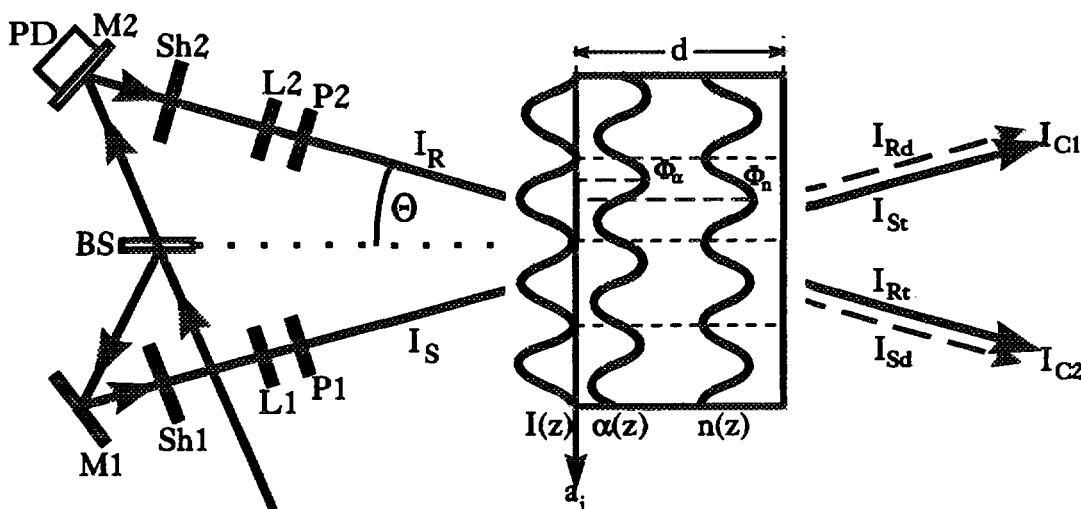


Figure 1: Principle experimental arrangement for holographic measurements

The intensities I_R and I_S and polarizations \vec{E}_R and \vec{E}_S of the two beams can be adjusted by $\lambda/2$ -plates L_1, L_2 and polarizers P_1, P_2 . Every beam can be blocked by shutters Sh1, Sh2. With the piezo-driver PD the phase between R and S can be shifted. The superposition of the two coherent plane waves R and S results in interference pattern with a sinusoidal intensity modulation $I(z)$ along the crystallographic axis a_i . In photorefractive materials the index of refraction is modulated by the light intensity, so that a grating is written with wavelength $\Lambda (|\vec{K}| = \frac{2\pi}{\Lambda})$ and a phaseshift of ϕ_n with respect to the incoming interference pattern $I(z)$. In photochromatic substances the absorption coefficient α is modulated but with a phase-shift of ϕ_α . These gratings are called *elementary holographic gratings*. The Bragg-condition for diffraction at these gratings is:

$$\lambda = 2\Lambda \sin \theta$$

whereby λ is the irradiation wavelength and θ the Bragg-angle which is automatically fulfilled for the writing beams R and S. If for instance Sh1 is closed, a diffracted and transmitted intensity I_{Rd} and I_{Rt} can be measured. The ratio of diffracted and incoming intensity gives the diffraction efficiencies $\eta_R := \frac{I_{Rd}}{I_R}$ and $\eta_S := \frac{I_{Sd}}{I_S}$, respectively. Kogelnik [1] has calculated for thick holographic gratings the dependence of η on Δn and $\Delta \alpha$:

$$\eta = e^{-\frac{2\alpha d}{\cos \theta}} \left[\sin^2\left(\frac{\pi \cdot \Delta n \cdot d}{\lambda \cdot \cos \theta}\right) + \sinh^2\left(\frac{\Delta \alpha \cdot d}{2 \cos \theta}\right) \right] \quad (1)$$

Here, α is the absorption coefficient and d the hologram thickness. The maximum efficiency of thick photochromic gratings is about $\eta = 4\%$ compared to photorefractive gratings, which reach a maximum diffraction efficiency of $\eta = 100\%$. Therefore, we will discuss in the following the behaviour of photorefractive crystals. In dependence on the irradiation time and intensity the grating is build up, so that a dynamical process of the diffracted intensity can be measured, as shown in figure 2 for $Sr_{0.69}Ba_{0.39}Nb_2O_6 : Ce$ (Strontium-Barium-Niobat (SBN)), doped with 0.48% Cerium):

The diffraction efficiency η increases during the writing process forming the grating. Saturation of $\eta = 16\%$ is reached at an exposure $Q=I \cdot t$ of $Q = 35 \frac{J}{cm^2}$ with the irradiation wavelength $\lambda = 632.8nm$. Knowing the absorption coefficient at this wavelength, the refraction index Δn can be calculated via (1) as $\Delta n = 1.4 \cdot 10^{-4}$.

Discussing photorefractive gratings (phase gratings), the diffracted waves are $\pi/2$ -phase shifted with respect to the incoming waves [2]. Neglecting absorption, the resulting transmitted intensities I_{C1} and I_{C2} during the writing process are influenced by the interference of the transmitted and diffracted waves:

$$I_{C1} = I_S(1 - \eta) + I_R\eta + 2\sqrt{I_R I_S} \sqrt{\eta(1 - \eta)} \cdot \sin \phi_n$$

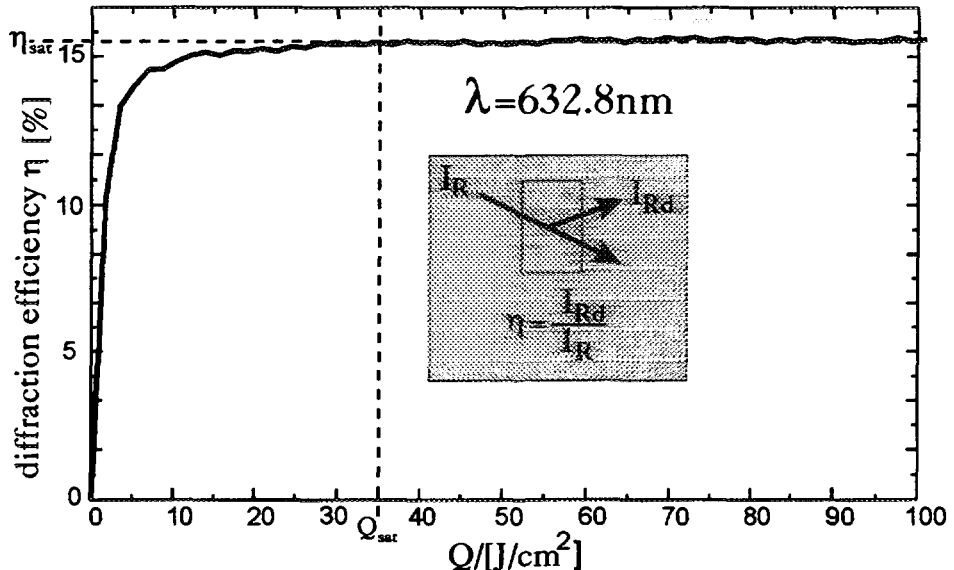


Figure 2: Diffraction efficiency η versus exposure $Q = I \cdot t$ for SBN:Ce.

$$I_{C2} = I_R(1 - \eta) + I_S\eta - 2\sqrt{I_R I_S} \sqrt{\eta(1 - \eta)} \cdot \sin\phi_n$$

The first two terms describe the transmitted intensity (incoming intensity minus diffraction loss) and the gain of diffraction. The third term contains the interference of the diffracted and transmitted waves, the so called coupling-term. In dependence on the phase-shift ϕ_n the energy is transferred from I_{C2} to I_{C1} . For the special case, that the incoming intensities I_S and I_R are equal $I_R = I_S = I_0$ and the phase-shift is $\phi_n = 90^\circ$, the coupling formula reduces to:

$$\frac{I_{C1}}{I_o} = 1 + 2\sqrt{\eta(1 - \eta)}$$

$$\frac{I_{C2}}{I_o} = 1 + 2\sqrt{\eta(1 - \eta)}$$

For a diffraction efficiency of $\eta = 0.5$ we finally get:

$$\frac{I_{C1}}{I_o} = 2 \text{ and } \frac{I_{C2}}{I_o} = 0.$$

so that the whole energy is transferred from I_{C2} into I_{C1} .

The condition $\phi_n = 90^\circ$ is found in acentric photorefractive crystals, so that we can decide between centrosymmetrical and acentric photorefractive materials by measuring the intensities I_{C1} and I_{C2} .

Such a behaviour is shown in figure 3 for a Cerium doped (0.48 wt. %) SBN-crystal: $Sr_{0.61}Ba_{0.39}Nb_2O_6 : Ce$.

The crystal was illuminated with red light of a HeNe-laser ($\lambda = 632.8nm$) and equal intensities of the R and S waves $I_R = I_S = I_0$. The difference of I_{C1} and I_{C2} demonstrates clearly that $\phi_n \neq 0$. SBN belongs to the acentric pointgroup

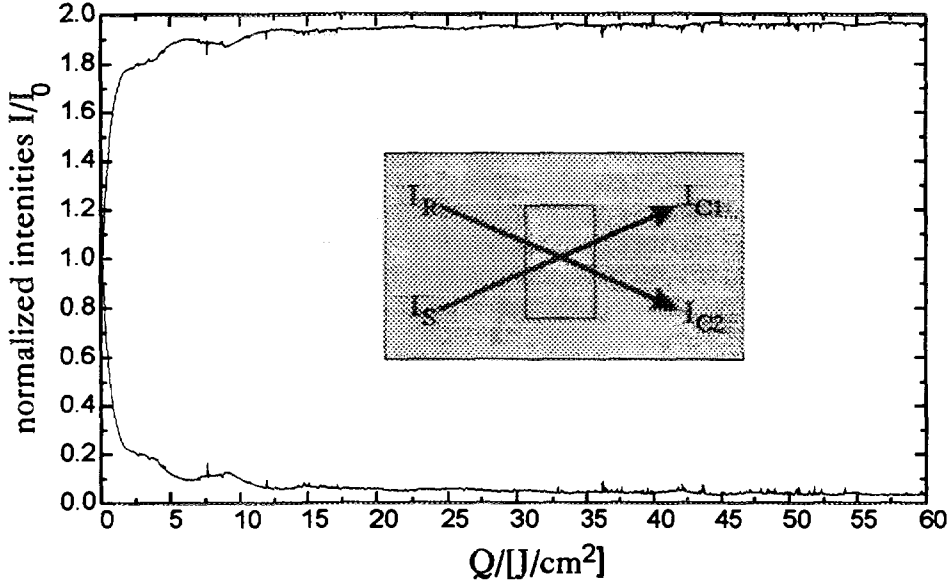


Figure 3: Transmitted intensities I_{C1} and I_{C2} during the writing process for $\eta = 0.5$; $I_R = I_S = I_0$

4mm, which determines the phaseshift between the interference pattern and the modulation of the index of refraction theoretically to $\phi_n = 90^\circ$ ($\pi/2$ -phase-grating). Experimentally we get with $\frac{I_{C1}}{I_0} = 1.9$ and $\eta = 0.5$: $\phi_n = 90^\circ$.

A further important parameter is the optical amplification Γ of I_{C1} with respect to decreasing I_{C2} , defined as:

$$\Gamma = \frac{1}{d} \ln \left(\frac{I_{C1} \cdot I_{Rt}}{I_{C2} \cdot I_{St}} \right)$$

whereby d is the hologram thickness. A real optical amplification takes place if Γ exceeds the absorption coefficient of the material: $\Gamma > \alpha$, which is the case in SBN:Ce. From the dependence of Γ on the Bragg-angle we can calculate the effective number of photorefractive centers N_{eff} excited during the writing process [3]. The photorefractive effect is determined by the transition: $Ce^{3+} \rightarrow Ce^{4+}$.

$$\Gamma(\theta) = \frac{A \cdot \sin \theta}{1 + B^{-2} \sin^2 \theta} \cdot \frac{e1 \cdot e2}{\cos \theta}; \quad (2)$$

where the material parameters in two coefficients A,B are given by:

$$A = r_{eff} \zeta(k) \frac{8\pi^2 n^2 k_B T}{e \lambda^2}$$

$$B = \frac{e \lambda}{4\pi} \left(\frac{N_{eff}}{\epsilon \epsilon_0 k_B T} \right)^{\frac{1}{2}}$$

Here, $e1$ and $e2$ are the polarization directions of the optical beams, n is the refractive index, $\frac{k_B T}{e}$ is the thermal energy per charge, λ is the irradiation

wavelength, ϵ is the dielectric constant, $\zeta(k)$ is the electron-hole competition factor, r_{eff} is the effective electrooptic coefficient.

The dependence of Γ on the Bragg-angle θ for SBN:Ce is shown in figure 4 for a light polarization parallel to the crystallographic c-axis (polar axis).

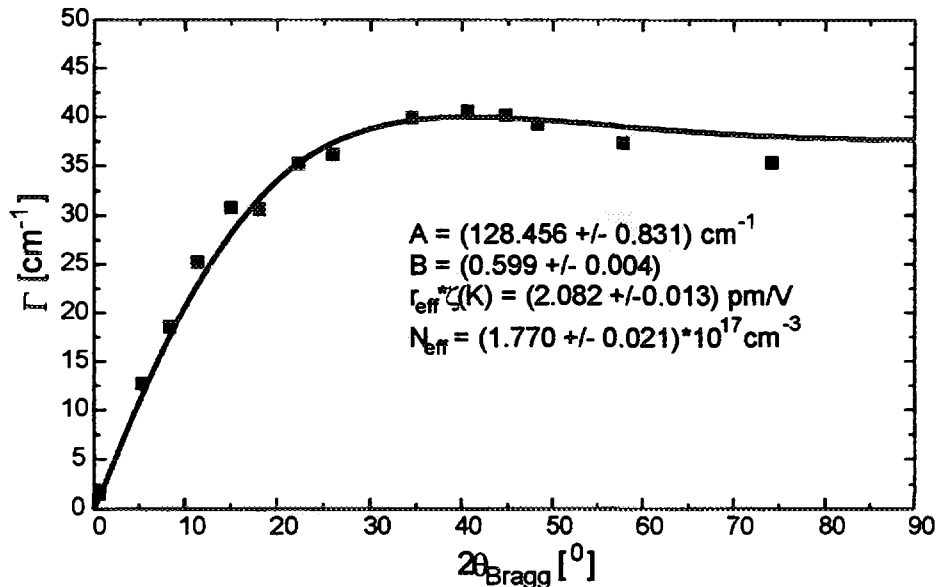


Figure 4: Optical amplification Γ in dependence on the Bragg-angle θ

Fitting equation 2 to the measured values shown in figure 4, N_{eff} and r_{eff} can be determined as: $N_{eff} = 1.77 \cdot 10^{17} [\text{cm}^{-3}]$; $r_{eff} \zeta(k) = 2.082 [\frac{\text{pm}}{\text{V}}]$.

For holographic storage at least three steps are necessary: Excitation of photorefractive centers, carrier transport and recombination. This is shown schematically in figure 5

In a one-center-model the carriers are excited in the region of the modulated irradiating light $I(z)$ and move into the dark regions. A new modulation of charge density results and with this a space charge field E_{sc} , which modulates the refractive index Δn via the electrooptic coefficient r_{ij} :

$$I \rightarrow \Delta\rho \rightarrow E_{sc} \rightarrow \Delta n \sim r_{ij} \cdot E_{sc}$$

Typical values of Δn are lying in the range of $\Delta n \sim 10^{-4}$. The modulation of Δn opens the possibility to write information in a crystal by holography. High density can be reached by focussing the laser light and by writing holograms at different Bragg-angles, since the deviation from the Bragg-angle is very small, as shown in figure 6 for $LiNbO_3$:

The diffracted intensity of a written hologram is detected by rotating the crystal in the range of $-20^\circ \leq \theta \leq +20^\circ$. At the full width of half maximum $\Delta\theta < 0.1^\circ$

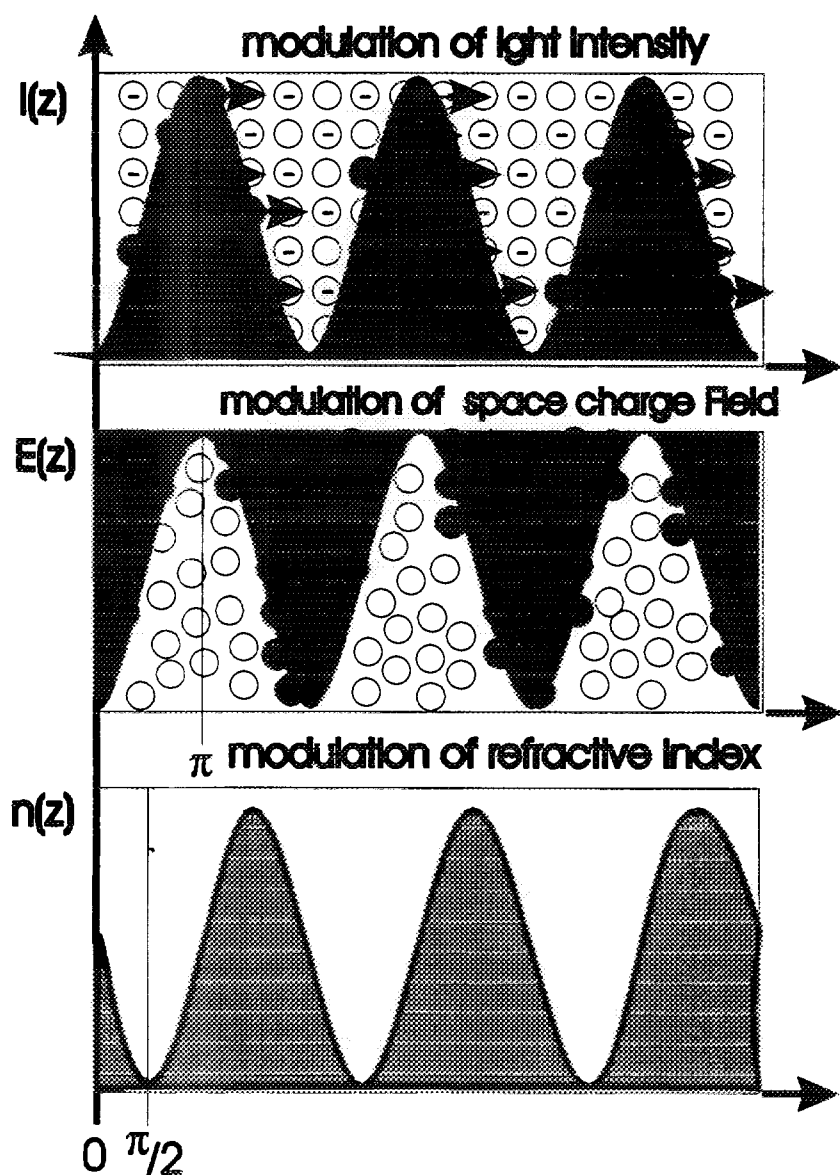


Figure 5: Holographic storage in photorefractive materials via the electrooptic effect

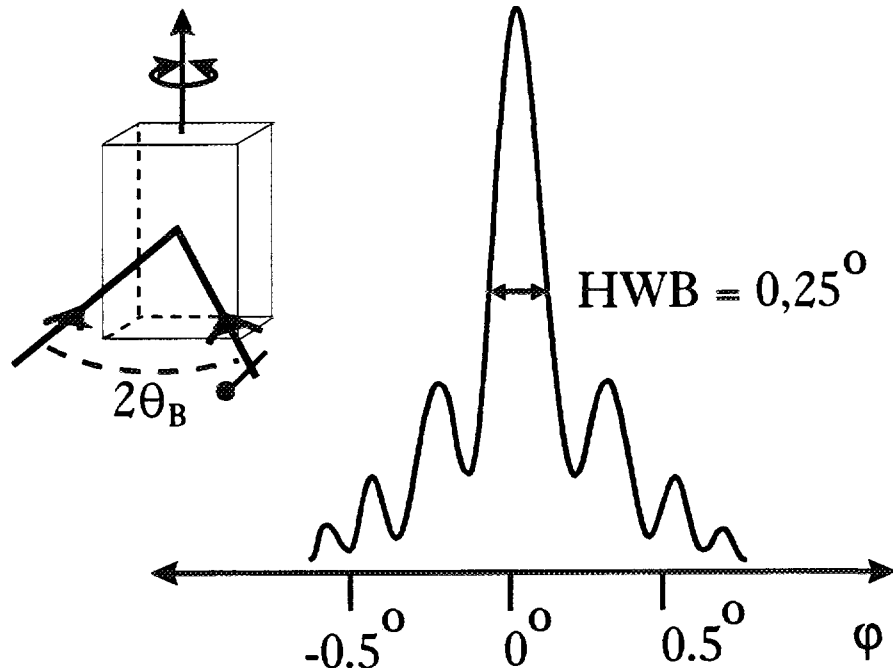


Figure 6: Efficiency in dependence from the deviation of the Bragg-angle

for a crystal thickness of $d = 1\text{mm}$:

$$\Delta\theta \sim \frac{1}{d}$$

so that in steps of about 0.1° holograms can be written.

However, if we want to read the information by detecting the diffraction efficiency η , the space charge modulation will be destroyed, since we are irradiating the crystal with a homogeneous light intensity. Therefore, the hologram must be fixed. This can be done by two different techniques: Thermal fixation and electric fixation. The standard technique of thermal fixation of the space charge is done by heating the crystal to about $T = 150^\circ\text{C}$ [4]. At this temperature the bonds of the always present O-H-ions are broken and the protons move in order to compensate the space charge. Homogeneous irradiation now destroys the space charge grating but the protons are pinned and form the grating. Below $T = 80^\circ$ the stability can be guaranteed for at least 100 years. In order to reduce the time for a thermal fixation, we irradiate the written hologram with a short intensive laser puls in the frequency range of the O-H vibration ($\nu \approx 3600\text{cm}^{-1}$) to destroy the O-H bond.

Electric fixation means, that space charge is compensated by ferroelectric domains. As shown in figure 7 a short electric puls of about 750 V and 0.1 second is applied after the hologram is written.

In the beginning of the reading process after fixation no diffraction efficiency can be found. This homogenous irradiation destroys the space charge modulation,

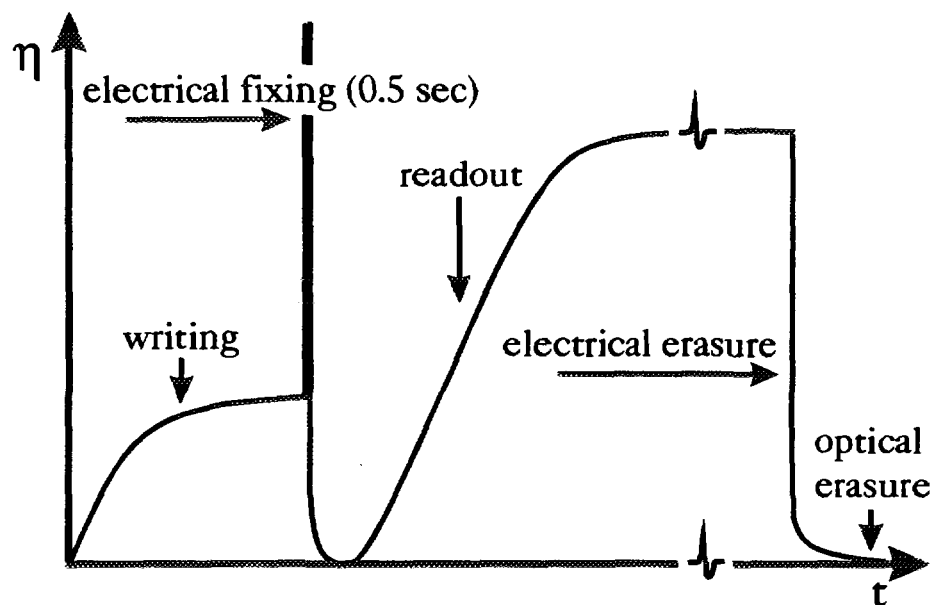


Figure 7: Electric fixation and read-out

but not the new domain structure around the space charge. η increases, since the domain modulations form the new grating, which produce higher diffraction efficiency. About 750 V are needed because the coercitivity of SBN:Ce lies in this region. In the same way the written information can be erased with a pulse of about 1700 V, which forms mono-domain structure in the crystal.

To write digitized information into the crystal a digitizer, called page composer, is put into the signal beam. This is a liquid-crystal, divided in regions of $20 \cdot 20(\mu\text{m})^2$ which can be separately opened or closed for light transmission. The signal beam with the digitized information is focussed onto the crystal together with the reference beam to write the hologram and fixed by a short pulse of an IR-laser afterwards. In figure 8 two different reading devices are presented.

The first one has a high storage capacity by angle-multiplexing, which needs a lot of time in random access operation. About 100° per second can be realized. The second one works like a CD-ROM with a rotating single crystal and the information is read by area-multiplexing, performed with multiplexed optical fibres. In both cases the diffracted information is focussed into a high speed CCD-array. Every hologram contains 1MByte, so that about 100 TByte can be stored. With optical fibres one can reach a reading velocity of 1MByte/1μsec.

Holographic storage by metastable electronic states

In a second part we want to apply the above given results, found in a lot of single crystals (LiNbO_3 , LiTaO_3 , SBN , BaTiO_3 , etc.), on new photorefractive substances, in which the photorefractive effect bases upon the existence of metastable

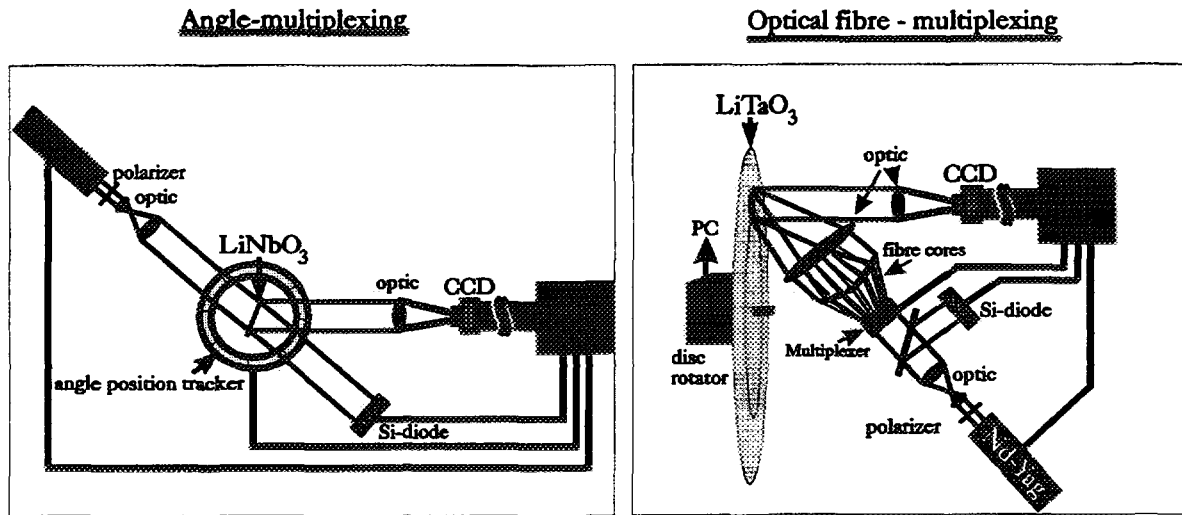


Figure 8: Reading devices for holographic storage: Angle multiplexing and optical fibre-multiplexing

electronis states in contrast to electron drift or diffusion.

Such states can be excited in substances of $X_n[Fe(CN)_5NO] \cdot YH_2O$, $K_2[RuCl_5NO]$ and $K_2[Ru(NO_2)_4(OH)(NO)]$, which all contains the nitrosyl-molecule as a ligand. All anions have central atoms of Fe, Ru and Os, surrounded by six ligands, forming distorted octaedra. The best investigated material is $Na_2[Fe(CN)_5NO] \cdot 2H_2O$ called sodium nitroprusside (SNP) [5]. The structure of the molecule and unite cell is shown in figure 9:

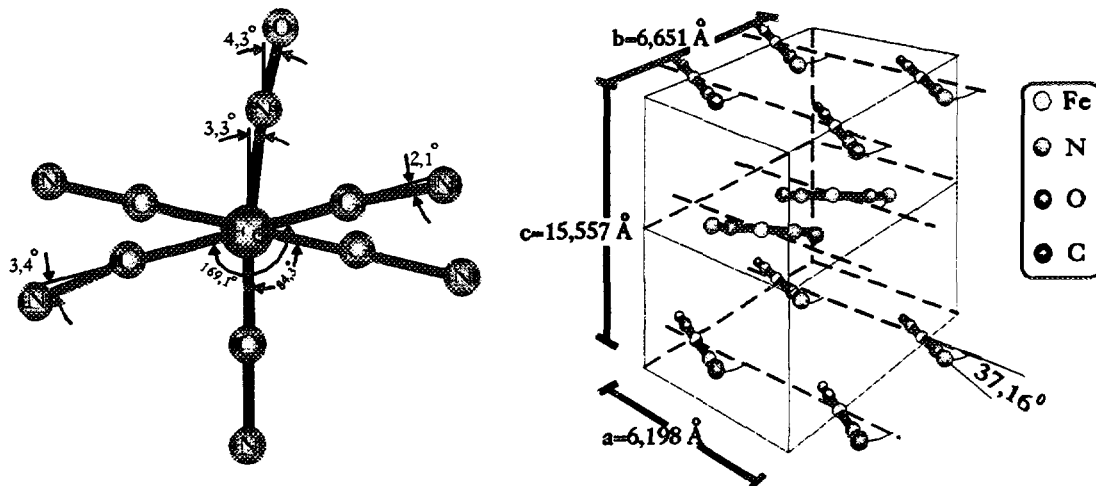


Figure 9: Structure of the SNP-molecule and the unite cell

SNP crystallizes in the orthorhombic space group $Pnnm$, with four molecules per unite cell ($Z=4$). The $[Fe(CN)_5NO]^{2-}$ anions have quasi tetragonal structure

4m, since the Fe-N-O axis deviates from the 4-axis [6], as shown in figure 9. Two metastable electronic states (SI, SII) can be excited by irradiation with light in the wavelength range of 350-580 nm. As given in figure 10 the complete reversible deexcitation can be performed with light in the range of 600-1200 nm, whereby a transfer from SI into SII is possible with light in the infrared region (900-1200nm).

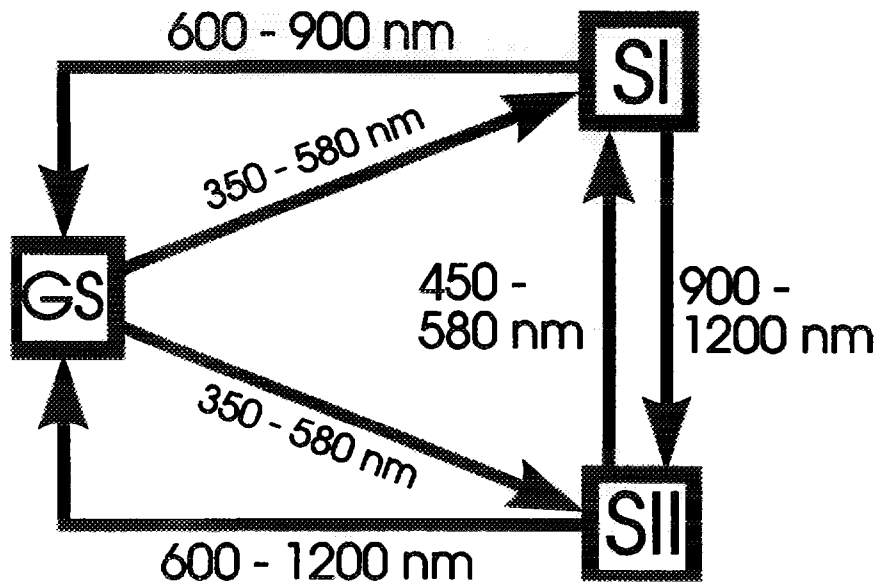


Figure 10: Dependence of the two metastable states SI and SII in SNP on the irradiation light

The difference between ground- and metastable states can be understood by Mößbauer spectroscopy. SNP is a NBS-standard for velocity calibration of Mößbauer drives. The spectra in figure 11 show the quadrupole splitting QS, isomer shift IS and line width Γ of all three states [7].

The maximum of the population is 50% (SI) and 35% (SII). QS increases, IS is shifted to more positive values and Γ increases. The anions in the ground state are completely unaffected by the anions in SI or SII since all Mößbauerparameters of GS are unchanged. The quadrupole splitting depends on the electron density of the 3d and 4p states:

$$QS \sim (3d_{x^2-y^2} - 3d_{z^2}) + (3d_{xy} - 3d_{xz,yz}) + \text{const.}(4p_{x,y} - 4p_z)$$

so that a rearrangement of electron density in the 3d- and/or 4p-states takes place. The isomer shift depends on the s-electron-density. The linebroadening especially in SII indicates an oscillation of the electric field gradient. From angle dependent Mößbauer spectroscopy we can say, that the quasi 4m symmetry of

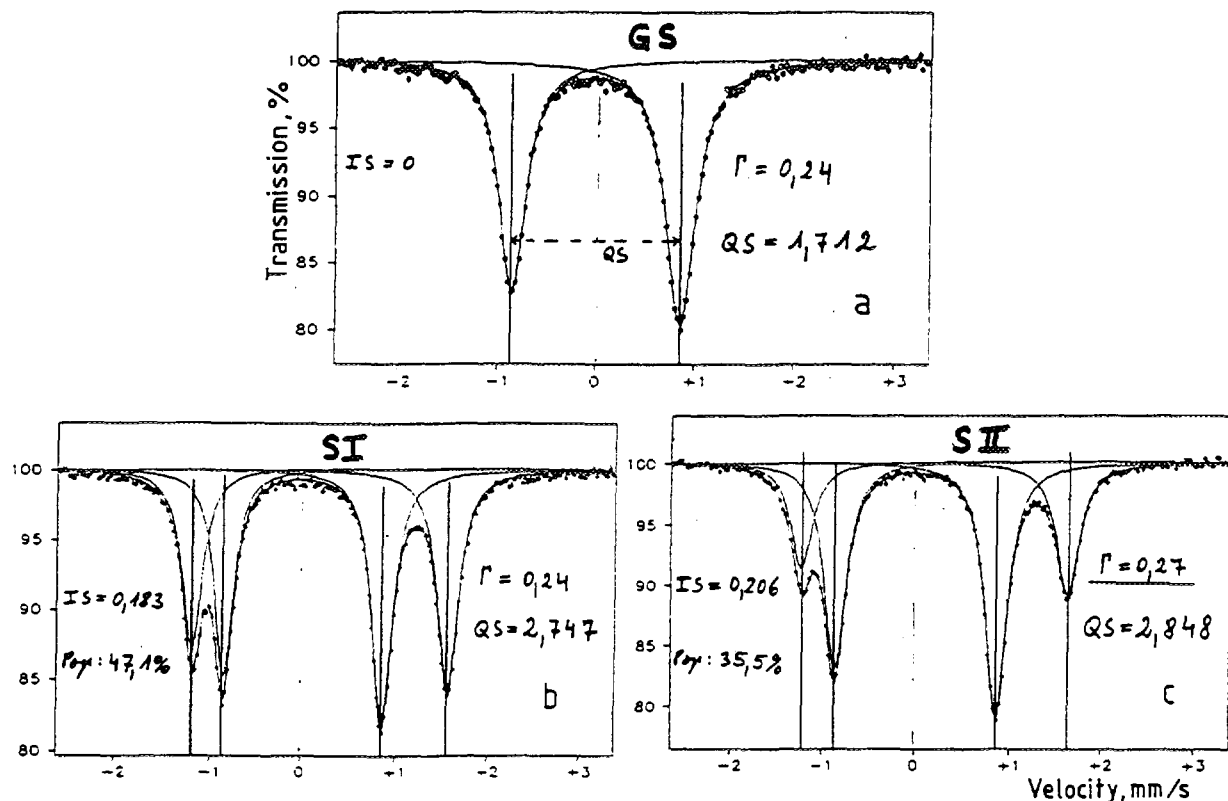


Figure 11: Mößbauer spectra for all three states in SNP

the anion is unchanged in the new metastable states. The sign of the electric field gradient is positiv and its direction is one and the same in all states.

A complete structure analysis with a population of 50% in SI is made by J. Schefer et al. [6] using neutron diffraction, to avoid a possible depopulation during the measurement. The main result is, that the space group is again $Pnnm$ and only the Fe-N and N-O bonds increase by 4 pm and 0.8 pm, respectively. Refinement into subgroups of $Pnnm$ gives no better R-value.

The same result could be found by polarized Infrared- and Raman spectroscopy combined with the Badger-rule [8]. In figure 12 a typical change of the $\nu(N - O)$ stretching vibrations, the $\nu(Fe - N)$ stretching and $\delta(Fe - VO)$ bending modes are shown for the ground and metastable state SI.

The new lines are underlined. With the Badger-rule, corrected by Herschbach and Laurie [9], we can calculate in the harmonic approximation the interatomic distances of the N-O and Fe-N bonds in SI knowing the distance of the ground state:

$$r_{SI} = r_{GS} + 2 \cdot b_{ij} \cdot \log \left(\frac{\nu_{GS}}{\nu_{SI}} \right)$$

Here, r_{SI} and r_{GS} are the equilibrium bond lengths of the metastable state SI and ground state, respectively, b_{ij} is a constant for bonds between atoms from

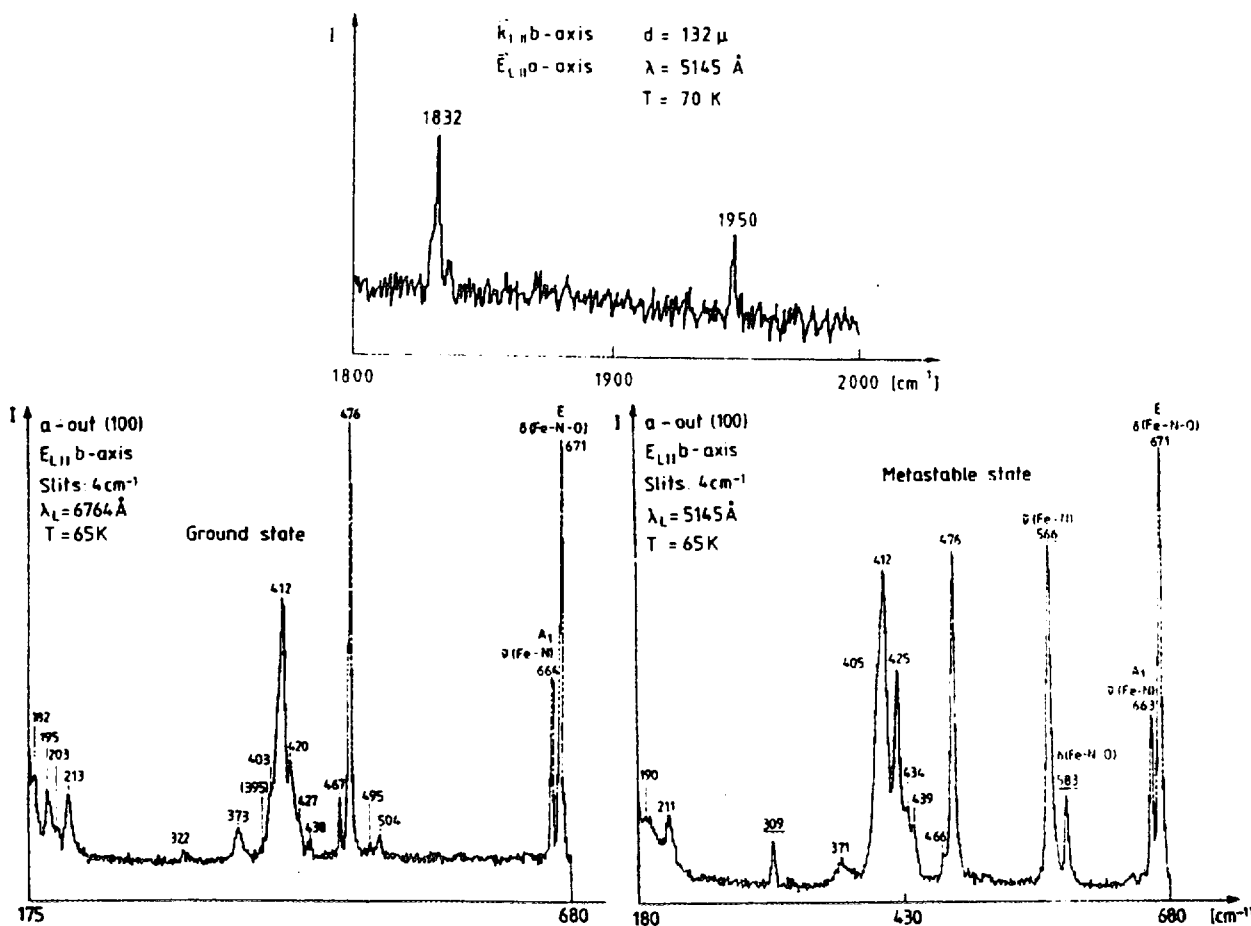


Figure 12: Raman-spectrum of SNP

row i and j of the periodic table and ν_{GS}, ν_{SI} are the wavenumbers in GS and SI of the Fe-N and N-O stretching vibrations. The differences $r_{SI} - r_{GS}$ are a factor 2 larger as found by neutron diffraction. The polarization behaviour of the vibrations in GS and SI are exactly the same and the twofold degenerate modes (i.e. $\delta(FeNO)$) do not split. Therefore, a second independent method with which we can determine the local change of the bondstrength, demonstrate that no phase transition in another spacegroup takes place. Only the electron density along the Fe-N-O direction and at the Fe-central atom is rearranged in such a way, that the polarizability increases, which can be used in order to write holographic gratings into the crystal. The modulation is formed by the difference of ground state and metastable state. Since the new states can be populated with blue-green light, quenched with red light and transferred (SI → SII) with light in the near infrared spectral range, holographic gratings can be written in a very large spectral region.

In figure 13 the efficiency η is shown as a function of exposure Q .

During the irradiation with $\lambda = 514nm$ the diffracted efficiency η increases to the maximum value $\eta = 78\%$ and decays exponentially to zero. Such a high efficiency indicates the existence of phase gratings. According to Kogelnik [1] the

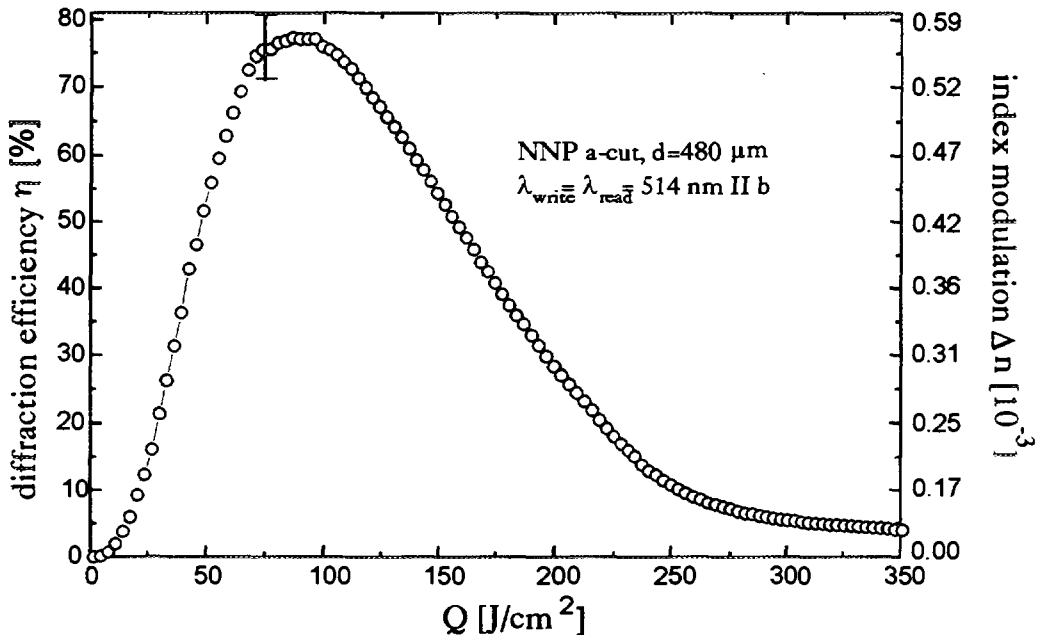


Figure 13: Diffraction efficiency in SNP

modulation of the refractive index Δn can be calculated by

$$\eta = \sin^2 \frac{\pi \cdot \Delta n \cdot d}{\lambda \cdot \cos \theta}$$

where d is the thickness of the hologram, λ the irradiation wavelength and θ the Bragg angle. The hologram thickness can be determined by rotating the crystal around the Bragg angle (Rocking curve). From the line width given in figure 14 we get $d=(450 \pm 30)\mu\text{m}$ so that the modulation of the refractive index through the whole crystal yields $\Delta n = 5.8 \cdot 10^{-4}$, typical for inorganic substances.

From the fact that no phase transition occurs during the writing process, we can assume that the phase shift between the interference light modulation and the refractive index modulation is zero, which is also a demonstration for the centrosymmetric space group $Pnnm$. However the surprising result is shown in figure 15:

The beam-coupling analysis with $\lambda = 633\text{nm}$ reveals the existence of $\pi/2$ -phase grating in contrast to our assumption based on the above discussed measurements. In figure 15 we have normalized I_{C1} and I_{C2} to the change of the absorption during the population. The gain factor at $Q = 8[\frac{\text{J}}{\text{cm}^2}]$ exceeds with $\Gamma = 28.2\text{cm}^{-1}$ the absorption coefficient $\alpha = 5\text{cm}^{-1}$, so that SNP is an optical amplifier. The same result can be found at other wavelengths. In order to verify the existence of 90° -phase grating we have shifted the phase of the incoming beams to each other by the piezo-driver PD shown in figure 1. In figure 16 I_{C1} and I_{C2} have reciprocal behaviour, which yields by a Fourier-transformation again $\pi/2$ -phase grating. This means, that in the macroscopic range of about $1\mu\text{m}$ lattice constant of the

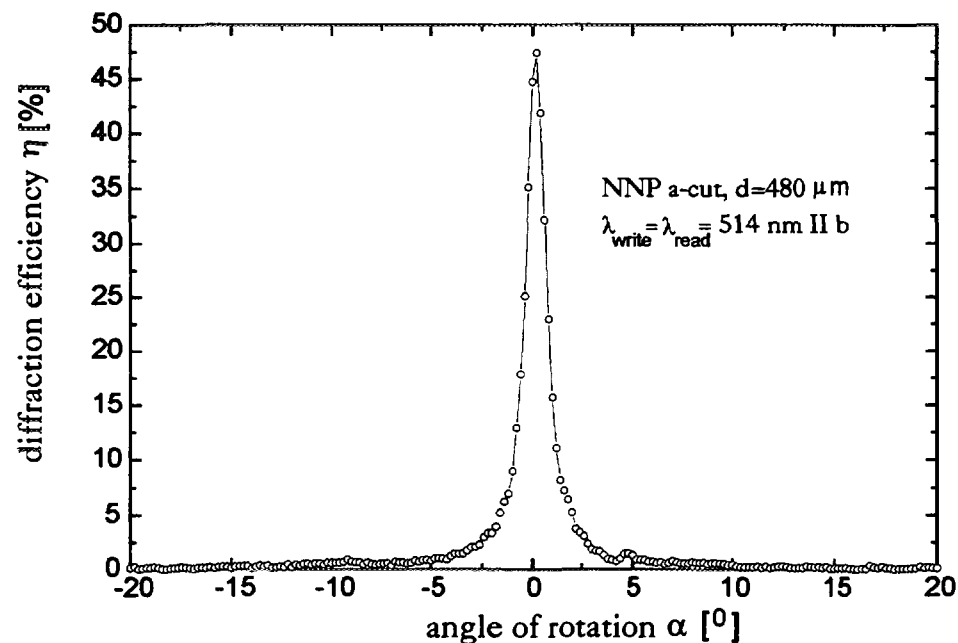


Figure 14: Deviation from the Bragg-angle in SNP

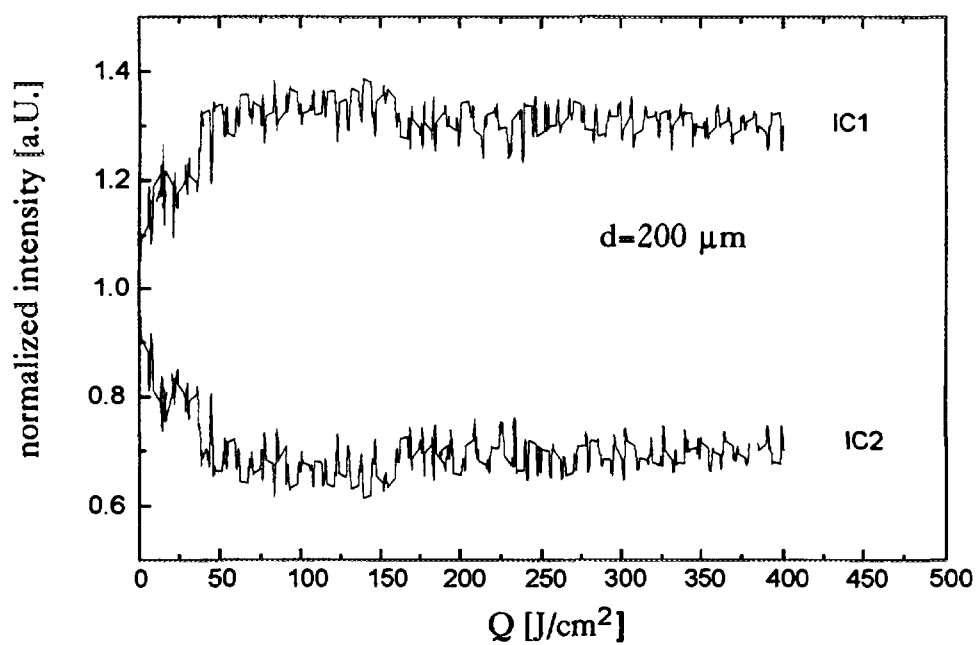


Figure 15: Transmitted intensities I_{C1} and I_{C2} in SNP

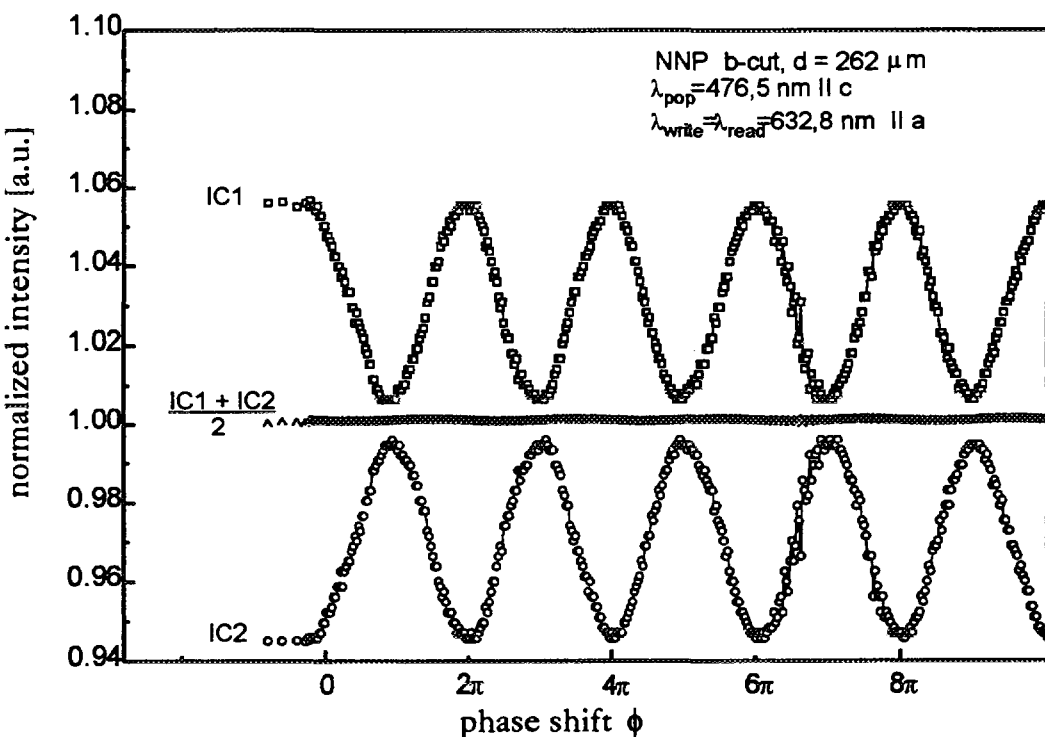


Figure 16: Beamcoupling analysis in SNP

hologram, the phase modulation is shifted in the crystal, which is only possible in acentric crystals. From this point of view a phase transition into the subgroup mm2, m, 2 or 1 takes place. But the problem is now, that in SBN:Ce for instance, electron transport is responsible for the $\pi/2$ -grating. In SNP excitation of the new states, however, is a local effect inside the anion, no transport behaviour could be found so far. In order to get clarity in the question of the phase transitions we have irradiated the crystal with orthogonal polarized laser beams, one is vibrating parallel to the crystallographic a-axis the other parallel to the b-axis. In such a configuration no hologram can be written since the light modulation is zero. As shown in figure 17 in the orthorhombic system the axis n_a, n_b of the optical indicatrix are lying parallel to the crystallographic axes a,b.

The orthogonal polarized electric field vectors E_a, E_b are independent and not influenced by the crystal system. If, however, a phase transition into the monoclinic (m,2) or triclinic (1) point group takes place, the main axes of the indicatrix differ from the crystallographic axes and the components of the electric field vectors E_a, E_b with respect to the indicatrix axes have to consider. In this case the modulation inside the crystal is not zero and holograms can be written. Such a measurement is shown in figure 18:

With orthogonal polarized light holograms can be written. The diffraction efficiencies are $\eta \sim 90\%$ and $\eta \sim 5\%$. Analyzing the polarisation of the transmitted and diffracted waves, shown in the insert of figure 18, the diffracted waves are

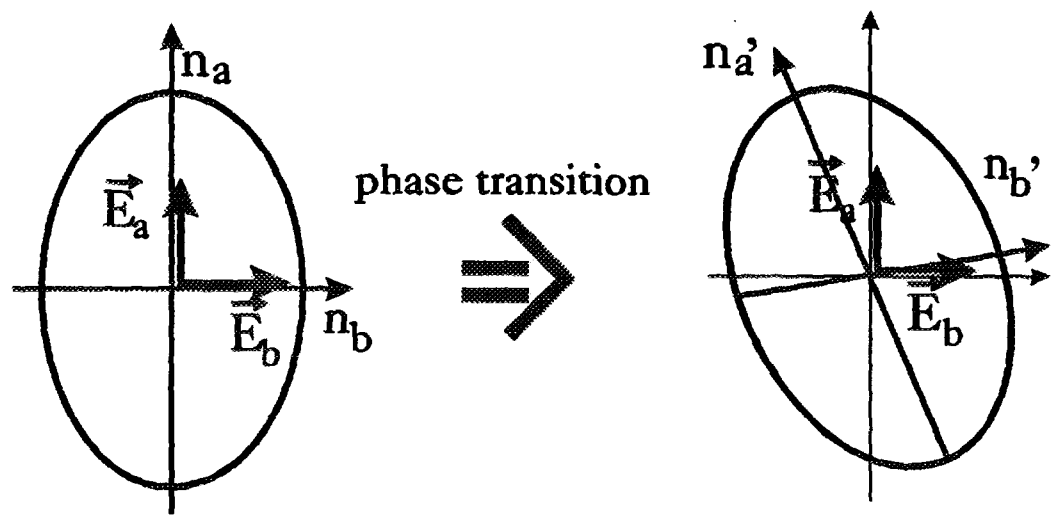


Figure 17: Orthogonal polarized waves and change of the indicatrix by phase transition

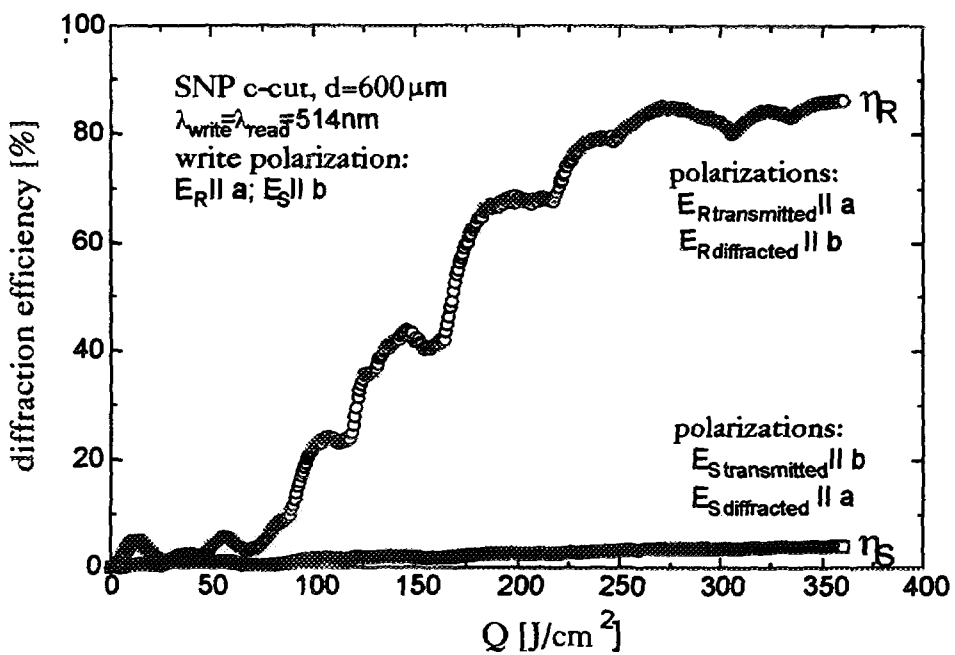


Figure 18: Diffraction efficiency of a grating written with orthogonal polarized beams

orthogonal to the incoming waves while the polarization of the transmitted waves is unaffected. Therefore, the transmitted beam I_{St} and the diffracted beam I_{Rd} have the same polarization, they can interfere with each other and a grating can be built up inside the crystal. Since outside the crystal the modulation is zero, a further physical effect must be the initiator. As shown in figure 18 the diffraction efficiency remains at low values up to an exposure of $Q = 50 \left[\frac{J}{cm^2} \right]$ and increases to $\eta = 90\%$ for higher exposure. This dynamical behaviour can be explained by holographic scattering as a trigger process. As shown in figure 19 holographic light scattering can be detected, so that in a ring, outside of the direct beam, light is scattered in other directions and with perpendicular polarisation with respect to the incoming beam.

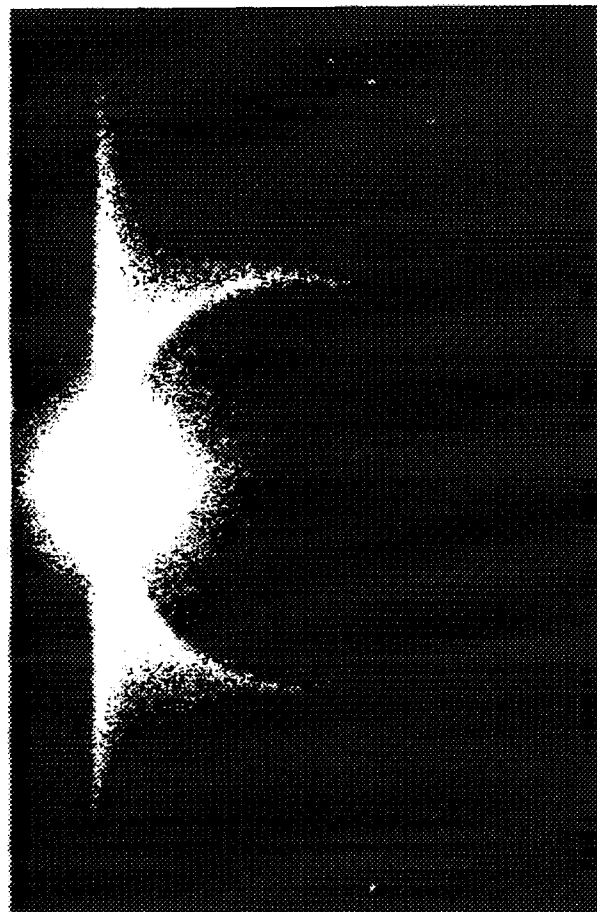


Figure 19: Holographic scattering in SNP

The scattered light can interfere inside the crystal with I_R or I_S and a grating is written. Subsequently, the diffracted intensities of I_R and I_S superimpose the scattered light, because of their higher intensity. Phase transitions into

the monoclinic or triclinic point groups are not necessary for the explanation of holograms written with orthogonal polarized light.

Two questions are unresolved: the existance of $\pi/2$ -phase gratings and the rotation of the polarisation. Further measurements are needed for clarity.

In summary, holographic information storage can reach storage capacities of about 100 TByte and and read-out velocities of 1MByte/ μ sec by multiplexing of optical fibres. The fixation techniques are thermal fixation by short laser pulses of infrared laser light or electric fixation by electric pulses.

Applications of holography on metastable electronic states which are new information storage systems, reveal a lot of informations about these new states and demonstrates that holography is a very important tool analysing solid state problems.

THIS WORK WAS SUPPORTED BY THE DEUTSCHE FORSCHUNGS GEMEINSCHAFT (PROJECT WO 618/1-1).

References:

- [1] H.Kogelnik, Bell. syst. Tech. J. **48**, 2909-2947 (1969)
- [2] L.Solymar, D.J.Cooke, Volume Holography and Volume Gratings, Academic Press, London 1981
- [3] R.A.Vazquez, F.R.Vachss, R.R.Neurgaonkav, M.D.Ewbank, J.Opt.Soz.Am. **B8**, 1932 (1991)
- [4] D.L.Staebler, J.J.Amodei, Ferroelectrics **3** 107 (1972)
- [5] Th.Woike, W.Krasser, H.Zöllner, W.Kirchner, S.Haussühl Z Phys. D **D25**, 351 (1993)
- [6] M.Rüdlinger, J.Schefer, G.Chevrier, H.U.Giedel, S.Haussühl, G.Heger, P.Schweiss, T.Vogt, Th.Woike, H.Zöllner, Z.Phys. **B83**, 125 (1991)
- [7] Th.Woike, W.Kirchner, Hyuang-sang Kim, S.Haussühl, V.Rusanov, V.Angelev, S.Ormandjiev, Ts. Bonchev, A.N.F. Schroeder, Hyperfine interactions **77**, 265 (1993)
- [8] R.M. Badger, J.Chem.Phys. **2**, 128 (1934)
- [9] D.R.Herschbach, V.W.Laurie, J.Chem.Phys. **35**, 458 (1961)



PRINCIPLES OF THE MEASUREMENT OF RESIDUAL STRESS BY NEUTRON DIFFRACTION

G.A. WEBSTER and A.N. EZEILO

Department of Mechanical Engineering

Imperial College, London, SW7 2BX, UK

ABSTRACT

The presence of residual stresses in engineering components can significantly affect their load carrying capacity and resistance to fracture. In order to quantify their effect it is necessary to know their magnitude and distribution. Neutron diffraction is the most suitable method of obtaining these stresses non-destructively in the interior of components. In this paper the principles of the technique are described. A monochromatic beam of neutrons, or time of flight measurements, can be employed. In each case, components of strain are determined directly from changes in the lattice spacings between crystals. Residual stresses can then be calculated from these strains. The experimental procedures for making the measurements are described and precautions for achieving reliable results discussed. These include choice of crystal planes on which to make measurements, extent of masking needed to identify a suitable sampling volume, type of detector and alignment procedure. Methods of achieving a stress free reference are also considered. A selection of practical examples is included to demonstrate the success of the technique.

1. Introduction

The presence of residual stresses in engineering components can significantly affect their load carrying capacity and resistance to fracture. Residual stresses can be introduced into components during fabrication and as a result of creep and plastic deformation incurred during use. Manufacturing processes which can produce residual stresses include welding, forging, bending and machining operations. An illustration of how plastic bending can generate a residual stress distribution is shown in Fig 1. A characteristic of residual stress distributions is that they must satisfy load equilibrium. They are incurred because the material which remains elastic attempts to revert to its initial state but is constrained from doing so by the permanently yielded material. As a consequence, regions of material which have previously yielded in tension develop a compressive residual stress whereas those which were plastically deformed in compression generate tensile residual stresses. Normally compressive residual stresses in components are beneficial since they inhibit fracture processes and tensile residual stresses are detrimental as they assist cracking [1,2].

Several techniques [3] are available for measuring residual stresses. They include X-ray diffraction [4], neutron diffraction [5,6], hole drilling [7], slicing [8] and boring [9] methods. In all cases, strains are measured and then stresses calculated. With the mechanical procedures, the component is cut, bored or drilled to produce a relaxed stress state. These procedures are therefore, at least, partially destructive. The original residual stress distribution is evaluated by analysis of the changes in strain that are obtained during the machining operations. By contrast, the diffraction methods are non-destructive. Although the X-ray technique is well established, it is restricted to near surface determinations of residual stress as X-rays interact strongly with orbiting electrons and are absorbed after penetrating less than 100 μm in most metals. This procedure can be used to obtain sub-surface measurements by progressive surface layer removal but then it becomes destructive like the mechanical methods. Only the neutron diffraction technique is capable of measuring residual stresses non-destructively within the interior of components. This is because the uncharged neutrons only react weakly with electrons so that they can penetrate several centimetres into most metals.

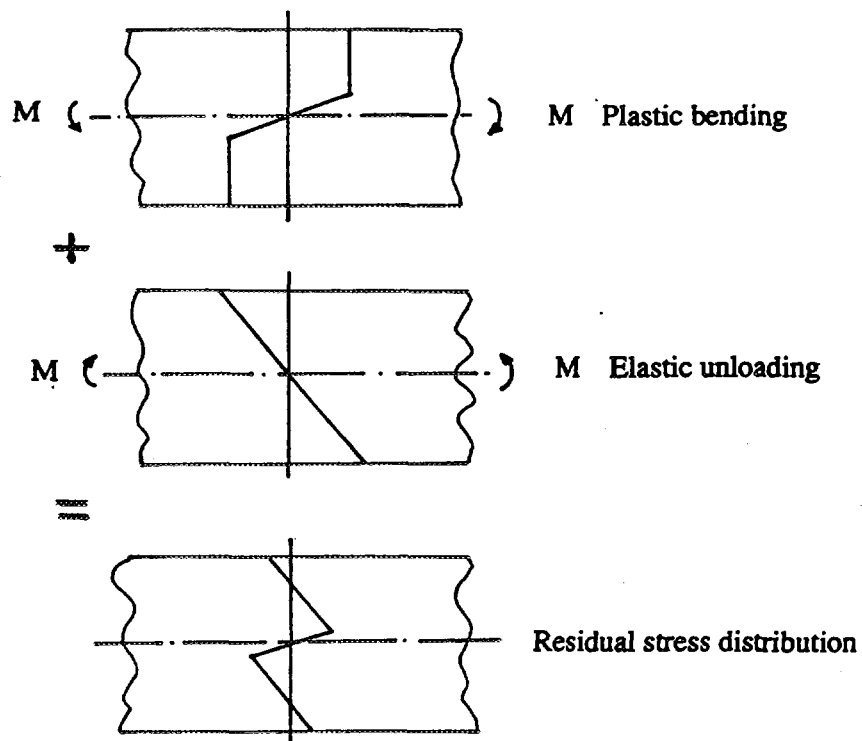


Fig 1 Generation of a residual stress field by plastic bending

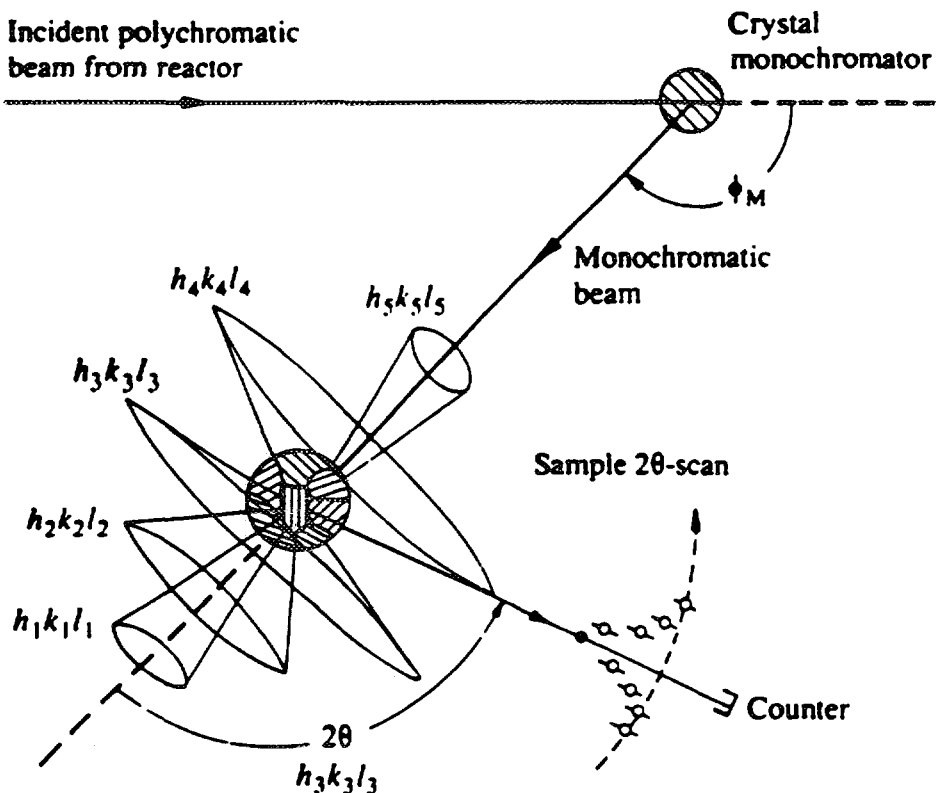


Fig 2 Scattering Debye Scherrer cones from a polycrystalline material subjected to a monochromated neutron beam [10]

In this paper the principles of the neutron diffraction method for measuring residual stresses are presented. The precautions needed to ensure reliable results are discussed. It is shown how stresses can be calculated from measured strains. Examples of several engineering applications are included to illustrate the success of the technique.

2. Principles of the Technique

2.1 Introduction

The neutron is a fundamental particle of mass $m = 1.675 \times 10^{-27}$ kg. Its velocity is directly related to its energy or wavelength through de Broglie's relation so that for a velocity v and Planck's constant h , the wavelength is given by;

$$\lambda = \left(\frac{h}{mv} \right) \quad (1)$$

The neutron reacts weakly with matter and as such can penetrate several centimetres into most metals thus making it ideal for the examination of materials. When neutrons impinge on a material they are scattered by the nucleus. The scattering process can be elastic or inelastic. The process is termed elastic if there is no energy transfer between the neutron and the nucleus. With elastic scattering the scattered wave can interfere with scattered waves from nearby nuclei and produce localised maxima in neutron intensities according to the Bragg equation. For this to occur the distance between the planes of nuclei (d -spacing) must be of the same order of magnitude as the neutron wavelength. Fast neutrons produced in nuclear reactors are moderated to produce thermal neutrons which have wavelengths of the order of 0.1 nm which is comparable to the crystal spacings in metals and are therefore appropriate for measuring the d -spacings in most engineering materials. The Bragg equation is given by;

$$n\lambda = 2d_{(hkl)} \sin\theta_{(hkl)} \quad (2)$$

where n is an integer, d is the distance between sets of parallel (hkl) crystal planes and θ is the scattered angle. From the above expression it can be seen that the interatomic distances between sets of (hkl) reflections can be obtained when λ and θ are known. Two methods are described for obtaining d .

2.2 Monochromatic Beam

It is possible to filter out from a white (polychromatic) beam, neutrons having the same wavelength. This is done using a monochromator and allows a monochromatic beam to impinge on a sample. Figure 2 shows the scattering of neutrons with the Debye Scherrer cones from a polycrystalline material subjected to a monochromatic neutron beam. Each diffraction cone corresponds to different crystallographic spacings d . The maxima for a family of crystallographic planes, denoted by the Miller indices (hkl) , are given by the Bragg equation (2). An illustration of the diffracted neutron intensity with scattering angle for mild steel is indicated in Fig 3. Keeping the wavelength constant the Bragg equation can be differentiated to produce the following,

$$0 = 2\Delta d \sin\theta + 2d \cos\theta \Delta\theta \quad (3)$$

so that the lattice strain ϵ in the direction of the scattering vector is given explicitly as

$$\epsilon = \frac{\Delta d}{d} = -\Delta\theta \cot\theta \quad (4)$$

Hence if a shift $\Delta\theta$ in the diffraction peak can be measured, the strain can be obtained. To calculate absolute values of strain the unstressed lattice spacing d_0 (and hence the

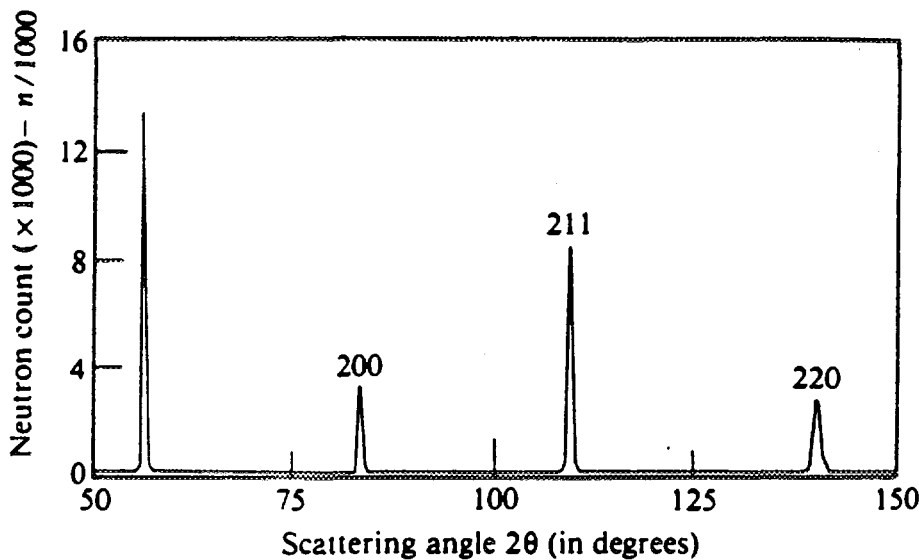


Fig 3 Diffraction pattern for steel

unstressed reference angle $2\theta_0$) must be known. Obtaining the unstressed lattice spacing is more of an art than a science and is based largely on experience [11]. Typical methods used by most researchers include (i) measurements on a powder sample of the material, (ii) carrying out a force balance across a section of the component, and (iii) determining the value of 2θ in a region of the component where little stress is expected e.g. at corners.

2.3 Time of Flight

An alternative approach to having a monochromatic beam impinge on a sample is to use an intermittent white beam composed of a range of neutron wavelengths (velocities). The time it takes for neutrons to travel the distance L from a moderator to the detector after scattering from the sample is, from Eq (1),

$$t = \left(\frac{\lambda mL}{h} \right) \quad (5)$$

Shorter wavelength neutrons will clearly reach the detector first. The time at which neutrons reach a detector at a fixed angle 2θ can be measured. This is called Time of Flight (TOF) diffraction. Keeping 2θ fixed and differentiating the Bragg equation, for $n=1$ gives

$$\Delta\lambda = 2 \sin \theta \Delta d \quad (6)$$

or by combining Eqs. (5) and (6),

$$\frac{\Delta\lambda}{\lambda} = \frac{\Delta d}{d} = \frac{\Delta t}{t} = \varepsilon \quad (7)$$

It is possible therefore from Eq (7) to obtain a profile of neutron intensity vs time or wavelength identical in profile to figure 3 but with time of flight or d-spacing values replacing the 2θ axis. Hence a shift Δt in the diffraction peak can be used to obtain strain measurements. TOF techniques are typically used in pulsed neutron sources. Because the full diffraction pattern is obtained profile refinement techniques may be used to obtain engineering strain. Here, rather than measure the shift of a single peak,

the whole diffraction pattern is analyzed to produce an overall lattice parameter. This can be compared with the lattice parameter for unstressed material to give the engineering strain. The same problems are encountered in establishing a stress free reference as when using a monochromatic beam.

2.4 Engineering Material Issues

The two properties of most interest to engineers when making neutron diffraction measurements are the absorption and scattering characteristics of the material. Also of interest are grain size and texture. Table 1 shows various neutron scattering parameters for some elements which comprise the majority component of many common engineering alloys [12]. Absorption is exponential and statistical errors vary approximately as the square of the counting time. It is possible to define an "economic thickness" x through which reasonably good quality data should be possible in these materials.

Table 1 Scattering Properties of Common Engineering Materials

<i>Element</i>	<i>Fe</i>	<i>Ni</i>	<i>Ti</i>	<i>Al</i>
Neutron scattering length b (nm)	9.5	10.3	-3.4	3.5
Intensity (αb^2)	90.3	106.1	11.6	12.3
Absorption coefficient μ (mm ⁻¹)	0.12	0.18	0.05	0.01
50% transmission thickness (mm)	5.8	3.9	13.9	69.3
10% transmission thickness (mm)	19.2	12.8	46.1	230.3
1% transmission thickness (mm)	38.4	25.6	92.1	460.5
"Economic thickness" $b^2 e^{-\mu x} = 1$ (mm)	37.5	25.9	49.0	250.6

The scattering length b is an indication of the number of neutrons scattered from a nucleus for the same number of incident neutrons. The absorption coefficient μ is an indication of the number of neutrons absorbed by the material. The ideal material for engineering strain measurements would be one having a very high scattering length b and a very small absorption coefficient μ . This would allow high quality data to be obtained at very large depths. It can be seen that nickel and steel scatter neutrons well but have a higher absorption coefficient than titanium and aluminium. So for example the thickness of a titanium or aluminium specimens would not be of particular concern for neutron strain measurements although their poor scattering properties would. The high absorption coefficients of nickels and steels make specimen thickness critical.

3. Determination of Stress from Strain

For a uni-axial stress state, when the elastic strain ϵ in the direction of stressing is known, the stress σ can be calculated from,

$$\sigma = E \cdot \epsilon \quad (8)$$

where E is the elastic modulus of the material. However, in general a multiaxial stress state will exist in many components. In this case, for an isotropic material, the stress tensor σ_{ij} at a point will be given in terms of the elastic strain tensor ϵ_{ij} by,

$$\sigma_{ij} = \frac{E}{(1 + v)} \epsilon_{ij} + \frac{vE}{(1 + v)(1 - 2v)} \delta_{ij} \epsilon_{kk} \quad (9)$$

where v is Poisson's ratio, $\delta_{ij} = 1$ for $i = j$, $\delta_{ij} = 0$ for $i \neq j$, i and j take values of 1, 2 or 3 and ϵ_{kk} is defined as the summation

$$\varepsilon_{kk} = \varepsilon_{11} + \varepsilon_{22} + \varepsilon_{33} \quad (10)$$

for coordinate directions, 1, 2 and 3.

For anisotropic materials Eq (9) must be written in terms of the elastic stiffness constants C_{ijkl} of the material as,

$$\sigma_{ij} = C_{ijkl} \varepsilon_{kl} \quad (11)$$

where C_{ijkl} relates the stresses in the directions ij to the strains in directions kl .

It is evident from these equations that to define the strain tensor completely at a point, neutron diffraction measurements in six orientations are required. However, when the principal directions are known, three orientations will suffice because the shear stresses and strains on the principal planes are zero. When the principal directions coincide with the coordinate directions x , y and z for an isotropic material Eq (9) simplifies to,

$$\sigma_x = \frac{E}{(1+v)(1-2v)} [(1-v)\varepsilon_x + v(\varepsilon_y + \varepsilon_z)] \quad (12a)$$

$$\sigma_y = \frac{E}{(1+v)(1-2v)} [(1-v)\varepsilon_y + v(\varepsilon_x + \varepsilon_z)] \quad (12b)$$

$$\sigma_z = \frac{E}{(1+v)(1-2v)} [(1-v)\varepsilon_z + v(\varepsilon_x + \varepsilon_y)] \quad (12c)$$

In practice, from a knowledge of the fabrication procedures or loading conditions imposed on a component, it is often possible to infer the principal directions. Clearly, by making use of this information neutron measurement times can be halved. When plane stress conditions or plane strain conditions prevail, measuring times can be further reduced. A plane stress state is most likely to exist in thin sheet and a plane strain state in thick plate.

4. Experimental Method

4.1 Introduction

There are a number of constraints and factors to be considered when performing an experiment and these may affect the experimental method adopted. There is a time constraint; neutrons are expensive and engineering measurements typically use a very small proportion of the neutron beam. There are geometry constraints as the space in which the samples are mounted restricts the examination of large or heavy components. There is a sample thickness constraint as thicker samples require longer measuring times. Other factors to be considered are the nature of the beam (monochromatic, white), type of detectors used and the accuracy needed. All these influence the experimental method that can be employed.

4.2 Choice of (hkl) Reflection

In most residual stress experiments a monochromatic neutron beam is used. The neutron intensity profile of a single (hkl) reflection is measured and the shift in the centre of the peak is related to the strain at that point. A single crystal is anisotropic by virtue of the structure of its unit cell and the bonding between atoms. Most engineering materials however are polycrystalline with random orientations of the crystallites which ensure bulk isotropy. It is possible therefore for the different (hkl) reflections to experience different strain levels while subjected to the same stress.

Calibration experiments performed by pulling tensile specimens *in situ* in a neutron beam can generate the elastic constants relating to a particular (hkl) reflection and allow engineering stress to be obtained from specific (hkl) strains. Figure 4 shows the response obtained when a steel bar was pulled beyond the yield point in the neutron beam on ENGIN at ISIS, Rutherford, UK [13]. This figure shows the elastic anisotropy of selected (hkl) reflections compared with bulk strain gauge measurements. It has also been observed that if a material is subjected to uniform tensile straining in the plastic region, on unloading different levels of residual stresses are found to be obtained from different (hkl) reflections. This is due to the effects of local slip and constraints between neighbouring grains. It is therefore important for accurate stress measurements that an (hkl) reflection is used that develops little or no residual stress after uniform straining into the plastic region. For steels it has been found that the (211) or (200) reflections are suitable. In aluminium and nickel alloys the (311) reflection is most appropriate.

Practical considerations when selecting an (hkl) reflection are a good neutron peak intensity above the background (signal to noise), a well defined Gaussian shape, a narrow width and a diffraction angle close to 90° for good sampling volume shape. It is seen from Eq. (4) that maximum angular resolution is obtained at large Bragg angles near to back scattering when $\tan\theta$ is large, but the best spatial resolution occurs at $2\theta = 90^\circ$ when the gauge volume has a rectangular cross-section. In practise a compromise between angular and spatial resolution is made depending on the particular problem that is being investigated and the resolution characteristics of the instrument.

4.3 Masking of the Neutron Beam

Engineers often want to know the variation of residual stress within a component. To do this the neutron beam is usually masked using a strongly neutron absorbing material such as cadmium or boron carbide. The effect of this is to produce a gauge volume within the sample defined by the masking used on the incident and diffracted beams as illustrated in Fig 5 [14]. The measured strains are averages within this sampling volume and therefore in principle this volume is made as small as is practically possible considering the time constraints. The shape of the sampling volume is dependent on the masking size and the 2θ angle of measurement. Typical gauge volumes used are $2 \times 2 \times 2$ mm and $1 \times 25 \times 1$ mm.

4.4 Set-up Procedure

Stress gradients in engineering components can be as high as 2000 MPa/mm. Precise location of the specimen and the point of strain measurement is critical. It is therefore essential that the location of the centroid of the sampling volume is known to within 0.1mm. Also because the component is usually translated and rotated in the beam to permit the measurement of at least 3 orthogonal strain components, it is important that the strains are measured at the same point in the sample following a rotation. There are very few purpose built instruments for residual stress measurements and as such diffractometers typically have to be set up before an engineering stress experiment. There are a number of techniques for making sure that the precise path of the incident and diffracted neutron beam is known. The centre of rotation of the ω -table is usually made a reference. A fine pin is usually positioned on the ω -table at the height of the beam and rotated until there is no translation of the pin during rotation when observed using carefully positioned telescopes [15]. The telescopes are then locked on the pin defining the centre of rotation of the ω -table. The objective is then to mask the incident neutron beam such that it is focussed on the centre of the ω -table. This is achieved by adjusting the masking on the input side using micrometer controls. Having achieved this the masking on the exit side of the beam is obtained, usually by scattering off of a steel pin. Once the centre of rotation of the ω -table is known as well as the direction of the neutron beam, lasers may be used to make the mounting of specimens easier and faster.

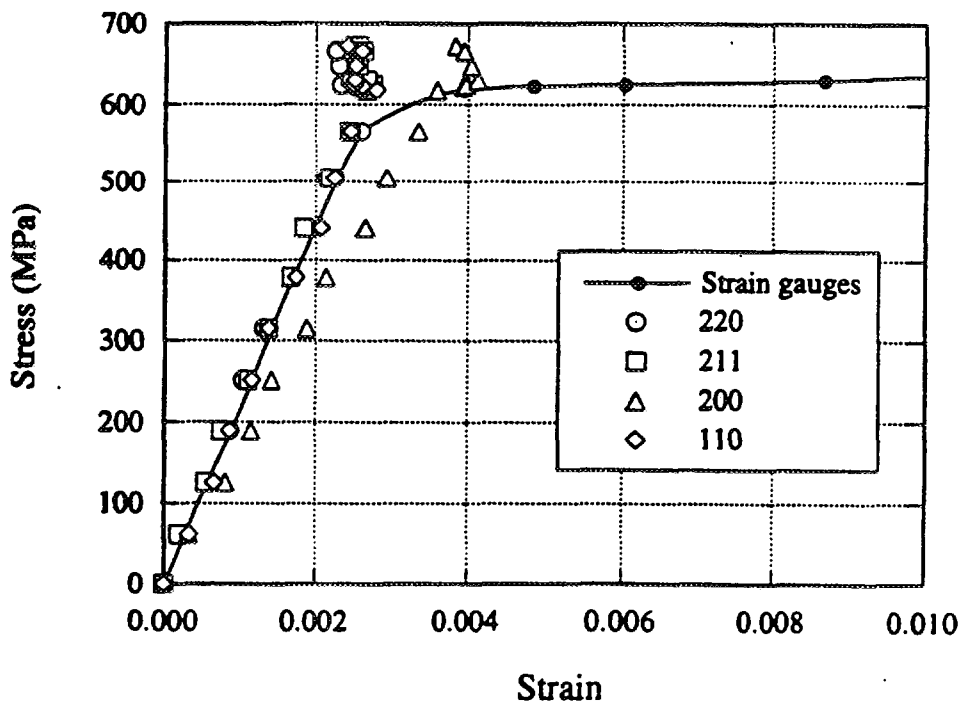


Fig 4 Elastic anisotropy of selected (hkl) reflections compared with strain gauge measurements

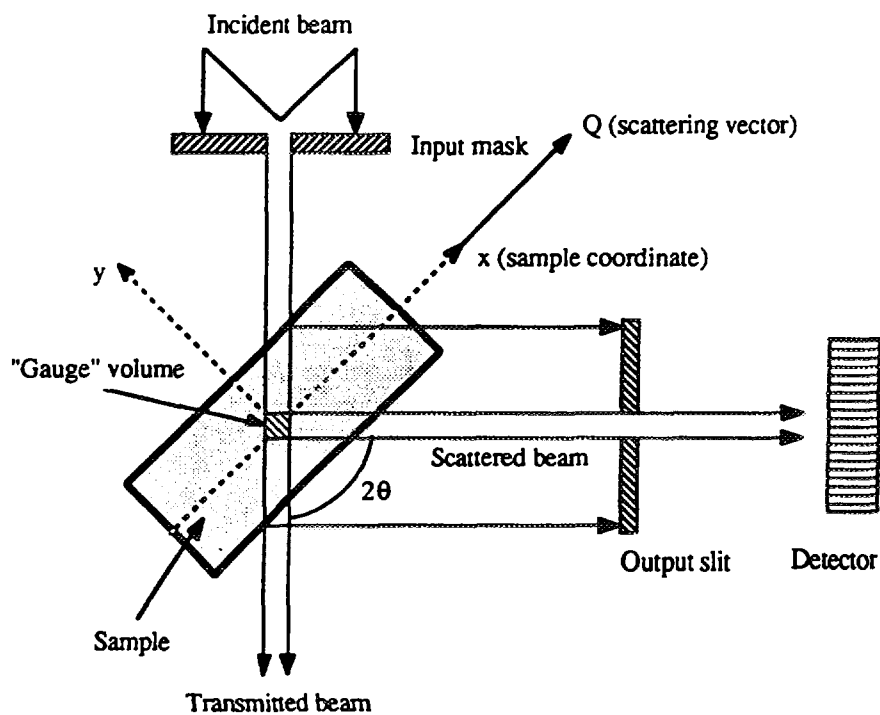


Fig 5 Masking of neutron beam to identify sampling (gauge) volume

4.5 Type of Detector

Engineering strain measurements using neutrons differ from conventional diffractometry in a number of ways. Engineers typically measure the intensity distribution of a single peak to a high accuracy while in diffraction a whole profile is measured with less accuracy. Engineers normally reduce the size of the incident beam on the sample to improve spatial resolution; in diffraction a large beam aperture is normally used. These combined provide a severe challenge and a large amount of expertise is focused on the efficient use of the detectors to reduce the time for measurements.

The simplest form of detector is a single detector, usually with sollers in front to improve angular sensitivity. The detector is usually scanned in small steps about a diffraction peak. An example of this type of detector is provided on instrument HB4 at the HFR, Petten, Holland.

Some diffractometers are equipped with a multi-detector. This is in principle an arrangement of single detectors in a bank at angular intervals. Instrument D1A at the ILL Grenoble, France, is fitted with a multidetector, having 25 He³ detectors in a bank at 6° intervals. For engineering strain measurements only a single detector is used unless the angular discrimination between the detectors in the bank is small.

Finally there is the position sensitive detector (PSD), where the position at which the neutrons impinge on the detector is known. This type of detector allows measurements to be made faster than with single detectors as the entire intensity profile can be obtained over a region of 2–4° without scanning the detector. There are however precautions to be taken when using PSD's for stress measurements as it has been observed that large peak shifts occur at surfaces in powder samples. Careful positioning of the masking slits in front of the specimens as well as the use of correction software on the data can be used to overcome these problems. Instrument D20 at the ILL is fitted with a PSD as well as ENGIN at ISIS.

4.6 Data Analysis

Where a number of single diffraction peaks are obtained at various locations in the specimen, the peak profile is usually approximated to a function that best fits the data. The natural shape is that of a Gaussian. The Gaussian fit provides the following information; peak intensity, peak position, full width at half maximum (FWHM) and the background intensity. Shifts in peak position indicate macrostrain, variations in the intensity usually indicate texture while variations in the FWHM indicate stress gradients or extent of plasticity. In TOF diffraction the scattered neutron intensity profile is often approximated with a combination of statistical functions for example a convolution of a Gaussian instrumental term and an exponential moderator pulse term.

5. Practical Applications

In order to illustrate the application of neutron diffraction for measuring residual stress a number of practical cases will be considered. Examples involving shallow and steep stress gradients through homogeneous and inhomogeneous materials will be included. Where appropriate comparisons will be made with other experimental methods and numerical analysis techniques.

5.1 Autofrettaged Ring

The highest tensile stresses in thick-walled cylinders which are subjected to internal pressure loading are generated at the bore. When this pressure is pulsating, it can cause fatigue cracks to initiate at the bore. Once formed, a crack will continue to propagate through the wall until a leak or burst occurs. One way of enhancing the resistance to fatigue failure of a thick-walled cylinder used for high pressure applications is to produce a compressive residual stress at the bore prior to use. This can be achieved by subjecting the cylinder to an initial 'over-pressure' to cause tensile yielding at the bore. This process is called autofrettage. It is commonly applied to gun-barrels and to pressure vessels in the chemical process industry.

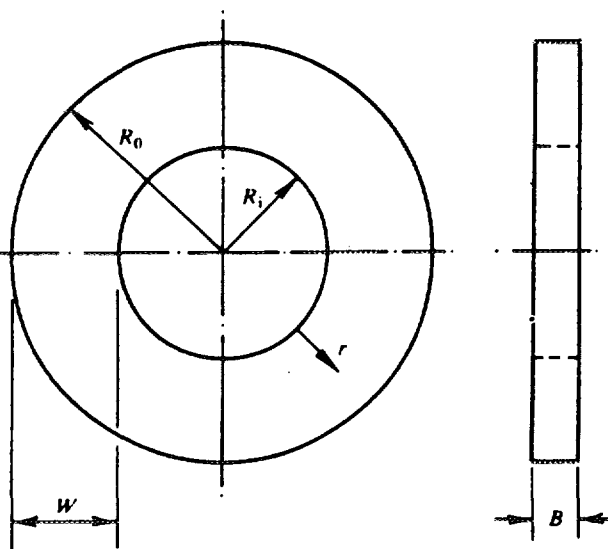


Fig 6 Dimensions of autofrettaged ring specimen.

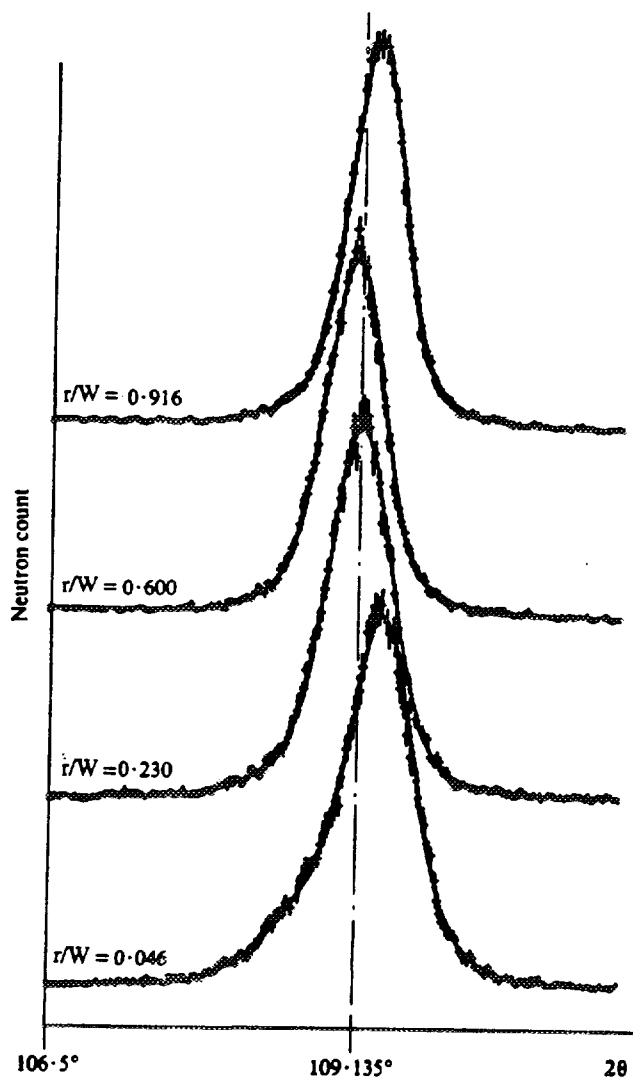


Fig 7 Peak profile for the (211) reflection at different radial positions through the autofrettaged ring specimen

Figure 6 shows the dimensions of a ring specimen which was removed from an autofrettaged steel cylinder for residual stress measurement by neutron diffraction and by the established Sashs boring technique for comparison [6]. The neutron diffraction determinations were made using instrument D1A at the ILL. The specimen was clamped in a support which permitted it to be translated horizontally and vertically through the neutron beam. Masks were used to identify an 8 mm long by 1.8 mm cross-section sampling volume. This sampling volume was then traversed in steps in the radial direction r across the ring width W and shifts in the peak profile for the (211) reflection obtained.

An example of the results recorded for the hoop orientation is presented in Fig 7 where the curves have been displaced vertically for clarity. Also shown in this figure is the zero strain reference position corresponding to $2\theta = 109.135$ degrees. This was obtained by sampling a large volume of unstressed material. As indicated from Eq (4), a shift in the peak to lower angles than the zero strain position corresponds to extension, and to high angles to compression. A change from compression near to the bore to tension at about mid-radius and back to compression towards the outer diameter is clearly apparent. Similar measurements were made for the axial and radial orientations and Eqs (12) used to calculate the residual stresses.

An illustration of the residual stresses which were determined for the hoop direction are shown in Fig 8. Good agreement is achieved with the Sashs boring method and with a modification of this process involving machining from the outer diameter (OD) [6]. The high beneficial compression generated at the bore by the autofrettage treatment is clearly evident.

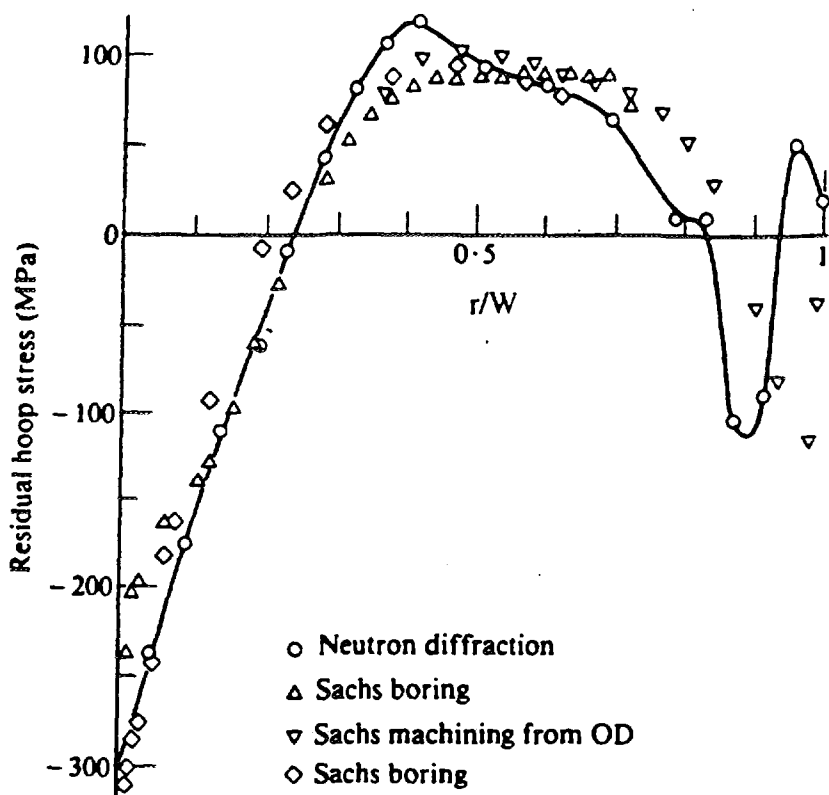


Fig 8 Comparison of residual hoop stresses determined by the neutron diffraction and Sachs methods.

5.2 Shot Peening

It is possible to improve the fatigue performance of engineering components by introducing beneficial compressive residual stresses at the surface which can inhibit crack initiation and growth. Shot peening is a mechanical surface treatment process where many small beads are fired at the surface to be treated. This process causes material at the surface to yield keeping the bulk of material elastic. This results in the generation of residual stresses at the surface. The shot peening process parameters determine the magnitudes and the distribution of the induced stresses as well as the depth of plastic deformation. The region of interest when determining the residual stresses is very shallow, of the order of 0.5mm from the surface.

It is possible to measure the residual stresses in peened material by stepping the sampling volume through the surface region in the principal directions as shown in Fig 9. Usually a matchstick shaped sampling volume is used to exploit the symmetry from the peening process. The data requires deconvolution to correct for the positions of the centroid of the sampling volume. After deconvolution the residual stresses are calculated using Eqs (12).

Residual stresses measured in a shot peened specimen is shown in Fig 10. These results show compressive stresses at the surface close to the yield stress of the material. There is a rapid reduction in the compressive stresses to zero in 0.3mm. Also of interest is the subsurface tensile stresses measured with neutrons which is often not seen when using X-rays [16]. These results show the importance of neutrons in discovering subsurface stresses non-destructively.

5.3 Welds

Residual stresses are associated with most welds. This is because of the high thermal gradients which are generated during the heating and cooling processes. These lead to local plastic deformation which can introduce residual stresses of the order of the yield stress of a material. The precise residual stress distribution produced depends on the weld geometry and sequence of operations employed.

An example of a double vee butt weld in an aluminium alloy plate is shown in Fig 11. The weld was made in several passes as indicated. Measurements of residual stress along the centre line of the weld were determined by neutron diffraction and afterwards by progressive layer removal using strain gauges [11]. The results for the transverse stress distribution are indicated in Fig 12. Since no stress free weld metal was available, and as measurements on stress free base material were regarded as unreliable because of its different chemical composition, the stress free reference angle θ_0 for the neutron diffraction method was obtained by satisfying load equilibrium. This produced a value of $2\theta_0 = 105.92^\circ$. The influence of an error of 0.01 degrees is also shown. This causes a change in stress of 15 MPa. It is evident that there is close agreement between the neutron and 'layering' techniques. The welding process causes an approximately symmetrical residual stress pattern with peak tension near the top and bottom surfaces and maximum compression at the centre.

5.4 Laser surface treatment

Localised heat treatment by laser surface melting is able to produce a hard surface layer and generate residual stresses. The stresses are introduced by a combination of differential plastic deformation and volumetric changes associated with the microstructural transformations occurring on quenching. A hard surface offers improved resistance to corrosion and wear whilst residual stresses influence the fatigue behaviour of the material. It is possible for either tensile or compressive residual stresses to be introduced at the surface depending on the process route adopted. In order to optimise the laser treatment process it is therefore advantageous to select a process that introduces compressive near surface stresses as these will inhibit the initiation of fatigue cracks.

Neutron diffraction residual stress measurements have been made on a 12% chromium martensitic stainless steel after laser surface remelting to a depth of 0.23mm [17]. A microstructural examination revealed 3 layers, a 0.23mm melted zone, a 0.23mm intermediate heat affected zone and the remainder base material. The specimen

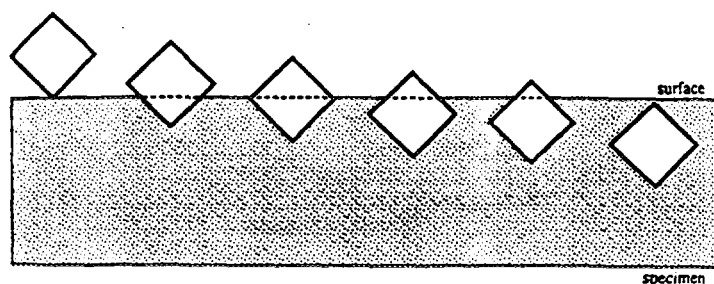


Fig 9 Traverse of sampling volume through a surface

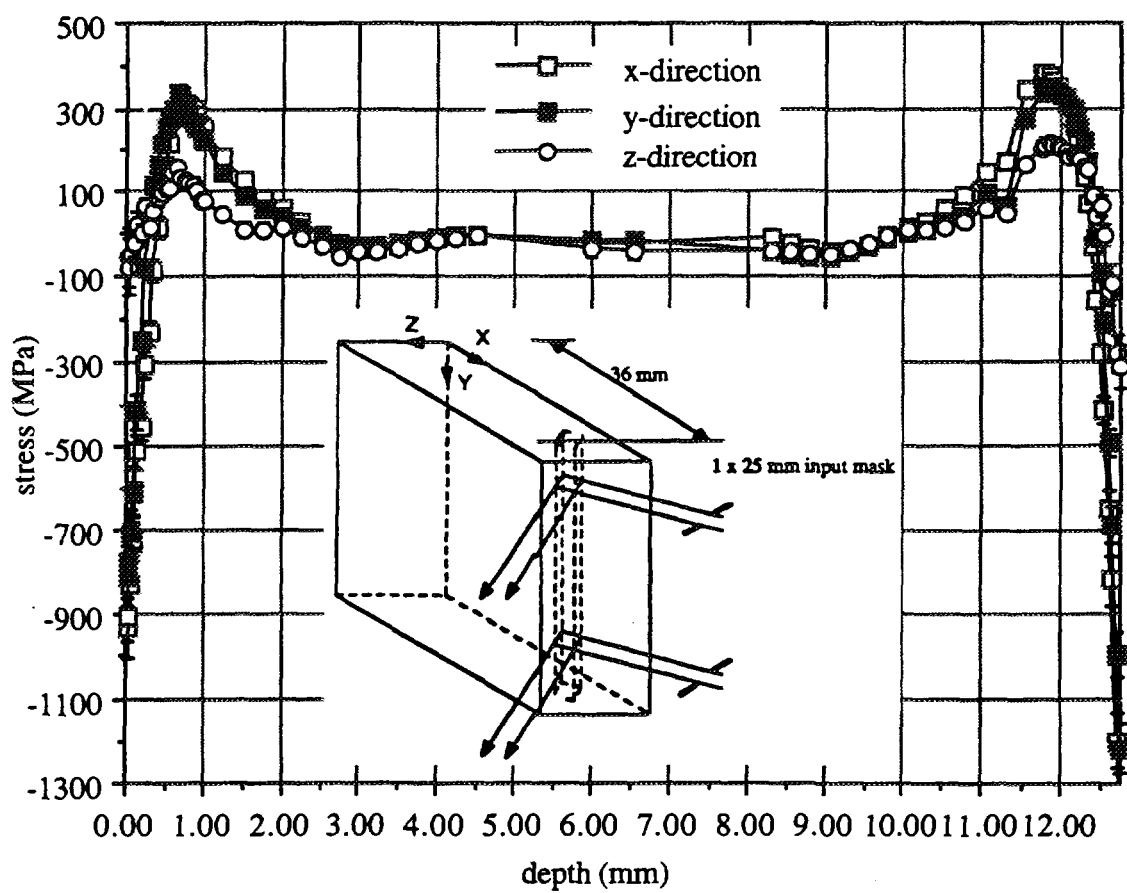


Fig 10 Residual stresses generated by shot peening in a Udimet 720 plate

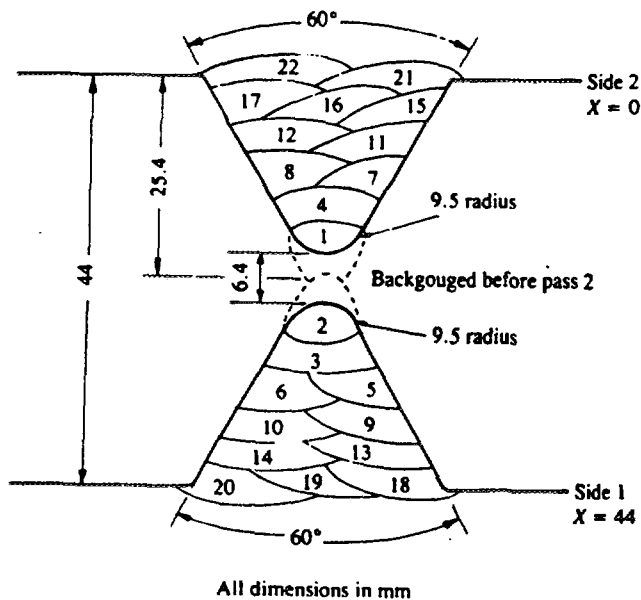


Fig 11 Vee butt weld in aluminium alloy plate showing welding sequence

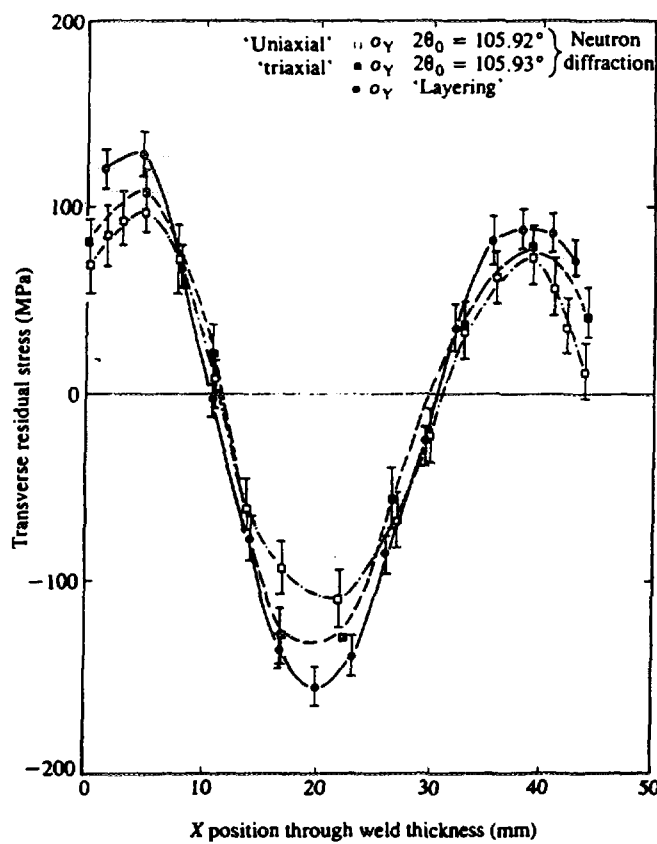


Fig 12 Comparison of transverse σ_Y residual stress

was mounted in D1A at the ILL with a neutron wavelength of 0.19 nm. In order to achieve high spatial resolution the beam dimensions at the specimen were reduced to a matchstick shape measuring 0.33 x 0.33 x 25 mm. The (211) set of crystallographic planes was used at a diffraction angle of 109°. Measurements were made in three orthogonal directions and stresses calculated using Eq (12). As a consequence of the microstructural variations across the specimen, the value of the unstressed d-spacing (d_0) had to be obtained for each microstructural region. This was achieved by obtaining the d_0 value at the surface in the melted layer and also in the bulk material and assuming a linear variation for intermediate material.

Results are shown in Fig 13 for in-plane (x-direction) residual stresses with neutron diffraction measurements compared with X-rays. Similar results were obtained in the other in-plane direction (y-direction). Calculations are also shown for a constant value of d_0 throughout the material. For the set of laser processing parameters used compressive stresses are produced close to the surface although substantial tensile stresses are generated subsurface. These measurements reveal the importance of using appropriate values of the unstressed lattice spacing in materials with varying microstructures in neutron diffraction stress calculations.

5.5 Cold hole expansion

Discontinuities in engineering load bearing structures act as stress raisers. In particular, bolt holes and rivet holes are the source of many engineering failures and it is common for cracks to initiate at the bore of these holes during cyclic loading. Cold hole expansion is established as a standard technique for improving the fatigue life of engineering components as the compressive residual stresses produced at the bore inhibit the initiation and growth of fatigue cracks. The process involves driving a mandrel, in most cases with a split sleeve, through the bore to cause yield in tension adjacent to the bore. Elastic recovery introduces compressive residual stresses in the bore region. In order to predict the fatigue life enhancement due to cold hole expansion, it is critical to know the residual stress distribution resulting from the expansion process.

Residual stresses have been measured in a specimen containing a central circular hole of 5 mm diameter after 4.8% expansion at the bore and subsequent fatigue loading of 105,000 cycles from 0 - 400 MPa to determine the redistribution of residual stresses due to the fatigue loading [18]. The material examined was a nickel base superalloy Inconel 718.

Experiments were made on D1A at the ILL using the (311) reflection at $2\theta_0 = 123.255^\circ$. Measurements were made in the hoop, radial and axial directions using a sampling volume of 2mm^3 . The sampling volume shape was chosen to optimise measuring sensitivity. All measurements were made along the centre line of each specimen to provide average values.

Figure 14 shows the results in the hoop direction only. This shows high compressive stresses at the bore close to the monotonic yield stress of the material following the expansion process. It is clear that the fatigue cycling has resulted in some redistribution of the residual stress state. The main effect was to cause relaxation adjacent to the bore to values close to the cyclic yield stress of the material.

Finite element calculations using the commercial code ABAQUS were also used to predict the induced residual stress state and the redistributed stresses after fatigue cycling. In calculating the redistributed stresses the cyclic stress-strain properties of the material were used. Only results following the fatigue cycling are shown in Fig 14. They model the process satisfactorily agreeing with the neutron diffraction measurements.

6. Conclusions

The principles of the neutron diffraction method for measuring residual stresses have been described. Use of a monochromatic beam of neutrons and time of flight measurements have both been considered. In each case, it has been shown how components of strain, which can be converted into stresses, can be determined directly

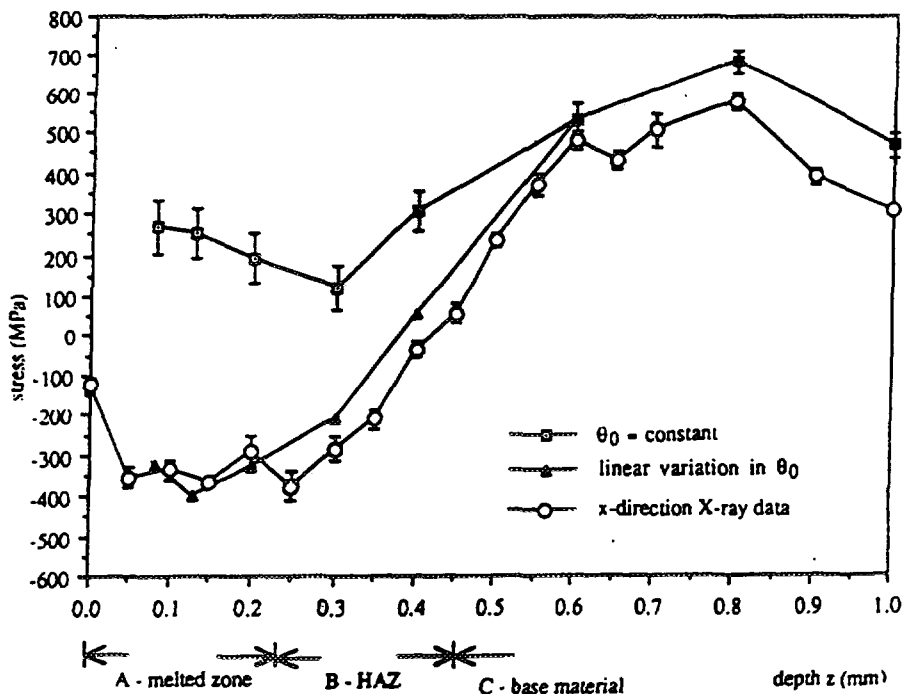


Fig 13 Residual stress measurement along the laser traverse direction for a laser surface treated specimen

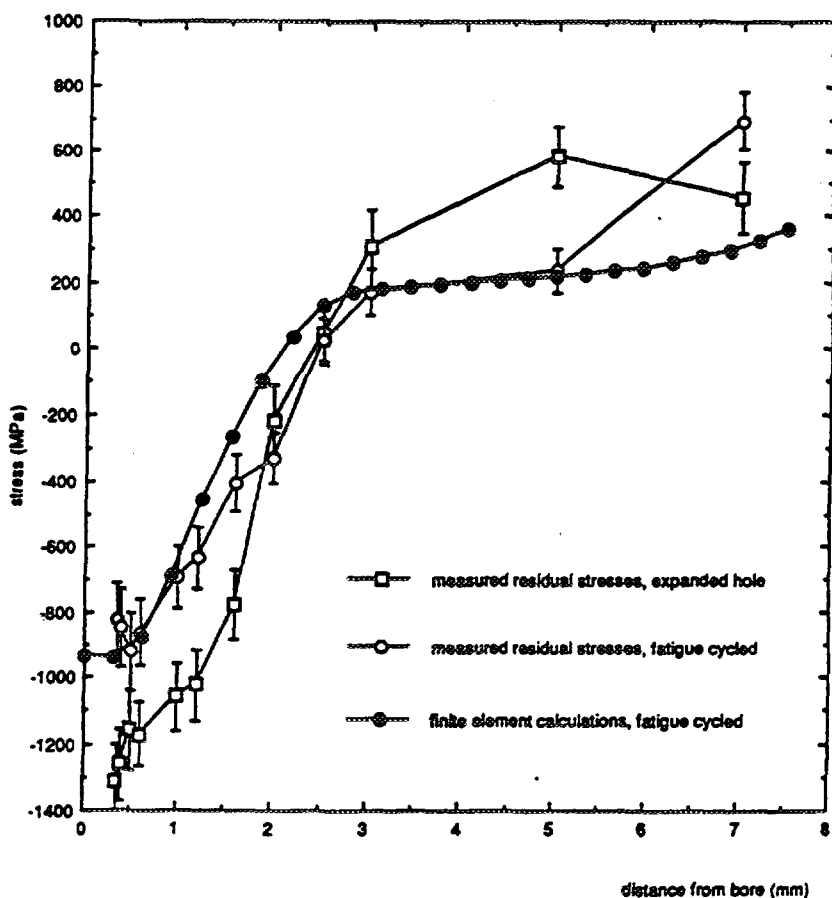


Fig 14 Comparison between hoop residual stresses around an expanded hole before and after fatigue cycling

from changes in the lattice spacings between crystals. The experimental procedures and precautions needed for achieving reliable results have been discussed. Advice has been given on choice of crystal planes on which to make measurements, shape and size of sampling volume to be employed, type of detector to use, alignment procedure to adopt and how to achieve a stress free reference.

A selection of practical examples involving shallow and steep stress gradients through homogeneous and inhomogeneous materials have been considered to demonstrate the applicability of the technique.

7. References

1. Stacey, A. & Webster, G.A., 'Influence of residual stress on fatigue crack growth in thick-walled cylinders', ASTM Symposium 'Analytical and Experimental Methods of Residual Stress Effects in Fatigue', (Eds R.L. Champoux, J.H. Underwood, and J.A. Kapp), ASTM STP 1004, American Society for Testing and Materials, 1988, 107-121.
2. Webster, G.A., 'Propagation of fatigue cracks through residual stress fields', *Fatigue & Stress*, (Ed H.P. Lieurade), IITT International, Gournay-sur-Marne, France, 1989, pp 9 - 20.
3. Parlame, A.J.A., 'The determination of residual stresses: a review of contemporary measurement techniques'; in *Residual stresses in welded construction and their effect*, 1978 (Welding Institute, Cambridge), pp 63-78.
4. Hughes, H., 'X-ray techniques for residual stress measurements', *Strain*, 1967, **3**, 26-31.
5. Allen, A., Andreani, C., Hutchings, M.T., And Windsor, C.G., 'Measurements of internal stress within bulk materials using neutron diffraction', *NDT International*, 1981, **14**, 249-254.
6. Stacey, A., Macgillivray, H.J., Webster, G.A., Webster, P.J. & Ziebeck, K.R.A., 'Measurement of residual stresses by neutron diffraction', *J.of Strain Analysis*, **20**, 1985, 93-100.
7. Beaney, E.M. And Proctor, E., 'A critical evaluation of the centre hole technique for the measurement of residual stresses', *Strain*, 1974, **10**, 7-14.
8. Williams, J.G., Hodgkinson, J.M. And Gray, A., 'The determination of residual stresses in plastic pipe and their role in fracture', *Polymer Engng Sci.*, 1981, **21**, 816-821.
9. Sachs, G., 'Der nachweis immerer spannungen in stangen und rohren', *Zeits. Metall.*, 1927, **19**, 352-357.
10. Allen, A.J., Hutchings, M.T. and Windsor, C.G. , 'Neutron diffraction methods for the study of residual stress fields', *Adv. Phys.*, 1985, **34**, 445-473.
11. Smith, D.J., Leggatt, R.H., Webster, G.A., Macgillivray, H.J., Webster, P.J. And Mills, G, 'Neutron diffraction measurements of residual stress and plastic deformation in an aluminium alloy weld', *J. Strain Analysis*, **23**, No 4, 1988, 201-211.
12. Webster, P.J., 'The neutron strain scanner', *Kerntechnik*, 1991.
13. Ezeilo, A.N., Webster, G.A., Webster, P.J. And Wang, X., 'Characterisation of elastic and plastic deformation in a nickel superalloy using pulsed neutrons', *Physica B*, 180 & 181, 1992, 1044-1046.
14. Webster, P.J., Wang, X. and Mills, G., 'Problems with railway rails', in *Measurement of Residual and Applied Stress Using Neutron Diffraction*, (Eds M.T. Hutchings and A.D. Krawitz), Kluwer Academic Publishers, Netherlands, 1992, 517-524.
15. Webster, P.J., 'Spacial resolution and strain scanning' *ibid*, 235-251.
16. Ezeilo, A.N., Webster, P.S., Webster, G.A. And Webster, P.J., 'Development of the neutron diffraction technique for the determination of near surface residual stresses in critical gas turbine components', *ibid*, 535-543.

17. Ezeilo, A.N., Webster, G.A., Webster, P.J., Roth, M. & Muster, W.J., 'Comparison of X-ray and neutron diffraction determinations of residual stresses in a laser treated martensitic steel', Proc. of the 2nd European Conf on Adv Materials and Processes (Eds T.W. Clyne and P.J. Withers), Euromat 91, 3, Cambridge, 1991, 389-394.
18. Ezeilo, A.N., Webster, G.A., Webster, P.S. & Webster, P.J., 'Influence of cyclic loading on residual stress distribution caused by cold hole expansion', Proc 4th Int. Conf on Residual Stress, Baltimore, USA, June 1994, Soc. Exp. Mechanics, 1994, 1275-1284.

MAGNETISM: A SUPRAMOLECULAR FUNCTION

S. DECURTINS, R. PELLAUX, H.W. SCHMALLE

Institut für Anorganische Chemie, Universität Zürich,
Winterthurerstrasse 190, CH-8057 Zürich, Switzerland

and

P. FISCHER

Laboratorium für Neutronenstreuung, ETH/PSI
CH-5232 Villigen PSI, Switzerland

ABSTRACT

The field of molecule-based magnetism has developed tremendously in the last few years. Two different extended molecular — hence supramolecular — systems are presented. The Prussian-blue analogues show some of the highest magnetic ordering temperature of any class of molecular magnets, $T_c = 315$ K, whereas the class of transition-metal oxalate-bridged compounds exhibit a diversity of magnetic phenomena. Especially for the latter compounds, the elastic neutron scattering technique has successfully been proven to trace the magnetic structure of these supramolecular and chiral compounds.

1. Introduction

Why should chemists become enthusiastic about magnetism ? Isn't it that the world of "real" magnets, dominated by physics and material science, goes on in its preoccupation with metals, objects that are opaque, shiny, and go clang when they hit the floor. These materials do not overlap much with the kind of compounds that chemists make in their flasks and beakers. Furthermore, the information-storage industry relies heavily on transition-metal oxides, whether simple binary ones like $\gamma\text{-Fe}_2\text{O}_3$ and CrO_2 or complex solid solutions based on the garnet or ferrite structures. Given that so many conventional magnetic materials are available with Curie temperatures far above room-temperature, not to mention high coercive and remanent fields, it is worth asking why much effort should be devoted to the synthesis of so called molecule-based magnetic materials.

All these points in question which are taken from a short perspective, entitled "The Chemistry of Magnets", and written by Peter Day, should call the reader's attention to this novel and exciting research field of molecular magnetism [1].

When did the research activities in the area of molecule-based magnetism start ? The first genuine molecular compound displaying a ferromagnetic transition was described by Wickman et al. as early as 1967 [2]. This compound, a chlorobis(diethyldithiocarbamato)iron(III), exhibiting an intermediate spin $S = 3/2$, orders ferromagnetically at 2.46 K. Since then, over the years, a scientific community has been established throughout the world focusing on the aspects of molecular magnetism and an increasing

number of international conferences have turned up a lot of new chemistry and brought synthetic chemists into close contact with physics and material science. Especially since 1989, there have been five International Conferences on Molecule-Based Magnets organized in the United States, in Japan, and in Europe, which demonstrates that the study of the magnetic properties of molecule-based materials has become an important focus of scientific interest [3,4].

There are several features of potential practical impact that distinguish magnetic materials based on molecules from their analogues consisting of continuous ionic or metallic lattices. Examples would include the search for materials combining two- or more functional properties, e.g. magnetism and transparency for magneto-optical applications or the design of mesoscopic molecules possessing large magnetic moments. Synthetic methods will also be quite different and consequently, magnetic thin films might be deposited with methods such as solvent evaporation.

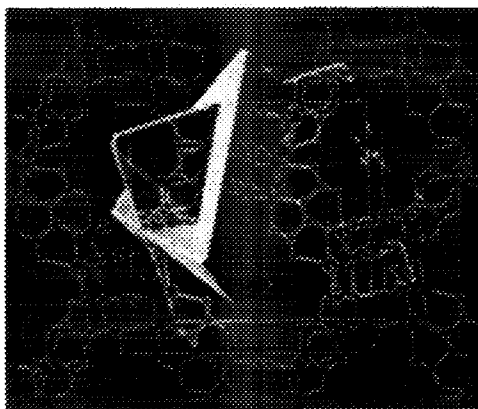


Fig. 1: Chemistry is moving from molecular magnetochemistry to solid state supramolecular magnetochemistry. Single crystal of a chiral 3D network compound with transition-metal ions as spin carriers [22].

A brief comment of the characteristics of the elements that constitute a magnetic molecular solid will give us a feeling of the extension, complexity and wide diversity of magnetic phenomena that can be found in these materials. A magnetic molecular solid can be formed by free radicals, transition-metal ions, rare earth ions and diamagnetic ligands. Any combination of these components is possible although only the free radicals can form a magnetic molecular solid by themselves. In the following, we will concentrate only on coordination compounds, where the importance of transition-metal ions as spin carrier centers stems at least from three main reasons: i) transition-metal to ligand interactions are extremely variable, thus the building up of novel, higher-dimensional architectures can profit very much from the coordination algorithm of the metal ions as well as from the availability of various bridging ligand systems; ii) transition-metals are prone to quick and reversible redox changes, hence supramolecular functions like energy- and charge-transfer processes can anticipate from it; iii) the collective features of components bearing free spins may result in supramolecular assemblies exhibiting molecule-based magnetic behavior, whereby the critical role of the dimensionality of the compounds is simultaneously taken into account. Accordingly, molecular precursors implying transition-metal ions entail the synthesis of ferro- and antiferromagnetic systems with a tuneable critical temperature.

To sum up, molecular magnetism is by essence of supramolecular nature. It results from the collective features of components bearing free spins and on their arrangement in organized assemblies. Accordingly, it is the supramolecular chemistry, the design of systems exhibiting molecular self-organization, which expresses the strategy of the

synthetic chemist of creating novel materials which combine a selected set of properties, for instance from the areas of photophysics, photochemistry, magnetism and electronics.

In the following, two different, supramolecular systems will be discussed. The Prussian-blue analogues reveal compelling results with respect to high critical temperature and tuneable magnetic phase transitions also with electronic and optical stimuli, whereas the supramolecular transition-metal oxalate systems have been chosen to demonstrate the possibilities of the elastic neutron scattering technique for elucidating the magnetic structures in extended two- and three-dimensional molecular systems.

2. The Prussian-Blue Analogues

The Prussian-blue analogues represent a cornerstone in the field of molecular magnetism. In fact, the latest striking example in the field of molecular magnetism is the Prussian-blue-like phase which has been reported in 1995 to behave as a magnet below a critical temperature of 315 K [5]. Fig. 2 depicts the thermal dependence of the magnetization of this organometallic magnet. That specific solid, as well as other analogues prepared from hexacyanometalate building blocks consistently show some of the highest magnetic ordering temperature of any class of molecular magnets. For example, compounds with stoichiometries $\text{Cs}_2\text{Mn}[\text{V}(\text{CN})_6]$, $[\text{NEt}_4]_{0.5}\text{Mn}_{1.25}[\text{V}(\text{CN})_5]\cdot 2\text{H}_2\text{O}$ and $\text{V}[\text{Cr}(\text{CN})_6]_{0.86}\cdot 2.8\text{H}_2\text{O}$ exhibit magnetic ordering temperatures of 125 K, 230 K and 315 K respectively [5,6]. Typically and obviously when looking at the stoichiometries, these compounds have to be characterized as amorphous, non-stoichiometric solids. Therefore, Fig. 3 exhibits only an idealized unit cell of a three-dimensional cubic structure.

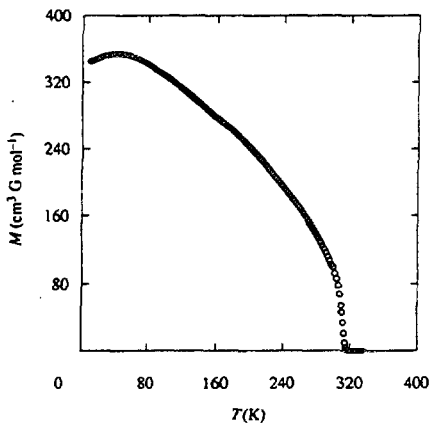


Fig. 2: Thermal dependence of the magnetization of the dark blue solid $\text{V}[\text{Cr}(\text{CN})_6]_{0.86}\cdot 2.8\text{H}_2\text{O}$ in low applied field ($H = 10 \text{ G}$) [5]. Note, that $T_c = 315 \text{ K}$.

Prussian-blue, a pigment obtained by the reaction of the diamagnetic $[\text{Fe}(\text{CN})_6]^{4+}$ complex anion with the Fe^{3+} cation is the first synthetic coordination compound to be reported already in 1710 [7]. It owes its name to the color of the deep blue precipitate of $\text{Fe}_4[\text{Fe}(\text{CN})_6]_3\cdot 15\text{H}_2\text{O}$. Thereby, the intense absorption band at 700 nm is due to a transition from the ground state to an excited state in which an electron is transferred from an Fe(II) to an Fe(III) site, thus the compound may be considered as the archetype of mixed valence compounds, containing two identical metals in different oxidation states.

Prussian-blue's attraction for chemists and physicists lies not only in its optical properties but also in its magnetic properties. The compound shows a long-range magnetic ordering at $T_c = 5.6 \text{ K}$ [8]. The critical temperature is low, because only the Fe(III) sites carry a spin, whereas the Fe(II) sites are diamagnetic. Therefore, the magnetic interaction

must occur between next-nearest ions through the 10.6 Å long Fe(III)-C-N-Fe(II)-N-C-Fe(III) linkages. The possibility of propagating magnetic interactions is due to the strong spin delocalization from the metal ions towards its nearest neighbors. The presence of strong spin densities on the nitrogen and carbon atoms of the cyano groups has been experimentally observed by polarized neutron diffraction [9].

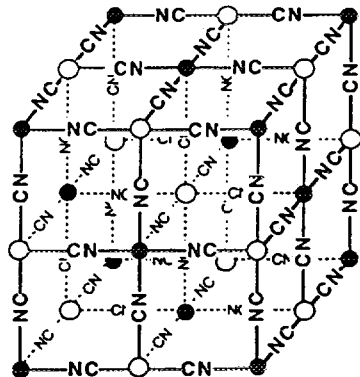


Fig. 3: Idealized unit cell of the three-dimensional, face-centered cubic structure: (●), (○) are different metal ions. Water molecules and interstitial ions in the unit cell were omitted for clarity.

The substitution of Fe(II) and Fe(III) by other ions A and B leads to a family of compounds with the rock salt structure. In these compounds, molecular hexacyanometalate anions $[B(CN)_6]^{P^-}$ and the metallic cation A^{q+} occupy alternate vertices of the cubes, where the A-N-C-B distance is about 5 Å. When paramagnetic ions are used, compounds with various magnetic properties are created. Babel was the first, in 1982, to reach a high Curie temperature of 90 K with a ferrimagnetic Cr(III)/Mn(II) system [10]. Since then, the Curie temperatures continued to increase by varying the A and B ions and finally 315 K is reached with a Cr(III)/[V(II)-V(III)] compound [5]. In that particular case, the V(II)-Cr(III) and V(III)-Cr(III) interactions are strongly antiferromagnetic, and the compound behaves as a ferrimagnet with a high critical temperature. In addition to the value of the critical temperature, the saturation magnetization and the coercivity are also important characteristics of a magnetic material. In the present case, the saturation magnetization is limited to 0.15 Bohr magnetons, owing to the weak value of the resulting spin per repeat unit. The coercivity is also weak: at 10 K, the value of the coercive field is only 10 Oe; at least 100 Oe would be needed to be useful in recording media.

Overall and most importantly, a room-temperature molecular magnet is realized and prospectively, molecular electronics may emerge from such kind of molecular magnets. Only recently, Hashimoto et al. reported the synthesis of molecule-based ferrimagnetic thin films with high critical temperatures by means of a simple electrochemical route [11]. The compounds are mixed-valence chromium cyanides, for example $[Cr^{II}_{0.36}Cr^{III}_{1.76}(CN)_6] \cdot 2.8H_2O$ for $T_c = 270$ K, and their magnetic phase transitions could be controlled electrochemically after the film preparation. Fig. 4 demonstrates that these materials can be switched from ferrimagnetism or paramagnetism, e.g. between 100 K and 240 K depending on the stoichiometry.

In addition to the electrochemical tuning of molecule-based magnets, another possibility is the induction of a magnetic phase transition by optical stimuli. This effect was demonstrated with the report of a photoinduced magnetization change observed in a cobalt-iron cyanide [12]. Fig. 5 illustrates this effect with the field-cooled magnetization versus temperature curves.

This concise report about the Prussian-blue analogues with their high critical temperatures and tuneable magnetic phase transitions through electrical and optical stimuli demonstrates adequately the targets of the ongoing research in the field of molecule-based magnetic materials.

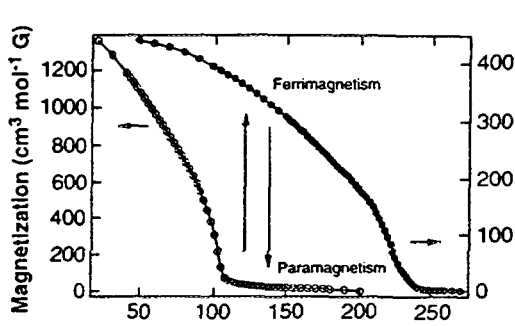


Fig. 4: Magnetic bistability induced by the redox reaction of Cr(III) in the mixed-valence chromium cyanides. FCM versus temperature before (■) and after (□) electrochemical reduction [11].

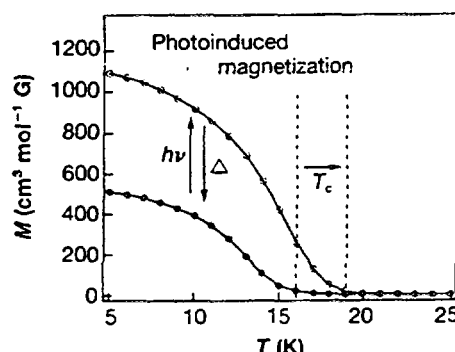


Fig. 5: FCM versus temperature curves at $H = 5$ G before (●) and after (○) red light irradiation of a cobalt-iron cyanide. The magnetization enhanced by illumination ($h\nu$) can be removed by thermal treatment (Δ) above T_c [12].

3. The Supramolecular Transition-Metal Oxalate Compounds

3.1. The System

A successful molecular design of metal-complex magnets which are based on trioxalatochromium(III) building blocks (compare Fig. 6B), has been reported in 1992 [13]. Within a series of layered, oxalate-bridged bimetallic compounds, ferromagnetic ordering behavior has been shown to occur at temperatures < 14 K. Since then, a variety of analogous two-dimensional (2D), bimetallic assemblies, also with mixed-valency stoichiometries, have been prepared and characterized [14-20]. Overall, many of these layered compounds exhibit ferro-, ferri- or antiferromagnetic long-range ordering behavior and in some cases they show at least evidence for short-range interactions. Furthermore, as an extension to the structurally two-dimensional compounds, it seemed likely, that also three-dimensionally-bridged metal assemblies could be realised. Accordingly, on the basis of a chiral template, namely a tris-bipyridine transition-metal complex (compare Fig. 6A), three-dimensional (3D), homo- and heterometallic oxalate-bridged frameworks have been synthesized [21-23].

As expected, these supramolecular host/guest compounds reveal an interesting structural topology, and in addition, many of them show a long-range magnetic ordering behavior as well as various kinds of photophysical properties. Given that an astonishing diversity of magnetic phenomena is generated by these polymeric 2D and 3D framework compounds and that a large body of experimental results is reported from magnetic susceptibility and magnetization studies, very limited experience has been gained so far from elastic neutron scattering experiments aimed at elucidating the spin structure in the magnetically ordered state. Therefore, we focus on some results of neutron scattering experiments with the 2D and 3D oxalate-bridged transition-metal compounds [20,23].

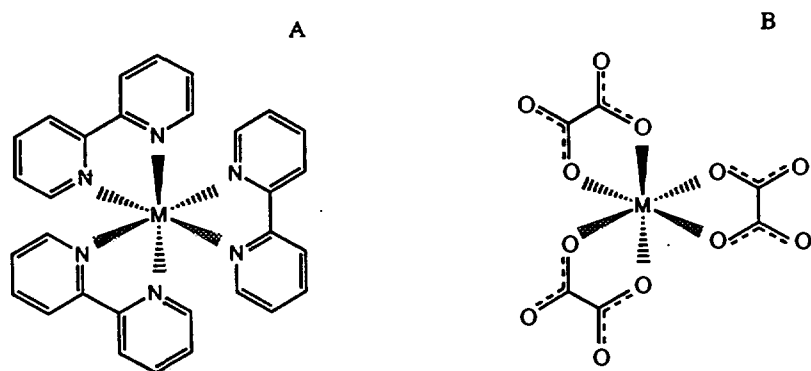


Fig. 6: Schematic representations of the two chiral (the Λ -isomers are shown) preorganized cationic (A) and anionic (B) coordination entities. M = transition-metal ion as spin carrier center.

In addition, an overview about possible photophysical processes occurring in the 3D supramolecular host/guest compounds is presented. Thereby, we address the basic idea in the field of molecular magnetism, namely to engineer novel molecular compounds that are not only magnetic but which also possess additional characteristics, for instance in the field of photophysics [22,25].

3.2. Basic Structural Principles

The oxalate ion, $C_2O_4^{2-}$, is well known to be an attractive ligand, because its ambidentate coordinating ability enables the construction of homo- and bimetallic chain- and layer-structures, and even the formation of three-dimensionally connected transition-metal frameworks. In the following, we will discuss some basic ideas which are relevant for the understanding of the two- and three-dimensional framework topologies. Both structure types are formally composed of $[M^{z+}(ox)_3]^{(6-z)}$ - building blocks, whereby each of these units represents a three-connected point. These subunits which are predestined to create extended network motifs, may polymerise in principle in two ways. Thereby, one alternative leads to a 2D honeycomb layer compound, whereas in the other possible arrangement, an infinite 3D structure is formed. In the former case, building blocks of different chirality are alternately linked and consequently, the bridged metal ions are confined to lie within a plane, as it is illustrated in Fig. 7a. Consequently, a layered structure motif will result. In contrast, as it is depicted in Fig. 7b, an assembling of building blocks of the same chiral configuration will lead to a 3D framework structure.

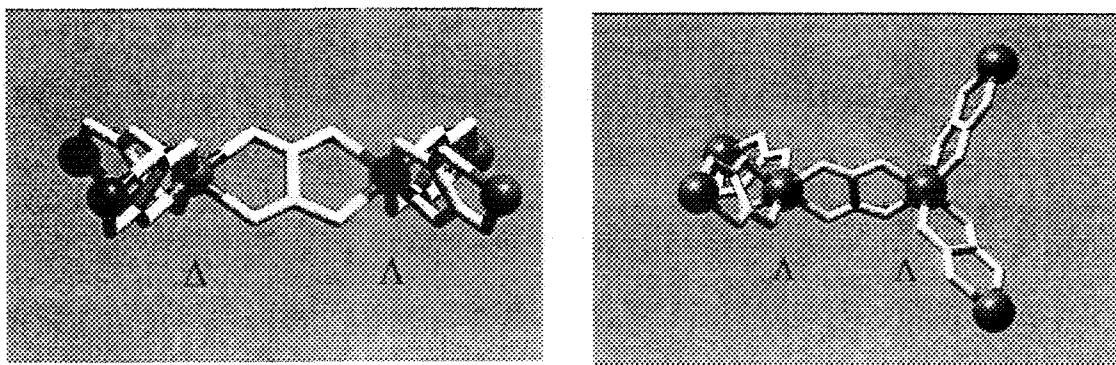


Fig. 7: Chiral $[M^{z+}(ox)_3]^{(6-z)}$ - building blocks assembled with a) alternating chiral configuration, b) equal chiral configuration.

As a next step, simple topological rules will be applied in order to define the number of subunits which are needed to build closed circuits, hence, extended framework motifs. Fig. 8 illustrates the way that two dimeric subunits may be combined to form the planar honeycomb network. In an analogous manner, it can easily be seen from Fig. 9, that two tetrameric subunits are needed to build closed circuits composed of ten metal centers, which in sum define the three-dimensional decagon framework structures.

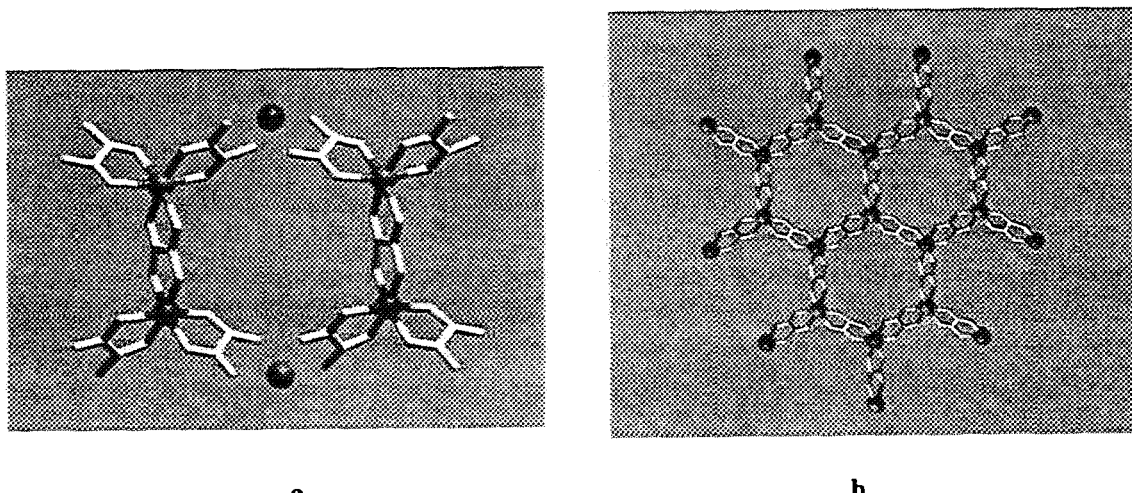


Fig. 8: a) Two dimeric units of the alternating chirality type are necessary to form a closed hexagon ring;
b) the resulting planar network motif.

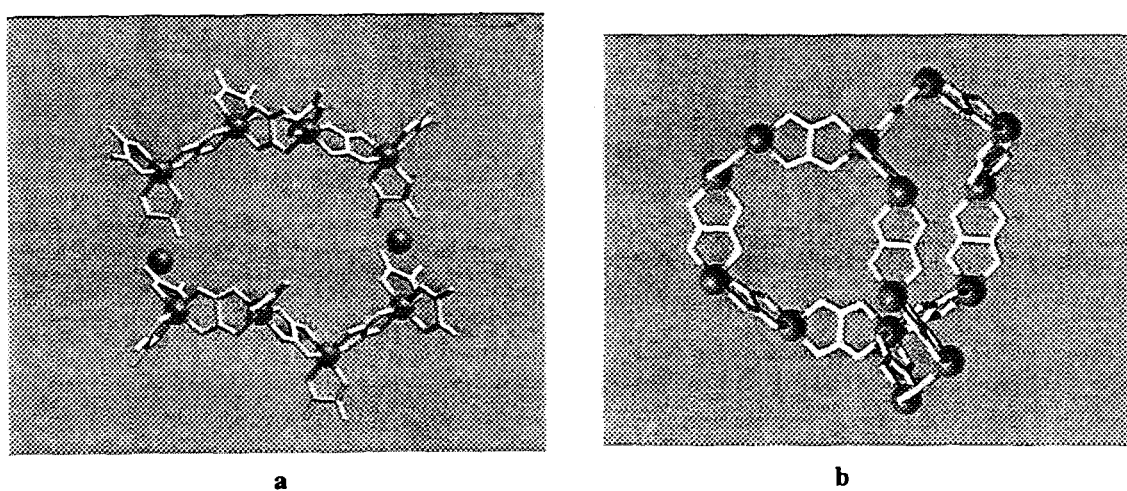


Fig. 9: a) Two tetrameric units of the same chirality type are necessary to form a closed decagon ring;
b) a fragment of the 3D, chiral framework.

3.3. The Honeycomb Layer Structure

The discrimination between the formation and crystallization either of a 2D or a 3D framework structure relies on the choice of the templating counterion. Evidently, the template cation determines the crystal chemistry. In particular, $[XR_4]^+$ ($X = N, P$; $R =$ phenyl, n-propyl, n-butyl, n-pentyl) cations initiate the growth of 2D layer structures containing $[M^{II}M^{III}(ox)_3]_n^{n-}$, $M^{II} = V, Cr, Mn, Fe, Co, Ni, Cu, Zn$; $M^{III} = V, Cr, Fe$, network stoichiometries. The structures consist of anionic, 2D, honeycomb networks which are interleaved by the templating cations. Although these 2D compounds are not chiral, they express a structural polarity due to the specific arrangement of the templating

cations (see Fig. 10). These organic cations which are located between the anionic layers, determine the interlayer separations. From single-crystal X-ray studies, these distances have been determined to the values 9.94 Å, 9.55 Å, 8.91 Å, and 8.20 Å for the n-pentyl, phenyl, n-butyl, and n-propyl derivatives [14,15,18,20].

3.4. The Chiral 3D Structure

The cationic, tris-chelated transition-metal diimine complexes, $[M(bpy)_3]^{2+/3+}$, act as templates for the formation and crystallization of the 3D decagon framework structures [21-23]. As outlined above, the topological principle implies for the 3D case, that only subunits of the same chiral configuration are assembled. Consequently, the uniform anionic 3D network-type with stoichiometries like $[M^{II}_2(ox)_3]_{n}^{2n-}$, $[M^I M^{III}(ox)_3]_{n}^{2n-}$ or $[M^{II} M^{III}(ox)_3]_{n}^{n-}$ is chiral, as it is composed of $2n$ centers exhibiting the same kind of chirality. Naturally, this chiral topology is in line with the symmetry elements which are present in the crystalline state of the 3D frameworks, which in sum constitute either one of the enantiomorphic cubic space groups $P4332$ or $P4132$ for the former and the cubic space group $P213$ for the latter bimetallic stoichiometries. Thereby, the $2n$ metal ions occupy special sites with a three-fold symmetry axis. Fig. 11 depicts a stereo view of the decagon network topology.

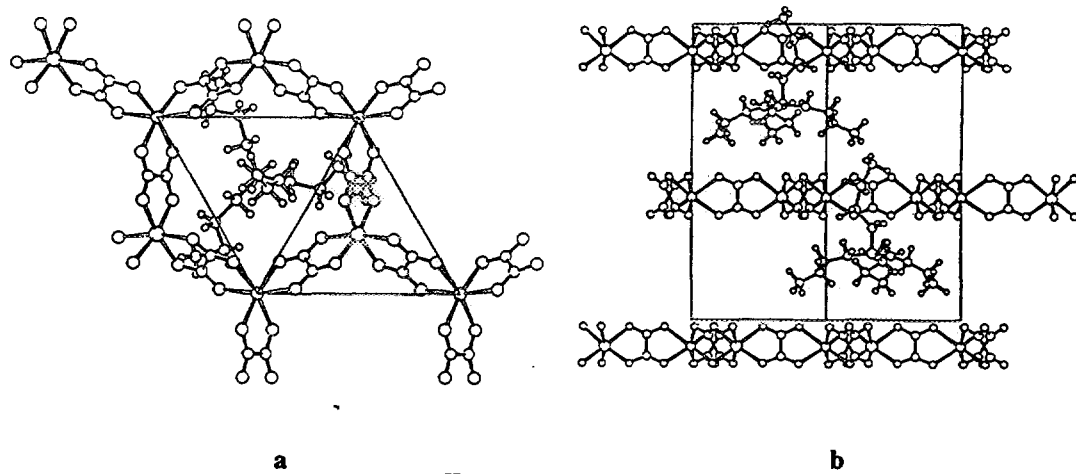


Fig. 10: Sector from the $[N(n\text{-butyl})_4][Mn^{II}Fe^{III}(ox)_3]$ layer compound. a) [001] projection; b) [110] projection [20].

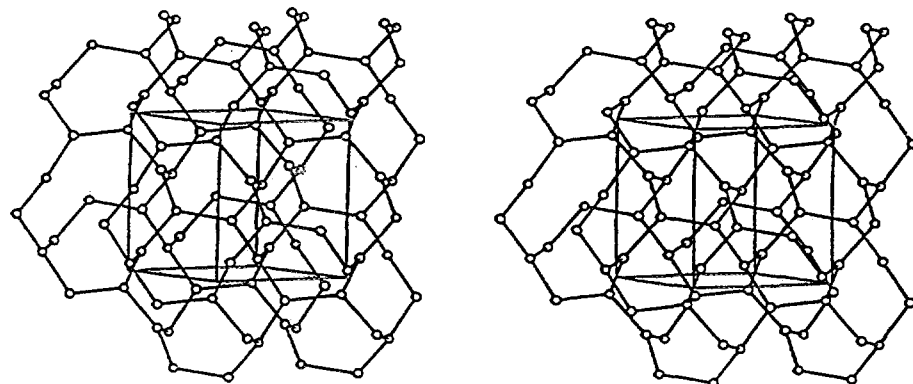


Fig 11: Stereo view of the 3-connected 10-gon (10,3) network topology.

3.5. Magnetic Structure of a 2D Ferromagnet

The layer compound with stoichiometry $[A][Mn^{II}Cr^{III}(ox)_3]$, is known to exhibit a transition to a ferromagnetically ordered state at $T_C = 6$ K [13-15,20]. A single-crystal field-dependent magnetization experiment with the compound $[N(n\text{-propyl})_4][Mn^{II}Cr^{III}(ox)_3]$, revealed a distinct anisotropic behavior such that the easy-axis of magnetization is lying predominantly in the direction of the c-axis, thus perpendicular to the hexagonal network [20]. As it is illustrated in Fig. 12, with the parallel orientation of the external field to the c-axis, the saturation is reached in a field of $H \approx 0.1$ T, while the saturation field in the perpendicular direction is $H > 0.3$ T. This finding is in accordance with the results of the neutron scattering experiments (vide infra).

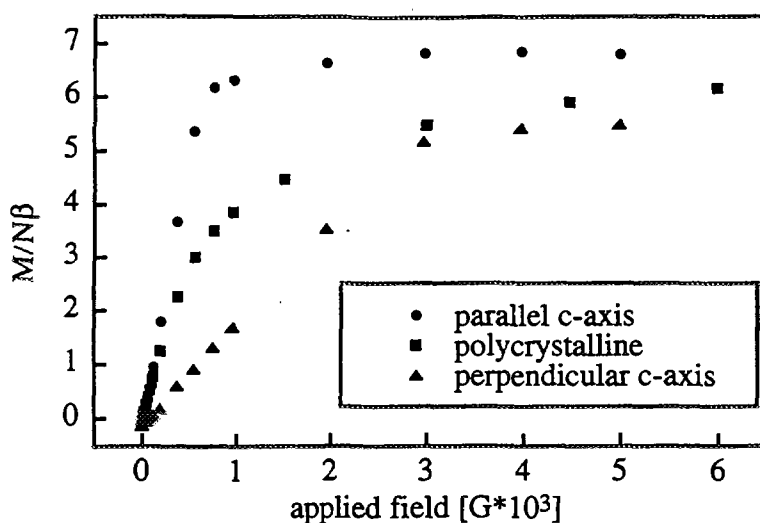


Fig. 12: Plot of the field dependence of the magnetization for a single-crystal of $[N(n\text{-propyl})_4][Mn^{II}Cr^{III}(ox)_3]$ at $T = 4.2$ K [20].

In order to verify the magnetic long-range ordering character below $T_C = 6$ K, and to elucidate experimentally the magnetic structure of that ferromagnetic compound, an elastic neutron scattering study was undertaken with a polycrystalline sample with $A^+ = [P(C_6D_5)_4]^+$ [20]. First, the structural part of the diffraction pattern had to be examined from room-temperature down to liquid-helium temperatures. Fig. 13 shows a profile matching of a 1.8 K neutron diffraction pattern of the polycrystalline sample. The refined unit cell parameters within space group R32 show the values $a=b=18.749(3)$ Å, $c=111.89(3)$ Å. The c-axis was formerly determined from a single-crystal X-ray measurement at room-temperature within space group R3c to a value of $c=57.283(24)$ Å [15]. The doubling of the c-axis as a result from the refinement of the neutron diffraction pattern, is interpreted to originate either from a superstructure phenomenon or from a twinning effect.

Furthermore, as anticipated from the magnetic susceptibility data, a difference in the peak intensities due to long-range ferromagnetic ordering of the magnetic moments from the Mn^{2+} and Cr^{3+} ions could be detected from the neutron diffraction experiment at the temperatures 1.8 K and 12 K. Fig. 14 illustrates the observed [$I(1.8\text{ K}) - I(12\text{ K})$] and calculated magnetic neutron diffraction patterns. Thereby it has to be noted, that the increase of the intensities corresponds to a propagation vector $\mathbf{k} = 0$. The temperature dependence of the dominant magnetic intensity at $2\Theta = 69.1^\circ$ indicates an ordering

temperature of 6.0(5) K, in good agreement with the magnetic susceptibility measurements. The observed enhancement in some of the Bragg reflections proves the presence of long-range magnetic interactions within this structurally two-dimensional compound. Finally, the best agreement between observed and calculated neutron intensities was achieved with a collinear ferromagnetic arrangement of both the Mn^{2+} and Cr^{3+} spins along the c-axis.

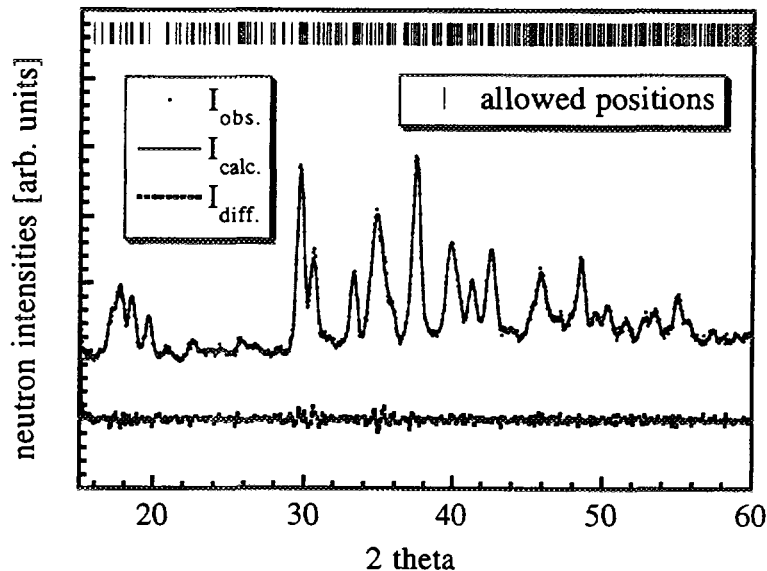


Fig. 13: Observed neutron diffraction pattern of a polycrystalline sample of $[P(C_6D_5)_4][Mn^{II}Cr^{III}(ox)_3]$ at $T = 1.8$ K with the profile matching plot for space group R32. $\lambda = 2.398$ Å [20].

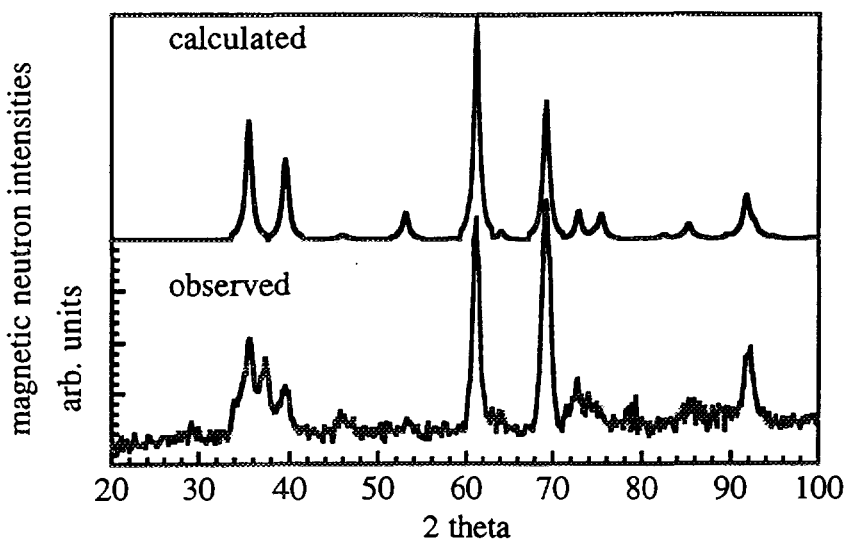


Fig. 14: Observed [difference $I(1.8$ K) - $I(12$ K)] and calculated magnetic neutron diffraction patterns of a polycrystalline sample of $[P(C_6D_5)_4][Mn^{II}Cr^{III}(ox)_3]$; $\lambda = 4.766$ Å. The calculation is based on a ferromagnetic spin configuration parallel to the c-axis [20].

3.6. Magnetic Structure of a 3D Antiferromagnet

The existence of a magnetically ordered phase for the compound $[Fe(bpy)_3][Mn^{II}2(ox)_3]$ could be deduced from magnetic susceptibility measurements,

which revealed a rounded maximum at about 20 K in the χM versus T curve (thus $T_N < 20$ K) as well as a Weiss constant Θ of -33 K in the $1/\chi M$ versus T plot [21]. As anticipated, an increase of the intensities due to long-range antiferromagnetic ordering of the spins from the Mn^{2+} ions could be detected with the neutron diffraction experiments performed in the temperature range from 30 K to 1.8 K with a deuterated polycrystalline sample [23]. Fig. 15 illustrates the observed [difference $I(1.8\text{ K}) - I(30\text{ K})$], calculated and difference magnetic neutron diffraction patterns. The increase of the intensities corresponds to a propagation vector $\mathbf{k} = 0$, thus the magnetic unit cell is equal to the chemical cell.

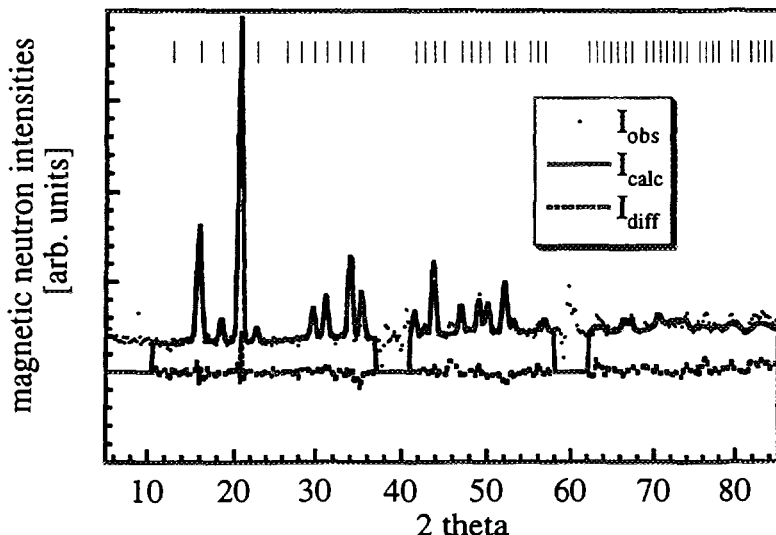


Fig. 15: Observed [difference $I(1.8\text{ K}) - I(30\text{ K})$], calculated and difference magnetic neutron diffraction patterns of a polycrystalline sample of $[Fe^{II}(dg-bpy)_3][Mn^{III}_2(ox)_3]$; $\lambda = 2.5154\text{ \AA}$ [23].

The best agreement between observed and calculated magnetic neutron intensities was achieved with a collinear, antiferromagnetic arrangement of the Mn^{2+} moments according to the three-dimensional irreducible representation τ_4 , which is derived from the enantiomorphic pair of the chiral, cubic crystallographic space groups $P4_332 / P4_132$ [24]. Thus a two-sublattice spin configuration has been proven to occur. Naturally, in the present experiment, no information about a preferred direction of the magnetic moments with respect to the crystallographic axes can be gained from the polycrystalline sample with cubic symmetry. Fig. 16 depicts the pattern of the magnetic structure within the 3D manganese(II) network.

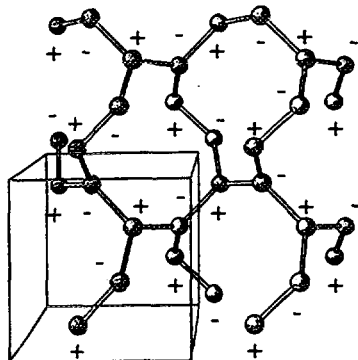


Fig. 16: A scheme of the AF, collinear configuration of the magnetic moments originating from the Mn^{2+} ions, which constitute the chiral 3D network compound [23].

3.7. A Short Comment on Photophysical Properties

Chemical variation and combination of metal ions of different valencies in the oxalate backbone of the two- and three-dimensionally bridged frameworks as well as in the tris-bipyridine cations offer unique opportunities for studying a large variety of photophysical processes, such as light-induced electron transfer and excitation energy transfer in the solid state [22,25]. In this report we will comment on some observations of the excitation energy transfer processes within the 3D, supramolecular host/guest compounds. Depending upon the relative energies of the excited states of the chromophores, energy transfer is observed either from the guest system with the tris-bipyridine cations as donors to the host system where the oxalate-backbone acts as acceptor sites or vice versa. In addition, energy migration, that is excitation energy transfer between identical chromophores, occurs within the host as well as within the guest system [25]. The following stoichiometries $[\text{Ru}_{1-x}\text{Os}_x(\text{bpy})_3][\text{NaAl}(\text{ox})_3]$ and $[\text{Ru}(\text{bpy})_3][\text{NaAl}_{1-x}\text{Cr}_x(\text{ox})_3]$ are chosen to illustrate with examples these specific photophysical properties.

Fig. 17 shows the luminescence spectra of three representative compounds. If Al^{3+} is replaced by Cr^{3+} , the $[\text{Ru}(\text{bpy})_3]^{2+}$ luminescence from the spin-forbidden MLCT transition is completely quenched and the sharp luminescence bands characteristic for the zero-field components of the $^2\text{E} \rightarrow ^4\text{A}_2$ transition of octahedrally coordinated and trigonally distorted Cr^{3+} are observed at $14'400 \text{ cm}^{-1}$. This is a clear indication for very efficient energy transfer from the initially excited $[\text{Ru}(\text{bpy})_3]^{2+}$ to $[\text{Cr}(\text{ox})_3]^{3-}$.

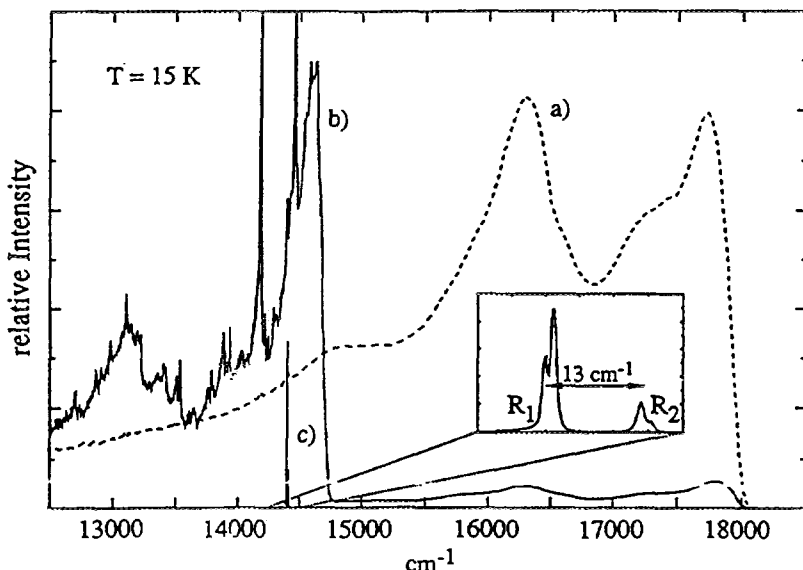


Fig. 17: Luminescence spectra at $T = 15 \text{ K}$ of a) $[\text{Ru}(\text{bpy})_3][\text{NaAl}(\text{ox})_3]$; b) $[\text{Ru}_{1-x}\text{Os}_x(\text{bpy})_3][\text{NaAl}(\text{ox})_3]$, $x=1 \text{ \%}$; c) $[\text{Ru}(\text{bpy})_3][\text{NaCr}(\text{ox})_3]$; $\lambda=476 \text{ nm}$.

Not only acceptors on the oxalate backbone may quench the $[\text{Ru}(\text{bpy})_3]^{2+}$ luminescence. Replacing a fraction of the $[\text{Ru}(\text{bpy})_3]^{2+}$ by $[\text{Os}(\text{bpy})_3]^{2+}$ results in luminescence from $[\text{Os}(\text{bpy})_3]^{2+}$ and a quenching of the $[\text{Ru}(\text{bpy})_3]^{2+}$ luminescence, too. Indeed, the energy transfer to $[\text{Os}(\text{bpy})_3]^{2+}$ is even more efficient than to $[\text{Cr}(\text{ox})_3]^{3-}$. This is due to the higher oscillator strength of the MLCT absorption on $[\text{Os}(\text{bpy})_3]^{2+}$ as compared to the spin allowed d-d transition on $[\text{Cr}(\text{ox})_3]^{3-}$. Fig. 18 summarizes within a schematic representation these different photophysical processes.

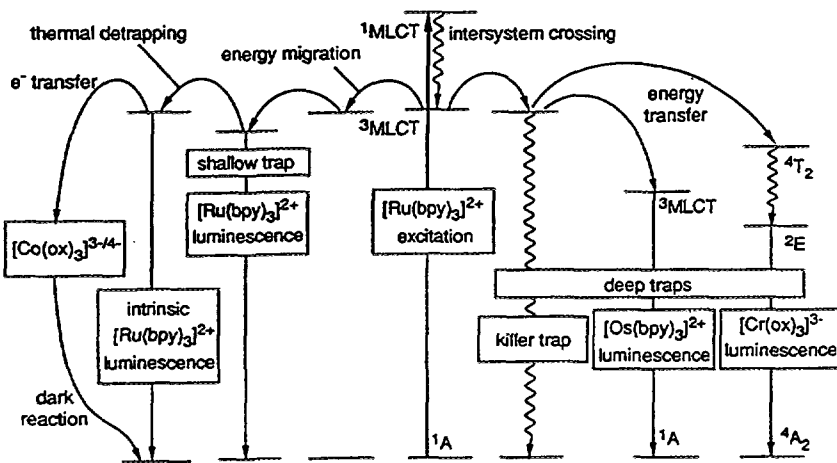


Fig. 18: Schematic representation of different photophysical processes observed in $[\text{Ru}_{1-x}\text{Os}_x(\text{bpy})_3][\text{NaAl}_{1-x}\text{Cr}_x(\text{ox})_3]$

4. Conclusions and Perspectives

Molecular magnetism is a new field of research which has emerged over the past decade or so. The heart of the field concerns the design and synthesis of molecular assemblies that show bulk properties such as long-range magnetic ordering combined with an additional supramolecular function, for example in the field of photophysics. The outlined results of the neutron diffraction experiments on the supramolecular transition-metal oxalate compounds have successfully proven to trace the spin configuration defining the antiferro- and ferromagnetic phases in a 3D and 2D molecular framework compound. The short comment on the photophysical energy-transfer processes within the 3D compounds points to another exciting aspect in the study of molecule-based magnetic materials.

The V International Conference on Molecule-Based Magnets, convened in July 1996 in Osaka, Japan, focused upon several key aspects that directly relate to the design, preparation, and physical study of molecule/polymer based magnets and high spin molecule/polymer systems. The VI International Conference is already announced for 1998 to be hosted in France. The field indeed is now a thriving branch of interdisciplinary science.

5. References

1. P. Day, *Science* **261** (1993) 431.
2. H.H. Wickman, A.M. Trozzolo, H.J. Williams, G.W. Hull, and F.R. Merritt, *Phys. Rev.* **155** (1967) 563.

3. Proceedings of the IV International Symposium on Molecule-Based Magnets; J.S. Miller, A.J. Epstein, Eds.; *Mol. Cryst. Liq. Cryst.*, Sect. A **271-274** (Gordon & Breach, London, 1995).
4. O. Kahn, *Molecular Magnetism* (VCH, Weinheim, 1993).
5. S. Ferlay, T. Mallah, R. Ouahès, P. Veillet, and M. Verdaguer, *Nature* **378** (1995) 701.
6. W.R. Entley, and G.S. Girolami, *Science* **268** (1995) 397.
7. Misc. Berolinensia ad Incrementum Sci. **1** (Berlin, 1710) 337.
8. R.M. Bozorth, H.J. Williams, and D.E. Walsh, *Phys. Rev.* **103** (1956) 572.
9. B.N. Figgis, E.S. Kucharski, and M. Vrtis, *J. Am. Chem. Soc.* **115** (1993) 176.
10. W.D. Griebler, and D. Babel, *Z. Naturforsch.* **37b** (1982) 832.
11. O. Sato, T. Iyoda, A. Fujishima, and K. Hashimoto, *Science* **271** (1996) 49.
12. O. Sato, T. Iyoda, A. Fujishima, and K. Hashimoto, *Science* **272** (1996) 704.
13. H. Tamaki, Z.J. Zhong, N. Matsumoto, S. Kida, M. Koikawa, N. Achiwa, Y. Hashimoto, and H. Okawa, *J. Am. Chem. Soc.* **114** (1992) 6974.
14. L.O. Atovmyan, G.V. Shilov, R.N. Lyubovskaya, E.I. Zhilyaeva, N.S. Ovanesyan, S.I. Pirumova, and I.G. Gusakovskaya, *JETP Lett.* **58** (1993) 766.
15. S. Decurtins, H.W. Schmalle, H.R. Oswald, A. Linden, J. Ensling, P. Gütlich, and A. Hauser, *Inorg. Chim. Acta* **216** (1994) 65.
16. W.M. Reiff, J. Kreisz, L. Meda, and R.U. Kirss, *Mol. Cryst. Liq. Cryst.* **273** (1995) 181.
17. C. Mathonière, C.J. Nuttall, S.G. Carling, and P. Day, *Inorg. Chem.* **35** (1996) 1201.
18. S.G. Carling, C. Mathonière, P. Day, K.M.A. Malik, S.J. Coles, and M.B. Hursthouse, *J. Chem. Soc., Dalton Trans.* (1996) 1839.
19. A. Bhattacharjee, S. Iijima, and F. Mitzutani, *J. Magn. Magn. Mater.* **153** (1996) 235.
20. R. Pellaux, H.W. Schmalle, R. Huber, P. Fischer, T. Hauss, and S. Decurtins, *Inorg. Chem.*, submitted.
21. S. Decurtins, H.W. Schmalle, P. Schneuwly, J. Ensling, and P. Gütlich, *J. Am. Chem. Soc.* **116** (1994) 9521.
22. S. Decurtins, H.W. Schmalle, R. Pellaux, P. Schneuwly, and A. Hauser, *Inorg. Chem.* **35** (1996) 1451.
23. S. Decurtins, H.W. Schmalle, R. Pellaux, R. Huber, P. Fischer, and B. Ouladdiaf, *Adv. Mater.*, in press.
24. O.V. Kovalev, *Representations of the Crystallographic Space Groups* (Gordon & Breach, Reading, 1993).
25. M.E. von Arx, A. Hauser, H. Riesen, R. Pellaux, and S. Decurtins, *Phys. Rev. B*, submitted.



THE METAL-INSULATOR TRANSITION OF $RNiO_3$ PEROVSKITES What can we learn from neutron diffraction?

MARIA LUISA MEDARDE

*Laboratory for Neutron Scattering, ETH Zürich & Paul Scherrer Institute
CH-5332 Villigen PSI, Switzerland.*

ABSTRACT

$RNiO_3$ perovskites (R = rare earth) provide a remarkable opportunity to study the relationship between structural and physical properties since by moving along the 4f rare earth series, the evolution of several transport and magnetic properties can be nicely correlated to the steric effects associated with the lanthanide contraction. The most appealing example is probably the metal-insulator transition discovered for the compounds with $R \neq La$, whose critical temperature T_{M-I} increases with decreasing size of the rare earth ion. In this lecture, a summary of the most relevant neutron diffraction results on this system is presented. Moreover, the nickelates are used as an example to illustrate the performances of the diffractometers HRPT and DMCG to be installed at the SINQ.

1. Why $RNiO_3$ perovskites?

Very few systems allow the study of the relationship between structural changes and physical properties in such a clear way as $RNiO_3$ perovskites (R = rare earth). Synthesized for the first time by Demazeau *et al.* [1] in 1971 and completely forgotten for almost twenty years, these compounds have regained interest since the discovery of high temperature superconductivity and giant magnetoresistive effects in other perovskite-related systems.

Although the nickelates do not display any of these exotic properties, they are, together with cuprates and manganites, one of the rare families of oxides which show metallic conductivity. Moreover, resistivity measurements have revealed the existence of a very sharp metal-insulator (M-I) transition in the compounds with $R \neq La$ [2, 3] (see figure 1a). The evolution of T_{M-I} along the series can be correlated with the degree of deviation of each compound from the ideal perovskite structure, which increases as La is substituted by the smaller rare earth ions. Moreover, the M-I transition is accompanied by a small expansion of the unit cell volume (about 0.2%, see figure 1b) [4]. For the earliest members of the series ($PrNiO_3$ and $NdNiO_3$), a sudden appearance of 3D (three-dimensional) ordered magnetic moments at the Ni sites has also been observed simultaneously with the electronic localization. In contrast, for the remaining rare earths, the onset of the Ni magnetic ordering takes place at a temperature T_N considerably lower than T_{M-I} (see figure 1c).

In spite of some theoretical calculations [5], which suggest a charge-transfer nature for the gap, the mechanism responsible for the M-I transition is controversial at the present time [6]. Although several origins can be considered, the main difficulty, especially for the Pr and Nd compounds is to establish the hierarchy between the three kinds of effects (structural, electronic and magnetic) which coexist at T_{M-I} .

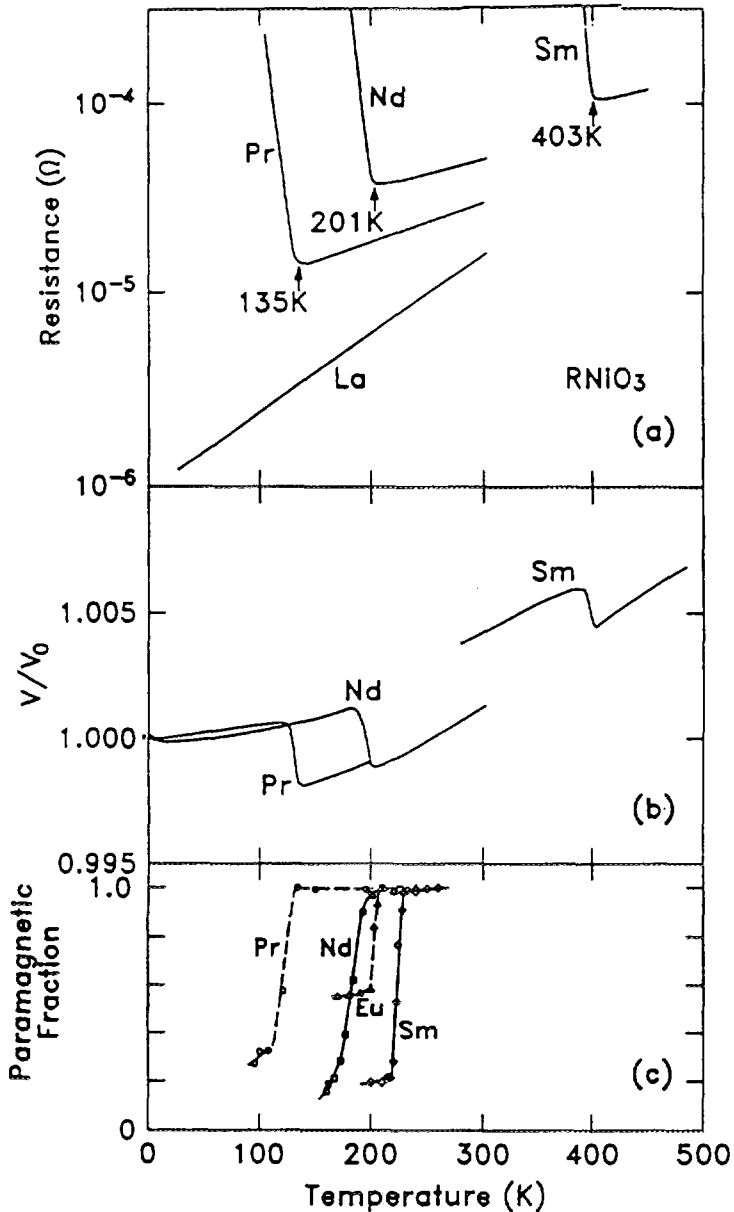


Figure 1.

- a) Electrical resistance of LaNiO_3 , PrNiO_3 , NdNiO_3 and SmNiO_3 showing their metal-insulator transitions.
- b) Temperature dependence of the relative unit cell volume showing the anomaly at T_{M-I} .
- c) Paramagnetic fraction as determined from muon⁺ - spin - rotation experiments, which drops suddenly at the antiferromagnetic ordering temperature (from ref. [3], reproduced with permission of the authors).

In this lecture, a summary of the most important neutron diffraction results on this system will be presented. The main objective will be to show how this technique has been the fundamental tool for the understanding of the unusual properties concomitant with the M-I transition. In addition, the nickelates will be taken as example for a comparison of the performances of 5 constant wavelength neutron diffractometers (2 from ILL, one from the reactor Saphir and two from SINQ). Thus, in each section, the description of the experimental results and the subsequent interpretation will be followed by a computer simulation showing what would be obtained on each instrument.

3. Resolution functions of the diffractometers D2B, D1B, DMC, DMCG and HRPT

The diffractometers chosen for the simulation are D2B and D1B (currently at the ILL), HRTP and DMCG (to be installed at the SINQ) and DMC (operating at the reactor Saphir until end 1993). Three of them are optimised for high resolution (HR) structural studies (D2B, HRPT and DMC in HR mode) whereas the three remainders are more suitable for applications where high neutron fluxes (HI) are required. The resolution functions of each diffractometer, calculated with the technical parameters listed on table I, are displayed in Fig. 2. The best resolution corresponds to D2B, followed by HRPT, DMC (HR), DMC (HI), D1B and DMCG. The fluxes at the sample position are inversely proportional to the resolution. Note that the "first day" operating conditions have been chosen for HRPT and DMCG (HI modes). When the nominal neutron flux will be reached (≈ 2 times larger), other options allowing higher resolution measurements will be also operative (see the notes of Peter Fischer's lecture).

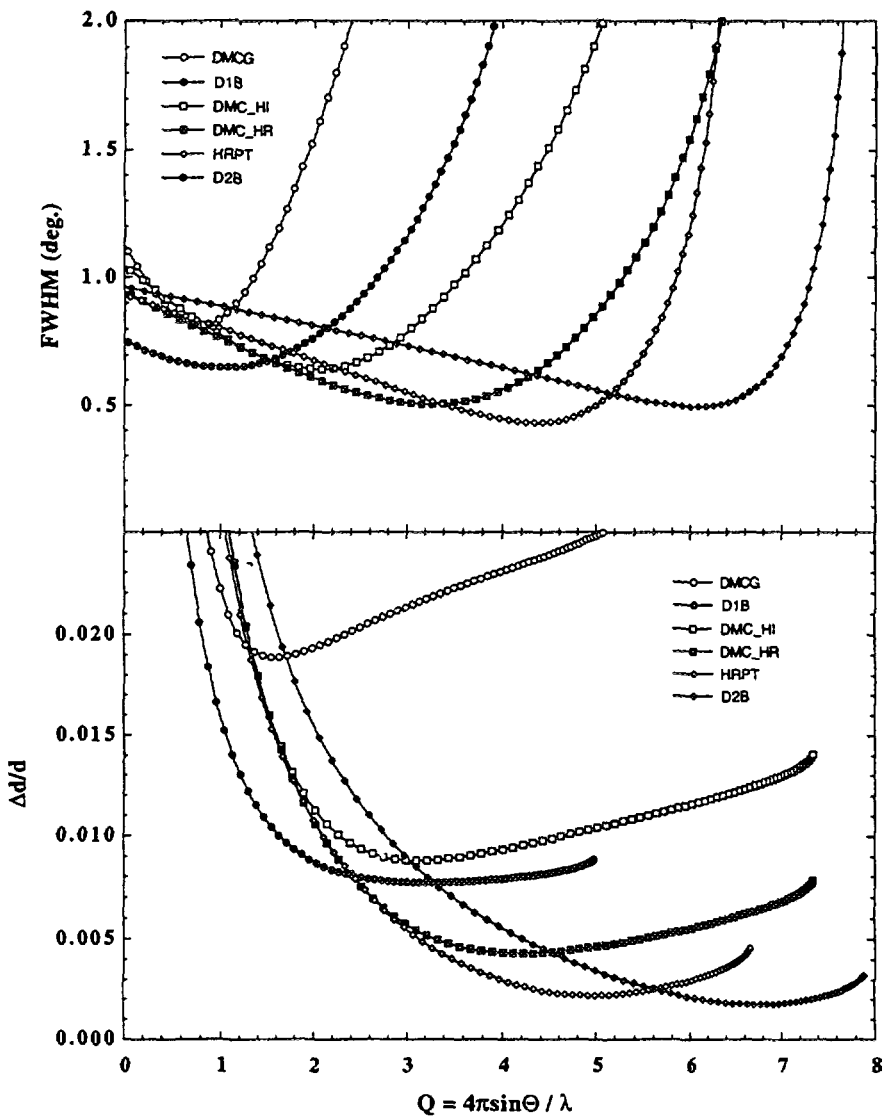


Figure 2. Resolution functions of the 5 diffractometers as a function of Q. a) FWHM. b) $\Delta d/d$.

Instrument	θ_M	Reflection	β	λ	U	V	W
D2B (HI) ⁽¹⁾	135	Ge 335	20	1.594	0.1525	-0.3682	0.3032
HRPT (HI) ⁽²⁾	120	Ge 511	13	1.886	0.2963	-0.5132	0.2835
DMC (HR)	60	Ge 311	20	1.71	0.8485	-0.8398	0.2915
DMC (HI)	60	Ge 311	20	1.71	2.6667	-1.5396	0.3588
D1B	44.22	PG 002	40	2.52	1.0540	-0.4520	0.1880
DMCG (HI) ⁽²⁾	40.80	PG 002	40	2.338	9.0863	-2.7198	0.2835

Table I. Some technical parameters of the diffractometers. Here, θ_M is the take-off angle of the monochromator, β is the mosaic spread, λ is the wave length and U, V and W the coefficients of the Cagliotti, Paoletti and Ricci formula for FWHM [7].

(1) These parameters correspond to the old monochromator working on HI mode. Since spring 1996 D2B is equipped with a new composite Ge 335 monochromator.

(2) First-day conditions.

3. Crystallographic structure of $RNiO_3$ perovskites

From the structural point of view, the $RNiO_3$ compounds are orthorhombically distorted perovskites [8]. The aristotype of this structural family, whose chemical formula can be written in a general way as ABX_3 , is the mineral "perovskite" ($CaTiO_3$). The ideal cubic structure, which is displayed by $CaTiO_3$ above 900 °C, consists of a 3D array of corner-sharing BX_6 octahedra, located at the nodes of a simple cubic lattice (see Fig. 3). At the center of the unit cell ((1/2 1/2 1/2) position) there is room for the A cation, which will fit perfectly if the following condition is fulfilled:

$$d_{A-X} = d_{B-X} \sqrt{2} \quad (1)$$

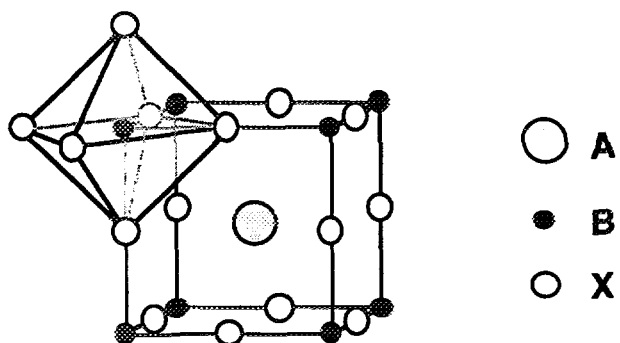


Figure 3. The ideal perovskite structure.

The stability of the perovskite structure requires X to be an anion and B a cation showing preference for octahedral coordination. The A position must be occupied by a cation with the adequate oxidation state (in order to assure the electrical neutrality) and whose size satisfies the condition (1). In the case of the $RNiO_3$ perovskites, the rare earth

is too small to satisfy this criterion. Thus, the NiO_6 octahedra, which have been found to remain practically undistorted along the series, are tilted to fill the extra interstitial space. These rotations cause the unit cell to be smaller and more distorted than the ideal cubic cell. Since the magnitude of this distortion is related to the relative distances $d_{\text{Ni}-\text{O}}$ and $d_{\text{R}-\text{O}}$, it can be discussed in terms of the tolerance factor [9] defined as

$$t = d_{A-X} / d_{B-X} \sqrt{2} \quad (2)$$

Experimentally, it is observed that when t is slightly less than 1, the NiO_6 octahedra are rotated around the [111]-axis [10]. For even smaller t , the octahedra tilt around the [110] and [001] directions, resulting in the orthorhombic GdFeO_3 structure [11]. For $t < 0.7$ other, non-perovskite structures are preferred[8].

The crystallographic structure of the nickelates with $\text{R} \neq \text{La}$ is orthorhombic (Pbnm space group with a unit cell two times larger than the cubic parent shown in Fig. 3). LaNiO_3 is, however, rhombohedral (space group $\text{R}\bar{3}\text{c}$) and displays a unit cell 6 times larger. In figure 4 we have represented the variation of the lattice parameters as a function of the tolerance factor. From this picture we deduce that the orthorhombic distortion, which becomes more important with decreasing radius of the rare earth ion, is stable from $t \approx 0.861$ (Lu) to $t \approx 0.922$ (Pr). In the case of LaNiO_3 , the high value of the tolerance factor allows the less distorted rhombohedral structure to be stabilized.

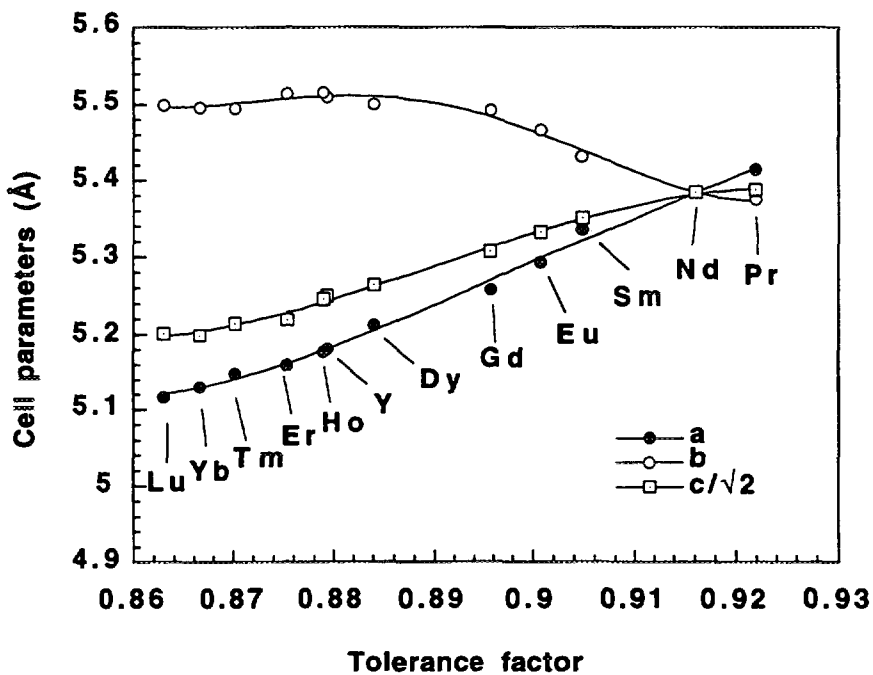


Figure 4 Variation of the cell parameters as a function of the tolerance factor in the RNiO_3 series.

An interesting trend, which has been observed in all the presently available nickelates, is the quasi-invariance of the average Ni-O distance (see Fig. 5). The NiO_6

octahedra behave approximately as rigid bodies, the departure from the ideal perovskite structure along the series being due to their cooperative tilts. The cosine of the tilt angle ω is, to a first approximation, a *linear* function of T_{M-I} .[12] Although this tendency has to be tested for the remaining nickelates (from EuNiO_3 to LuNiO_3), it strongly suggests that this angle is the relevant structural parameter controlling the evolution of T_{M-I} along the series.

4. Structural changes across the M-I transition

The variation of the unit cell volume is the result of a small increase in the Ni-O distance (0.2 %) and a simultaneous decrease of the Ni-O-Ni superexchange angle θ (0.4 %, see Fig. 5). Here, θ is defined as $\theta = \pi - 2\omega$, where ω is the tilt angle of the NiO_6

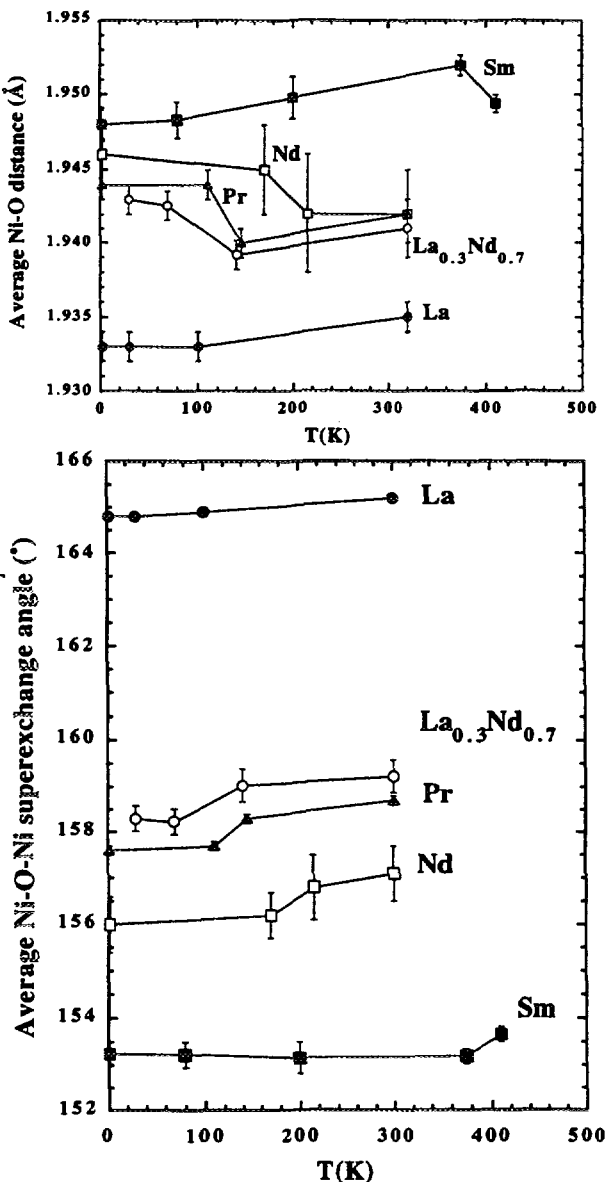


Figure 5. Thermal evolution of a) the average Ni-O distance and b) the average Ni-O-Ni angle for RNiO_3 .

octahedra. The collective displacement of O atoms, shown schematically in figure 6, corresponds to coupled tilts of the octahedra in the sense of increasing rotation angles around the *b* and *c* axes. In other words, the structural changes simply consist of an enhancement of the orthorhombic distortion. Thus, within the experimental uncertainty imposed by the resolution, the crystallographic structure at $T < T_{M-I}$ is also well described in the space group Pbnm.

A very interesting feature of this subtle structural transition is that the oxygen displacements seem to be merely a regular accommodation of the perovskite framework to the sudden enhancement of the Ni-O distance. All happens as if a certain (probably electronic in origin) mechanism produces at $T = T_{M-I}$ a sudden increase of the Ni-O distance and then, the structure reacts in a purely steric way by increasing the tilt angle of the octahedra. The magnitude and sign of the variation of the Ni-O-Ni angle θ can be easily derived by using the following expression [4]

$$\Delta\theta_{Ni-O-Ni} \approx -275(d_{R-O} / d_{Ni-O}^2 \sqrt{2})\Delta d_{Ni-O} \quad (3)$$

The substitution of Δd_{Ni-O} by the observed value across the transition obtained from neutron diffraction measurements ($\approx 0.0035 \text{ \AA}$) yields to $\Delta\theta_{Ni-O-Ni} \approx -0.46^\circ$. This is the expected $\Delta\theta$ value if steric effects predominate. Looking at the figure 4, we see that it has the same sign and the same order of magnitude as the $\Delta\theta$ experimentally determined.

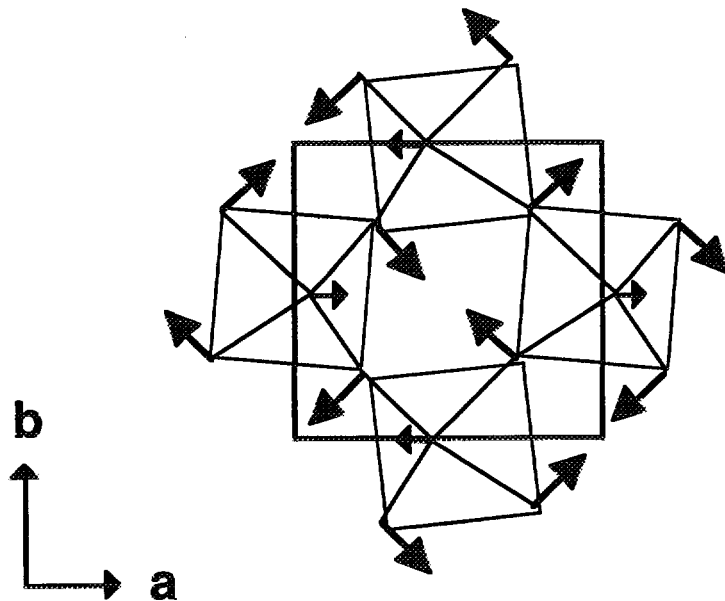


Figure 6. Scheme of the atomic displacements across the metal-insulator transition.

Fig. 7 shows the neutron diffraction patterns of PrNiO_3 calculated by using the λ , angular range and resolution functions of the 6 diffractometers described in section 2. The counting statistics is the same for all the patterns (15000 neutron counts). Note that in the abscises we have used Q instead of 2θ in order to facilitate the comparison between the 6 sets of data.

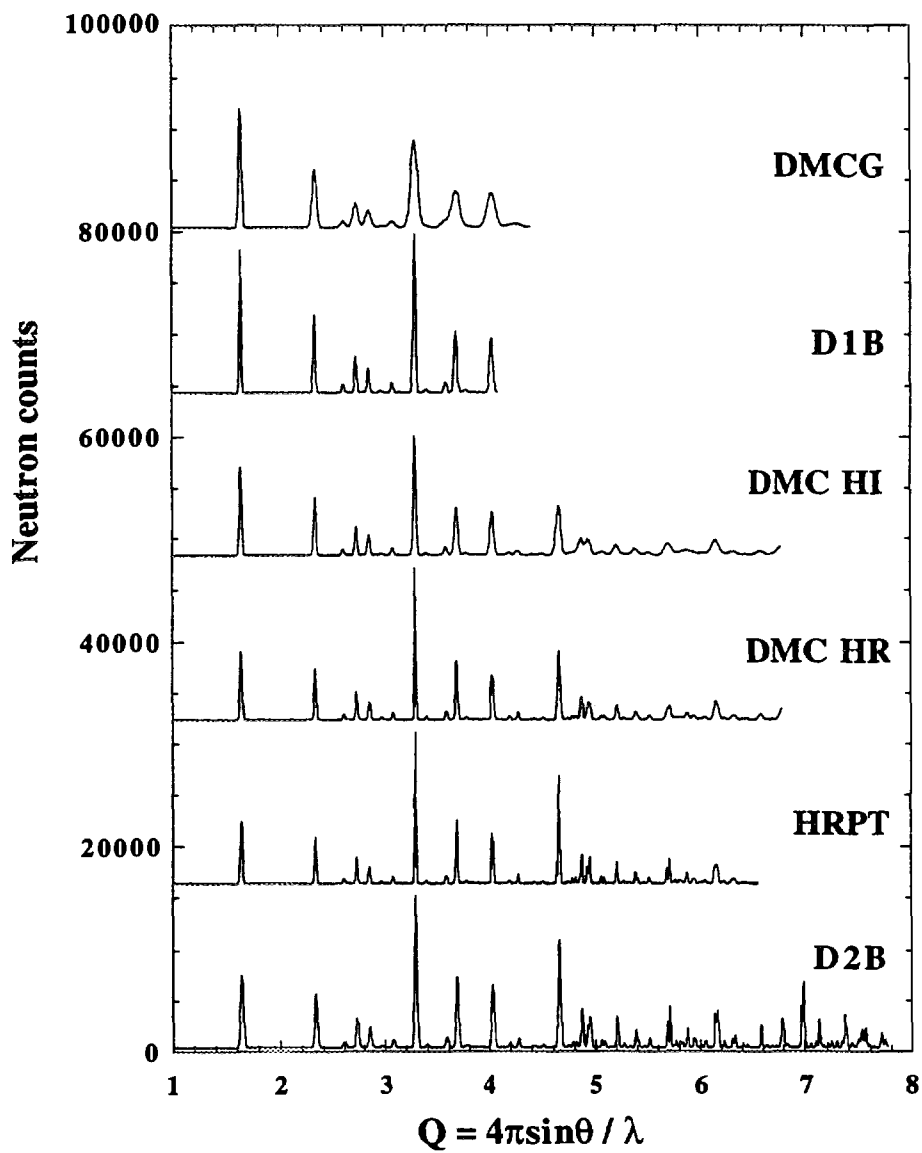


Fig. 7. Calculated neutron diffraction patterns of PrNiO_3 .

Figs. 8 and 9 show the values of the average Ni-O distance d_{Ni-O} and the average Ni-O-Ni superexchange angle θ obtained from Rietveld refinements of those patterns. Note that the small variations of d_{Ni-O} and θ at T_{M-I} are only observable with D2B, HRPT and DMC (HR). With the other diffractometers, the size of the errors is too large to separate the points before and after the M-I transition. Note also that HRPT is a very promising machine for such kind of studies. Taking into account that the simulation was made by using the "first day" SINQ conditions, it is reasonable to expect resolutions and counting times very close of that of D2B when the nominal source conditions will be operative.

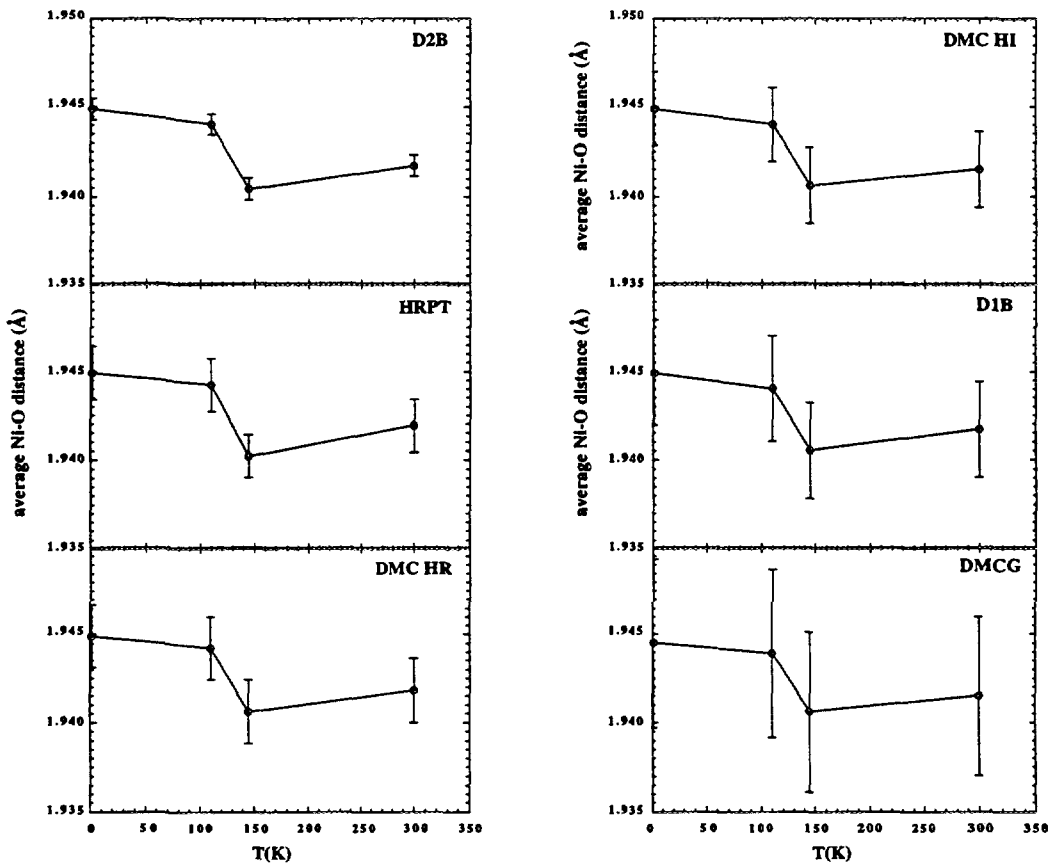


Fig. 8. Temperature dependence of the average Ni-O distance for PrNiO_3 (note the step at $T_{M-I} = 130\text{K}$). The data are the results of the Rietveld refinements performed for the simulated powder neutron diffraction data displayed in Fig. 7.

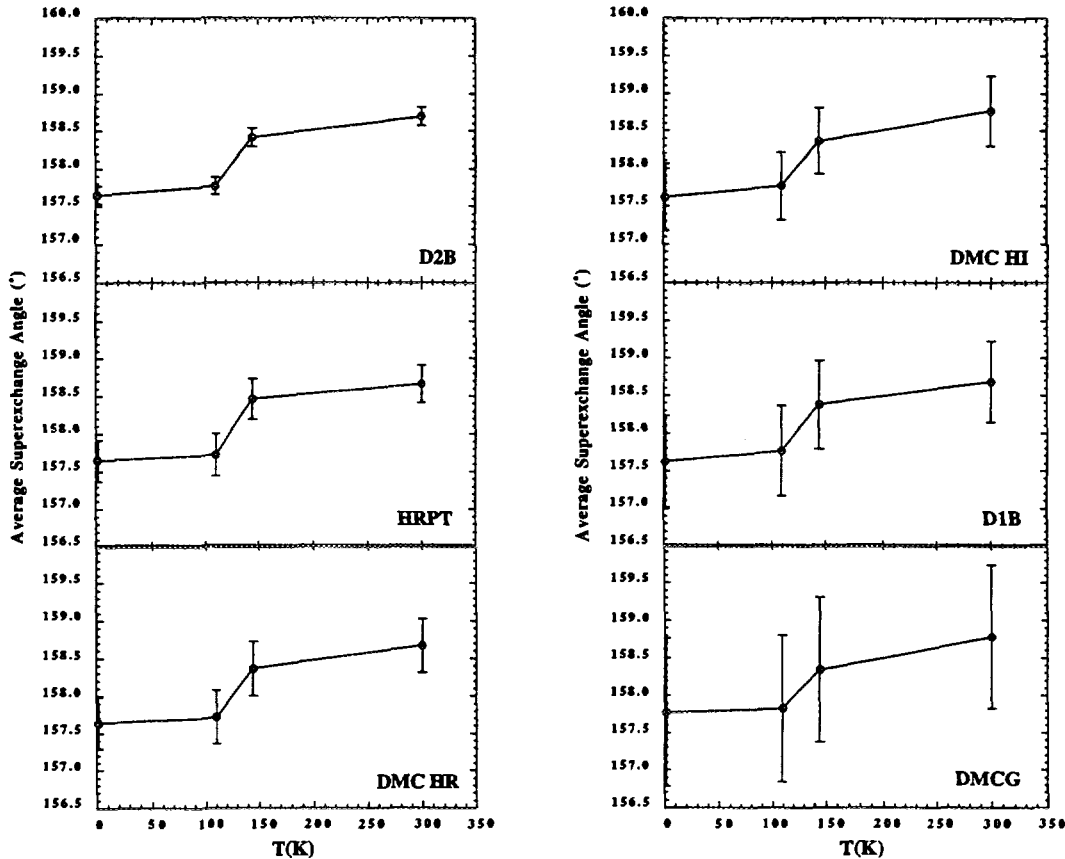


Fig. 9. Temperature dependence of the average Ni-O-Ni superexchange angle for PrNiO_3 (note the step at $T_{M-I} = 130\text{K}$). The data are the results of the Rietveld refinements performed for the simulated powder neutron diffraction data displayed in Fig. 7.

5. Magnetic structure

5.1. Ni sublattice

The proposed magnetic structure (Ni sublattice) for PrNiO_3 , NdNiO_3 and SmNiO_3 [13, 14] is shown in figure 10 ($\mathbf{k} = (1/2 \ 0 \ 1/2)$, $\mu_{\text{Ni}} \approx 1\mu_B$). The most interesting (and surprising!) feature of such a magnetic arrangement is that it supposes the existence of an equal number of ferromagnetic (F) and antiferromagnetic (AF) couplings between nearest-neighbours. In other words, each Ni magnetic moment is coupled with three of its six nearest-neighbors via an AF interaction (full lines), whereas the coupling with the three remainders is F (dotted lines). As far as we know, this magnetic arrangement is unprecedented in an oxide with perovskite structure.

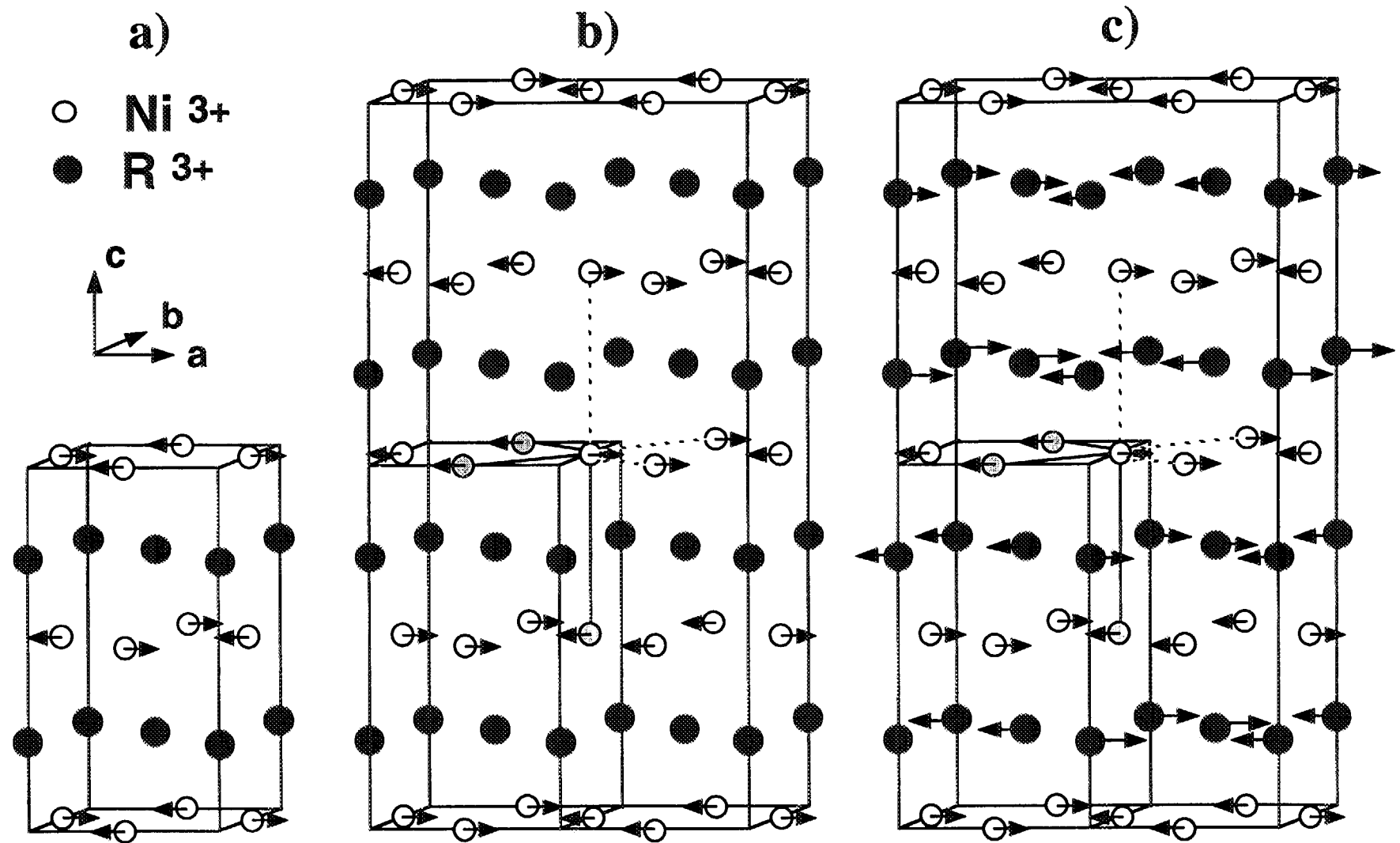


Fig. 10. Magnetic structure of RNiO_3 perovskites. a) as predicted by Demazeau. b) As found experimentaly (only Ni sublattice). c) The same as b) but by including the rare earth sublattice.

5.2. Rare earth sublattice

Whereas in PrNiO_3 no traces of cooperative magnetic ordering have been found in the Pr sublattice, the sharp rise of some magnetic reflections observed below ≈ 30 K indicate the existence of induced magnetic ordering of the rare earth moments in NdNiO_3 and SmNiO_3 .

The proposed magnetic structure below 30 K [14, 15] is shown in figure 10c. Notice that, due to the particular arrangement of the Ni magnetic moments, the exchange field at the R^{3+} positions is practically zero in half of them ($z=3/8, 7/8$) and different from zero in the other half ($z=1/8, 5/8$). The consequence is the existence of two different values for the rare earth magnetic moment (big and small arrows at the R positions in figure 9c) which, at $T = 1.5$ K are $2.0(2)$ - $0.8(2)$ μ_B and $0.33(5)$ - ≈ 0 μ_B for NdNiO_3 and SmNiO_3 , respectively.

5.3. Comparison of the diffractometers

Due to the smallness of the Ni magnetic moment in RNiO_3 perovskites ($\approx 1\mu_B$), high intensity neutron diffraction experiments were necessary to determine the magnetic structure. The very first were made on D1B. After 10 minutes, a spectrum with about 35000 counts (larger nuclear peak) was obtained. The reflections associated to the three-dimensional magnetic ordering were about 40 times smaller than the largest nuclear reflection. With the statistics of such a pattern, the magnetic moment of Ni can be determined with an accuracy of about 5% ($0.87(5)\mu_B$).

The approximate counting times needed to get the same statistics with the other diffractometers are displayed in table II. Note the difference between the high resolution and high intensity instruments. Note also that DMCG, even operating with the first-day conditions, will be a very promising machine for magnetic studies (just 4 times slower than D1B).

A comparison of the sensibilities of the 6 instruments for equal counting times has been performed by simulating the PrNiO_3 patterns which would be obtained on each instrument after 10 minutes. The refined magnetic moments of Ni are displayed on the last column of table II. Although in almost all the cases the errors are smaller than the refined value (DMC in high resolution mode is the only exception), it is clear that the large counting times needed to get a reasonable accuracy prevent the use of the three high resolution machines for this kind of studies.

Instrument	2θ step	angular range	detector positions	counting time	refined μ_{Ni} (μ_B)
D1B	0.2	80	1	1 (1)	0.87(5)
DMCG (HI)	0.2	80	1	4 (2)	0.86(5)
DMC (HI)	0.2	80	1	10 (1)	0.9(2)
DMC (HR)	0.1	135	4	160 (1)	1(4)
HRPT (HI)	0.1	160	1	20 (2)	0.8(4)
D2B (HI)	0.1	160	25	20 (1)	0.8(4)

Table II. Measuring conditions, counting times and values of the refined Ni magnetic moment for the 5 diffractometers.

(1) Determined experimentally.

(2) Estimated taking into account a) the calculated SINQ flux ("first day"), the detector efficiencies and, for DMCG, the material of the neutron guide.

6. Interpretation of the magnetic structure: the orbital ordering

In RNiO_3 perovskites, the Ni^{3+} ions have the $3d^7$ configuration. Because they are located in octahedra with relative small Ni-O distances ($\approx 1.94\text{\AA}$), the crystal field leaves the degeneracy of the 3d orbitals in the way shown in Fig. 11. As the energy separation between the t_{2g} and e_g levels is large enough to overcome the first Hund rule, the triplet t_{2g} is completely occupied. The remaining electron is then in the doubly degenerated e_g level, giving rise to the experimentally observed magnetic moment ($\approx 1\mu_B$) (note that, if the crystal field splitting were smaller than the intra-atomic exchange energy, the moment of Ni would be $\approx 3\mu_B$)

If this single e_g^1 electron is located either in the $3d_{x^2-y^2}$ or in the $3d_{z^2-r^2}$ orbitals, the Goodenough-Kanamori rules predict the existence of AF coupling between the $S=1/2$ Ni^{III} low spin magnetic moments. The expected magnetic structure is shown in figure 10a. The experimentally observed arrangement in PrNiO_3 and NdNiO_3 is, however, very different (Fig. 10b), and it is in contradiction to a uniform distribution of the e_g orbital.

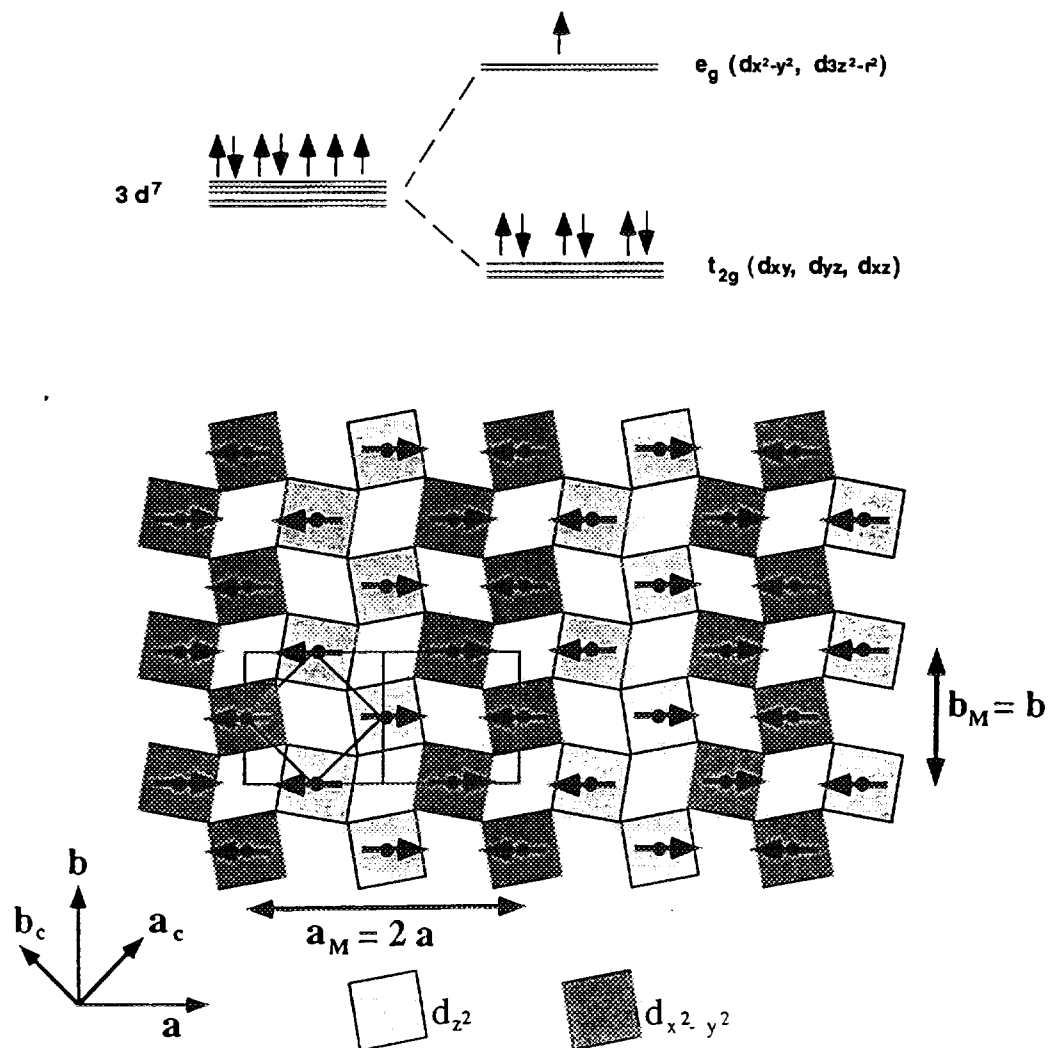


Figure 11. a) Schema of the crystal field splitting of the Ni 3d orbitals in an octahedral environment.
b) Schematic representation of the orbital superlattice in the nickelates.

A possible explanation has been proposed by García Muñoz *et al.* [13] following the theoretical calculations of Cyrot and Lyon-Caen [16]. These authors suggest that *the actually observed magnetic structure results from the set-up of an orbital superlattice*. Thus, whereas the t_{2g} orbitals are expected to be fully occupied, the $3d_{x^2-y^2}$ and the $3d_{3z^2-r^2}$ orbitals are probably not degenerate due to the orthorhombic distortion. But the difference in energy between them may be very small, perhaps not very different from the intra-atomic ferromagnetic exchange. Thus, the competition between intraatomic exchange correlations and the energy gain by the electrons occupying the lower energy orbital can lead to a ground state in which the lattice breaks up into two sublattices, each with predominantly one of the $3d_{x^2-y^2}$ or the $3d_{3z^2-r^2}$ orbitals half occupied. The nearest neighbouring Ni atoms with the e_g electron in the same orbital will be then AF coupled and those with a different orbital occupancies will prefer to align their $S = 1/2$ spins parallel. This situation is schematically shown in figure 11.

Another mechanism which may induce an orbital ordering is the cooperative Jahn-Teller effect. This is for example the case of LaMnO_3 [17]. In this compound, the electronic configuration of Mn^{3+} is $t_{2g}^3 e_g^1$. To break the degeneracy of the e_g^1 orbitals, a strong elongation of the MnO_6 octahedra takes place. Thus, the $3d_{3z^2-r^2}$ orbital has lower energy than the $3d_{x^2-y^2}$ and the e_g^1 electron will be exclusively located in it. In this case the orientation of the e_g orbitals can be directly deduced from the alternating arrangement of the elongated MnO_6 octahedra. In RNiO_3 perovskites, however, *no appreciable Jahn-Teller distortion has been observed, the existence of an orbital superlattice being invoked uniquely to explain the existence of such an unusual magnetic structure*.

If the orbital ordering produces a significative distortion of the NiO_6 octahedra, it could be possible to observe superstructure peaks corresponding to the propagation vector $\mathbf{k} = (1/2 \ 0 \ 1/2)$ in the paramagnetic insulating state. The ideal nickelate to test this hypothesis is SmNiO_3 because in it, the magnetic and the M-I transition are well separated (for Pr and Nd the reflections associated to the orbital superlattice will be superimposed to the magnetic reflections). Thus, we have attempted to detect the signature of the orbital ordering (that we assume to be established in the insulating regime) by a high intensity neutron diffraction measurement on D1B. The difference pattern between low (insulating state) and high (metallic state) temperature is shown in Fig. 12.

We could not see any indication of superstructure peaks. However, we could find an upper limit for their size. Taking into account that the most intense peak has 5×10^6 counts and that the statistical noise is about 500 counts, the superstructure reflections, if existing, should be at most 10^4 times smaller than the largest diffraction peak. Our conclusion is that, if the orbital ordering exists, it is not possible to detect it with the available neutron fluxes for powder neutron diffraction. Single crystals and/or high intensity x-ray synchrotron investigations are then of absolute necessity to unambiguously state that the orbital ordering is a relevant concept in these materials. Another possibility is that our ideas about superexchange interactions are too simplistic and the Googenough-Kanamori rules do not apply to the present system. In any case, the existence of other subtle interactions able to stabilize the observed spin arrangement should not be disregarded.

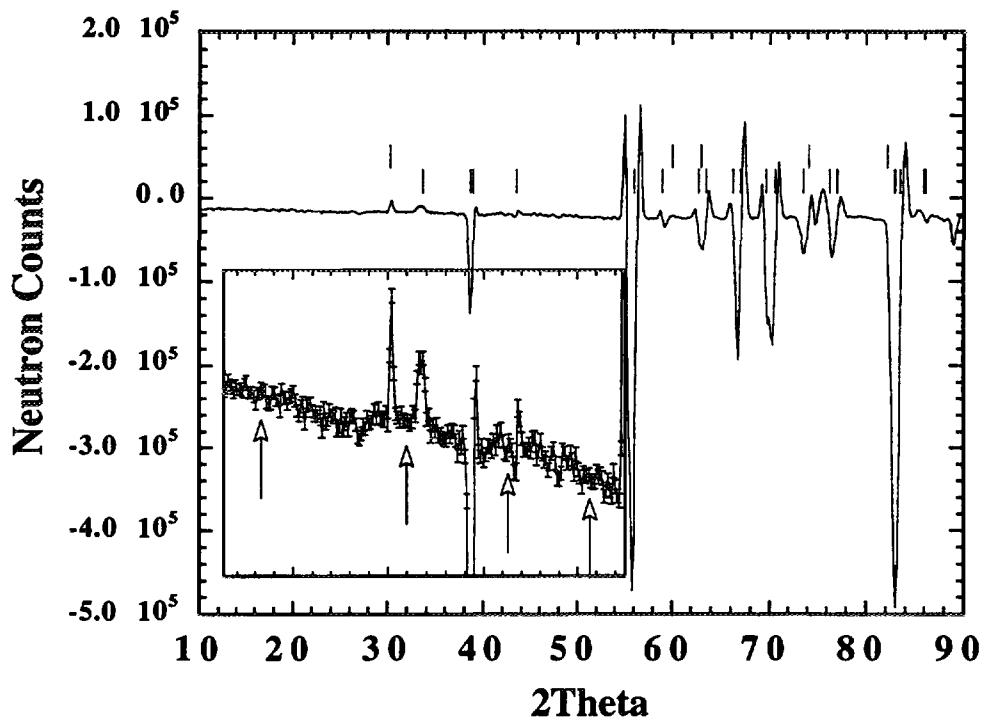


Fig. 12. Difference pattern showing the absence of superstructure peaks in the insulating paramagnetic state of SmNiO_3 . The arrows indicate the positions corresponding to the propagation vector $\mathbf{k} = (1/2 \ 0 \ 1.2)$.

6. Acknowledgements

The author is grateful to Peter Fischer for helpful discussions, as well as for providing the technical parameters of the diffractometers HRPT and DMCG. The help of Stephan Rosenkranz in the elaboration of some figures and the careful reading of the manuscript by Joël Mesot are also kindly acknowledged.

7. References

- 1- G. Demazeau, A. Marbeuf, M. Pouchard and P. Hagenmuller, J. Solid State Chem. **3**, 582 (1971).
- 2- P. Lacorre, J. B. Torrance, J. Pannetier, A. I. Nazzal, P. W. Wang and T. C. Huang, J. Solid State Chem. **91**, 225 (1991).
- 3- J. B. Torrance, P. Lacorre, A. I. Nazzal, E. J. Ansaldi and C. Niedermayer, Phys. Rev. B **45**, 8209 (1992).
- 4- J. L. García-Muñoz, J. Rodríguez-Carvajal, P. Lacorre and J. B. Torrance, Phys. Rev. B **46**, 4414 (1992).
- 5- J. B. Torrance, P. Lacorre, C. Asavaroengchai and R. Metzger, J. Solid State Chem. **90**, 168 (1991).
- 6- M. Medarde, A. Fontaine, J. L. García-Muñoz, J. Rodríguez-Carvajal, M. d. Santis, M. Sacchi, G. Rossi and P. Lacorre, Phys. Rev. B **46**, 14975 (1992).
- 7- G. Caglioti, A. Paoletti and F. P. Ricci, Nucl. Instr. **3**, 223 (1958).

- 8- J. B. Goodenough and J. M. Longo, in *Landolt-Börnstein, New series, Group III, Magnetic and Other Properties in Oxides and Related Compounds*, edited by A. M. H. K.H. Hellwege (Springer-Verlag, 1970), Vol. 4a, p. 126.
- 9 - V. M. Goldsmith, Geochemische Verteilungsgesetze der Elemente VII, VIII **28**, (1927).
- 10 - A. Wold, B. Post and E. Banks, J. Am. Chem. Soc. **79**, 4911 (1957).
- 11 - S. Geller, J. Chem. Phys. **24**, 1236 (1956).
- 12 - M. Medarde *et al.*, in preparation.
- 13 - J. L. García-Muñoz, J. Rodríguez-Carvajal and P. Lacorre, Europhys. Lett. **20**, 241 (1992).
- 14 - J. Rodríguez-Carvajal, S. Rosenkranz, M. Medarde, P. Lacorre and V. Trounov, submitted.
- 15 - J. L. García-Muñoz, J. Rodríguez-Carvajal and P. Lacorre, Phys. Rev. B **50**, 978 (1994).
- 16 - M. Cyrot and C. Lyon-Caen., J. Phys. (Paris) **36**, 253 (1975).
- 17 - S. Quezel-Ambrunaz, Bull. Soc. Franc. Miner. Crist. **91**, 339 (1968).



INCOMMENSURATE PHASE TRANSITIONS

R. Currat
*Institut Laue-Langevin, BP 156X
 38042 Grenoble, France*

ABSTRACT

We review the characteristic aspects of modulated crystals from the point of view of inelastic neutron scattering. We discuss the phenomenological Landau theory of the normal-to-incommensurate displacive instability and its predictions concerning the fluctuation spectrum of the modulated phase. General results on the form of the normal-mode eigenvectors and on the inelastic scattering channels through which they couple to the probe are established using the superspace approach. We illustrate these results on a simple discrete model system and we review available inelastic neutron scattering data on several displacively modulated compounds.

1. Introduction.

1.1. Modulated crystals as quasiperiodic structures

There are three main classes of solids which are known to lack translational periodicity, in the conventional sense, while retaining a high degree of structural order [1,2]. These are the modulated crystals, the composite systems (intercalates, epitaxial or intergrowth compounds) and the quasicrystals. They share the common property that their Fourier spectrum is characterised by sharp diffraction peaks whose labeling requires more than three integer indices. This implies that a proper description of their direct space structure involves more independent periodicities or independent length scales than the number of space dimensions. They are said to be *quasiperiodic*.

Modulated crystals make up the simplest class of quasiperiodic solids, insofar as their diffraction pattern can be separated into fundamental reflections ($m_r=0$) and m^{th} order satellites:

$$\mathbf{K} = h\mathbf{a}_1^* + k\mathbf{a}_2^* + l\mathbf{a}_3^* + \sum_{r=1}^d m_r \mathbf{k}_r \quad (1)$$

For an incommensurate structure, the d modulation vectors $\mathbf{k}_1, \mathbf{k}_2, \dots, \mathbf{k}_d$, and the three reciprocal vectors $\mathbf{a}_1^*, \mathbf{a}_2^*, \mathbf{a}_3^*$ are rationally independent.

1.2. Periodic reference structures

The fundamental reflections define a '*basic*' (or average) structure with ordinary 3-dimensional periodicity. This basic structure is related, but not always isomorphous, to the '*undistorted*' structure generated by continuously reducing the modulation amplitude(s) to zero [3]. The word '*modulation*' is used here in a generic sense, referring to any distortion or static perturbation, characterised by its own independent periodicity.

In many modulated compounds the undistorted structure can be obtained, not only through the above *gedanken* process, but also via an actual (continuous) phase transition. The undistorted phase corresponds to a normal crystalline phase, stable at high

temperature (say for $T > T_i$). Below T_i the modulated state develops, with the amplitude of the modulation(s) increasing continuously as the temperature is lowered.

The existence of a continuous transition at T_i implies a symmetry relationship between the crystalline and the modulated phases. This relationship can be formulated in the framework of the Landau theory of continuous phase transitions (see Sect. 2).

In general the modulation periodicity is temperature-dependent and *locks-in* at low temperature to a value that is commensurate with the periodicity of the basic structure. The lock-in transition is very different in nature from the incommensurate instability at T_i . Under certain symmetry conditions, McMillan [4] has shown that the modulated structure just above lock-in is highly non-sinusoidal and consists of regions where the local periodicity is essentially already commensurate (*commensurate domains*), separated by regions where the local periodicity is essentially the same as near T_i (*discommensurations*). As the system approaches lock-in, the discommensuration density decreases (and eventually vanishes), although generally the lock-in transition is found to be somewhat discontinuous.

1.3. Systems and mechanisms

Neutron studies of modulated structures date back to the discovery of helimagnetic order, several decades ago [5-6]. Since then, structural modulations have been identified in a wide range of insulating and metallic systems [1,7,8], by means of x-ray, neutron and electron diffraction techniques.

Structural modulations can be of two separate types: *displacive* waves which modulate the atomic lattice positions and *probability* waves which affect site occupation probabilities, as in disordered alloys or orientationally-disordered molecular crystals. Fig. 1 shows an example of a structural modulation with mixed displacive/occupation-probability character in sodium nitrite [9], one of the earliest known structurally modulated compounds [10].

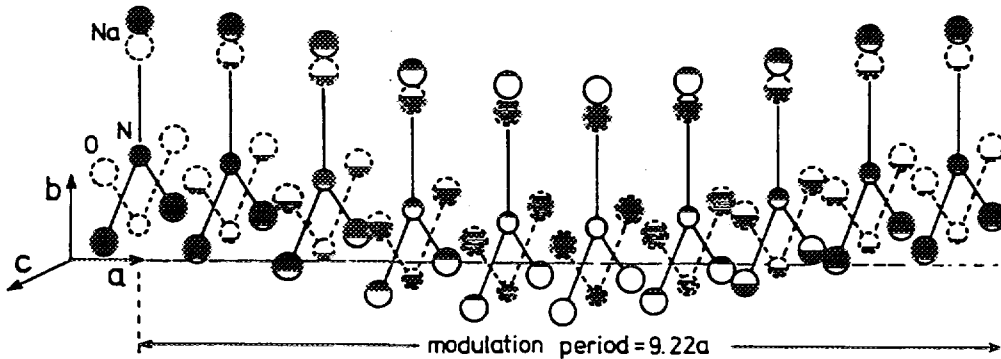


Fig. 1. Mixed order-disorder-displacive modulation in NaNO_2 . Na^+ and NO_2^- ions are found in two alternate positions (full and broken lines) with occupation probabilities proportional to the shaded areas. Probabilities and ionic shifts vary sinusoidally along a with a temperature-dependent periodicity of 8 to 10 a . After Kucharczyk and Paciorek [9].

The microscopic mechanisms which stabilise incommensurate modulated structures have not all been identified. In the magnetic case, the origin of the modulated state can often be traced back to the presence of antiferromagnetic second-neighbor interactions ($J_2 < 0$). The incommensurate state appears then as the best ordered compromise between *competing interactions* of different characteristic range [4,11]. Similar arguments have been applied to structurally modulated systems, e.g. in the case of the orientationally-modulated phase of the molecular crystal biphenyl [12].

Mechanisms based on *competing length scales*, rather than competing interactions are clearly at work in composite systems and adsorbed gases. The Peierls instability in low-dimensional metals can also be cast into this latter category, with the Fermi

wavevector of the electronic subsystem coexisting and competing with the ionic lattice periodicity.

1.4. Phasons

Modulated crystals are characterised by new types of excitations [13,14], corresponding to fluctuations in the phase and amplitude of the (thermally averaged) modulation wave. In the long-wavelength limit, the phase mode consists in an overall phase shift of the modulation with respect to the underlying atomic lattice (*sliding mode*). For a well-behaved incommensurate modulation, i.e. one for which the atomic displacement field can be described in terms of analytic functions of space [15], such a phase shift costs no energy and the corresponding excitation branch is gapless. This regime is expected to hold in a finite temperature range below T_i , when the modulation wave is not too far from sinusoidal in shape.

In *real* solids, however, impurities and defects in the host lattice may pin the modulation and raise the sliding mode frequency to a finite value (*pinning frequency*), even though the modulation may be close to sinusoidal.

In the discommensuration limit, the phason branch becomes identical to the acoustic branch of the discommensuration lattice [14]. Its gapless character is not expected to survive, even in the pure system, because close enough to lock-in, lattice discreteness effects are bound to localise and pin the discommensurations (*intrinsic pinning*) [16].

Discrete microscopic models, such as the discrete frustrated ϕ^4 (DIFFOUR) model [17], are able to reproduce the gapless character of the phason branch in the sinusoidal regime and the opening of a phason gap as the discommensuration regime is approached.

1.5. Experimental studies

No model can however replace direct observation. Over the past two decades, a considerable amount of experimental work has thus been devoted to dynamical studies of incommensurate crystals. Raman scattering was used very effectively in the study of amplitude modes ('amplitudons'), in insulators [18, 19], while similar attempts on the phase mode, by Brillouin spectroscopy, proved unsuccessful. The origin of the difficulty was spelled out by Golovko and Levanyuk [20] who pointed out that in the wavelength range accessible by Brillouin scattering gapless phasons would be too overdamped (and pinned phasons, too weak) to be detectable by Brillouin spectroscopy.

Infra-red studies of the sliding mode are difficult because of the low frequency range (typically a few cm^{-1}) and stringent selection rules [21]. In the case of low-dimensional metals, the sliding mode is associated with electron *transport* via the moving charge-density-wave (CDW) and is thus *always* infra-red active, regardless of the symmetry of the atomic vibrations involved [22]. Evidence for pinned phasons have been reported in several CDW systems by far infra-red, microwave and mm-wave conductivity measurements. Pinning frequencies vary from 15 cm^{-1} (450 GHz) for KCP (i.e. $\text{K}_2\text{Pt}(\text{CN})_4\text{Br}\cdot 3\cdot 3 \text{ H}_2\text{O}$) [23] to 1.1 cm^{-1} (34 GHz) in the case of $(\text{TaSe}_4)_2\text{I}$ [24].

Neutron three-axis spectrometry offers direct and unique experimental possibilities for studying the excitation spectrum of modulated crystals. Due to the lack of translational invariance, the wavevector selection rules, which govern phonon scattering cross-sections in normal crystals, are relaxed, but not dramatically so, at least in *weakly* modulated crystals. Hence, as discussed in Sect. 3 below, the standard three-axis technique is found to be applicable without major modifications and the concepts of 'pseudo' dispersion curve and 'pseudo' Brillouin zone are still quite useful.

Most of the direct information available today on phasons and phason velocities results from high-resolution three-axis work. The advent of cold neutron sources and cold-source instrumentation made possible a number of detailed inelastic studies, some of which are reviewed in Sect. 5 below. These studies have had a major impact in the field. Without the contribution from inelastic neutron scattering (INS), the concept of phason

propagation in modulated crystals would probably be in the same speculative state as it was in the early 80's [25].

2. Landau theory of the normal-to-incommensurate phase transition.

2.1. Order parameters

We consider explicitly the case of a *displacive* instability, but the derivation of the order-disorder case follows by simple transposition, phonon normal coordinates and phonon (squared) frequencies being replaced by collective pseudo-spin coordinates and relaxation rates, respectively.

One assumes that the instability is driven by a single non-degenerate soft phonon branch whose frequency vanishes at T_1 for some characteristic wavevector \mathbf{k}_1 . In the present case, \mathbf{k}_1 is not a special high symmetry point in the Brillouin zone of the high-temperature (HT) phase:

$$\mathbf{k}_1 \neq \mathbf{0}, \mathbf{G}/2 \quad (2)$$

so that at least one of its components is not constrained by symmetry and may take irrational and, in general, temperature-dependent values.

The diffraction pattern of the LT phase ($T < T_1$) is characterised by additional satellite diffraction spots at incommensurate positions:

$$\mathbf{K} = \mathbf{G} + m \mathbf{k}_1 \quad (3)$$

where the integer m defines the order of the satellite.

The atomic displacements just below T_1 are written as:

$$u_{lj} = (2NMj)^{-1/2} e(j; \mathbf{k}_1) \exp\{i\mathbf{k}_1 \cdot \mathbf{R}_l\} \langle Q_{k_1} \rangle + \text{compl. conj.} \quad (4)$$

where the index $j = 1, \dots, s$ runs over all atomic sites in the HT unit cell and $e(\mathbf{k}_1)$ is the 3s-component soft mode eigenvector. $\langle Q_{k_1} \rangle$ and $\langle Q_{k_1}^* \rangle = \langle Q_{-k_1} \rangle$ form a pair of complex-conjugate order parameters:

$$(2/N)^{1/2} \langle Q_{\pm k_1} \rangle = \eta e^{\pm i\phi} \quad (5)$$

In the case of a monoatomic lattice, Eq. 4 reduces to:

$$u_l = \eta e \cos(\mathbf{k}_1 \cdot \mathbf{R}_l + \phi) \quad (6)$$

which identifies η and ϕ as the amplitude and phase of the modulation with respect to the parent lattice.

Note that even for sinusoidal displacements, as in Eqs. 4 and 6, higher-order diffraction satellites are present. This is a consequence of the non-linear relationship between the displacements u_{lj} and the scattered amplitude $F(\mathbf{K})$:

$$F(\mathbf{K}) = \langle \sum_j b_j \exp\{i\mathbf{K} \cdot (\mathbf{R}_{lj} + u_{lj})\} \rangle \quad (7)$$

For a monoatomic lattice, neglecting fluctuations, we get:

$$\begin{aligned} \exp\{i\mathbf{K} \cdot u_l\} &= \exp\{i\eta \mathbf{K} \cdot e \cos(\mathbf{k}_1 \cdot \mathbf{R}_l + \phi)\} = \\ &\Sigma_m i^m J_m(\eta \mathbf{K} \cdot e) \exp\{i m (\mathbf{k}_1 \cdot \mathbf{R}_l + \phi)\} \end{aligned} \quad (8)$$

whence:

$$F_m(K) = (i e^{i\phi})^m b J_m(\eta |K| \cdot e^{-\Delta(K + m k_i)}) \quad (9)$$

No such complication occurs in the magnetic case or for the pure order-disorder case where the atomic scattering amplitudes, as opposed to the atomic positions, are modulated.

2.2. Landau free-energy near T_i

Within Landau theory the excess free-energy of the distorted phase is expressed as a polynomial expansion in powers of the order parameter(s), subject to symmetry restrictions imposed by the HT space group. For a single pair of condensed modes at $\pm k_i$ ($k_i \neq G/m$), the only translational invariants have the form:

$$N^{-m} \{ \langle Q_{ki} \rangle \langle Q_{-ki} \rangle \}^m = \eta^{2m} \quad (m=1, 2, \dots) \quad (10)$$

Hence:

$$F = F_0 + 1/2 A(k_i, T) \eta^2 + 1/4 B \eta^4 + \dots \quad (11)$$

where F_0 is the free-energy of the undistorted phase and one assumes:

$$\begin{aligned} A(k_i, T) &= \alpha (T - T_i) \\ B &> 0 \end{aligned} \quad (12)$$

Minimising Eq. 11 with respect to η yields:

$$\eta^2 = \begin{cases} 0 & T > T_i \\ \alpha(T_i - T) / B & T < T_i \end{cases} \quad (13)$$

To calculate the order-parameter susceptibility it is convenient to introduce the variables [14]:

$$\begin{aligned} P_1 &= 1/\sqrt{2} \{ Q_{ki} + Q_{-ki} \} = \eta \cos\phi \sqrt{N} \\ P_2 &= i/\sqrt{2} \{ Q_{ki} - Q_{-ki} \} = -\eta \sin\phi \sqrt{N} \end{aligned} \quad (14)$$

from which the free-energy is obtained in canonical form as:

$$F = F_0 + (\alpha/2N) (T - T_i) (P_1^2 + P_2^2) + (B/4N^2) (P_1^2 + P_2^2)^2 + \dots \quad (15)$$

Eq. 15 has the same form as the free-energy of the isotropic planar magnet ($n=2$; $d=3$), with the amplitude η and phase ϕ of the modulation playing the role of the modulus and orientation angle of the magnetisation, respectively.

2.3. Order-parameter susceptibilities

The rest of the derivation follows by analogy with the isotropic magnet case. One assumes a specific modulated state, characterised by a specific value of the phase ϕ (viz. a specific orientation of the magnetisation), say $\phi=0$:

$$\langle P_1 \rangle = \eta \sqrt{N} ; \quad \langle P_2 \rangle = 0 \quad (16)$$

The longitudinal and transverse static susceptibilities are defined as:

$$\chi^{-1}_{L,T} = N \partial^2 F / \partial P_{1,2}^2 = \alpha (T - T_i) + B/N \{ (P_1^2 + P_2^2) + 2 P_{1,2}^2 \} \quad (17)$$

where $P_{1,2}$ are evaluated in the equilibrium state (cf. Eqs. 16 and 13). For $T > T_i$ the two susceptibilities are identical:

$$\chi^{-1} = \alpha(T - T_i) \quad (18)$$

while for $T < T_i$:

$$\begin{aligned} \chi^{-1}_L &= 2 \alpha(T_i - T) \\ \chi^{-1}_T &= 0 \end{aligned} \quad (19)$$

The divergence of χ_T is related to the invariance of the free-energy with respect to an homogeneous change in the phase ϕ (see Eq. 11). The branch of excitations corresponding to phase fluctuations is expected to have vanishing frequency in the long-wavelength limit (Goldstone theorem). Phasons in incommensurate structures play the same role as magnons in isotropic magnets (see below for further discussion on this point).

2.4. Order-parameter fluctuation spectrum

One wishes to calculate the free-energy associated with long-wavelength order-parameter fluctuations. These involve soft branch normal coordinates of the type $Q_{\pm k_i \pm q}$, with $|q| \ll |k_i|$. The expansion of the free-energy to fourth order in the Q 's yields:

$$\begin{aligned} \delta F &= 1/2N \int dq A(k_i \pm q) Q_{k_i \pm q} Q_{k_i \pm q}^* \\ &\quad + (B/4N^2) \int dq dq' dq'' Q_{k_i+q} Q_{k_i+q'} Q_{k_i-q'}^* Q_{k_i+q+q'+q'}^* \end{aligned} \quad (20)$$

with the assumption that the fourth order coefficient B is constant in a neighborhood of $\pm k_i$. Below T_i this can be linearised as:

$$\begin{aligned} \delta F &= 1/2N \int dq \{ [\alpha(T - T_i) + q \Lambda q + 2B\eta^2] Q_{k_i \pm q} Q_{k_i \pm q}^* \\ &\quad + B\eta^2 [Q_{k_i+q} Q_{-k_i+q}^* + c.c.] \} \end{aligned} \quad (21)$$

where, in a product of four Q's, two have been set equal to their average value in the incommensurate phase.

In deriving Eq. 21 we have used a parabolic expansion of the soft-mode frequency around its minimum at $\pm \mathbf{k}_i$:

$$A(\mathbf{k}_i + \mathbf{q}) \approx A(\mathbf{k}_i - \mathbf{q}) = A(-\mathbf{k}_i + \mathbf{q}) = \alpha(T - T_i) + q\Lambda q + \dots \quad (22)$$

As a result the bilinear coupling term in Eq. 21 can be diagonalised using the same unitary transformation as in Eq. 14:

$$\begin{aligned} \delta P_1(\mathbf{q}) &= 1/\sqrt{2} \{ Q_{\mathbf{k}_i + \mathbf{q}} + Q_{-\mathbf{k}_i + \mathbf{q}} \} \\ \delta P_2(\mathbf{q}) &= i/\sqrt{2} \{ Q_{\mathbf{k}_i + \mathbf{q}} - Q_{-\mathbf{k}_i + \mathbf{q}} \} \end{aligned} \quad (23)$$

With the help of Eq. 13, the corresponding static susceptibilities are found as:

$$\chi^{-1}(\mathbf{q}) = \alpha(T - T_i) + q\Lambda q + \dots \quad (T > T_i) \quad (24a)$$

$$\chi^{-1}_L(\mathbf{q}) = 2\alpha(T_i - T) + q\Lambda q + \dots \quad (T < T_i) \quad (24b)$$

$$\chi^{-1}_T(\mathbf{q}) = q\Lambda q + \dots \quad (24c)$$

2.5. Soft modes below T_i

As usual, the above \mathbf{q} -dependent inverse static susceptibilities can be identified to mode frequencies (squared), provided the mode lineshapes are of the damped harmonic oscillator (DHO) type. If not (and the present theory gives no information on lineshapes), they only relate to the frequency-integrated response of the modes (via Kramers-Krönig).

The real space fluctuating displacements δu_l associated with the variables $\delta P_1(\mathbf{q})$ and $\delta P_2(\mathbf{q})$ can be obtained starting from Eq. 4. For a monoatomic lattice one gets:

$$\delta u_l = (e/2\sqrt{N}) \sum_{\mathbf{q}} Q_{\mathbf{k}_i + \mathbf{q}} \exp\{i(\mathbf{k}_i + \mathbf{q}) \cdot \mathbf{R}_l\} + Q_{-\mathbf{k}_i + \mathbf{q}} \exp\{i(-\mathbf{k}_i + \mathbf{q}) \cdot \mathbf{R}_l\} \quad (25)$$

or using Eq. 23:

$$\delta u_l = (e/\sqrt{2N}) \sum_{\mathbf{q}} \{ \delta P_1(\mathbf{q}) \cos(\mathbf{k}_i \cdot \mathbf{R}_l) + \delta P_2(\mathbf{q}) \sin(\mathbf{k}_i \cdot \mathbf{R}_l) \} e^{i\mathbf{q} \cdot \mathbf{R}_l} \quad (26)$$

On the other hand by differentiating Eq. 4 near $\phi = 0$ we obtain:

$$\delta u_l = e \{ \delta \eta \cos(\mathbf{k}_i \cdot \mathbf{R}_l) - \eta \delta \phi \sin(\mathbf{k}_i \cdot \mathbf{R}_l) \} \quad (27)$$

Comparing Eqs. 26 and 27, the variable $\delta P_1(\mathbf{q})$ is identified as a long-wavelength amplitude fluctuation, while $\delta P_2(\mathbf{q})$ has the dimension of a phase fluctuation multiplied by the static amplitude η .

To summarize, Landau theory predicts a classic soft mode behavior for the amplitude branch (cf. Eq. 24b), while the phase branch appears as a temperature-independent acoustic-like branch (Eq. 24c), emanating from first-order satellite reflections.

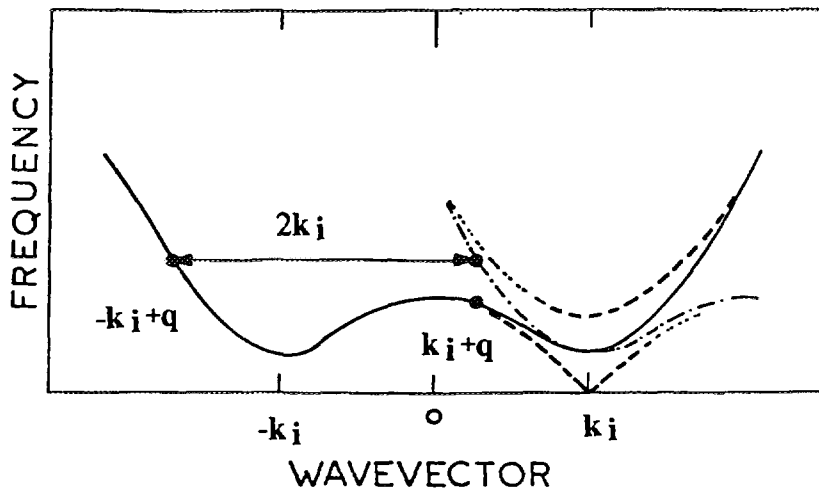


Fig. 2. Phase and amplitude branches (broken lines) as obtained from the diagonalisation of the interaction between $\pm k_i + q$ soft-mode normal coordinates: soft-mode dispersion curve: solid line; same shifted by $2k_i$: dash-dotted line.

Fig. 2 illustrates graphically the reconstruction of the soft mode dispersion near k_i arising from the diagonalisation of the bilinear interaction between Q_{k_i+q} and Q_{-k_i+q} , below T_i (last term in Eq. 21).

2.6. Damping

An important difference between phasons and true Goldstone modes, such as acoustic modes in ordinary crystals or magnons in isotropic magnets, lies in the lifetime of the phasons which remains finite as $q \rightarrow 0$. The damping arises from the fact that atomic motions involved in phase (or amplitude) fluctuations are *inhomogeneous* on a microscopic scale and are thus affected by ordinary anharmonic (i.e. dissipative) interactions [20, 26].

In practice one assumes a phason spectral response of the DHO type:

$$S_\phi(q, \omega) = (kT \Gamma_\phi / \pi) \{ [\omega^2 - \omega_\phi^2(q)]^2 + \omega^2 \Gamma_\phi^2 \}^{-1} \quad (28)$$

with $\omega_\phi^2(q) = \chi^{-1} T(q) = q \Lambda q$, as in Eq. 24c. The damping coefficient Γ_ϕ is slowly varying in q and comparable in magnitude to the soft mode damping coefficient above T_i . In the limit $q \rightarrow 0$, the phason response becomes approximately Lorentzian:

$$S_\phi(q, \omega) = (kT / \pi \Gamma_\phi) \{ \omega^2 + \gamma_\phi^2(q) \}^{-1} \quad (29)$$

with a q -dependent half-width given by:

$$\gamma_\phi(q) = q \Lambda q / \Gamma_\phi \quad (30)$$

Numerical estimates for Λ and Γ_ϕ yield values for $\gamma_\phi(q)$ in the range 10-100 MHz, for q values relevant to Brillouin scattering. This is comparable with the best attainable instrumental resolution. In a Brillouin scattering experiment much of the phason response will thus be hidden in the Rayleigh line. With neutron scattering it is essential to work on systems with low soft-mode damping and to select the q - and T -range judiciously (See Sect. 5).

3. Normal modes in modulated crystals.

3.1. General

The results obtained in the preceding section are limited in several respects. They refer to the renormalisation of the soft phonon branch in a neighborhood of the first order satellites at $\pm k_i$, where the quadratic expansion of the soft mode dispersion is assumed to be valid [Note that in Fig. 2 we consider the case $q \parallel k_i$. The case $q \perp k_i$ may be quite different if k_i lies along a two-fold symmetry axis, as is often the case. Then the even-order expansion of the soft-mode dispersion is valid by symmetry, and the degeneracy between Q_{ki+q} and Q_{-ki+q} holds without restrictions on the magnitude of $q \perp k_i$]. Furthermore Landau theory, as formulated above, is only applicable in the temperature range where the sinusoidal regime is valid.

There are at least two other (more general) lines of approach to the problem of the dynamics of modulated crystals. The first one is to make use of the superspace formalism, originally developed as a tool to handle the crystallography of quasiperiodic systems [27]. Its application to the dynamics of modulated crystals, as proposed by Janssen [28], will be outlined in Sects. 3.2 to 3.4 below.

The other approach consists in treating the incommensurate system as a high-order commensurate system, to which standard lattice-dynamical methods can be applied. Janssen and Tjon [17] have developed this approach with great success in the context of the DIFFOUR model and some of their results will be reviewed in Sect. 4 below.

3.2 The superspace approach

When the modulation periodicity is given in terms of a single pair of modulation wavevectors $\pm k_i$, the atomic positions are labeled as $R_{lj} + f_j(k_i, R_l + \phi)$, where $R_{lj} = R_l$

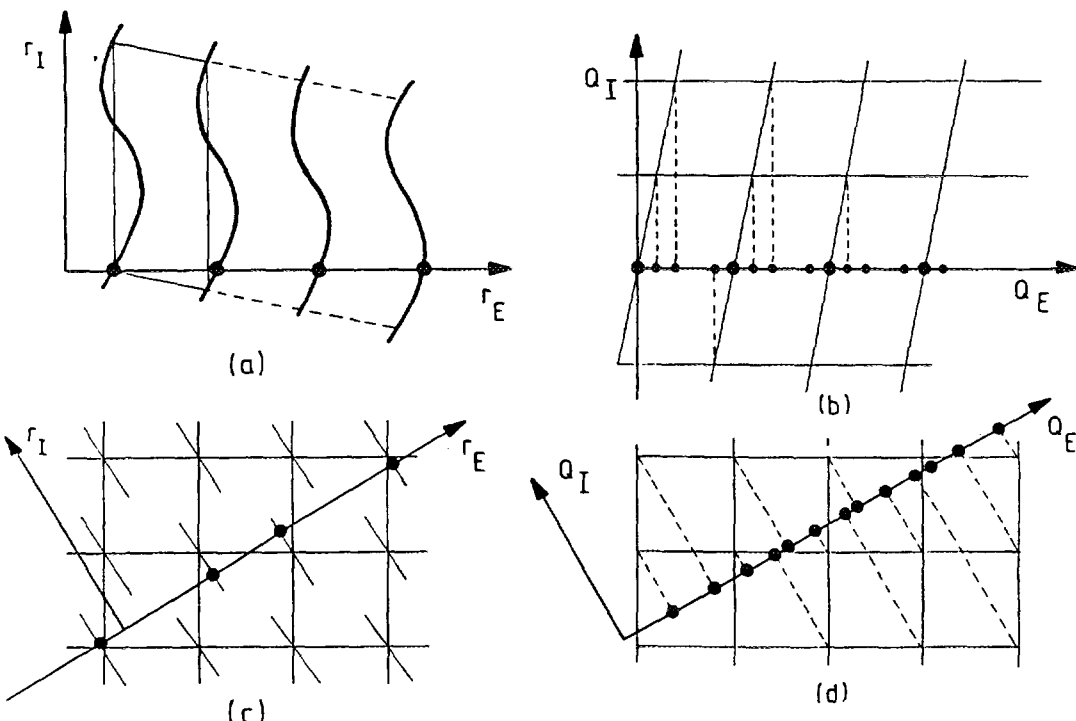


Fig. 3. Relationship between superspace periodicity and physical space quasiperiodicity: (a) displacively modulated 1D crystal in direct space; (b) same in reciprocal space; (c) 1D quasicrystal in direct space; (d) same in reciprocal space.

$+R_j$ refers to the unmodulated positions and f_j is periodic with period 2π ($j=1,\dots,s$). A particular physical system is characterised by a specific value of the phase variable, say $\phi=0$. Each such system, considered alone, is nonperiodic. However there are ways in which these systems can be "arranged" in order to define a new collective entity, a super-system, which will have periodicity.

This is sketched in Fig. 3a, for a physical system consisting in a 1D monoatomic modulated crystal. The horizontal axis, labeled r_E , is physical space and the atomic positions are shown as closed circles. The vertical axis, labeled r_I , corresponds to the ϕ -axis. One can think of the picture as showing the set of all possible physical systems, corresponding to all possible values of the variable ϕ , stacked on top of each other along the ϕ -axis. The wavy lines are the atomic trajectories as the variable ϕ is changed continuously. These trajectories generate a 2D object which is clearly *periodic* in 2D space. The corresponding reciprocal lattice is shown in Fig. 3b. The projections of the nodes of the 2D rec. lattice onto 1D physical rec. space (Q_E axis in Fig. 3b), generate the set of fundamental and satellite reflections characteristic of the 1D modulated crystal.

This simple example illustrates the link between the periodic superspace object and its physical quasiperiodic counterpart: *intersection in direct space, projection in Fourier space*. The concept of superspace periodicity and superspace symmetry has proved useful in the context of modulated crystals, composite systems and quasicrystals. It enables one to deal with commensurate and incommensurate systems on the same footing and to make use of standard crystallographic and group-theoretical methods in both cases[29, 30].

Similarly, one may obtain the normal modes of the modulated crystal as the restriction to 3D physical space of the normal modes of the 4D periodic structure ($3+d$ in the general case of Eq. 1). Because of lattice periodicity the displacement field associated with the normal modes of the higher-dimensional structure may be written as *Bloch waves*, i.e. for $d=1$:

$$u^k_{lj\phi} = M_j^{-1/2} \exp(-ik \cdot R_l) U^k_{j(\phi+k_i \cdot R_l)} \quad (31)$$

where U^k_j is periodic:

$$U^k_{j(\phi)} = \sum_m A^k_{jm} \exp(im\phi) \quad (32)$$

As shown by Janssen [28], both vectors u and k can be taken to be parallel to 3D physical space without loss of generality. In particular k is restricted to the first Brillouin zone of the basic lattice. The atomic displacements of the modulated crystal are obtained by setting $\phi=0$ in Eq. 31:

$$u^k_{lj0} = M_j^{-1/2} \sum_m \exp\{(-ik + m k_i) \cdot R_l\} A^k_{jm} \quad (33)$$

Eq. 33 suggests that an excitation of nominal wavevector k can be described as a linear superposition of normal modes of the basic structure, with wavevectors k , $k \pm k_i$, $k \pm 2k_i, \dots$. As such it can participate in inelastic scattering processes at $K = G - k$, $G - k \pm k_i$, $G - k \pm 2k_i, \dots$ with scattering strengths proportional to the appropriate eigenvector component A^k_{jm} . Physically, this mixing process can be viewed as arising from Bragg scattering of the phonons of the basic structure by the periodic potential of the modulation.

3.3. Brillouin zones, dispersion curves and gaps

In an ordinary crystal normal modes are characterised by a wavevector defined in the first Brillouin zone and a branch index $v = 1, 2, \dots, 3s$. The corresponding eigenfrequencies generate dispersion curves $\omega_v(\mathbf{k})$ with gaps at the Brillouin zone boundaries. In an inelastic scattering experiment performed at a fixed momentum transfer \mathbf{K} , the probe, say, the neutron beam, interacts with excitations of wavevector \mathbf{k} defined through:

$$\mathbf{K} + \mathbf{k} = \mathbf{G} \quad (34)$$

where \mathbf{G} is a reciprocal lattice vector.

In an incommensurately modulated crystal the 3D Brillouin zone has collapsed to zero volume since an infinite number of points within the basic structure's Brillouin zone have become "zone centers". Due to the infinite number of zone boundary points which have thus been introduced, an infinite number of frequency gaps should in principle appear in the excitation spectrum.

In practice, however, most of the new zone centers correspond to high-order satellite peaks whose intensities, for small modulation amplitudes, converge rapidly to zero. The frequency gaps at the corresponding zone boundaries will scale accordingly. It is thus possible to draw the dispersion of the new normal modes in the Brillouin zone of the basic structure. The wavevector associated with each new eigenfrequency is defined by continuity, using the correspondence between normal modes of the modulated and basic structures. The new dispersion curves should look essentially continuous, except for a few gaps at low-order zone-boundary points, given by:

$$\mathbf{k}_{\mathbf{G},m} = 1/2 (\mathbf{G} + m \mathbf{k}_i) \quad (m = 0, \pm 1, \pm 2, \dots) \quad (35)$$

The situation described in Fig. 2 refers to the frequency gap at $\mathbf{k} = \mathbf{k}_0, 2 = \mathbf{k}_i$. Note that strictly speaking (i.e. in order to conserve the same number of modes in the modulated and basic structures) the phason dispersion should be restricted to the range $|\mathbf{k}| < |\mathbf{k}_i|$ ($|\mathbf{k}| > |\mathbf{k}_i|$ for the amplitudon branch). The gap is thus equal to the difference between amplitudon and phason frequencies at \mathbf{k}_i .

Experimentally, one does not expect the amplitudon (phason) response to switch on (off) abruptly as \mathbf{k} goes through \mathbf{k}_i . Therefore in Fig. 2 the phason dispersion was not stopped abruptly at \mathbf{k}_i , but was shown to vanish progressively for \mathbf{k} increasing beyond \mathbf{k}_i . The same applies to the amplitudon branch for \mathbf{k} decreasing below \mathbf{k}_i .

The phase mode observed for $\mathbf{k} < \mathbf{k}_i$ corresponds to an excitation of nominal wavevector \mathbf{k} observed through its fundamental component ($A_{jm=0}^k$ in Eq. 33), while for $\mathbf{k} > \mathbf{k}_i$, the phase mode corresponds to an excitation of nominal wavevector $\mathbf{k} - 2\mathbf{k}_i$, seen near \mathbf{k}_i through its $m=2$ component. Both modes are linear combinations of the original soft-mode coordinates $Q_{\mathbf{k}_i+\mathbf{q}}$ and $Q_{-\mathbf{k}_i+\mathbf{q}}$, and are observed near \mathbf{k}_i through their $Q_{\mathbf{k}_i+\mathbf{q}}$ component.

3.4. Inelastic scattering channels

In an ordinary crystal the scattering strength of a phonon of wavevector \mathbf{k} and eigenvector $\mathbf{e}(\mathbf{k})$, in a scattering process characterised by a momentum transfer $\mathbf{K} = \mathbf{G} - \mathbf{k}$, is given by the squared modulus of the one-phonon inelastic structure factor:

$$H_{\mathbf{k}}(\mathbf{K}) = \sum_j b_j M_j^{-1/2} e^{-W_j(\mathbf{K})} e^{i\mathbf{K} \cdot \mathbf{R}_j} \{ \mathbf{K} \cdot \mathbf{e}(j;\mathbf{k}) \} \quad (36)$$

Eq. 36 can be generalised to the case of an excitation in a modulated crystal [31]. For an excitation of nominal wavevector \mathbf{k} and a momentum transfer $\mathbf{K} = \mathbf{G} - \mathbf{k} - n\mathbf{k}_i$, one gets:

$$H_k(K) = \sum_j b_j M_j^{-1/2} e^{-W_j(K)} e^{iK \cdot R_j} \sum_m \{K \cdot A_{jm}^k\} B_{j;n-m}(K) \quad (37)$$

where the B's are related to the Fourier coefficients of the static modulation function:

$$e^{iK \cdot f_j(\phi)} = \sum_n B_{jn}(K) e^{in\phi} \quad (38)$$

In the sinusoidal case the B's correspond to Bessel functions, as in Eq. 8.

The last summation in Eq. 37 above, shows that the excitation of wavevector k contributes at $K=G-k-nk_i$ through several channels. The term $m=n$ yields a contribution proportional to A_{jn}^k , as expected. But there are a number of other channels corresponding to other values of m . It can be shown that the $n+1$ terms corresponding to $m=0, 1, \dots, n$ all scale as the n^{th} power of the modulation amplitude and are thus comparable in magnitude.

The origin of these additional channels is purely geometrical. They arise from the fact that the fluctuating displacements are attached to the *modulated* atomic positions, whereas Eq. 37 is written in terms of the unmodulated positions R_j . When going from the unmodulated case of Eq. 36 to the modulated case of Eq. 37, the phase factor $\exp(iK \cdot R_j)$ in Eq. 36 becomes:

$$\exp\{iK \cdot [R_j + f_j(k_i, R_j) + \phi]\} = \exp(iK \cdot R_j) \cdot \exp\{iK \cdot f_j(k_i, R_j) + \phi\} \quad (39)$$

and the Fourier expansion of the last exponential factor introduces the summation over the B's appearing in the final result.

Experimentally, the presence of the additional "parasitic" channels is a major source of complication. In particular they are responsible for the detection of long-wavelength *acoustic* modes near satellite reflections, which must then be distinguished from *acoustic-like* phasons (see Sects. 4 and 5 below).

4. A commensurate model.

4.1. The DIFFOUR model: static aspects

The vibrational spectrum of incommensurate crystals can be modeled very effectively using commensurate approximants. The discrete frustrated ϕ^4 model (DIFFOUR) has proved quite useful in this context [17], because it is well suited to simulate displacive phase transitions. The model consists in a linear chain of identical particles, embedded in a 3D crystal. The particles interact along the chain via nonlinear first-neighbor and linear second- and third-neighbor interactions. Denoting the position of the particles by $a + u_n$, where a is the lattice constant, the potential energy reads:

$$V = \sum_n \alpha/2(u_n - u_{n-1})^2 + \gamma/4(u_n - u_{n-1})^4 + \beta/2(u_n - u_{n-2})^2 + \delta/2(u_n - u_{n-3})^2 \quad (40)$$

The model always has the original equidistant configuration ($u_n = 0$) as a solution with extremal energy. The harmonic oscillations around this configuration have frequency given by:

$$m \omega_k^2 = 4 \{ \alpha \sin^2(k/2) + \beta \sin^2 k + \delta \sin^2(3k/2) \} \quad (41)$$

For fixed β and δ all frequencies are real for α greater than a critical value α_i , but for $\alpha = \alpha_i$ the mode at the minimum of the dispersion becomes unstable. If one considers α as T-dependent, this is a *soft mode*. For $-6 < \beta/\delta < 2$ and $\delta > 0$, the instability occurs with wavevector k_i given by:

$$\cos k_i a = -(\beta + 2\delta)/4\delta \quad (42)$$

which is, generally, incommensurate. Below α_i the ground-state is modulated and generally incommensurate.

The phase diagram, i.e. the ground-state configuration as a function of the parameters, and the structure of the solutions have been studied in detail. In general, most of the properties of the model agree well with the picture arising from the phenomenological theory. There is a soft-mode leading to an instability at a wavevector k_i given by Eq. 42. Below the transition there is a region where the modulation is to a good approximation sinusoidal with an amplitude that varies as $(\alpha_i - \alpha)^{1/2}$. For lower values of α there is a lock-in transition, and in the region close to this transition the modulated structure may be described as consisting of nearly commensurate domains separated by discommensurations.

The same potential energy can also be written in terms of the difference variables $x_n = u_n - u_{n-1}$:

$$V = \sum_n A/2 x_n^2 + C/4 x_n^4 + B x_n x_{n-1} + D x_n x_{n-2} \quad (43)$$

where $A = \alpha + 2\beta + 3\delta$; $C = \gamma$; $B = \beta + 2\delta$; $D = \delta$. For negative values of A this is the potential energy for a chain of particles, each in a double well potential, with harmonic first- and second-neighbor interactions.

4.2. Dynamics in the commensurate approximation

Both versions of the model can be analysed for vibrations around the modulated configurations. The first version is translationally invariant and exhibits an acoustic branch while the second version does not. In practice the model parameters are tuned in order to yield a high-order *commensurate* ground-state. The (finite) set of linearised coupled equations of motion can then be solved by standard numerical techniques.

For sufficiently high commensurabilities, i.e. $k_i = 2\pi L/N$ with $N > 10$, one finds that the vibrational spectrum closely approximates that of the incommensurate system. In particular, the phason frequency is found to *vanish* within computational accuracy. Fig. 4a shows the eigenfrequency spectrum, plotted in the Brillouin zone of the unmodulated chain, for the non-translationally invariant version of the model (Eq. 43) and for parameter values yielding a sinusoidal ground-state with $k_i/2\pi = 6/37$. The quantities plotted are the A_{km} coefficients (cf. Eq. 33) which are obtained by Fourier analysis of the commensurate eigenvectors. Specifically, the horizontal bars in the figure have lengths proportional to $|A_{km}|$ and are centred on $(k + m k_i; \omega_k)$ for each eigenfrequency ω_k and all values of m for which the values of the coefficients $|A_{km}|$ are significant. The same plot for the unmodulated chain would show a single optic branch with a minimum at $k_i/2\pi = 6/37$ and all bars would be of same length. The spectrum reconstruction near k_i is seen to be in good qualitative agreement with the predictions of the phenomenological theory (Fig. 2). Note also the small gap at $k_{1,-2} = 25/74 = 0.338$ (cf. Eq. 35). A similar result is shown in Fig. 4b for the translationally-invariant version of the model, also in the sinusoidal regime, with $k_i/2\pi = 8/27$.

Fig 4c shows the spectrum obtained for the same parameter values as in Fig. 4a, except for a lower value of α , i.e. for a lower temperature. The modulation is now much more developed and far from sinusoidal. The system looks more like a sequence of domains with the stable commensurate structure $k_c = 6/36 = 1/6$, separated by discommensurations. Each eigenfrequency appears now at several locations in the zone, reflecting the fact that the $|A_{km}|$'s are significant for a number of different m values.

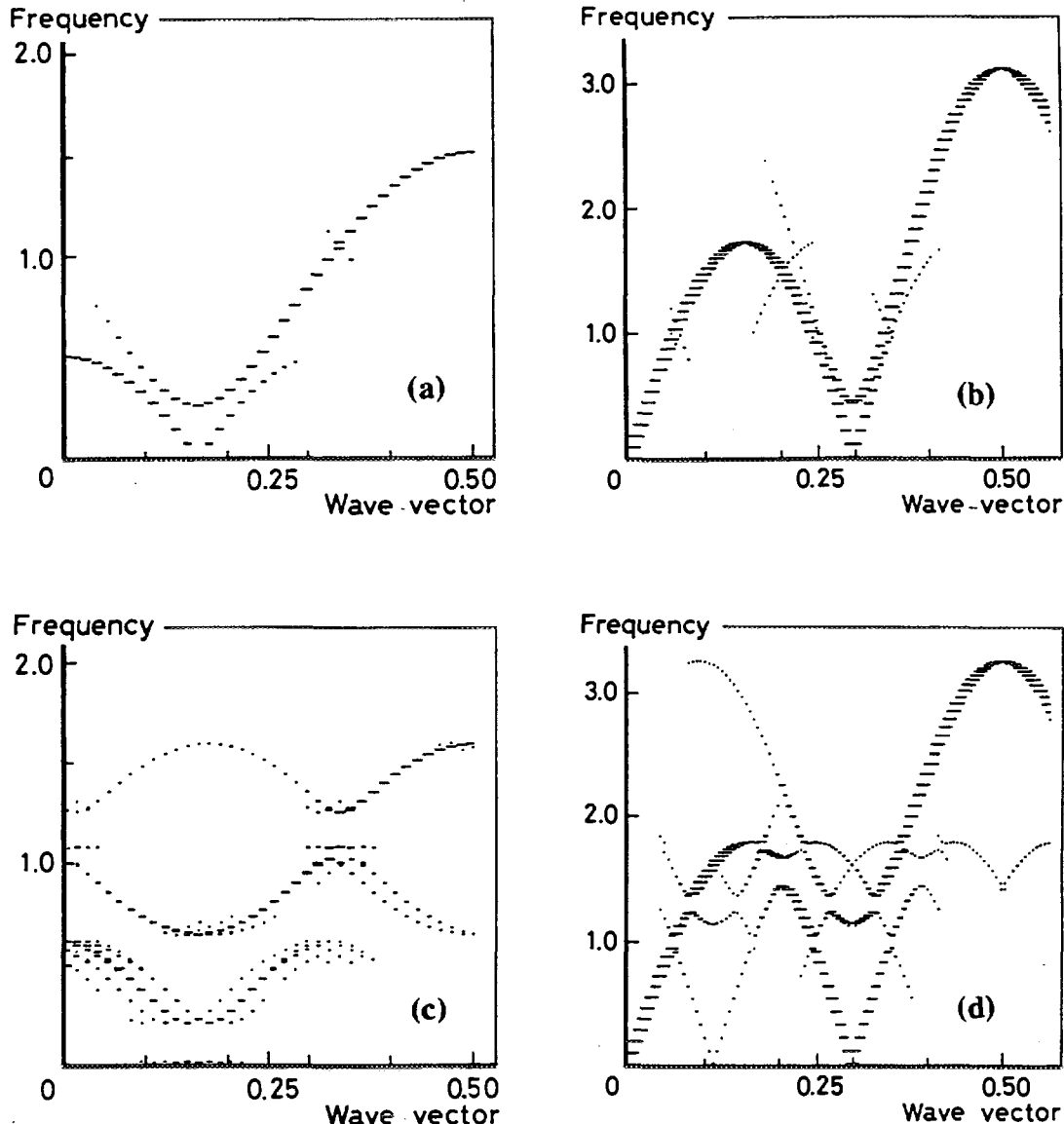


Fig. 4. Eigenvector Fourier components A_m^k with DIFFOUR : (a) and (c) : non-translationally invariant version; (b) and (d) : translationally invariant version; (a) and (b) : sinusoidal regime; (c) and (d) : discommensuration regime. After Janssen and Currat [57].

The bars close to the horizontal axis in the region $0.1 < k/2\pi < 0.2$, correspond to vibrations of the discommensuration lattice. These vibrations are pinned due to lattice discreteness. There is a large gap above this band and the next band starts at about 0.22 in reduced frequency units. This latter frequency corresponds to the *commensurate phason* frequency, i.e. to oscillations of the phase of the modulation in the commensurate 1/6 domains. These regions are pinned by the 1/6 commensurability potential, which is strong on the present energy scale, as attested by the significant stability range of the commensurate 1/6 phase [32]. The amplitudon band starts at about 0.63 and the gap at $k_{1,-2} = 0.338 * 2\pi$ is much more apparent than in Fig. 4a.

Fig. 4d shows the same system as in Fig. 4b but at lower temperature. There the commensurability effects (towards 1/3 in that case) are not as marked as in Fig. 4c, although a small phason gap is already present at $k_i = 8/27 * 2\pi$.

4.3. Discussion

The predictions of the present model are a very useful guide for the interpretation of inelastic neutron spectra. One should keep in mind, however, that the spectra shown in Fig. 4a-d correspond to *only one* of the possible scattering channels: namely, the $m = n$ term in Eq. 37. In that sense, they do not reflect the full complexity of the experimental situation. In the case shown in Fig. 4d, for example, one would expect to observe an acoustic branch originating at the first-order satellite position, *in addition* to the phason branch ($m = 0$ term in Eq. 37 with $n = 1$). The strength of this acoustic branch will be controlled by the magnitude of the coefficients B_1 's and hence by the magnitude of the satellite elastic structure factor itself. It should become visible at large enough modulation amplitudes.

Another shortcoming of the model is the absence of a third-order anharmonic term in the potential energy: Eqs. 40 and 43. This is a serious oversimplification, since such terms, once linearised, can induce mixing between k and $k + k_i$ modes, e.g. between long-wavelength acoustic phonons and long-wavelength phasons. The net result of such a mixing process is to blur the distinction between the two types of excitations. We shall see in the following Sections how these difficulties can be addressed experimentally.

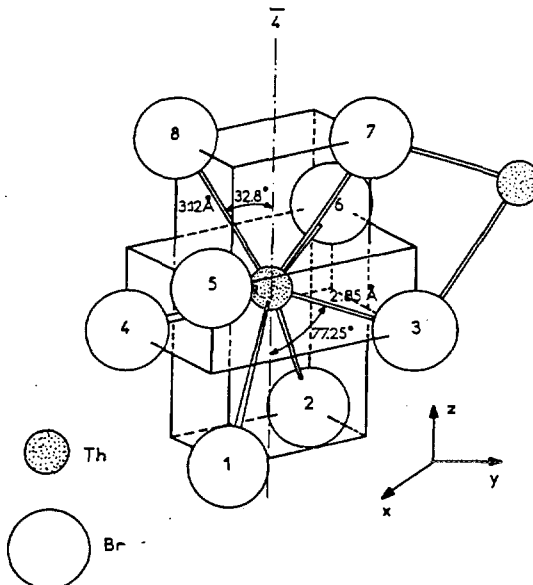
5. Inelastic neutron scattering results

5.1. $\beta\text{-ThBr}_4$

The structure of $\beta\text{-ThBr}_4$ at room temperature is shown in Fig. 5.

Fig. 5. Primitive unit cell of $\beta\text{-ThBr}_4$.

The two Th^{4+} ions are located at $(0,0,0)$ and $(0,1/2,1/4)$. The conventional body-centred tetragonal cell ($a = b = 8.93 \text{ \AA}$; $c = 7.96 \text{ \AA}$) contains 4 formula units. The space group is D_{4h}^{19} and the primitive cell contains two formula units. The 8 bromine ions are located at equivalent sites and can be chosen in such a way as to make up the first and second coordination shells of the Th^{4+} ion at the origin, as shown in the figure. The symmetry of the thorium site is D_{2d} ($42m$) and the inversion center is located halfway between the two thorium ions. After Bernard et al. [35].



Raman work [33] followed by neutron diffraction studies [34, 35, 36] has revealed the occurrence of a structural phase transition at $T_i = 95 \text{ K}$ towards a modulated structure with modulation wavevector:

$$\mathbf{k}_i = \zeta_i \mathbf{c}^* = 0.310 \pm 0.005 \text{ c}^* \quad (44)$$

The displacive nature of the transition was confirmed by the observation of a soft phonon branch by INS as shown in Fig. 6. The symmetry representation of the soft branch ($T > T_i$) and the detailed description of the modulated ionic displacements ($T < T_i$) were established on the basis of first-order satellite intensity measurements:

$$u_{lj} = \eta \{ \cos\theta e_1(j) \cos(k_i \cdot R_{lj} + \phi) + \sin\theta e_2(j) \sin(k_i \cdot R_{lj} + \phi) \} \quad (45)$$

where e_1 and e_2 are two normalised basis vectors with B_{1u} and B_{2g} symmetry respectively; ϕ is an arbitrary phase angle; the index j runs over the 8 bromine sites, as labeled in Fig. 5. Figure 7 illustrates the ionic displacements involved in the e_1 and e_2 components: rotations and twists of the bromine shells about the $\bar{4}$ axis. Their relative weights in the soft-mode eigenvector is determined by the value of the mixing angle θ ($\theta \approx 20^\circ$).

Fig.6. Dispersion curves for the longitudinal acoustic (LA), transverse acoustic (TA) and soft optic modes, propagating along $[0 0 \zeta]$: (O) 300 K
(▲) 150 K; (□) 120 K; (●) 101 K; $T_i = 95$ K.

After Bernard et al. [35].

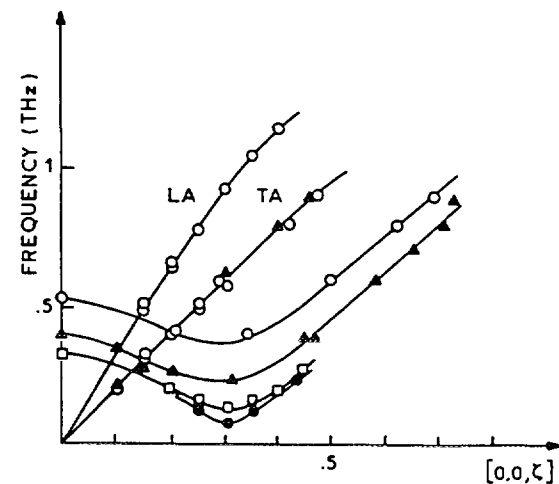
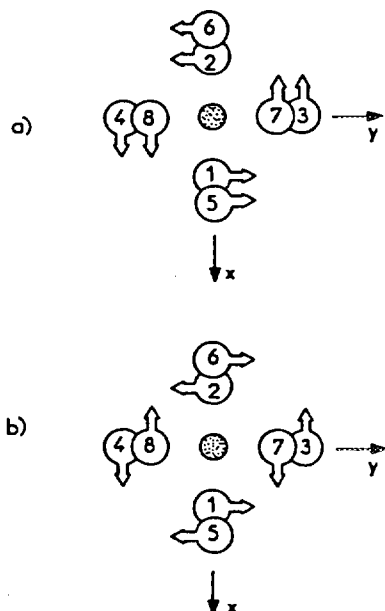


Fig. 7. Projection of unit cell along $\bar{4}$ -axis showing:
(a) the B_{1u} and (b) the B_{2g} components of the soft-mode eigenvectors. All arrows have equal lengths and correspond to equal amplitudes for the 8 Br^- ions. The Th^{4+} ions remain at rest. After Bernard et al. [35].

The only temperature-dependent quantity in Eq. 45 is the modulation amplitude η , which grows from $\eta = 0$ at T_i to $\eta \approx 0.02$ at 0 K, where $a = 8.93$ Å is the cell edge. The value of the modulation wavevector, ζ_i in Eq. 44, remains constant. Even at low temperatures no significant higher-order satellite intensities are observed. Hence the modulated displacements can be described as a small perturbation on the basic structure and the sinusoidal approximation of Eq. 45 should hold throughout.

This is confirmed by the detailed analysis of the crystal-field transitions of dilute U⁴⁺ impurities, substituting for Th⁴⁺, which indicates that a sinusoidal model for the crystal-field-level modulations is adequate [37, 38].

Fig. 8 shows the INS spectra observed near the strong $(2 3 1-\zeta_j)$ satellite reflection at $T = 81$ K = $T_i - 14$ K. The data were collected using the cold-source three-axis spectrometer IN12, operated in the up-scattering mode with a fixed incident neutron energy of 4.9 meV. The instrumental vanadium-resolution was 25 GHz.

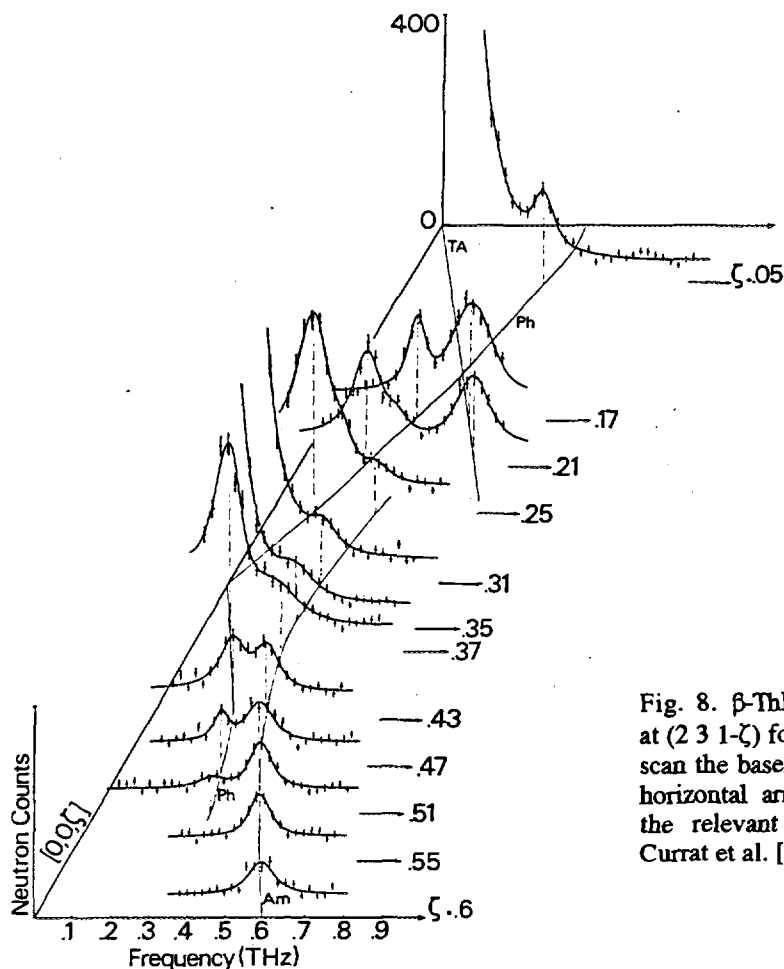


Fig. 8. β -ThBr₄: constant- q scans at (2 3 1- ζ) for $T = 81$ K. For each scan the baseline is indicated by a horizontal arrow pointing toward the relevant value of ζ . After Currat et al. [36].

Three excitation branches are observed:

- an acoustic-like branch originating at the (2 3 0.69) satellite position ($\zeta = 0.31$ in the figure).
- an optic-like branch with a minimum at the satellite position
- a transverse acoustic (TA) branch originating at the (2 3 1) fundamental reflection.

The slope of the first branch is close to that of the TA mode. However its intensity is much larger than expected for an acoustic mode near a first-order satellite reflection. From Eq. 37 with $n = 1$, the inelastic structure factor for a TA mode of wavevector $k \ll k_i$ at $K = G - k_i - k$ is written as (to leading order in η):

$$H_{k,ac}(G - k_i - k) = \sum_j b_j M_j^{-1/2} e^{-W_j(K)} e^{iK \cdot R_j} \times \{ (K \cdot A_{kj,ac}) B_{1j}(K) + (K \cdot A_{kj,ac}) B_{0j}(K) \} \quad (46)$$

The second term in Eq. 46 reflects the modulation-induced mixing between the TA mode (k, ac) and the soft-mode coordinate Q_{k_i+k} . However for $k \parallel k_i \parallel c^*$ this mixing is forbidden due to rotational selection rules [34]. Hence, in that case, Eq. 46 reduces to:

$$\begin{aligned} H_{k,ac}(G - k_i - k) &= \sum_j b_j M_j^{-1/2} e^{-W_j(K)} e^{iK \cdot R_j} (K \cdot A_{kj,ac}) B_{1j}(K) \\ &= (K \cdot \alpha_{k,ac}) F_1(G - k_i) \end{aligned} \quad (47)$$

where, for a long-wavelength acoustic mode, the mass-weighted eigenvector $M_j^{-1/2} A_{k,ac}^{(j)}$ can be replaced by a j -independent polarisation vector $\alpha_{k,ac}$. F_1 is the elastic structure factor of the satellite at $K = G - k_j$. With the help of Eq. 47 one readily shows that:

$$|H_{k,ac}(G - k_j - k)| / |H_{k,ac}(G - k)| = |F_1(G - k_j)| / |F_0(G)| \quad (48)$$

From the observed intensity of the TA branch near (2 3 1) and the known intensity ratio of the (2 3 1) and (2 3 0.69) Bragg intensities, one concludes that the acoustic-like dispersion originating at (2 3 0.69) is approximately two orders of magnitude too intense to be of acoustic origin, and is thus identified as the phason branch.

Similarly the optic branch is identified as the amplitude mode. Its observed frequency at $\zeta=0.31$ is consistent with the frequency of the $q=0$ amplitude mode, as deduced from the Raman data of Hubert et al. [33].

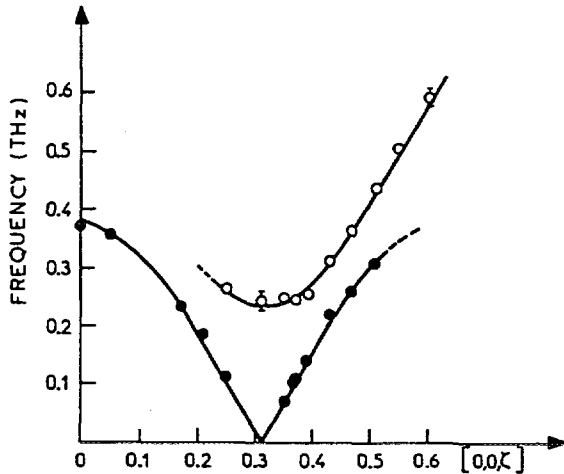


Fig. 9. Phase (●) and amplitude (○) modes in β -ThBr₄ at 81 K. The plotted frequencies are obtained from a damped harmonic oscillator fit of the spectra in Fig. 8. After Currat et al. [36].

The analysis of the spectra in Fig. 8 using DHO response functions yields the quasi-harmonic frequencies of the phase and amplitude modes, as shown in Fig. 9. Note the analogy with the behavior shown in Fig. 4a. The fitting procedure also yields the values of the mode damping coefficients. Values in the range 50–90 GHz are found for both the amplitude and phase modes, with no detectable trend as a function of wavevector. The phason velocity is in good agreement with the curvature of the soft-mode dispersion near its minimum above T_i , as required from Eq. 24c. The experimental points in Fig. 9 give no indication of a phason gap at $q=0$ ($\zeta=0.31$). If such a gap exists, its magnitude may not exceed 40 GHz.

Similar spectra at lower temperatures show a rapid renormalisation of the amplitude mode upon cooling while the phase mode becomes sharper, particularly at small wavevectors, but its integrated intensity, corrected for the effect of thermal population, remains essentially constant.

Most of the above observations are consistent with the predictions of the phenomenological theory and of model calculations, in the sinusoidal regime.

5.2. Deuterated biphenyl (C₁₂D₁₀)

Fig. 10 shows the room-temperature structure of biphenyl (phase I). As already mentioned, this is one of the few systems where the competing interactions which lead to the incommensurate state have been identified [12, 37].

The modulated variable is the torsional angle (ϕ in Fig. 10a) between the molecular phenyl rings. There are in fact two successive modulated phases (II and III), corresponding to wavevectors of the form:

$$k_I = \begin{cases} \pm(\delta_a a^* - \delta_c c^*) \pm (1-\delta_b)b^*/2 & T_{II} < T < T_I \\ \pm(1-\delta_b)b^*/2 & T < T_{II} \end{cases} \quad (49)$$

for phases II and III respectively. The temperature dependence of the quantities δ_a , δ_b , δ_c is shown in Fig. 11, for the deuterated compound.

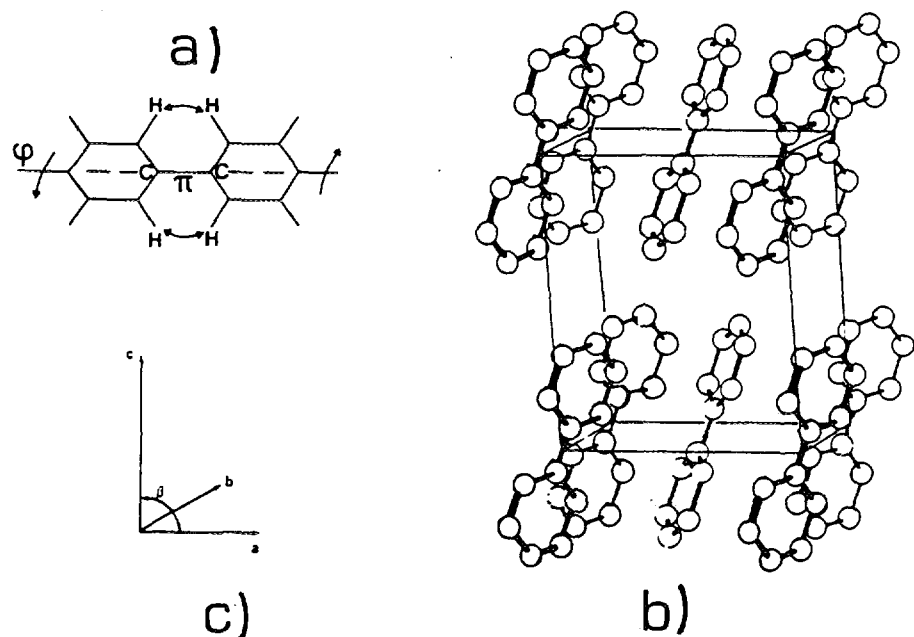


Fig. 10. Structure of biphenyl in phase I: (a) The molecule and its torsional angle φ due to ortho-hydrogen repulsion; (b) The $P2_1/a$ unit cell; (c) The crystallographic axes orientation ($a = 8.11 \text{ \AA}$; $b = 5.56 \text{ \AA}$; $c = 13.61 \text{ \AA}$; $\beta = 92^\circ$). After Cailleau [38].

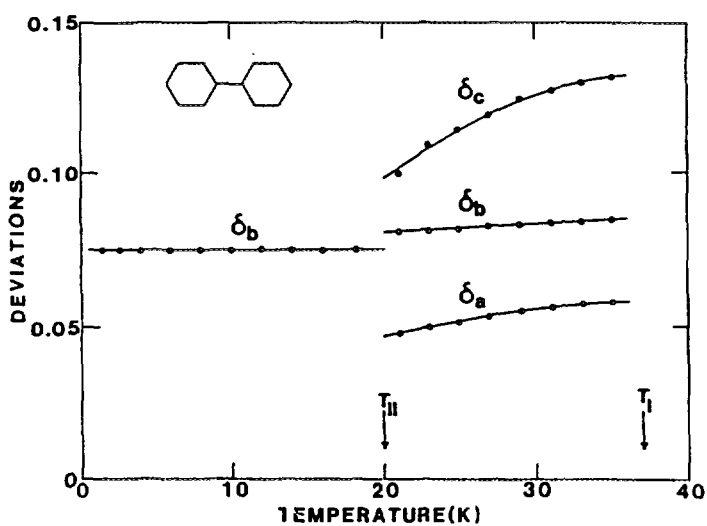


Fig. 11. Temperature dependence of the components of the modulation wavevector:

$$k_I = \pm(\delta_a a^* - \delta_c c^*) \pm (1-\delta_b)b^*/2$$

After Cailleau et al. [39].

In phase II the star of \mathbf{k}_I has four arms, corresponding to a 4-component order parameter and a superspace dimensionality of $3 + 2 = 5$. As far as INS is concerned, the situation is complex, since, in principle, two phason branches and two amplitudon branches can be simultaneously observed.

Studies in the partially commensurate phase III are comparatively much simpler. Also the lower temperature range considerably reduces the mode linewidths.

Fig. 12 shows the dispersion of the soft-phonon branch along the two-fold axis \mathbf{b}^* in phase I. The true frequency minimum is slightly displaced from the high-symmetry direction. The soft-mode linewidth is in the range 100–150 GHz near T_I (as compared to ≈ 70 GHz in the case of $\beta\text{-ThBr}_4$).

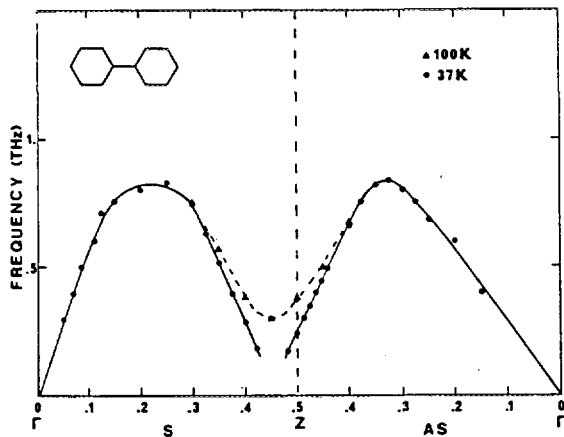


Fig. 12. Dispersion of the soft phonon branches along the \mathbf{b}^* direction in an extended zone representation. The branches are, respectively, symmetric (S) and anti-symmetric (AS) with respect to the 2_1 screw axis. They are pairwise degenerate at the zone boundary Z-point (Lifshitz invariant); (\blacktriangle) 100 K and (\bullet) 37 K.
After Cailleau [38].

Inelastic spectra obtained in phase III near a strong first-order satellite reflection are shown in Fig. 13, where a propagating excitation is clearly seen. The corresponding dispersion relation is plotted in Fig. 14, as a function of reduced wavevector along \mathbf{a}^* . The observed slope is substantially lower than the slope of the lowest acoustic mode, as obtained from Brillouin [41] and neutron scattering measurements [38] in that temperature range: the distinction between phase and acoustic modes is here straightforward. The amplitude branch is already too far up in frequency at 10 K and is not observable in the above measurements.

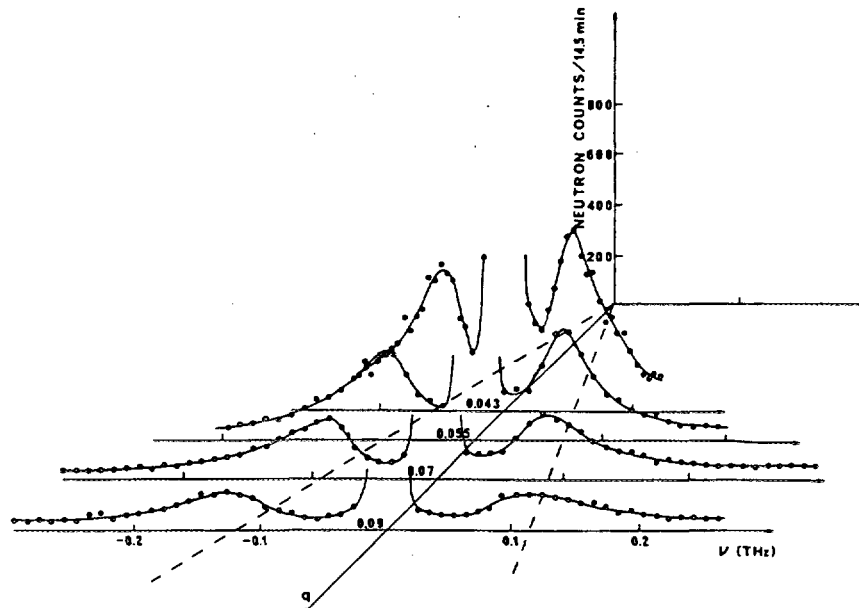


Fig. 13. Constant- q scans near the satellite reflection ($2 \frac{1}{2}(1+\delta_b) 0$) for several reduced wavevectors along \mathbf{a}^* , at $T = 10$ K (phase III). After Cailleau et al. [40].

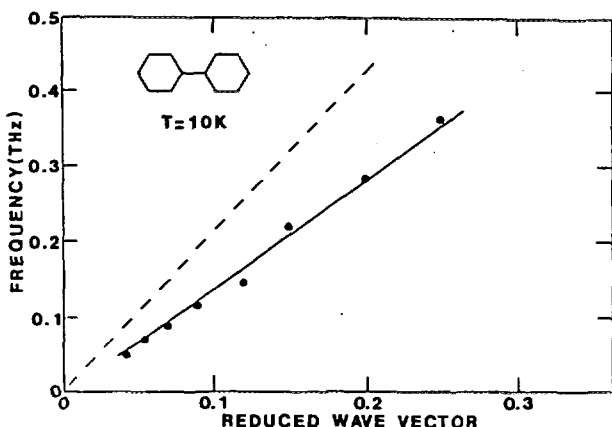


Fig. 14. Phase-mode dispersion along the a^* direction in phase III of deuterated biphenyl. The slope of the lowest acoustic mode is shown as a broken line. After Cailleau [38].

The intermolecular interactions which favor a coplanar molecular configuration, as in phase I, can be enhanced by hydrostatic pressure. Fig. 15 shows the (P,T) phase diagram for deuterated biphenyl, as deduced from neutron diffraction data [42]: as expected, the modulated phases II and III are progressively destabilised with increasing pressure.

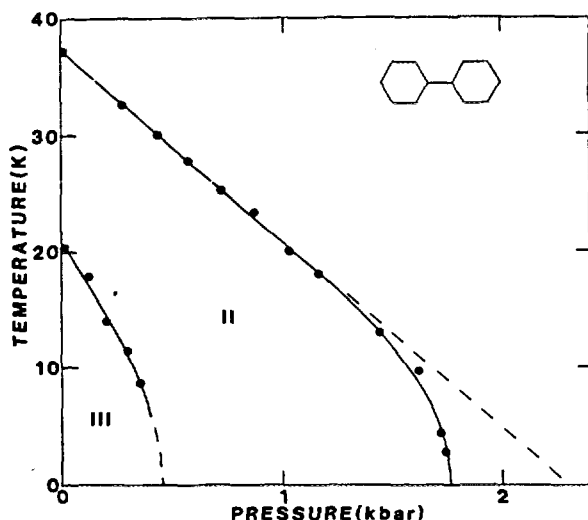


Fig. 15. Pressure-temperature phase diagram of deuterated biphenyl. After Cailleau et al. [42].

Cailleau and cow. [39] have taken advantage of this situation to study the low-frequency dynamics in all three phases, at low temperature (3K) where damping effects can be further reduced. Below the critical pressure separating phases I and II, the splitting of the soft mode into phason- and amplitudon-like excitations could be observed [43, 44].

5.3. Potassium Selenate (K_2SeO_4)

As the prototype of the A_2BX_4 family, K_2SeO_4 is one of the best studied dielectric materials exhibiting an incommensurate phase [45]. At room temperature this compound has orthorhombic symmetry ($Pnam$ - D_{2h}^{16}) with four formula units per cell. At $T_i = 129$ K, it undergoes a continuous transition towards a modulated state with modulation wavevector:

$$k\delta = 1/3(1-\delta)a^* \quad (50)$$

The incommensurability parameter δ is temperature-dependent and vanishes on approaching $T_C = 94$ K, leading to a commensurate 3a superstructure below T_C .

INS measurements [46, 47] indicate that the transition at T_i is displacive, as seen in Fig. 16. The microscopic lattice-dynamical origin of the instability has been discussed by Haque and Hardy [48] and Bussmann-Holder et al. [49].

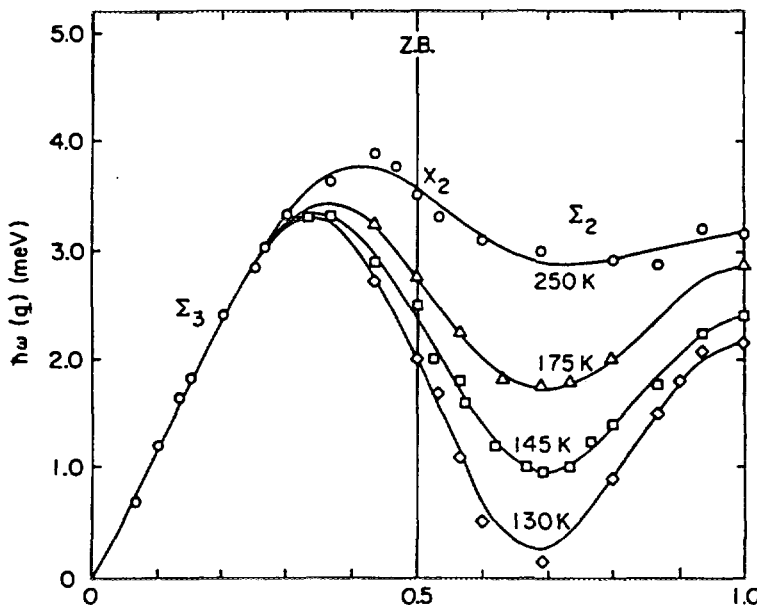


Fig. 16. Soft phonon dispersion in K_2SeO_4 (extended zone scheme). After Axe et al. [47].

A detailed x-ray diffraction study by Yamada and Ikeda [50] indicates that at 113 K the modulated ionic displacements are adequately described in a quasi-sinusoidal approximation. Near T_C , however, a number of experimental results [51-53] favor a description in terms of discommensurations.

Fig. 17 shows the expected temperature behavior for the $k = \pm k_\delta$ soft modes: in a simple sinusoidal model, the amplitudon frequency ω_η renormalises upwards while the phason frequency ω_ϕ remains at zero frequency until T_C .

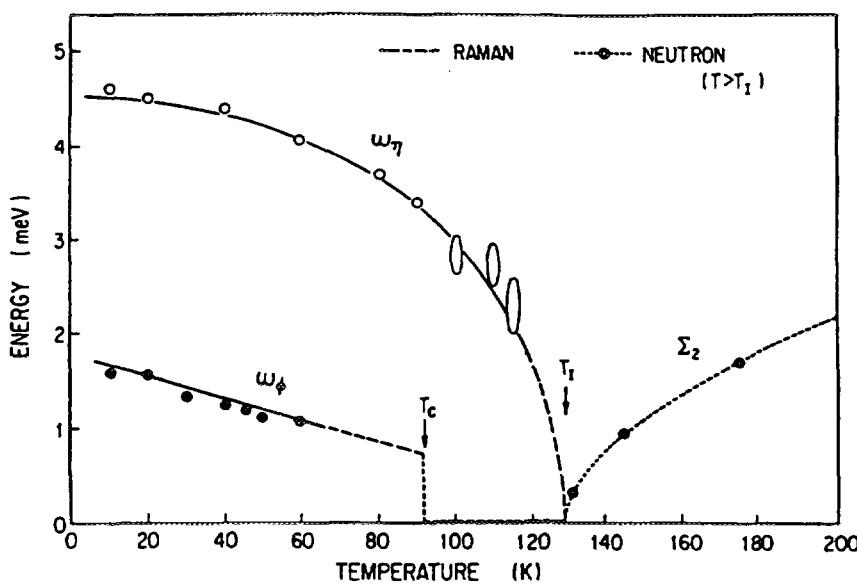


Fig. 17. Temperature behavior of $k = k_\delta$ soft mode ($T > T_i$) and $q = 0$ phase and amplitude modes ($T < T_i$). After Axe et al. [47].

Below T_C the phase mode continues as a zone-centre optic mode of the new 3a superstructure, with finite frequency (commensurate phason). It can be observed by Raman scattering in appropriate geometries.

A major obstacle in the study of the soft-mode response in K_2SeO_4 , is the large value of the soft-mode damping coefficient Γ_s . Fig. 18 shows the soft-mode lineshape at $k = k_\delta$ and $T = 139$ K ($= T_i + 10$ K), as obtained from high-resolution INS measurements [54]: the lineshape is already critically damped, with a DHO-fitted value of ≈ 350 GHz for Γ_s .

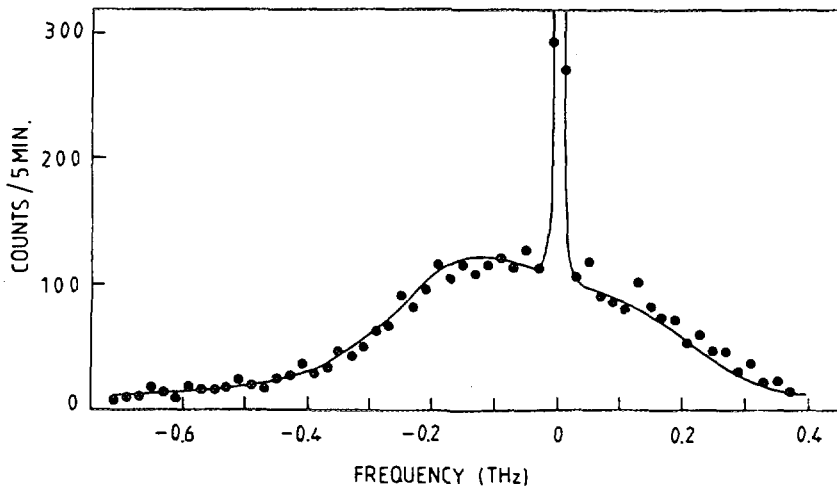


Fig. 18. Soft-mode lineshape in K_2SeO_4 at $T = 139$ K: Constant- q scan at $(1+k_\delta \ 0 \ 2)$. Solid line: DHO fit with $\omega_\phi = 250 \pm 5$ GHz, $\Gamma_\phi = 350 \pm 20$ GHz. After Quilichini and Currat [54].

Typical lineshapes in the incommensurate phase are shown in Fig. 19 for $q \parallel a^*$ and $T = 120$ K ($= T_i - 9$ K). The overdamped spectra correspond to the phase-mode response alone, since at that temperature the amplitude-mode response is much weaker and lies largely outside of the frequency range of the measurements. In Fig. 19 a comparison is made with the TA-mode response, measured at equivalent reduced wavevectors, near a fundamental reflection: the two modes have very different lineshapes and can hardly be confused.

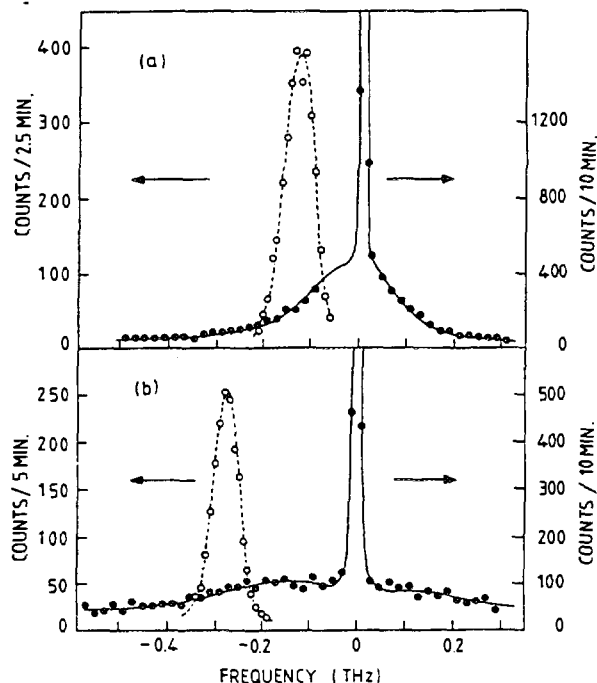


Fig. 19. Phason and TA-phonon lineshapes at equivalent reduced wavevectors ($T = 120$ K): (a) $q = 0.046 a^*$
(b) $q = 0.096 a^*$
TA data (\circ) and phason data (\bullet) are collected near $(0 \ 0 \ 2)$ and $(1+k_\delta \ 0 \ 2)$, respectively.
After Quilichini and Currat [54].

Phase-mode spectra of the type shown in Fig. 19 have been collected for several temperatures in the incommensurate phase and analyzed by fitting to DHO functions. For overdamped spectra, however, the fitting procedure becomes unreliable because strong correlations occur between best-fit values of ω_ϕ and Γ_ϕ and, in practice, additional assumptions must be introduced.

Here we use the general result from Sect. 2.6, that the damping of the phase mode should be closely related to that of the soft mode above T_i , and therefore should be slowly varying in q and T . Values for $\Gamma_\phi(q, T)$ were obtained by interpolating between $\Gamma_s(k\delta, T)$ ($T > T_i$) and the Raman-determined values of the commensurate phase-mode damping for $T < T_c$. As shown in Fig. 20, a linear interpolation appears to be justified.

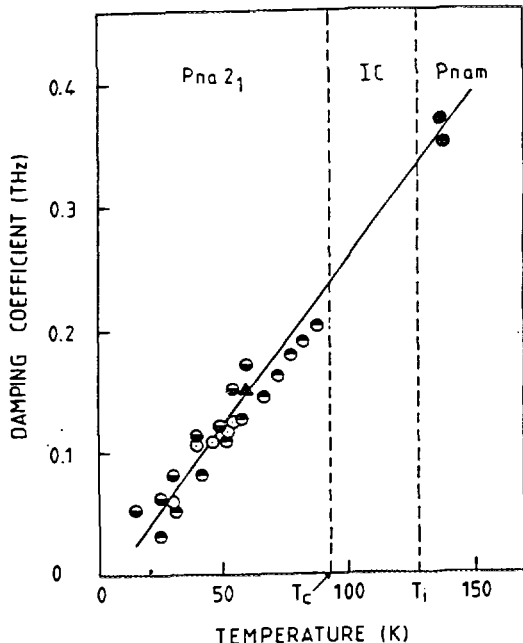


Fig. 20. Damping coefficient of soft mode ($T > T_i$) and commensurate phase mode ($T < T_c$), as deduced from analysis of neutron and Raman spectra:

(●) Ref. [54]; (◐) Ref. [58]
(◑) Ref. [59]; (○) Ref. [60]
After Quilichini and Currat [54].

The resulting values of $\omega_\phi(q)$ for $T_c < T < T_i$, are shown in Fig. 21.

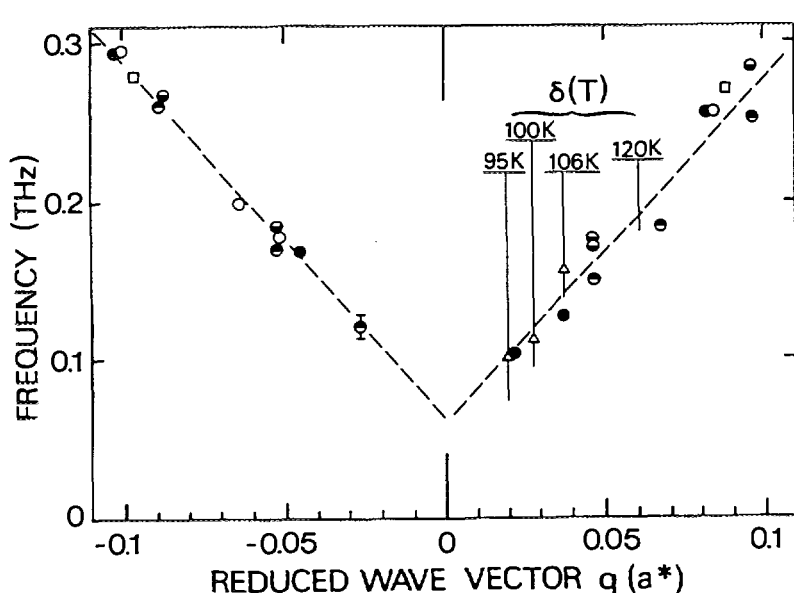


Fig. 21. Phason dispersion in incommensurate K_2SeO_4 for q/a^* : neutron results at 120 K (◐, ●); 110.5 K (□); 100 K (○); 96 K (●), Ref. [54]; Raman results (Δ) corresponding to 95 K, 100 K and 106 K from left to right, Ref. [55]. After Quilichini and Currat [54].

As before the origin of wavevectors is the first-order satellite reflection at $(1+k\delta 0 2)$. Also shown in Fig. 21 are the Raman data of Inoue and Ishibashi [55] for the phason frequency at a wavevector $q_D=\delta(T) a^*$. In the discommensuration regime this latter position corresponds to the zone boundary of the discommensuration lattice. The Raman mode is thus a precursor, in the incommensurate phase, of the commensurate phason.

The data suggest a temperature-independent dispersion for the phase-mode, with a gap of 70-100 GHz at $q=0$. Such a gap is expected close to T_c , but not at 120 K when the sinusoidal approximation should be valid.

At the moment there is no satisfactory explanation for this result, which rests heavily on the assumption of a DHO lineshape for the phase mode. Gooding and Walker [56] have pointed out that coupling between phasons and acoustic modes could produce lineshape distortions such as to mimic the presence of a gap. The detailed consequences of their model have not been tested experimentally.

6. Concluding remarks.

The examples discussed above concern the low-frequency excitation spectrum of simple displacively-modulated systems. They illustrate the capabilities and limitations of coherent inelastic neutron scattering. Cold-source 3-axis spectrometry is the most appropriate technique whenever energy and momentum space resolutions must be simultaneously controlled.

Current developments aim at exploring the dynamics of other types of modulated crystals and other aspects of their excitation spectrum. One obvious extension consists in studying the renormalisation of *hard modes*, below the normal-to-incommensurate transition. As for the soft phonon branch, gaps open at $k_{G,m} = 1/2 (G + m k_i)$ ($m = \pm 1, \pm 2, \dots$), and the corresponding gap modes may become optically active. Extensive comparisons between model predictions and measured spectra (neutron and optical) are thus possible [61]. In principle, the study of the reconstruction of the phonon spectrum in the modulated state provides direct and selective information on the spatial derivatives of the interatomic force-constants.

Away from the sinusoidal regime, the excitation spectrum becomes more and more pathological when referred to the Brillouin zone of the parent crystal. In the discommensuration limit a new picture emerges in which phase fluctuations take the form of collective vibrations of the discommensuration array. In discrete models, a phason gap is predicted due to pinning of the discommensurations by the underlying crystal structure. All these delicate features are well established theoretically and it would be instructive to find out whether or not they survive in real systems. The high momentum space resolution required for such studies unfortunately exceeds the present capabilities of neutron 3-axis spectrometry.

Progress has been achieved in the field of charge-density-waves, where the specific difficulties associated with the observation of CDW excitations by INS are now better appreciated. These include large and strongly dispersive damping effects, steep Kohn anomalies and strong 1D fluctuations above the 3D ordering temperature. In these respects the molybdenum bronzes, such as $K_{0.3} MoO_3$ and $Rb_{0.3} MoO_3$, have more favorable characteristics [62,63] than the Pt-chain (KCP) and organic compounds studied earlier [64]. Another difficulty specific to the CDW case, is the polar (infra-red active) character of the $q = 0$ phase-mode. In the low temperature Peierls insulating state, when screening by residual free carriers can be ignored, the $q = 0$ phason frequency will exhibit LO-TO splitting and angular dispersion, just like a zone center polar mode in a dielectric crystal.

The dynamics of modulated structures with several amplitude and phase degrees of freedom has been often discussed. Such structures result from instabilities where the star of the critical wavevector has more than two arms ($n > 2$). The case $n=4$ is found in $BaMnF_4$ [65] and biphenyl in phase II, while quartz [66,67] and berlinitite ($AlPO_4$) correspond to $n=6$ and $(TaSe_4)_2I$ to $n=8$ [68]. In each case, the structure of the low-

frequency spectrum depends on the number of order-parameter components actually condensed, an information not always known with certainty. As shown in the case of biphenyl [43, 44], the study of the low-frequency excitations, while of interest in itself, can help to distinguish between single-q and multiple-q states.

Phasons have also been studied in the context of composite crystals, such as the mercury-chain compound $\text{Hg}_{3-x}\text{AsF}_6$ [69] or the urea inclusion compounds [70]. In such systems phasons correspond to the relative motion of the two incommensurate sublattices along the direction of incommensurability. Their long-wavelength dynamics and their coupling to the elastic degrees of freedom have been discussed by Finger and Rice [71] and Brand and Bak [72]. In the context of quasicrystals, phasons refer to structural defects with hopping dynamics in the μeV range [73].

References

1. T. Janssen, and A. Janner, *Adv. Phys.* **36** (1987) 519.
2. T. Janssen, *Acta Cryst. A* **47** (1991) 256.
3. V. Heine, and E. H. Simmons, *Acta Cryst. A* **43** (1987) 289.
4. W. L. McMillan, *Phys. Rev. B* **14** (1976) 1496.
5. A. Yoshimori, *J. Phys. Soc. Jpn.* **14** (1959) 807.
6. A. Herpin, P. Meriel, and J. Villain, *Compt. Rend.* **249** (1959) 1334.
7. R. Blinc, and A. P. Levanyuk, eds., *Incommensurate Phases in Dielectrics* (Elsevier Science, Amsterdam, 1986).
8. P. Monceau, ed., in: *Electronic Properties of Inorganic Quasi-One-Dimensional Materials* (Reidel, Dordrecht, 1985), p. 139.
9. D. Kucharczyk, and W. A. Paciorek, *Acta Cryst. A* **41** (1985) 466.
10. S. Tanisaki, *J. Phys. Soc. Jpn.* **16** (1961) 579.
11. R. J. Elliott, *Phys. Rev.* **124** (1961) 346.
12. V. Heine, and S. L. Price, *J. Phys. C* **18** (1985) 5259.
13. A. W. Overhauser, *Phys. Rev. B* **3** (1971) 3173.
14. A. D. Bruce, and R. A. Cowley, *J. Phys. C* **11** (1978) 3609.
15. S. Aubry, in: *Solitons in Condensed Matter Physics*, ed. by A.R. Bishop and T. Schneider (Springer, Berlin, 1978), p. 264.
16. D. A. Bruce, *J. Phys. C* **13** (1980) 4615.
17. T. Janssen, and J. A. Tjon, *J. Phys. C* **16** (1983) 4789.
18. M. V. Klein, in: *Light Scattering near Phase Transitions*, ed. by H. Z. Cummins, and A. P. Levanyuk (North-Holland, Amsterdam, 1983), p. 503.
19. H. Poulet, and R. M. Pick, in: *Incommensurate Phases in Dielectrics*, ed. by R. Blinc, and A. P. Levanyuk (North-Holland, Amsterdam, 1986), Vol. 1, p. 315.
20. V. A. Golovko, and A. P. Levanyuk, *Sov. Phys. JETP* **54** (1981) 1217.
21. J. Petzelt, *Phase Transitions* **2** (1981) 155.
22. P. Lee, T. M. Rice, and P. W. Anderson, *Sol. St. Commun.* **14** (1974) 703.
23. P. Brüesch, S. Strässler, and H. R. Zeller, *Phys. Rev. B* **12** (1975) 219.
24. S. Donovan, Y. Kim, B. Alavi, L. Degiorgi, and G. Grüner, *Sol. St. Commun.* **75** (1990) 721.
25. R. Pynn, *Nature* **281** (1979) 433.
26. R. Zeyher, and W. Finger, *Phys. Rev. Lett.* **49** (1982) 1833.
27. P. M. de Wolff, *Acta Cryst. A* **30** (1974) 777.
28. T. Janssen, *J. Phys. C* **12** (1979) 5381.
29. T. Janssen, and A. Janner, *Physica A* **126** (1984) 163.
30. A. Yamamoto, *Acta Cryst. A* **38** (1982) 87.
31. R. Currat, and T. Janssen, *Sol. St. Phys.* **41** (1988) 201.
32. T. Janssen, in: *Incommensurate Phases in Dielectrics*, ed. by R. Blinc, and A. P. Levanyuk (North-Holland, Amsterdam, 1986), Vol. 1, p. 67.
33. S. Hubert, P. Delamoye, S. Lefrant, M. Lepostollec, and M. Hussonnois, *J. Sol. St. Chem.* **36** (1981) 36.
34. R. de Kouchkovsky, M. F. Le Cloarec, and P. Delamoye, *Mat. Res. Bull.* **16** (1981) 1421.
35. L. Bernard, R. Currat, P. Delamoye, C. M. E. Zeyen, S. Hubert, and R. de Kouchkovsky, *J. Phys. C* **16** (1983) 433.
36. R. Currat, L. Bernard, and P. Delamoye, in: *Incommensurate Phases in Dielectrics*, ed. by R. Blinc, and A. P. Levanyuk (North-Holland, Amsterdam, 1986), Vol. 2, p. 161.
37. T. Janssen, *Jpn. J. Appl. Phys.* **24** (1985) 747.
38. H. Cailleau, in: *Incommensurate Phases in Dielectrics*, ed. by R. Blinc, and A. P. Levanyuk (North-Holland, Amsterdam, 1986), Vol. 2, p. 72.
39. H. Cailleau, J. C. Messager, F. Moussa, F. Bugaut, C. M. E. Zeyen, and C. Vettier, *Ferroelectrics* **67** (1986) 3.
40. H. Cailleau, F. Moussa, C. M. E. Zeyen, and J. Bouillot, *J. Physique* **42** (1981) C6-704.

41. C. Ecolivet, M. Sanquer, J. Pellegrin, and J. De Witte, *J. Chem. Phys.* **78** (1983) 6317.
42. H. Cailleau, A. Girard, J. C. Messager, Y. Delugeard, and C. Vettier, *Ferroelectrics* **54** (1984) 597.
43. F. Moussa, P. Launois, M. H. Lemée, and H. Cailleau, *Phys. Rev. B* **36** (1987) 8951.
44. P. Launois, M. H. Lemée, H. Cailleau, F. Moussa, and J. Mons, *Ferroelectrics* **78** (1987) 137.
45. J. D. Axe, M. Iizumi, and G. Shirane, in: Incommensurate Phases in Dielectrics, ed. by R. Blinc, and A. P. Levanyuk (North-Holland, Amsterdam, 1986), Vol.2, p. 1.
46. M. Iizumi, J. D. Axe, G. Shirane, and K. Shimaoka, *Phys. Rev. B* **15** (1977) 4392.
47. J. D. Axe, M. Iizumi, and G. Shirane, *Phys. Rev. B* **22** (1980) 3408.
48. M. S. Haque, and J. R. Hardy, *Phys. Rev. B* **21** (1980) 245.
49. A. Bussmann-Holder, H. Büttner, and H. Bilz, *Ferroelectrics* **36** (1981) 273.
50. N. Yamada, and T. Ikeda, *J. Phys. Soc. Jpn.* **53** (1984) 2555.
51. M. Horioka, and A. Sawada, *Ferroelectrics* **66** (1986) 303.
52. M. Fukui, and R. Abe, *J. Phys. Soc. Jpn.* **51** (1982) 3942.
53. T. Kobayashi, M. Suhara, and M. Machida, *Phase Transitions* **4** (1984) 281.
54. M. Quilichini, and R. Currat, *Sol. St. Commun.* **48** (1983) 1011.
55. K. Inoue, and Y. Ishibashi, *J. Phys. Soc. Jpn.* **52** (1983) 556.
56. R. J. Gooding, and M. B. Walker, *Phys. Rev. B* **36** (1987) 5377.
57. T. Janssen, and R. Currat, in: Incommensurate Crystals, Liquid Crystals, and Quasicrystals, ed. by J. F. Scott, and N. A. Clark (Plenum, New York, 1987) p. 19.
58. M. Wada, A. Sawada, Y. Ishibashi, and Y. Takagi, *J. Phys. Soc. Jpn.* **42** (1977) 1229.
59. H. G. Unruh, W. Eller, and G. Kirf, *Phys. Stat. Sol. A* **55** (1979) 173.
60. M. Quilichini, unpublished.
61. T. Rasing, P. Wyder, A. Janner, and T. Janssen, *Phys. Rev. B* **25** (1982) 7504.
62. B. Hennion, J. P. Pouget, and M. Sato, *Phys. Rev. Lett.* **68** (1992) 2374.
63. J. P. Pouget, B. Hennion, and M. Sato, *J. Physique IV* **3** (1993) C2-215.
64. R. Comes, and G. Shirane, in: Highly Conducting One Dimensional Solids, ed. by J. T. Devreese, R. P. Evrard, and V.E. van Doren (Plenum, New York, 1979).
65. D. E. Cox, S. M. Shapiro, R. A. Cowley, M. Eibschutz, and H. J. Guggenheim, *Phys. Rev. B* **19** (1979) 5754.
66. M. B. Walker, and R. J. Gooding, *Phys. Rev. B* **32** (1985) 7412.
67. M. Vallade, V. Dvorak, and J. Lajzerowicz, *J. Physique* **48** (1987) 1171.
68. J. E. Lorenzo, R. Currat, P. Monceau, B. Hennion, and F. Levy, *Phys. Rev. B* **47** (1993) 10116.
69. I. U. Heilmann, J. D. Axe, J. M. Hastings, G. Shirane, A. J. Heeger, and A. G. MacDiarmid, *Phys. Rev. B* **20** (1979) 751.
70. S. van Smaalen, and K. D. M. Harris, *Proc. R. Soc. London A* **452** (1996) 677.
71. W. Finger and T. M. Rice, *Phys. Rev. B* **28** (1983) 340.
72. H. Brand and P. Bak, *Phys. Rev. A* **27** (1983) 1062.
73. S. Lyonnard, G. Coddens, R. Bellissent, Y. Calvayrac, and P. Fabi, in: Proceedings of the 5th International Conference on Quasicrystals, ed. by C. Janot, and R. Mosseri (World Scientific, Singapore, 1995) p. 367.



Martensitic Phase Transitions

Winfried Petry and Jürgen Neuhaus

*Physik Department E13, Technische Universität München,
D-85748 Garching, Germany*

Many elements transform from a high temperature bcc phase to a more dense packed low temperature phase. The great majority of these transitions are of 1st order, displacive and reconstructive. The lattice potentials which govern these martensitic transitions can be probed by inelastic neutron scattering, thereby answering fundamental questions like: Will the transition be announced by dynamical or static lattice fluctuations? What are the trajectories for the displacements needed for the transformation? Does the vibrational entropy stabilize the high temperature phase? Are the unusual transport properties in these materials related to their ability to transform?

1 INTRODUCTION

Almost half of the elements condense in the open bcc structure. With very few exceptions these bcc phases transform into a close packed structure at lower temperature or under pressure [1]. Among the exceptions those with magnetic transitions will be noted: Pure iron solidifies at 1809 K in the bcc δ -phase and undergoes a first transition to fcc γ -Fe at 1665 K. Very unusual it transforms with decreasing temperature back to a bcc α -phase at 1184 K. Within this α -phase a magnetic transition occurs at 1042 K below of which α -Fe is ferromagnetic. Pure cobalt solidifies immediately in a closed packed fcc structure and has its ferromagnetic transition within this β -phase at 1388 K. On further cooling it transforms to hcp α -Co at 693 K without any apparent influence on its magnetic properties.

In all cases the transitions are *displacive* and of *first order*. They are mostly *reconstructive* in the sense that the high temperature/low pressure or parent phase and the product phase are not related by a group-sub group relation. Rather, the product phase reconstructs a new structure belonging to a different symmetry group. This reconstruction is achieved by homogenous lattice distortive strains and/or by shuffles. A lattice distortive strain is a homogenous strain that transforms one lattice into another. A shuffle is a coordinated movement of atoms that produces in itself no lattice distortive deformations but alters the symmetry of the crystal. A shuffle deformation can be expressed by a lattice wave modulation of a short wavelength, typically in the order of one to a few nearest neighbour distances. The lattice correspondence observed between parent and product phase defines a structural unit in the parent phase that under the action of homogeneous strain and/or shuffle transforms into a unit of the product phase. Discerning this lattice correspondence does not mean that the actual trajectory for the displacive deformation is known, many ways through real space produce identical lattice correspondences.

Firstly, the question will be addressed whether the actual trajectory for the displacements during the transition can be deduced from the dynamical response of the lattice. In harmonic approximation the phonon frequencies $\omega(\bar{q})$ are given by the eigenequation

$$\omega^2(\bar{q}) \cdot \bar{e}(\bar{q}) = \overline{\overline{D}}(\bar{q}) \cdot \bar{e}(\bar{q}) \quad (1)$$

with \bar{q} the phonon wave vector and $\bar{e}(\bar{q})$ the eigen- or polarizationvector. In high symmetry directions the latter describe longitudinal and transversal displacements. For monoatomic systems the components of the dynamical matrix $\overline{\overline{D}}(\bar{q})$

$$D_{\alpha\beta}(\bar{q}) = \frac{1}{M} \sum_m \phi_{\alpha\beta}^{mn} \cdot \exp\{i\bar{q}\bar{r}^m - \bar{r}^n\} \quad (2)$$

can be expressed in terms of the Fourier transform of the force constants ϕ which are the second order derivatives of the interatomic potentials. For convenience the summation in eq (2) restricts to a small number of nearest neighbour shells. Translational symmetry of the lattice implies that the possible solutions for the eigenfrequencies $\omega(\bar{q})$ can be projected into one reciprocal unit cell. In the limit of long wave length $\bar{q} \rightarrow 0$, i.e. when the lattice is seen by the phonon as a continuum $\omega(\bar{q})$ depends linearly on q .

$$\omega^2(\bar{q}) \cdot \rho = C_{ij}(\bar{q}) \cdot q^2 \quad (3)$$

Here ρ means the mass density and cubic symmetry reduces the elastic constants C_{ij} to a bulk modulus $K = 1/3(C_{11} + 2C_{12})$ expressing the static compressibility $\chi = 1/K$ and the two independent shear moduli C_{44} and $C' = 1/2(C_{11} - C_{12})$. Eq. (1-3) indicate how lattice vibrations probe the lattice potential in 3 dimensions.

It is expected that the transition occurs in such a direction where low energy phonons or particularly low elastic constants indicate a weak repulsive interaction for displacements. *Where in reciprocal space shall we find the low energy phonons? At very short momentum transfer \bar{q} or at large \bar{q} close to the Brillouin zone boundaries?* Answering these questions will tell us whether long wavelength shears or short wavelength shuffles dominate the transformation. Following this idea we expect dynamical precursors for a transition of first order. Eventually these dynamical anomalies become stronger the closer the temperature approaches the transition. These dynamical precursors are the fingerprint of the approaching transition, but we will learn that at the same time they are the cause for stabilizing the open bcc structure. *It is interesting to speculate whether these large amplitude phonons freeze to static displacements and thereby cause elastic precursors.* Discussion on this question deeply involves the role of defects and nucleation for the transition. The great resemblance of elastic and inelastic diffuse scattering will give us an intuitive picture of the liquid-like motions of rows of atoms along the nearest neighbour direction. Finally we show how the tendency of these elements to transform into close packed structures dominates other physical properties: *anomalies in the transport mechanism, strongly anharmonic lattice potentials etc.*

Most of this holds for transitions from bcc \rightarrow close packed structures. *But what happens if the reverse transition occurs? - or a transition within close packed structures like fcc \rightarrow hcp?* Observing the dynamical response of iron and cobalt will partly answer this question.

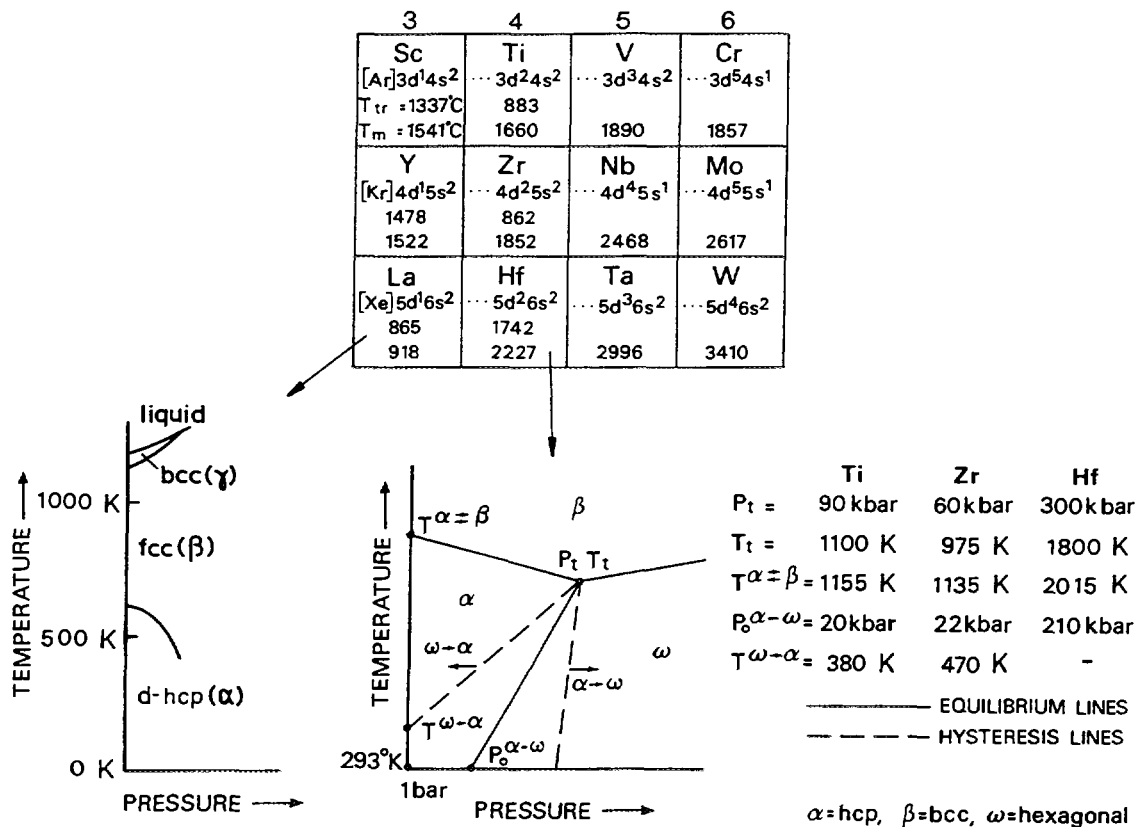


Fig. 1: Transition temperatures T_0 and phase diagrams for the early transition elements.

Metallurgists and physicists do not agree on a unique definition of what is meant by a martensitic phase transition. Originally the term was introduced for the segregation of a bct phase within γ or austenitic steel during cooling down in honour of the German metallurgist A.Martens. Soon the expression was extended to all kinds of displacive transitions. Throughout this paper martensitic transitions are discussed in a more physical sense: i) The transition occurs instantaneously, and is virtually independent of time. ii) The amount of transformation is a characteristic of the temperature, i.e. a hysteresis exists. iii) The transformation is very reversible. In general the same single crystal is obtained after a temperature cycle. In reality this is difficult to achieve due to experimental constraints. iv) Insofar as alloys are concerned, no change occurs in the chemical composition and almost no change in volume is observed. v) There exists a definite orientational relation between the parent and product phase. In general a habitus plane is common to parent and product phase. vi) No group-subgroup relation exists between the two structures. The product phase reconstructs its own group symmetry. For the above reasons martensitic transitions are of 1st order, they are displacive and reconstructive. The latter makes them different from a whole class of 2nd order transitions like the ferroelectric transition in SrTiO₄. For a recent review of some of the principles we refer to [2].

Martensitic transformations are mainly studied in binary or tertiary alloys, particularly if the shape memory effect is of primary interest. However, if the basic physical properties are addressed, it is extremely helpful to return to elementary systems. In general the structural properties of monoatomic solids are better defined. The influence of all kinds of defects can be thoroughly controlled and phenomena induced by host-defect interactions are expected to be of minor importance. Further, quite a number of martensitic transitions in the elementary systems occur at high temperatures, i.e. thermal equilibrium during the transition is easily achieved. The inherent drawback is the difficult experimental access to single crystals in the high temperature phase – this is also the reason why experimental information on high temperature martensitic transitions is scarcely available. Indeed recent progress in studying high temperature martensitic transitions is due to the development of reliable in-situ growth methods of parent phase single crystals during the experiment [3].

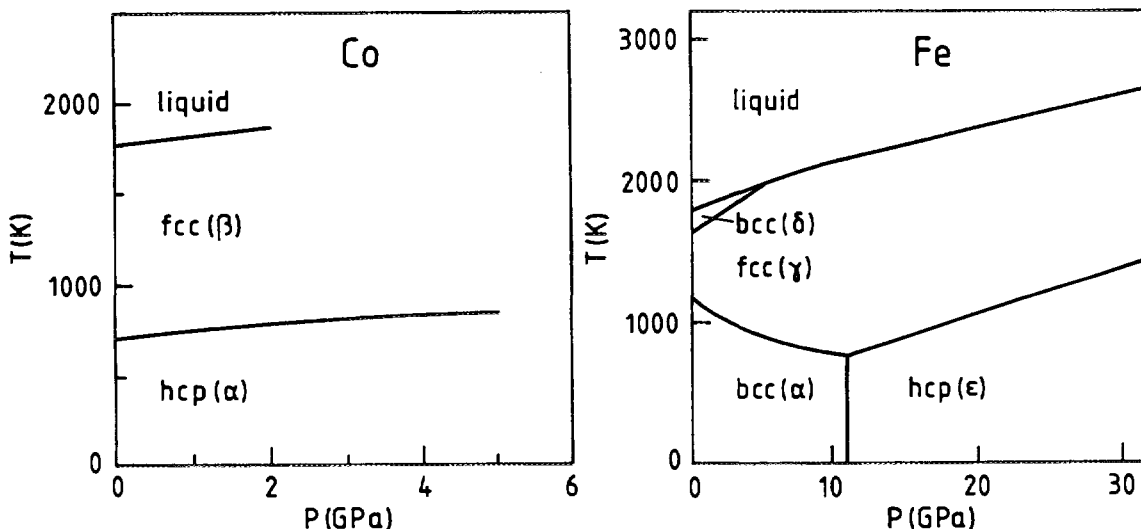


Fig. 2: Phase diagrams for iron and cobalt.

Being interested in dynamical properties of the transition, the choice of experimental methods is almost limited to inelastic neutron scattering. Whereas elastic constants are conventionally measured by ultrasonic methods, this is no longer feasible for the high temperature phases. Further, elastic constants contain only direct information about long wavelength shears. Dynamical instabilities towards opposite shuffles of neighbouring planes have to be explored in full reciprocal and energy space which is only accessible through inelastic neutron scattering.

2 TRANSITIONS FROM BCC → CLOSE PACKED STRUCTURES

Prominent examples for transitions from the open bcc structure to closest packed structures are the alkali, earth alkali and the group 3 and 4 transition elements. Transitions in Li or Na to 9R+fcc and 9R+hcp occur at 75 K and 35 K, respectively. These were among the earliest elementary systems in which one was looking for dynamical precursors of the martensitic phase transition. Despite a considerable effort by neutron scattering experiments [4,5] the outcome was to a certain extent disappointing: Dynamical precursors close to the transition temperature are virtually absent. Elastic precursors have been observed but their strength and location in \vec{q} -space often depend on

the thermal history of the crystal. Recent ab initio [6] and thermodynamic [7] calculations describe some of the reasons: Energetically the different closest packed structures are hardly separable and the actual product phase is strongly influenced by the initial crystal quality and thermal history.

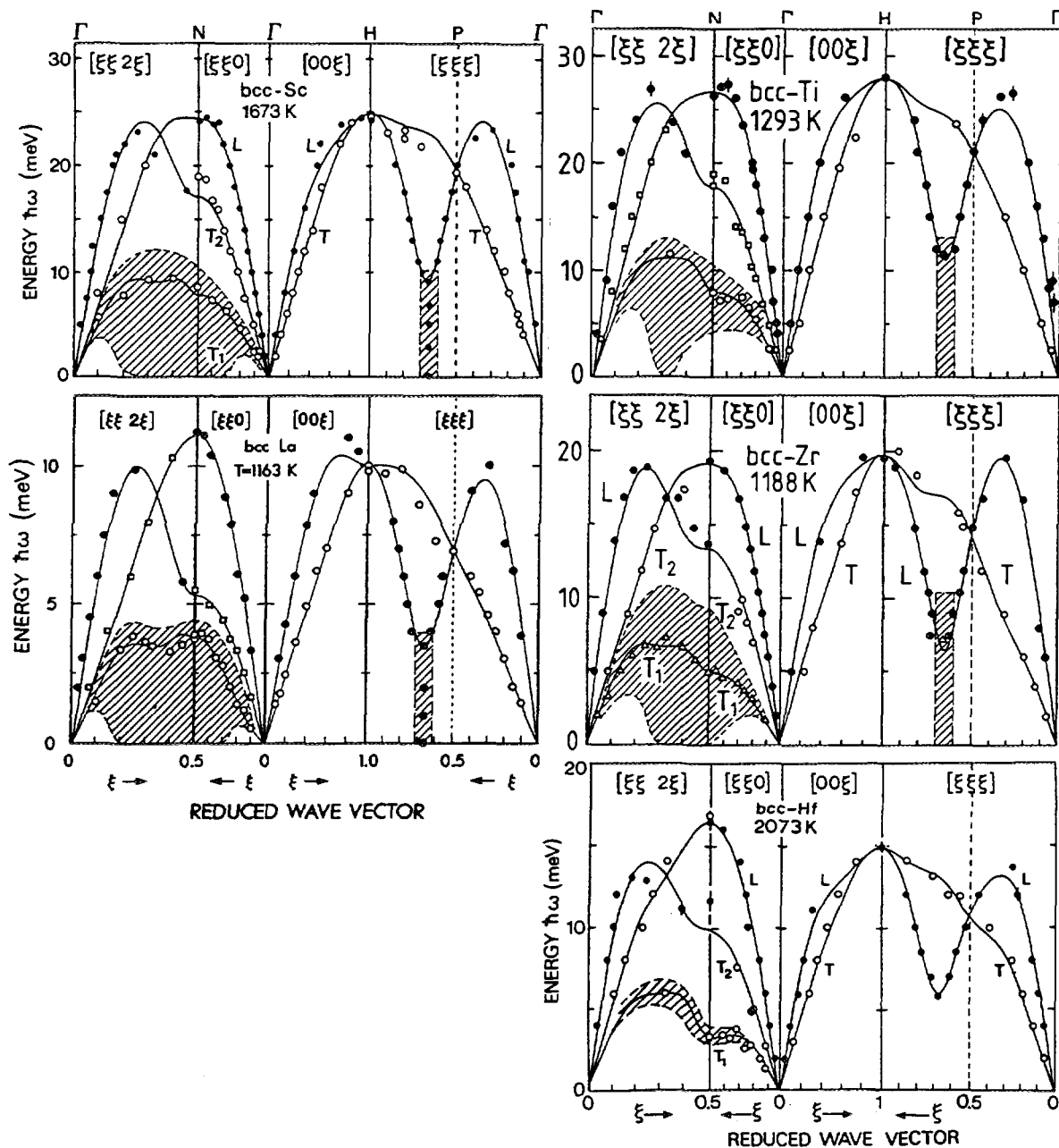


Fig. 3: Measured phonon dispersions in the bcc phase of group 3 and 4 metals. Shaded areas indicate regions of inelastic diffuse scattering or strongly damped phonons. [10-14]

The situation is very different in the early transition metals. As indicated in Fig. 1, Sc, Y, La, Ti, Zr and Hf all transform into the hcp structure. For the group 4 elements an additional transition to the ω -phase under moderate pressure is known. As an exception, La first transforms to fcc and then to double-hcp. Stassis and collaborators [8] were the

first to measure the phonon dispersion of β -Zr by cycling a large α -single grain through the α - β transition. More detailed measurements could be made by the in-situ growth technique developed more recently [9]. Fig. 3 gives a synopsis of the measured phonon dispersions in the parent bcc phase of these elements [10-14].

The dispersions in Fig. 3 greatly resemble one another, i.e. the phonons at higher energy scale roughly with the square root of the mass and the lattice constant, thereby following the homology rule. Most evidently all dispersions are dominated by a few unusual properties: i) At $\xi = 2/3$ the longitudinal $L[\xi\xi\xi]$ phonon branch shows a pronounced dip. ii) The whole transverse $T_1[\xi\xi 0]$ phonon branch with $[1\bar{1}0]$ polarisation is of low frequency when compared to other transverse phonons. iii) The same holds true for the off symmetry $T_1[\xi\xi 2\xi]$ phonon branch. iv) The low energy phonons are strongly damped. As indicated by the shaded area the intensity of these damped phonons reaches down to zero energy transfer.

2.1 The $bcc \rightarrow \omega$ transition

The atomic displacements achieved by a longitudinal phonon in $[\xi\xi\xi]$ direction with $\xi = 2/3$ have a particular crystallographic meaning for the bcc structure. As shown in Fig. 4, for a stationary wave at $\xi = 2/3$ two of three neighbouring (111) planes move towards each other, whereas every third plane stays at rest. When the two moving planes collapse the perfect ω structure is achieved. During the second half of the wave, the planes move in the opposite direction and approach the plane at rest. Distortions in these directions are called anti- ω distortions. From symmetry, it is evident that the restoring forces involved for distortions into the ω or anti- ω structure are different.

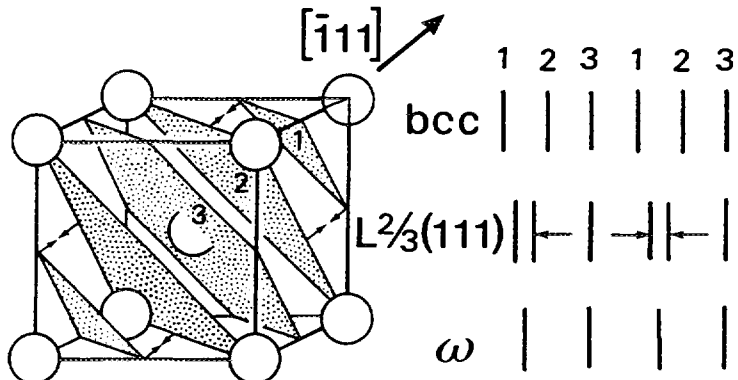


Fig. 4: Scheme of the $bcc \rightarrow \omega$ transition.

The ω lattice can be described as an hexagonal cell, with the c axis along the $\langle 111 \rangle_{bcc}$ direction and the a axis along the $\langle 110 \rangle_{bcc}$ direction. Thus the crystallographic relation between ω and β reads

$$(111)_{bcc} \parallel (001)_\omega \text{ and } [\bar{1}01]_{bcc} \parallel [010]_\omega$$

Fig. 5 illustrates what is meant by the shaded area in Fig. 3 at $L2/3(111)$. *Coherent* intensity is measured down to zero (!) energy transfer and even has its maximum at zero energy. Further, the small elastic peak on top of the broad inelastic scattering distribution

is of purely incoherent origin and therefore does not represent any coherent elastic scattering. The latter is of particular importance because any static embryo of the ω -phase causes elastic diffuse scattering at $\bar{Q} = 4/3(111)$, i.e. at the scattering vector \bar{Q} where the spectra in Fig. 5 have been measured. Therefore the absence of this "truly" elastic scattering means that within the time window of the method ($\leq 10^{-10}$ s) no stable ω -embryo exists.

Taking resolution effects into account, the broad inelastic distribution can be reproduced by a damped oscillator, the scattering law of which reads

$$S(Q, \omega) = f(Q) \frac{1}{1 - e^{-\hbar\omega/k_B T}} \cdot \frac{\Gamma \hbar\omega}{(\hbar^2(\omega^2 - \omega_0^2))^2 + (\Gamma \hbar\omega)^2} \quad (4)$$

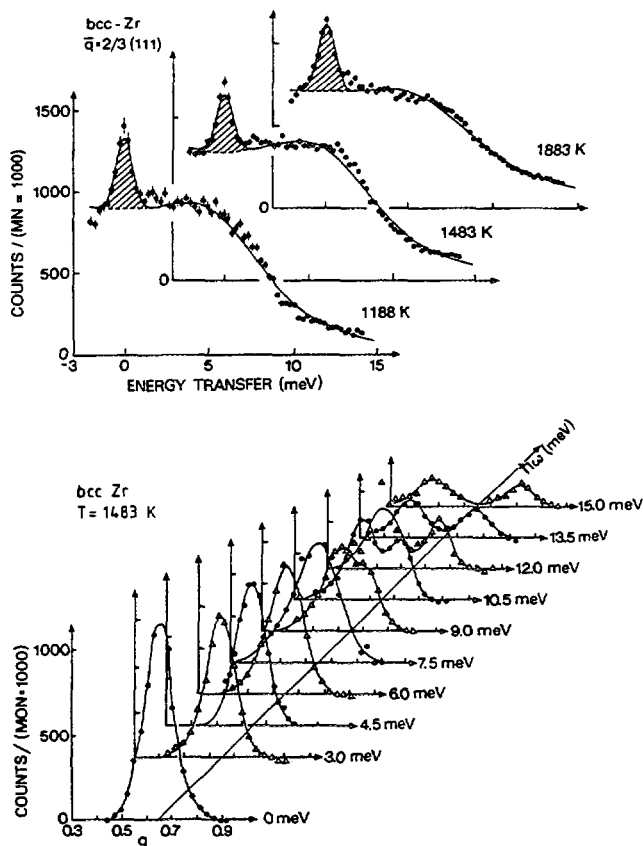


Fig. 5: The L2/3(111) phonon measured at $\bar{Q} = 4/3(111)$. Top: Const. q-scans at different temperatures. The elastic peak on top of the broad energy distribution is of purely elastic incoherent origin. Bottom: The evolution of the dispersion around $\bar{Q} = 4/3(111)$ towards a region of diffuse inelastic intensity is visualized by a series of const. E-scans. For the elastic scan the incoherent intensity has been subtracted [11].

With the exception of β -Hf, the actual damping term Γ observed for the different elements in Fig. 3 is larger than the resonance frequency ω_0 itself. This means that the L2/3(111) phonon has an extremely short lifetime, the amplitude of the corresponding displacement is over-damped after one period of the vibration. This short lifetime of the L2/3(111) excitation has to be well separated from the question of how this phonon

propagates in real space. Along $L[\xi\xi\xi]$ direction a strong dispersion is observed whereas in the vicinity of $\vec{Q} = 4/3(111)$ and in directions perpendicular to $[\xi\xi\xi]$, i.e. in $T[\xi\xi\bar{2}\xi]$ and $T[\xi\bar{\xi}0]$ only a very weak dispersion is observed. Translated to real space this means that the displacements corresponding to the $L2/3(111)$ phonon propagate along the [111] chains but neighbouring [111] chains mostly do not follow. Considering both, the short lifetime and the localized character of this phonon, propagation perpendicular to [111] is *liquid-like*.

In the single-oscillator approximation, the amplitude u_0 of a vibration is given by

$$u_0 = \left(\frac{2k_B T}{m} \right)^{1/2} \cdot \frac{1}{\omega_0} \quad (5)$$

The phonon energies at $L2/3(111)$ are in the order of 3-10 meV corresponding to displacements from 0.4-0.75 Å at the transition temperature T_0 . These values are comparable to the displacements needed for the bcc $\rightarrow \omega$ transition. Whereas these large displacements are certainly indicative for the weakness of the bcc lattice towards the ω transformation their absolute values have to be taken with caution, eq. (5) is only a crude approximation, and inserting the mass of a single atom is probably not justified.

As depicted in Fig. 6 the open bcc structure is characterized by chains of nearest-neighbour (NN) atoms in [111] directions. Out of all phonons in the $L[\xi\xi\xi]$ branch, the phonon at $\xi = 2/3$, i.e. $\lambda = \sqrt{3}/3 a$, is the only one which leaves the [111] chains undisturbed. Thus atoms along [111], i.e. the direction with shortest distances between the atoms and therefore strong restoring forces, do not alter their distance. The phonon frequency is low because it is determined by restoring forces between the chains which are weaker (because they do not compress the NN chains). All the other modes with [111] propagation will change the distances of the atoms along the chains, thus giving rise to extra restoring forces leading to higher energies.

This purely geometrical argument is valid for *all* bcc structures and therefore cannot explain the difference in softening of the $L2/3(111)$ phonon in different transition elements. Whether this general weakness of the bcc lattice towards the ω -structure is enhanced or not depends on the filling of the d-electrons. Ab initio calculations by Ho et al [15] show that in bcc Zr the valence charge density is concentrated in d bonds which run in chains along (111) direction with very little interaction between neighbouring chains, i.e. the valence charge is highly localized along these [111] chains. As mentioned before, the $L2/3(111)$ phonon is the only one which leaves the [111] chains undisturbed, and does not compress or stretch the highly localized d bonds. The validity of these considerations is underlined by results from similar calculations for bcc Mo [15]. Here the d bonds entangle the [111] chains. Therefore the $L2/3(111)$ phonon is not expected to have a particularly low frequency, perfectly agreeing with the experimentally determined phonon dispersion of Mo. Fig. 7 shows the valence charge distribution in the (110) plane for bcc Zr and Mo, respectively. To visualize the effect of these charge distributions on the restoring forces, the densities in Fig. 7 are force weighted, i.e. shown for small displacements. Chromium which is chemically equivalent to Mo may serve as an example of a phonon dispersion for a bcc element exhibiting almost no dip at $L2/3(111)$ -

see Fig. 8. The electronic calculations as presented in Fig. 7 are ground state calculations. How important finite temperature can be is also shown in Fig. 8. The dispersion of Cr at 1773 K has changed considerably and very much resembles of that of the group 3 and 4 transition metals.

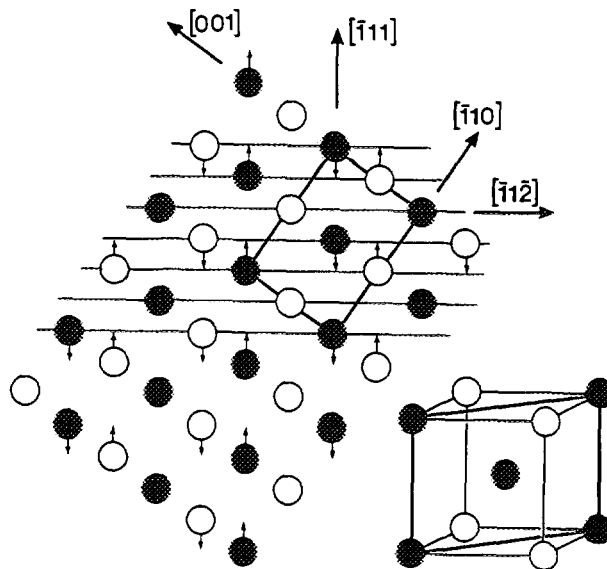


Fig. 6: Displacements of the atoms in a (110) plane due to a L2/3(111) phonon.

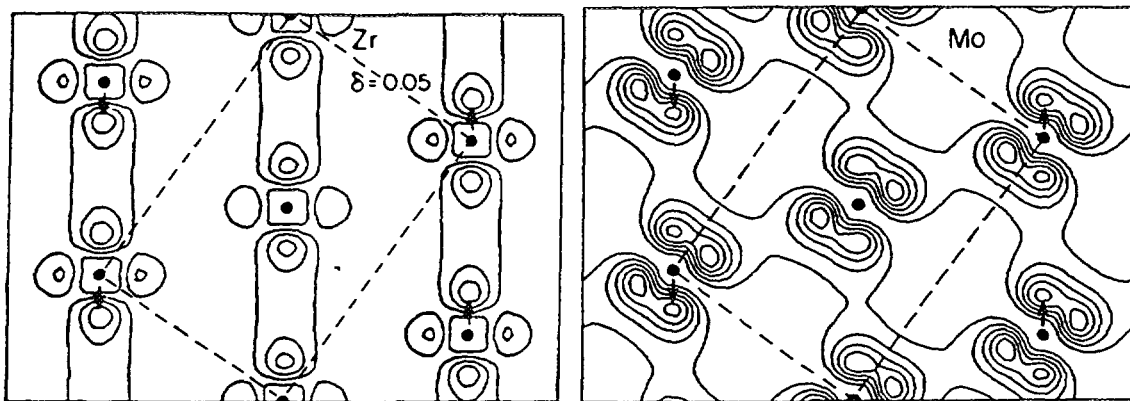


Fig. 7: Contour plots of the valence charge density in the bcc (110) plane. Densities are force weighted [15,16].

Returning to our initial interest that of the $\text{bcc} \rightarrow \omega$ transition, we summarise the experimental observations: i) The high temperature bcc phases show large amplitude fluctuations towards the ω structure. These excitations do not alter with temperature and are also observed in bcc metals of group 3 which do not transfer to the ω phase. The low restoring force for the shear motion of the [111] chains towards each other is therefore a property inherent to the open bcc structure. For a more fundamental ab-initio explanation on the basis of the electronic configuration, we refer to literature [15]. ii) The L2/3(111) shuffle alone transforms the bcc lattice to a ω lattice. There is no need for any long wavelength shear. iii) In pure metals no static precursors of the parent phase are observed. As only dynamical precursors exist, the description of a homogenous transition is more appropriate.

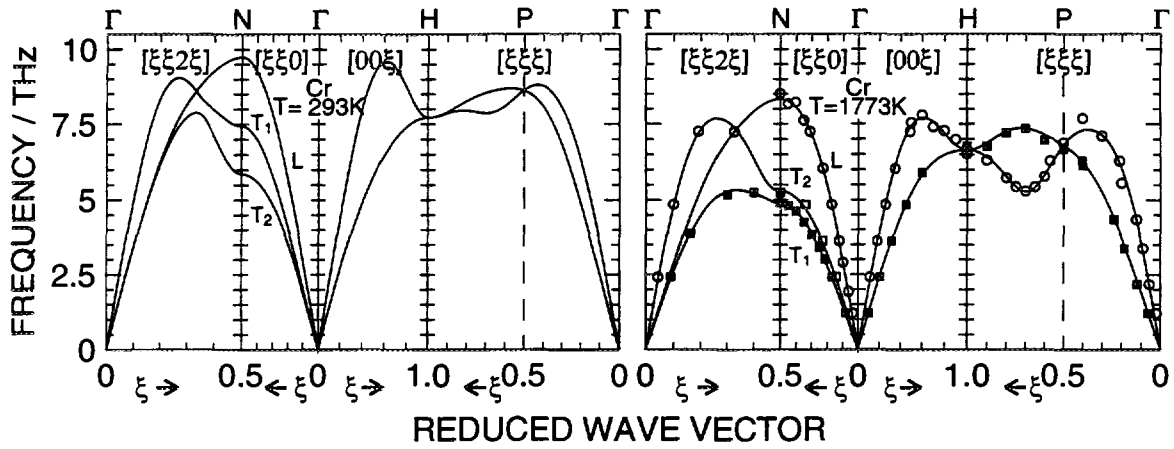


Fig. 8: Dispersion of Cr measured at RT[16] and 1773 K[17]

2.2 The bcc \rightarrow hcp transition

The crystallographic relation for the bcc \rightarrow hcp transition has been established by Burgers [18].

$$(110)_{\text{bcc}} \parallel (00.1)_{\text{hcp}} \text{ and } [\bar{1}11]_{\text{bcc}} \parallel [\bar{2}1.0]_{\text{hcp}}$$

The transformation can be achieved by the combined displacements of two phonons. The transverse zone boundary phonon $T_{11/2}(110)$ at the N point with a displacement of neighbouring (110) planes in opposite $[\bar{1}\bar{1}0]$ directions by $\delta = a \cdot \sqrt{2}/12$ achieves the hcp stacking sequence. Two equivalent long wavelength shears – for instance $(1\bar{1}2)[\bar{1}11]$ and $(\bar{1}12)[\bar{1}\bar{1}1]$ – squeeze the bcc octahedron to a regular hcp one, thereby changing the angle from 109.5° to 120° . This Burgers mechanism is illustrated in Fig. 9.

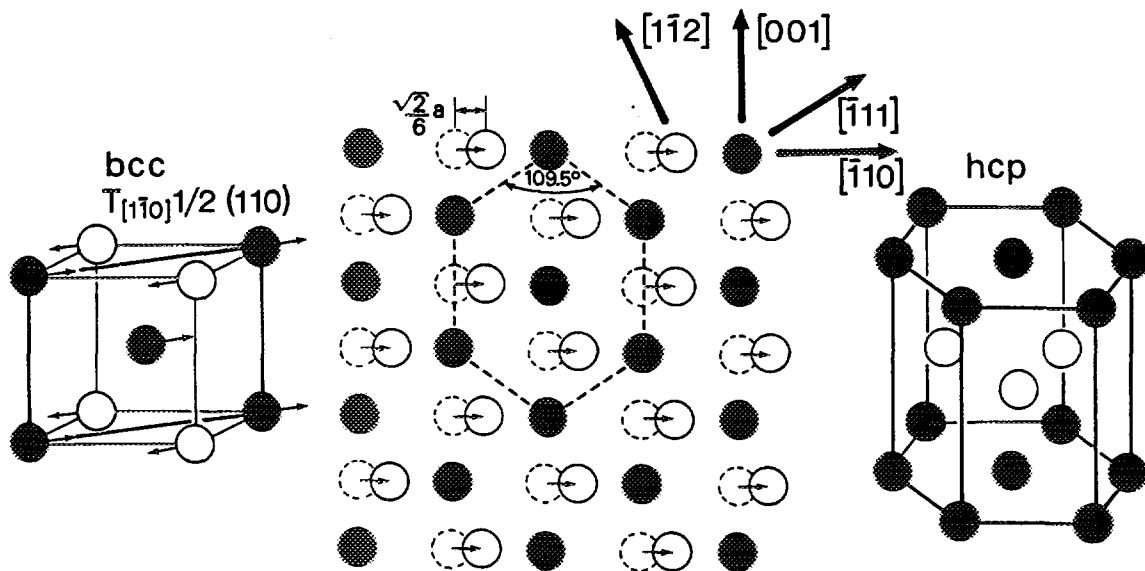


Fig. 9: Scheme of the bcc \rightarrow hcp transition (Burgers mechanism).

The $T_{11/2}(110)$ phonons in Fig. 3 are of even lower energies than the so-called ω phonons, i.e. the bcc lattice exhibits very low restoring forces for shuffling neighbouring (110) planes into opposite [110] directions. As for the ω point these phonons are strongly damped. Contrary to what has been observed at the ω point, the $T_{11/2}(110)$ phonon energy considerably decreases on approaching the martensitic transition temperature - see Fig. 10. Because the bcc \rightarrow ω transition is driven by an increase in the pressure, the temperature variation does not alter the related L2/3(111) phonon. The bcc \rightarrow hcp transition however, is driven by temperature and therefore the related $T_{11/2}(110)$ phonon decreases with decreasing temperature. Nevertheless the martensitic transition occurs at finite energy.

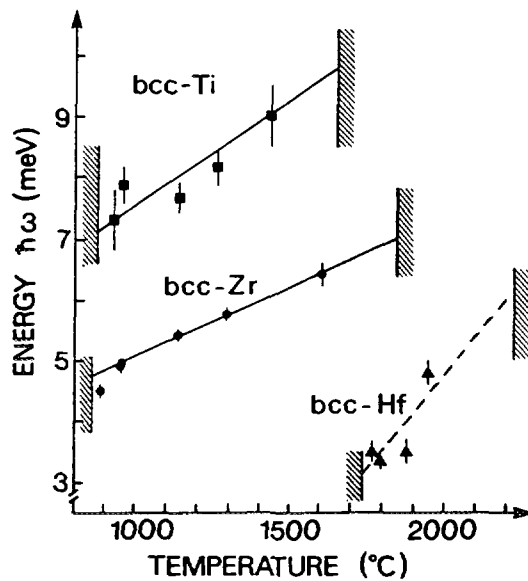


Fig. 10: Temperature dependence of the $T_{11/2}(110)$ phonon in β -Ti, β -Zr and β -Hf [21].

The shears needed to complete the transition are those given by the initial slope of the $T_1[\xi\xi 2\xi]$ phonon branch. The elastic constant along this direction is rather low, i.e. one finds low restoring forces for this motion. Recent thermodynamic approaches [19,20], which use an expansion of the free energy in terms of dynamical displacements have suggested that a small softening of the relevant low-energy phonon is sufficient to produce a lower minimum of the free energy required to obtain the product phase. The order parameter in the expansion of free energy is related to the *average* atomic displacements of the phonons which are associated with the transition.

The fact that the $T_{11/2}(110)$ phonon and the initial slope of the $T_1[\xi\xi 2\xi]$ branch are of little value do not unequivocally prove that the actual trajectory of the atoms during the transition follow the Burgers mechanism. Computations of energy landscapes may be helpful in filling this argumentative gap. For the pressure induced bcc \rightarrow hcp transition in Ba Chen et al [22] calculated the valley of lowest internal energy as a function of the Burgers shuffle and the homogeneous strain needed to squeeze the octahedron - Fig. 11. As it turns out, this valley of lowest energy for the combined deformation follows exactly the trajectory assumed in the Burgers mechanism.

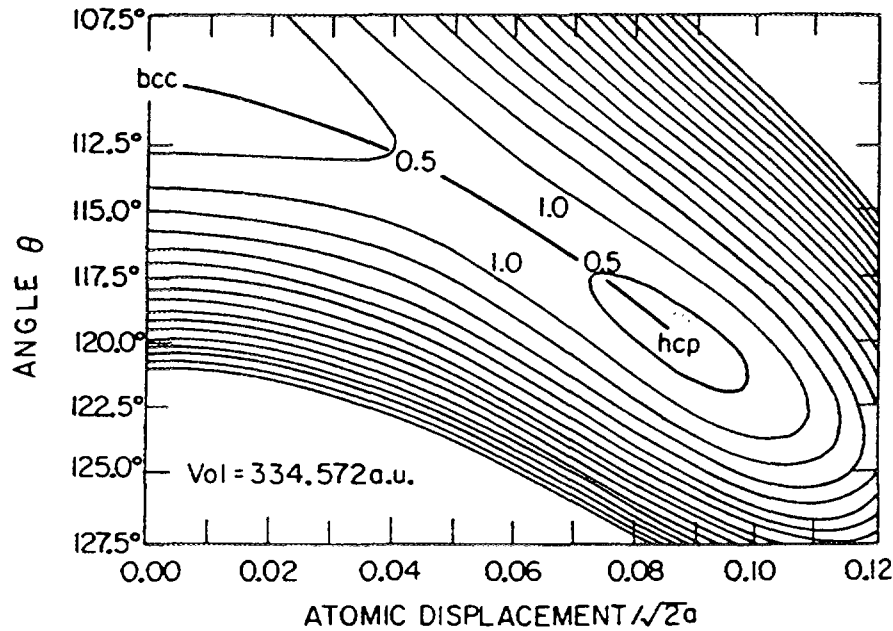


Fig. 11: Energy landscape for the bcc \rightarrow hcp transition in Ba [22]. The transition is supposed to occur along the valley of lowest energy. Θ is the angle of the octahedron, displacements are along [110] as indicated in Fig. 6.

We conclude that low frequencies along the $T_1[\xi\xi 0]$ phonon branch which further decrease upon approaching T_0 are indicative for the Burgers mechanism. Different to the ω transition, the bcc \rightarrow hcp transformation needs a combination of a short wavelength shuffle and a homogenous lattice strain.

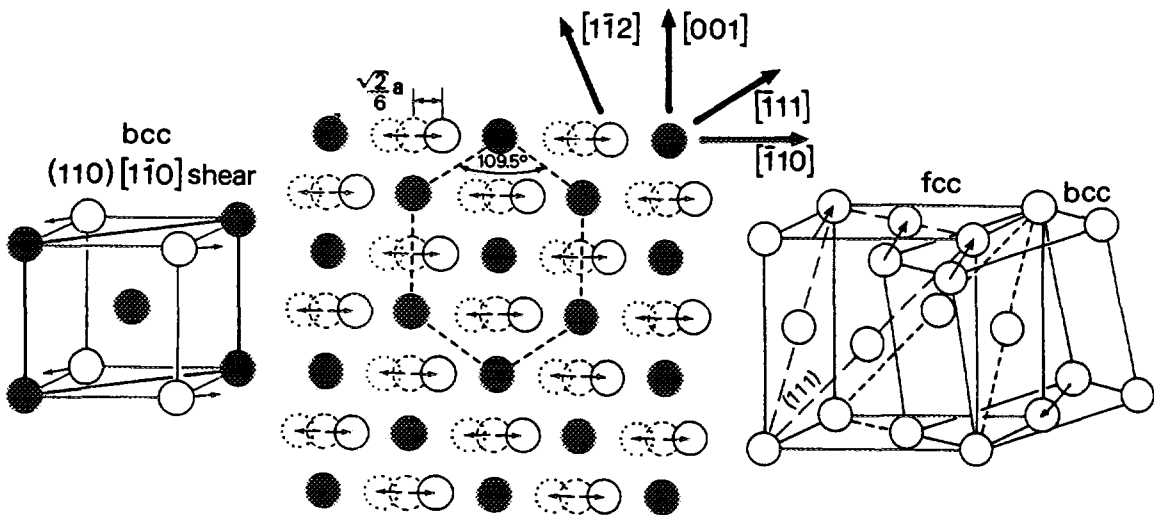


Fig. 12: Scheme of the bcc \rightarrow fcc transition.

2.3 The bcc \rightarrow fcc transition

Before discussing the $\gamma \rightarrow \beta$ transition in La as an example for the bcc \rightarrow fcc transformation, we have to recover some arguments concerning the relation of the

phonons involved in the ω and hcp transition. The longitudinal displacements of the (111) planes for the L2/3(111) phonon can also be viewed as a shearing of neighbouring [111] rows in opposite directions [23], i.e. $L2/3(111) \equiv T_{[1\bar{1}\bar{1}]} 1/3(112)$. Noting also the identity $T_{[01\bar{1}]} 1/2(112) \equiv T_{[\bar{1}\bar{1}0]} 1/2(110)$ the phonons related to the two above mentioned transitions are no longer isolated points in reciprocal space but are part of the valley of the transverse low energy phonons along $[\xi\xi 2\xi]$ propagation.

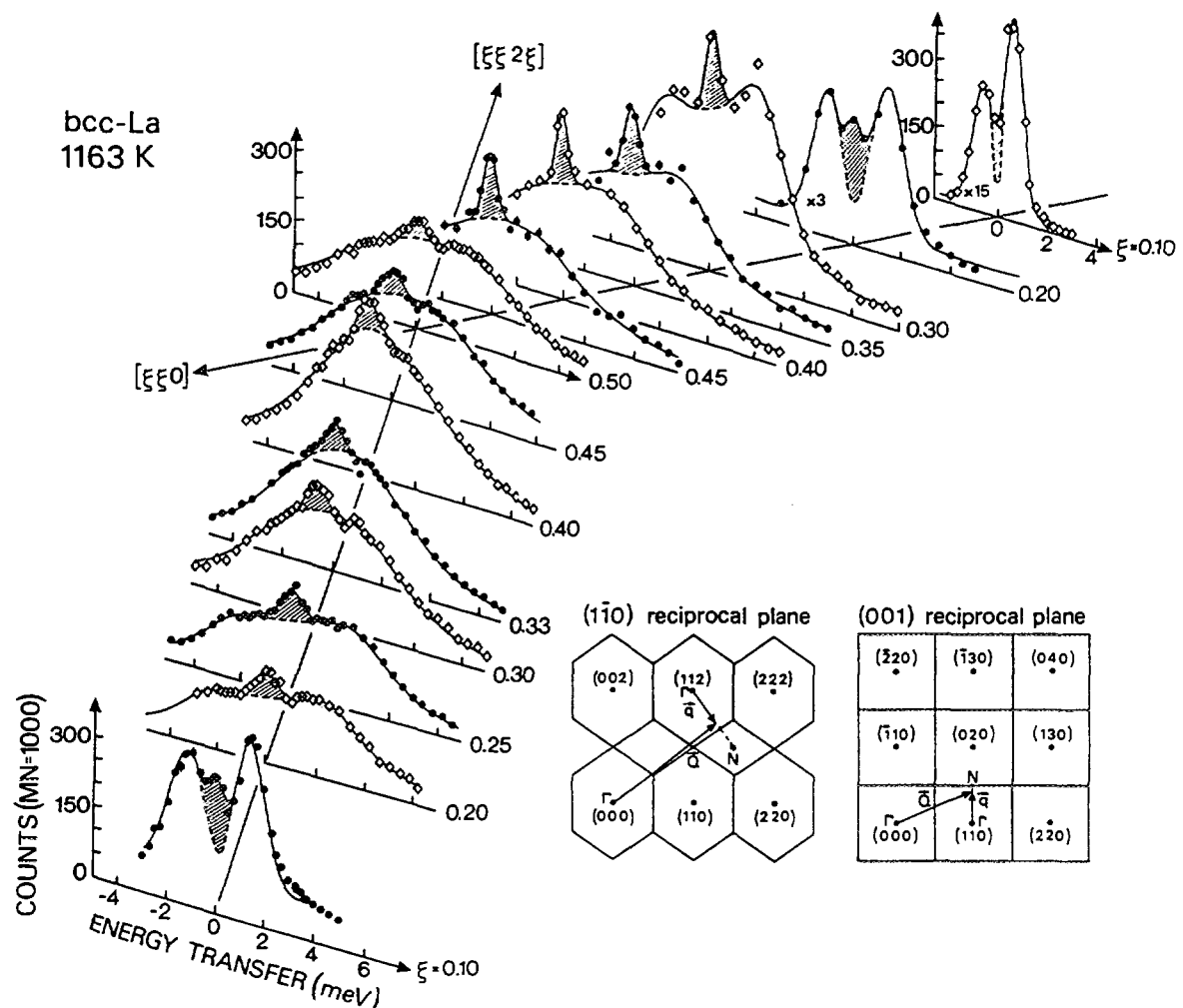


Fig. 13: Low energy and damped phonons along $T_1[\xi\xi 2\xi]$ and $T_1[\xi\xi 0]$ in γ -La [14].

Now, the dispersion of γ -La shows the same anomalies as the other high temperature bcc phases but instead of transforming to ω or hcp, it first transforms into fcc - see Fig. 1. Both fcc and hcp are closest packed structures and differ only by their stacking sequence of the basal plane. As for the bcc \rightarrow hcp transition a short wavelength shuffle shifts the ABAB... sequence of $(110)_{bcc}$ planes to an ABAB... sequence of densely packed basal planes. But a further $(110)[1\bar{1}0]_{bcc}$ long wavelength shear is needed to change to the ABCABC... sequence of $(111)_{fcc}$ planes - see Fig. 12. Hence this mechanism is analogous to the Burgers mechanism, as both transitions preserve the interlayer distance of the original $(110)_{bcc}$ plane and thus the repulsive effect of one layer with respect to the

other. The essential difference is that for the bcc \rightarrow fcc transition a further long wavelength strain of $(110)_{\text{bcc}}$ planes into $[1\bar{1}0]$ direction is needed. The corresponding elastic constant $C' = 1/2(C_{11}-C_{12})$ is given by the initial shape of the $T_1[110]$ phonon branch. Indeed a very low C' is found in γ -La, which is best expressed by the unusual high asymmetry parameter for the two shear constants $A = C_{44}/C' \approx 10$ [14]. Similar considerations hold for the $\delta \rightarrow \gamma$ transition in Fe. Also in δ -Fe a large $A = 7.1$ is found [24].

The dominating role of C' is confirmed by thermodynamic considerations. Assuming no volume change through the $\gamma \rightarrow \beta$ transition, it can be shown that the local restoring forces tending to oppose the change into the fcc phase solely depend on the shear constant C' , i.e. a small C' alone already indicates low potential barriers for a bcc \rightarrow fcc transition.

2.4 Consequences of the martensitic transition

The dynamics of the high temperature bcc phases of the group 3 and 4 metals is dominated by a valley of phonons of unusual low energy and strong damping along $[\xi\xi 2\xi]$ and $[\xi\xi 0]$ propagation. The example demonstrating this for γ -La is depicted in Fig. 13. Along this valley in the 4 dim. \vec{Q} - ω space, we find all the large amplitude fluctuations one needs to transform the bcc lattice to ω , hcp, fcc or related structures like 7R, 9R, d-hcp etc... Which of these locks in at the transition can hardly be determined from the phonons themselves, it depends on subtle details of the free energy of the product phase.

2.4.1 What stabilizes bcc?

The other question as to why bcc is stable at high temperature although considerable fluctuations towards close packed structures are observed is easier to answer. Knowing the phonon dispersions in the parent and product phase, vibrational entropy changes ΔS_v at the transition temperature can be calculated rather precisely in *quasiharmonic* approximation [25].

$$S_v = -3k_B \int d\omega Z(\omega) \{ n(\omega) \ln n(\omega) - [1+n(\omega)] \ln [1+n(\omega)] \} \quad (6)$$

$$\Delta S_v = S_{v, \text{above } T_c} - S_{v, \text{below } T_c}$$

where $n(\omega) = (\exp\{\hbar\omega/k_B T\} - 1)^{-1}$. A comparison with the known excess enthalpy $\Delta S_{tot}, T_M$ of the bcc \rightarrow close packed transition –see Table 1 – shows that roughly 2/3 of the excess enthalpy is due to the vibrational entropy. The latter is dominated by the low-energy phonons. The remaining $\Delta S_{tot} - \Delta S_v = \Delta S_{el}$ can then be ascribed to the difference in electronic entropy ΔS_{el} . For the particular case of δ -Fe [24] the change in vibrational entropy is even larger than the total entropy change, i.e. electronic contributions destabilize the bcc high temperature phase in Fe. Consequently, the role of these transverse energy phonons is two fold: *they are due to the instability of the bcc lattice towards a martensitic transition but in the same instance bcc is stabilized due to their contribution to the vibrational entropy*.

These considerations are not limited to the elementary systems. Ultrasonic and neutron measurements on a series of Cu based tertiary shape memory alloys [23,26] show

similar low energy phonons as in the group 3 and 4 metals. In particular large anisotropy parameters A are found. Hence it can be concluded that in the Cu based alloys also, the martensitic transformation is practically a pure vibrational driven transition [26].

Table 1: Vibrational ΔS_v and total entropy changes ΔS_{tot} at the bcc \rightarrow close packed transition

	T_0 (K)	ΔS_v (k _B /atom)	ΔS_{tot} (k _B /atom)
Ti	1156	0.29	0.42
Zr	1135	0.26	0.40
La	1138	0.26	0.30
Fe($\delta \rightarrow \gamma$)	1665	0.11	0.06

2.4.2 Defect driven condensation of static displacements

Static displacement towards the product phase but still within the parent phase have been reported in many alloyed systems. Prominent examples are the ω phase alloy Zr_{0.8}Nb_{0.2} [27] and the shape memory alloys Ni_{1-x}Al_x [28] and Ni_{0.5}Ti_{0.5}[29]. It was one of the surprises of the neutron measurements in β -Zr and other pure metals that no truly elastic scattering has been observed at these points in reciprocal space where the phonons are overdamped. *From this arises the question to which extent these static precursors of the martensitic transition are defect related or alternatively generic to the transition.*

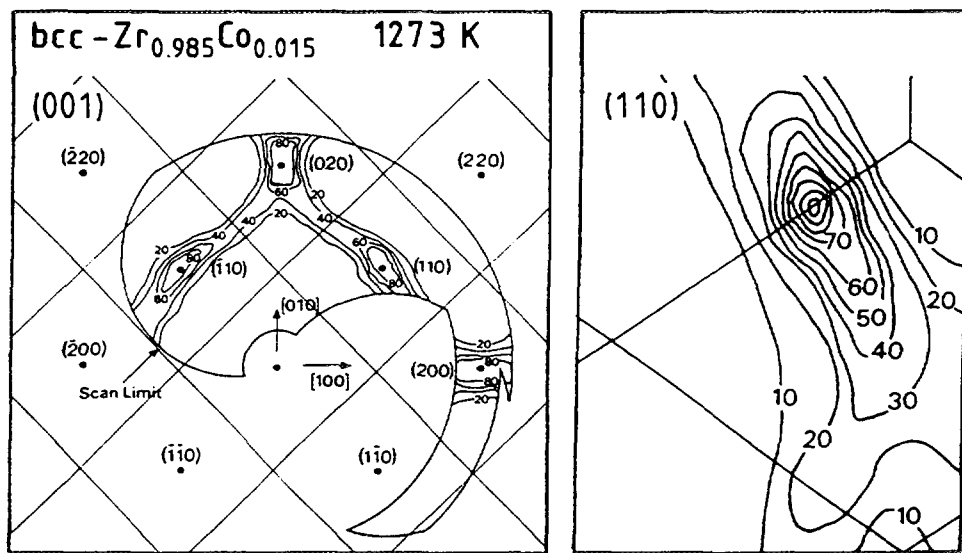


Fig. 14 "Truly" diffuse scattering in bcc-Zr due to alloying of 1.5 at % Co [30].

A first answer is quickly given: A considerable part of what has been reported in literature about elastic precursors related to martensitic transitions is simply due to heterogeneous co-existence of product and parent phase. Reasons for this co-existence might be temperature gradients, concentration gradients, impurity driven phase separation, thermal non-equilibrium conditions etc ... A representative example of how gaseous impurities are the driving force for a strongly temperature dependent segregation has been reported for α -precipitates in β -Zr due to oxygen and nitrogen contamination [21].

As stated before diffuse scattering at zero energy transfer in pure samples of the bcc high temperature phase is of inelastic nature. The situation changes upon alloying. With increasing amount of impurities the elastic intensity increases at certain regions in reciprocal space with respect to the neighbouring inelastic intensity. The *difference* between both is then due to *truly elastic* diffuse scattering [11,30]. In reciprocal space this additional elastic diffuse intensity is found exactly along the valley of the low energy and strongly damped phonons. Fig. 14 gives the example of β -Zr alloyed with 1.5 at % Co [30]. Almost similar diffuse patterns are observed for impurities of a so different nature as O, N, Co, or Nb [31]. Only the strength of the effect changes.

In the pure elements the displacements towards the close packed structures are of purely dynamical nature. The existence of diffuse elastic scattering in the presence of point defects indicates that parts of the fluctuations freeze to static displacements. This can be understood in terms of a Kanzaki force analysis. Then, in the limit of low defect concentrations the diffuse scattering cross section can be written [32]:

$$\frac{d\sigma}{d\omega} = c_h c_d \left\langle \left| L(\bar{Q}) + i b_h \bar{Q} \tilde{u}(\bar{q}) + \dots \right|^2 \right\rangle e^{-2w} \quad (7)$$

c_h, c_d are the host and defect concentrations and b_h, b_d the corresponding coherent scattering lengths. For substitutional defects the Laue term $L(\bar{Q}) = b_d - b_h$ becomes independent of \bar{Q} . $\tilde{u}(\bar{q})$ is the Fourier transform of the defect caused displacements in real space $\bar{u}(\bar{r})$. For sufficiently small displacements these are formally ascribed to short ranged Kanzaki forces $\bar{f}(\bar{r}_n)$

$$u_{\alpha}^m = \sum_{\beta, n} G_{\alpha\beta}^{mn} \cdot f_{\beta}^n \quad (8)$$

$$G_{\alpha\beta}^{mn} = \int_{1/BZ} D_{\alpha\beta}^{-1}(\bar{q}) \cdot e^{i\bar{q}(\bar{r}_m - \bar{r}_n)} d\bar{q} \quad (9)$$

The dynamical matrix $\overline{\overline{D}}(\bar{q})$ - eq. (2) - which enters into eqs. (8-9) relates the static displacements to the phonon dispersion or lattice potential. As seen in eq. (7) the diffuse elastic scattering is proportional to the scattering vector \bar{Q} times the Fourier transform of the displacement field $\tilde{u}(\bar{q})$. In main symmetry directions such as $<111>$ or $<110>$ the dynamical matrix contains only the square of the longitudinal and transverse phonon energies. Therefore, independently of any model for the displacement field, the diffuse intensity is already proportional to $(\hbar\omega)^4$. *Consequently, diffuse intensity strongly correlates with low energy phonons.* Physically that means that in the presence of defects dynamical fluctuations freeze into static displacements. In the case of β -Zr it could be shown that the displacement field in the presence of defects is a superposition of all the displacements for which low energy phonons are observed [30]. Assignments like diffuse scattering due to ω -embryos are oversimplifications, they arise from measurements of the diffuse scattering only in the $[110]$ plane and oversee its 3-dimensional character.

The absense of elastic precursors is not limited to transitions in monoatomic pure samples. The measurements on a series of Cu based shape memory alloys by Manosa and co-workers [33] confirm the observation that diffuse elastic scattering which might be related to the martensitic transition can be avoided if the alloys are carefully prepared and annealed.

Keeping in mind that at least in the examples cited above diffuse elastic scattering is rather a consequence of defects in the parent phase, than a property inherent to the martensitic transition, a scenario which describes the martensitic transition as a uniform transformation driven by a free energy difference seems to be appropriate. Heterogenous nucleation at defects might play a role for the transition in cases where they are present, however, they are certainly not a necessary prerequisite for the martensitic transformation.

2.4.3 Local symmetry breaking

It is evident from Figs 5 and 13 that the transverse phonons along $[\xi\xi 2\xi]$ and $[\xi\xi 0]$ are strongly damped. Close to or at the BZ boundary the lifetime of the excitations are only of the order of a few vibrational periods. Phonon-phonon interactions can be seen as the physical origin behind these short lifetimes. In a first approximation one-phonon events decay into two one or more phonons, and vice versa multi-phonon events combine to one phonon. Interference effects due to this multi-phonon creation and annihilation have been observed and discussed initially for the quantum solid ^4He . In a theory reviewed by Glyde [34] alterations of the one-phonon scattering law $S(Q, \omega)_1$ phonon are expressed in terms of the observed damping $\Gamma(\bar{q})$

$$S(\bar{Q}, \omega)_{\text{interf.}} = S(\bar{Q}, \omega)_{1\text{phonon}} \left\{ 1 + A(\bar{Q}, \bar{q}) + B(\bar{Q}, \bar{q}, \omega, \omega_0(\bar{q}), \Gamma(\bar{q})) \right\} \quad (10)$$

A first contribution A alters the one-phonon scattering law for apparently equivalent loci in reciprocal space, and a further contribution B affects the one-phonon line shape itself. These latter alterations are explicitly expressed in terms of the damping $\Gamma(\bar{q})$.

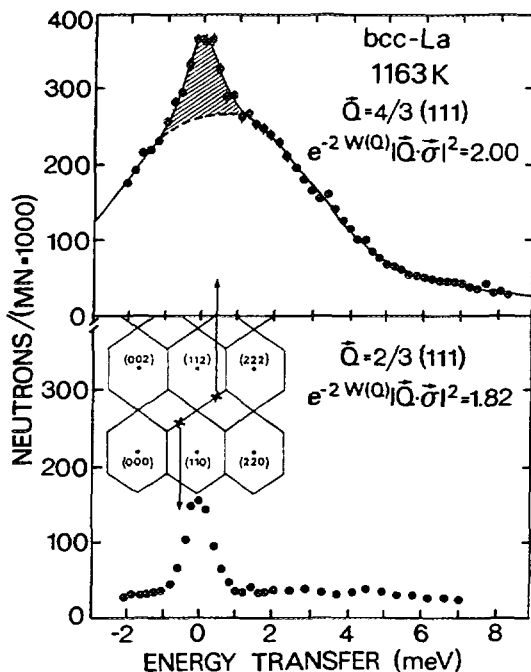


Fig. 15: The L2/3(111) phonon measured in γ -La at two different but equivalent loci in reciprocal space. The one-phonon structure factor $f(\bar{Q})$ for the two points differs by only 10 % [14].

Fig. 15 gives strong evidence for this apparent breaking of cubic symmetry. Measurements of the L2/3(111) phonon in γ -La at different but equivalent \bar{q} -values result in a completely different dynamical response. By no means can this be explained by the \bar{Q} -dependent structure factor of the one-phonon scattering law $f(\bar{Q})$, which varies for the actual case by 10%. We will not go into detail concerning a quantitative analysis rather present the physical picture which emerges. Because L2/3(111) phonon intensities and line shapes are so different at equivalent points in reciprocal space, we have to conclude that the displacements due to the L2/3(111) phonon locally break the bcc symmetry. (111) planes fluctuate towards the ω structure, however during the second half of the wave period amplitudes are so damped that displacements towards the anti- ω structure are strongly suppressed [14,35].

2.4.4 Anomalous diffusion

At half the melting temperature T_m self diffusivities $D(T)$ in the elementary bcc structures vary by roughly 8 orders of magnitude [36]. Elements with martensitic transitions show the highest diffusivity rate whereas the most stable bcc metals of group 6, Cr, Mo, and W have particularly low diffusivities. Direct [37] and indirect measurements [36] of the diffusion mechanism lead to the conclusion that despite the great variety in D , one and the same mechanism is responsible for the self diffusion in all bcc metals, namely the diffusion via nearest neighbour vacancies. *The question, why $D(1/2T_m)$ differs so much, if the same mechanism is valid, remains.* Of course it is appealing to suspect a relation between the tendency of the bcc metals to undergo phase transitions and their unusual diffusivities. In Fig. 16 the possible connection is shown: The L2/3(111) as well as the T_{11/2}(110) phonon displace the lattice in such a way that atoms are pushed into the direction of an eventually present nearest neighbour vacancy. As argued before, these displacements are of large amplitude in those metals which exhibit "weak" bcc structures, i.e. the phonons tell us that migration barriers are extraordinarily low. Of course diffusion is not only promoted by the two phonons shown in Fig. 16 but by the whole set of displacements related to the tendency of the bcc metals to undergo transitions.

This idea has been worked out more quantitatively [38] and the migration barrier H^m could be expressed in terms of a purely structural term $\alpha \cdot a^2$ characteristic for *all* bcc phases and a term explicitly reflecting the dynamical response of the actual lattice

$$H^m = \alpha \cdot a^2 \left(\int \frac{Z(\omega)}{M\omega^2} d\omega \right)^{-1} \quad (11)$$

Here a is the lattice constant, M the atomic mass, and the weighting of the phonon density of states $Z(\omega)$ by ω^{-2} guarantees the dominating influence of the low energy phonons.

This model which relates the diffusion anomalies in bcc metals to varying migration barriers has been very successful in explaining the different experimental facts: i) The calculated H^m is close to the measured values, ii) the pronounced chemical group systematics observed in the diffusivity and H^m is reproduced and iii) migration barriers

are established as temperature dependent quantities, with gradients in opposite directions for bcc metals as different as β -Zr and Cr. Fig.17 compares calculated and measured H^m and also indicates the lattice dynamical reason for the systematic variation of H^m .

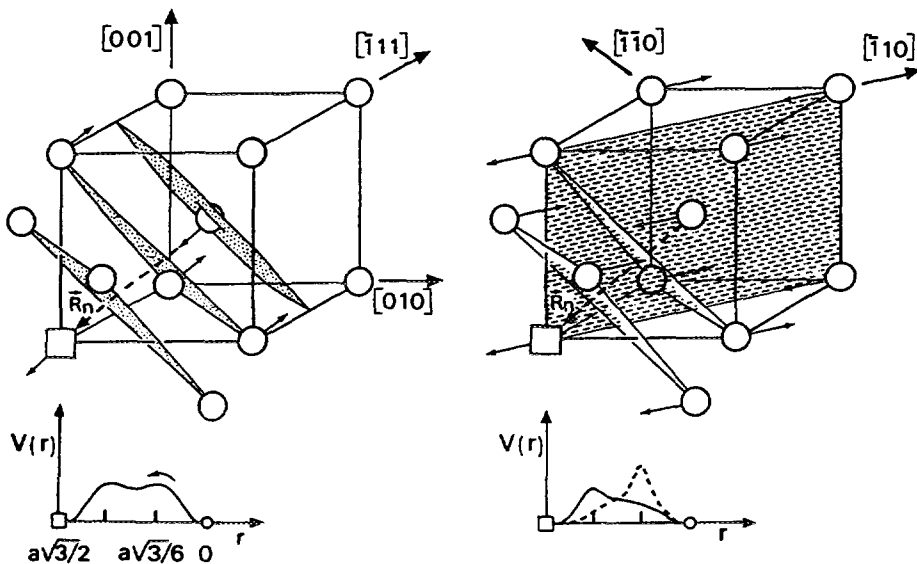


Fig. 16: The displacements of the L₂/3(111) (left) and the T₁1/2(110) phonon (right) push the centered atom in direction of an eventually present nearest neighbour vacancy. At the left a quasi-static double peak potential is seen by the migrating atom. At the right the phonon itself alters the barriers which it has to overcome during a vibrational period [36].

3 TRANSITIONS FROM CLOSE PACKED STRUCTURES → BCC

The most straight forward examples are the transitions of the low temperature α or hcp phases of the group 4 metals Ti, Zr or Hf to high temperature bcc. No dynamical precursors have been found so far, which is in itself not astonishing. As known from ground state calculations [39] hcp is the structure with the lowest internal energy and as argued before bcc is mainly stabilized by vibrational entropy of the bcc phase itself.

A more promising example could be the invar system Fe₃Pt. Here a strong composition and ordering dependent martensitic transition from a high temperature fcc phase to a low temperature bcc phase is found [40]. According to the Nishiyama-Wassermann rule

$$(111)\text{fcc} \parallel (110)\text{bcc} \text{ and } [1\bar{1}0]\text{fcc} \parallel [001]\text{bcc}$$

(111)[11̄2] shuffles are needed to transform the fcc ABCABC... stacking sequence to a ABAB... stacking sequence of (110)_{bcc} planes. Despite several precise neutron and ultrasonic measurements particularly along the T_[11̄2][ξξξ] branch no anomalies evidently connected to the transition could be identified [41,42]. Instead a pronounced decrease of the T_[1̄10]1/2(110) phonon similar to that observed in the bcc metals was found in the austenitic fcc phase [41]. Whether the displacements of this phonon are related to the transition remains to be solved.

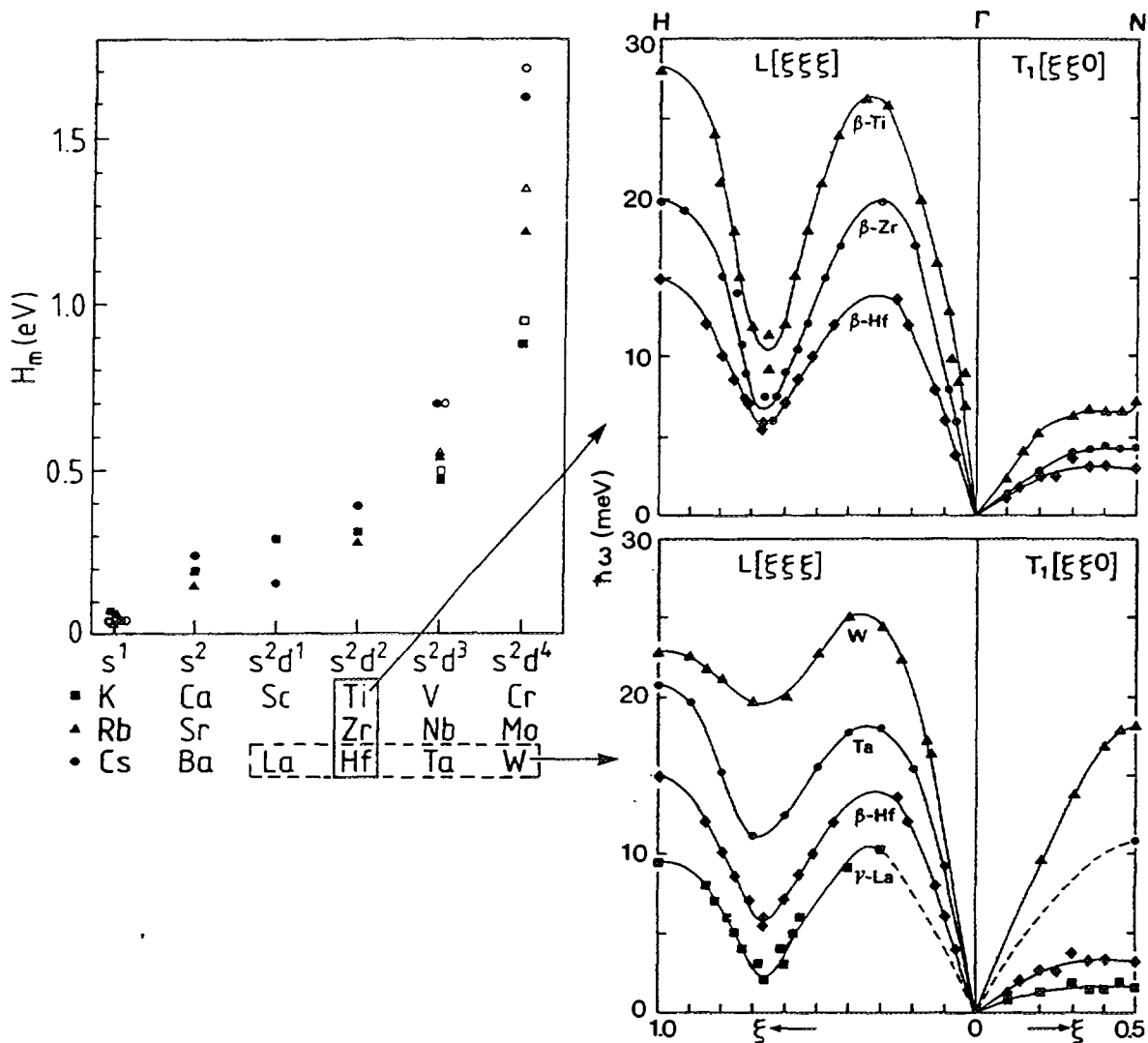


Fig. 17: Left: Migration barriers H_m^m calculated (black symbols) according to the model of phonon controlled diffusion and compared to measured values (open symbols). Right: Explanation of the chemical group systematics by low energy phonons [38].

4 THE FCC \rightarrow HCP TRANSITION

Co is an often discussed example. At $T_0 = 695$ K the high temperature phase of fcc-Co transforms to the low temperature hcp structure. For the transition closest packed stacking sequences have to change from ABCABC... to ABAB... Several models have been proposed for the transition, for instance Shapiro and Moss [43] postulate the coherent superposition of two $(111)[11\bar{2}]_{\text{fcc}}$ shuffles with wavelength of $\lambda_1=3d_{111}$ and $\lambda_2=6d_{111}$, and more recently Folkins and Walker [44] showed a transition path which is the sum of a modulation and a strain. However, experiments so far are at variance to all these explanations. Firstly, most of the experiments were done on alloyed crystals [43] and secondly, recent careful measurements along $T_{[11\bar{2}]}[\xi\xi\xi]_{\text{fcc}}$ in pure Co in the fcc as well as in the hcp phase [45] did not reveal any dynamical anomaly related to the transition. The only experimental hint that Co indeed transforms by shearing $(111)_{\text{fcc}}$ planes comes from relatively low energies of the $T[\xi\xi\xi]$ phonon branch at short as well as long wavelengths.

A very pronounced phonon anomaly, has been found in fcc or β -La which transforms upon cooling at 609 K to d-hcp. At $\xi = 0.42$ the dispersion along $T[\xi\xi\xi]$ branch exhibits a strong temperature dependent dip [46]. However, this example might not be conclusive. The anomaly is only present in metastable β -La below room temperature.

5 SUMMARY

From phonon measurements, shuffles have been identified which promote the transition from bcc towards ω , hcp or fcc. With the exception of the bcc $\rightarrow \omega$ transition the shuffles alone cannot transform the lattice, further homogenous strains are needed. In none of the cited examples do elastic precursors or defects play any obvious role during the transition, which favours the picture of a free energy driven uniform transformation of the entire crystal. The phonon dispersions in the transition elements of group 3 and 4 indicates low restoring forces for fluctuations not only towards one discrete close packed structure but to all of them. The one which locks in at the transition cannot be judged from the phonons alone but is rather a question of subtle details of the internal energy.

The tendency of the bcc metals to transform has severe consequences on the physical properties of these metals. Vibrations in these crystals behave liquid-like along certain directions in reciprocal space. The inelastic response breaks cubic symmetry and can only be explained by phonon-phonon interaction. These dynamical fluctuations promote both the stability of bcc by entropy and the transformation because they are indicative for low restoring forces. Further, self diffusion in bcc can be explained by low migration barriers, the height of which is given by the low energy phonons probing the harmonic part of the migration potential.

The situation is much less clear for the reverse transition, namely close packed \rightarrow bcc. No shuffle can be identified, only low shear constants are observed. The situation is similar for the transition within closest packing. Further experiments on better defined, if possible, elementary systems and at transitions at high temperature are necessary. Whereas high temperature certainly hinders the experimental access, it is the best way to guarantee the observation of the martensitic transitions in thermal equilibrium and due to the higher thermal energy, pinning of the transition on defects is less probable.

6 REFERENCES

- [1] Young D.A., Phase diagrams of the elements (University of California Press, Berkeley, 1991)
- [2] Delaey L., in Phase Transformations, Material Sience and Technology Vol.5, Vol ed. P. Haasen (VCM Weinheim 1991) pp.339
- [3] Petry W., Flottmann T., Heiming A., Trampenau J., Alba M. and Vogl G., *Phys. Rev. Lett.* **61** (1988) 722
- [4] Schwarz W., Blaschko O. and Gorgas I., *Phys. Rev. B* **44** (1991) 6785; Smith H.G., Berliner R., Jorgensen J.D., Nielsen M. and Trivisonno J., *Phys. Rev. B* **41** (1990) 1231
- [5] Schwarz W., Blaschko O. and Gorgas I., *Phys Rev. B* **46** (1992) 14448; Smith H.G., Berliner R., Jorgensen J.D and Trivisonno J., *Phys. Rev. B* **43** (1991) 4524; Blaschko O. and Krexner G., *Phys. Rev. B* **30** (1984) 1667
- [6] Ye Y.Y., Chan C.T., Ho K.-M. and Harmon B.N., *Int.J. Supercomput. Appl.* **4**, (1991) 111

- [7] Gooding R.J. and Krumhansl J.A., *Phys. Rev. B* **38** (1988) 1695; Gooding R.J., Ye Y.Y., Chan C.T., ho K.-M. and Harmon B.N., *Phys. Rev. B* **43** (1991) 13626
- [8] Stassis C., Zarestky J., Wakabayashi N., *Phys. Rev. Lett.* **41** (1978) 1726; Stassis C. and Zarestky J., *Solid State Comm.* **52** (1984) 9
- [9] Flottmann Th., Petry W., Serve R. and Vogl G., *Nucl. Instr. & Methods A* **260**, (1987) 165
- [10] Petry W., Heiming A., Trampenau J., Alba M., Schober H.R. and Vogl G., *Phys. Rev. B* **43** (1991) 10933
- [11] Heiming A., Petry W., Trampenau J., Alba M., Herzig C., Schober H.R. and Vogl G., *Phys. Rev. B* **43** (1991) 10948
- [12] Trampenau J., Heiming A., Petry W., Alba M., Herzig C., Miekeley W. and Schober H.R., *Phys. Rev. B* **43** (1991) 10963
- [13] Petry W., Trampenau J., Herzig C., *Phys. Rev. B* **48** (1993) 881
- [14] Güthoff F., Petry W., Stassis C., Heiming A., Hennion B., Herzig C. and Trampenau J., *Phys. Rev. B* **47** (1993) 2563
- [15] Ho K.-M., Fu C.-L. and Harmon B.N., *Phys. Rev. B* **28** (1983) 6687; *Phys. Rev. B* **29** (1984) 1575
- [16] Shaw W.M., Muhlestein L.D., *Phys. Rev. B* **4** (1971) 969
- [17] Trampenau J., Petry W., Herzig Ch., *Phys. Rev. B* **47** (1993) 3132
- [18] Burgers W.G., *Physica* **1** (1934) 561
- [19] Lingard P.-A. and Mouritsen O.G., *Phys. Rev. Lett.* **57** (1986) 2458
- [20] Krumhansl J.A. and Gooding R.J., *Phys. Rev. B* **39** (1989) 3047
- [21] Heiming A., Petry W., Trampenau J., Alba M., Herzig C. and Vogl G., *Phys. Rev. B* **40** (1989) 11425
- [22] Chen Y., Ho K.-M. and Harmon B.N., *Phys. Rev. B* **37** (1988) 283
- [23] Guenin G., Rios Jara D., Morin M., Delaey L., Pynn R. and Gobin P.F., *J. Physique (Paris), Colloque* **43** (1982) C4-597
- [24] Neuhaus J., Nicolaus K., Petry W., Hennion B., Krimmel A., to be published
- [25] Schober H.R. and Petry W. in *Structure of Solids, Material Science and Technology*, Vol 1, Vol. ed. V. Gerold (VCH-Weinheim 1993) pp.289
- [26] Planes A., Manosa L., Rios-Jara D. and Ortín J., *Phys. Rev. B* **45** (1992) 7633; Manosa L., Planes A., Ortín J. and Martínez B., *Phys. Rev. B* **48** (1993) 3611
- [27] Noda Y., Yamada Y. and Shapiro S.M., *Phys. Rev. B* **40** (1989) 5995
- [28] Shapiro S.M., Yang B.X., Noda Y., Tanner L.E. and Shryvers D., *Phys. Rev. B* **44** (1991) 9301
- [29] Müllner M., Tietze H., Eckold G. and Assmus W. in *Proc. Int. Conf. Martensitic Transformations, ICOMAT 86*, Nara (Japan), ed. I. Tamura (The Japan Inst. of Metals 1987) pp.159
- [30] Heiming A., Petry W., Vogl G., Trampenau J., Schober H.R., Chevrier J. and Schärf O., *Z. Phys. B* **85** (1991) 239
- [31] Petry W., *Phase Transitions* **31** (1991) 119
- [32] Bauer G.S., in *Treatise on materials science and technology* ed. by G. Kostorz, Vol 15 (Academic Press, New York 1979) p. 291
- [33] Manosa L., Zarestky J., Lograsso T., Delaney D.W. and Stassis C., *Phys. Rev. B* **48** (1993) 15708
- [34] Glyde H.R., *Can. J. Phys.* **52** (1974) 2281
- [35] Dubos O., Petry W., Trampenau J. and Hennion B., unpublished
- [36] Petry W., Heiming A., Herzig C. and Trampenau J., *Defect & Diffusion Forum* **75** (1991) 211

- [37] Vogl G., Petry W., Flottmann T. and Heiming A., *Phys. Rev. B* **39** (1989) 5025
- [38] Schober H.R., Petry W. and Trampenau J., *J. Phys. Condens. Matter* **4** (1992) 9321
- [39] Pettifor D.G.. in Structure of Solids Material Science and Technology, Vol 1, Vol. ed. V. Gerold (VCH-Weinheim 1993) pp.61
- [40] Wassermann E.F. in Ferromagnetic Material Vol 5, eds K.H. Buschow, E.P. Wollfarth (North Holland, Amsterdam 1990) pp.240
- [41] Noda Y. and Endoh Y., *J. Phys. Soc. Japan* **57** (1988) 4225
- [42] Kawald U., Schulenberg P., Bach H., Pelzl J., Eckold G. and Saunders A., *J. Appl. Phys.* **70** (1991) 6537
- [43] Shapiro S.M. and Moss S.C., *Phys. Rev. B* **15** (1977) 2726
- [44] Folkins I. and Walker M.B., *Phys. Rev. Lett.* **65** (1990) 127
- [45] Strauß B., Frey F., Petry W., Trampenau, J. Nicolaus K., Shapiro S.M., Bossy J., *Phys. Rev. B*, in press
- [46] Stassis C., Smith G.S., Harmon B.N., Ho K.-M. and Chen Y., *Phys. Rev. B* **31** (1985) 6298



IDENTIFICATION OF DIFFERENT MAGNETIC MODES IN CsFeCl₃ BY POLARISATION ANALYSIS

BRUNO DORNER

Institut Laue Langevin, BP156, F-38042 Grenoble, France

and

BORIS TOPERVERG¹, MARKUS BAEHR², DANIEL PETITGRAND³

- 1) *St Petersburg Nuclear Physics Institut, Gatchina, 188350 St. Petersburg, Russia*
- 2) *Hahn Meitner Institut, Glienicker Str.100, D-14109 Berlin, Germany*
- 3) *Laboratoire Léon Brillouin, CEA-Saclay, 91191 Gif-Sur-Yvette, France*

ABSTRACT

CsFeCl₃ is a quasi 1D magnetic system with a singlet groundstate. The Fe²⁺ ion has an effective spin S = 1. Experimental results in a magnetic field applied perpendicular to the anisotropy axis show that the excited states (doubly degenerate in zero field) split and shift to higher frequencies with increasing field. The splitting of the high frequency modes is very small compared to the instrumental resolution. Only polarisation analysis of inelastic neutron scattering made it possible to observe the splitting everywhere in reciprocal space. The frequency shift of the two modes with field is different such that a mode crossing appears for fields below about 4 Tesla.

1. Introduction

CsFeCl₃ is one compound out of the family AFeX₃, with A = Rb, Cs and X = Cl, Br, where the Fe²⁺ ion has an effective spin S = 1. It crystallises in the hexagonal space group P6₃ / mmc. FeCl₆ octahedra form chains in c-direction by face sharing. These chains are separated by the Cs-ions and form a quasi one dimensional magnetic system [1], see Fig. 1.

From basic quantum mechanics we know that an isolated spin S = 1 has three states with respect to a quantisation axis (z-direction) which we will call the anisotropy axis in the following. There are three values for the quantum number m :

$$\begin{aligned}
 m &= -1 & \rightarrow s^z &= -1 \\
 m &= 0 & \rightarrow s^z &= 0 \\
 m &= +1 & \rightarrow s^z &= +1
 \end{aligned}$$

where s^z is the projection of the spin on the anisotropy axis. $s^z = 0$ means that in this state the magnetic moment averages out to zero.

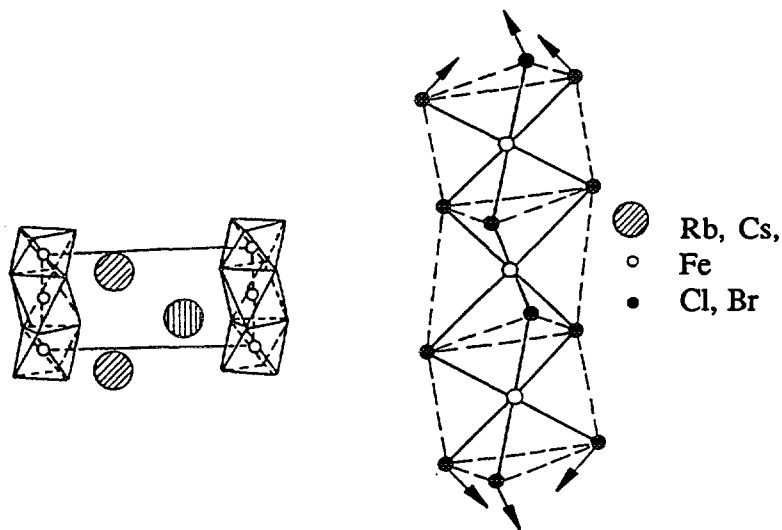


Fig. 1 : The structure of $AFeX_3$ with $A = Rb, Cs$ and $X = Cl, Br$

The crystal electric field in the $AFeX_3$ materials produces an anisotropy $D(S^z)^2$ with a positive value of D . This anisotropy creates a splitting between the $m = \pm 1$ (degenerate doubled state) and the $m = 0$ singlet ground state. In the $RbFeX_3$ systems this local singlet ground state goes at low temperatures over to a x-y or easy plane system, where the interactions between neighbouring spins create long range order with the magnetic moments perpendicular to the z-axis with the frustrated 120° structure.

In $CsFeCl_3$ the exchange interactions are not strong enough to create long range magnetic order at low temperatures. Due to the strong anisotropy D the whole system remains in a singlet ground state for temperature $T \rightarrow 0$.

Note that a negative value for D produces an Ising system, where the $m = \pm 1$ doublet is the ground state.

Let us consider the Hamiltonian for a 1D system with only nearest neighbour interactions (super exchange) :

$$H = -2J \sum_i S_i S_{i+1} + D \sum_i (S_i^z)^2 \quad (1)$$

Positive or negative values for J describe ferromagnetic or antiferromagnetic coupling along the chains.

For $D < 8|J|$ the systems ($RbFeCl_3$, $RbFeBr_3$) exhibit long range order at low temperatures with an easy plane. For $D > 8|J|$ the systems ($CsFeCl_3$, $CsFeBr_3$) remain in a singlet ground state with no magnetic moment. $D >$ or $< 8|J|$ would be the conditions for ideal 1-D systems. The real $AFeX_3$ materials have also an interaction J' between the chains and the correct conditions reads $D >$ or $< 8|J| + 12|J'|$.

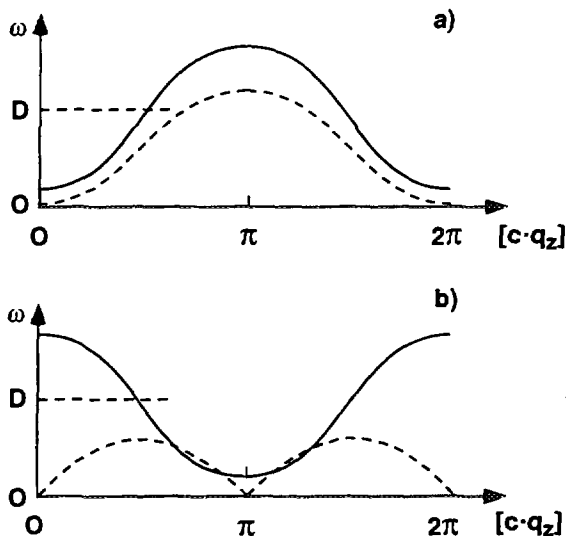


Fig. 2 : Schematic dispersion curves for magnetic excitations in 1-D systems. Full lines correspond to singlet groundstate systems, where D is the anisotropy parameter, see Eq. 2 :

a) for $J > 0$ and b) for $J < 0$. For comparison the magnon dispersion curves for a 1-D Heisenberg ferromagnet (a) and a 1-D Heisenberg antiferromagnet (b) are given by dashed lines.

The magnetic excitations (better called excitons than magnons) in a singlet ground state system are shown schematically in Fig. 2 for positive and negative values of J . The dispersion is given by [2] :

$$\omega(q_z) = \sqrt{D^2 - 8JD \cos(cq_z)} \quad (2)$$

Note that positive (RbFeCl_3 , CsFeCl_3) or negative (RbFeBr_3 , CsFeBr_3) values for J shift the lowest frequency from 0 to π . For comparison the dispersion curves in the absence of an anisotropy are given also in Fig. 2.

For the 1D Heisenberg ferromagnet ($S = 1$) it reads

$$\omega(q_z) = 4J[1 - \cos(cq_z)] \quad (3)$$

and for the 1D Heisenberg antiferromagnet ($S = 1$) :

$$\omega(q_z) = 4|J| |\sin(cq_z)| \quad (4)$$

c is in all expressions given above the distance between magnetic neighbours and q_z is the wavevector of the excitation with the dimension [$2\pi/c$].

In the 1D Heisenberg Antiferromagnet the dispersion curves are doubly degenerate due to time reversal symmetry.

In the singlet ground state systems the dispersion curves are doubly degenerate for another reason : the excited state contains $m = \pm 1$. An applied magnetic field splits this degeneracy, see Fig. 3. If the field is applied parallel to the anisotropy axis, the Zeeman splitting of the excited state leads to two modes one with increasing frequency and one with decreasing frequency. The states remain pure in the quantum number m . Only two modes can be observed by inelastic neutron scattering, because a transition from $m = -1$ to $m = +1$ would require a change in spin $\Delta S = 2$. A neutron which has the spin $1/2$ can only transfer $\Delta S = 0$ or 1 . The mode with decreasing frequency can be considered as a soft mode which creates a phase transition to long range order [3].

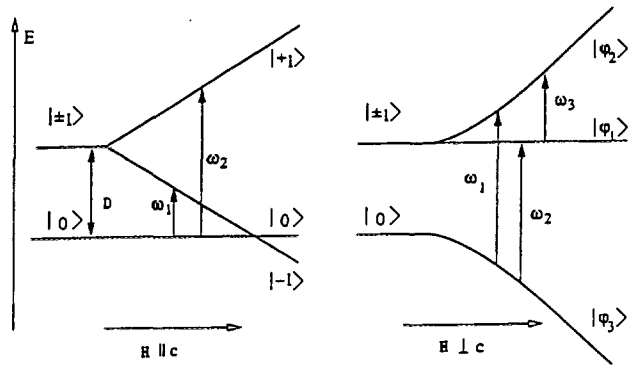


Fig. 3 : The level schemes for CsFeCl_3 in fields applied either parallel or perpendicular to the anisotropy axis.

If the field is applied perpendicular to the anisotropy axis, the degeneracy is also lifted, but both modes shift to higher frequencies. This field breaks the symmetry of the anisotropy axis and the new eigenfunctions φ_1 to φ_3 contain a field dependent mixture of the states $m = 0, \pm 1$. Therefore three modes ω_1 to ω_3 can principally be observed by neutron scattering. In reality, the thermal occupation of the φ_1 state is too small to observe the transition ω_3 . The detailed behaviour of CsFeCl_3 in a field applied perpendicular to the anisotropy axis will be discussed in the following.

2. Theoretical Aspects

In CsFeCl_3 the interactions between nearest $|J_1|$ and next nearest $|J_2|$ neighbours along the chains have to be taken into account and also the interaction between chains J' . The full Hamiltonian [4] reads

$$H = -2J_1 \sum_i S_i S_{i+1} - 2J_2 \sum_i S_i S_{i+2} - J' \sum_{i,j} S_i S_j + D \sum_i (S_i^z)^2 + g\mu_B H^x \sum_i S_i^x \quad (5)$$

g is the Landé factor, μ_B is the Bohr magneton and H^x the field applied perpendicular to the chain axis.

The applied field creates an internal magnetisation which leads to a renormalisation of the spectrum. Therefore the Landé factor is replaced by a field dependent factor \hat{g} [4]. A further renormalisation occurs from the field dependence of the spin correlation function. The factors Q_x and $Q_y = Q_z = Q_{yz}$, which are equal to one at zero field, are the corresponding correction factors.

At zero field the dispersion curve reads, similar to Eq. (2) :

$$\omega_{1,2}(q) = \sqrt{D^2 - 2DJ_q} \quad (6)$$

with

$$J_q = 4 \{ J_1 \cos(q_z) + J_2 \cos(2q_z) + J' (2 \cos(q_y) [\cos(q_y) + \cos(q_x)] - 1) \} \quad (7)$$

Under the field applied perpendicular to the anisotropy axis, the modes split into :

$$\omega_1(q) = \sqrt{\Delta^2 - 2Q_x J_q D^2 / \Delta} \quad (8)$$

$$\omega_2(q) = \sqrt{[(D + \Delta)/2]^2 - J_q(D + \Delta)Q_{yz} + [2Q_{yz}\hat{g}\mu_B H^x J_q / \Delta]^2} \quad (9)$$

with

$$\Delta = \sqrt{D^2 + 4(\hat{g}\mu_B H^x)^2} \quad (10)$$

There are 7 parameters to be determined by the experiment : $J_1, J_2, J, D, \hat{g}, Q_x, Q_{yz}$. We consider the first 4 parameters as being independent of the applied field. They will be determined from results at zero field and kept constant at applied fields.

Now we have to evaluate, which spin operators are involved in the different transitions. In the absence of an external field the creation and annihilation operators between the levels $m = 0$ and $m = \pm 1$ are :

$$\begin{aligned} S^+ &= S^x + iS^y \\ S^- &= S^x - iS^y \end{aligned} \quad (11)$$

see Fig. 4. These operators remain valid for a field $H_{||}$ applied along the anisotropy axis.

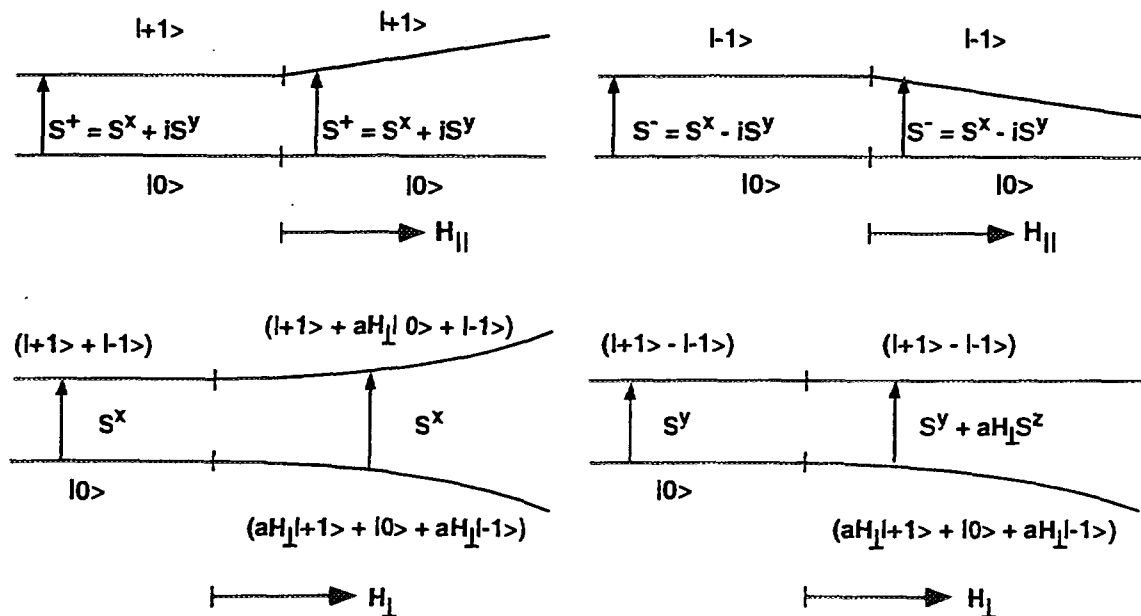


Fig. 4: The transition-operators between different states. The states are given in components of $m = +1, m = 0$ and $m = -1$. At zero field the doubly degenerate excited states can equally well be defined as $|+1\rangle ; | -1\rangle$ or as $(|+1\rangle + |0\rangle) ; (|+1\rangle - |0\rangle)$. The upper and lower parts correspond to fields applied parallel or perpendicular to the anisotropy axis. a is constant at low field.

In zero field we can redefine the doubly degenerate excited states as a linear combination of $m = +1 : |+1\rangle$ and of $m = -1 : |-1\rangle$. Now the operator S^x leads from $|0\rangle$ to $(|+1\rangle + |-1\rangle)$ and the operator S^y from $|0\rangle$ to $(|+1\rangle - |-1\rangle)$. This separation leaves the physical behaviour in zero field unchanged. Still both operators S^x and S^y lead from $|0\rangle$ to the doubly degenerate states.

The picture changes as soon as an infinitesimal field is applied perpendicular to the anisotropy axis. Then the states $(|+1\rangle + |-1\rangle)$ and $(|+1\rangle - |-1\rangle)$ adopt an infinitesimal splitting and S^x leads to one and S^y to the other state. With increasing field the lowest and the highest states get admixtures of other m states proportional to H_{\perp} , see Fig. 4.

The higher transition (in the local picture of Fig. 4), ω_1 , corresponds exclusively to S^x fluctuations, while the lower one, ω_2 , corresponds to S^y and with increasing field also to S^z fluctuations.

Polarised neutrons have certain selection rules [5]. In our case, where the field $H_{\perp} = H^x$ was applied vertically, (i.e. perpendicular to the experimental plane which includes the anisotropy axis) the S^x fluctuations, which are parallel to the field, and in turn the mode ω_1 are visible only in the "non spin flip" (NSF) channel. At the same time the S^y and S^z fluctuations, which are perpendicular to the field, and thus the mode ω_2 show up in the "spin flip" (SF) channel. This separation of the modes was used in the experiment described in the following.

A short word to the intensities corresponding to S^{xx} , S^{yy} and S^{zz} . The calculations predict that S^{xx} decreases and S^{zz} increases quadratically with the field, while S^{yy} shows only slow variation.

A geometrical factor influences the intensities also, because only components of fluctuations perpendicular to the momentum transfer Q contribute. This geometrical factor is one for S^x fluctuation, because they are always perpendicular to Q . But the intensity of mode ω_2 is weighted by $S^{yy} \sin^2 \alpha + S^{zz} \cos^2 \alpha$, where α is the angle between Q and the y direction $[\xi, \xi, 0]$. Therefore, if Q is parallel to the y-direction the mode ω_2 is only visible due to the S^z fluctuations, which are vanishing for zero field and increase linearly with the field H_{\perp} .

3. Experiment

The instrument IN14 at ILL with cold neutrons is equipped for inelastic scattering with polarisation analysis. A vertically curved pyrolytic graphite monochromator is followed by a supermirror polarising bender. A horizontally curved Heusler crystal (Cu_2MnAl) analyser determines simultaneously energy and polarisation after scattering. In this set-up, with a magnetic guide field all along the neutron path, the polarisation of the bender (neutrons parallel to the magnetisation) is opposite to the Heusler crystal which reflects neutrons with polarisation opposite to the magnetisation. The reason is that in the Heusler crystal the sum of the nuclear scattering lengths, together with their phase factors, is negative for the (111) reflection. Therefore in the position "flipper off" (the flipper was positioned in front of the analyser) only neutrons which underwent a spin flip in the scattering process can reach the detector. In the following we do not quote the flipper position, but only "SF" or "NSF".

A Be-filter in front of the analyser reduced the higher order contamination. The sample of 0.5 cm^3 was mounted in a superconducting magnet with vertical field up to 6 Tesla. The axes [110] (y-direction) and [001] (z-direction) of reciprocal space were oriented in the experimental plane, perpendicular to the field in x-direction.

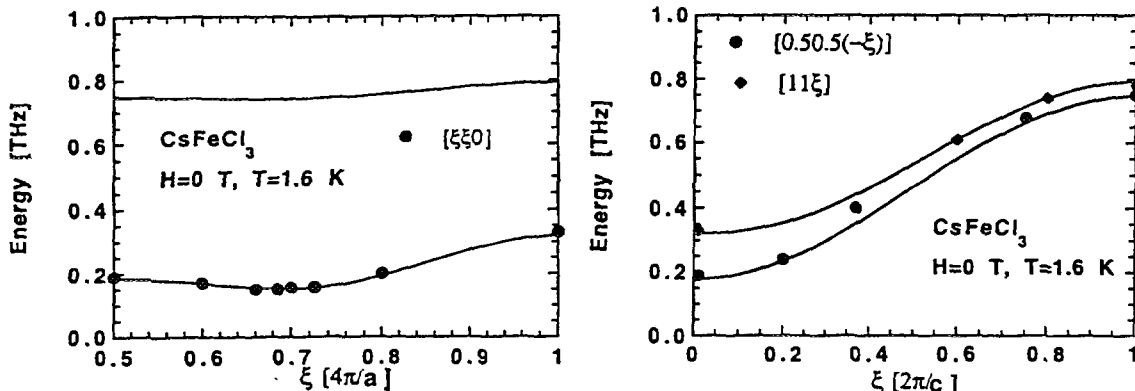


Fig. 5 : Dispersion curves of the magnetic excitations in zero field.

We have earlier experimental results, obtained without polarised neutrons [6], see Fig. 5. Therefore we repeated only a selected number of scans at zero field. The fitted parameters were in good agreement with earlier results :

$$\begin{aligned} D &= 0.524(3) & [\text{THz}] \\ J_1 &= 0.0637(8) & [\text{THz}] \\ J_2 &= -0.0096(1) & [\text{THz}] \\ J' &= -0.0043(1) & [\text{THz}] \end{aligned} \quad (12)$$

The splitting of the low frequency modes, (for $q_z = 0$ and 2 in reciprocal space) could easily be observed within the resolution of the spectrometer, see Fig. 6.

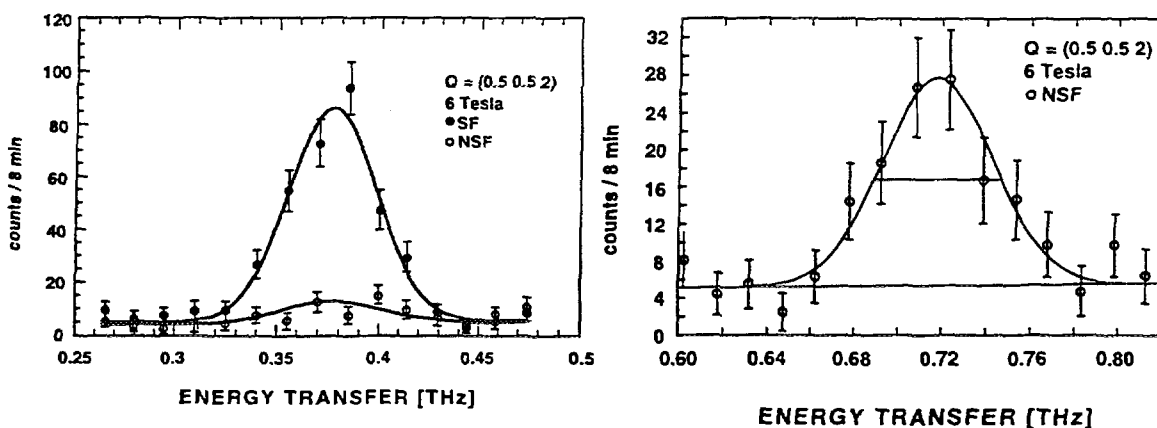


Fig. 6 : The modes ω_2 on the left and the mode ω_1 on the right in the "low frequency" region ($q_z = 0$ or 2), where the mode splitting is much larger than the instrumental resolution.

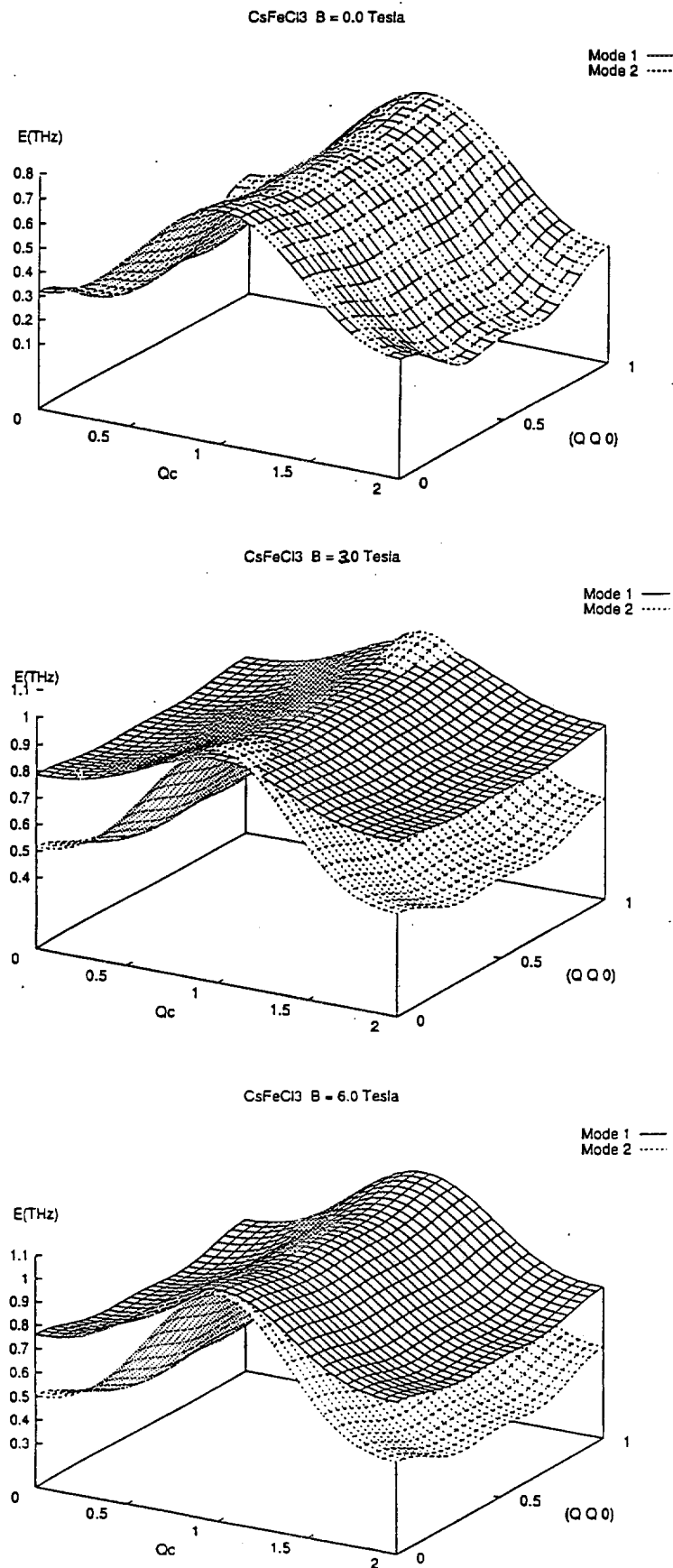


Fig. 7 : Sheets of dispersion for the modes ω_1 and ω_2 for two dimensions in reciprocal space at 0.3 and 6 Tesla.

We measured a few signals from the two modes in the "SF" and "NSF" channel, to verify experimentally that ω_1 appears in the "NSF" channel and ω_2 in the other, see Fig. 6. In Fig. 6a, we measured the "SF" and the "NSF" channels for the mode ω_2 which had strong intensity in the "SF" channel. The very weak intensity in the "NSF" channel appears due to non perfect performance of the instrument. The polarisation produced by the bender and the Heusler analyser is only close to 100 % and the flipper is not perfect either. The ratio of the main signal to the intensity leaking through is called the flipping ratio. It was in our case about 15.

Our main interest in the investigation with polarised neutrons concentrated on the high frequency excitations, where a mode crossing was predicted [4]. Fig. 7 gives the calculated dispersion sheets at 0.3 and 6 Tesla, where the field dependent parameters were taken from fits to the new experimental data. Our data sets at 3 and 6 Tesla are quite complete, see Figs. 8. The parameters obtained by the fitting procedure are :

Table I

Field	\hat{g}	Q_x	a_x	Q_{yz}	a_{yz}
0 Tesla	-	1	-	1	-
3 Tesla	3.97(1)	1.23(1)	0.0256(6)	1.061(5)	0.0064(1)
6 Tesla	4.25(1)	1.96(1)	0.0267(6)	1.15(1)	0.0043(1)

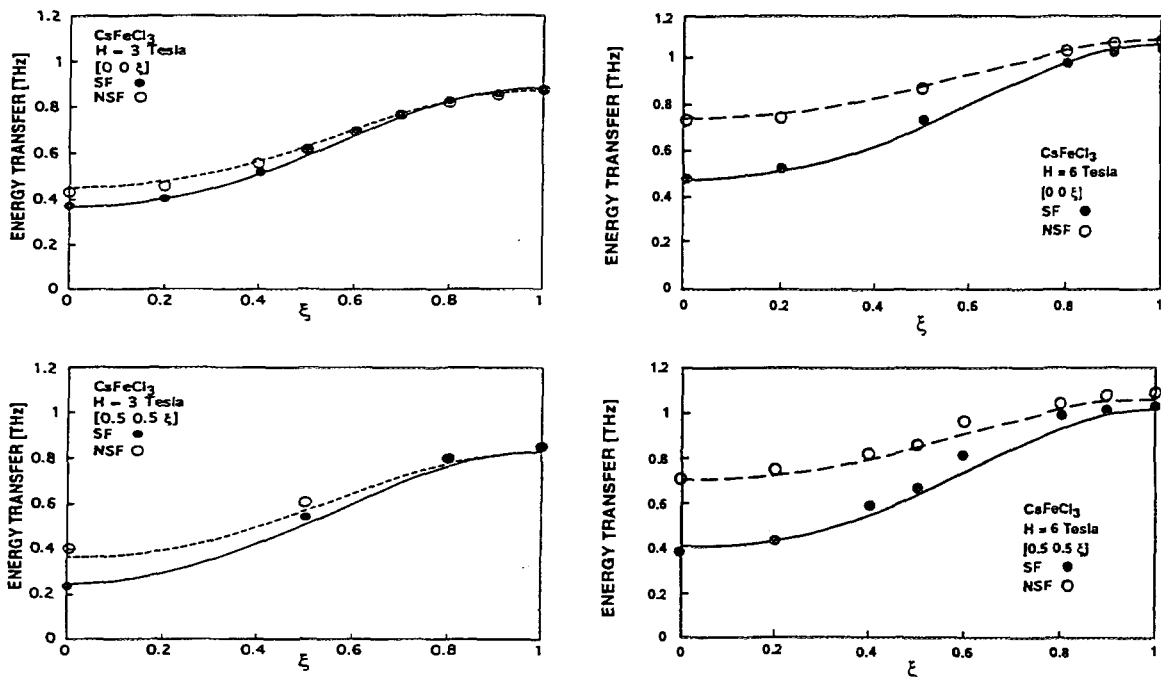


Fig. 8 : Dispersion curves of the magnetic excitations at 3 and 6 Tesla for two directions parallel to the anisotropy axis.

The high value for \hat{g} around 4 was already obtained earlier [6] when we analysed the data with another theoretical approach [7]. The field dependence of the parameters Q_x and Q_{yz} is expected to be

$$Q = 1 + aH^2 \quad (13)$$

The values for a are given in Table I above. Apparently the relation of Eq. (13) applies very well for Q_x but less for Q_{yz} .

The results at 6 Tesla clearly show that the mode ω_1 has always higher frequencies than the mode ω_2 . But they are so close together that only the polarised neutron technique made it possible to separate the modes. Fig. 9 shows the "SF" (ω_2 mode) and "NSF" (ω_1 mode). The separation of the centers of these signals is rather small. A serious experimentalist does not invest too much confidence into only two scans. Therefore we performed many scans at different positions of reciprocal space in the high frequency region. The results look similar to Fig. 9 and give convincing evidence for the separation of the modes.

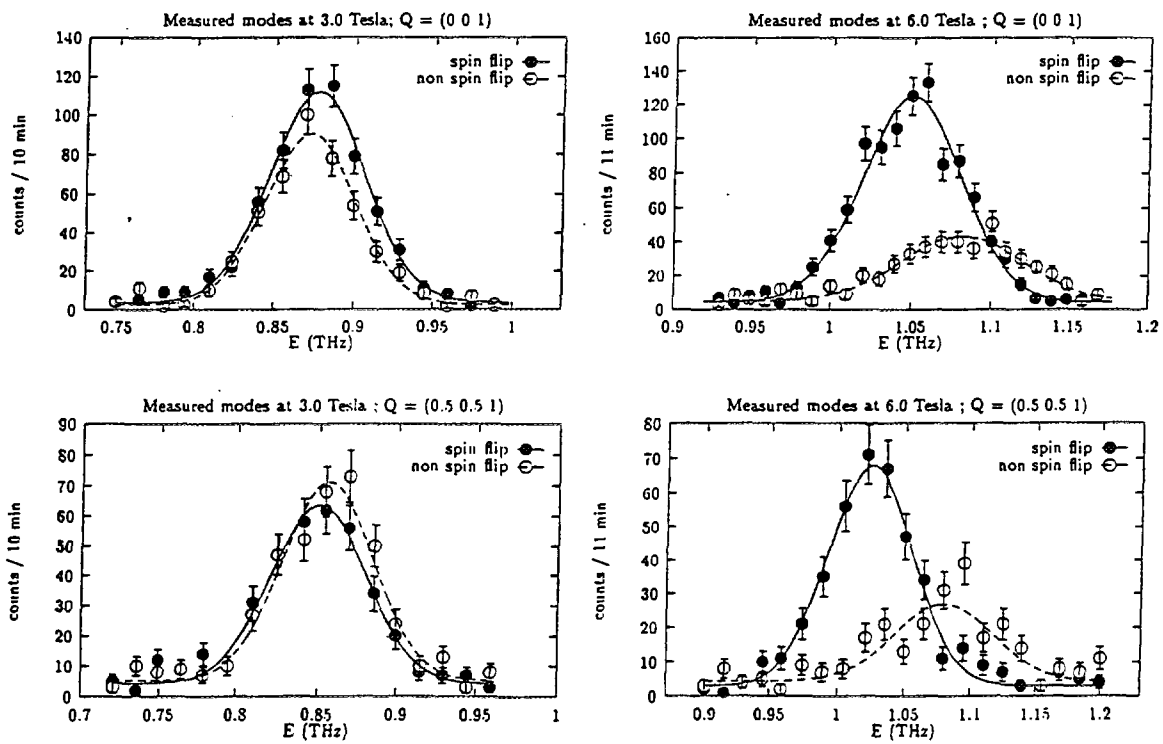


Fig. 9 : Scans at $Q = (001)$ and $Q = (0.5 0.5 1)$ at fields of 3 and 6 Tesla.

At 3 Tesla the situation is more delicate, because around the (001) and the equivalent (111) points in reciprocal space the mode ω_2 has the higher frequency. Fig. 9 shows scans also at 3 Tesla, where the inversion can be seen in the scan at (001) , while

the scan at (0.5 0.51) shows the same sense of shift at 3 and at 6 Tesla. Again at 3 Tesla the multitude of scans confirms the picture given in Fig. 7.

After this principal observation of the crossing of modes ω_1 and ω_2 , we performed selected scans at 2, 2.5, 3.5 and 4 Tesla. The results show that the mode ω_1 has everywhere the highest frequency for fields higher than about 4 Tesla.

The experiment with polarisation analysis separates the signals for the ω_1 and ω_2 modes everywhere in reciprocal space. As shown above, therefore their frequencies could be determined everywhere. But the frequencies are not the only information which can be extracted from the data. The intensities of the modes and their dependence on field and frequency can be analysed and compared with theoretical predictions [4]. This analysis is not yet terminated.

4. Conclusion

We applied a magnetic field perpendicular to the anisotropy axis in the singlet ground state system CsFeCl_3 . We observed that the modes which are degenerate at zero field split into two. The mode ω_1 corresponds to S^x fluctuations and is therefore visible in the "NSF" channel. The second mode ω_2 corresponds to S^y and S^z fluctuations as theoretically predicted and appears in the "SF" channel.

The shift of frequency with increasing field is different for the two modes. This leads to the effect that up to about 4 Tesla there appears a crossing of the two modes such that ω_2 has in certain regions of reciprocal space a higher frequency than ω_1 . This observation is in accordance with recent theoretical predictions [4]. The experimental verification was only possible due to the use of polarised neutrons.

5. References

1. D. Visser and A. Harrison, *J. de Physique* **49**, C8 (1988) 1467.
2. P.A. Lingård, *Physica* **120B** (1983) 190.
3. M. Steiner, K. Kakurai, W. Knop, B. Dorner, R. Pynn, U. Happek, P. Day and G. McLean, *Solid State Commun.* **38** (1981) 1179.
4. B. Toperverg, B. Dorner, A. Sonntag and D. Petitgrand, *Phys.Rev. B* submitted.
5. R.M. Moon, T. Riste and W.C. Koehler, *Phys. Rev.* **181** (1969) 920.
6. B. Schmid, B. Dorner, D. Petitgrand, L.P. Regnault and M. Steiner, *Z. Phys.* **B95** (1994) 13.
7. P.A. Lingård and B. Schmid, *Phys. Rev.* **B48** (1993) 13636.



**SPIN-LATTICE INTERACTIONS STUDIED BY
POLARISED AND UNPOLARISED INELASTIC SCATTERING
APPLICATION TO THE INVAR PROBLEM**

P.J.BROWN

Institut Laue Langevin Avenue des Martyrs, 38042 Grenoble, France

ABSTRACT

A semi-quantitative analysis is given of some of the ways in which spin-lattice interactions can modify the cross-sections observable in neutron scattering experiments. This analysis is applied to the scattering from the invar alloy Fe₆₅Ni₃₅ using a model in which the magnetic moment is a function of the near neighbour separation. This model has been applied to clarify the results of inelastic scattering experiments carried out on Fe₆₅Ni₃₅ using both polarised and unpolarised neutrons. The extra information obtainable using polarised neutrons as well as the difficulties and limitations of the technique for inelastic scattering are discussed.

1. Introduction

Inelastic neutron scattering provides a powerful tool with which to study the interaction between the magnetic and vibrational degrees of freedom in crystals. When combined with a polarised incident beam and polarisation analysis of the scattered neutrons a maximum of information about the scattering process is obtained. Up to the present time the polarised technique has been little used mainly due to the difficulty of doing such experiments with relatively inefficient neutron polarisers. Recently however interest in the stability of magnetic moments in metals, and recognition of the important influence which the interatomic distances can have upon this has provided new motivation for such studies.

One of the better known examples of a macroscopic property mediated by spin-lattice interaction is the invar effect. In invar alloys the magnetic and lattice degrees of freedom interact in such a way that in a certain range of temperature, the invar temperature, the thermal expansion coefficient becomes very small. Although there is as yet no complete explanation of the effect it is generally agreed that around the invar temperature the increase in interatomic distance due to lattice vibrations is compensated by a decrease in the effective atomic volume brought about by a change in the magnetic state [1,2]. Recently it has become possible to carry out spin-polarised band structure calculations with reasonable accuracy. Two new calculations for the invar alloy Fe₆₅Ni₃₅ have been made [3,4] both of which indicate an incipient instability in the alloy at around the invar composition due to the existence of nearly degenerate states with different symmetries, magnetic moments and atomic volumes. It is supposed that it is the population and depopulation of these states driven by the lattice vibrations which gives rise to the invar property.

2. Cross-sections for inelastic magnetic scattering

The cross-sections for magnetic inelastic scattering of neutrons from an ordered magnetic material were first evaluated by Halpern and Johnson in their classical paper [5]. Here we use the form of the double differential cross-section given by Squires [6](p138) for spin-only scattering by moments localised at the nodes of a Bravais lattice:

$$\begin{aligned} \frac{d^2\sigma}{d\Omega dE'} &= (\gamma_n r_0)^2 \frac{k'}{k} \sum_{\alpha\beta} (\delta_{\alpha\beta} - \kappa_\alpha \kappa_\beta) \sum_{l'} \sum_l |F(\mathbf{Q})|^2 \delta(E - E' + \hbar\omega) \\ &\times \sum_{\lambda\lambda'} p_\lambda \langle \lambda | S_{l'}^\alpha \exp[-i\mathbf{Q} \cdot \mathbf{R}_{l'}] | \lambda' \rangle \left\langle \lambda' \left| \exp[i\mathbf{Q} \cdot \mathbf{R}_l] S_l^\beta \right| \lambda \right\rangle \quad (1) \end{aligned}$$

Here γ_n is the neutron magnetic moment in nuclear magnetons and r_0 the classical electron radius; \mathbf{Q} is the scattering vector, and κ a unit vector parallel to it. $F(\mathbf{Q})$ is the magnetic form factor, \mathbf{R}_l the position of the atom at lattice site \mathbf{l} and S_l^β the β component of its spin. E and k are the energy and wavevector of the incident neutron, λ represents the initial state of the scattering system and p_λ its probability. The primed symbols are the final state values. The second line of Eq. 1 which contains the matrix elements for the scattering process can be written [6]

$$\frac{1}{2\pi\hbar} \int_{-\infty}^{\infty} \left\langle \hat{S}_{l'}^\alpha(0) \exp(i\mathbf{Q} \cdot \hat{\mathbf{R}}_{l'}(0)) \times \exp(-i\mathbf{Q} \cdot \hat{\mathbf{R}}_l(t)) \hat{S}_l^\beta(t) \right\rangle \exp(-i\omega t) dt \quad (2)$$

where $\hat{\mathbf{R}}_l(t)$ and $\hat{S}_l^\beta(t)$ are the time dependent Heisenberg operators

$$\hat{\mathbf{R}}_l(t) = \exp[i\mathcal{H}t/\hbar] \mathbf{R}_l \exp[-i\mathcal{H}t/\hbar] \quad (3)$$

$$\hat{S}_l^\beta(t) = \exp[i\mathcal{H}t/\hbar] \hat{S}_l^\beta \exp[-i\mathcal{H}t/\hbar] \quad (4)$$

The angle brackets in Eq. 2 indicate the thermal average of the enclosed operator at the temperature of the system.

In order to see how the cross-sections are evaluated it is assumed to start with that there is no correlation of either the magnitudes or the directions of the magnetic moments of the atoms with their displacements $\mathbf{u} = \mathbf{R}_l - \mathbf{l}$. In this case the thermal average of Eq. 1 can be factorised into the product of an average depending only on the atomic displacements and one depending only on magnetic fluctuations. Each of these averages is written as the sum of a constant part given by its value after infinite time, and a time-varying part. Thus

$$\left\langle \exp[-i\mathbf{Q} \cdot \hat{\mathbf{R}}_{l'}(0)] \exp[i\mathbf{Q} \cdot \hat{\mathbf{R}}_l(t)] \right\rangle = I_{ll'}(\mathbf{Q}, \infty) + I_{ll'}(\mathbf{Q}, t) \quad (5)$$

and

$$\left\langle \hat{S}_{l'}^\alpha(0) \hat{S}_l^\beta(t) \right\rangle = J_{ll'}^{\alpha\beta}(\infty) + J_{ll'}^{\alpha\beta}(t) \quad (6)$$

The product of Eq. 5 and Eq. 6 expands to give four terms:

- (i) $I_{ll'}(\mathbf{Q}, \infty) J_{ll'}^{\alpha\beta}(\infty)$ which is the cross-section for elastic magnetic scattering
- (ii) $I_{ll'}(\mathbf{Q}, t) J_{ll'}^{\alpha\beta}(\infty)$ that for magneto-vibrational scattering. This term is elastic in the magnetic system and inelastic in the phonon system. For a ferromagnet with spins parallel to z it gives scattering with the same \mathbf{q} , \mathbf{Q} and ω dependence as phonon scattering by the atomic nuclei except that the $\sigma_{coh}/4\pi$ which occurs in the nuclear phonon cross-section is replaced by

$$\left(\frac{\gamma_n r_0}{2}\right)^2 |F(\mathbf{Q})|^2 (1 - \kappa_z^2) \langle \mathbf{S}^z \rangle^2 = M_{\perp}^2 \quad (7)$$

in the magneto-vibrational cross-section. Both cross-sections are proportional to

$$\frac{(\epsilon \cdot \mathbf{Q})^2}{\omega} \rightarrow \left[\frac{(\epsilon \cdot \mathbf{Q})^2}{v\mathbf{q}} \right]_{lim(\mathbf{Q} \rightarrow 0)} \propto \mathbf{Q} \quad (8)$$

where ϵ is the polarisation of the phonon, v the phonon velocity and \mathbf{q} the reduced wavevector.

- (iii) $I_{ll'}(\mathbf{Q}, \infty) J_{ll'}^{\alpha\beta}(t)$ gives scattering inelastic in just the spin system. This can include excitations corresponding to both longitudinal fluctuations and transverse fluctuations (Spin waves).
- (iv) $I_{ll'}(\mathbf{Q}, t) J_{ll'}^{\alpha\beta}(t)$ scattering inelastic in both the phonon and spin systems.

3. Spin-lattice interaction in invar

If there is a significant spin-lattice interaction then the assumption that the magnetic state of an atom is independent of its displacement from the lattice node is no longer valid. There are several mechanisms which can give rise to such interactions; these include the Jahn Teller effect, quadropolar couplings, and magnetovolume effects. It is this latter mechanism which is probably important in invar alloys. All the recent electronic structure calculations for the Fe-Ni invar alloys, which are reviewed by [3], agree that there are states of nearly equal energy amongst which those with lower moment correspond to smaller atomic volumes. The different versions differ only in the actual composition of the states and on whether there are just two states or whether there is a continuum of states. For the present discussion these differences are unimportant and we shall adopt a very simple model in which we suppose that as a result of this peculiar band structure the atomic magnetic moment is a function of the nearest neighbour separation, or from the other point of view that there is a force between neighbouring atoms which depends on the magnitude of their moment. Suppose that this interaction leads to a linear dependence of the magnitude of the moment on the strain in the near neighbour bonds. Then as a first approximation the spin operators $\hat{\mathbf{S}}$ can be renormalised so that

$$\hat{\mathbf{S}}_i = \hat{\mathbf{S}}_{0i} \left(1 - \sum_{\alpha\beta} x^{\alpha\beta} \varepsilon_i^{\alpha\beta} \right) \quad (9)$$

where $x^{\alpha\beta}$ is a matrix of coefficients which depend on the physics of the magnetic moment fluctuation and $\varepsilon_i^{\alpha\beta}$ is the strain tensor at site i due to the lattice vibrations.

It can be seen qualitatively that such a model will lead to additional terms in the inelastic scattering cross-section because it introduces a correlation between the moment fluctuations and the lattice displacements. If the electronic transitions which lead to the modification of the moment take place on a much shorter time-scale than the phonon frequencies the most important new contribution is to the magneto-vibrational scattering.

4. Magneto-vibrational scattering with spin-fluctuations driven by interatomic strain

Assuming the assumptions made above are valid and the renormalisation given by Eq. 9 is small the spin operators S_l can be replaced by $S_{0l} \exp[-\hat{\xi}_l]$ where $\hat{\xi}_l$ is an operator which gives the fractional deviation in the magnitude of the moment at lattice site l from its mean value. The dependence of the moment on the atomic displacements is now completely contained in the operator $\hat{\xi}$ so it is again possible to factorise Eq. 5 but as the more complex expression

$$\langle \exp[-i\mathbf{Q} \cdot \hat{\mathbf{R}}_{l'}(0) - \hat{\xi}_{l'}(0)] \exp[i\mathbf{Q} \cdot \hat{\mathbf{R}}_l(t) - \hat{\xi}_l(t)] \rangle \times \langle S^\alpha \beta_{0l'}(0) S_{0l}^\beta(t) \rangle \quad (10)$$

and this may be developed to give four terms similar to those enumerated in section 3. The thermal average which determines the magneto-vibrational scattering becomes

$$\langle \exp[-i\mathbf{Q} \cdot \hat{\mathbf{R}}_{l'}(0) - \hat{\xi}_{l'}(0)] \exp[i\mathbf{Q} \cdot \hat{\mathbf{R}}_l(t) - \hat{\xi}_l(t)] \rangle \times \langle S_{0l'}^\alpha(0) S_{0l}^\beta(\infty) \rangle \quad (11)$$

For a ferromagnet with spins parallel to z the spin dependent term in the cross-section reduces to

$$\begin{aligned} & \left(\frac{\gamma_n r_0}{2}\right)^2 |F(\mathbf{Q})|^2 \sum_{\alpha\beta} (\delta_{\alpha\beta} - \kappa_\alpha \kappa_\beta \langle S_{0l'}^\alpha(0) S_{0l}^\beta(\infty) \rangle) \\ &= \left(\frac{\gamma_n r_0}{2}\right)^2 |F(\mathbf{Q})|^2 (1 - \kappa_z^2) \langle S_0^z \rangle^2 = M_{0\perp}^2 \end{aligned} \quad (12)$$

The operators $\hat{\mathbf{R}}_l = \mathbf{l} + \hat{\mathbf{u}}_l$ can be expressed in terms of the phonon annihilation and creation operators \hat{a} and \hat{a}^+ since

$$\hat{\mathbf{u}}_l = \left(\frac{\hbar}{2m_a N}\right)^{1/2} \sum_s \frac{\epsilon_s}{\sqrt{\omega_s}} (\hat{a}_s \exp[i\mathbf{q}_s \cdot \mathbf{l}] + \hat{a}_s^+ \exp[-i\mathbf{q}_s \cdot \mathbf{l}]) \quad (13)$$

where m_a is the mass of the atom and the sum is over the N phonon modes with wave-vector \mathbf{q}_s , frequency ω_s and polarisation ϵ_s in the 1st Brillouin zone. The strain operator $\partial \hat{\mathbf{u}} / \partial \mathbf{l}$ can also be written in terms of the operators \hat{a} and \hat{a}^+

$$\hat{\xi}_l = \left(\frac{\hbar}{2m_a N}\right)^{1/2} \sum_s \sum_{\alpha\beta} \left(\frac{x^{\alpha\beta} q_s^\alpha \epsilon_s^\beta}{\sqrt{\omega_s}} i (\hat{a}_s \exp[i\mathbf{q}_s \cdot \mathbf{l}] - \hat{a}_s^+ \exp[-i\mathbf{q}_s \cdot \mathbf{l}]) \right) \quad (14)$$

and we define

$$\Xi_s = \sum_{\alpha\beta} x^{\alpha\beta} q_s^\alpha \epsilon_s^\beta \quad (15)$$

Following [6] (p29) we write the thermal average

$$\begin{aligned} & \left\langle \exp \left[-i\mathbf{Q} \cdot \hat{\mathbf{R}}_{l'}(0) - \hat{\boldsymbol{\xi}}_{l'}(0) \right] \exp \left[i\mathbf{Q} \cdot \hat{\mathbf{R}}_l(t) - \hat{\boldsymbol{\xi}}_l(t) \right] \right\rangle \\ &= \exp[-i\mathbf{Q} \cdot (\mathbf{l}' - \mathbf{l})] \langle \exp U \exp V \rangle \end{aligned} \quad (16)$$

with

$$U = -i\mathbf{Q} \cdot \hat{\mathbf{R}}_{l'}(0) - \hat{\boldsymbol{\xi}}_{l'}(0) = -i \sum_s \hat{a}_s(g_s + \gamma_s) + \hat{a}_s^+(g_s - \gamma_s) \quad (17)$$

$$V = i\mathbf{Q} \cdot \hat{\mathbf{R}}_l(t) - \hat{\boldsymbol{\xi}}_l(t) = i \sum_s \hat{a}_s(h_s - \eta_s) + \hat{a}_s^+(h_s^* + \eta_s^*) \quad (18)$$

$$\begin{aligned} g_s &= \left(\frac{\hbar}{2m_a N} \right)^{1/2} \frac{\mathbf{Q} \cdot \boldsymbol{\epsilon}_s}{\sqrt{\omega_s}}, \quad \gamma_s = \left(\frac{\hbar}{2m_a N} \right)^{1/2} \frac{\Xi_s}{\sqrt{\omega_s}} \\ h_s &= \left(\frac{\hbar}{2m_a N} \right)^{1/2} \frac{\mathbf{Q} \cdot \boldsymbol{\epsilon}_s}{\sqrt{\omega_s}} \exp(i(\mathbf{q} \cdot \mathbf{l} - \omega_s t)) \\ \eta_s &= \left(\frac{\hbar}{2m_a N} \right)^{1/2} \frac{\Xi_s}{\sqrt{\omega_s}} \exp(i(\mathbf{q} \cdot \mathbf{l} - \omega_s t)) \end{aligned} \quad (19)$$

The magneto-vibrational cross-section can then be expanded

$$\begin{aligned} \left(\frac{d^2\sigma}{d\Omega dE'} \right)_{MV} &= \frac{k'}{k} \frac{N}{2\pi\hbar} M_{0\perp}^2 \exp \langle U^2 \rangle \sum_l \exp[i\mathbf{Q} \cdot \mathbf{l}] \\ &\times \int_{-\infty}^{\infty} \exp \langle UV \rangle \exp[-i\omega t] dt \end{aligned} \quad (20)$$

$$\begin{aligned} \langle U^2 \rangle &= - \sum_{\lambda} p_{\lambda} \sum_{ss'} \langle \lambda | (\hat{a}_s(g_s + \gamma_s) + \hat{a}_s^+(g_s - \gamma_s)) \\ &\times (\hat{a}_{s'}(g_{s'} + \gamma_{s'}) + \hat{a}_{s'}^+(g_{s'} - \gamma_{s'})) | \lambda \rangle \\ &= - \sum_{\lambda} \sum_s (g_s^2 - \gamma_s^2) \langle \lambda | \hat{a}_s \hat{s}_s^+ + \hat{a}_s^+ \hat{a}_s | \lambda \rangle \end{aligned} \quad (21)$$

so that the Debye Waller term becomes

$$\exp \langle U^2 \rangle = \exp \left[-\frac{\hbar}{2m_a N} \sum_s \frac{(\mathbf{Q} \cdot \boldsymbol{\epsilon}_s)^2 - \Xi_s^2}{\omega_s} \langle 2n_s + 1 \rangle \right] = \exp(-2W') \quad (22)$$

where $\langle n_s \rangle$ is the probability of the state n_s at the temperature of the system. The one-phonon cross-section is obtained from the term in $\langle UV \rangle$ in the expansion of $\exp \langle UV \rangle$.

$$\begin{aligned} \langle \lambda | UV | \lambda \rangle &= \sum_{ss'} \langle \lambda | (\hat{a}_s(g_s + \gamma_s) + \hat{a}_s^+(g_s - \gamma_s)) \\ &\times (\hat{a}_{s'}(h_{s'} - \eta_{s'}) + \hat{a}_{s'}^+(h_{s'}^* + \eta_{s'}^*)) | \lambda \rangle \end{aligned} \quad (23)$$

giving

$$\begin{aligned} \langle UV \rangle &= \sum_s (g_s + \gamma_s)(h_s^* + \eta_s^*) \langle n_s + 1 \rangle + (g_s - \gamma_s)(h_s - \eta_s) \langle n_s \rangle \\ &= \left(\frac{\hbar}{2m_a N} \right) \sum_s \frac{1}{\omega_s} \left((\mathbf{Q} \cdot \boldsymbol{\epsilon}_s + \Xi_s)^2 \exp[-i(\mathbf{q} \cdot \mathbf{l} - \omega_s t)] \langle n_s + 1 \rangle \right. \\ &\quad \left. + (\mathbf{Q} \cdot \boldsymbol{\epsilon}_s - \Xi_s)^2 \exp[i(\mathbf{q} \cdot \mathbf{l} - \omega_s t)] \langle n_s \rangle \right) \end{aligned} \quad (24)$$

The cross-section for magneto-vibrational scattering by one phonon creation is thus

$$\begin{aligned} \left(\frac{d^2\sigma}{d\Omega dE'} \right)_{MV+} &= \frac{k'}{k} \frac{(2\pi)^3}{2m_a v_0} M_{0\perp}^2 \exp(-2W') \sum_s \sum_{\tau} \frac{(\mathbf{Q} \cdot \boldsymbol{\epsilon}_s + \Xi_s)^2}{\omega_s} \langle n_s + 1 \rangle \\ &\quad \times \delta(E - E' - \hbar\omega_s) \delta(\mathbf{Q} + \mathbf{q} - \boldsymbol{\tau}) \end{aligned} \quad (25)$$

where $\boldsymbol{\tau}$ is a reciprocal lattice vector.

5. Inelastic experiments with polarised neutrons

5.1 The polarised neutron cross-sections

The full range of cross-sections which can be measured on a triple-axis spectrometer with a polarising monochromator and analyser were discussed by [7]. Rather more information can be obtained if it is possible to measure all three components of the scattered polarisation rather than just the z-component [8]. General expressions for the cross-section for polarised neutrons and for the polarisation of the scattered beam are given in [9]. In the experiments to be described here an unpolarised incident beam was scattered from a magnetised sample and the separate intensities of neutrons scattered with spins parallel and antiparallel to the magnetisation direction were measured. So as not to make the expressions too complicated the discussion will be limited to this special case. The double differential cross-section for joint nuclear and magnetic scattering has the form

$$\frac{d^2\sigma}{d\Omega dE'} \propto \sum_{ll'} \sum_{\sigma\sigma'} p_{\sigma} p_{\lambda} \left| \left\langle \lambda\sigma \left| \exp[-i\mathbf{Q} \cdot \mathbf{R}_{l'}] (\hat{\mathbf{T}}_{l'} \cdot \hat{\sigma} + \hat{\mathbf{M}}_{Ql'} \cdot \hat{\sigma}) \right| \lambda'\sigma' \right\rangle \right|^2 \quad (26)$$

Here $\hat{\sigma}$ is the neutron spin operator, $\hat{\mathbf{T}}$ the neutron nuclear interaction operator and $\hat{\mathbf{M}}_Q$ the neutron magnetic interaction operator, the latter is subscripted \mathbf{Q} to indicate that it only has components perpendicular to \mathbf{Q} . We now simplify Eq. 26 by first assuming that there is no alignment of nuclear spins and then neglecting all terms which contribute to incoherent scattering only. The remaining neutron nuclear interaction is then just described by a scalar scattering length b which is the same at every site. The two intensities measured are given by the cross-sections $\sigma^{++} + \sigma^{-+}$ and $\sigma^{--} + \sigma^{+-}$. In the experiment \mathbf{Q} is confined to the horizontal plane and is perpendicular to the magnetisation. It is convenient to define axes \mathbf{z} parallel to the magnetisation direction \mathbf{y} parallel to \mathbf{Q} and \mathbf{x} completing the right-handed

orthogonal set. Then

$$\sigma^{++} \propto \sum_{ll'} \sum_{\lambda\lambda'} p_\lambda |\langle \lambda | \exp[-i\mathbf{Q} \cdot \mathbf{R}_l] (b + M_{zl}) | \lambda' \rangle|^2 \quad (27)$$

$$\sigma^{--} \propto \sum_{ll'} \sum_{\lambda\lambda'} p_\lambda |\langle \lambda | \exp[-i\mathbf{Q} \cdot \mathbf{R}_l] (b - M_{zl}) | \lambda' \rangle|^2 \quad (28)$$

$$\sigma^{-+} \propto \sum_{ll'} \sum_{\lambda\lambda'} p_\lambda |\langle \lambda | \exp[-i\mathbf{Q} \cdot \mathbf{R}_l] M_{zl} | \lambda' \rangle|^2 \quad (29)$$

and $\sigma^{+-} = \sigma^{-+}$. The cross-section of Eq. 27 expands to give four terms each of which can be expressed in terms of thermal averages as in section 2. The polarisation dependent terms are those containing products of magnetic and nuclear interactions, they have the same magnitude but opposite signs in σ^{++} and σ^{--} . They may be written

$$\begin{aligned} \left(\frac{d^2\sigma}{d\Omega dE'} \right)_{pol} &= \int_{-\infty}^{\infty} \left(\langle b \exp[-i\mathbf{Q} \cdot \hat{\mathbf{R}}_{l'}(0)] \exp[i\mathbf{Q} \cdot \hat{\mathbf{R}}_l(t) \hat{M}_{zl}] \rangle \right. \\ &\quad \left. + \langle \exp[-i\mathbf{Q} \cdot \hat{\mathbf{R}}_{l'}(0)] \hat{M}_{zl} b \exp[i\mathbf{Q} \cdot \hat{\mathbf{R}}_l(t)] \rangle \right) dt \end{aligned} \quad (30)$$

This polarisation dependent part of the cross-section can be factorised into space and spin dependent parts in the same way and with the same assumptions as can the purely magnetic cross-section (section 2) and gives rise to polarisation dependent magneto-vibrational scattering. The cross-sections σ^{+-} and σ^{-+} are zero for this type of scattering which is elastic in the spin system, so long as the magnetisation is perpendicular to \mathbf{Q} . Eq. 30 can be evaluated using the assumptions and methods of section 4 as

$$\begin{aligned} \left(\frac{d^2\sigma}{d\Omega dE'} \right)_{pol} &= \left(\frac{\hbar}{2m_a N} \right) b M_{0\perp} \exp[-(W + W')] \sum_s \frac{1}{\omega_s} \\ &\quad \times \int_{-\infty}^{\infty} \left(\mathbf{Q} \cdot \boldsymbol{\epsilon}_s (\mathbf{Q} \cdot \boldsymbol{\epsilon}_s + \Xi_s) \exp[-i(\mathbf{q} \cdot \mathbf{l} - \omega_s t)] \langle n_s + 1 \rangle \right. \\ &\quad \left. + \mathbf{Q} \cdot \boldsymbol{\epsilon}_s (\mathbf{Q} \cdot \boldsymbol{\epsilon}_s - \Xi_s)) \exp[i(\mathbf{q} \cdot \mathbf{l} - \omega_s t)] \langle n_s \rangle \right) dt \end{aligned} \quad (31)$$

The ratio between the two intensities measured with momentum transfer $\mathbf{Q} = \tau - \mathbf{q}$ and energy loss $\hbar\omega_s$ corresponding to a phonon mode with wave vector \mathbf{q} frequency ω_s and polarisation $\boldsymbol{\epsilon}_s$ is therefore

$$\frac{\sigma^{++}}{\sigma^{--}} = \frac{1 + 2\gamma + \gamma^2}{1 - 2\gamma + \gamma^2} \quad (32)$$

with

$$\gamma = \frac{M_{0\perp}}{b} \exp[W - W'] \left(\frac{\mathbf{Q} \cdot \boldsymbol{\epsilon}_s + \Xi_s}{\mathbf{Q} \cdot \boldsymbol{\epsilon}_s} \right) \quad (33)$$

5.2 Experimental considerations

Figure 1 shows a set of typical dispersion curves for a fcc ferromagnetic metal along

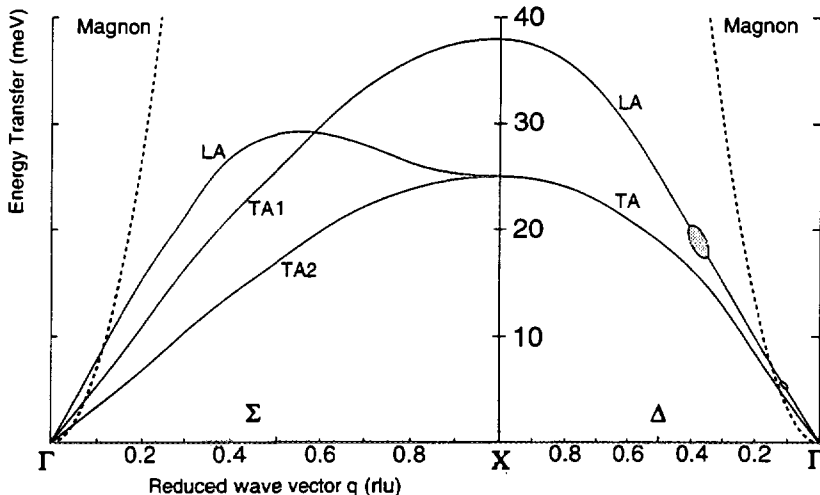


Fig. 1. Typical dispersion curves for a fcc ferromagnetic metal in the (100) Δ and (110) Σ directions. The dashed curve represents the magnon excitation and the full curves the longitudinal acoustic (LA) and transverse acoustic (TA) modes. The small shaded ellipsoids indicate the expected resolution of the instrument.

the symmetry directions Δ (100) and Σ (110). In general the magnon branch which is parabolic at low q will cross the phonon branches, which are linear, at some finite energy and in the vicinity of this cross-over the two will not be well resolved. Typical resolution ellipsoids which might be obtained with the triple axis polarised neutron spectrometer IN20 at ILL with a Cu 200 monochromator, a Heusler 111 (polarising) analyser and collimation starting from the source of $30' 40' 40' 40'$ are indicated. With this shape of ellipsoid constant energy scans which cross both the magnon and phonon wave-vectors will show relatively sharp peaks. These peaks can be fitted using Gaussian line shapes to obtain the positions, intensities and widths of the magnon and phonon peaks superposed on a uniform background. The spectra obtained for opposite final spin states can be analysed together and the positions and widths of corresponding peaks constrained to be equal. The quantity γ defined in Eq. 33 which gives the ratio of magnetic to nuclear scattering is calculated from the ratio of the heights of the phonon peaks for opposite spin states using Eq. 32 modified to include corrections for incomplete polarisation and spin reversal.

$$\frac{I^+}{I^-} = \frac{1 + 2P\gamma + \gamma^2}{1 - 2Pe\gamma + \gamma^2} \quad (34)$$

where P is the polarisation and e the flipper efficiency

6. Polarisation dependence of the phonon cross-section in $\text{Fe}_{65}\text{Ni}_{35}$

Experiments using the technique described above were carried out on a single crystal of $\text{Fe}_{65}\text{Ni}_{35}$ [10]. The crystal was in the form of a cube $12 \times 12 \times 12$ mm with edges parallel to [110], [001] and [110], it was mounted on IN20 with the [110] edge vertical in a vertical field produced by a pair of superconducting Helmholtz coils. The field at the sample was set to 2T which is sufficient for saturation at 100 K,

the temperature of the experiment. The monochromator, analyser and collimation were as described above and the spectrometer was used in the constant k_f mode with k_f either 4.1 or 2.662 \AA^{-1} depending on the energy transfer. A graphite filter was used to eliminate high order contamination of the beam. Dispersion curves for the phonon and magnon modes in the (111) and (001) directions taken from the published work [11,12] are drawn in Fig. 2. They show the magnon mode crossing the LA (111) phonon mode at $\approx 12 \text{ meV}$ and the LA (001) phonon mode at $\approx 7 \text{ meV}$. A series of constant energy scans were carried out which are indicated by the shaded oblongs in Figure 2. Those in the (111) directions were based on the 111 reciprocal lattice point and those in the (001) direction on 002. In each scan the scattered intensity was measured at each point first with the flipper on and then with it off. The scattered intensity for both polarisation states obtained in the scans was fitted as indicated above but introducing the additional constraint that the centres of peaks at $\tau + q$ and $\tau - q$ in scans at the same energy should be at equal q . When one of the peaks in a scan was identified with a magnon it was constrained to have the same peak heights for both polarisation states. These extra constraints were found to improve the determination of the background which is a critical factor in obtaining a correct intensity ratio. The centres of the fitted peaks are plotted as circles (phonons) and triangles (magnon) in Figure 2. In the scans at energies between 7 and 15 meV it was not possible to separate the phonon and magnon intensities, and this severely reduces the amount of information that can be obtained. Unresolved peaks are shown by superposed triangles and circles in Figure 2.

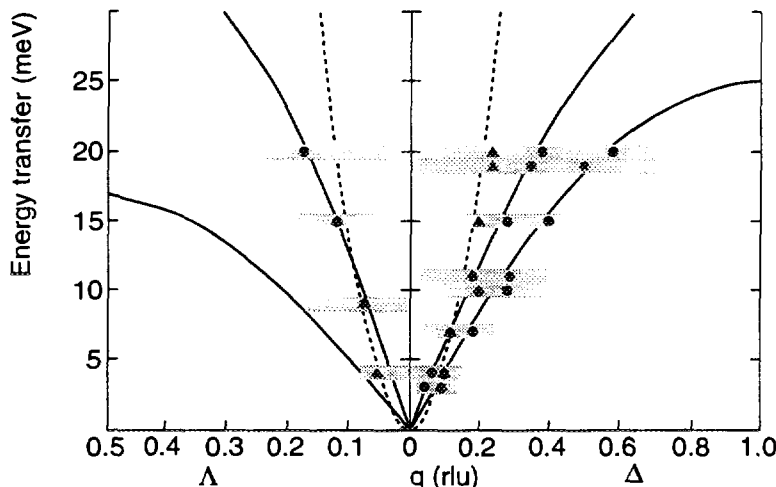


Fig. 2. Dispersion curves for $\text{Fe}_{65}\text{Ni}_{35}$ in the (100) and (111) directions. The magnon mode [12] is shown as the dashed curve and the LA and TA phonon modes [11] as solid curves. The ranges of the constant energy scans [10] are shown as open oblongs and the positions of the peaks of the excitations observed within them as \blacktriangle (magnon) and \bullet (phonon).

In the absence of spin lattice interaction the ratio

$$\gamma = M_{\perp}/\bar{b} \quad (35)$$

where \bar{b} is the mean nuclear scattering length per site. The only Q dependence of γ is through the magnetic form factor $F(Q)$ (Eq. 7). Fig. 3 shows the magnetic

contribution to the scattering $M_{\perp} = \gamma \bar{b}$, derived from the scans over the two phonon modes, plotted against Q . It can be seen that for the LA 111 phonon there appears to be a reduction in the scattering with increasing $|q|$ which is not observed in the LA 100 phonon. For the LA phonons Ξ is proportional to q so the model developed in section 4 predicts that the intensity should rise on one side of $q=0$ and fall on the other. As for the Debye Waller term $\exp[W - W'] = \exp[\Xi^2]$ it should increase the intensity on either side of $q = 0$ since Ξ^2 must be positive.

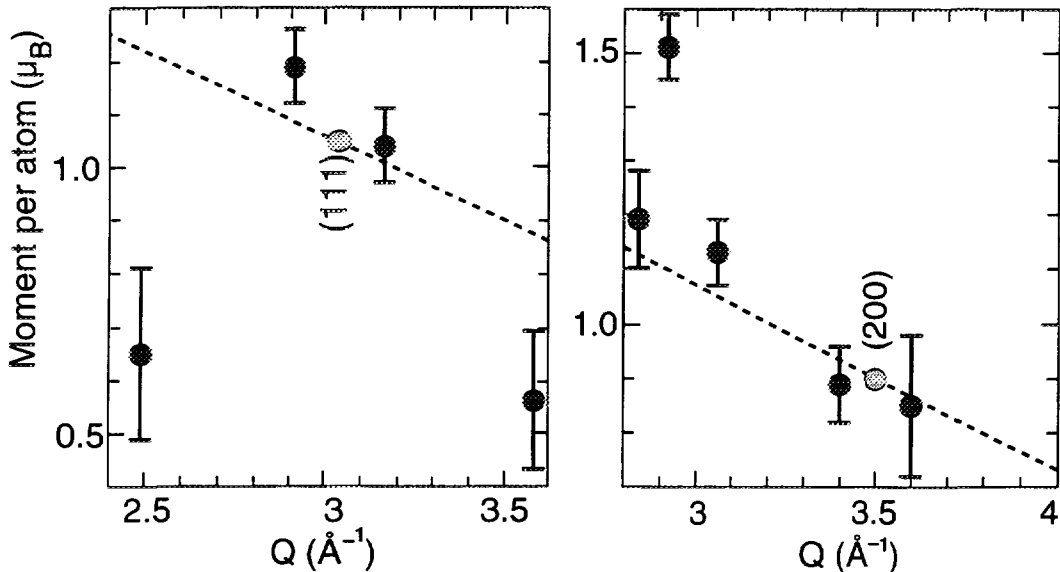


Fig. 3. The magnetic scattering amplitude observed in the LA 111 (a) and LA 100 phonon modes as a function of Q . The dashed line shows the Q dependence expected from the magnetic form factor.

It is quite easy to see qualitatively that these predictions are specific to the simple model (Eq. 7) and that the results are quite sensitive to its specific form. The expression given in Eq. 7 for the renormalisation of the spin corresponds to a model in which the moment decreases with positive strain and increases with negative strain. The greater the phonon amplitude the greater is the moment fluctuation which is giving rise to the extra scattering: hence the positive Debye-Waller term. The correlation between the sense of the moment fluctuation and the sense of the strain leads to the phase relationship between the normal scattering and the moment fluctuation scattering implicit in the term $\mathbf{Q} \cdot \epsilon - \Xi$. The simple model proposed in section 3 presupposes a continuum of states having moments both smaller and larger than that for no strain. As an alternative suppose there were only states with lower moment than the zero strain value and these were excited only for positive strains, then the function giving the moment deviation would be more complex than that of Eq. 8 and in particular would contain additional terms which were even functions of the strain. In principle it is possible to expand any reasonable functional form giving the moment in terms of the strain as a Fourier series and to apply the methods of section 4 to it term by term. Unfortunately the algebra becomes rather cumbersome. The effect of terms even in the strain can be seen by taking the simplest even function:

$$S = S_0 \cos(\hat{\xi}) = \frac{1}{2} S_0 (\exp[i\hat{\xi}] + \exp[-i\hat{\xi}]) \quad (36)$$

The Fourier series has just two terms $n = \pm 1$ so there are four terms in the product which gives the thermal average. The important point to note is that in each term γ_s and η_s are imaginary so that the product $\langle U^2 \rangle + \langle V^2 \rangle$ becomes $(\mathbf{Q} \cdot \boldsymbol{\epsilon})^2 + \Xi^2$. It is the same for all four terms. In the sum of $\langle UV \rangle$ all the terms containing Ξ cancel out. For this even function therefore the ratio of magnetic to nuclear scattering is given by

$$\gamma = \frac{M_{0\perp}}{b} \exp \left[-\frac{W\Xi^2}{(\mathbf{Q} \cdot \boldsymbol{\epsilon})^2} \right] \quad (37)$$

7. Study of the "forbidden" TA mode

Whilst determining the optimum energies and wavevectors for the polarised neutron experiments described in the previous section an unexpected third peak was found in the spectrum of excitations with wavevectors in the (001) directions. This excitation which has the same dispersion as the transverse acoustic (TA) mode was seen in scans along reciprocal space direction (100) with either [001] or [011] perpendicular to the scattering plane, although in neither case does the polarisation vector for the TA mode have a component parallel to the scattering vector ($Q_h 00$). This excitation is referred to as the "forbidden" acoustic mode.

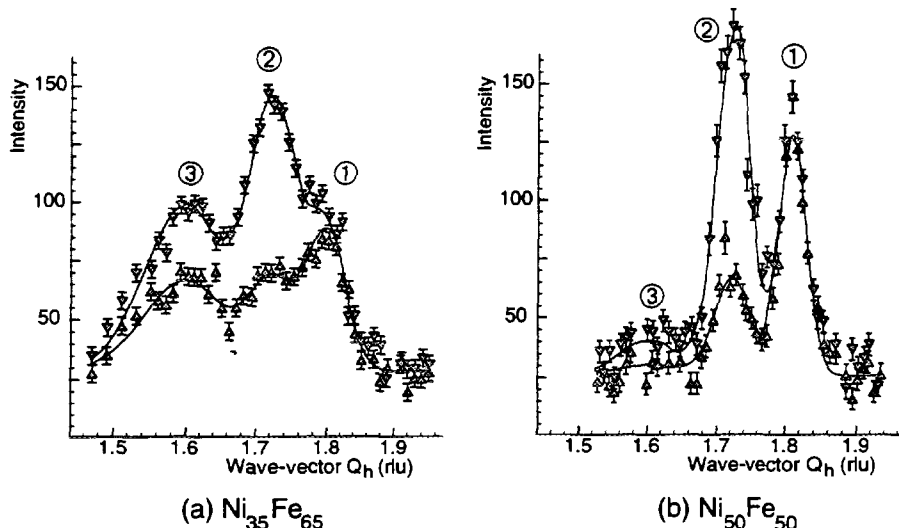


Fig. 4. Scans along $(00Q_h)$ at 100 K with a constant energy transfer of 15 meV for (a) $\text{Fe}_{65}\text{Ni}_{35}$ and (b) $\text{Fe}_{50}\text{Ni}_{50}$. Points marked ∇ are for scattered polarisation parallel and Δ antiparallel to the field direction. The peak marked 1 was identified with the magnon mode, that marked 2 with the LA phonon; the peak marked 3 is the "forbidden mode".

The scans which showed this extra mode were repeated under different experimental conditions e.g. by changing the final wavevector but the "forbidden" mode was observed in all experiments. However measurements carried out under identical experimental conditions on a Ni crystal failed to reveal the "forbidden" mode. Figure 4 shows the intensities of the two opposite polarisation states in scans along $(0, 0, Q_h)$ from $Q_h = 1.48 - 1.96$ with a constant energy transfer of 15 meV for (a) the $\text{Fe}_{65}\text{Ni}_{35}$ crystal and (b) a crystal of composition $\text{Fe}_{50}\text{Ni}_{50}$. The "forbidden"

mode which is labelled (3) is clearly visible in (a) but is at the limit of significance in (b). It appears that the occurrence of this mode is intrinsic to the Invar composition.

It has been suggested [13] that the TA 100 mode can be observed in the 100 direction because local orthorhombic distortions of the cubic site symmetry perturb the dynamical matrix elements and allow mixing of the TA and LA modes, but it is difficult to invoke mode mixing which is strong enough to account for its large intensity. Further experiments have therefore been undertaken [14] to obtain more information about this “forbidden” mode. These experiments seek to examine its Q dependence by making measurements in the 1st Brillouin zone.

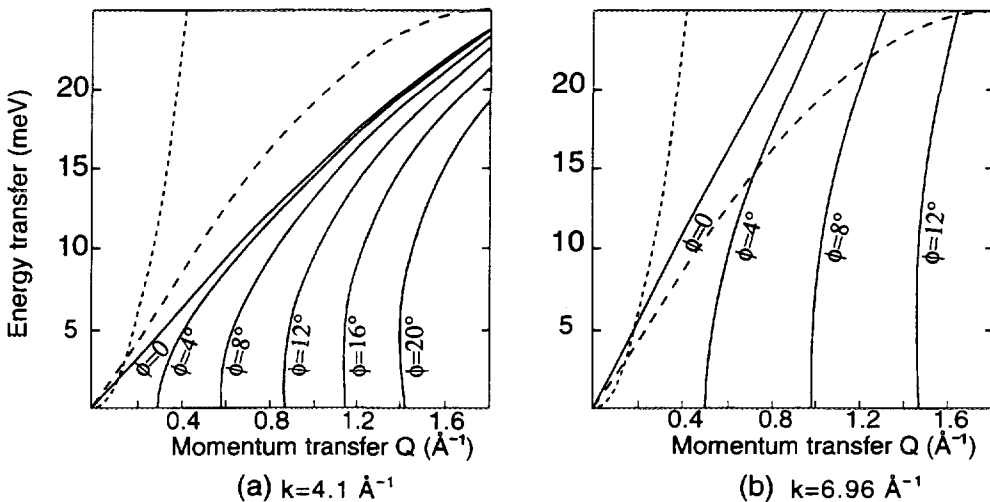


Fig. 5. The range of energy and momentum transfer accessible with a given scattering angle ϕ for (a) An incident energy of 35 meV ($k = 4.1 \text{ \AA}^{-1}$) and (b) 100 meV ($k = 6.96 \text{ \AA}^{-1}$). The dispersion of the magnon, and the LA and TA (100) phonon modes are shown as dashed curves.

7.1 Experimental

The conditions under which neutron scattering can take place are determined by the energy and momentum conservation rules:

$$E - E' = \frac{\hbar^2}{2m} (k^2 - k'^2) \quad (38)$$

$$\hbar \mathbf{Q} = \hbar(\mathbf{k} - \mathbf{k}') \quad (39)$$

where $E - E'$ is the energy transfer and \mathbf{k} and \mathbf{k}' are the incident and final neutron wavevectors. Eq. 39 can be rewritten in terms of the scattering angle ϕ as

$$Q^2 = k^2 + k'^2 - 2|\mathbf{k}||\mathbf{k}'| \cos(\phi) \quad (40)$$

When carrying out triple axis spectroscopy it is usual to fix the magnitude of either \mathbf{k} or \mathbf{k}' and vary the other in order to provide the energy transfers required. As the energy transfer is increased the momentum transfer increases, and therefore in order to close the scattering triangle, Eq. 40, ϕ must also increase. In order to carry out scans at finite energy transfers in the first Brillouin zone it is necessary to increase either \mathbf{k} or \mathbf{k}' . The range of energy and momentum transfer required is

determined by the dispersion of the "forbidden" mode. If Eq. 38 is substituted into Eq. 40 the range of momentum - energy space accessible for given incident neutron wavevector can be determined. The results are shown in Figure 5 for incident neutron energies 35 meV ($k=4.1 \text{ \AA}^{-1}$) and 100 meV ($k=6.96 \text{ \AA}^{-1}$) respectively. The dispersion curves for the magnon ($D=143 \text{ meV \AA}^2$) and the "forbidden" mode (24 meV \AA^{-1}) along the [100] direction are superposed. From these figures it is clear that the "forbidden" mode is not observable in the first zone for any scattering angle if the incident energy is only 35 meV which was the maximum used in previous experiments. Increasing the incident energy to 100 meV enables the mode to be observed for energy transfers above 15 meV at a scattering angle of 4 degrees. Experimentally the minimum usable scattering angle is 2.5 degrees. By careful selection of the incident energy it is therefore possible to investigate the dispersion of the "forbidden" mode in the first Brillouin zone for energy transfers greater than 15 meV.

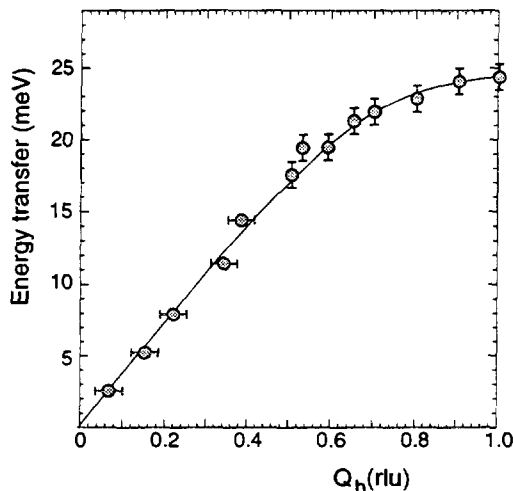


Fig. 6. The dispersion of the "forbidden mode" in $\text{Fe}_{65}\text{Ni}_{35}$ measured in the 1st Brillouin zone. The solid line represents the dispersion curve determined for the TA (100) phonon mode [11].

The experiment was carried out on the same single crystal of $\text{Fe}_{65}\text{Ni}_{35}$ as used in previous neutron experiments [1]. The crystal was mounted with the [1\bar{1}0] axis vertical inside a variable temperature cryostat on the triple axis spectrometer IN1 at ILL Grenoble. IN1 is located on the hot source which provides the high energy incident neutrons needed for the experiment. The exterior tail of the cryostat was increased to a diameter of 1.0 m in order to reduce the background scattering at small scattering angles. As in previous experiments the temperature was initially set to 100 K well below the Curie temperature of 550 K but later scans were also carried out at room temperature and above the Curie temperature at 570 K.

The spectrometer was set up with a vertically focusing Cu (200) monochromator and the scattered beam was also analysed using a Cu (200) crystal. In order to work in the first zone close to the straight through position it was necessary to tighten the collimation before and after the specimen to 20'. The spectrometer was operated throughout in the constant \mathbf{k}' mode with \mathbf{k}' set to 5.7 \AA^{-1} for the majority of scans although for some it was necessary to increase \mathbf{k}' to 6.6 \AA^{-1} . As

a further check that the "forbidden" mode was intrinsic to the material some scans were repeated with the curvature of the monochromator set to zero i.e. flat, to improve the vertical resolution and, as expected, there was no change in the observed excitations.

An initial longitudinal scan along (001) with an energy transfer of 18 meV showed a strong excitation centred at $q = 0.48$ which was identified with the "forbidden mode". The dispersion of this mode was measured out to the zone boundary and is shown in Figure 6 where it is compared with that of the TA 100 phonon measured by [11]. The constant \mathbf{Q} scans from $\mathbf{Q} = 0.7$ out to the zone boundary were repeated at 300 K, the dispersion was found to be unchanged, but the intensity was diminished indicating the primarily magnetic character of the scattering. Finally a constant \mathbf{Q} scan was carried out at the zone boundary at T=550 K ($T_c=500$ K) which is compared with that obtained at 100 K in Fig. 7. Only a small fraction of the intensity remains.

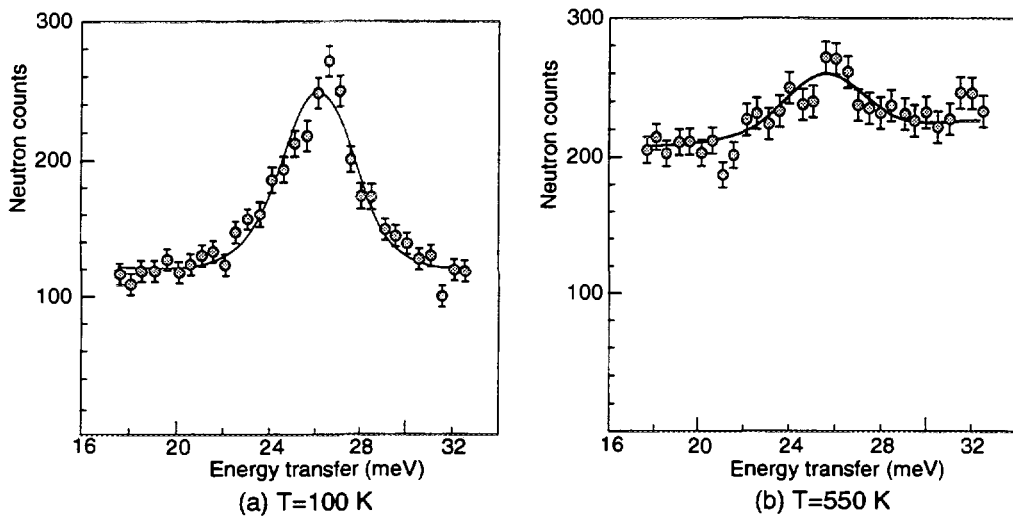


Fig. 7. Constant \mathbf{Q} scans showing the "forbidden mode" at the boundary of the 1st Brillouin zone $\mathbf{Q} = (100)$ at temperatures of (a) 100 K and (b) 550 K.

These experiments strongly suggest that the origin of the scattering in the "forbidden" mode is not directly due to the displacements of the atoms from their ideal positions but to a secondary effect, such as that suggested in section 2, induced by such displacements. For the former the physics of the scattering process gives an intensity proportional to $\mathbf{Q} \cdot \epsilon$ as $q \rightarrow 0$ Eq. 7 which is incompatible with the observed behaviour. On the other hand if the scattering is due to magnetic fluctuations driven by the TA100 phonons then, as was shown in section 4, the intensity is proportional to Ξ^2 , so long as there are odd terms in the dependence of the moment on the strain. For the TA 100 phonon Ξ is proportional to q and to the component x_{12} of the coupling matrix. A dependence on q rather than Q will explain the strength of the scattering in the 1st Brillouin zone, but a non-zero coefficient x_{12} is also necessary. Fig. 8 illustrates how this might arise; it shows the 100 plane of the fcc structure with the displacements corresponding to the TA 100 phonon indicated in an exaggerated way. The perturbation of the crystal field due to the strain is to first order the superposition of a rotation and an orthorhombic distortion. The former couples the $t_{2g}(xy)$ states with the $\epsilon_g(x^2 - y^2)$ states and

the latter couples with their spatial extent. Transitions from high moment (HM) to low moment (LM) states might well be induced by this distortion. According to the band structure calculations [3], the LM iron moments on the low moment side of the magneto-volume instability are mostly of t_{2g} character while HM iron atoms are mostly of e_g character, whereas on the other side of the instability the reverse is true.

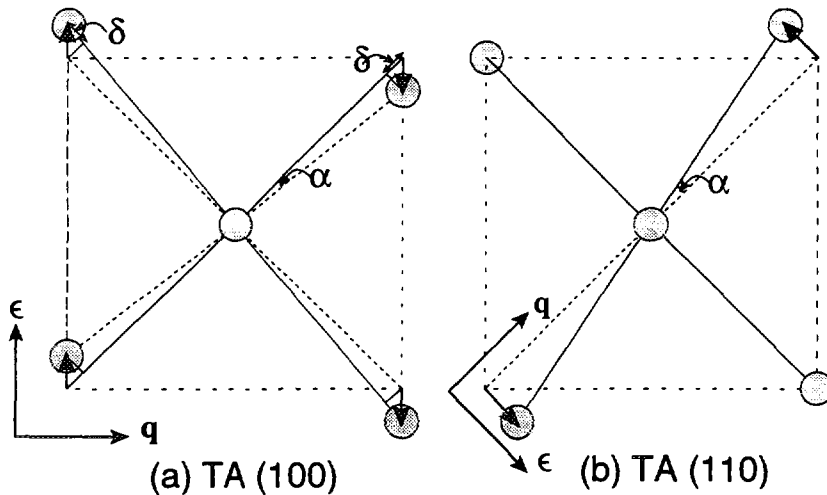


Fig. 8. Strain induced in the nearest neighbour environment of atoms in the the 110 plane of an fcc structure by (a) the TA 100 and (b) the TA 110 lattice modes. In (a) the first order strain corresponds a rotation α coupled to an orthorhombic distortion δ , whereas in (b) it is a rotation only.

It is therefore possible that magnetic fluctuations driven by the lattice vibrations can give rise to scattering which has the characteristics of the “forbidden” mode.

8. Conclusions

It has been shown that measurements of the polarisation dependence of the phonon intensity in a ferromagnet can give new information about the interactions between the magnetic and vibrational degrees of freedom. To obtain meaningful results however the phonon and magnon excitations must be sufficiently well resolved, and sufficiently well fitted to ensure that there is no contamination from the magnon in the scattering ascribed to the phonon. This requires better resolution and statistical precision than that needed just to determine the peak positions. Nevertheless polarisation dependent scans made in the region where the magnon and phonon cross, can be used to distinguish the phonon and magnon peaks and to recognise anticrossing behaviour.

In the foregoing sections a very crude model of a possible mechanism of spin-lattice interaction was introduced and some of its consequences for the neutron scattering cross-sections developed. Many physical details have been omitted from this model, including whether the magnetic moment fluctuations which couple to the lattice modes are solely longitudinal. In addition the initial assumption, that the time-scale of the magnetic moment fluctuations is much shorter than that of the lattice vibrations, must break down when the energy difference between the

competing magnetic states becomes comparable with the energy of the phonon which couples them. It is not therefore to be expected that there will be more than qualitative agreement between the predictions of the model and the experiment. Some significant physics does however emerge from the experimental data which any more sophisticated model must contain.

- (1) There is an interaction between the LA phonons and the magnetic system which leads to a variation of the ratio of magnetic to nuclear scattering with q additional to that expected from the form factor. This is not present in the TA modes.
- (2) The interaction of the magnetic system with the TA (100) phonon leads to a strong scattering cross-section even when the phonon polarisation is perpendicular to the scattering vector ("forbidden mode"). The scattering is probably mainly due to magnetic moment fluctuations driven by, and coupled to the TA 100 phonon mode. No such scattering is observed in the TA 110 mode, suggesting that distortive as well as torsional strain is involved in the coupling.
- (3) The polarised neutron data together with the low Q results show that the "forbidden" mode must have a small but significant nuclear contribution. Some mode mixing such as that suggested by [13] must therefore occur.
- (4) The exact positions of the phonon and magnon peaks near to the cross-over give little evidence for any coupling between the transverse magnetic (spin-wave) excitations and the LA 100 lattice vibrations.

Most of this new information has been obtained from the polarisation dependence of the intensity of the inelastic scattering. One may conclude that when spin-lattice interactions are important it may well be worth taking the extra time needed to measure the polarisation dependence of their inelastic spectra.

9. References

1. E.F. Wasserman in *Ferromagnetic Materials Vol. 5* eds. K.H. Buschow and E.P. Wohlfarth, (North Holland, Amsterdam) (1990)
2. E.G. Moroni and T. Jarlborg *Physica B* **161** (1989) 115
3. P. Entel, E. Hoffmann, P. Mohn, K. Schwarz and V.L. Moruzzi *Phys. Rev.B* **47** (1993) 8706
4. S. Lipinski *J. Mag. Magn. Mater.* **140-144** (1995) 233
5. O. Halpern and M.H. Johnson *Phys. Rev.* **55** (1939) 898
6. G.L. Squires *Introduction to the theory of thermal neutron scattering* Cambridge University Press, Cambridge (1978)
7. R.M. Moon, T. Riste and W.C. Koehler *Phys. Rev.* **181** (1969) 920
8. P.J. Brown J.B. Forsyth and F. Tasset *Proc. Roy. Soc. Lond. A* **442** (1993) 147
9. M. Blume *Phys. Rev.* **130** (1963) 1670

10. P.J. Brown, I.K. Jassim, K.-U. Neumann and K.R.A. Ziebeck *Physica B* **161** (1989) 9
11. Y. Endoh *J. Mag. Magn. Mater.* **10** (1979) 177
12. S. Ondero, Y. Ishikawa and K.J. Tajima *J. Phys. Soc. Japan* **50** (1981) 1513
13. S. Lipinski, K.-U. Neumann and K.R.A. Ziebeck *J. Phys.: Condens. Matter* **6** (1995) 9773
14. P.J. Brown, B. Roessli, J.G. Smith, K-U. Neumann and K.R.A. Ziebeck *J. Phys.: Condens. Matter* **8** (1996) 1527



MAGNETIC DIFFUSE SCATTERING: A THEORISTS PERSPECTIVE

M.W. LONG,

*School of Physics, Birmingham University, Edgbaston,
Birmingham, B15 2TT, United Kingdom*

ABSTRACT

We attempt to show that magnetic diffuse scattering is the natural probe for *frustrated antiferromagnetism*. Comparison between nuclear and magnetic diffuse scattering compares the range of atomic clustering with the range of the magnetic impurity. At low temperature frustration is expected to lead to large differences which are a natural signature for the relevance of such frustration effects. We provide some elementary examples in first-row transition metals which display fairly dramatic effects.

1. Basic Concepts

Magnetic diffuse scattering from antiferromagnets is a fairly difficult experiment[1]. To tackle such a measurement the desire must be strong and the rewards must be significant. The point to this article is to establish that magnetic diffuse scattering has a specific function which is rather difficult to fulfill with other probes; The investigation of *non-collinear* spin systems. The structure of the article is to use simple models and pictures to explain why *elastic* magnetic diffuse scattering is in a fairly unique position to provide interesting information about the existence and nature of non-collinear spins.

Any good textbook on neutron scattering will provide an introduction to magnetic diffuse scattering[2]. In this article we will need only the simple idea that the elastic scattering is:

$$I(\mathbf{k}) \propto \langle \mathbf{S}^\perp(-\mathbf{k}) \cdot \mathbf{S}^\perp(\mathbf{k}) \rangle$$

where:

$$\mathbf{S}^\perp(\mathbf{k}) = \hat{\mathbf{k}} \times [\mathbf{S}(\mathbf{k}) \times \hat{\mathbf{k}}]$$

is the component of the total-spin density, $\mathbf{S}(\mathbf{k})$, perpendicular to the direction of momentum transfer, \mathbf{k} . This spin-density is then split into two parts, with an average, denoted $\langle \mathbf{S}(\mathbf{k}) \rangle$, together with 'fluctuations' away from this average, denoted $\delta \mathbf{S}(\mathbf{k})$. The average is usually very narrow and constitutes Bragg scattering, controlling any magnetic order:

$$I_{Bragg}(\mathbf{k}) \propto \langle \mathbf{S}^\perp(-\mathbf{k}) \rangle \cdot \langle \mathbf{S}^\perp(\mathbf{k}) \rangle$$

whereas the fluctuations are usually fairly broad:

$$I_{\text{Diffuse}}(\mathbf{k}) \propto \langle \delta \mathbf{S}(-\mathbf{k}) \cdot \delta \mathbf{S}(\mathbf{k}) \rangle$$

Although this development is very appealing, and should be used as an intuitive tool, there is a minor difficulty as to the meaning of the average: This could be a thermal average or alternatively an average of many representatives of statically disordered systems. Both possibilities make sense, but often we make use of a third description, allowing the average to correspond to the *pure* state without disorder and then the ‘fluctuations’ are interpreted as *static* distortions away from this pure state. This third description involves *cross terms* between the Bragg and Diffuse scattering which we ignore because the Bragg scattering is so narrow.

In order for diffuse scattering to be important, we require that spins are significantly fluctuating away from their average. Thermal fluctuations are only severe in the vicinity of a magnetic phase transition, and consequently there has been some interest in this area[3]. Static disorder, ie substituted atoms with a different moment, also lead to spin defects which lead to diffuse scattering. Since magnetism is usually dominated by interactions between neighbours, any spin defect has the potential to spread out via these interactions. Unfortunately, in most spin structures there are many neighbours to any particular spin and so the loss of one provides only a small effect. Only near the phase transition, where the average field is severely weakened, is the loss of a neighbour expected to be crucial, and so there has been some investigation into the role of disorder at magnetic phase transitions[3]. At low temperature, where the spins have settled down into their classical order, the role of disorder is dull. The cause of this is obvious from figure 1:

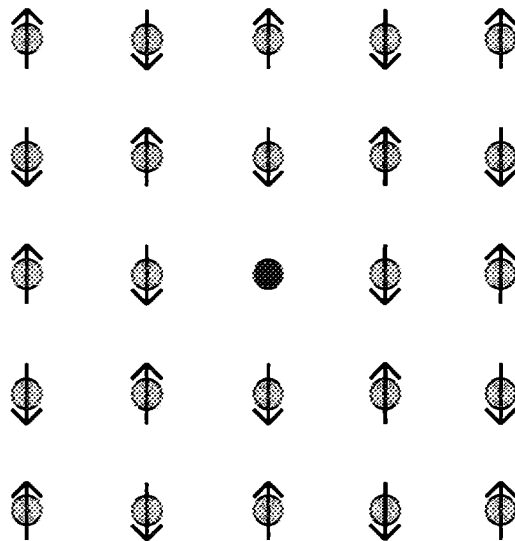


Figure 1: Ground-state spin configuration for the square lattice in the presence of a substitutional impurity with zero moment

The depicted spin arrangement is clearly the ground-state at zero temperature, and the impurity has not spread out *at all!* There remains some diffuse scattering, however, due to the missing spin. If we use:

$$\mathbf{S}(\mathbf{k}) = \frac{1}{N} \sum_j e^{i\mathbf{k} \cdot \mathbf{R}_j} \mathbf{S}_j$$

where \mathbf{R}_j is the atomic position of the spin (ie we ignore form factors), and the normalisation is a trifle abnormal, then:

$$I_{\text{Diffuse}} \propto |\mathbf{S}_0|^2 \left[1 - (\hat{\mathbf{k}} \cdot \hat{\mathbf{S}})^2 \right]$$

is a fairly uniform diffuse ‘background’ containing only information about the quantisation direction of the omitted spin.

If we are intending to use the disorder to *probe* the underlying magnetism, this ‘uniform’ background coming from the disorder itself is extremely dull and physically uninteresting. Fortunately, there is a clear physical way to assess this effect, *nuclear elastic diffuse scattering*. When considering magnetic diffuse scattering, one should first compare it to the associated nuclear profile, and then the *differences* are a probe of the underlying magnetism. For the current example of figure 1, it is clear that there is no difference and hence we will find nothing out.

Now let us consider the example depicted in figure 2:

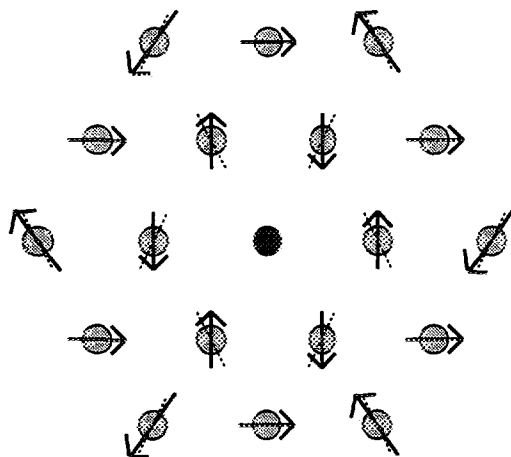


Figure 2: Ground-state spin configuration for the triangular lattice in the presence of a substitutional impurity with zero moment

this is the elementary triangular lattice with the so-called 120° phase as the ground-state. This time there is a clear extended magnetic impurity bound to the substituted impurity. There will be associated magnetic diffuse scattering with spatial structure, signifying the existence of frustration in the magnetism.

How may we interpret the difference between the frustrated and unfrustrated systems? There are two simple ideas that provide an explanation: Firstly, in the unfrustrated system all the spins are parallel to each other. The local fields that the spins exert on each-other are also consequently parallel. If a particular spin is removed, all its neighbours feel a reduced field, but due to the fact that they still have *some* neighbours they do not change orientation. The frustrated magnet has *non-collinear* spins. When a particular spin is extracted, any neighbouring spin which is not parallel will then feel a change in its local field direction and will rotate. This effect will then spread out as neighbours of neighbours feel this reorientation. Secondly, frustrated magnets involve non-trivial *degeneracy*. As well as the normal quantisation direction, corresponding to

rotating all the spins together, there are additional ground-states for frustrated magnets involving changes in relative orientations between spins. These additional ground-states may be generated from an understanding of the broken *point-group* symmetries of the magnet. For the current case, the broken symmetry is that of inversion, and there is a discrete degeneracy described by the *chirality* of the spiral. These two ground-states are depicted in figure 3:

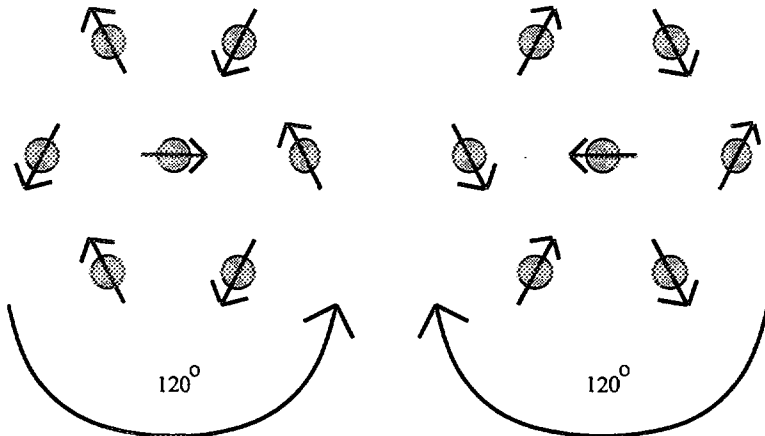


Figure 3: The two triangular lattice ground-states with opposite chirality

The idea is that one may add a ‘localised’ portion of the state with the opposite chirality to form the impurity. If the two depicted portions are added, then the spin in the middle is cancelled whilst the surrounding cage is reoriented. This second picture is very much more useful in general for the short-range distortion. When we look at the longer-range spreading out of the magnetic impurity, however, we find a different effect: Locally, far from the impurity, the dominant magnetic distortion is that of a *uniform rotation*, leading to scattering of the *original* order but weakly rotated in spin-space. The *sense* of this uniform rotation is a strong function of space, and one can see six quadrants for which nearest-neighbour quadrants rotate in opposite directions. This basic picture for a magnetic impurity will be seen to be quite general: The cause of the magnetic impurity is a second state at low energy which can locally make use of the change in bonds around the impurity. This leads to short-range distortion in real-space. This local distortion, which is often characterised by a specific point-group symmetry, then induces a longer-range distortion which spreads out using the ‘softest’ modes, usually the uniform rotations or Goldstone modes associated with the classical breaking of global spin-symmetry.

For the case of a simple spiraling antiferromagnet, this analysis leads to a prediction: If the domain structure of the sample permits a non-trivial chirality for the Bragg spots, then the diffuse peaks at the same sites would be expected to have *opposite* chirality.

The advent of domains into the argument introduces a second style of frustrated antiferromagnet and an important associated domain problem: Multiple- \mathbf{Q} states or multiple-spin-density-waves. This type of magnet involves a broken rotation symmetry in the point group, and then *several* possible Bragg spots which can be rotated onto each-other by this rotation. This style of magnet is best explained by example. We have selected the square lattice with sizeable next-nearest-neighbour exchange ($2J_2 > J_1$),

for which there are a variety of ground-states:

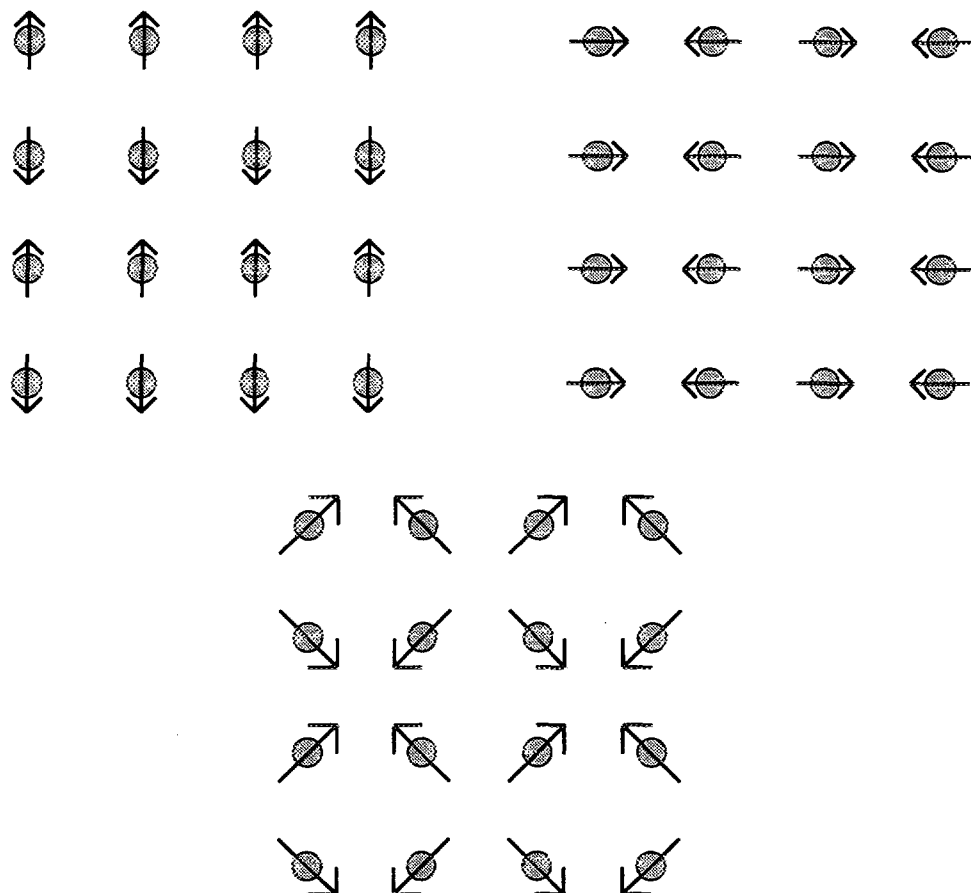


Figure 4: Three frustrated ground-states to the square lattice.

The first two ground-states are collinear phases involving different Bragg spots; The first with both Bragg spot *and* quantisation direction parallel to the y -axis and the second parallel to the x -axis. The third ground-state is a 'linear' superposition of the first two, and involves non-collinear spins. The fundamental problem with this type of magnetism is caused by *magnetic domains*. If we have a sample with a collinear structure but equal numbers of domains of the two pictured types, then in principle at the Bragg level this mixture is indistinguishable from the depicted non-collinear spin arrangement. In practice, the magnetoelastic coupling is usually sufficient to provide a measurable tetragonal distortion, but for the case of a double-spin-density-wave, when both Bragg spots are present at the local level, then no static distortion is anticipated and the dichotomy remains. There are a variety of techniques which purport to answer this question: Applying uniaxial stress or a magnetic field close to the transition temperature can measurably alter the domain populations. Mossbauer would also be expected to distinguish the two orientations of the moments in the two cases. We would like to propose magnetic diffuse scattering as a possible technique.

Magnetic diffuse scattering around a magnetic impurity is a *local* probe and hence is expected to depend only on the domain containing the impurity, this is the physical motivation to its use. Our previous interpretation provides the simple intuitive argument for the technique. There should be very low magnetic diffuse scattering in the collinear phases, but very strong scattering in the non-collinear phases. The likely

ground-state configuration for the double-spin-density-wave state is:

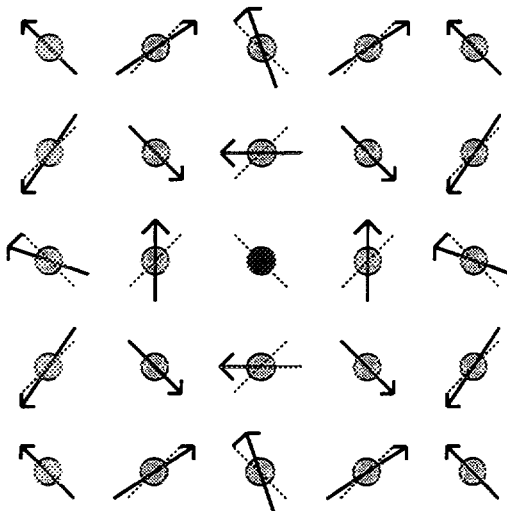


Figure 5: Ground-state spin configuration for the frustrated square lattice in the presence of a substitutional impurity with zero moment

Once again, it is useful to interpret the magnetic impurity in terms of the other degenerate ground-states. Since there are two Bragg spots, one would quite naturally presume that by shifting intensity between these two Bragg spots one could relax the spins around the impurity: *This is not true!* When restricted to next-nearest-neighbour bonding, one can see that this ground-state splits into two *unfrustrated* and independent ground-states. Since the phenomenon is controlled by the frustration, the bound state must involve the ground-state for the case of nearest-neighbour bonds, the elementary Neel state on the square lattice. Indeed, the elementary Neel state readily provides a good picture for the short-range distortion encountered in the vicinity of the substituted atom. Combining our ground-state with the rotated Neel state depicted in figure 6:

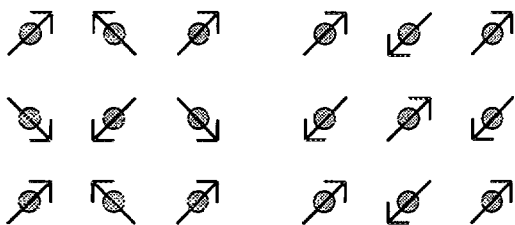


Figure 6: The square-lattice ground-state with its locally trapped magnetic impurity we can readily explain the local distortion. The central moment is seen to locally cancel, whereas the surrounding shell rotates. For this case the trapped magnetic impurity involves a state which can be energetically quite far removed from the ground-state, albeit remaining a turning point. The short-range magnetic diffuse scattering is expected to be centred on the Neel Bragg spots, and well away from the underlying frustrated Bragg spots.

For this impurity, the point-symmetry is non-trivial: The lines $x = \pm y$ mark *nodes* in the distortion. Inside any of the four remaining quadrants, we recognise that the distortion is another double-spin-density-wave, but with the spin axes *reversed*. The diffuse scattering is again expected to be ‘opposite’ to the Bragg scattering. For this case, there are two distinct Bragg spots, and each is associated with an orthogonal spin

direction for the Bragg scattering. The long-range diffuse scattering should be peaked around the same positions, but the associated spin directions are reversed. This shows up very easily through the angular dependence of the scattering, ie the $(1 - \hat{k}_z^2)$ factor. Usually, there are Bragg spots which are extinguished because their momentum transfer is parallel to the spin orientation. For the current case, these vanishing Bragg spots are those closest to the origin. Since the diffuse scattering is associated with a perpendicular spin direction it should be maximal here.

The conclusions of this section are fairly simple: In collinear spin structures the magnetic diffuse scattering should 'mirror' the nuclear diffuse scattering. In non-collinear spin structures the magnetic diffuse scattering should be strongly enhanced over the nuclear diffuse scattering. This magnetic scattering should be peaked around the Bragg sites but should have 'opposite polarisation'. For a spin-spiral this means that the diffuse scattering should have opposite chirality, whereas for the multiple-spin-density-wave case, the associated spin orientation should be rotated.

We close this section with some quite crucial practical considerations which *must* be kept in mind when physical systems are being investigated through substitutional impurities and their associated magnetic defects. As with probes like μ -SR, where the technique involves a sizeable change in the physics where it acts, the impurity itself can *mask* the underlying magnetism and provide misleading information. The magnetic impurity must be fully understood before deductions about the underlying magnetism are attempted.

This simple idea that non-collinear spin structures can easily deform to accommodate spin defects, has radical consequences: Each doped impurity would gain more magnetic energy in a non-collinear state than a collinear state. At some doping level this energy can dominate the energy saving from being in the collinear phase and cause a *phase transition*. This possibility is very real, as will be demonstrated in the next section, and is also quite confusing because there can be phenomena associated with the impending phase transition that confuse interpretation. The stabilisation of collinear phases is normally on a smaller energy-scale than the basic magnetism; Quantum fluctuations prefer a collinear phase, but on the magnetic energy scale reduced by $1/S$. Spin-orbit coupling can tie the spins to the lattice directions, preferring collinear states, but this effect is very weak for first-row transition metals. Sympathetic structural distortions also prefer collinear states, where the bonds are at their most anisotropic. Since these effects are quantitatively dominated by the magnetic energy, substitutional impurities can cause phase transitions at quite low concentrations, eg $\sim 10\%$.

The degeneracy previously referred to in frustrated antiferromagnets is usually *not* pure in the real physical systems. Firstly, there are associated structural distortions with any symmetry broken ground-state, and these provide macroscopic energy differences between the states degenerate in a pure system. Such effects provide a natural *range* for the magnetic impurity, which in their absence would decay only as a power law. Secondly, the spin-orbit effects, although weak, also serve to provide a *range* for the impurities and must be considered very carefully in practice.

2. First-row transition metals: Manganese in particular

In this section we will look at the particular example of γ -Manganese, ie manganese quenched into a face-centre-cubic lattice, as a real physical system in which these phenomena abound. Probably the most interesting alloy is $\gamma\text{-Mn}_{1-x}\text{Ni}_x$ [4]. As the nickel concentration is increased from zero, there are a sequence of phase transitions at low temperature; The pure manganese is tetragonal $c < a$, which transits to orthorhombic $c < b < a$, which transits to tetragonal $c > a$, which transits finally to cubic near $x \sim 1/4$. This is interpreted as a ‘cascade’ of additional spin-density-waves: The alloy starts out with a single- \mathbf{Q} , transits to two unequal \mathbf{Q} ’s, transits to an equal double- \mathbf{Q} , and finally transits to a triple- \mathbf{Q} . This is precisely the overwhelming influence of the disorder causing phase transitions as we previously discussed. The collinear phase is held in place by the static distortions and consequent saving in magnetic energy from partially unfrustrating the bonds. Paramagnetic impurities destabilise this distortion and gain more energy from their ability to relax neighbouring moments around the disorder, overwhelming the small unfrustrating energy saving.

Magnetic diffuse scattering is an excellent probe for this behaviour. Unfortunately, only the cubic phase has been investigated[5]. The predicted magnetic ground-state would be the triple- \mathbf{Q} state:

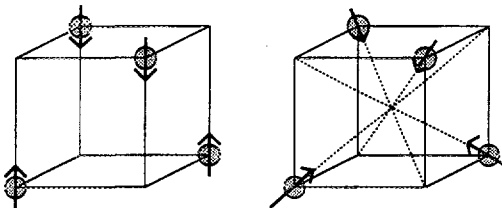


Figure 7: A single- \mathbf{Q} state and a triple- \mathbf{Q} state for the face-centre-cubic lattice type I antiferromagnetism

Since this phase has non-collinear spins, we would anticipate a large amount of magnetic diffuse scattering. A huge amount of diffuse scattering has been observed, indeed at first this diffuse scattering was erroneously deemed to be Bragg scattering and a quite bizarre canted spin-state was originally proposed in this type of alloy.

The magnetic diffuse scattering has well defined spatial structure which can be well fit using an impurity model allowing two shells of neighbours to reorient subject to Heisenberg interactions[5]. Although the basic picture is well described by this isolated impurity model, the *amplitude* for the scattering is not well described. For this alloy there is a high concentration of impurities, nigh on 25%, and hence the impurities clearly overlap with each-other. When two impurities overlap, they do so *in phase* and so the expected scattering is *four* times a single impurity, and not twice as would be expected if the impurities were incoherent. There must be a length-scale over which this orientational coherence is lost, but we found no clear way to experimentally probe this idea directly and so left this area uninvestigated. Clearly a theoretical method for describing such orientational disorder should be developed.

The magnetic diffuse scattering was exactly as anticipated for the triple- \mathbf{Q} structure and quite unlike that expected in a multi-domain single- \mathbf{Q} sample. Of course, at

a practical level, the structural distortions were the obvious physical signal as to the magnetic structure.

The next most interesting alloy of this system is $\gamma\text{-Mn}_{1-x}\text{Cu}_x$, which shows fairly unique behaviour amongst the analysed possibilities. Unlike many of the other alloys, there is no sequence of structural transitions and the system goes smoothly over from tetragonal $c < a$ to cubic. The excitement was caused by the *magnetic diffuse scattering* from the collinear spin state, however, where giant perpendicular magnetic impurities had become trapped around the doped copper sites[6]. This is very difficult to understand given our previous prediction that collinear magnets cannot respond to paramagnetic impurities. One crucial difference between the copper and nickel alloys is that the copper atoms cluster whereas the nickel atoms anti-cluster. There is a strong nuclear diffuse peak in the copper case, but the magnetic diffuse peak is many times stronger[6]. As we shall see, this clustering is an important clue.

The resolution to the predicament is *local spontaneous symmetry breaking*. In the same way that global phase transitions can be controlled by spontaneous symmetry breaking, so can the formation of local impurities. The physical idea is that if the system is very close to a phase transition, then only a small change in bond strengths would push it into a new phase. The large local change around an impurity can stabilise this second phase, but only in the vicinity of the impurity[7]. For the simple case of the frustrated square lattice, with $2J_2 \sim J_1$, the Neel state can be locally unstable to the formation of a small impurity of the type depicted in figure 8:

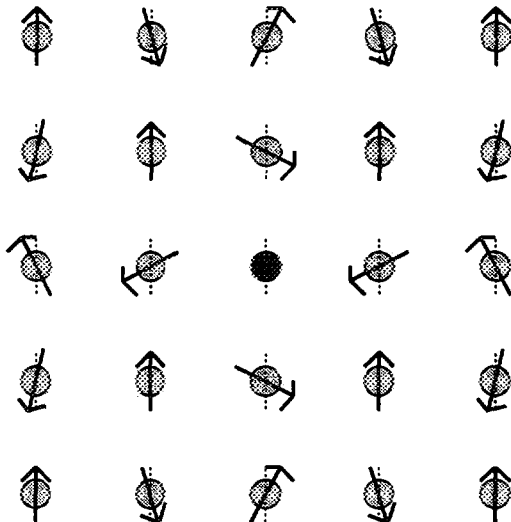


Figure 8: A magnetic impurity of new symmetry bound to a paramagnetic impurity in the unfrustrated square-lattice ground-state

The four spins surrounding the impurity feel a reduced penalty from the weakened nearest-neighbour field and take full advantage of the next-nearest-neighbour field. It is important to realise that the two perpendicular spin components are *independent*; The perpendicular moment is self-trapped, gaining nothing from the underlying spin-state. The only coupling between the two moments is via the spin constraints.

There are a variety of subtleties that need to be understood when interpreting this eventuality: Firstly, the immediate physical prediction would be that diffuse scattering

would appear in the vicinity of Bragg spots associated with the spin-density-waves *not* present in the underlying order, and that this magnetic diffuse scattering would be perpendicular to the long-range order. This is *not* the dominant observed scattering experimentally! Although such scattering is believed to be present, and further to be related to the fundamental cause of the effect, it is overtaken by important details. The crucial concept here is the length-scale over which the magnetic impurity spatially decays: There are *two* such length-scales. Firstly, the collinear phase is relatively stable and consequently there is an energy penalty from trying to trap spin-density around another Bragg spot. This penalty in the experimental system is high and the trapped impurity decays very fast over only a couple of unit cells. Secondly, magnetism with the same spatial structure as the underlying order but *perpendicular* to it decays only on a length-scale controlled by the spin-orbit coupling, which is very small in these experiments and so this decay is much slower, involving tens of unit cells or more. The dominant effect is that the quick decaying magnetic impurity trapped around the other Bragg spots acts as a *source* for perpendicular magnetism associated with the *original* Bragg spots. At first sight, this would then explain the observed scattering, which is centred on the existing extinguished Bragg spots, but is perpendicular to underlying long-range order. Unfortunately, the theoretical calculation of such diffuse scattering provides figure 9[7]:

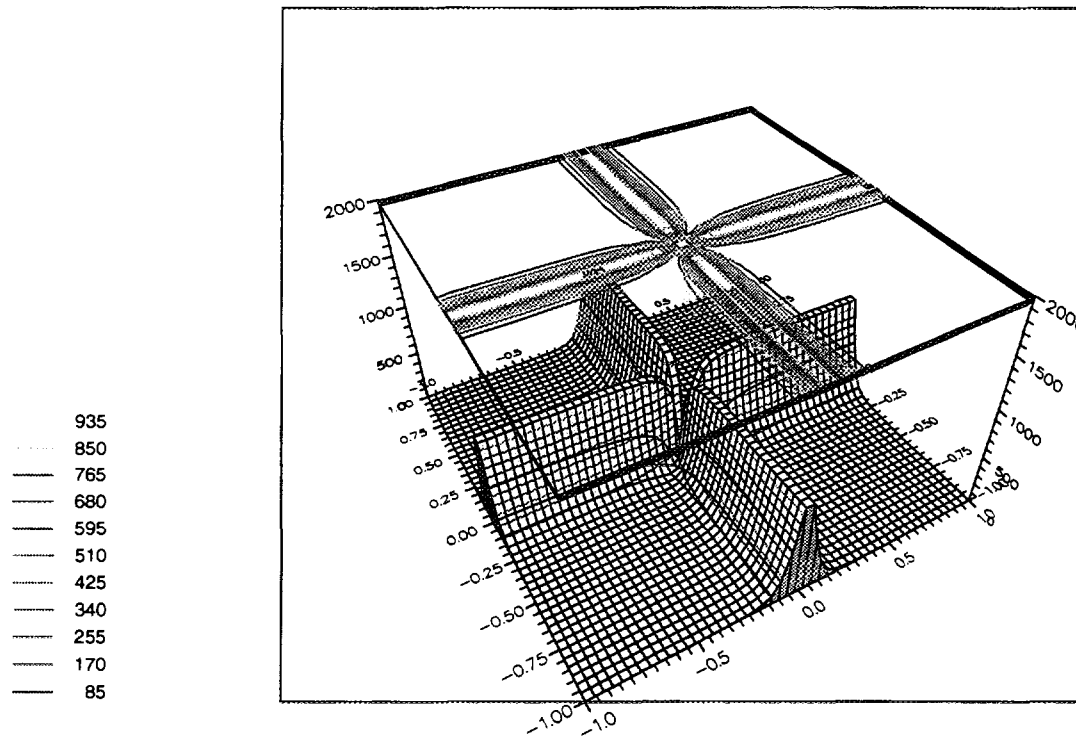


Figure 9: The diffuse scattering from a paramagnetic impurities in the face-centre-cubic lattice

Disaster! The fast decay around the other Bragg spots is observed but no long-range component at the classical Bragg spot in the centre.

The resolution of this ‘paradox’ is also quite subtle. The trapped impurity moments that we are analysing have curious symmetry: They have non-trivial *point* symmetry. The depicted impurity in figure 8 has two reflection planes and *d*-like symmetry.

It is this property that eliminates the central peak! The ‘wavefunction’ to the impurity is $W(\mathbf{k}) \sim (k_x^2 - k_y^2)$ near the central peak, and then the magnetic diffuse scattering is of the form[7]:

$$I(\mathbf{k}) \sim \frac{|W(\mathbf{k})|^2}{\epsilon(\mathbf{k})^2}$$

in terms of the ‘dispersion’ for static moments, $\epsilon(\mathbf{k})$. The numerator and denominator are both $O(k^4)$ and hence no peak is expected. The modeling here requires some explanation: Elementary impurity calculations performed on elementary Heisenberg models and variants. For these calculations there are two major inputs. Firstly, there is the underlying energy expenditure for laying down spin-density at any position in reciprocal-space, and this is the quantity $\epsilon(\mathbf{k})$. Secondly, there is the local impurity potential and its corresponding bound state wavefunction, which we denote by $W(\mathbf{k})$. This wavefunction contains the information about the point-symmetry of the bound-state and is quite crucial in assessing whether or not the longer-range distortion will be visible in any experiment. The details are provided elsewhere[7].

When we consider an impurity with only a single reflection plane, a p -like symmetry, a less symmetric impurity is expected:

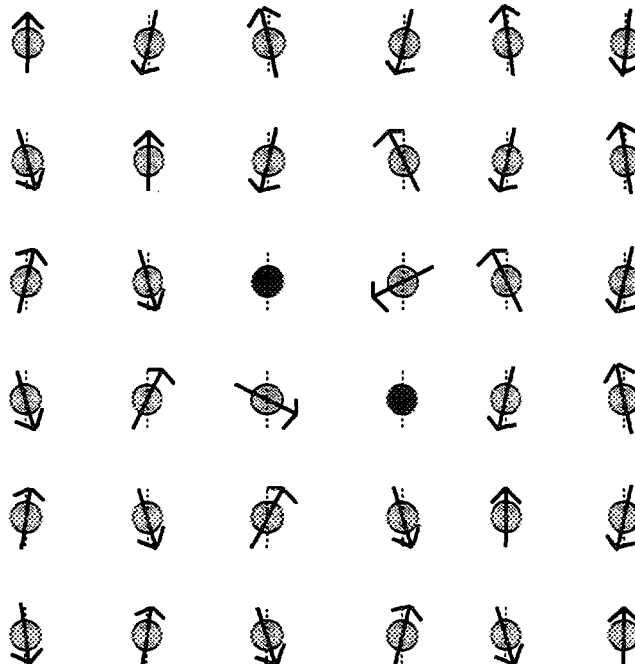


Figure 10: A magnetic impurity of new symmetry bound to a pair of paramagnetic impurities
This magnetic impurity is expected to have a ‘wavefunction’ of the form, $W(\mathbf{k}) \sim (k_x^2 - k_y^2)$, and hence provides a healthy divergence for the central peak. This divergence is cut off by the spin-orbit coupling, and still has non-trivial point-symmetry which must be reinstated by averaging over many such impurities of all possible orientations. Once some of these ‘details’ have been included, we are led to a theoretical profile of

the form depicted in figure 11:

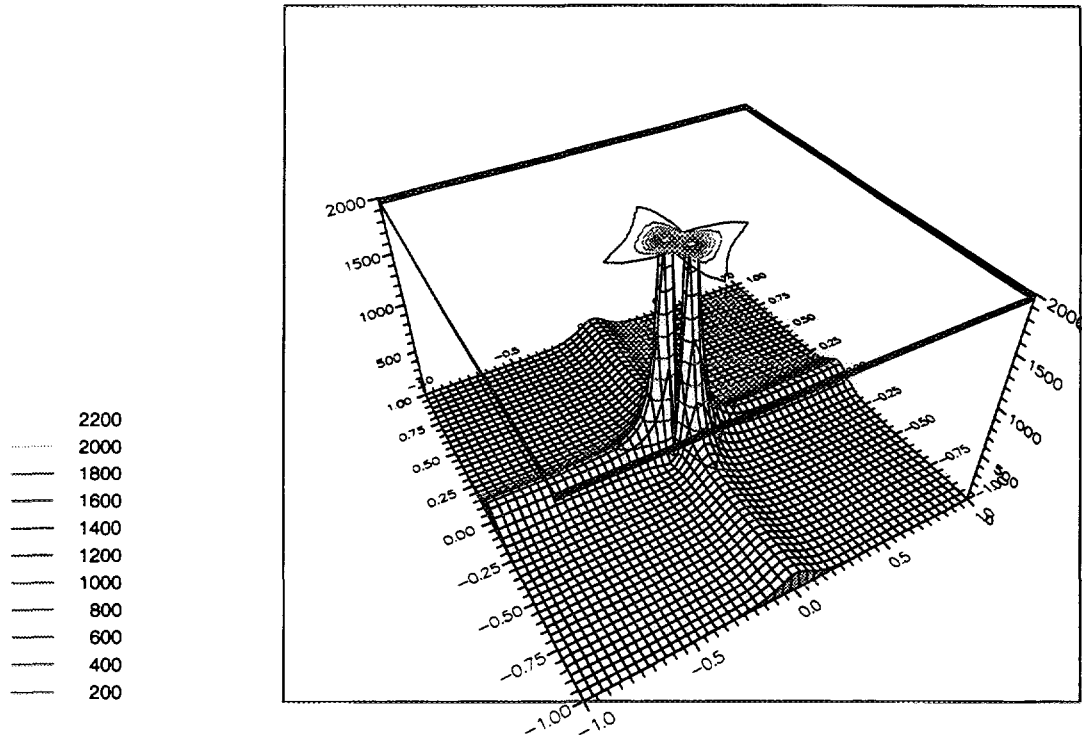


Figure 11: The diffuse scattering from a pair of paramagnetic impurities in the face-centre-cubic lattice

a healthy central peak is observable as in the experiments. In order to observe a large central peak, we need a sizeable probability of finding magnetic impurities with a *p*-like symmetry. The clustering present in the copper alloy provides many such pairs whereas the anti-clustering in the nickel alloys would be expected to strongly reduce their contribution in an equivalent experiment.

The conclusions from these experiments demonstrate how careful one must be in interpreting magnetic diffuse scattering. The magnetic impurity spreads out away from the defect in quite a subtle way. There are short-range effects attributable to the *cause* of the impurity, but the longer-range effects which are easier to detect experimentally come from the ‘softest modes’ in the system which are associated with the underlying magnetism but in a perpendicular spin direction.

We close this section with a fairly sophisticated comment. One of the most exciting areas in fundamental magnetism is that with zero temperature classical degeneracy, such as the Kagome net with the physical example $\text{SrCr}_{8-x}\text{Ga}_{4+x}\text{O}_{19}$ [8]. These systems are theoretically expected to have macroscopic degeneracy even at zero temperature, having continuous degrees of freedom in the ground-state manifold. One theoretical surprise is that the disorder in the system does not strongly stabilise a preferred ground-state. The materials are very ‘messy’, and using the arguments already presented, one might have anticipated the *most* non-collinear state to become stable, since in this phase one would expect the most effective relaxation around impurities. Experimentally no classical order has as yet been found, which requires investigation. The simplest theoretical approaches provide an explanation: With only the minor restriction that one needs to use all three spin dimensions, *the energy of a magnetic impurity is independent*

of the ground-state spin configuration. This quite remarkable result explains why there is no strong force from the static disorder. The magnetic diffuse scattering profile is strongly dependent on the underlying ground-state, and so it makes great sense to investigate the diffuse scattering with the intention of trying to deduce something about the underlying magnetism. The path to understanding such scattering would not be short, as the rather simpler transition metal examples have shown.

3. Conclusions

Collinear magnets involve local fields which are parallel to a unique direction in space, the direction along which all the spins are aligned. At low temperature, when the system is disordered with paramagnetic impurities, the resulting random fields are still expected to be parallel to this unique direction and as such, lead to forces which want either to elongate or to contract the spins along their length. Spins are *very* stiff against magnitude changes and so the result of the disorder is expected to be pitifully weak and dull. Non-collinear magnets, which necessarily involve frustration, have neighbouring spins which are not parallel, and when one is removed the other feels a field which desires to reorient it. This reorientation spreads out into the system and can lead to a sizeable magnetic impurity trapped near the paramagnetic impurity. This magnetic defect leads to magnetic diffuse scattering which is the hallmark of the non-collinear state. The spatial structure of the impurity is a probe of the underlying magnetic state, and through theoretical modeling can be used to understand the magnetism.

This technique of using the magnetic diffuse scattering around paramagnetic disorder is both experimentally difficult and interpretationally taxing. The disorder is a strong physical perturbation and as such can provide new physics which masks the underlying magnetism under investigation. Each experimental system must be analysed on merit and imagination must be used theoretically.

The fundamental idea is that collinear spin systems yield scattering of a similar form to the nuclear diffuse scattering, but non-collinear systems show much enhanced scattering. The spatial structure of this additional magnetic scattering is then a local probe of the susceptibility of the underlying magnetism to magnetic defects. Unfortunately, in some situations even a collinear spin state can exhibit these magnetic impurities. This situation is a precursor to a possible magnetic transition and amounts to a *local* breaking of a spin symmetry. The phase transition is when these local impurities become coherent across the sample. The experimental method of assessing whether one has *local symmetry breaking* or a real non-collinear spin state is non-trivial. The use of the different ranges for the diffuse scattering worked for the γ -Mn systems, but there is no guarantee as to its use in more anisotropic magnets. Sadly, one must look at each case carefully with few preconceptions.

The physical interpretation for the *cause* of the magnetic impurities is the binding of localised components of a *second* low-energy state. This second ground-state is usually related to the first by some point-group symmetry which can be employed in analysis of the scattering, but this is not a necessity. This magnetic impurity then acts as a *source* for longer-range ‘tails’ with possibly different properties: The dominant diffuse peak may well exhibit similar properties to the existing magnetism but perpendicular in spin-space. The shorter-range surrounding scattering may well be more instructive.

The experimental area of investigating non-collinear states through their magnetic impurities is as yet underdeveloped, and we await to see it used as a prime source of investigation rather than as a source of corroboration.

We believe that this technique should be seriously considered for the class of classically degenerate magnets such as the Kagome Net, because the theory is so intriguingly pathological.

4. References

1. T.J.Hicks, *Nucleonika* **24** (1979) 795
2. S.W.Lovesey, *Theory of Neutron Scattering from Condensed Matter*, (Clarendon Press, Oxford, 1984)
3. S.W.Lovesey, *Proc. Phys. Soc* **89** (1967) 625, 893
4. Honda N, Tanjii Y and Nakagawa Y, *J. Phys. Soc. Jap.* **41** (1976) 1931
5. M.W.Long and O.Moze, *J.Phys: Condens. Matter* **2** (1990) 6013
6. O.Moze and T.J.Hicks, *Phys. Rev.* **B46** (1992) 915
7. M.W.Long and A.Bayri, *J.Phys: Condens. Matter* **5** (1993) L15
8. X.Obradors, A.Labarta, A.Isalgue, J.Tejada, J.Rodriguez and M. Pernet, *Solid State Commun.*, **65** (1988) 189

Magnetic Excitations Studied with Time-of-Flight Spectroscopy

BRIAN RAINFORD

Department of Physics, University of Southampton
Southampton SO17 1BJ, England.

ABSTRACT

An introduction to time-of-flight neutron spectroscopy is presented in the context of the study of magnetic materials. Examples are taken from the class of rare earth and actinide magnetic materials known as "strongly correlated electron" systems.

1. Introduction

Inelastic neutron scattering has had a profound impact on the understanding of magnetism at the microscopic level. It is the only technique which allows us to probe the dynamical susceptibility $\chi(Q, \epsilon)$ over a large range of wavevectors and energies. At the forefront of modern magnetism research is a broad class of phenomena, collectively known as "strongly correlated electron" systems, which include Kondo lattice, heavy fermion and intermediate valence materials and also high temperature superconductors, Mott-Hubbard insulators, etc. Time-of-flight spectroscopy has played an import role in the characterisation of these materials, so I have focussed on this area of magnetism when providing illustrations.

2. The time-of flight technique

In the usual "direct geometry" time-of-flight spectrometer a pulsed monochromatic neutron beam, with energy E_i and wavevector k_i , is produced either by Bragg reflection from a monochromator crystal or by two or more phased Fermi choppers. This beam is scattered by the sample into a large detector bank, and the time of arrival of each neutron is recorded. The energies E_f and wavevectors k_f of the scattered neutrons are determined from their time of flight between the sample and the detector bank. The time-of-flight, τ , is the inverse neutron velocity and can be related to the neutron energy by $E(\text{meV}) = 5.228 \times 10^6 / \tau^2$ and to the wavelength by $\lambda(\text{\AA}) = 3.956 \times 10^{-3} \tau$, where the time-of-flight is in units of microseconds per metre. The great advantage of time-of-flight spectrometers for studying inelastic neutron scattering is that the detector solid angle may be made very large. This allows the scattering law $S(Q, \omega)$ to be measured at a large number of wavevector transfers Q simultaneously. Clearly this is of special benefit if the scattering law varies with Q in an easily predicted way: for example in crystal field spectroscopy we normally work with samples in which the interactions between the magnetic ions are weak, so that the only Q dependence of the cross section comes from the magnetic form factor $F^2(Q)$, which is well known and slowly varying.

The neutron energy transfer ϵ and wavevector transfer Q are given by the conditions

$$\epsilon = E_i - E_f \quad (1)$$

$$Q^2 = k_i^2 + k_f^2 - 2k_i k_f \cos\phi \quad (2)$$

where ϕ is the scattering angle of the detector. Note that both the energy and momentum

transfers vary with the time-of-flight. The accessible region of Q, ε space can be found by combining (1) and (2) as follows

$$\frac{\hbar^2}{2m} Q^2 = 2E_i - \varepsilon - 2\sqrt{E_i(E_i - \varepsilon)} \cos \phi \quad (3)$$

This equation allows us to plot the locus of the neutron in Q, ε space as a function of time-of-flight and scattering angle. Figure 1 shows this plot for a number of scattering angles and an incident energy of 10 meV.

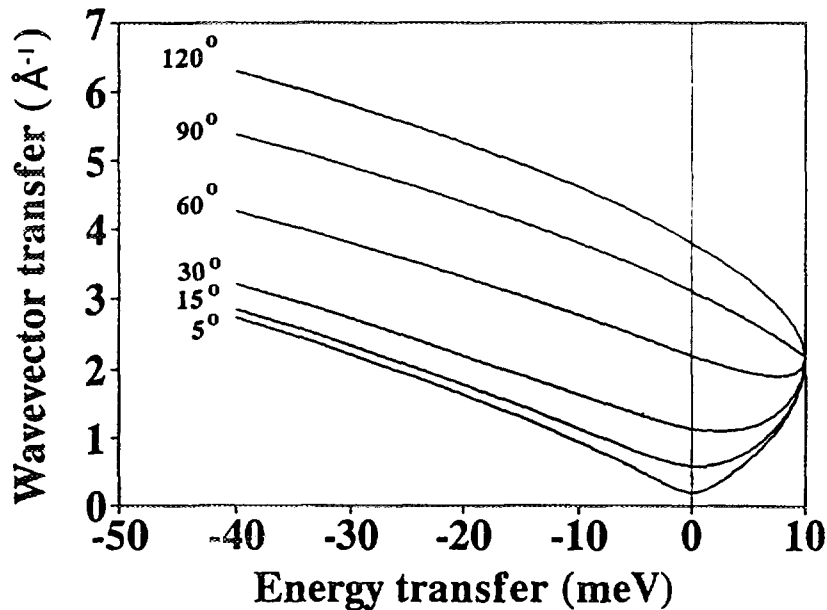


Fig.1 Locus of neutron in (Q, ε) space from (3) for $E_i = 10$ meV and various scattering angles.

The time-of-flight cross section is related to the normal energy differential cross section by

$$\frac{d^2\sigma}{d\Omega dE_f} = \tau^3 \frac{\hbar}{m} \frac{d^2\sigma}{d\Omega d\tau} \quad (4)$$

What this means in practice is that the energy width $\Delta\varepsilon$ of a given time channel (width $\Delta\tau$) varies as the inverse cube of the time-of-flight! Let us look at a real example: suppose we have an incident neutron energy of 10 meV and the spectrometer has a 3 m flight path and 8 μ sec time channels. At the elastic channel ($\omega = 0$) the channel width in energy will be 0.07 meV, well matched to an energy resolution of 1% of E_i . However for an energy transfer of -30 meV (neutron energy gain with $E_f = 40$ meV) the channel width in energy is 0.59 meV, and for an energy transfer of +6 meV (neutron energy loss, with $E_f = 4$ meV) the energy width of a single time channel is only 0.02 meV! One can get around this strongly non-linear feature of time-of-flight spectra by using variable width time channels in the data collection software.

For reactor or quasicontinuous spallation sources like SINQ the time between neutron pulses is determined by the period of the Fermi chopper. As an example, for a curved slot Fermi chopper spinning at 240Hz, giving one pulse per revolution, the period between pulses would be $(1/240) \times 10^6 = 4167 \mu\text{sec}$. This defines the time frame: if we then have 512 time channels with channel width 8 μsec , we would be collecting data for 4096 μsec out of the

total of 4167 μ sec, with a gap of 71 μ sec between frames. If we assume a 3 m flight path as above, the slowest neutron which will be detected will have a time-of-flight of roughly $4096/3 = 1365.3 \mu$ sec/m, or an energy of 2.8 meV (i.e. if $E_i = 10$ meV, this would correspond to an energy transfer of +7.2 meV). The problem is that it is possible for even slower neutrons to emerge from the sample, and these will be travelling so slowly that they will appear in the next, or subsequent, time frames. This is known as "frame overlap". The frame overlap neutrons are well spread out over the time channels (because of the τ^3 factor above) and so appear usually as a rather flat background. If this is bothersome the only solution is to chop out every second pulse, or two pulses out of three with a "frame overlap chopper". This problem does not arise at pulsed neutron sources like ISIS, since the source repetition period (20 ms) is much longer than the typical useful time frame.

The energy resolution of time-of-flight spectrometers has contributions arising from the burst time of the neutron pulse and the uncertainty in measuring the time-of-flight. The latter depends on the length of the flight path, the time channel widths, the effective thickness of the detectors and also the sample dimensions. As always there is a trade-off between resolution and intensity: longer flight paths gives better energy resolution, but a smaller solid angle coverage of a given detector. The neutron pulse width can be decreased by choice of the chopper slit package geometry or by increasing the rotation speed of the choppers, but there is a clear upper limit here determined by engineering considerations. The HET and MARI spectrometers at ISIS and IN5 at ILL are designed for a resolution at the elastic channel of about 1% of E_i , while the rebuilt IN4 spectrometer at ILL will have $\Delta E/E_i$ between 2 and 5%.

3. Separation of Magnetic Scattering from Phonon Scattering

Before discussing examples of magnetic scattering it is worth considering methods for separating the magnetic scattering from phonon scattering, which is always present.

The technique of polarisation analysis, as employed on the D7 time-of-flight instrument at ILL, allows a complete separation of magnetic and phonon scattering in a sample [1]. However there is a large intensity penalty involved in producing polarised beams and in analysing the polarisation of scattered beams, which makes such experiments time consuming. It is often possible to effect an approximate magnetic-phonon separation without using polarisation analysis. The general principle depends on the fact that the magnetic cross section falls off at large Q values because of the magnetic form factor $F^2(Q)$, while the phonon cross section increases with Q. The first approach is to use a "phonon blank": this is a sample in which the magnetic species of the original sample is replaced by a non-magnetic element which is as close as possible chemically and in mass number. For example if one were studying the magnetic response of CeCu_2Si_2 then a suitable phonon blank would be LaCu_2Si_2 [2]. One would expect that the phonon scattering in the La compound would be very similar to that of the Ce compound. A straight subtraction of the LaCu_2Si_2 data from the CeCu_2Si_2 data would not necessarily work, however, since La has a larger nuclear scattering length than Ce. A better approach is to assume that the Q dependence of the phonon scattering in the two samples is the same, and to use the LaCu_2Si_2 data to define a scaling function for the CeCu_2Si_2 phonon cross section in (Q, ϵ) space. This scaling function can then be used to extrapolate back the data from high Q (where the magnetic scattering is negligible) to smaller wavevectors.

A second approach is to use Monte Carlo simulations for the phonon scattering [2]. In the incoherent approximation the one phonon scattering cross section is

$$\frac{d^2\sigma}{dQd\varepsilon} = \frac{N\sigma_{inc}}{8\pi M} \frac{k_f}{k_i} Q^2 e^{-2W} \frac{Z(\varepsilon)}{\varepsilon} [n(\varepsilon) + 1] \quad (5)$$

where $Z(\varepsilon)$ is the phonon density of states and $[n(\varepsilon) + 1]$ is the detailed balance (population) factor. The Q^2 dependence would suggest that phonon scattering at small Q is negligible. This is not true, however, since the Q^2 dependence leads to a high probability of multiple scattering processes through large angles. This multiple scattering is found to be isotropic to a very good approximation: most of the phonon scattering measured at small Q arises from two or more scattering events. Osborn [2] has shown how to model the total phonon cross section (not just the one phonon term given in (5)), given the phonon density of states. This may then be used as the kernel in a Monte Carlo simulation of the multiple phonon events. A reasonable approximation to the density of states may be extracted from high Q data using (5), since the single phonon cross section dominates at high Q . Fig.2 shows the results of Monte Carlo simulations for $Y\text{Mn}_2$ at 200 K [3]. We find that, in practice, the phonon

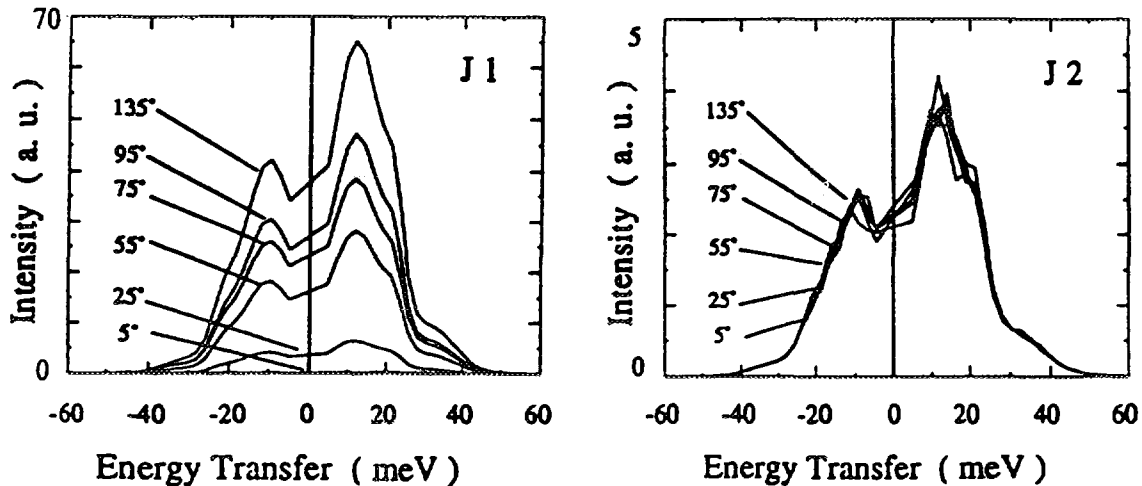


Fig.2 Monte Carlo simulation of phonon scattering in $Y\text{Mn}_2$ at different scattering angles. J_1 corresponds to single scattering and J_2 to double scattering events: note that J_2 is isotropic.

scattering can be well represented here by

$$S(Q, \varepsilon) = A(\varepsilon) + B(\varepsilon)Q^2 \quad (6)$$

where $B(\varepsilon)$ is due to the single scattering events and $A(\varepsilon)$ arises from multiple scattering. This simple representation of the phonon scattering in (6) leads to a third approach for separating magnetic from phonon scattering. Let us suppose that the only Q dependence of the magnetic scattering results from the magnetic form factor. We can then write the total scattering law as

$$S(Q, \varepsilon) = A(\varepsilon) + B(\varepsilon)Q^2 + C(\varepsilon)F^2(Q) \quad (7)$$

where $C(\varepsilon)$ represents the magnetic scattering. Assuming we have a normalised data set $D(Q, \varepsilon)$, which has been corrected for detector efficiencies and solid angles, we can perform a simple linear least squares fit of (7) to the data for each value of the energy transfer ε . Suppose there are M values of the momentum transfer Q_j ; then for a specific energy transfer

ε_i chi-squared is

$$\chi_i^2 = \sum_{j=1}^M [D(Q_j, \varepsilon_i) - A(\varepsilon_i) - B(\varepsilon_i)Q_j^2 - C(\varepsilon_i)F^2(Q_j)]^2 / \sigma^2(Q_j, \varepsilon_i)$$

where $\sigma(Q_j, \varepsilon_i)$ is the statistical error of the data point $D(Q_j, \varepsilon_i)$. It is straightforward to minimise χ_i^2 with respect to the coefficients A, B and C. This gives three simultaneous equations from which $A(\varepsilon_i)$, $B(\varepsilon_i)$ and $C(\varepsilon_i)$ may be found. As an example of this method Fig. 3 shows the phonon density of states (derived from B(ε) using (5)) and the magnetic cross section C(ε) for CeAgSn derived from the energy gain part of a data set collected on IN6 at 200K. The incident neutron energy was 3.1 meV and the 19 detector groups had elastic Q values ranging from 0.2 to 2.0 \AA^{-1} . The structure in the magnetic cross section arises from crystal field excitations. In this case the A(ε) term was found to be negligibly small.

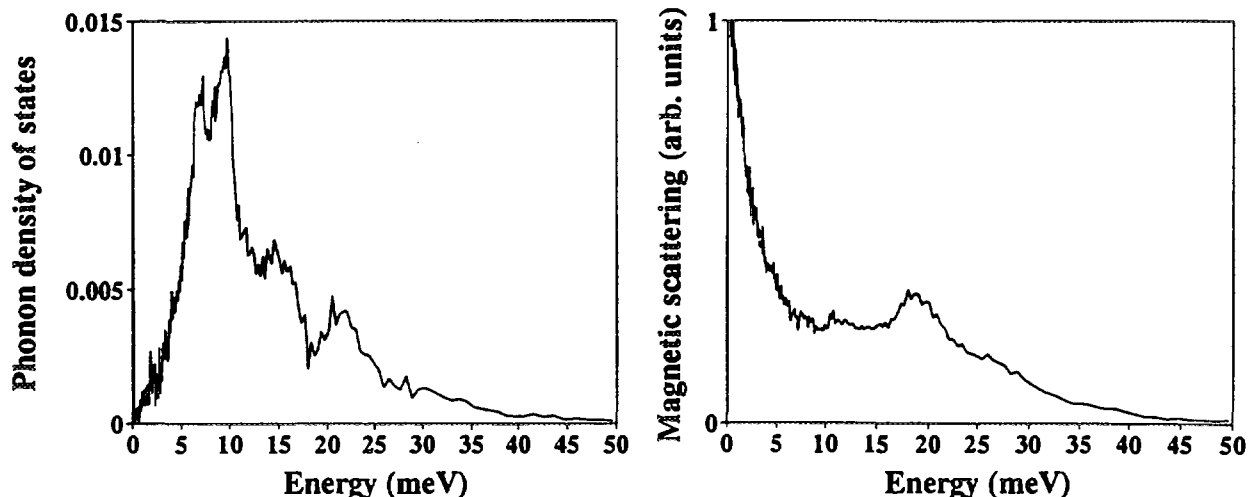


Fig.3 Phonon density of states and magnetic scattering in CeAgSn at 200 K separated using the least squares method. The data consisted of 19 detector groups with $Q_d = 0.2$ to 2.0\AA^{-1} . The magnetic scattering shows a quasielastic peak and broadened crystal field (CF) excitations at 19 and 30 meV. The weak peak near 11 meV arises from an excited state CF transition.

4. Magnetic cross sections.

The basic cross section for magnetic scattering can be written in the form

$$\frac{d^2\sigma}{dQdE_f} = (\gamma r_0)^2 \frac{k_f}{k_i} \left[\frac{1}{2} g F(Q) \right]^2 \sum_{m,n} P_m | \langle m | J_\perp(Q) | n \rangle |^2 \delta(\varepsilon - E_m + E_n) \quad (7)$$

where P_m is the thermal population of the state $|m\rangle$ and

$$J_\perp(Q) = \sum_j \exp(-iQ \cdot R_j) \hat{Q} \times J_j \times \hat{Q} \quad (8)$$

where \hat{Q} is a unit vector parallel to the momentum transfer. Here we have used the "dipole approximation" for the scattering from the orbital magnetic moment [4] which is valid for moderately large momentum transfers. For iron group materials where the orbital moment is quenched $\frac{1}{2}gJ$ is replaced by the spin S. The symbol \perp reminds us that the magnetic scattering is due to the component of the magnetisation (or J) lying in the plane perpendicular

to the momentum transfer \mathbf{Q} . This is a consequence of the vector nature of the interaction of the neutron's magnetic moment with the spin and orbital magnetic moments of the electrons in the sample. The square of the matrix element in (7) introduces a dot product $\mathbf{J}_\perp \cdot \mathbf{J}_\perp$ which can be simplified by using Cartesian components:

$$\mathbf{J}_\perp \cdot \mathbf{J}_\perp = \sum_{\alpha, \beta} (\delta_{\alpha\beta} - \hat{Q}_\alpha \hat{Q}_\beta) J^\alpha J^\beta ,$$

where $\alpha, \beta = x, y, z$. We can now write the cross section in terms of the component of the scattering law $S(Q, \varepsilon)$:

$$\frac{d^2\sigma}{d\Omega dE_f} = (\gamma r_0)^2 \frac{k_f}{k_i} [\frac{1}{2} g F(Q)]^2 \sum_{\alpha, \beta} (\delta_{\alpha\beta} - \hat{Q}_\alpha \hat{Q}_\beta) S^{\alpha\beta}(Q, \varepsilon) , \quad (9)$$

with

$$S^{\alpha\beta}(Q, \omega) = \sum_{m, n} P_m \langle m | J_\alpha(Q) | n \rangle \langle n | J_\beta(-Q) | m \rangle \delta(\varepsilon + E_m - E_n) . \quad (10)$$

If the system has the property that J_z^{tot} is a constant of the motion (i.e. it commutes with the Hamiltonian) then (9) simplifies further, in that only terms with $\beta = \alpha$ appear:

$$\frac{d^2\sigma}{d\Omega dE_f} = (\gamma r_0)^2 \frac{k_f}{k_i} [\frac{1}{2} g F(Q)]^2 \sum_{\alpha} (1 - \hat{Q}_\alpha^2) S^{\alpha\alpha}(Q, \varepsilon) , \quad (11)$$

By using the integral representation of the delta function:

$$\delta(\varepsilon + E_i - E_f) = \frac{1}{2\pi\hbar} \int_{-\infty}^{\infty} e^{i(\varepsilon + E_i - E_f)t/\hbar} dt ,$$

we can write (10) in terms of the correlation function

$$S^{\alpha\beta}(Q, \varepsilon) = \frac{1}{2\pi\hbar} \int_{-\infty}^{\infty} \langle J_\alpha(Q, 0) J_\beta(-Q, t) \rangle e^{-i\varepsilon t/\hbar} dt . \quad (12)$$

Invoking the fluctuation-dissipation theorem we can relate the time Fourier transform of the correlation function in (12) to the imaginary part of the dynamical susceptibility:

$$S^{\alpha\beta}(Q, \varepsilon) = \frac{N}{\pi(g\mu_B)^2} [n(\varepsilon) + 1] \text{Im} \chi^{\alpha\beta}(Q, \varepsilon) , \quad (13)$$

where the detailed balance factor

$$n(\varepsilon) + 1 = \frac{1}{1 - e^{-\varepsilon/k_B T}} = -n(-\varepsilon) . \quad (14)$$

Note that $\text{Im} \chi(\varepsilon)$ is an odd function of ε . Although these different forms may seem unnecessarily complicated, they do convey extra physical insight: the correlation function can readily be visualised in terms of the way a spatial component of the magnetisation decays with time. Similarly in (13) we can imagine the neutron's magnetic moment setting up a field which varies in space and time like $\exp[i(Q.r - \omega t)]$ with $\omega = \varepsilon/\hbar$. The system's response to this field is a magnetisation $M^\alpha(Q, \omega) = \chi^{\alpha\beta}(Q, \omega) B^\beta(Q, \omega)$, and the neutron scattering is related to the dissipative part of this response.

An important result in relation to the dynamical susceptibility is the Kramers-Kronig relation which relates the real and imaginary parts:

$$\text{Re } \chi^{\alpha\beta}(Q, 0) = \frac{1}{\pi} \int_{-\infty}^{\infty} \frac{\text{Im } \chi^{\alpha\beta}(Q, \varepsilon)}{\varepsilon} d\varepsilon . \quad (15)$$

If our scattering system is in the classical limit (i.e. $\varepsilon \ll k_B T$ for all ε) then the detailed balance factor (14) becomes $n(\varepsilon)+1 \approx k_B T/\varepsilon$. Inserting this result into (13) leads to a useful sum rule:

$$\int_{-\infty}^{\infty} S^{\alpha\beta}(Q, \varepsilon) d\varepsilon = \frac{N}{(g\mu_B)^2} k_B T \chi^{\alpha\beta}(Q) . \quad (16)$$

$\chi(Q)$ here is $\text{Re}\chi(Q, 0)$ as in (15). In this limit an experiment carried out without energy analysis yields a total scattering cross section proportional to $k_B T \chi(Q)$; this result should be used with caution, however. It is perhaps safer to extract $\chi(Q)$ from inelastic scattering experiments, by relating the scattering law to $\text{Im } \chi(Q, \varepsilon)$ using (13), then using Kramers-Kronig (15). A final useful form for the scattering law can be written as:

$$S^{\alpha\beta}(Q, \varepsilon) = \frac{N/\hbar}{(g\mu_B)^2} \frac{\varepsilon/k_B T}{1 - \exp(-\varepsilon/k_B T)} k_B T \chi^{\alpha\beta}(Q) F^{\alpha\beta}(Q, \varepsilon) . \quad (17)$$

The advantage of this version is that the scattering law is clearly expressed in terms of a line shape function $F^{\alpha\beta}(Q, \varepsilon)$ which is an even function of ε and has unit area:

$$\int_{-\infty}^{\infty} F^{\alpha\beta}(Q, \varepsilon) d\varepsilon = 1$$

The other factors are $k_B T \chi(Q)$, which governs the integrated response of the system and the population factor $(\varepsilon/k_B T)/[1 - \exp(-\varepsilon/k_B T)]$ which is well behaved in the limit $\varepsilon/k_B T \rightarrow 0$.

5. Spectroscopy and spin dynamics of rare earths and actinides.

5.1 Crystal field spectroscopy.

The magnetic properties of a free ion are determined by its spectroscopic ground state, as given by Hund's rules, namely the multiplet $|L, S, J, m\rangle$ with $(2J+1)$ values of the magnetic quantum number m in the range $-J < m < J$. However when the ion is incorporated into a solid it experiences a potential with the point symmetry of its local crystalline environment. The $(2J+1)$ fold degeneracy of the ground multiplet is lifted by this "crystal field" and the resulting eigenstates are linear combinations of the $|J, m\rangle$ states:

$$|\Psi_i\rangle = \sum_{j=1}^{2J+1} \alpha_{ij} |J m_j\rangle . \quad (18)$$

These states, and their corresponding eigenvalues ε_i , result from diagonalising the crystal field Hamiltonian H_{CF} in the space of $|J, m\rangle$ states. The symmetries and degeneracies of the Ψ_i are determined by the symmetry of H_{CF} . The crystal field Hamiltonian can be written in a particularly simple form [5]:

$$H_{CF} = \sum_{lm} A_l^m \langle r^l \rangle \Theta_l^m O_l^m = \sum_{lm} B_l^m O_l^m . \quad (19)$$

The A_l^m or B_l^m are the crystal field parameters and the Stevens' operators O_l^m are polynomials in the components of the angular momentum operators J_x, J_y and J_z which transform under rotations in the same way as the corresponding spherical harmonics Y_l^m . Only even values of $l=2,4,6$ need be considered in the sum (19) with values of $|m| \leq l$. The matrix elements of most of the Stevens' operators are tabulated by Hutchings [5] and Abragam and Bleaney [6].

The crystal field splittings have a profound effect on the magnetic properties. As the temperature is lowered the thermal population of the excited CF states decreases: as a result the effective magnetic moment of the ion is temperature dependent. At very low temperatures only the ground state Ψ_0 is populated, and the magnetic moment $\langle \mu_\alpha \rangle = g\mu_B \langle \Psi_0 | J_\alpha | \Psi_0 \rangle$, with $\alpha = x,y,z$, can be substantially reduced compared to the free ion moment, and in general is also anisotropic since $\langle \mu_x \rangle$ is not necessarily the same as $\langle \mu_z \rangle$. In the extreme case where Ψ_0 is a singlet $\langle \Psi_0 | J_\alpha | \Psi_0 \rangle = 0$, for $\alpha = x,y,z$, i.e. the magnetic moment is totally quenched by the crystal field. The susceptibility is in general anisotropic: the crystal field is the origin of the magnetocrystalline anisotropy. It is important therefore to be able to characterise the crystal field, which means determining the CF parameters B_l^m in (19).

Inelastic neutron scattering is now widely established as a tool for crystal field spectroscopy, especially in metals and opaque materials where optical spectroscopy is difficult [7]. Crystal field splittings are usually in the range 1 to 100 meV, well matched to thermal neutron energies. We are normally concerned with systems in which the magnetic ions are independent (spin-spin correlations can be ignored), so that the scattering law is Q independent: the scattering law has the form of (11) with $J_a(Q)$ replaced by J_a . The neutron can excite CF transitions between different $|\epsilon\rangle$ states according to the magnetic dipole

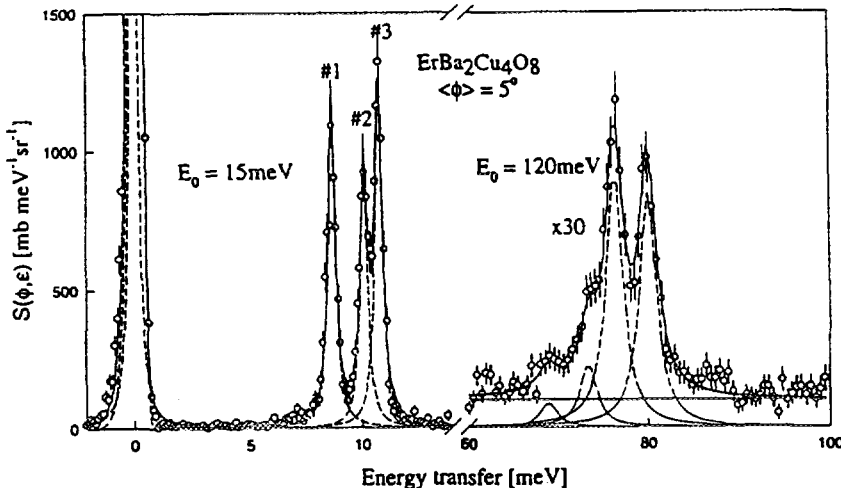


Fig.4 Crystal field excitation spectrum for $\text{ErBa}_2\text{Cu}_4\text{O}_8$ measured with 15 meV and 120 meV incident neutrons [8]. The solid line is the fitted profile from the CF model; the dotted curves show individual transitions.

selection rule $\Delta m = 0, \pm 1$. As an example Fig.4 shows the CF spectrum for the Er^{3+} ($J=15/2$) ion in the high temperature superconductor $\text{ErBa}_2\text{Cu}_4\text{O}_8$ [8]. The Er ion in this compound is at a site with orthorhombic symmetry, for which H_{CF} has nine parameters, namely $B_2^0, B_2^2, B_4^0, B_4^2, B_4^4, B_6^0, B_6^2, B_6^4$ and B_6^6 . These have been determined using the energies and intensities of the seven transitions shown in Fig.4. It is often not at all easy to determine the CF parameters from the neutron spectrum. For example the Ce^{3+} ion in an environment with low point symmetry splits into three doublets, so we would expect only two inelastic

transitions; yet there might be up to eight CF parameters, so the problem is underdetermined. Bulk susceptibility data on a single crystal can be very useful in this situation. If a large single crystal were available then the angular variation of the neutron transition intensities would give a great deal more information than measurements on a polycrystalline sample.

The superposition model for the crystal field [9] is often useful when dealing with low symmetry environments. Here the CF potential is expressed in terms of three intrinsic parameters \bar{A}_2 , \bar{A}_4 and \bar{A}_6 which represents the cylindrically symmetric potential between the magnetic ion and each of its ligands. The CF parameters are given by

$$B_l^m = \Theta_l \sum_i \bar{A}_l(R_i) K_l^m(\theta_i, \phi_i), \quad (20)$$

as a sum over the nearest neighbour ligands at (R_i, θ_i, ϕ_i) , with the K_l^m factors determined entirely by the geometry of the local environment. The point is that within a given rank e.g. $l=4$ or $l=6$ all the B_l^m are related by (20). The dependence of the $\bar{A}_l(R)$ on distance is usually given by a power law R^{-t} with t large (in the range 6-10 for $l=4$ or 6), so that only nearest neighbours ligands are important. This appears to work well for rank 4 and rank 6 terms, but is less reliable for second parameters. Newman and Ng have shown that nearly all contributions to the CF potential obey the superposition principle (20), including overlap, covalency and other hybridisation terms.

5.2 Spin lattice relaxation

At any finite temperature the environment of a magnetic ion is constantly being modulated by lattice vibrations. The crystal field therefore has a dynamic component which causes the magnetic moment to flip at a rate determined by the lattice temperature. This is referred to as spin-lattice relaxation; it leads to a finite lifetime for the electronic state and therefore a finite linewidth for CF excitations. In metals another contribution to the linewidth arises from the exchange coupling of the local moment to the spins of the conduction electrons:

$$H_{sf} = -(g - 1) \Im J \cdot s. \quad (21)$$

In the simplest case of a CF transition between two singlet states $|0\rangle$ and $|1\rangle$, separated in energy by $\Delta = \epsilon_1 - \epsilon_0$, the linewidth is given by [7]:

$$\Gamma = \pi [(g - 1) \Im \rho(E_F)]^2 M_{01}^2 \Delta \coth(\Delta/2k_B T), \quad (22)$$

where $\rho(E_F)$ is the conduction electron density of states at the Fermi energy and

$$M_{01}^2 = \sum_{\alpha=x,y,z} |\langle 0 | J_{\alpha} | 1 \rangle|^2.$$

For $k_B T \gg \Delta$ the linewidth varies linearly with temperature, since $\Delta \coth(\Delta/2k_B T) \approx 2k_B T$. This is known as Korringa relaxation. The dynamical susceptibility for the two singlet level system can be written [7]

$$\chi(\epsilon) = M_{01}^2 (P_0 - P_1) L t_{\delta=0} \left[\frac{1}{\epsilon + \Delta + i\delta} - \frac{1}{\epsilon - \Delta + i\delta} \right]. \quad (23)$$

If the limit of $\delta \rightarrow 0$ is taken the imaginary part of the susceptibility just yields two delta functions, centred at $+\Delta$ and $-\Delta$, corresponding to energy loss and energy gain CF transitions, in accord with (10). We can include the effect of spin-lattice relaxation by replacing imaginary part δ by the linewidth Γ , i.e we take the pole in the dynamical susceptibility to

move off the real axis. The scattering law then has the form

$$S(Q, \varepsilon) = \frac{N}{\pi(g\mu_B)^2} \frac{M_{01}^2(P_0 - P_1)}{1 - \exp(-\varepsilon/k_B T)} \left[\frac{\Gamma}{(\varepsilon - \Delta)^2 + \Gamma^2} - \frac{\Gamma}{(\varepsilon + \Delta)^2 + \Gamma^2} \right], \quad (24)$$

i.e. the delta functions are replaced by Lorentzian functions: overall the lineshape in (24) is that of a damped harmonic oscillator.

The temperature variation of the linewidth of the peak labelled #1 in Figure 4 is shown in Fig. 5 [10], together with the same data for the related high temperature superconductor $\text{ErBa}_2\text{Cu}_3\text{O}_7$. While the underlying trend follows the $\coth(\Delta/2k_B T)$ variation of (22), there are two cusp-like anomalies, one at T_c the superconducting transition temperature, the other at a temperature T^* , 30-40 K above T_c . The interpretation of the anomaly at T_c is that it arises when the superconducting energy gap is resonant with the crystal field splitting, due to the build-up of electronic density of states above the gap, along the lines of the Hebel-Slichter coherence peak in NMR. The implication of the second cusp-like anomaly at T^* is that an energy gap (or pseudogap) persists in the normal state. The presence of a pseudogap appears to be a characteristic of the normal state of high T_c superconductors with less than optimal doping. Other indications include transport measurements (thermopower) [11] and angle-resolved photoemission (ARPES) [12]. It appears that the nature of the superconductivity changes with doping concentration: it is BCS-like at greater than optimal doping (i.e. the energy gap develops at T_c , the onset of long-range phase coherence). For less than optimal doping the onset of superconductivity at T_c resembles a Bose condensation of a gas of paired hole states, which have already formed at a temperature above T_c .

5.3 Kondo lattice compounds, heavy fermions.

Measurements of the form of the dynamical response has been extremely informative in the context of the Kondo lattice problem. Inelastic neutron scattering gives one of the best ways of characterising the broad range of behaviours which are found in this field [13].

The Kondo effect arises from the sf Hamiltonian (21) when \mathfrak{S} is negative, i.e. the exchange coupling between the local moment and the conduction electrons is

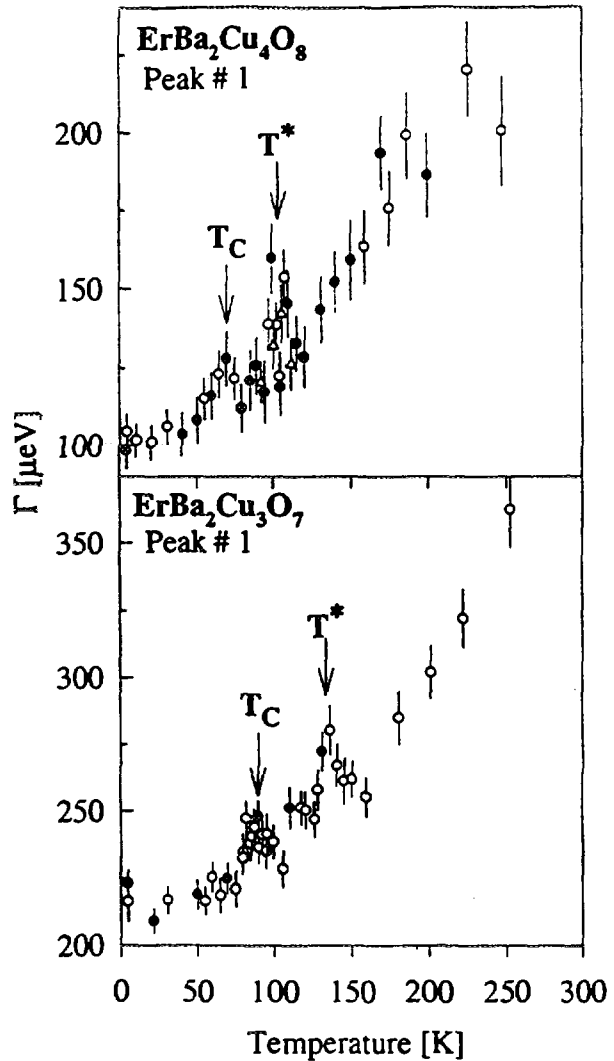


Fig.5 Linewidth of peak #1 (Fig.4) as a function of temperature, together with corresponding data for the related compound $\text{ErBa}_2\text{Cu}_3\text{O}_7$. Note the two cusp-shaped anomalies at T_c and T^* in each case.

antiferromagnetic. In the single ion Kondo effect the ground state is a magnetic singlet state, pictured as a many-body state in which the spin degrees of freedom of the local moment are compensated by oppositely polarised conduction electrons. The gradual formation of this many-body state at low temperatures leads to a temperature independent susceptibility and to the famous $-\ln(T)$ anomaly in the resistivity. As might be expected there are also pronounced effects on the spin dynamics: the dynamical response is a quasielastic Lorentzian

$$F(Q, \varepsilon) = \frac{1}{\pi} \frac{\Gamma}{\Gamma^2 + \varepsilon^2} \quad (25)$$

for which the Korringa law (22) would predict $\Gamma \propto T$ (limit of $\Delta \rightarrow 0$). However it is found that $\Gamma(T)$ has a low temperature intercept $\Gamma(0)$ of order $k_B T_K$, where T_K is the Kondo temperature, and that the temperature dependence $\Gamma(T)$ is closer to $T^{1/2}$ than linear. Fig.6 shows the linewidth data for CuFe with only 100ppm Fe, which shows the expected temperature variation. This is one of the very few dilute transition metal Kondo systems to have been studied [14]. It is necessary to work with very dilute alloys, since spin-spin (RKKY) interactions between transition metal impurities kill the Kondo effect and leads to spin glass behaviour. This is not the case for rare earth and actinide impurities, however, where even an ordered lattice of cerium, ytterbium or uranium ions can show the Kondo effect. There are two major reasons why the Kondo effect survives in "Kondo lattice" systems, firstly the RKKY interactions for Ce and Yb ions are relatively weak (because of the $(g-1)$ factor in (21)), but also the large orbital angular momenta of f electrons leads to many $(2J+1)$ distinct scattering channels for the conduction electrons. Kondo lattice behaviour is found in many intermetallic compounds of cerium and ytterbium. Typically these display anomalies at high temperature which are characteristic of the Kondo effect, e.g. $-\ln(T)$ dependence of the resistivity, so it appears as though the lattice behaves as a collection of independent Kondo impurities. However at low temperatures the resistivity is often found to drop to a low value with $\rho(T) \approx \rho_0 + AT^2$, a form expected for a Fermi liquid. This suggests that a many-body ground state has formed consisting of fermion quasiparticles which obey Bloch's theorem. The effective masses of these quasiparticles (as estimated from the Sommerfeld constant $\gamma = [C_p(T)/T]_{T=0}$) is found to be enormous, of order 10^2 - 10^3 times the bare electron mass. Such compounds are therefore known as "heavy fermion" materials. De Haas-van Alphen studies show that there are indeed Fermi surface orbits with huge effective masses. Such compounds tend to show either no long range magnetic order, or antiferromagnetism with extremely small magnetic moments ($10^{-2} \mu_B$). The Kondo effect, tending to form a non-magnetic ground state, is in competition with the RKKY interaction, which leads to magnetic order. Both interactions depend on the coupling constant $\mathfrak{S}\rho(E_F)$ which appears in (22), viz. the Kondo temperature T_K is given in Wilson's theory by

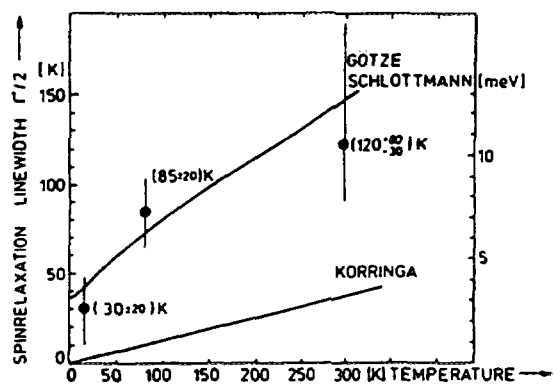


Fig.6 Temperature dependence of the linewidth of the magnetic response for dilute Fe impurities (100ppm) in Cu [14]. The theoretical curve is calculated for a Kondo alloy with a Kondo temperature $T_K = 25$ K.

$$k_B T_K = D \left(\frac{1}{2 \mathfrak{S} \rho} \right)^{\frac{1}{2}} \exp \left(-\frac{1}{2 \mathfrak{S} \rho} \right) , \quad (25)$$

where D is the bandwidth, while the RKKY exchange interaction is

$$J(R_{ij}) = 12 \pi v(g-1)^2 \mathfrak{S}^2 \rho(E_F) \mathcal{F}(2k_F R_{ij}) , \quad (26)$$

where $\mathcal{F}(x) = [\sin(x) - x \cos(x)]/x^4$ and v is the number of conduction electrons per formula unit. With increasing \mathfrak{S} there is a cross-over from a region where the RKKY interaction dominates (with magnetically ordered ground states) to the regime where the Kondo effect dominates and magnetic order is suppressed [15]. Heavy fermions are found near the critical value of $(\mathfrak{S} \rho)_c$ at which magnetic order is just suppressed. For smaller values of $\mathfrak{S} \rho$ Kondo lattice compounds usually display relatively well defined crystal field splittings and a magnetically ordered ground state. As an example of what can be learned from time-of-flight spectroscopy in this context, Fig. 7 shows the quasielastic linewidths for a series of alloys $\text{CeRu}_2\text{Si}_{2-x}\text{Ge}_x$ at 15 K [16].

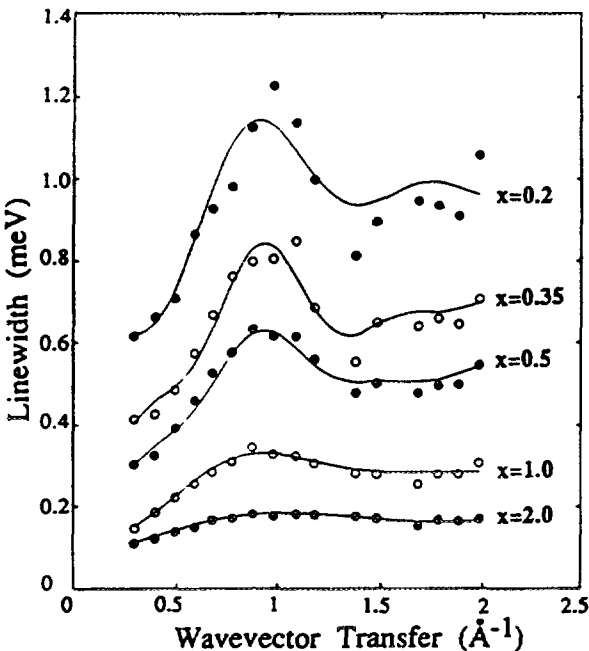


Fig. 7 Linewidths at 15 K for the alloys $\text{CeRu}_2\text{Si}_{2-x}\text{Ge}_x$ showing modulation as a function of the wavevector.

CeRu_2Si_2 is a heavy fermion material with $\gamma \approx 340 \text{ mJ/mole-K}^2$, while CeRu_2Ge_2 is a ferromagnet with $T_C = 7 \text{ K}$. The linewidths show a smooth decrease in magnitude with increasing Ge concentration, x (and cell volume), reflecting the decreasing size of the coupling constant \mathfrak{S} . From the data we estimate that the Kondo temperature, T_K , decreases from a value of 22 K for CeRu_2Si_2 to a value of only 2 K for CeRu_2Ge_2 . The other feature of the data is the pronounced modulation of the line width with wavevector, due to the intersite RKKY coupling. The data were fitted to a simple RPA theory in which the dynamical response is given by

$$\chi(Q, \varepsilon) = \frac{\chi_0(\varepsilon)}{1 - J(Q)\chi_0(\varepsilon)} , \text{ where}$$

$\chi_0(\varepsilon) = \frac{i\Gamma_0}{\varepsilon + i\Gamma_0}$, is the single ion response. Taking the imaginary part of $\chi(Q, \varepsilon)$ leads to

a Lorentzian lineshape with a Q dependent width: $\frac{1}{\varepsilon} \chi(Q, \varepsilon) = \frac{\chi(Q) \Gamma(Q)}{\varepsilon^2 + \Gamma(Q)^2}$

where $\chi(Q) = \chi_0/[1 - \chi_0 J(Q)]$ and $\Gamma(Q) = \Gamma_0[1 - \chi_0 J(Q)]$. The single ion linewidth Γ_0 derived from the data (Fig. 8) [16] shows a form similar to (22) in which both the intercept (proportional to $k_B T_K$) and the gradient (proportional to $(\mathfrak{S} \rho)^2$) vary smoothly with Ge concentration. The inset shows this scaling, together with a fit (solid line) to (25) for the

variation of T_K with δp . The agreement with single ion Kondo scaling is tolerably good.

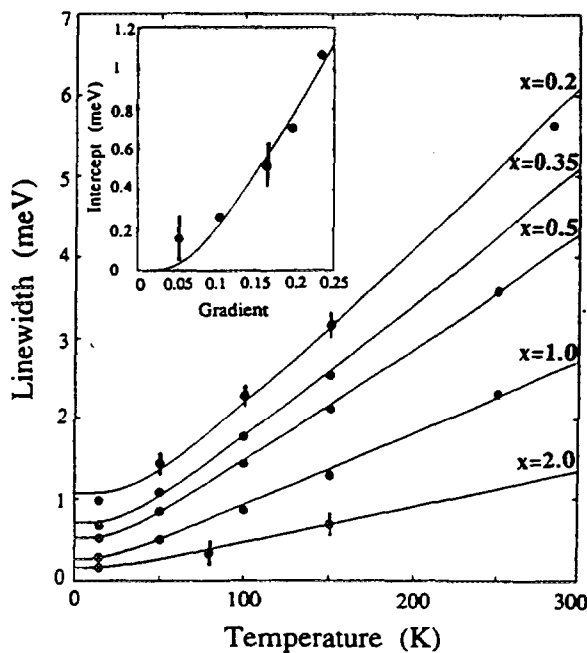


Fig.8 Temperature variation of single ion component of linewidth Γ_0 for $\text{CeRu}_2\text{Si}_{2-x}\text{Ge}_x$ alloys. The inset shows the scaling of the gradients with the intercepts of $\Gamma_0(T)$, compared with the predictions of single ion Kondo theory (25) (solid line).

moment behaviour, to a low temperature intermediate valence phase. The crystal structure remains the same through the transition but there is a small increase (0.45%) in the cell volume. The character of the dynamical response changes completely at the phase transition [18]: the paramagnetic scattering (Fig.9a) at high temperature extends out to about 15 meV

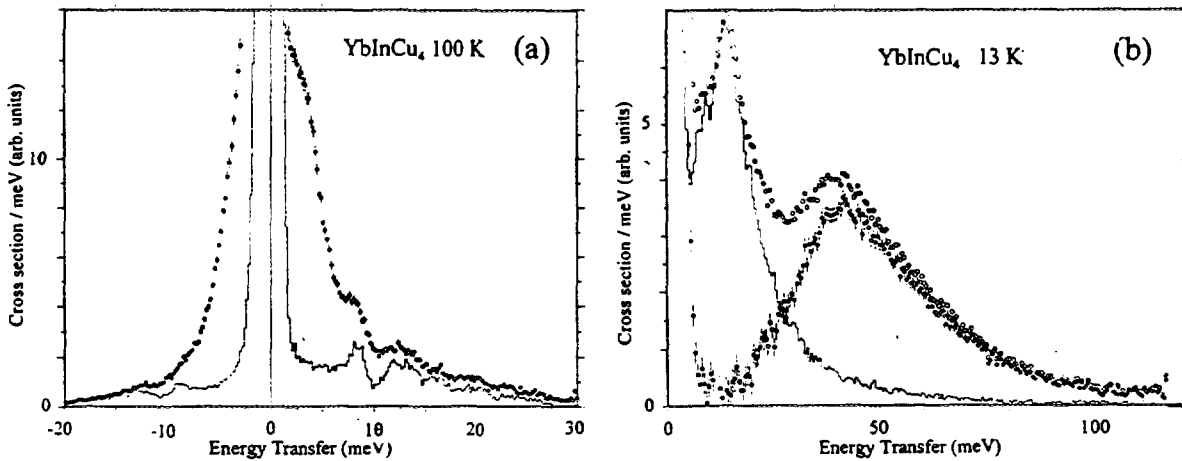


Fig.9 (a) High temperature inelastic neutron spectrum for YbInCu_4 ; filled circles: total scattering in low angle bank; histogram: phonon scattering estimated from scaling scattering in high angle bank. (b) Low temperature response in YbInCu_4 ; open circles: total scattering in low angle bank; histogram: estimated phonon scattering; filled circles: estimated magnetic response (total-phonon).

5.4 Intermediate valence.

For $\delta p \gg (\delta p)_c$ there is a cross-over to a distinct behaviour which is labelled as "intermediate valence". In this limit the sf hybridisation is strong enough to cause a temporal fluctuation in the valence state of the magnetic ion: $4f^n = 4f^{n-1} + 5s^1$, with an electron hopping between the atomic-like f state and a conduction band state. The rate of this hopping is fast enough to change the spin dynamics (and therefore the magnetic properties) completely. The susceptibility becomes weakly temperature dependent, usually with a maximum at a finite temperature. The crystal field splittings are washed out and the dynamical response at low temperature is characterised by a broad Q independent inelastic line. A rather dramatic example of this behaviour is found in the case of YbInCu_4 . This compound (cubic Laves C15b structure) has a remarkable first order phase transition [17] from a high temperature phase, in which the Yb ion displays local

and arises from thermally broadened CF excitations centred at 3-4 meV. In contrast the response at low temperatures (Fig.9b) consists of a broad inelastic line centred at 42 meV, with scattering extending out beyond 100 meV. Very similar behaviour is found in another system CeNi_{1-x}Co_xSn in which the cerium ion undergoes a first order valence transition, for Co concentrations near x=0.38 [19]. The lineshape of the scattering in the intermediate valence state has been derived for a single magnetic impurity in the "non-crossing approximation" (NCA) by Kuramoto and Muller-Hartmann [20]:

$$\frac{1}{\varepsilon} \text{Im } \chi(\varepsilon) = \frac{C \alpha}{u^2(u^2 + 4\alpha^2)} \left[\alpha \ln[(1-u^2)^2 + 4u^2\alpha^2] + |u| \left[\frac{\pi}{2} - \tan^{-1} \left(\frac{1-u^2}{2|u|\alpha} \right) \right] \right]$$

where $u = \varepsilon/\varepsilon_K$ and $\alpha = \sin(\pi \langle n_f \rangle / N)$. Here ε_K is a characteristic Kondo energy, $\langle n_f \rangle$ is the mean occupancy of the 4f level and N is the degeneracy of the 4f state.

5.5 Non-Fermi liquid scaling.

The ground states of heavy fermions are characterised by a single energy scale, namely the Fermi energy E_F of the quasiparticles. This is reflected in the temperature dependences of the resistivity: $\rho(T) \approx \rho_0 + AT^2$, heat capacity: $C(T) \approx \gamma T$ and susceptibility $\chi(T) \approx \chi_0$ for $T \ll E_F/k_B$. Recently certain uranium and cerium alloys have been found [21] to display weak power law divergences in the susceptibility, linear dependence of $\rho(T)$ and logarithmic divergences in the heat capacity $C(T) \approx -T \ln T$. These observations suggest that the low frequency excitations are no longer characteristic of fermionic quasiparticles. Theoretical approaches suggest that the divergences arise from the proximity to a zero temperature critical point, leading to scale invariant behaviour where the only energy scale is the absolute temperature. It has been argued that the normal state of the high temperature superconductors also falls into this class. We would expect the spin dynamics to reflect the same type of scaling. This has been shown in greatest detail in work on UCu_{4-x}Pd_x alloys with x=1.0 and 1.5 [22]. UCu₅ is a Kondo lattice antiferromagnet with $T_N = 15$ K and $T_K \approx 80$ K. The antiferromagnetism is rapidly suppressed by the substitution of Cu by Pd, so that UCu₄Pd and UCu_{3.5}Pd_{1.5} show no long range magnetic order down to 10 mK. Inelastic neutron scattering measurements show a

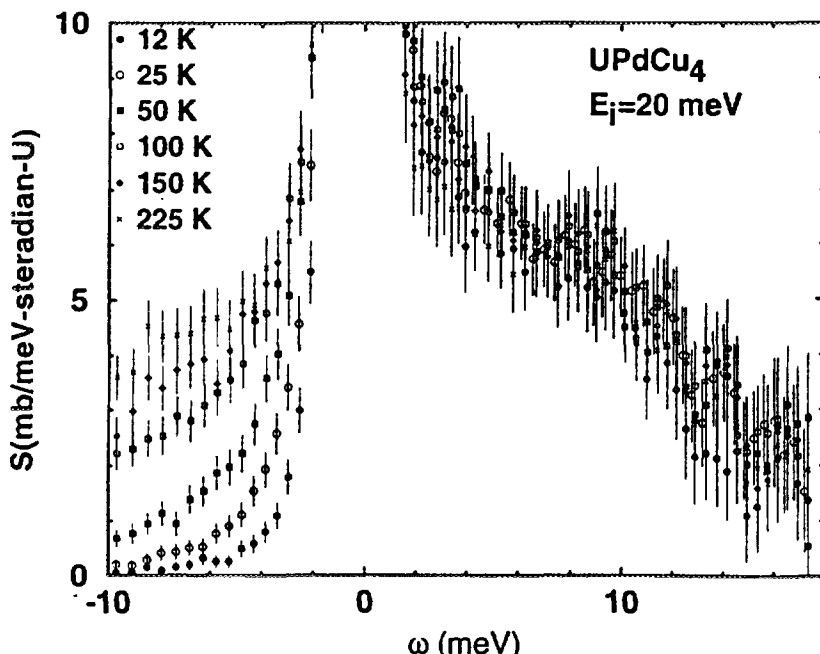


Fig.10 Scattering law $S(\varepsilon)$ for UCu₄Pd: note that the energy loss cross section appears to be independent of temperature from 12 K to 225 K.

broad Q independent response with two power-law regimes: for $\epsilon > 20$ meV, $\text{Im}\chi(\epsilon) \sim \epsilon^{-1}$, whereas for $\epsilon < 20$ meV, $\text{Im}\chi(\epsilon) \sim \epsilon^{-\frac{1}{3}}$. Remarkably the scattering law $S(\epsilon)$ was found to be independent of temperature (for $\epsilon > 0$) (Fig.10) so that the dynamical susceptibility must follow a scaling function $\epsilon^{\delta} Z(\epsilon/k_B T)$ from 1.5 K to 300 K, with $\delta = \frac{1}{3}$ and $Z(\epsilon/k_B T) \approx \tanh(\epsilon/\alpha k_B T)$ ($\alpha \approx 1.2$) (Fig.11). With this scaling a Kramers-Kronig analysis (15) predicts that the static susceptibility should vary as $T^{-\delta}$: this agrees with the measured bulk susceptibility from 1 K to 300K. The absence of Q dependence in the scattering suggests a

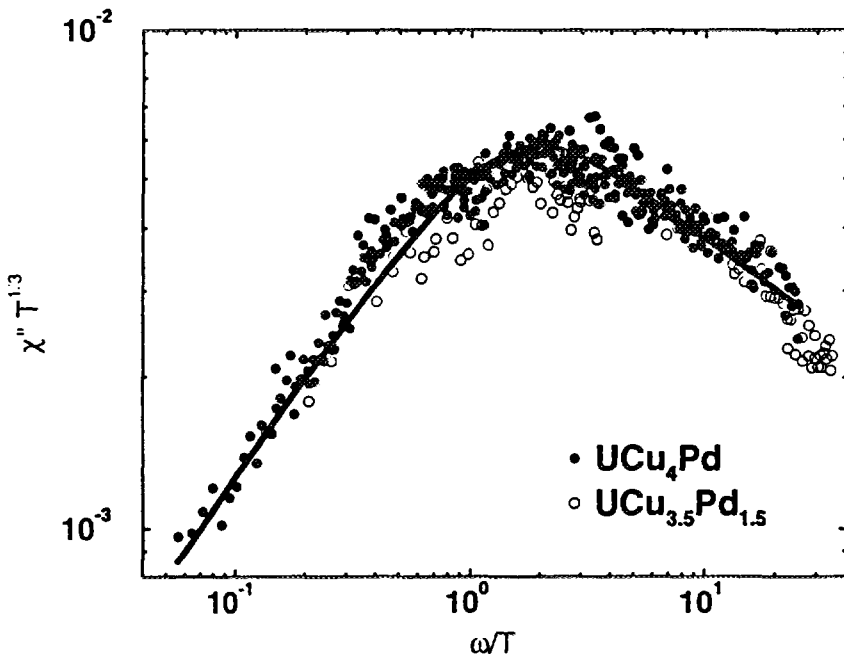


Fig.11 Plot to show scaling behaviour of $\text{Im}\chi(\epsilon)$ for UCu_4Pd and $\text{UCu}_{3.5}\text{Pd}_{1.5}$ alloys for $\epsilon < 25$ meV; solid line: $\text{Im}\chi(\epsilon, T) T^{1/3} \approx (T/\epsilon)^{1/3} \tanh(\epsilon / 1.2 k_B T)$.

single-impurity critical point at $T=0$, and the magnetic response reflects the low frequency collective excitations of the relevant order parameter. A number of microscopic models, such as the "multi-channel Kondo effect", predict single impurity critical behaviour, though it is difficult to establish the microscopic origin of this behaviour in a particular case.

6. The (near) future: MAPS

Most of the examples in section 5 relate to work on polycrystalline samples in situations where the Q dependence of the magnetic cross section is weak. Traditionally the assumption has been that magnetic systems showing strong Q dependence, e.g. the spin wave dispersion in a single crystal, are studied on triple axis spectrometers, which have the flexibility to define a particular track in (Q, ϵ) space along which $S(Q, \epsilon)$ may be studied. Recent experience at the ISIS pulsed neutron source has changed this perspective in a number of ways:

- (i) For problems involving high energy transfers (> 50 meV), time-of-flight spectroscopy does much better than the triple axis spectrometer. This is because for large values of E_i the energy resolution of the triple axis is inevitably poor, since the monochromator take-off angle $2\theta_M$ is low and $\Delta E_i \approx k_i^3 \cot(\theta_M)$. Low values of $2\theta_M$ lead also to severe background problems. On the other hand time of flight machines can work with $\Delta E_i/E_i \approx 1\%$,

independent of E_i , with good signal-to-noise and none of the spurious processes which plague crystal monochromator instruments.

(ii) In the study of excitations in linear chain magnets it is possible to make effective use of a large detector bank at low angles, when the crystal is oriented with the chain axis along \mathbf{k}_i . Since the dispersion perpendicular to the chains is small in a 1-D magnet, there is no azimuthal Q variation and the whole detector bank may be summed. This gives a huge gain in counting rate, compared to a triple axis (on MARI there are 160 detectors at scattering angles below 15°!). This has been used to great effect in the study of a number of 1-D systems, for example KCuF_3 , [23].

(iii) Modern computing power has brought increasingly sophisticated techniques for data visualisation. We have the possibility of extracting from time-of-flight data information about a whole dispersion surface, not just along specific (Q, ε) tracks. As long as the dispersion surface can be modelled theoretically, then there is no need to constrain scans to high symmetry directions. This approach has shown its power in the recent study of the spin wave dispersion in the "colossal magnetoresistive" (CMR) material $\text{La}_{1-x}\text{Pb}_x\text{MnO}_3$ using the HET spectrometer [24].

The new MAPS spectrometer, currently being built at ISIS, is the first time-of-flight machine designed from its inception for single crystal studies. Design features include continuous detector coverage in the range $\pm 30^\circ$ and compact detector elements to give good angular resolution in the q_\perp direction. The aim is to provide as much control over the resolution function as possible and to allow specific (Q, ε) tracks to be selected in software from neighbouring detector elements.

7. Acknowledgements

I would like to thank Drs D.T. Adroja, Ray Osborn, Eugene Goremychkin and Prof. Meigan Aronson for their input and numerous valuable discussions. Financial support has been provided by EPSRC (GR/J87435) and NATO CRG.931257.

8. References

- [1] O.Schaerp and H.Capellmann, *Physica Status Solidi (a)* **135** (1993) 359.
- [2] E.A.Goremychkin and R.Osborn, *Phys. Rev. B* **47** (1993) 14280; R.Osborn, *private communication*.
- [3] S.J.Dakin, *Ph.D. Thesis* (1992), Southampton University (unpublished).
- [4] S.W.Lovesey, *Theory of Neutron Scattering from Condensed Matter*, vol.2, (Oxford University Press, 1984).
- [5] M.T.Hutchings, *Solid State Physics* (ed. Seitz and Turnbull) **16** (1964) 227.
- [6] A.Abragam and B.Bleaney, *Electron Paramagnetic Resonance of Transition Metal Ions*, (Oxford University Press, 1970).
- [7] P.Fulde and M.Loewenhaupt, *Adv. Phys.* **34** (1986) 589.
- [8] E.A.Goremychkin, B.D.Rainford, D.B.Currie, M.T.Weller and A.T.Boothroyd, *Physica* **C235** (1994) 1665.
- [9] D.J.Newman and B.Ng, *Rep. Prog. Phys.* **52** (1989) 699.
- [10] E.A.Goremychkin, B.D.Rainford, R.Osborn, D.B.Currie and M.T.Weller, to be published.
- [11] J.L.Tallon, J.R.Cooper, P.de Silva, G.V.M.Williams and J.W.Loram, *Phys. Rev. Lett* **75** (1995) 4114.
- [12] H.Ding et al. *Nature* **382** (1996) 51.
- [13] M.Loewenhaupt and K.H.Fischer, in *Handbook on the Physics and Chemistry of Rare Earths and Actinides*, eds. K.A.Gschneidner and L.Eyring, Vol.16 (Elsevier, 1993).
- [14] M.Loewenhaupt, *J. Magn. Magn. Mater.* **2** (1976) 99.
- [15] S.Doniach, *Physica* **B91** (1977) 231.
- [16] B.D.Rainford and S.J.Dakin, *Phil. Mag. B* **65** (1992) 1357.
- [17] I.Felner and I.Nowik, *Phys. Rev. B* **33** (1986) 617.
- [18] A.Severing, B.D.Rainford and D.T.Adroja, to be published; A.Severing, E.Gratz, B.D.Rainford and K.Yoshimori, *Physica* **B163** (1990) 409.
- [19] D.T.Adroja, B.D.Rainford, J.M.de Teresa, A.del Moral,M.R.Ibarra and K.S.Knight, *Phys. Rev. B* **52** (1995) 12790.
- [20] Y.Kuramoto and E.Müller-Hartmann, *J. Magn. Magn. Mater.* **52** (1985) 122.
- [21] M.B.Maple et al. *J.Low Temp. Phys.* **95** (1994) 225; B.Andraka and G.R.Stewart, *Phys. Rev. B* **47** (1993) 3208.
- [22] M.C.Aronson, R.Osborn, R.A.Robinson, J.W.Lynn, R.Chau, C.L.Seaman and M.B.Maple, *Phys. Rev. Lett.* **75** (1995) 725.
- [23] S.E.Nagler, D.A.Tennent, R.A.Cowley, T.G.Perring and S.K.Satija, *Phys. Rev. B* **44** (1991) 12361; D.A.Tennent et al., *Phys. Rev. Lett.* **70** (1993) 4003.
- [24] T.G.Perring, ISIS report 1995 (see illustration on front cover and Fig.2.27, vol.1).

NEXT PAGE(S)
left BLANK

DYNAMICS OF POLYMERS

U. BUCHENAU

*Institut für Festkörperforschung, Forschungszentrum Jülich
Postfach 1913, D-52425 Jülich, Federal Republic of Germany*

ABSTRACT

Neutron scattering from amorphous polymers allows to switch from incoherent to coherent scattering in the same substance. The power of the tool for the study of the picosecond dynamics of disordered matter is illustrated for polybutadiene, polycarbonate and polystyrene. The results suggest a mixture of sound waves and localized modes, strongly interacting with each other, in the picosecond range.

1 Introduction

The picosecond dynamics of disordered matter, though heavily studied [1], is poorly understood. One finds much more low frequency motion than in corresponding crystalline substances. This is not only true at low temperatures, where glasses exhibit tunneling states [2] and localized low frequency vibrations coexisting with the sound waves [3, 4], but also at the glass transition temperature, when the undercooled liquid freezes in to form a glass.

The question of the present paper is: What can we learn about the picosecond dynamics of disordered matter (solid or undercooled liquid) by inelastic neutron scattering? For that question, measurements on amorphous polymers are particularly useful for the following reasons:

- (i) By chemical tailoring of the regularity of the polymer chain, one can easily achieve enough chemical disorder to avoid crystallization at all temperatures, even for the long times needed in a neutron measurement
- (ii) As already mentioned in the abstract, one can measure the incoherent scattering in a protonated sample and the coherent scattering in a deuterated sample
- (iii) There is a clear separation of interactions: the elastic constants, which determine the sound waves, are due to the van der Waals interaction between different polymer chains, while any localized mode requires changes of the configuration of one or more single chains
- (iv) While the sound velocities do not vary drastically from polymer to polymer, one has a wide range of glass transition temperatures, such as $T_g = 186K$ in polybutadiene and $T_g = 423K$ in polycarbonate.

Most of the inelastic neutron scattering data from glasses collected so far focus on the spectra and their temperature dependence. These are indeed interesting; as examples, we will discuss those of polybutadiene and polycarbonate in the second section of the paper. The quantitative evaluation shows an excess of additional modes in the meV region over the expectation for the density of sound waves from the known sound velocities. At low temperatures, these additional modes appear as a broad peak

at about 2 meV, the so-called boson peak. At higher temperatures, the additional scattering looks more like a broad quasielastic line.

However, one quickly realizes that the spectra alone do not tell enough. This is obvious from the many different interpretations of the spectra in the literature: mode coupling theory [5], fast relaxations [6] related to Ngai's coupling model [7] or a mixture of vibrations and relaxations [8]. In particular, neither the spectra nor their temperature dependence allow to decide what kind of modes one deals with. In order to get information about the eigenvectors of the motion, one needs to study the momentum transfer dependence of the inelastic scattering. That task is more difficult than a simple measurement of the spectra. It requires good measurements from thin samples in order to be able to manage the multiple scattering corrections.

In section 3, we will treat the momentum transfer dependence of the incoherent scattering, which contains information on the localization of the modes (more generally speaking, information on the dynamical heterogeneity of the motion). Section 4 deals with the information obtainable from the momentum transfer dependence of the coherent scattering. That possibility is only now beginning to be exploited; the next years will probably bring more detailed information on the eigenvectors of the picosecond motion than what we have now.

2 Neutron spectra

If one does a neutron time-of-flight experiment on an amorphous protonated polymer sample at low temperatures - 50 or 100 Kelvin -, the evaluation is easy and straightforward. One can neglect the small coherent part of the scattering, because the large incoherent scattering cross section of the proton (81 barns!) dominates. At the low frequencies of the order of 1 meV, one still can be sure that the scattering from the proton reflects the dynamical behaviour of the polymer chain. Since the atomic mean square displacements of the protons are small, the one-phonon approximation [9] is still accurate:

$$S_{inc}(Q, \omega) = e^{-2W} \left[\delta(\omega) + \frac{\hbar Q^2}{2M} f_B \frac{g(\omega)}{\omega} \right]. \quad (1)$$

In this equation, e^{-2W} is the Debye-Waller factor connected with the mean square displacement of the protons (we will come back in more detail to the Debye-Waller factor in the next section), Q is the momentum transfer of the scattering process, $\hbar\omega$ is the energy transfer, M is the mass of an appropriate microscopic unit (in the polymers usually the mass of a single monomer) and $g(\omega)$ is the vibrational density of states of the sample, normalized conventionally to three states per mass unit. The Bose factor f_B approaches the classical limit $k_B T / \hbar\omega$ at low enough frequencies (T temperature). Consequently, the spectrum at low frequencies and not too low temperatures measures $g(\omega)/\omega^2$. By referring the inelastic intensities to the elastic line, one can extract that quantity without any adaptable parameter. This is a first demonstration of the quantitative character of the neutron scattering tool in this contribution; there will be more to follow.

Fig. 1 shows the vibrational density of states of polybutadiene, obtained from time-of-flight neutron data [8] and plotted as $g(E)/E^2$ against the energy transfer $E = \hbar\omega$. Let us first focus on the 60 Kelvin data. They show a broad boson peak at

2.3 meV. At low frequency, the scattering extrapolates to a constant value. That is what one expects on the basis of the sound wave picture (the Debye model). According to the Debye model, the vibrational density of sound wave states $g_D(\omega)$ is given by

$$g_D(\omega) = \frac{3\omega^2}{\omega_D^3} = \frac{V_m}{6\pi^2} \left[\frac{1}{v_l^3} + \frac{2}{v_t^3} \right] \omega^2, \quad (2)$$

where V_m is the volume of a monomer and v_l and v_t are the longitudinal and transverse sound velocities, respectively. The arrows in Fig. 1 were calculated from ultrasonic [10] and Brillouin measurements [11] of the sound velocities using eq. (2). Since the density of the sound waves increases with ω^2 , the corresponding classical scattering spectrum is simply a frequency-independent constant. The spectrum at 60 Kelvin starts from that expected constant at low frequencies (note there is no adaptable parameter in this comparison!) and then shows an excess of modes over that constant value by a factor of two at the boson peak.

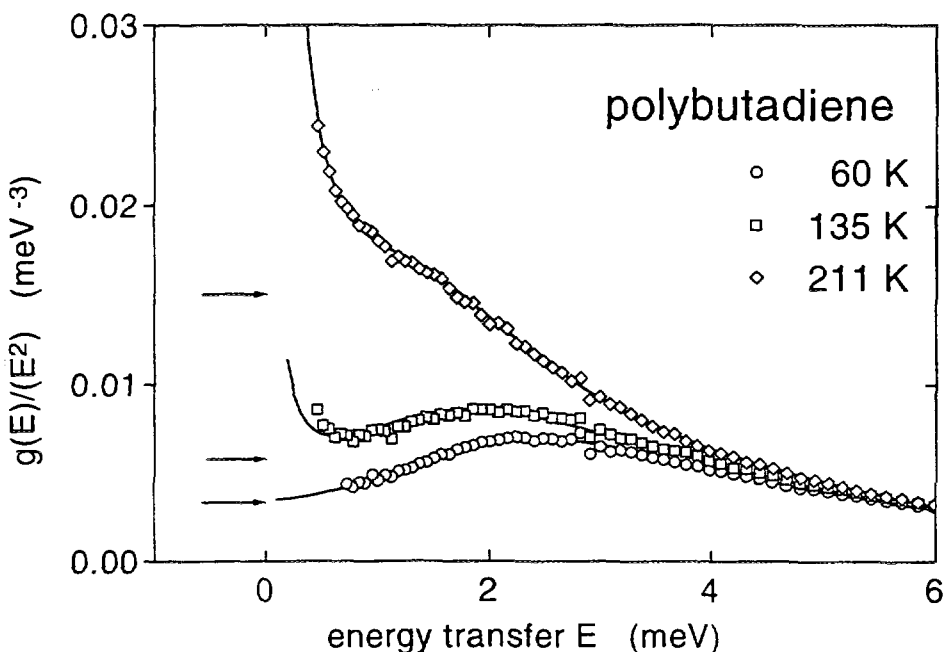


Fig. 1. Neutron spectra of polybutadiene, evaluated in terms of a vibrational density of states $g(E)/E^2$ and plotted against the energy transfer $E = \hbar\omega$ at three different temperatures. The arrows show the Debye density of states calculated from ultrasonic [10] and Brillouin [11] data. The continuous lines are fits in terms of the vibration-relaxation model [8].

The interpretation of the 60 K spectrum in terms of a vibrational density of state is further supported by the good agreement of specific heat data between 3 and 10 Kelvin with values calculated from the neutron vibrational density of states. Again, there is no adaptable parameter in that comparison.

With rising temperature, the spectra reveal a strongly anharmonic behaviour at the low frequency end. Nevertheless, one can still present the results in terms of an effective vibrational density of states, though the strong rise at low frequency indicates a quasielastic signal, usually ascribed to some relaxational motion.

Fig. 1 illustrates the central problem for the understanding of the dynamics of disordered matter: On one hand, the quasielastic shape of the scattering at higher temperatures implies relaxational dynamics, as for instance postulated by the mode coupling theory [5] or the coupling model [7]. The concept of relaxational dynamics is certainly valid at lower frequencies. On the other hand, there is a strong decrease of the sound velocities at the Brillouin frequencies (about 10 GHz, corresponding to an energy transfer of 40 μeV). If one calculates the corresponding increase of the density of sound wave states from eq. (2) (note that the sound velocities enter with the third power!), one gets the three arrows in Fig. 1. Thus one does not know for sure whether one deals with picosecond relaxations or with a softening of meV vibrations or a mixture of both. That insecurity has led to a confusing variety of different theories and models which are often hard to understand and difficult to disprove. Most probably, the final explanation will have to contain both a vibrational softening and an onset of a fast relaxational motion. We will come back to this problem in section 4.

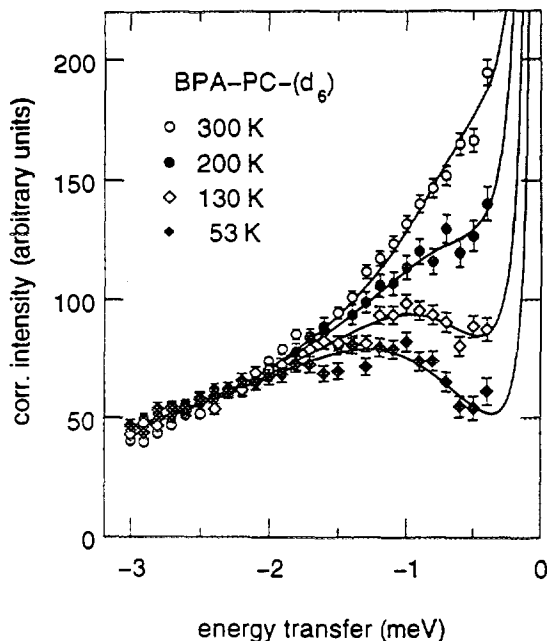


Fig. 2. Bose- and Debye-Waller scaled neutron spectra of polycarbonate [12] at different temperatures.

In most glass formers, that anharmonic change of the spectra sets in at or at least near to the glass transition temperature. However, there are notable exceptions. One of them is polycarbonate [12], shown in Fig. 2. The Bose and Debye-Waller scaled spectra of Fig. 2 show the same anharmonic effects as those in polybutadiene, but at temperatures much lower than the glass transition temperature of 423 Kelvin (in fact, at more or less the same temperature as in polybutadiene with its much lower glass transition temperature). A complementary example is vitreous silica [13], which shows no visible relaxation or vibrational softening even 200 Kelvin above the glass transition. These two examples suggest there is no direct connection between the picosecond dynamics and the glass transition. In fact, there should not be any such connection. The glass transition, defined pragmatically as the point in temperature

where the structural relaxation of the undercooled liquid takes minutes to hours to reach equilibrium, has nothing to do with the motion on the picosecond time scale. On the other hand, one can easily imagine an indirect connection: In most glass formers, the thermal expansion increases by a factor of two to three at the glass temperature. Thus it is no wonder that one finds a quicker developement of the anharmonic effects above the glass temperature in many glasses.

3 Q dependence: incoherent

From eq. (1), one would think the Q dependence of the incoherent scattering is rather trivial, namely e^{-2W} for the elastic line and $Q^2 e^{-2W}$ for the inelastic scattering. Since $2W = \langle (\mathbf{Q} \cdot \mathbf{u})^2 \rangle$, where \mathbf{u} is the atomic displacement, one expects a linear decrease of the logarithm of the elastic intensity with Q^2 . As we shall see, however, one finds deviations from that expectation in glasses. The explanation of these deviations is most probably connected with localized modes at low frequencies.

Localized low frequency modes in disordered matter were first discovered in numerical work on model glasses [4, 14, 15, 16, 17, 18]. The evidence is not fully conclusive, because the modes tend to delocalize with increasing cell size and the influence of long wavelength modes is missing.

In real glasses, there is no direct evidence so far. One does find low frequency vibrations coexisting with the sound waves and giving rise to the boson peak in Raman and neutron scattering [19]. If there is a continuous crossover from the low-barrier tunneling states [2] to these additional vibrational modes, one would expect them to be localized. Such a crossover has been postulated in the soft potential model [20]. An evaluation of low-temperature specific heat data in terms of that model [21] estimates a number of twenty to hundred atoms partaking in a single vibrational mode, in good agreement with the numerical work [4, 14, 15, 16, 17, 18]. One begins to understand vibrational localization in porous solids [22], but the physical reason for the vibrational localization in disordered bulk matter is not yet clear.

Very recently [23], incoherent inelastic neutron scattering was used to measure the localization of low frequency vibrational modes in glasses. The method was applied to two amorphous polymers, polystyrene and polybutadiene.

The method works as follows: Consider a localized low frequency mode at a frequency ω_s . For simplicity, let us assume N_s atoms with the total mass M_s and vibrating with the same amplitude u_s (though not necessarily in the same direction) in that mode. For $k_B T \gg \hbar\omega_s$,

$$\langle u_s^2 \rangle = \frac{k_B T}{M_s \omega_s^2}. \quad (3)$$

As an example, the low frequency vibrations in amorphous selenium seem to be localized to twenty atoms [21]. At the boson peak frequency (1.4 meV), one calculates a mean square displacement $\langle u_s^2 \rangle$ of 0.012 \AA^2 for such a localized mode at 100 K. The average mean square displacement measured at that temperature [24] is 0.009 \AA^2 for a single direction. Thus the mean square displacement contribution from the localized mode at a participating atom exceeds the average contribution from all the other modes, at least in the direction of vibration of the localized mode. Since it

is precisely that direction which is sampled in the inelastic neutron scattering from the localized mode, one expects to see an increase of the effective Debye-Wallerfactor exponent in the one-phonon scattering at the mode frequency.

The contribution of atom i participating in the mode to the one-phonon scattering [9] from the localized mode is given by

$$S_{i,loc}^{(1),inc}(\mathbf{Q}, \omega) = \frac{1}{2} e^{-2W_i(\mathbf{Q})} Q^2 \langle u_s \rangle^2 \cos^2 \theta \delta(\omega \pm \omega_s). \quad (4)$$

Here θ is the angle between the direction of vibration of atom i in the mode and the direction of the momentum transfer vector \mathbf{Q} . The Debye-Wallerfactor $W_i(\mathbf{Q})$ is given by

$$2W_i(\mathbf{Q}) = (\bar{\alpha} + \langle u_s^2 \rangle \cos^2 \theta) Q^2, \quad (5)$$

where $\bar{\alpha} Q^2$ describes the contribution from all other modes.

Averaging over θ and the participating atoms, one finds that the one-phonon scattering from the localized mode is seen with a Debye-Wallerfactor $2W = (\bar{\alpha} + \Delta\alpha)Q^2$ where

$$\Delta\alpha = \frac{3}{5} \langle u_s^2 \rangle. \quad (6)$$

Measuring $\Delta\alpha$ through the Q dependence of the inelastic scattering, one can determine the localization of the mode.

The inelastic scattering does not only contain the one-phonon term, but also multiphonon terms [9], which give a negative contribution to the effective Debye-Waller exponent in the inelastic scattering. They result from all possible combinations of different vibrations, so their calculation is rather cumbersome. However, there is an easy way to take them into account, at least to a reasonable approximation. One fits the Q -dependence of the full inelastic intensity at a given energy $\hbar\omega$ by the one-phonon form

$$S^{(1),inc}(Q, \omega) = f(\omega) Q^2 e^{-\alpha(\omega) Q^2} \quad (7)$$

over the whole relevant frequency range of the spectrum. Thus one gets at each frequency two parameters, namely the initial slope $f(\omega)$ against Q^2 at small Q and the effective Debye-Waller-exponent $\alpha(\omega)$. The latter contains the $\Delta\alpha$ of the one-phonon scattering which one is looking for.

In order to extract $\Delta\alpha$, one can compare the fitted values of the effective Debye-Waller-exponents $\alpha(\omega)$ with those calculated in the gaussian approximation. The gaussian approximation assumes for each atom a gaussian probability distribution around its position at time zero. The time-dependent width $\gamma(t)$ of that probability distribution is assumed to be the same for each atom and each spatial direction. $S(Q, \omega)$ is then obtained as the Fourier transform in time of the intermediate scattering function

$$I(Q, t) = e^{-\gamma(t) Q^2}. \quad (8)$$

The gaussian approximation has been found to be reasonably accurate in high resolution experiments on polymers at elevated temperatures [25, 26], but seems to fail at lower temperatures in other substances [27, 28], indicating an influence of localized low-frequency modes at low temperatures.

Equating the Q^2 coefficients in the expansions of $S(Q, t)$ and of the Fourier transform of $S(Q, \omega)$, one finds

$$\gamma(t) = \int_{-\infty}^{\infty} f(\omega)(1 - \cos \omega t)d\omega. \quad (9)$$

Thus one can calculate the full gaussian scattering from $f(\omega)$ alone and fit the scattering law with the one-phonon form, eq. (7), to see what the effective Debye-Waller exponent in the measurement range should be without any localized modes. The difference can then be attributed to the localization.

In ref. [23], time-of-flight data on amorphous protonated *cis-trans* polybutadiene [8] and amorphous polystyrene [29] were evaluated along these lines. The validity of the procedure was checked by a measurement of a 98 % crystalline *trans* polybutadiene sample. All data were taken on the spectrometer IN6 at the HFR at Grenoble with a wavelength of the incoming neutrons of 4.1 Å. At that particular wavelength one has the largest Q-range available at the instrument and an exceptionally high intensity.

The comparison of experiment and theory requires substantial corrections for self absorption, resolution tails, multiple scattering and coherent scattering contributions. This is illustrated in Fig. 3, which shows raw and corrected data. The dashed line shows the result of a global fit of the whole dataset in terms of gaussian scattering. The deviations from that fit are larger than the statistical error of the measurement, but they are smaller than the corrections, which therefore require due care.

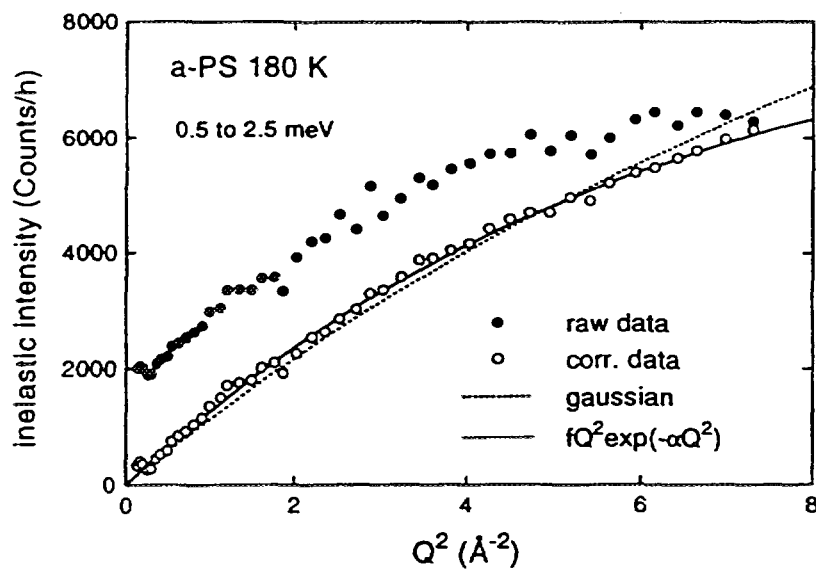


Fig. 3. Q dependence of the inelastic scattering from polystyrene between 0.5 and 2.5 meV at 180 K, showing a comparison of raw and corrected data and the difference between gaussian and nongaussian fits.

The self absorption correction is a standard procedure which requires good knowledge of the scattering, absorption and shape of the sample. The correction for tails of the elastic line are small at the chosen wavelength because of the sharp cutoff of the beryllium filter. Only the energy gain part of the spectrum was used; the other part

was calculated via detailed balance. After subtracting the tails, the inelastic scattering from single-scattering processes must extrapolate to zero for zero Q . This can be used to judge the quality of the multiple scattering correction. After subtracting multiple scattering, the curves did indeed extrapolate to zero at zero Q for all frequencies. Once this is guaranteed, it is possible to extrapolate $S(Q, \omega)$ for higher frequencies to small Q . This allows a final normalization correction using $\int S_{inc}(Q, \omega) d\omega = 1$, to remove the remnants of coherent scattering.

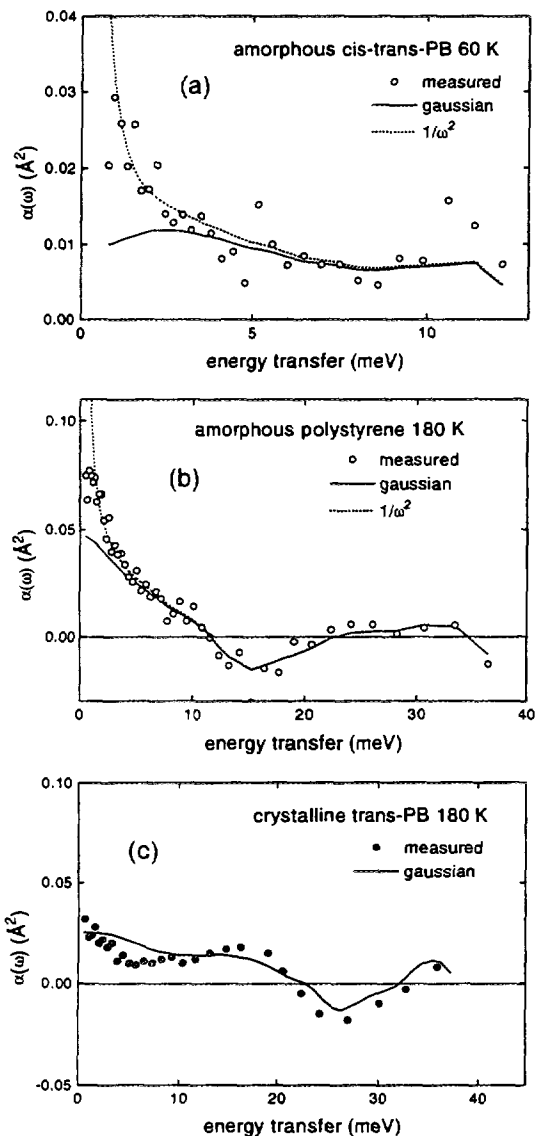


Fig. 4. Comparison of measured and calculated $\alpha(\omega)$. The dotted line adds a $1/\omega^2$ term to the gaussian calculation. (a) Amorphous *cis-trans* polybutadiene at 60 K (b) Amorphous polystyrene at 180 K (c) Crystalline *trans* polybutadiene at 180 K.

After correcting, one can fit the Q dependence of an inelastic channel with the one-phonon term, eq. (7). The one-phonon form with an effective adapted Debye-Waller factor turned out to describe the data within experimental error for all three samples

at all frequencies and temperatures. Fig. 1 shows an example for the quality of the fit. Repeating the same fit up to frequencies of $3k_B T$, one gets a set of $f(\omega)$ from which one can determine the gaussian values for the effective Debye-Waller exponents $\alpha(\omega)$.

Fig. 4 compares the Debye-Waller exponents $\alpha(\omega)$ fitted to the measured data with those determined from the gaussian approximation for three different examples. The first in Fig. 4 (a) shows amorphous *cis-trans* polybutadiene at 60 K (glass transition temperature 183 K). One observes deviations from the gaussian values at low frequencies, consistent with a mass M_s of 580 atomic units (eleven monomers) participating in a single localized mode. The second example in Fig. 4 (b) is amorphous polystyrene at 180 K, well below its glass transition temperature of 373 K. One finds good agreement between experiment and gaussian calculation above 5 meV (note that at 15 meV the Debye-Waller exponent becomes negative, because the density of states is low and the multiphonon scattering prevails), but at low frequencies one finds deviations. These deviations again seem to follow the $1/\omega^2$ behaviour predicted by eq. (3) down to about 1 meV within experimental error (below 1 meV one expects a slower increase of $\langle u_s^2 \rangle$ due to the anharmonicity and to the sound wave contribution to the inelastic scattering [21]). From the prefactor, one calculates (via equs. (1) and (4)) a total mass M_s of 650 atomic units (about six polystyrene monomers).

The crystalline sample in Fig. 4 (c) shows no deviation at the lowest frequency (the deviations around 5 meV are probably due to the stronger effects of the remnant coherent scattering which is much sharper in Q). The absolute values are about the same as those of the amorphous sample at a three times lower temperature. Since the mean square displacement of the crystalline sample increases essentially linearly with temperature, this implies much smaller values in the crystalline polymer.

It is interesting to relate the nongaussian behaviour of the inelastic data to the corresponding nongaussian behaviour of the elastic line. The Q dependence of the elastic line of the incoherent scattering for an ensemble of N gaussian scatterers with different mean square displacements is given to order Q^4 by

$$\frac{1}{N} \sum_{i=1}^N e^{(-\alpha_i Q^2)} \approx e^{(-\bar{\alpha} Q^2 + \frac{1}{2} (\bar{\alpha}^2 - \bar{\alpha}'^2) Q^4)}, \quad (10)$$

where $\bar{\alpha}$ and $\bar{\alpha}'^2$ are the averages of α_i and α_i^2 , respectively. The dimensionless coefficient $(\bar{\alpha}^2 - \bar{\alpha}'^2)/\bar{\alpha}^2$ is denoted as the *nongaussianity* A_0 .

The nongaussianity parameter A_0 can be calculated from the equations

$$\bar{\alpha} = \int_{-\infty}^{\infty} f(\omega) d\omega \quad A_0 = 2 \frac{\int_{-\infty}^{\infty} f(\omega) \alpha(\omega) d\omega}{\bar{\alpha}^2} - 1 \quad (11)$$

where the integrals are taken over the inelastic part of the scattering. For polystyrene at 180 K, one finds a value of 0.52, much higher than the value 0.09 anticipated from the factor of two between the average mean square displacements of the five protons on the phenyl ring and the three protons on the chain [30]. However, the value is in good agreement with recent triple axis measurements of the elastic line of polystyrene over a large Q range [31]. For polybutadiene, A_0 is 0.55 at 60 K and decreases to 0.35 at 135 K, in excellent agreement with a recent backscattering measurement on the IN13 at the ILL Grenoble [32].

All three measurements indicate a marked decrease of the nongaussianity towards higher temperatures (Fig. 5). A gradual delocalization of the vibrational modes has been also observed in numerical work [17]. Another simulation [15] shows localized modes in low-temperature amorphous ice, but no vibrational localization in room-temperature water. One should note, however, that the criterion for localization of the neutron measurement differs from the eigenmode criterion of the simulations. Two weakly coupled localized modes on two neighbouring groups of atoms appear as two eigenmodes extended over both groups in the simulation, but as two separate modes in a measurement of the atomic mean square displacements.

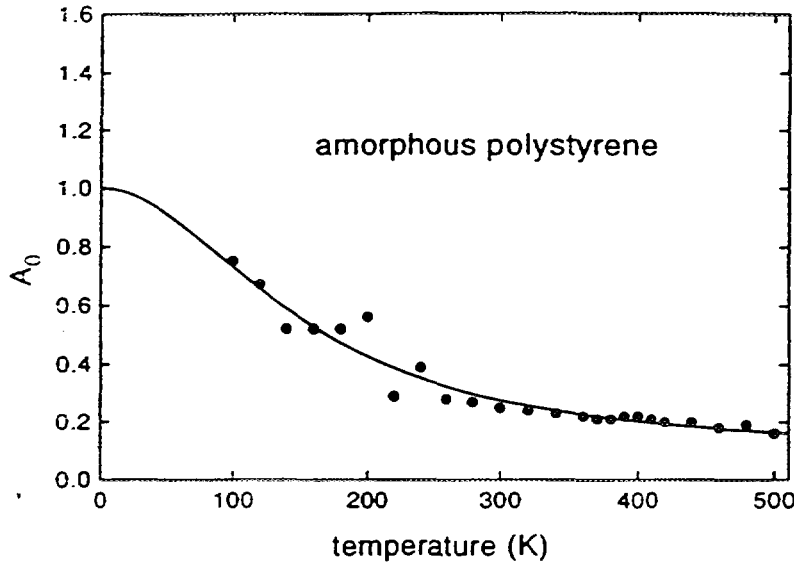


Fig. 5. Temperature dependence of the nongaussianity parameter A_0 in polystyrene. The line is a guide to the eye.

The interpretation of the data in terms of a single kind of localized modes oversimplifies the real situation in many ways. In particular, a full treatment will have to take the sound waves and their interaction with the localized modes into account. Such a treatment, however, requires a theoretical understanding which is not yet available. The next section deals with coherent neutron scattering measurements which shed some light on this aspect of the picosecond dynamics.

4 Q dependence: coherent

Many evaluations of coherent inelastic neutron data concentrate on the frequency dependent spectra, following the mode-coupling assumption [33] of a decoupling of the Q and ω dependence. For polybutadiene, a well-studied glass former [8], one finds, however, strong deviations from the decoupling assumption [34]. While at low frequencies the inelastic spectra exhibit a pronounced sound wave like coherent form factor indicating long wavelength excitations, at higher frequencies more localized vibrations prevail.

The sample was fully amorphous deuterated (1,4)-*cis-trans* polybutadiene with a molecular weight of 100.000 atomic units. The data were taken on the spectrometer IN6 at the HFR at Grenoble with a wavelength of the incoming neutrons of 4.1 Å.

Fig. 6 (a) shows the intensities in the elastic window (resolution width 150 μeV) at the two temperatures 20 and 293 K (the glass transition temperature is 186 K). At low momentum transfer Q , one finds a small amount of small angle scattering, possibly due to some impurities and essentially temperature independent. Around 1.5 \AA^{-1} , there is a pronounced peak due to interchain correlations (correlations between *different* chains lying side by side and attracted towards each other by van der Waals forces). The continuous line through the 20 K data points is a fit with an appropriate form, describing the peak at 1.5 \AA^{-1} by the three parameters of a Lorentzian.

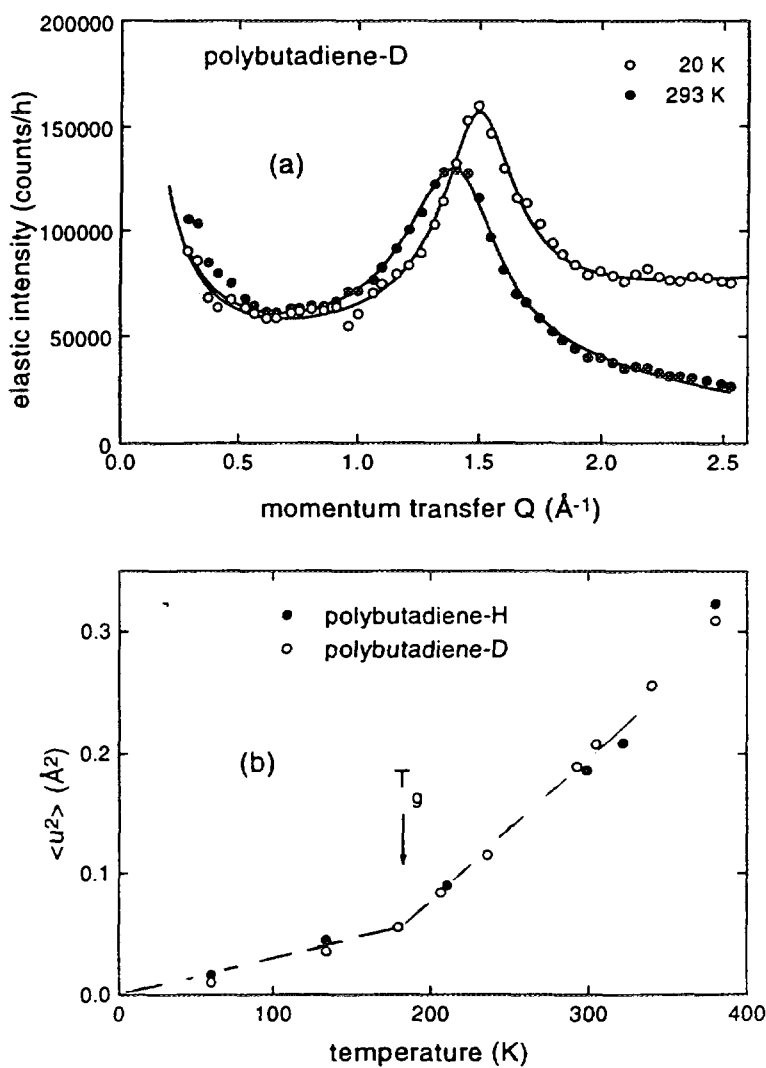


Fig. 6. (a) Q dependence of the elastic window scattering from polybutadiene at 20 and 293 K, together with the fits described in the text; (b) comparison of mean square displacements from the Debye-Waller factors $2W = Q^2 < u^2 >$ of protonated and deuterated polybutadiene.

It turned out to be possible to describe the elastic window data at higher temperatures by the same form, adapting only the three parameters of the Lorentzian and the exponent $2W = \langle u^2 \rangle Q^2$ of a Debye-Waller factor. The continuous line through the 293 K data shows the fit at room temperature. The Debye-Waller factors determined in this way agree within experimental error with those determined from the incoherent scattering of protonated samples (Fig. 6 (b)). This shows that one has a reasonable quantitative description of the elastic window intensity $S(Q, 0)$, which will be needed for the quantitative treatment of the inelastic scattering.

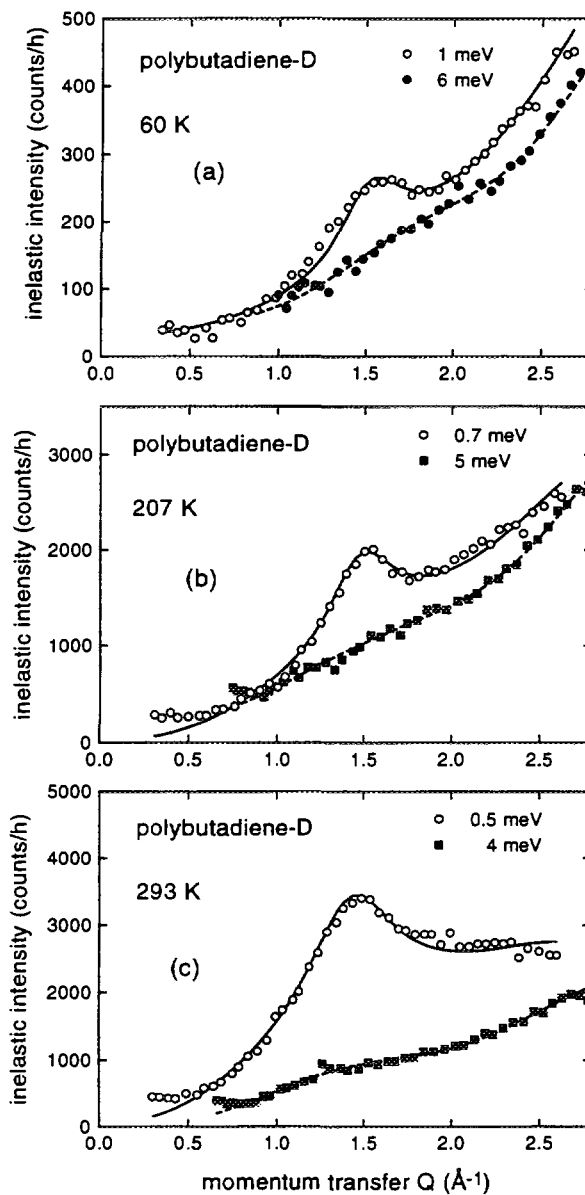


Fig. 7. Q dependence of the inelastic scattering from polybutadiene at different frequencies (a) at 60 K (b) at 207 K (c) at 293 K, together with the fits described in the text.

Fig. 7 shows the Q dependence of the inelastic scattering for two different frequencies, one near to the elastic window and the other one at a slightly higher frequency, around 5 meV. One sees immediately that the decoupling approximation is not valid:

the Q dependence near to the elastic line reproduces the peak at 1.5 \AA^{-1} and the one at higher frequency does not. This holds for all three sets of data in Fig. 7, from well below the glass temperature up to high above.

Even without quantitative analysis, the data in Fig. 7 demonstrate the existence of two different kinds of low frequency motion. The first is a correlated motion of neighbouring polymer chains and dominates at low frequencies. The second is an uncorrelated motion of different polymer chains which prevails at frequencies above two to three meV.

While the idea of two different kinds of low frequency motion is new in the field of undercooled liquids, it is a well-established concept for amorphous solids [2, 3, 20, 35]. The understanding of the low temperature properties of glasses requires sound waves interacting with localized excitations. These localized excitations appear as tunneling states [2], localized vibrations [3] or low-barrier relaxations, depending on the local details which determine their mode potentials [20]. In this picture, well-defined sound waves exist only at frequencies up to about two meV. At higher frequencies, they get overdamped by the rising number of localized vibrations [35].

A very similar picture is suggested by the data in Fig. 7. One has a correlated motion of different chains - e. g. sound waves - at low frequency and local modes which interact with the sound waves and dominate the spectrum at slightly higher frequencies. The continuous and broken lines in Fig. 7 represent a fit of the data in terms of that picture. Basically, the Q -dependence of the sound wave part was assumed to follow a $Q^2 S(Q, 0)$ curve, while the dynamic structure factor of the additional excitations was chosen to be close to a simple $Q^2 e^{-2W}$ dependence. In detail, the fit was more complicated, taking the explicit formulae of Carpenter and Pelizzetti [36] for the sound wave part and assuming a frequency-dependent Debye-Waller factor to account for the influence of multiphonon scattering effects [23]. Contrary to neutron [37] and x-ray [38] Brillouin scattering where longitudinal modes in the first Brillouin zone are observed, the Carpenter and Pelizzetti treatment is based on umklapp processes which enable the observation of both longitudinal and transverse sound waves at higher Q . The important feature of that analysis is that it allows to determine in a reasonably quantitative way a frequency-dependent density of sound waves as well as a frequency-dependent density of additional excitations.

Fig. 8 shows the result of this analysis for three temperatures. As in the case of the Debye-Waller factors, the total temperature-dependent effective density of states agrees within experimental error with the one determined from incoherent spectra of protonated polybutadiene (see Fig. 1), showing the internal consistency of the analysis. Here, however, that density of states is decomposed into sound wave and additional parts. In the low temperature glass phase (Fig. 8 (a)), the sound wave part first rises for frequencies below the boson peak and then decreases for frequencies above, in qualitative agreement with expectation for sound waves interacting with a broad distribution of local resonant modes. At the glass transition (Fig. 8 (b)), the decrease sets in at considerably lower frequencies, consistent with a sizeable vibrational softening of both the sound waves and the additional vibrations.

In the undercooled liquid at 237 K (Fig. 8 (c)), the sound wave signal looks like a broad quasielastic line and does in fact account for a large part of the intensity previously attributed to the famous fast picosecond process. Note that the sound wave part extrapolates accurately to the Debye density of states calculated from

acoustic [10] and Brillouin data [11] for longitudinal and transverse sound waves (the arrows in Fig. 8).

Thus, using the inelastic coherent formfactors as a fingerprint, we find that a sizeable part of the low frequency dynamic structure factor stems from correlated, in-phase molecular motions related to the sound waves. The correlation range ξ of this cooperative motion may be estimated from the width in Q of the sound wave form factor $\xi = 2\pi/\Delta Q \approx 15\text{\AA}$.

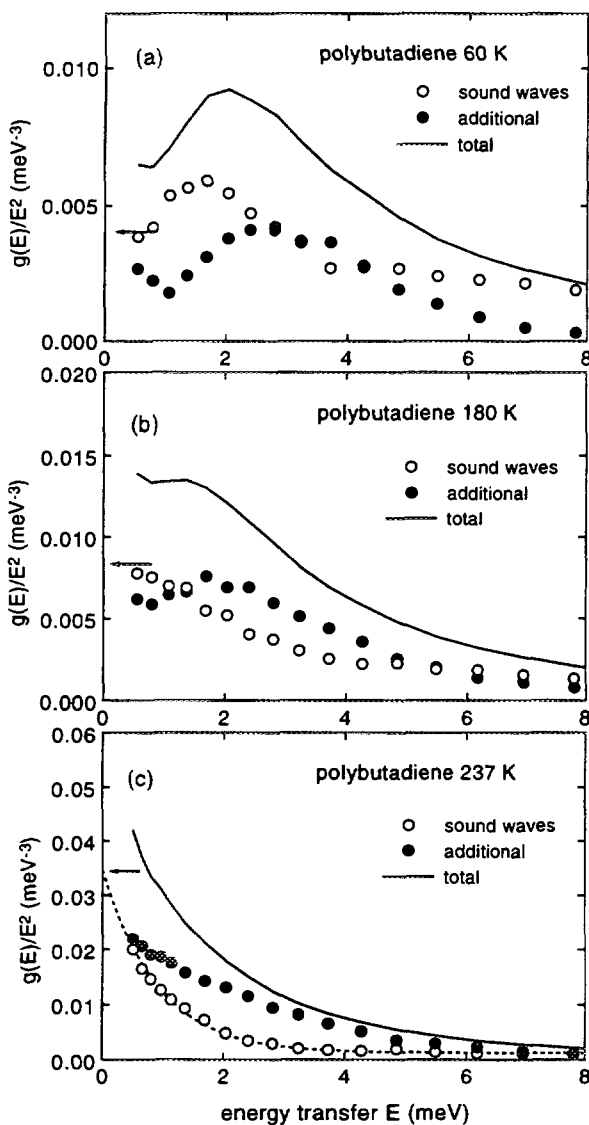


Fig. 8. Fit results in terms of a total effective density of states vs. frequency, plotted as density of states over frequency squared and decomposed into a sound wave and an additional excitation part (a) at 60 K (b) at 180 K (c) at 237 K. The arrows denote the Debye density of states calculated from acoustic [12] (at 77 K) and Brillouin [13] data.

Superimposed there is a vibrational pattern whose form factor does not deviate significantly from the conventional $Q^2 e^{-2W}$ incoherent phonon form factor within

the Q range of the measurement. In principle, one must reckon with a frequency dependence of such a vibrational form factor. Moreover there might be an interference term between sound wave like and additional excitations. However, since it turned out to be possible to fit all spectra at different temperatures and frequencies with a sum of the sound wave form factor and just one additional contribution, these other features are probably weak and can be disregarded.

These data show experimentally the essential role of long range correlated motion in the low frequency inelastic scattering from glasses and undercooled liquids. This raises questions on the models commonly applied to the phenomenon of the dynamic glass transition:

(i) Treating all low frequency excitations on the same footing in a single dynamic equation, the mode coupling theory of the glass transition [33] predicts the already mentioned decoupling of the frequency dependent spectral function from the Q dependent form factors. The possibility of important dynamic phenomena on significantly differing length scales and thereby giving rise to explicitly frequency dependent form factors is not considered so far.

(ii) In a recent approach following the coupling model of Ngai [7], Colmenero et al [8, 6] interpreted the short time dynamics of undercooled polymer melts in terms of local conformational transitions unaffected yet by the interaction with other chains. The picture is supported by the activation energies for the time scale of the fast process which agree with local rotational barriers in different polymers. Such a local picture of the fast process, however, will have difficulties to explain the cooperativity of the low frequency motion expressing itself in terms of a pronounced sound wave form factor.

(iii) Finally, also the vibration-relaxation model [8] which starting from the soft potential model [20] assumes double minimum potentials providing possibilities for soft vibrations and at the same time for over barrier jumps, cannot easily account for the observed cooperativity.

Although the strong decrease of the longitudinal and transverse sound velocities has been well known from Brillouin data [39], its consequence for the dynamic response of a glass forming material in the meV regime has never been realized before. The experimental results displayed here require the inclusion of the sound waves and their interaction with other excitations in any future attempt to understand the anomalous low frequency dynamics of glass forming polymers and probably that of other glass formers as well.

References

- [1] Proceedings of the Conference "Dynamics of Disordered Materials II", Grenoble 1993, *Physica A* **201**, Nos. 1-3
- [2] W. A. Phillips (ed.), *Amorphous Solids: Low temperature properties*, (Berlin: Springer 1981)
- [3] U. Buchenau, M. Prager, N. Nücker, A.J. Dianoux, N. Ahmad and W.A. Phillips, *Phys. Rev. B* **34**, 5665 (1986)
- [4] H. R. Schober and B. B. Laird, *Phys. Rev. B* **44**, 6746 (1991)

- [5] W. Götze, in *Liquids, Freezing and the Glass Transition*, edited by J. P. Hansen., D. Levesque and J. Zinn-Justin, (North-Holland, Amsterdam 1991) p. 287
- [6] J. Colmenero, A. Arbe and A. Alegria, Phys. Rev. Lett. **71**, 2603 (1993)
- [7] K. L. Ngai, Comments Solid State Pys. **9**, 128 (1979)
- [8] R. Zorn, A. Arbe, J. Colmenero, D. Richter and U. Buchenau, Phys. Rev. E **52**, 781 (1995)
- [9] W. Marshall and S. W. Lovesey, *Theory of thermal neutron scattering*, (Clarendon Press, Oxford 1971), p. 80 ff
- [10] A. Bhattacharya, T. L. Smith and A. C. Anderson, J. Noncryst. Solids **31**, 395 (1979)
- [11] B. Strube (private communication)
- [12] U. Buchenau, C. Schönfeld, D. Richter, T. Kanaya, K. Kaji and R. Wehrmann, Phys. Rev. Lett. **73**, 2344 (1994)
- [13] A. Wischnewski, A. J. Dianoux and U. Buchenau (unpublished)
- [14] C. Oligschleger and H. R. Schober, Physica A **201**, 391 (1993)
- [15] M. Cho, G. R. Fleming, S. Saito, I. Ohmine and R. M. Stratt, J. Chem. Phys. **100**, 6672 (1994)
- [16] J. Hafner and M. Krajci, J. Phys.: Condens. Matter **6**, 4631 (1994)
- [17] S.D. Bembeneck and B. B. Laird, Phys. Rev. Lett. **74**, 936 (1995)
- [18] R. Fernandez-Perea, F. J. Bermejo and E. Enciso, Phys. Rev. B **53**, 6215 (1996)
- [19] V. K. Malinovsky, V. N. Novikov, P. P. Parshin, A. P. Sokolov and M. G. Zemlyanov, Europhys. Lett. **11**, 43 (1990)
- [20] V. G. Karpov, M. I. Klinger and F. N. Ignat'ev, Zh. Eksp. Teor. Fiz. **84**, 760 (1983) [Sov. Phys- JETP **57**, 439 (1983)]
- [21] U. Buchenau, Yu.M. Galperin, V.L. Gurevich, and H.R. Schober, Phys. Rev. B **43**, 5039 (1991).
- [22] T. Nakayama, K. Yakubo and R. L. Orbach, Rev. Mod. Phys **66**, 381 (1994)
- [23] U. Buchenau, C. Pecharroman, R. Zorn and B. Frick Phys. Rev. Lett. **77**, 659 (1996)
- [24] U. Buchenau and R. Zorn, Europhys. Lett. **18**, 523 (1992)
- [25] T. Kanaya, K. Kaji and K. Inoue, Macromolecules **24**, 1826 (1991)
- [26] J. Colmenero, A. Arbe, A. Alegria and K. L. Ngai, J. Non-Cryst. Solids **172-174**, 229 (1994)

- [27] W. Doster, S. Cusack and W. Petry, *Nature* **337**, 754 (1989)
- [28] F. Fujara, W. Petry, R. M. Diehl, W. Schnauss and H. Sillescu, *Europhys. Lett.* **14**, 563 (1991)
- [29] K. Linder, B. Frick and U. Buchenau, *Physica A* **201**, 112 (1993)
- [30] B. Frick, U. Buchenau and D. Richter, *Colloid Polym. Sci.* **273**, 413 (1995)
- [31] T. Kanaya (private communication)
- [32] R. Zorn (unpublished)
- [33] W. Götze, in *Phase Transitions and Relaxation in Systems with Competing Energy Scales*, ed. by T. Riste and D. Sherrington (Kluwer, Amsterdam 1993) p. 202
- [34] U. Buchenau, A. Wischnewski, D. Richter and B. Frick (unpublished)
- [35] U. Buchenau, Yu. M. Galperin, V. L. Gurevich, D. A. Parshin, M. A. Ramos and H. R. Schober, *Phys. Rev. B* **46**, 2798 (1992)
- [36] J. M. Carpenter and C. A. Pelizzari, *Phys. Rev B* **12**, 2391 (1975)
- [37] J. Teixeira, M. C. Bellissent-Funel, S. H. Chen and B. Dorner, *Phys. Rev. Lett.* **54**, 2681 (1985)
- [38] F. Sette, G. Ruocco, M. Krisch, U. Bergmann, C. Masciovecchio, V. Mazzacurati, G. Signorelli and R. Verbeni, *Phys. Rev. Lett.* **75**, 850 (1995)
- [39] For a review on Brillouin scattering from polymers see J. K. Krüger, in *Optical Techniques to Characterize Polymer Systems*, ed. H. Bässler (Elsevier, Amsterdam 1989), p. 429



POLYMERS AND COLLOIDS

PETER SCHURTERBERGER
Institut für Polymere, ETH Zürich,
CH-8092 Zürich, Switzerland

ABSTRACT

A wealth of structural information from colloid and polymer solutions on a large range of length scales can be obtained using small angle neutron scattering (SANS) experiments. After a general introduction to the field of soft condensed matter, I shall give a few selected examples on how SANS combined with suitable contrast variation schemes can be used to extract information on the size and conformation of polymer coils in solution and in the melt, and on the local structure and flexibility of polymerlike micelles and microemulsions.

1. Introduction

During the last 10 - 20 years colloid and polymer sciences have undergone a 'renaissance', which has not only manifested itself in the creation of a new name, the term 'soft condensed matter', but indeed resulted in a considerable gain of understanding of the structural and dynamic properties of these complex fluids. The reason for this progress was on the one hand the realization of the existence of close analogies to established areas in theoretical physics such as between polymers and magnetic systems or field theory, or between colloidal suspensions and simple liquids. On the other hand, the availability of new experimental techniques such as dynamic light scattering or neutron scattering has also been instrumental in this development.

When talking about soft condensed matter, we generally consider three different areas: polymers, colloids and so-called association colloids or surfactant systems (see Fig. 1). Polymer sciences has greatly advanced in particular through the work of P. G. de Gennes, who for example demonstrated the existence of universal behavior (expressed through so-called scaling laws) for different physical properties of polymer solutions and melts. In such a treatment, the basic idea is to concentrate on global properties, i.e. on the dependence of observable physical properties such as the overall coil dimension (characterized for example by its radius of gyration, R_g) on chain length, concentration or a few basic interaction parameters, and reduce the polymer molecule to an idealized model omitting all chemical details. A classical model for such a description is the random walk with N completely independent steps as the simplest idealization of a flexible polymer chain consisting of N monomers in solution or in a melt. This simple model does in fact provide a very good description of the conformation of flexible polymer chains in theta solvents (where the different contributions to long range interactions between segments cancel and the polymer solution exhibits a pseudo-ideal behavior analogous to the Boyle point of gases) or melts. Additionally, one can for example take into account interactions between

neighbouring monomers (i.e., include the local 'chemistry') as done in the wormlike chain model, or include excluded volume interactions by modelling the polymer chain as a self-avoiding random walk.[1-3] SANS can then be used as a very good test of the predictions from the various theoretical models in order to assess their validity under various experimental conditions as will be demonstrated in the second chapter of this presentation.

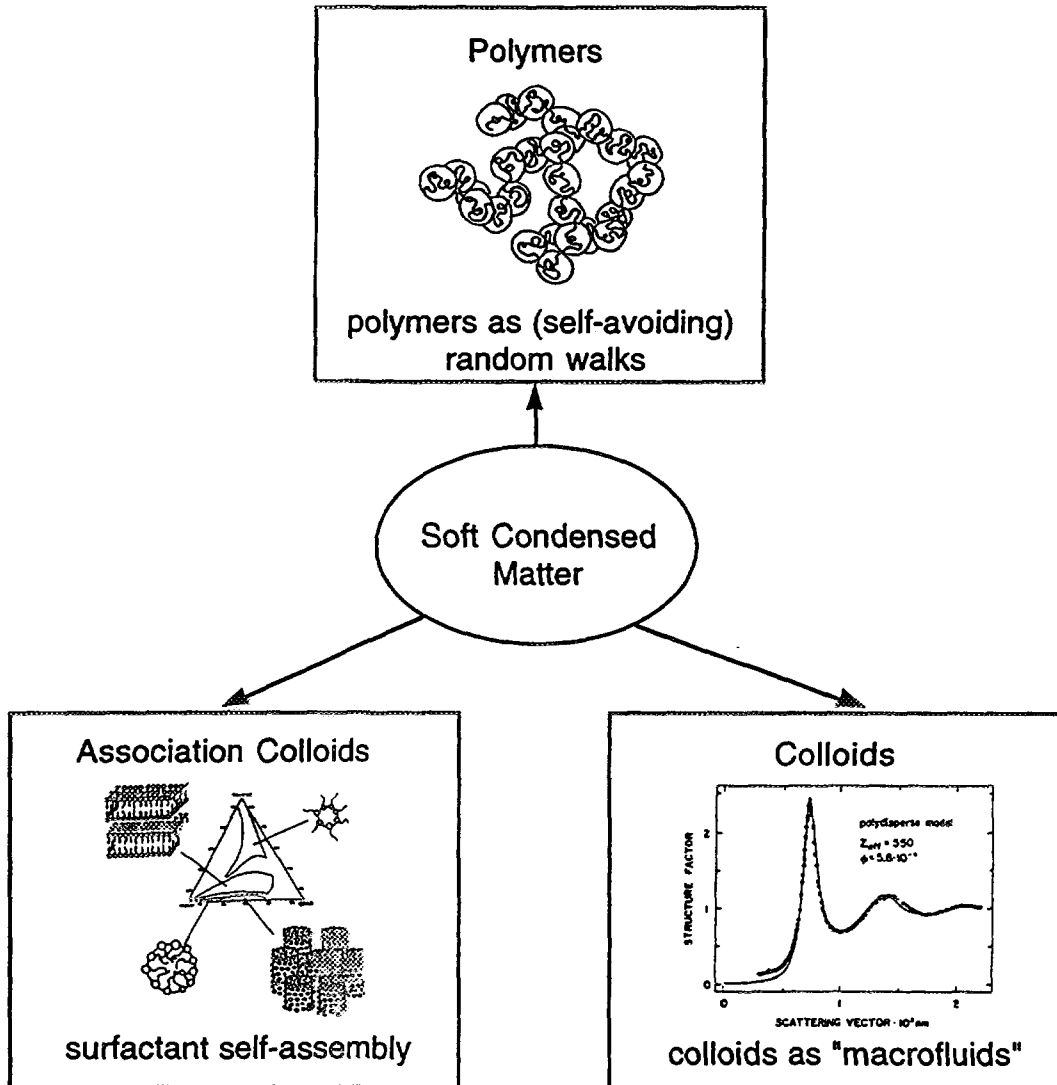


Fig. 1: An overview over some important areas in soft condensed matter

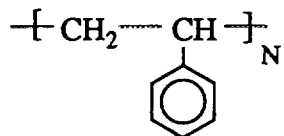
In colloidal suspensions, considerable progress in the understanding of questions such as the effect of interparticle interactions on the structure and stability of colloidal suspensions has been achieved by making analogies to simple fluids such as liquid argon. The idea is to make a typical coarse graining ansatz and consider a collection of colloidal particles as a 'macrofluid' dispersed in a continuous medium, i.e., the solvent is treated as a quasi-inert continuum that is defined through its macroscopic properties such as density, index of refraction and dielectric constant only. One can then apply the well known tools from statistical mechanics derived for simple liquids in order to create

a link between the suspension structure and the interaction potential.[4, 5] In this respect it is important to realize that the potential used as an input in the statistical mechanical treatment is a 'potential of mean force', and that the osmotic pressure now plays the role of the pressure in the corresponding atomic or molecular systems. SANS offers a very valuable tool to test these theoretical models and to obtain information on interparticle interactions and suspension structure.[4, 5]

Surfactants in solution exhibit a complex aggregation behavior as a result of a delicate balance of opposing forces.[6] An important aspect of surfactant systems is the relation between microstructure and phase equilibria. Several theoretical concepts based either on packing considerations of the surfactants in the aggregates or on the role of the bending elastic energy of the surfactant monolayer have provided us with a theoretical framework for a better understanding of these systems.[6, 7] In particular the 'flexible surface model', which is an interfacial description using curvature elasticity, has considerably advanced our understanding of many aspects of the complex phase behavior exhibited by surfactant systems.[7, 8] In these systems, SANS is a particularly powerful technique for determining structural properties on all length scales as it allows to specifically label certain components through contrast variation as will be demonstrated in chapter 3.

2. SANS from Polymer Solutions

In this chapter I shall discuss some structural aspects of linear polymers. As a classical example of such a polymer we can look at polystyrene:



where the number of repeat (or monomer) units, N, which is often called the degree of polymerization, can be as large as $> 10^6$. As already mentioned, the simplest possible

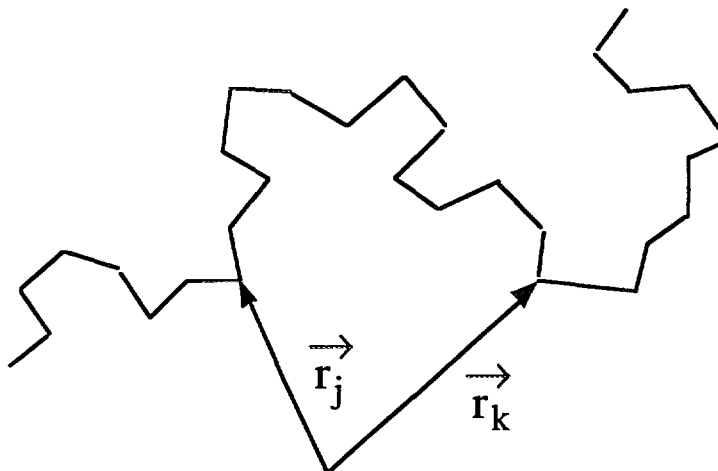


Fig. 2: Schematic representation of a random walk model of a linear polymer chain

model for the conformation of such a linear chain in solution is a random walk in three dimensions as shown schematically in Fig. 2.. The corresponding orientationally

averaged and normalized single particle scattering function $P(Q)$, which contains all the structural information on the conformation of the scattering object can then be calculated according to

$$P(Q) = \frac{1}{N^2} \sum_{j=1}^N \sum_{k=1}^N \left\langle \frac{\sin(Qr_{jk})}{Qr_{jk}} \right\rangle \quad (1)$$

where $r_{jk} = |\mathbf{r}_j - \mathbf{r}_k|$ is the distance between two scattering centres (monomers) and \mathbf{Q} is the scattering vector. For the random walk model, the evaluation of Eq. 1 is particularly simple due to the Gaussian distribution for the intersegmental distances and leads to the so-called Debye function

$$P(Q) = \frac{2(e^{-x} + x - 1)}{x^2} \quad (2)$$

where $x = \langle R_g^2 \rangle Q^2$ and $\langle R_g^2 \rangle$ is the mean square radius of gyration of the polymer coil. The Debye function results in the classical asymptotic behavior of $P(Q) \sim Q^{-2}$ for large values of x , which is the typical 'finger print' of a structure generated by a random walk. However, the local flexibility of polymer chains is basically caused by the potential energy of rotation about chemical bonds. While the random walk model assumes that the directions of individual chain segments are completely uncorrelated, i.e., that these rotations are completely unhindered, for 'real' polymers this is generally not true due to steric hindrances between side groups. Therefore, real chains are locally stiff, and it is only after a certain distance b (the Kuhn length or statistical segment length) along the chain that the direction of individual chain segments become completely uncorrelated and that the time averaged distance distribution function between two monomer units loses its local character and starts to obey Gaussian statistics. Furthermore, due to excluded volume effects between monomers we can expect that the ideal random walk model does not provide an adequate description of the stain statistics in good solvents, and that we have to use a self-avoiding random walk instead. This does not lead to Gaussian statistics for the distribution function of intersegmental distances and therefore does not allow for an easy evaluation of Eq. 1. Summarizing this short introduction to polymer statistics, we can point out the following characteristic features that we expect to find in data from scattering experiments with large single polymer coils in solution that cover a broad range of scattering vectors:

The data reveal a series of different regimes with a behavior characteristic of the various length scales of the chains: For very low values of Q ($1/Q < R_g$), i.e., in the so-called Guinier regime, the scattered intensity $I(Q)$ becomes insensitive to structural details and is dominated by the finite overall length of the particles, and we can determine the radius of gyration R_g of the particles. At intermediate Q (cross section radius $R_c \ll 1/Q \ll R_g$), $I(Q)$ becomes much more sensitive to the local aggregate structure, and polymer theory predicts for flexible polymer coils that $I(Q)$ should decay with a power law of the form $I(Q) \sim Q^{-x}$, where $x = 1.66$ for a self-avoiding random walk chain and $x = 2.0$ for an ideal random walk chain. At large values of Q , $I(Q)$ is controlled by distances over which polymers are rod-like rather than flexible, and we expect a crossover to an asymptotic Q^{-1} -dependence for $I(Q)$ which is typical for locally cylindrical structures. However, a real polymer is not an infinitely thin chain, and therefore the local cross section structure of the chains give rise to a cross section Guinier behavior and a strong decrease in the scattering intensity at still larger Q -values. The different characteristic regimes are demonstrated in Fig. 3.

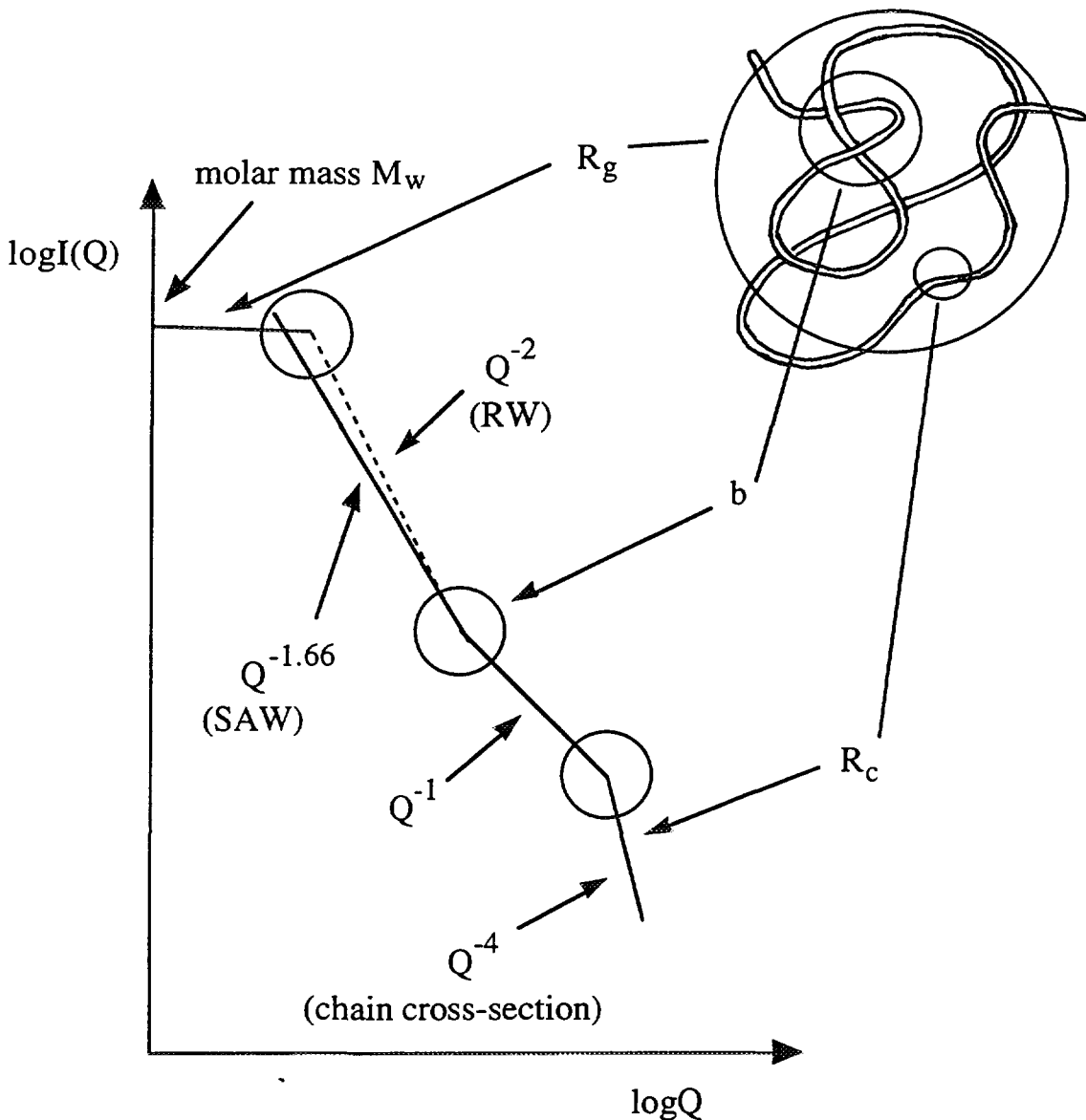


Fig. 3: Schematic plot of the asymptotic behavior of the scattering intensity $I(Q)$ versus scattering vector Q for polymers in solution. The crossover regions are denoted by circles (see text for details).

However, it is important to point out that the experimental verification of the asymptotic behavior can be quite difficult, and in particular the crossover from a flexible to a locally stiff chain that contains the very important information on the polymer flexibility is often masked by the local cross section structure. This can be demonstrated with data from partially deuterated polymer chains, where different parts of the monomer unit contribute differently to the overall intensity. The scattering functions of atactic polystyrene (PS) in carbon disulfide (CS_2) with different selective deuteration of the polymer have been determined by Rawiso et al. [9] using SANS. CS_2 is a good solvent for PS, and this is reflected in the scattering function which shows a $Q^{-1.7}$ -behavior at intermediate Q values. The data for a molar mass of $M_w = 50'000$ and three different selective deuterations ((i) fully deuterated, (ii) deuterated in the phenyl ring, and (iii) deuterated in the backbone) are shown in Fig. 4. CS_2 has a low scattering length density, C and D have a relatively large scattering length, and H has a negative

scattering length. Therefore it is mainly the deuterated parts of PS which contribute to the scattering from the polymer coil.

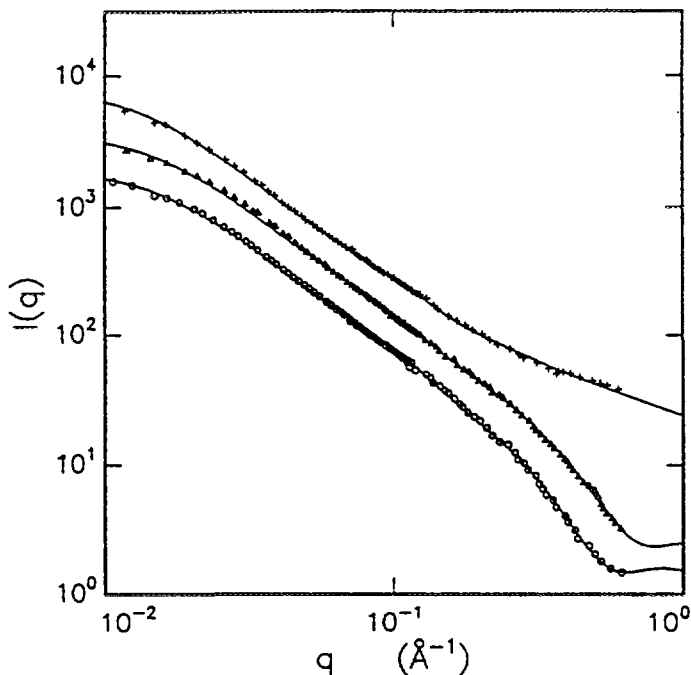


Fig. 4: Scattering functions for PS ($M_w \approx 50'000$) in CS_2 .[9] The lower data are for fully deuterated PS, the middle data for the phenyl ring and the upper data for the backbone deuterated. The curves are fits for a model scattering function that includes excluded volume effects.[10]

At low Q values we observe a well defined Guinier regime from which we can determine the molar mass (or contour length L) as well as the radius of gyration. However, we also immediately see from Fig. 4 that both for the fully deuterated as well as the phenyl ring deuterated samples the relatively large cross section radius of the chain leads to a direct cross-over from the asymptotic $Q^{-1.7}$ -behavior at intermediate Q values to the exponential decay in the cross section Guinier regime, thus completely masking the cross-over to the Q^{-1} -regime from which the Kuhn length b as a measure of the chain flexibility could be determined. It is only for the backbone deuterated sample, where the cross section radius is much smaller, that one is able to observe this part of the scattering function. In the original paper of Rawiso et al. the authors concentrated on the different asymptotic regimes in order to extract the maximum amount of data on the structure of PS in good solvents on all length scales, and no attempts were made to fit the data in the full Q range as the appropriate scattering functions for wormlike chains with excluded volume effects were not available. As a result of this unsatisfactory situation we started a series of off-lattice Monte Carlo simulations on semi-flexible polymer chains with and without excluded volume interactions.[11] The primary goal has been to obtain "experimental" data for the scattering function $P(Q)$ for semi-flexible chains with excluded volume effects with an accuracy of about 1 % in the range up to $Qb = 10$ and to parameterize them in such a way that they can be used for model fitting of experimental scattering data on polymer-like micelles. The model used is a discrete representation of the worm-like chain model of Kratky and Porod. The parameters of a

chain are the contour length L , and the statistical segment length b . In practice the chain is represented by N points along the contour, such that $L = Na$, where a is the point separation ("bond length"). For the excluded volume effects the finite cross section radius of the micelle was taken into account by placing hard spheres of radius $R = 0.1b$ at each point along the chain. Simulations were performed for chains with contour lengths of $L/b = 0.3, 0.6, 1.25, 2.5, 5, 10, 20, 40, 80, 160, 320$, and 640 . The accuracy of the resulting $P(Q)$ was estimated to be better than 1-2 % for $L/b \leq 160$ and 2-3 % for $L/b=320$ and 640 . The resulting $P(Q)$ have been parameterized using various methods in order to obtain numerical approximations that can be used in the analysis of "real" experimental data. The most accurate (and general) method used follows an approach used by Yoshizaki and Yamakawa in order to obtain $P(Q)$ for helical wormlike chains.[12] In this approach the scattering function can be written as

$$I(Q) = C_w \Delta\rho_m^2 S_{wc}(Q) S_c(Q) \langle M \rangle_w \quad (3)$$

where C_w is the polymer concentration (in weight per volume), $\Delta\rho_m$ is the average excess scattering length density per unit mass, $S_{wc}(Q)$ and $S_c(Q)$ are the normalized scattering functions of the infinitely thin wormlike chains and of the cross section, respectively, and $\langle M \rangle_w$ is the weight average molar mass. The scattering function $S_{wc}(Q)$ is given by

$$S_{wc}(Q, L, b) = [(1 - \chi(Q, L, b))S_{chain}(Q, L, b) + \chi(Q, L, b)S_{rod}(Q, L)]\Gamma(Q, L, b) \quad (4)$$

where $S_{chain}(Q, L, b)$ is the scattering function of a flexible chain with excluded volume effect,[13] $S_{rod}(Q, L)$ is the scattering function of a stiff rod,[14] $\chi(Q, L, b)$ is a cross-over function and $\Gamma(Q, L, b)$ corrects the crossover region. Explicit expressions for $\chi(Q, L, b)$ and $\Gamma(Q, L, b)$ are given elsewhere.[10] Such a scattering function indeed allows for a quantitative analysis of scattering data from semi-flexible chains over a broad Q -range as can be verified with the data from polystyrene in a good solvent shown in Fig. 4. A fit of Eqs. 3 and 4 to the experimental data is shown in Fig. 4. In the fit the local cross section structure of PS was approximated by a cylindrical shape, for which the corresponding cross section scattering function can be written as

$$S_c(Q) = \left(\frac{2J_1(R_c Q)}{(R_c Q)} \right)^2 \quad (5)$$

where $J_1(x)$ is the first order Bessel function and R_c the cross section radius.

The model scattering functions give almost perfect fits to the data over the entire range of Q values. The resulting values of the contour lengths L are in very good agreement with the calculated values based on the known molar mass and polydispersity for the three different samples. The Kuhn length is determined to be $b = 24.8 \text{ \AA}$, in good agreement with previous studies. The values for the cross-section radii that come out of the fit are also quite reasonable considering the molecular structure of the PS chain in solution as determined by other investigations. This clearly demonstrates that Eqs. 3 and 4 provide us with an analytical expression for the scattering cross section of polymers in good solvents capable of quantitatively reproducing the experimental features over an extended range of scattering vectors. This represents a major improvement compared to the previous characterization of

semiflexible polymers with small-angle scattering methods, where the analysis primarily relied on an individual interpretation of different Q-regimes based on asymptotic expressions. It also demonstrates the strength of SANS in the analysis of structural properties of polymers in solution, in particular when combined with contrast variation experiments and suitable model fits.

3. SANS from Polymerlike Micelles and Microemulsions

As pointed out in the introduction, surfactants in solution exhibit a complex aggregation behaviour as a result of a delicate balance of opposing forces.[6] Micellar solutions and microemulsions represent thermodynamically stable liquid dispersions containing surfactant aggregates, which can often be found in a large region of the phase diagram of 2- or multi-component surfactant systems.[15-17] In micellar dispersions, the aggregates are formed by self-assembly of surfactant monomers. While micelles are frequently spherical, they can also exhibit a sphere-to-rod transition and even grow to giant flexible and polymer-like aggregates. This micellar growth can be induced by a reduction in the so-called spontaneous curvature H_0 due to a change in a "control parameter" such as temperature (in nonionic surfactant systems), ionic strength (in ionic surfactant systems) or cosurfactant concentration, which subsequently results in a characteristic transition in the particle morphology from spheres to cylinders to lamellae.[8, 18, 19] Microemulsions are formed in 3- or multicomponent systems. The microemulsion aggregates have a liquid core (oil in oil-in-water (o/w), water in water-in-oil (w/o) microemulsions) which is surrounded and stabilized by a surfactant monolayer. They frequently possess a droplet-like structure, but they can also grow into large tubular or sponge-like and multi-connected structures.[8, 15] In addition to micellar and microemulsion phases, a number of liquid crystalline phases such as the lamellar (L_α), hexagonal (H) or cubic (I) phases or the so-called "sponge" phase (L_3) can be found.

A typical example for the phase behaviour of a ternary system with a nonionic surfactant of the ethylene oxide type is shown in Fig. 5. The surfactant-to-oil ratio is kept constant, and the temperature and the composition (characterized by the weight fraction of surfactant and oil) is allowed to vary, i.e., the system corresponds to a section through the phase prism as illustrated in Fig. 5(a). Three separate phases can be identified in the phase diagram shown in Fig. 5(b): A microemulsion phase, L, a lamellar liquid crystalline phase, L_α , and a second liquid phase, the so-called sponge or L_3 phase.[20] The relation between microstructure and phase equilibria is an important aspect of surfactant systems. Several theoretical concepts based either on packing considerations of the surfactants in the aggregates or on the role of the bending elastic energy of the surfactant monolayer have provided us with a theoretical framework for a better understanding of these systems.[6, 8, 21, 22] The sequence of phase transitions shown in Fig. 5(b) is, for example, in good agreement with the predictions of the flexible surface model.[8, 20] The phase transitions follow the trend of a decreasing mean curvature of the surfactant film with increasing temperature, i.e., are consistent with the strong temperature-induced variation of the spontaneous curvature for nonionic surfactants.[23] This temperature-induced variation of H_0 not only results in the appearance of phase transitions. It also causes variations of the microemulsion structure in the L-phase from almost monodisperse droplets at the lower phase boundary (the so-

called emulsification failure[8]) to anisotropic and possibly multiply-connected particles at the upper phase boundary.[20, 24, 25]

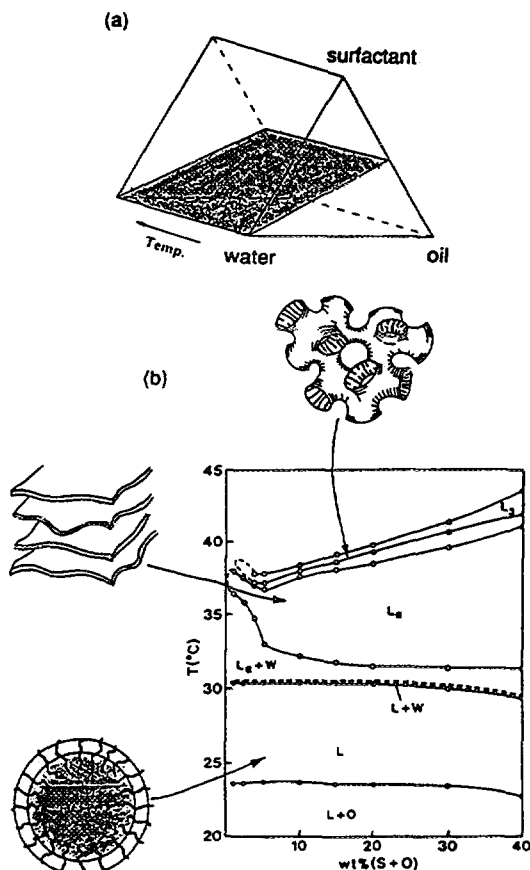


Fig. 5: (a) An illustration of the phase prism of a ternary system surfactant-water-oil. The shadowed region represents a plane through the phase prism defined by a constant surfactant-to-oil ratio (51.9/48.1 by weight). (b) Phase diagram of the system C₁₂E₅-D₂O-decane for a constant surfactant-to-oil ratio of 51.9/48.1 (see (a)), where temperature is plotted versus the total weight fraction of surfactant and oil. L denotes a liquid microemulsion phase, L_α is a lamellar liquid crystalline phase, and L₃ is an isotropic liquid phase often referred to as the "sponge phase" (adapted from ref. [8]).

It is this particular feature of micelles and microemulsions that makes scattering investigations of these systems so challenging. The micellar shape, the size distribution and the intermicellar interactions may depend strongly upon solution composition (e.g., surfactant concentration, ionic strength) and temperature, in contrast to other classical macromolecular systems such as polymers, biopolymers or lyophobic colloids. Therefore single particle properties such as the weight average molar mass M_w or the z-average mean square radius of gyration $\langle R_g^2 \rangle_z$ cannot be determined unambiguously from an extrapolation of the scattering data to infinite dilution. The neglect of this inherent property of surfactant systems and the various attempts to decouple micellar growth and intermicellar interactions have led to a number of controversies.

In the following paragraph I shall demonstrate that SANS can indeed provide important contributions to a better characterization of micellar structures in solution. It has been demonstrated in various reports that it is possible to find conditions where micelles or microemulsion particles grow dramatically with increasing surfactant concentration into giant cylindrical aggregates. These giant micelles normally have a high degree of flexibility, and their overall structure is generally well described by polymer theory.[18, 26] Several attempts have been made to demonstrate the existence of cylindrical micelles and to characterize the micellar structure using small-angle scattering experiments.[19, 27-34] The basis for such an approach comes from the fact that scattering experiments on polymers or polymer-like micelles covering a broad range of scattering vectors reveal a series of different regimes with a behavior characteristic of the various length scales of the chains as outlined in the previous paragraph (Fig. 3) These different characteristic regimes are indeed also found in solutions of polymerlike micelles as demonstrated in Fig. 6 with data from polymer-like lecithin reverse micelles, where results from static light and small-angle neutron scattering experiments have been combined. The particular example used is a microemulsion system in which giant polymerlike and tubular aggregates form. This formation of polymer-like structures upon the addition of trace amounts of water to almost spherical lecithin reverse micelles in organic solvents such as isoctane or cyclohexane has been demonstrated with a combination of light scattering and small-angle neutron scattering at low surfactant concentrations, which allowed verification of

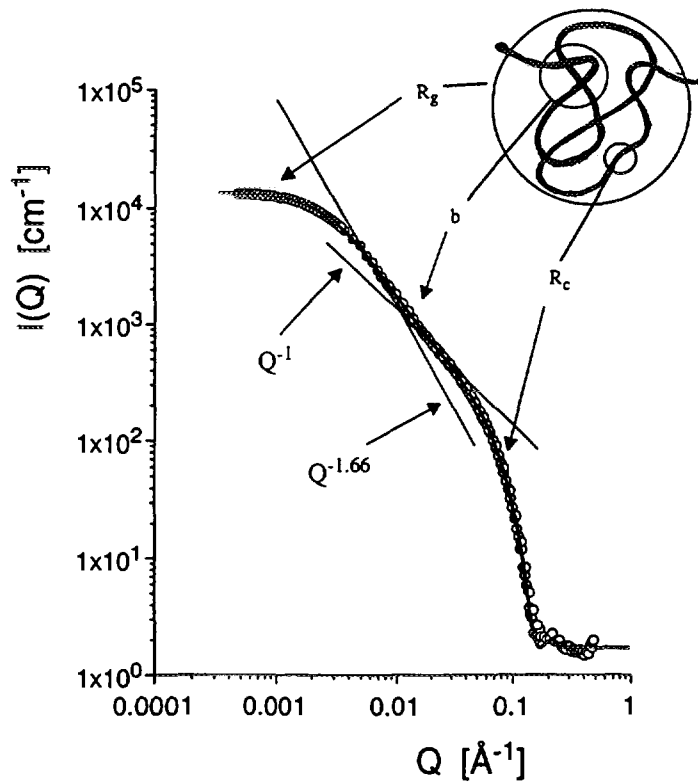


Fig. 6: Plot of scattering intensity $I(q)$ versus scattering vector q for solutions of soybean lecithin in deuterated isoctane (water-to-lecithin molar ratio $w_0 = 1.5$) at volume fraction $\phi = 0.0021$. Data shown is obtained from light (Δ) and neutron (\circ) scattering experiments. Also indicated are the regimes/length scales where a different characteristic q -dependence can be observed (see text for details).

the locally cylindrical structure of these reverse micelles and an estimate of the persistence length and overall dimensions.[43, 44]

In most previous studies, the data analysis primarily relied on an interpretation of different Q-regimes based on asymptotic expressions such as a Guinier approximation or the Debye equation for the low-Q part, the use of simple crossover relations for the incorporation of flexibility in the intermediate Q-range or a Guinier approximation for the high-Q part.[30-33, 35] However, in order to fully take advantage of the information content of the data it is desirable to perform a least squares analysis employing a model cross section as given for example by Eq. 3 for semiflexible polymers in good solvents. This is important, for example, in any attempt to determine the micellar flexibility characterized by the Kuhn length b , which is a key parameter in the interpretation of the micellar properties within the flexible surface model.[10, 34] Fig. 6 demonstrates that the scattering function developed for the wormlike chain model with excluded volume effects is indeed capable of quantitatively reproducing the experimental features of the SANS data from polymerlike micelles over an extended range of scattering vectors.

In the analysis of the local structure we can not only use model scattering functions as given by Eqs. 3-5, but we can try to extract detailed information on the local scattering length density profile of the micelles using a model-independent approach. This can be achieved through the indirect Fourier transformation (IFT) and square-root deconvolution (SQDEC) methods.[34, 36-39] The high-Q part of the polymer-like scattering intensity reflects the local cylindrical symmetry of the micelles, and the cross-section scattering intensity at $Q = 0$, $I_c(0)$, is directly related to the mass per length M_L .[40] While IFT uses the assumption that the cross-sectional contribution to the total scattering can be decoupled from the rest, it has the advantage that it does not rely on the low-Q part of the data used in the model fitting approach and that no specific model assumptions have to be made regarding the structure of the micelles except for the locally cylindrical symmetry. Therefore contributions from polydispersity of the overall size and interaction effects are minimized, which should result in a more reliable determination of the local micellar structure in micellar samples at finite concentrations.

Here I present experimental results from a detailed small-angle neutron scattering study of polymer-like lecithin reverse micelles (for details see [41, 42]). SANS experiments with polymer-like lecithin reverse micelles in cyclohexane provide an ideal test for the applicability of IFT and SQDEC methods. In cyclohexane, the water-induced formation of giant cylindrical micelles occurs at relatively high values of the molar ratio water-to-lecithin, w_0 , which according to the previously postulated model for the micellar structure should lead to a tubular arrangement with a well defined water core and a surfactant shell. One thus has the possibility to dramatically modify the cross-section excess scattering length density profile $\Delta\rho(r)$ by using deuterated cyclohexane as the solvent and either H_2O or D_2O . This is demonstrated in Fig. 7, where a schematic drawing of $\Delta\rho(r)$ versus the cross-section radius R_c is shown for $w_0 = 14$ and both H_2O as well as D_2O . From an application of the IFT and SQDEC methods to SANS data obtained on absolute scale, one should be able to resolve the corresponding variations in $\Delta r(r)$ and obtain quantitative agreement with the known scattering length densities of the water core and the lecithin headgroup and tail regions.

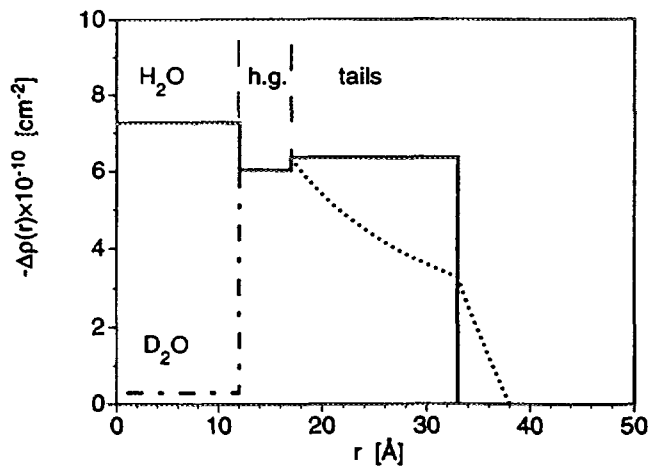


Fig. 7: Schematic representation of the expected radial cross-section excess scattering length density profiles for lecithin reverse micelles in deuterated cyclohexane with a molar ratio of water to lecithin $w_0 = 14$ with either H_2O ($\Delta\rho^{H_2O}(r)$, solid line) or D_2O ($\Delta\rho^{D_2O}(r)$, dashed-dotted line) as based on a simple model of tubular aggregates with a well defined water core and surfactant shell. Also shown is the result of a simple geometrical model that includes solvent penetration into the tail region as the dotted line.

The results from measurements with lecithin reverse micelles in deuterated cyclohexane at $w_0 = 14$ and a lecithin concentration of $C = 30 \text{ mM}$ (which corresponds to a total (surfactant plus water) weight concentration of $C_w = 30.6 \text{ mg/ml}$ for $w_0 = 14.0$) are summarized in Fig. 8. We see from Fig. 8 that the exchange of H_2O with D_2O indeed results in a significant variation of the Q dependence of the scattering intensity $I(Q)$. If H_2O is used, both water and lecithin have comparable scattering length densities. The expected radial cross-section excess scattering length density profile $\Delta\rho(r)$ can then be approximated by a simple step function modified by the solvent penetration into the chain region at higher values of r , which will cause a smoother decay of $\Delta\rho(r)$ (Fig. 7). This results in the typical monotonically decaying scattering pattern of a locally cylindrical particle with an intermediate Q^{-1} dependence of $I(Q)$ followed by an exponential (Guinier) decay due to the cross-section form factor.[34] However, when D_2O is used instead of H_2O , the reduced excess scattering length density in the water core of the tubular reverse micelles results in a pronounced shell contrast (see Fig. 7), and a well defined first minimum of the cross-section form factor now becomes visible at high Q values. Having seen that the scattering data qualitatively agrees with our expectations based on the structural model of tubular reverse micelles, we can try to extract much more quantitative information on the local micellar structure by applying the indirect Fourier transformation (IFT) method to the experimental data.[36, 37] Starting point is again the decoupling approximation given by Eq. 3. Provided that $R_g > b > R_c$, for $bQ \gg 1$ the high- Q asymptotic behavior can then be expressed by

$$I(Q) = \left(\frac{\pi}{Q}\right) 2\pi \int_0^\infty \tilde{p}_c(r) J_0(Qr) dr = \frac{\pi}{Q} I_c(Q) \quad (6)$$

where the normalized cross-section distance distribution function $\tilde{p}_c(r)$ is given by

$$\tilde{p}_c(r) = \frac{2\pi C_w}{M_L} \int_0^\infty \Delta\rho(r') \Delta\rho(r+r') r' dr' \quad (7)$$

and $J_0(x)$ is the zeroth order Bessel function. Note that $\tilde{p}_c(r)$ and $I_c(Q)$ contain a factor C_w/M_L , which is important for absolute normalization.

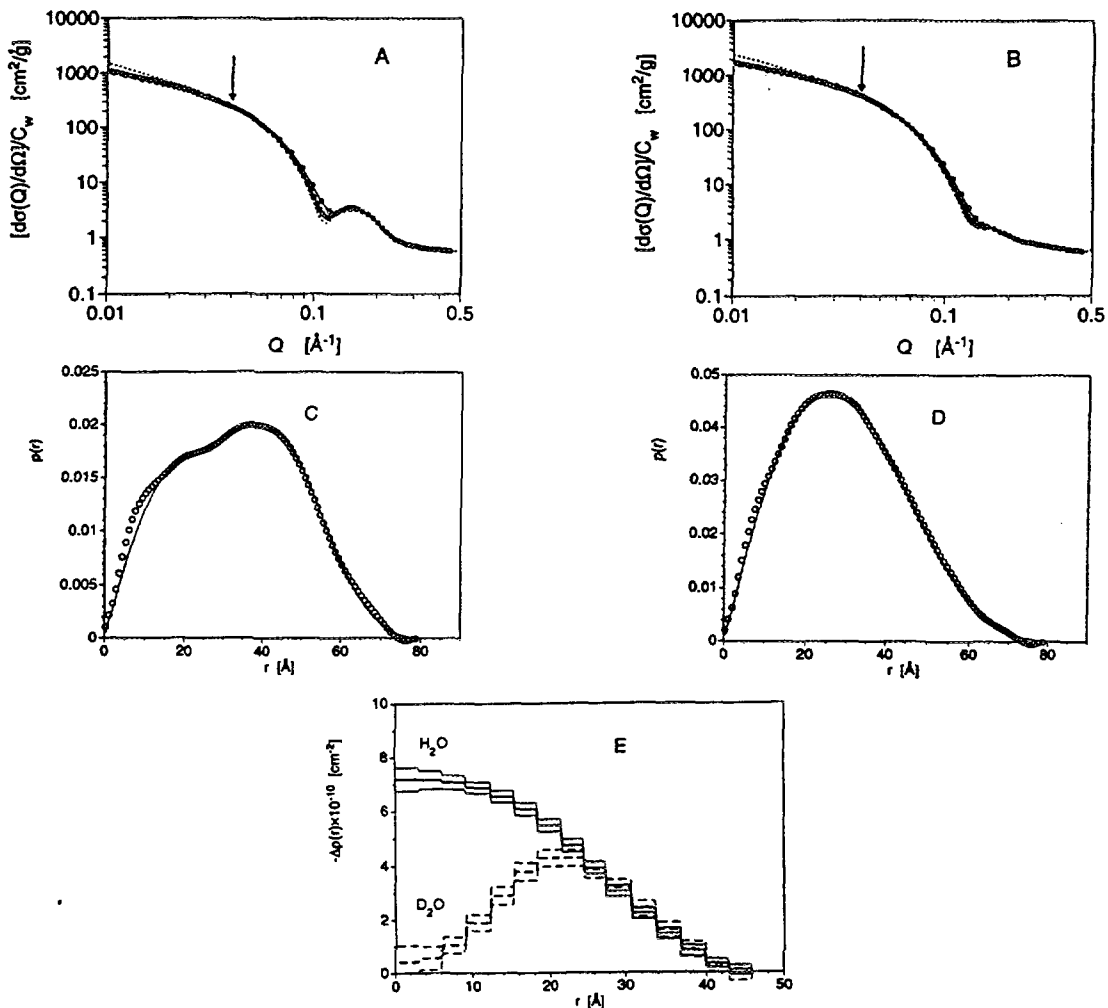


Fig. 8: A comparison of the experimental (o) and fitted (using the indirect Fourier transform method) normalized scattering intensity $[\mathrm{d}\sigma(Q)/\mathrm{d}\Omega]/C_w$ (A, B), the corresponding distance distribution functions $\tilde{p}_c(r)$ (C, D) and the radial cross-section excess scattering length density profiles (as obtained by the square-root deconvolution method) (E) for lecithin reverse micelles in deuterated cyclohexane at $w_0 = 14.0$: (A,B): $[\mathrm{d}\sigma(q)/\mathrm{d}\Omega]/C_w$ versus q for measurements with D_2O (A) and with H_2O (B). The solid lines correspond to the intensity smeared by the instrumental resolution, and the dotted line corresponds to the ideal intensity (Note that the data obtained with different combinations of neutron wavelength and sample-detector distance and the corresponding fitted curves are slightly shifted due to resolution effects.). Also shown by the arrow is the lower cut-off value of the q range used for the IFT. (C, D): $\tilde{p}_c(r)$ versus r as determined by IFT for measurements with D_2O (C) and with H_2O (D), respectively. Also shown as the full curves are fits to the data by the square-root deconvolution procedure for $\tilde{p}_c(r)$, resulting in the radial cross-section excess scattering length density profile $\Delta\rho^{H_2O}(r)$ (solid line) or $\Delta\rho^{D_2O}(r)$ (dashed line) shown in (E). The light lines in (E) indicate the errors in $\Delta\rho(r)$.

We can deduce a parameterized form of $\tilde{p}_c(r)$ through the IFT method. The lower limit $Q_{\min} = 0.04 \text{ \AA}^{-1}$ of the fitted Q -range (indicated by the arrows in Fig. 8) was chosen in accordance with the known Kuhn length of $b \approx 240 \text{ \AA}$.[32, 41] A very good fit of the experimental data can be achieved with the applied IFT method, and the thus

obtained $\tilde{p}_c(r)$ functions closely resemble the simulated functions for filled and hollow cylindrical particles (see for example Fig. 3 of ref. [41]). Furthermore, a well defined shoulder with an initially linear region below $r \leq 10 \text{ \AA}$ is also clearly visible and is most likely due to so-called diffuse longitudinal correlations as described in detail in ref. [41] (see Fig. 14 B in ref. [41]). The $\tilde{p}_c(r)$ functions vanish both in the "homogeneous cylinder" (H_2O) as well as in the "shell" (D_2O) contrast at approximately 70 \AA , thus qualitatively confirming the previously postulated geometrical model which would predict a cross-section radius $R_c \approx 30 \text{ \AA}$. Having determined $\tilde{p}_c(r)$, we can calculate the integral parameters of the micellar cross-section using the corresponding relations for the cross-section radius of gyration $R_{c,g}$

$$R_{c,g}^2 = \frac{\left(\int_0^\infty r^2 \tilde{p}_c(r) dr \right)}{\left(2 \int_0^\infty \tilde{p}_c(r) dr \right)} \quad (8)$$

the cross-section forward scattering intensity $I_c(0)$

$$I_c(0) = 2\pi \int_0^\infty \tilde{p}_c(r) dr \quad (9)$$

and the mass per unit length M_L in units g/cm given by

$$M_L = \frac{I_c(0)}{\Delta\rho m^2} \quad (10)$$

In addition to the evaluation of these integral parameters of the micellar cross-section, we can also aim at a quantitative estimate of the radial cross-section excess scattering length density profile $\Delta\rho(r)$ from the $\tilde{p}_c(r)$ functions using the SQDEC method as described in detail in ref. [41]. The resulting profiles $\Delta\rho(r)$ versus r in absolute units (cm^{-2}) as well as the agreement between $\tilde{p}_c(r)$ determined from IFT and fitted using SQDEC are also shown in Fig. 8 C-E. Except for the initial part of the $\tilde{p}_c(r)$ function, which is strongly influenced by diffuse longitudinal correlations and which therefore was not used in the fitting procedure, the fit using the SQDEC method results in good agreement. Moreover, the thus obtained excess scattering length density profiles $\Delta\rho(r)$ for H_2O and D_2O are in close agreement with the expectations based on the geometrical model and the known scattering length densities of lecithin and water. The clear difference in $\Delta\rho(r)$ at low values of r and the subsequent perfect overlap at higher values of r provides us with a first direct estimate of the extension of the water core. The values of approximately 20 \AA for the extension of the water into the headgroup region and approximately 22 \AA for the hydrophobic tail region are in good agreement with the geometrical dimensions of the lecithin molecule and the relative volumes of water, headgroup and tail region. Moreover, the entire data analysis has been performed in absolute units throughout, and no free parameters have been used to adjust the obtained $\Delta\rho(r)$ values such as to make them for example overlap in the tail region. The degree of overlap in the chain region between the data sets from samples with H_2O and D_2O is extremely good and provides us with a very sensitive test of the applied data normalization procedure. The cross-section excess scattering length density profiles given in Fig. 8 E provide us for the first time with a direct verification of the

previously postulated geometrical model of a tubular cross-section with a well defined water core and a surfactant shell for the structure of polymerlike lecithin reverse micelles.

3. Outlook

The preceding two sections have given a few selected examples on the application of SANS for a characterization of structural properties of soft condensed matter systems. These examples hopefully demonstrate how powerful a tool SANS can be in these areas, in particular when combined with contrast variation experiments and the application of suitable theoretical models. However, while these were quite classical examples of the application of SANS to soft condensed matter research, with the advent of more powerful SANS instruments with very high neutron flux and large two-dimensional detectors becoming available (such as for example D22 at ILL), new possibilities for experiments under non-equilibrium conditions and time-resolved studies of structural transitions and phase transitions become feasible.

4. Acknowledgement

These lecture notes have greatly benefited from contributions made by Carolina Cavaco, Stefan Egelhaaf, Götz Jerke, and Jan Skov Pedersen.

5. References

- [1] P. G. de Gennes, *Scaling Concepts in Polymer Physics* (Ithaca, N.Y.: Cornell University Press, 1979)
- [2] H. Fujita, *Polymer Solutions* (Amsterdam: Elsevier, 1990)
- [3] H. Yamakawa, *Modern Theory of Polymer Solutions* (New York: Harper & Row, 1971); Vol. .
- [4] R. Klein and B. D'Aguanno In *Light Scattering, Principles and development*; W. Brown, Ed. (Oxford: Clarendon Press, 1996); pp 30.
- [5] R. J. Hunter, *Foundations of Colloid Science* (Oxford: Clarendon Press, 1986)
- [6] J. N. Israelachvili, *Intermolecular and Surfaces Forces*; 2 ed. (London: Academic Press, 1992)
- [7] D. F. Evans and H. Wennerström, *The Colloidal Domain: Where Physics, Chemistry, Biology and Technology Meet* (New York: VCH Publishers Inc., 1994)
- [8] S. A. Safran In *Structure and dynamics of strongly interacting colloids and supramolecular aggregates in solution*; S. H. Chen, J. S. Huang and P. Tartaglia, Ed. (Dordrecht: Kluwer Academic Publishers, 1992); Vol. 369; pp 237.
- [9] M. Rawiso, R. Duplessix and C. Picot, *Macromolecules* **20** (1987) 630.
- [10] J. S. Pedersen and P. Schurtenberger, *Macromolecules (submitted)* (1996)
- [11] J. S. Pedersen, M. Laso and P. Schurtenberger, *submitted to Phys. Rev. E* (1996)
- [12] T. Yoshizaki and H. Yamakawa, *Macromolecules* **13** (1980) 1518.
- [13] H. Utiyama, Y. Tsunashima and M. Kurata, *J. Chem. Phys.* **55** (1971) 3133.
- [14] T. Neugebauer, *Ann. Phys. (Leipzig)* **42** (1943) 509.
- [15] D. Langevin, *Annu. Rev. Phys. Chem.* **43** (1992) 341.
- [16] U. Olsson and Wennerström, *Adv. Colloid Interface Sci.* **49** (1994) 113.
- [17] D. F. Evans, D. J. Mitchell and B. W. Ninham, *J. Phys. Chem.* **90** (1986) 2817.

- [18] M. E. Cates and S. J. Candau, *J. Phys.: Condens. Matter* **2** (1990) 6869.
- [19] G. Porte, J. Marignan, P. Bassereau and R. May, *J.Phys.France* **49** (1988) 511.
- [20] U. Olsson and P. Schurtenberger, *Langmuir* **9** (1993) 3389.
- [21] J. N. Israelachvili, D. J. Mitchell and B. W. Ninham, *J.Chem.Soc.Farad.Trans.II* **72** (1976) 1525.
- [22] B. Lindman, U. Olsson, H. Wennerström and P. Stilbs, *Langmuir* **9** (1993) 625.
- [23] D. Anderson, H. Wennerström and U. Olsson, *J. Phys. Chem.* **93** (1989) 4243.
- [24] M. S. Leaver, U. Olsson, H. Wennerström and R. Strey, *J. Phys. II* **4** (1994) 515.
- [25] M. Leaver and U. Olsson, *Langmuir* **10** (1994) 3449.
- [26] P. Schurtenberger and C. Cavaco, *J. Phys. Chem* **98** (1994) 5481.
- [27] T.-L. Lin, S.-H. Chen, N. E. Gabriel and M. F. Roberts, *J. Phys. Chem.* **91** (1987) 406.
- [28] R. P. Hjelm, P. Thiagarajan and H. Alkan, *J.Appl.Cryst.* **21** (1988) 858.
- [29] R. P. Hjelm, P. Thiagarajan, D. S. Sivia, P. Lindner, H. Alkan and D. Schwahn, *Progr.Colloid.Polym.Sci.* **81** (1990) 225.
- [30] R. P. Hjelm, P. Thiagarajan and H. Alkan-Onyukse, *J.Phys.Chem.* **96** (1992) 8653.
- [31] P. Schurtenberger, R. Scartazzini, L. J. Magid, M. E. Leser and P. L. Luisi, *J. Phys. Chem.* **94** (1990) 3695.
- [32] P. Schurtenberger, L. J. Magid, S. King and P. Lindner, *J.Phys.Chem.* **95** (1991) 4173.
- [33] M. A. Long, E. W. Kaler, S. P. Lee and G. D. Wignall, *J. Phys. Chem.* **98** (1994) 4402.
- [34] J. S. Pedersen, S. U. Egelhaaf and P. Schurtenberger, *J. Phys. Chem.* **99** (1995) 1299.
- [35] J. Marignan, J. Appell, P. Bassereau, G. Porte and R. P. May, *J. Phys. France* **50** (1989) 3553.
- [36] O. Glatter, *J. Appl. Cryst.* **10** (1977) 415.
- [37] O. Glatter, *J. Appl. Cryst.* **13** (1980) 577.
- [38] O. Glatter, *J. Appl. Cryst.* **14** (1981) 101.
- [39] O. Glatter and B. Hainisch, *J. Appl. Cryst.* **17** (1984) 435.
- [40] O. Glatter In *International Tables for Crystallography*; A. J. C. Wilson, Ed. (Dordrecht: Kluwer Academic Publishers, 1992); Vol. C; pp 89.
- [41] J. S. Pedersen and P. Schurtenberger, *J. Appl. Cryst.* (in press)
- [42] P. Schurtenberger, G. Jerke, C. Cavaco and J. S. Pedersen, *Langmuir* **12** (1996) 2433.
- [43] P. Schurtenberger, L. J. Magid, S. M. King and P. Lindner, *J.Phys.Chem.* **95** (1991) 4173.
- [44] P. Schurtenberger, L. J. Magid, P. Lindner and P. L. Luisi, *Prog. Colloid Polym. Sci.* **89** (1992) 274.



Polymer Surfaces, Interfaces and Thin Films

Manfred Stamm

Max Planck-Institut für Polymerforschung

Postfach 3148, 55021 Mainz, Germany

ABSTRACT

Neutron reflectometry can be used in various ways to investigate surfaces, interfaces and thin films of polymers. Its potential comes mostly from the possibilities offered by selective deuteration, where a particular component can be made visible with respect to its activity at the interface. In addition the depth resolution is much better than with most other direct techniques, and details of the profiles may be resolved. Several examples will be discussed including the segment diffusion at the interface between two polymer films, the determination of the narrow interfaces between incompatible polymer blends and the development of order in thin diblock copolymer films.

1. Introduction

Neutron reflectivity techniques are used in various areas of polymer science for the investigation of polymer surfaces, interfaces and thin films. This includes interdiffusion, blending, roughening, development of surface induced order, adsorption or surface enrichment of components. Several excellent reviews of different aspects in this area have been published (see e.g. reviews by Russell [1,2], Stamm and Schubert [3,4], Richards and Penfold [5] and Foster [6]). In those studies quite often the particular surface and interface properties are in the focus, but it is also tried in many cases to use the thin films as model systems for the determination of properties and parameters of the bulk state, which otherwise cannot easily be obtained. An example in both respects are polymer blend systems, where the surface induced ordering of diblock copolymers is a typical surface phenomena, while the segment diffusion across the interface of two polymer films and the determination of the interface width in incompatible polymer blends is used to draw conclusion on segment mobility and blend compatibility also for the bulk state.

We will use polymer blends and copolymers also here as examples to demonstrate the possibilities of the neutron reflectivity technique. Polymer blends and copolymers are used in an increasing area of applications, since they offer a cost effective way and a large potential to design optimized materials with properties tailored to quite a specific use. Thus polymer blends, composites and light-weight reinforced polymer materials are utilized for instance in various parts of cars or airplanes with different demands on material properties, which in addition also differ from manufacturer to manufacturer. The materials industry has to meet those demands for an increasing spectrum of applications, which is impossible to do through the development of chemically completely new polymers. Therefore existing materials are tried to be modified or blended, and the understanding of microstructures and polymer-polymer interactions gains increasing importance.

For this reason the question of polymer miscibility is attributed great importance [7,8]. Most polymers turn out to be incompatible with each other. They form microphase separated structures, when they are mixed together. To obtain good mechanical properties good cohesion between phases is required, and different materials have to interpenetrate with each

other at the interface [9,10]. This interpenetration depends on the degree of miscibility of components and is generally neither easy to determine experimentally nor easy to predict theoretically. For most incompatible materials, the interface is not very wide and typically in the range of 1 to 20 nm, depending on compatibility. This can be nicely measure by neutron reflectometry in a multilayer set-up as shown in Fig.1. If two incompatible polymers in the melt are put into contact, some interpenetration will occur. The interface width increases with time reaching an equilibrium value, which according to mean field theory is determined by the segment interaction parameter χ . From a more detailed and systematic knowledge of the interface parameters (for instance the interface width σ in Fig.1) for different polymeric materials, one could expect to obtain a better understanding of polymer miscibility.

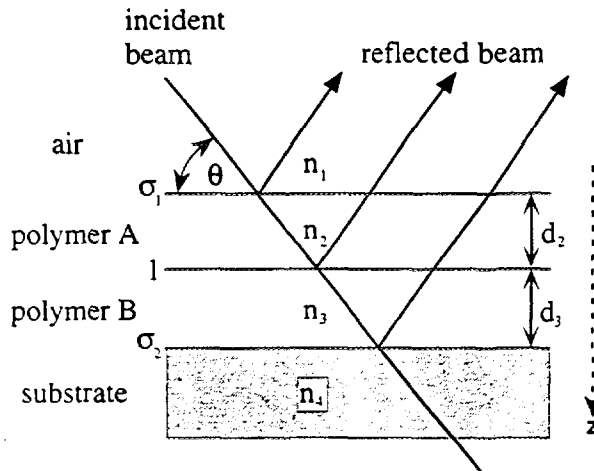


Fig. 1 Schematics of a neutron reflectivity experiment from two polymer films deposited on a substrate. Parameters indicated are film thicknesses d_i , indices of refraction n_i , interface widths σ_i and the angles of the incident and transmitted beam θ_i , respectively.

Besides equilibrium thermodynamic effects, other factors originating from sample preparation and experimental conditions also influence interface formation. Putting two films together, this includes the influence of initial surface roughness, surface composition and chain conformation at the surface of the films, which may largely depend on sample history. In specific cases it will be difficult to reach equilibrium, for instance when segment mobility is slow due to the vicinity of the glass transition T_g . It will generally be interesting to follow the time dependence of interface formation. Since the width for incompatible polymers is typically smaller than 20 nm, the resolution of techniques has to be adopted for a determination of interface width and profile [11,12,13]. Besides resolution requirements, a suitable contrast between components has to be present to be able to "see" the interface between the components. This contrast can be generated for neutron reflectometry, for example, by the suitable deuteration of one component. Neutron reflectometry is thus of quite general use, and also in multicomponent systems one component and its interfaces with other components can be made "visible" for neutrons. It is, however, in any case advisable to use other complementary surface and interface analysis techniques [11,12,13] including ellipsometry, x-ray reflectometry, interference microscopy, ion beam techniques, interface tension, electron microscopy or atomic force microscopy, which provide in many cases information, which cannot be obtained by neutron reflectivity alone and which helps considerably in the interpretation of the neutron results.

Since the technique of neutron reflectivity has already been introduced by the previous contributions, we will in the following only describe some specific aspects of polymers including contrast problems, sample preparation, and some instrumental details. Then we will

try to emphasize some of the advantages of neutron reflectometry as compared to the other most common techniques for the investigation of polymer surfaces and interfaces, and also will discuss some of the problems connected with this technique. We then will present some examples of polymer surfaces, interfaces and thin films demonstrating the possibilities and the potential of the technique in the area of polymer science.

2. General aspects for the application of neutron reflectometry to polymers

2.1 The contrast between components

Neutron reflectometry is a very versatile technique to investigate accurately interfacial aspects and thin films of polymers [1-6] since a contrast between components can in most cases be achieved by the deuteration of one component. It then provides a depth resolution typically of the order of 0.2 nm. The technique can be applied to practically all polymeric systems, provided one component can be deuterated. This might, however, require a significant effort from the chemical preparation side. Analogous to optics, one can specify a refractive index for neutrons :

$$n = 1 - (\lambda^2/2\pi) b \rho_n - i(\lambda/4\pi) \mu_n \quad (1)$$

$b\rho_n$ is the neutron scattering length density (b is the scattering length, ρ_n the particle number density), μ_n the linear absorption coefficient for neutrons, and λ the wavelength. The interaction between matter and neutrons is generally weak, and the refractive index n is very close to 1 (i.e. $n \sim 1-10^{-6}$). For neutrons true absorption is in most cases negligible. One may compare the situation to x-ray reflectometry, where the index of refraction is similarly given by an expression like equ.(1), but where $b \rho_n$ has to be replaced by $a_e \rho_e$. Here a_e and ρ_e now represent the classical electron radius and the electron density, respectively. To illuminate the contrast problem, the scattering densities for neutrons and x-rays for some materials are compiled in table 1. It is evident from a comparison of the deuterated and protonated materials that a large contrast can be obtained for neutrons by deuteration. In the case of x-rays, contrasts even for significantly different polymers are not large, and a typical situation is depicted in Fig. 2. Thus, X-ray experiments are only possible for the investigation of some particular polymer systems with large differences in the electron density, but neutron reflectometry proves to be a much more versatile technique due to the possibility to generate a huge contrast between components by deuteration. It should of course be kept in mind that deuteration also changes thermodynamics slightly, which, however, for many systems can be neglected.

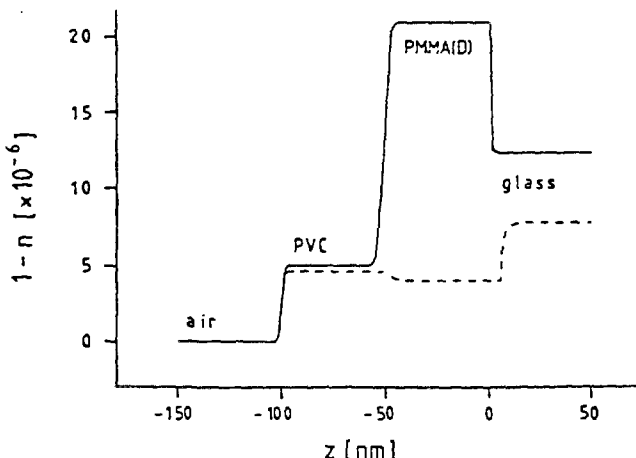


Fig. 2 Refractive index profile for neutrons (solid line) and x-rays (dashed line) of a layer system of PMMA and PVC on float glass

Compounds	chemical formulas	ρ [g cm ⁻³]	$a_e \rho_e$ [10 ¹⁰ cm ⁻²]	$b\rho_n(H/D)$ [10 ¹⁰ cm ⁻²]	μ_x [cm ⁻¹]	$\mu_n(H/D)$ [cm ⁻¹]
air/vacuum		0	0	0	0	0
PS	(C ₈ H ₈) _n	1.03	9.5	1.41/6.46	4	3.9/0.6
PMMA	(C ₅ H ₈ O ₂) _n	1.15	10.6	1.06/7.02	7	4.5/0.6
PVC	(C ₂ H ₃ Cl) _n	1.38	12.1	1.56/5.76	86	3.3/0.5
PBrS	(C ₆ H ₅ Br) _n	1.57	13.2	1.76/5.58	97	4.0/0.6
quartz	SiO ₂	2.3	19.7	4.20	85	0.2
silicon	Si	2.33	19.7	2.15	141	0.1
nickel	Ni(⁵⁹ Ni)	8.91	72.6	9.25 (12.9)	407	2.6
gold	Au	19.32	131.5	4.48	4170	3.3

Table 1. Characteristic data for the reflection of x-rays and neutrons at interfaces: mass density ρ_n , electron scattering densities $a_e \rho_e$, neutron scattering length densities $b\rho_n(H/D)$ for protonated (H) / deuterated (D) compounds, and linear absorption coefficients for X-rays and neutrons, μ_x (at a wavelength $\lambda = 0.154$ nm) and μ_n (at $\lambda = 0.1$ nm), respectively. The two values in some of the columns correspond to the H- and D- materials, respectively.

2.2 Sample preparation

Neutron reflectometry needs, however, a dedicated sample preparation, where relatively large (typically 5×10 cm²) thin films have for instance to be deposited on top of each other. Interfacial roughness (typically 1 nm or larger) also limits in some cases the resolution. A typical sample geometry is shown in Fig.1. A thin film of polymer A has been deposited by the floatation technique on top of a film of polymer B. Typical film thicknesses are in the range from 10 to 300nm, and to achieve a reasonable smoothness and surface roughness, spin coating techniques for the preparation of single films are used. A second film is mechanically deposited on another one by floating it off in a bath of water and picking it up with another film on a substrate. In this way even multilayer samples may be produced. Since both films are solid at room temperature, no interdiffusion takes place at the interface, but can be initiated by heating later. Water is removed by heating to a temperature below T_g under vacuum. Suitable substrates for film deposition are for instance float glass, silicon wafers or generally polished flat surfaces. Since the determination of a reflection curve takes between 2 to 12 h, samples are mostly annealed outside the reflectometer and then quenched for the neutron experiments below the glass transition temperatures of the materials. Because of the slow interdiffusion process of segments at the interface, samples sometimes have to be annealed for several days before the equilibrium interface width is achieved.

2.3 Instrumentation

There are generally two types of instruments existing described already before: single wavelength or time-of-flight reflectometers. The instrument TOREMA II at Geesthacht for instance utilizes a graphite monochromator and is operated at a fixed wavelength of 0.43nm (similar to [14]). In a reflectivity scan the sample is rotated and the reflected intensity recorded on the linear detector. In Geesthacht we are, however, presently constructing a new reflectometer PNR [15] at the end position of a neutron guide, which combines some of the elements of both set-ups (Fig.3). It utilizes a velocity selector, which allows in combination with a chopper the selection of a quite variable wavelength distribution (1 to 10%). Accordingly the intensity is significantly increased. The instrument may be operated in three different modes: (i) at fixed wavelength rotating the sample, (ii) at variable wavelength changing the wavelength with the velocity selector, or (iii) in TOF mode utilizing the chopper.

There are also polarization facilities and an area detector to also determine off-specular intensity.

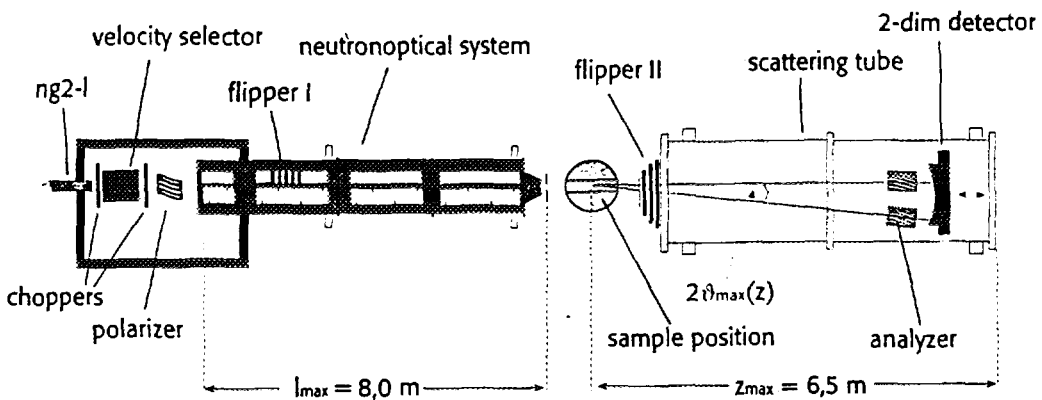


Fig. 3 Schematics of the polarized neutron reflectometer PNR at Geesthacht presently under construction.

2.4 Data analysis

The reflectivity as a function of the angle of incidence can be calculated from the refractive index profile using a matrix formalism [16]. Relevant parameters are indicated in Fig. 1. Error functions characterized by their variances σ_1^2 and σ_2^2 , respectively, are usually employed to describe the roughnesses of the interfaces air / polymer A and polymer B / substrate. A tanh-refractive index profile with the characteristic parameter l (see equ. (6a)) is commonly used between polymer A and B. Finally, the thicknesses d_2 and d_3 , and the refractive indices n_1 to n_4 are parameters for a fit, which, however, can be determined by separate measurements prior to the experiment for the determination of the interface width l . There are also techniques described for a model free fitting (see e.g. references in [4]). It is important to note that (specular) reflectivity techniques do not provide lateral information and reflection curves are averaged laterally over the sample (lateral coherence length is typically several micrometers). There is in principle the possibility to obtain lateral information from off-specular scans, which, however, in most experiments is not done for intensity reasons. Non-uniqueness of data analysis, which might be a problem in some more complicated cases of the application of the technique, is mostly not a problem for the analysis of a double layer system, since the starting situation is very well defined.

2.5 Advantages and limitations of the technique

There are several advantages of neutron reflectometry over other common interface analysis techniques. First the generation of the contrast by deuteration offers various possibilities. Thus for the same system also different contrasts may be chosen to reveal different aspects of the structure. Second the depth resolution of typically 0.2 nm is very good as compared to most other techniques. Thus also very thin interfaces can be still resolved and the resolution is mostly limited by the quality of the sample preparation. Third also hidden interfaces well within the material may be investigated. As an example neutrons can easily penetrate 10 cm of a silicon crystal to determine the interface between this crystal and a polymer in solution. Experiments under external fields (pressure, shear etc.) are therefore not so difficult. Finally the technique provides information also about various details of the shape of profile. This can be taken as an advantage, but in some cases may also turn out as a

disadvantage, since the interesting aspect may be hidden behind some other unexpected changes.

One thus might also note some of the disadvantages. The need of detailed model fits for the determination of parameters is certainly one of the main disadvantages. Those fit are usually not unique, and in some cases it turns out to be very time consuming to obtain reasonable fits. It is thus very helpful to obtain additional data on film thicknesses, roughnesses, surface enrichment of components etc. from other more direct techniques even if the resolution is much worse. Secondly the profile is averaged laterally, and it is very difficult to obtain information on lateral structures from neutron reflectivity alone. Here also other complementary techniques should be used. The large illuminated sample area thirdly poses severe requirements on the quality of the sample preparation, since samples have to be smooth on a nanometer-scale over several centimeters to achieve good depth resolution.

For a given problem it is thus very advisable to "compose" the sample already well in advance based on model calculations. One should try to obtain as much as possible additional information from complementary techniques, and it is hardly possible to obtain reliable results from multilayer systems or structured films without further knowledge about the sample.

3. Interfaces between incompatible polymers

As an example for the neutron reflectivity technique, where the good resolution together with a high contrast at the interface is needed, we will consider in some detail the formation of the narrow interfaces between incompatible polymers. In spite of the widespread use and application of incompatible polymer blends, only a limited number of experimental studies has been reported in literature. This is probably due to the fact that the narrow interface widths are hard to determine experimentally. Values reported from different techniques are then also not always compatible with each other and are scattered over quite a range. We will discuss some of the more recent investigations in more detail, where effect of compatibility, glass transition and temperature on interface width has been studied for several systems. A comparison of some data is given in table 2.

3.1 Theoretical aspects

For the description of phase behavior in polymer blends in a first approach the Flory, Huggins and Staverman (FHS) theory is used (for a review see e.g. [17]). With a lattice model a simple form for the free energy F_{FHS} of binary polymer blends including the segment interaction parameter χ is derived

$$\frac{F_{\text{FHS}}}{kT} = \frac{\phi \ln \phi}{N_1} + \frac{(1-\phi) \ln(1-\phi)}{N_2} + \chi \phi (1-\phi) \quad (2)$$

N_1 and N_2 are the degrees of polymerization, T is the temperature and ϕ is the concentration of one component. To discuss the problem of an interface between two polymers, equation (2) has to be extended by the so-called square gradient term $\kappa(\nabla\phi)^2$ introduced by Cahn and Hilliard [18] to take fluctuations into account. Due to different approximations there are different prefactors. A discussion of the prefactor is for instance also given in [19]. For the case, where structures are in the range of the radii of gyration (R_g) of components or smaller ($qR_g > 1$), one obtains a particular prefactor for the interface width $a_l = 2l$. An exact analytical solution for the volume fraction profile ϕ can be calculated for the case of infinite degrees of polymerization ($\chi N \gg 1$) using Euler-Langrange equation.

$$\phi(z) = \frac{1}{2} \left(1 + \tanh \frac{z}{l} \right) \quad (3)$$

where z is a coordinate across the interface and l is given by

$$l = \frac{a}{\sqrt{6\chi}} \quad (4)$$

a is the mean segment length of the components. For structures which are large compared to the radii of gyration ($qR_g \ll 1$) a different prefactor is derived

$$l = \frac{a}{\sqrt{9\chi}} \quad (5)$$

The influence of finite chain length on interface formation has been considered by several authors (for a review see e.g. [4, 17]). Three different methods yield slightly different expressions for the interface width l with finite chain length. Brosetta [20] derives the expression

$$l = \frac{a}{\sqrt{6\left(\chi - 2 \ln 2 \left(\frac{1}{N_1} + \frac{1}{N_2}\right)\right)}} \quad (6)$$

The fundamental result of the square gradient theory applied to the description of the interface between incompatible polymers is the direct connection of the interfacial width with the interaction parameter χ .

$$l \propto \chi^{-0.5} \quad (7)$$

In particular, computer simulations allow the incorporation of interactions and dynamics in a quite versatile way [21] and reveal asymmetry effects as well as the influence of fluctuations or capillary waves, which are mostly not included in analytic treatments. The analysis of experimental data on the basis of equ. (4) - (7) still has to be performed with care, since most experimental techniques measure an "apparent" interface width, which, due to lateral averaging, also contains the influence of lateral inhomogeneities, initial interfacial roughness due to preparation conditions and capillary waves or compositional fluctuations. Also not included in most theoretical treatments is the specific effect of chain ends, which may be enriched at the interface and which in general are of a different chemical nature as the rest of the chains including for instance some groups from the catalyst. The presence of a broad molecular weight distribution will also result in a broadening of the interface, in particular, if low molecular weight components are present. This effect can be estimated on the basis of equ. (6) and may lead to a fractionation of components at the interface.

3.2 Interfaces between Polystyrene(PS)/Polymethylmethacrylate (PMMA)

One of the most intensively studied incompatible blend systems is PS/PMMA. We have prepared a sample of a deuterated PS film ($M_w=720k$) on top of a protonated PMMA ($M_w=35k$) film by the floatation technique [22]. Both films were prepared by spin-coating from toluene solution. Substrates are float glass plates with a typical surface roughness of 1nm. Neutron reflectivity experiments have been performed at TOREMA II in Geesthacht. The reflectivity curves are shown in Fig. 4 before and after annealing for 24h at 140°C. Changes are observed in particular at large k_z corresponding to small interdiffusion distances. Also shown in Fig. 4 are the fit curves, which provide the interface widths. It changes from $a_l^0 = 3.0\text{nm}$ for the unannealed to $a_l^e = 4.6\text{nm}$ for the annealed sample. Also shown is a fit for the annealed sample assuming the interface width of the unannealed sample for the fit (Fig. 4c). This demonstrates the accuracy of the technique for the determination of the interface width, which is of the order of 0.4nm in this case. For the determination of the interdiffusion distance of the two materials one has to take the difference between the final and initial value,

$$a_l = \sqrt{(a_l^e)^2 - (a_l^0)^2} \quad (8)$$

The use of this equation assumes that the initial interfacial roughness does not change during annealing and that the two effects, interdiffusion and roughness, can be superposed. We similarly have performed experiments with PMMA materials of different molecular weights, showing the increase in interface width with decreasing molecular weight. The results are summarized in Fig. 5. Also shown in Fig. 5 is a fit curve based on equ.(6). From such a fit on the molecular weight dependence of the interface width one can obtain the two relevant parameters in equ.(6), the segment interaction parameter $\chi = 0.0326 (\pm 0.0058)$ and the segment length $a = 0.73 (\pm 0.13)\text{nm}$. From the measurement of interface parameters one thus can learn something about important thermodynamic quantities of this blend system. The segment interaction parameters for incompatible blend systems are not easy to obtain otherwise.

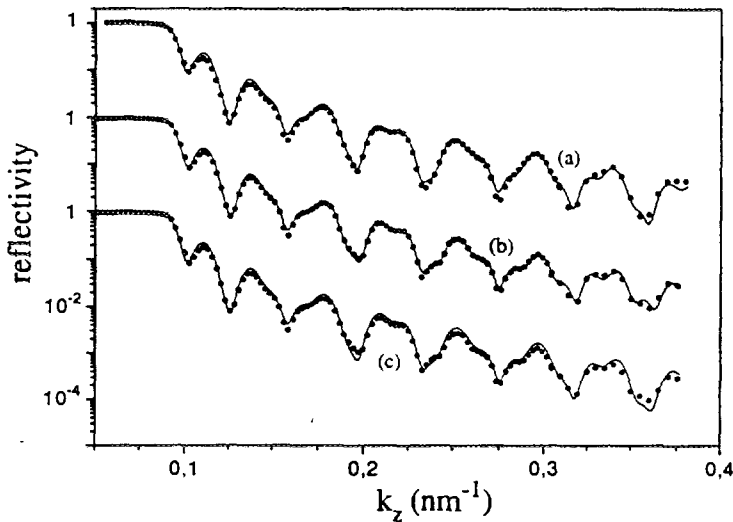


Fig. 4 Neutron reflectivity data and fits (solid lines) before (a) and after (b) annealing of a PS(D)/PMMA(H) double film system on a glass plate. The fit of curve (c) is performed with the interface width of the unannealed sample.

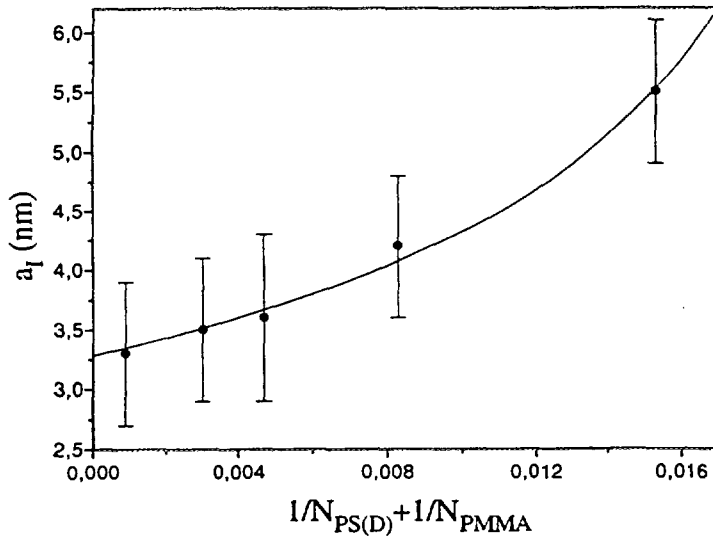


Fig. 5 Interface width of PS(D)/PMMA(H) as a function of the degree of polymerization. The solid line corresponds to a fit according to equ.(6) as explained in the text.

For comparison values of interface widths $a_l = 2l$ determined with different techniques are compiled in table 2. One of the most accurate values has been obtained by Anastasiadis et al. [23] with neutron reflectometry. It has been confirmed from other NR-studies of those authors with diblock copolymers, where also this interface width between lamellae is found to

be of the same size. The value of $a_i = 5.0\text{ nm}$ is also consistent with NR data of Fernandez et al. [23] after suitable recalculation of their original values. Both values are higher than the ones measured by us, but have not been corrected for initial roughness according to equ.(6). They can be expected to agree within error bars after the correction. Also, temperature dependent ellipsometry investigations [25] and transmission electron microscopy [26] yield similar results within error bars. Elastic recoil detection [27] on the other hand has to be taken with care, since, first, the profile is convoluted by the resolution function, which actually has a width of typically 12 nm and is thus much larger than the investigated interface width, and second, the oxygen profile is recorded, which might be influenced by contaminations of e.g. water at the interface.

Quite low values of the interface width are obtained when the interface width is calculated from interfacial tension data [19,28]. Those interface widths are approximately a factor of 2 smaller than the measured ones before correction for the initial roughness. End-group effects, capillary waves or surface contaminations on the other hand are usually not included in the theoretical treatments. End corrections and concentration fluctuation effects are considered in a recent calculation of Semenov [29], where he concludes that thermal fluctuations of the concentration at the interface can contribute as much as 2 nm to the interface width. In this approximation the coherence length of the reflection experiment enters, and results thus depend on experimental conditions. The agreement is good with a calculated interface width value obtained from a temperature dependent χ -value from SANS-experiments of diblock copolymers [30] on the basis of equ.(6).

Thus the neutron data are consistent with each other, if they are analyzed in a consistent way. They are also consistent with interfacial tension data, which can be taken as a proof of mean field theoretical concepts. Capillary waves and lateral fluctuations seem not to play an important role in the experiments or are already contained in the correction by equ.(6).

	a_i (nm)	T (°C)	$M_i(1)$ (10^3 g mol^{-1})	$M_i(2)$ (10^3 g mol^{-1})	Technique	Comments
PS/PMMA	5 ± 1	170	220	19	NR	—
	5.0 ± 0.5	170	110	107	NR	—
	$3-9 \pm 1$	140-170	180	151	ELLI	—
	5 ± 3	140	180	151	TEM	—
	8	140	180	151	ERD	Error not specified
	(2.6)	190	2-200	24	IT	Calculated from γ_∞
	(2.4)	199	2-43	10	IT	Calculated from γ_∞
	(4.9)	—	110	107	IT	Calculated from γ_∞ with fluctuation and end corrections
	(5.8)	150	13	14	SANS	Calculated from $\chi(T)$ of diblockcopolymer
	4.3-9.6 \pm 0.6		120-145	160	160	NR
PS/PBr _x S	$3.9-6.7 \pm 0.6$		142	100-1450	100-1450	NR, XR
	$3.5-4.9 \pm 0.4$		114-144	117	47	XR
						$x = 0.16-1.0$
						$x = 0.84-0.97$
						$x = 1.0$

Tab. 2 Interface widths of incompatible polymer systems determined by different techniques [4]

2.3 PS/poly(styrene-stat-para bromo styrene) (PBr_xS)

The blend system of PS and the statistical copolymer poly(styrene-stat-para bromo styrene) was chosen for systematic investigations of the dependence of interface width on

compatibility, since the compatibility between components can be easily tuned from completely compatible to highly incompatible by a change in the degree of bromination x . The molecular weight distribution of both partners is narrow. A systematic study of the change of the interface width with the degree of bromination has been performed by neutron reflectometry [31] and results are shown in Fig.6. At low x the interface width diverges, since the system becomes compatible. The functional form is fitted by a composition dependent χ -parameter, which contains the concentration-weighted individual segment-segment interaction parameters of components. Values at large x can be compared to other X-ray and neutron reflectivity data, as shown in table 2. The a_l -values quoted there are, for a better comparison, the ones which have not been corrected for initial surface roughness. There is a very good agreement between different data sets, if high molecular weight data are taken. Some of the differences between different data sets might be due to different temperatures, molecular weights, weight distributions and sample preparations. With some samples also the time dependence of the formation of an equilibrium interface has been followed [31], which is consistent with an initial $t^{0.25}$ -behavior and which then levels off to a constant value. In a compatible blend of PS/PBr_xS at low degree of bromination it has been shown by NR [32] that PS migrates to the interface. The form of the profile is consistent with an exponential decay. This system thus can serve as a nice model system with tunable compatibility and variable interface width.

4. Interdiffusion at the interface between compatible polymers

The interdiffusion between compatible polymers can proceed freely over large distances. Most interesting is, however, the segmental movement at early stages of interdiffusion. This can provide general information on the movement of segments of polymers in the melt, where for instance different time scales are discussed in the context of the reptation model. On the other hand this regime has very practical implications in the area of adhesion and welding, since the correlation between segment interdiffusion and mechanical strength at the interface is presently not very well understood. One might distinguish the "selfdiffusion" of a polymer into its deuterated analog versus the interdiffusion of one polymer into another compatible one. We will discuss mostly two cases, the already classical case of the diffusion of PS(H)/PS(D) as well as the interdiffusion of PMMA/PVC, where also the different chain mobilities play a dominant role.

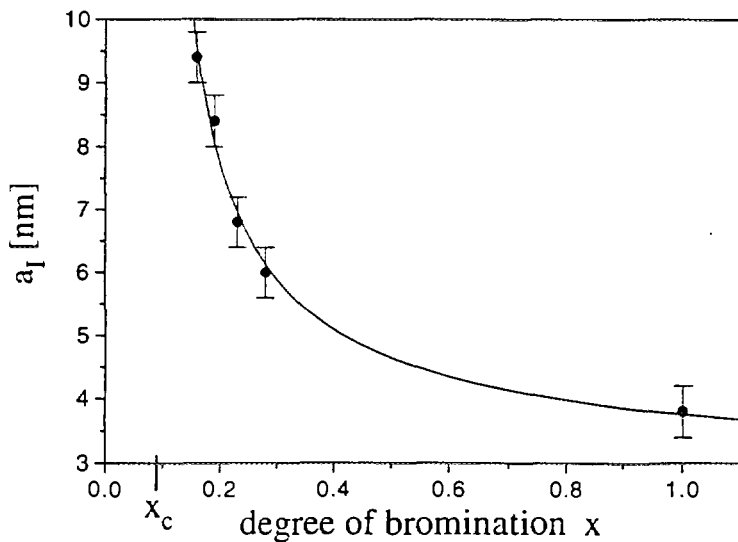


Fig. 6 Interface width as a function of the degree of bromination for the system PS(D)/PBr_xS(H) [31]. The solid line represents a fit according to theory.

4.1 Initial stages of segment diffusion at the interface

The interdiffusion of polystyrenes has been studied by several groups utilizing NR (for reviews see [1,2,3,5,6]). Again a deuterated PS-film is floated on a protonated one, and the broadening of the interface is followed by NR during a sequence of annealing procedures, where the sample is heated above the glass transition temperature (approx. 100°C) for a limited period of time, quenched to room temperature and investigated there. Thus with one sample the time evolution of the interface width can be studied. A typical example is given in Fig. 7, where the interface width is plotted versus the annealing time [33]. Clearly different regimes can be distinguished, which are consistent with the reptation predictions. According to the reptation model the diffusion of a chain in the melt is restricted by the entanglements with its neighboring chains. Different time regimes of segmental movement are predicted corresponding first to the movement in a virtual tube formed by the obstacles of the neighboring chains, while at later times the chain can reptate out of the tube. This behavior is nearly quantitatively observed for the movement of segments across the interface. One might on the other hand expect deviations from this ideal behavior due to distorted chain conformations at the interface, chain end effects etc. [3]. Those investigations are thus in strong support of the reptation picture, while the correlation with mechanical properties like adhesion is still not very well established.

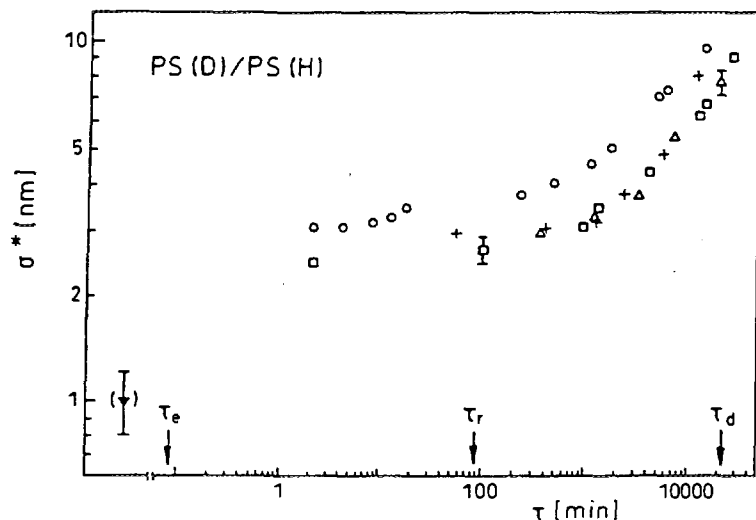


Fig. 7 Interfacial broadening as a function of annealing time for the system PS(D)/PS(H) [33]. The solid lines are guides to the eye. Typical times of the reptation picture are also indicated.

4.2 Influence of chain mobility on segment diffusion

For the case of the miscible blend system PMMA/PVC the mobilities of components are quite different due to different glass transition temperatures (116 and 75°C, respectively). Performing the interdiffusion experiment at a temperature of 114°C for instance, the PMMA material is still in its glassy state and cannot move. However, in a neutron reflectivity experiment (see Fig. 8) from a double layer system the dissolution of the immobile PMMA, being below its glass transition at the utilized temperatures, in the mobile component of PVC is observed [34]. This may be explained by a swelling and penetration of the PVC into the PMMA at the interface, leading to a dissolution. Correspondingly the interface moves into the direction of the PMMA film. Already at quite low concentrations of PMMA in PVC on the other hand the diffusion of PMMA to the surface is observed, resulting in a surface enriched layer of PMMA [35]. This is also seen in Fig. 8 at later diffusion times and can be confirmed by surface sensitive techniques like XPS or SSIMS.

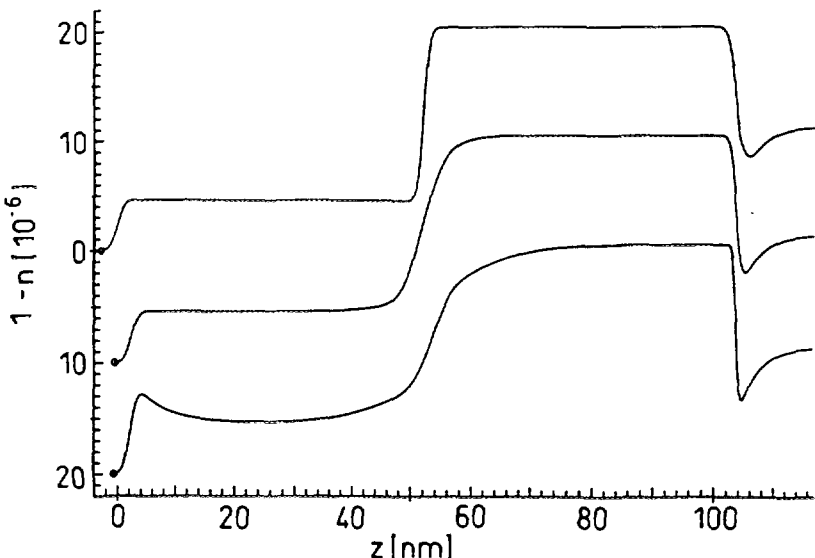


Fig.8 Refractive index profiles obtained from fits to neutron reflectivity curves at different times of annealing for the system PMMA(D)/PVC(H)[34].

5. Order in blockcopolymer thin films

In thin films of diblock copolymers the order induced by the interaction of the different blocks with the surface and substrate has been studied. This leads to a macroscopic ordering of the copolymer in the lamellar phase parallel to the surface. But also in the disordered phase there remains still some order in the vicinity of the surface, which decays with increasing distance.

A system well studied by NR is PS-b-PMMA, where in particular Tom Russell and coworkers have performed very extensive investigations (see reviews [1,2]). Thus it is shown [36] that a thin film in the ordered lamellar phase reveals a multilayered morphology parallel to the surface (Fig.9). The regular arrangement over large distances gives rise to Bragg peaks, while the Kiessig fringes are not resolved due to the large thickness of the film.

When a low molecular weight copolymer is heated into the disordered phase, the lamellar order in the film disappears, while some surface induced order close to the surface and substrate is retained (Fig.10). In subsequent investigations [37] it is shown that the profile at

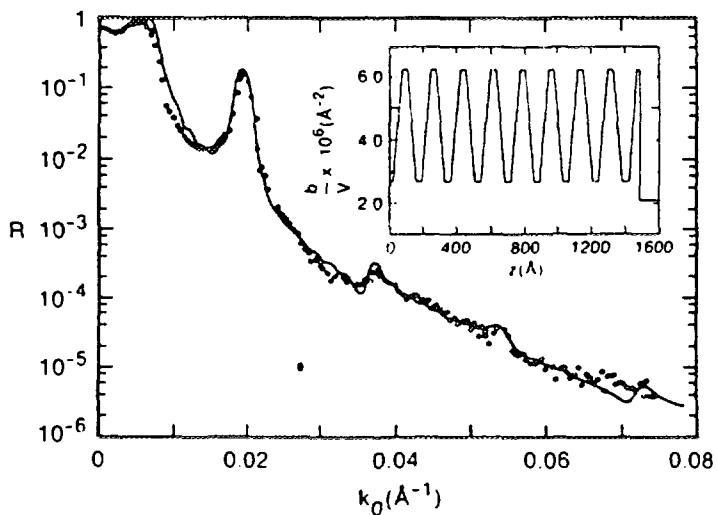
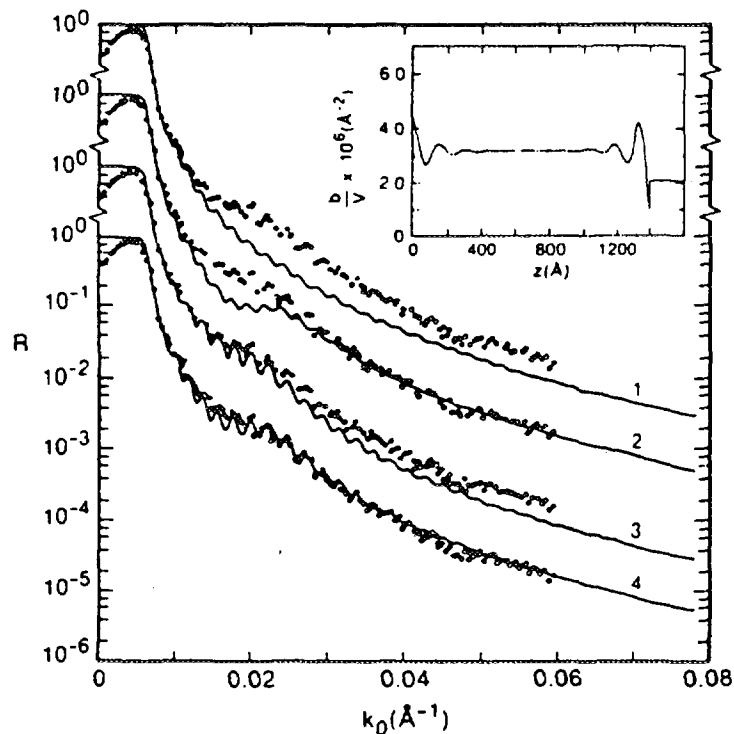


Fig.9 Neutron reflectivity curve and corresponding scattering length density profile (insert) of a thin diblock copolymer film of PS-b-PMMA annealed at 170°C for 24h (from [36]). The solid line corresponds to the fit with the shown profile.

the interface between the lamellae is best described by a hyperbolic tangent function, and that the width of the interface is 5nm. Thus there is no difference observed between the copolymers and the corresponding homopolymers. With very thin films the confined geometry gives rise to changes in the order. It also causes a change in the order-disorder transition temperature [38], which is increasing with decreasing film thickness.



*Fig.10 Neutron reflectivity curves of a thin PS-*b*-PMMA film in the disordered phase (from [36]). For comparison also fit curves with different model profiles are indicated: 1- uniform scattering length density, 2- exponentially damped cosine at the air interface, 3- at the substrate interface, and 4- from both interfaces. The curves have been offset by a factor of 10, respectively.*

6. Conclusions

Several examples of the application of neutron reflectivity for the investigation of polymer surfaces, interfaces and thin films have shown the potential of this technique in this area. Several other examples e.g. from the area of polymer adsorption from dilute solution to a solid wall, on the interfacial enrichment of copolymers in homopolymer films or the surface directed spinodal decomposition of polymer blends have not been treated. The technique, however, has been firmly established in the area of polymer science, and can provide information, which is otherwise hardly available.

Acknowledgments

I greatly acknowledge the contributions of Dr. B. Guckenbiehl, Dr. K. Kunz, Dr. D.W. Schubert and Dr. C. Bittorf to this work. Part of this work was supported by BMBF within grant 03-ST4MP2-1.

6. References

1. Russell, T.P., 1990. Mater. Sci. Reports 5: 171
2. Russell, T.P., 1991. Annual Review Materials Sci. 21: 249
3. Stamm, M., 1992. In: *Physics of Polymer Surfaces and Interfaces*. ed. I.C. Sanchez. Boston. Butterworth-Heinemann. 163
4. Stamm, M., Schubert, D.W., 1995. Annual Review Materials Sci. 25: 325
5. Richards, R.W., Penfold, J., 1994. Trends in Pol. Sci. 2: 5
6. Foster, M.D., 1993. Crit. Rev. Analyt. Chem. 24: 179
7. Olabisi, O., Robeson, L.M., Shaw, M.T., 1979. *Polymer-Polymer Miscibility*. New York. Academic Press. 370pp.
8. Utracki, L., 1989. *Polymer Alloys and Blends*. München. Hauser Publishers. 356pp.
9. Kausch, H.H., 1987. *Polymer Fracture*. Heidelberg. Springer Verlag
10. Brown, H.R., Ann. Rev. Mater. Sci. 21: 463
11. Stamm, M., 1992. Adv. in Pol. Sci. 100: 357
12. Tirrell, M., Parsonage, E.E., 1993. *Mater. Sci. and Techn.*, VCH, Weinheim, 12: 653
13. Allara, D.L., Zhang, P., 1994. Mater. Sci. and Techn., Vol. 2BII, VCH, Weinheim, 657
14. Stamm, M., Hüttenbach, S., Reiter, G., 1991. Physica B 173: 11
15. Bittorf, C., Stamm, M., Kampmann, R., Physica B, to be published
16. Lekner, J., 1987. *Theory of Reflection*, Martinus Nijhoff, Dordrecht
17. Binder, K., 1994. Advances in Pol. Sci. 112: 181
18. Cahn, J.W., Hilliard, J.E., 1958. J. Chem. Phys. 28: 258
19. Anastasiadis, S.H., Gancarz, I., Koberstein, J.T., 1988. Macromolecules 21: 2980
20. Broseta, D., Fredrickson, G.H., Helfand, E., Leibler, L., 1990. Macromolecules 23: 132
21. Müller, M., Binder, K., 1995. J.Chem.Soc.Faraday Trans. 91: 2369
22. Schubert, D.W., Stamm, M., 1996. Europhys.Lett., in press
23. Anastasiadis, S.H., Russell, T.P., Satija, S.K., Majkrzak, C.F., 1990. J. Chem. Phys. 92: 5677, and references therein
24. Fernandez, M.L., Higgins, J.S., Penfold, J., Ward, R.C., Shackleton, C., Walsh, D.J., 1988. Polymer 29: 1923.
25. Higashida, N., Kressler, J., Yukioka, S., Inoue, T., 1992. Macromolecules 25: 5259
26. Kressler, J., Higashida, N., Inoue, T., Heckmann, W., Seitz, F., 1993. Macromolecules 26: 2090.
27. Kressler, J., Zounek, A., Arai, E., Higashida, N., Sekimo, M., Inoue, T., to be published
28. Ellingson, P.C., Stand, D.A. Cohen, A., Sammler, R.L., Carriere, J., 1993. ACS/PMSE 69:183.
29. Semenov, A.N., 1994. Macromolecules 27: 2732; Semenov, A.N., to be published
30. Russell, T.P., Hjelm, R.P., Seeger, P.A. 1990. Macromolecules 23: 890.
31. Guckenbiehl, B., Stamm, M., Springer, T., 1994. Physica B 198: 127.
32. Guckenbiehl, B., Stamm, M., Springer, T., 1994. Colloids and Surfaces A86: 311.
33. Stamm, M., Hüttenbach, S., Reiter, G., Springer, T., 1991. Europhys. Lett. 14: 451.
34. Kunz, K., Stamm, M., 1994. Makromol. Chem., Macromol. Symp. 78: 105.
35. Kunz, K., Stamm, M., Harshorne, M., Affrossman, S., 1996. Acta Polymer. 47: 234.
36. Anastasiadis, S.H., Russell, T.P., Satija, S.H., Majkrzak, C.F., 1989. Phys.Rev.Lett. 62: 1852.
37. Anastasiadis, S.H., Russell, T.P., 1990. J.Chem.Phys. 92: 5677.
38. Menelle, A., Russell, T.P., Anastasiadis, S.H., Satija, S.H., Majkrzak, C.F., 1992. Phys.Rev.Lett. 68: 67.



LAYERED MAGNETS: POLARIZED NEUTRON REFLECTION STUDIES

HARTMUT ZABEL and ANDREAS SCHREYER
*Lehrstuhl für Experimentalphysik/Festkörperphysik
 Ruhr-Universität Bochum, D-44780 Bochum, Germany*

ABSTRACT

Neutron reflectivity measurements from extended surfaces, thin films and superlattices provides information on the chemical profile parallel to the film normal, including film thicknesses, average composition and interfacial roughness parameters. Reflectivity measurements with polarized neutrons are particularly powerful for analyzing the magnetic density profiles in thin films and superlattices in addition to chemical profiles. The basic theory of polarized neutron reflectivity is provided, followed by some examples and more recent applications concerning polarized neutron reflectivity studies from exchange coupled Fe/Cr superlattices.

1. Introduction

1.1. Neutron Optics

In the following we consider an elastic reflection experiment of unpolarized monochromatic neutrons. Furthermore, we assume that a collimated neutron beam impinges at a glancing angle Θ onto a flat and extended surface separating vacuum (air) and medium. The scattering vector $\mathbf{Q}_z = 2\mathbf{k}_{i,f} \sin(\Theta)$ points along the z -direction parallel to the surface normal, where $|\mathbf{k}_{i,f}| = 2\pi/\lambda$ is the magnitude of the incident and scattered wave vector. In vacuum the z -component of the neutron energy is

$$E = \frac{\hbar^2 \mathbf{Q}_z}{8m}, \quad (1)$$

where m is the neutron mass. At the interface between vacuum and medium the neutrons experience a potential step of height

$$V_n = \frac{2\pi\hbar^2}{m} n_A b. \quad (2)$$

Here n_A is the atomic number density and b is the coherent scattering length of the neutrons. The product $n_A b$ is usually referred to as the scattering length density. Total reflection occurs for $E \leq V_n$. Thus from Eqs. 1 and 2 for $E = V_n$ one obtains the critical scattering vector of total reflection:

$$Q_{c,z} = \sqrt{16\pi n_A b}. \quad (3)$$

Note that total reflection occurs only if the coherent scattering length b is positive, i.e. if $V_n > 0$. Then, for $Q < Q_c$ the neutron wave in the medium is exponentially damped within the medium, and for $Q > Q_c$ a Fresnel reflectivity is observed which drops

off with Q^{-4} . In case of thin films, Kiessig fringes are superimposed on the general Fresnel reflectivity due to the constructive interference of the neutron waves at inner and outer interfaces. Moreover, for multilayers with a periodic stack of layers along the z -direction and a repeat distance Λ , satellite reflections are observed at positions

$$Q_l = \sqrt{Q_c^2 + (l \frac{2\pi}{\Lambda})^2}, \quad (4)$$

where l is the order of the satellite reflection.

The true advantage of neutron reflectivity as compared to x-ray reflectivity measurements lies in the fact that neutrons carry a magnetic moment

$$\mu = \gamma_n \beta \sigma, \quad (5)$$

where $\gamma_n = -1.913$ is the gyromagnetic ratio of neutrons, and $\beta = e\hbar/2mc$ is the nuclear magneton. μ may interact with the magnetic induction \mathbf{B} in the sample, providing a magnetic potential for the neutrons

$$V_m = -\mu \cdot \mathbf{B} = -4\pi \mu \cdot \mathbf{M}. \quad (6)$$

Let us assume that a sample with a flat surface is in a ferromagnetic, single domain state and that the average magnetization vector \mathbf{M} makes an angle θ against the X-axis with a component $M_y = |\mathbf{M}|\sin(\theta)$ along the Y-axis, as indicated in Fig. 1. Furthermore, the magnetic moment of the incoming neutron beam shall be polarized parallel to the Y-axis.

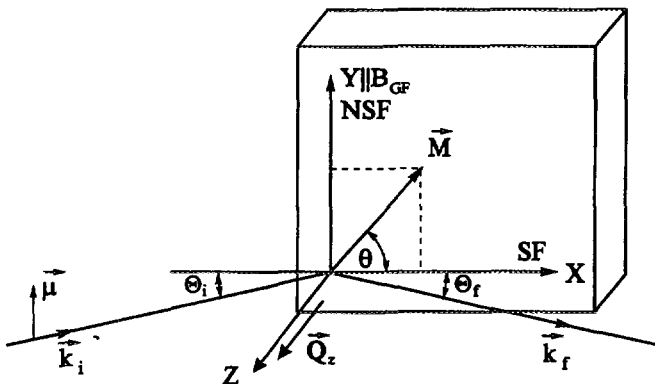


Figure 1: Schematic outline of the scattering geometry for polarized neutron reflectivity studies. The scattering triangle with the incident and final wavevectors \mathbf{k}_i and \mathbf{k}_f at glancing angles Θ against the surface is shown with the scattering vector \mathbf{Q}_z parallel to z . A small external neutron guide field \mathbf{B}_{GF} is oriented along the Y - axis to provide a polarization axis for the neutron magnetic moments μ parallel to Y. \mathbf{M} is the magnetization of the sample making an angle θ against the X-axis. Non-spin-flip or NSF scattering occurs for Y- and spin-flip or SF scattering for X-components of \mathbf{M} in the sample plane.

The neutron-sample scattering potential is modified according to:

$$V_{eff} = V_n \pm V_m, \quad (7)$$

where the (+) sign stands for a parallel alignment of μ and M_y (spin up) and the (-) sign for an antiparallel (spin down) alignment. Thus, for magnetic materials a bifurcation of the critical scattering vector occurs at small angles according to

$$Q_{c,z}(\pm) = \sqrt{16\pi n_A b_{eff}}, \quad (8)$$

where

$$b_{eff} = b \pm p \cos(\mu, \mathbf{M}) = b \pm p \sin(\theta). \quad (9)$$

Here $p = 2.695 n_B \times 10^{-4}$ nm is the magnetic scattering length, which is on the same order of magnitude as b and n_B is the number of Bohr magnetons. The variation of the scattering potential in a magnetic superlattice is shown schematically in Fig. 2(a) for the spin up (+) and in Fig. 2(b) for the spin down state (-) of the neutrons. The example is chosen such that the z -component of the kinetic energy E of the neutron beam is below the potential barrier of the magnetic layer in the (+) state, but above in the (-) state, demonstrating again the bifurcation of Q_c for magnetic materials.

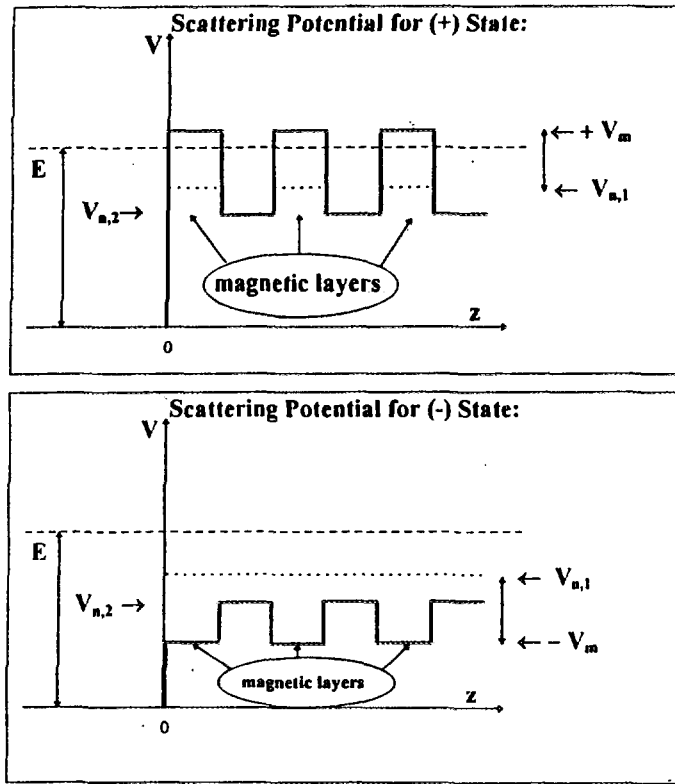


Figure 2: Scattering potential as seen by polarized neutrons in a magnetic multilayer with alternating ferromagnetic and non-magnetic layers. (a) shows the scattering potential for the spin up (+) state of the neutron and (b) for the spin down state (-). $V_{n,1}$ designates the nuclear potential of the magnetic material, $V_{n,2}$ the nuclear potential of the non-magnetic layer, and V_m the magnetic potential. Note that in the (+) state the z -component of the kinetic energy of the neutrons E lies below the potential height of the magnetic material causing a total reflection, whereas for the (-) state E is higher than all potential barriers.

As already pointed out, for magnetic materials the reflectivity of neutrons depends on the relative orientation of the sample magnetization vector \mathbf{M} and neutron moment μ , allowing to analyze the nuclear as well as the magnetic density profiles in the direction parallel to the surface normal. The X-component of the magnetization vector exerts a torque on the magnetic moment

$$\mathbf{T} = 4\pi (\mu \times \mathbf{M}), \quad (10)$$

which may flip the neutron spin during some optical path length from the up to the

down state. Therefore, the X-axis is called the spin-flip (SF) axis, while the Y-axis is the non-spin flip (NSF) axis.

It can easily be shown that for an unpolarized beam, the magnetic potentials average to zero. Therefore, the polarization of the incoming neutron beam is essential for analyzing the magnetic state of the sample. The method of polarized neutron reflectivity will be discussed more quantitatively in the following section.

1.2. Polarized Neutron Reflection

We refer again to Fig. 1 for the definition of the coordinate system and the polarization axis of the incoming monochromatic neutron beam. The incident neutron beam polarized parallel to the Y - direction shall be described by a wavefunction $\Psi_+(z)$, whereas a neutron spin - down state shall be described by a wavefunction $\Psi_-(z)$. The process of reflection of polarized neutrons is then described by the coupled system of Schrödinger equations:

$$\frac{\partial^2}{\partial z^2} \Psi_+(z) + \left[\frac{Q^2}{4} - \frac{2m}{\hbar^2} V_{++}(z) \right] \Psi_+(z) - \frac{2m}{\hbar^2} V_{+-}(z) \Psi_-(z) = 0 \quad (11)$$

$$\frac{\partial^2}{\partial z^2} \Psi_-(z) + \left[\frac{Q^2}{4} - \frac{2m}{\hbar^2} V_{--}(z) \right] \Psi_-(z) - \frac{2m}{\hbar^2} V_{-+}(z) \Psi_+(z) = 0 \quad (12)$$

For the case of a magnetic field in the sample plane, i.e. $\perp z$, the coefficients of the scattering potential V_{ij} are:

$$\begin{pmatrix} V_{++} & V_{+-} \\ V_{-+} & V_{--} \end{pmatrix} = \frac{2\pi\hbar^2}{m} n_A \left[\begin{pmatrix} b & 0 \\ 0 & b \end{pmatrix} + \begin{pmatrix} p_Y & p_X \\ p_X & -p_Y \end{pmatrix} \right]. \quad (13)$$

From Eq. 13 it follows that, apart from a constant factor, the scattering potential V_{ij} corresponds to the scattering length density of the form $n_A b_{eff} = n_A(b \pm p_{X,Y})$.

The following conclusions can be drawn. When V_{ij} with $i \neq j$ are zero, Eq. 11 and Eq. 12 are decoupled and only NSF scattering occurs, i.e. the neutrons maintain their spin state upon interaction with the sample. In this case, any magnetization vector \mathbf{M} has to be oriented along the Y-axis. Alternatively, any X-component of \mathbf{M} will induce SF scattering. Thus, by distinguishing between NSF and SF scattering, quantitative analysis of PNR data yields the *magnitude and orientation of magnetization vector \mathbf{M} in the sample plane*.

Solutions of Eq. 13 have been provided by several authors [1] [2] [3]. To analyze experimental data, theoretical reflectivities have to be calculated assuming a potential well structure $V_{ij}(z)$ composed of slabs of constant potential with sharp interfaces. Then a Parratt - type recursion formalism determines all transmitted and reflected amplitudes at each interface. Interface roughness, as it occurs in all realistic samples, is best taken into account by a large number of infinitely thin slabs of a gradually varying potential across an interface [4] [5].

In Fig. 3 a schematic outline of an angle dispersive reflectometer is shown with a spin - polarizer in the incident beam and a spin-analyzer in the scattered beam. Furthermore, spin π - flippers are placed between the polarizer and the sample and between the sample and the analyzer. A spin - down state is generated by activating a π - spin flipper in front of the sample. The second π - flipper after the sample verifies whether or not the neutron spin state has changed during the reflectivity process, since a supermirror in the exit beam acts as a spin - up filter. Thus, if both flippers

are de-activated, the NSF (+, +) cross section is measured. Alternatively, if both flippers are activated, the NSF (−, −) cross section is measured, and if one flipper is *on* while the other is *off*, the SF cross sections (+, −) and (−, +) are determined.

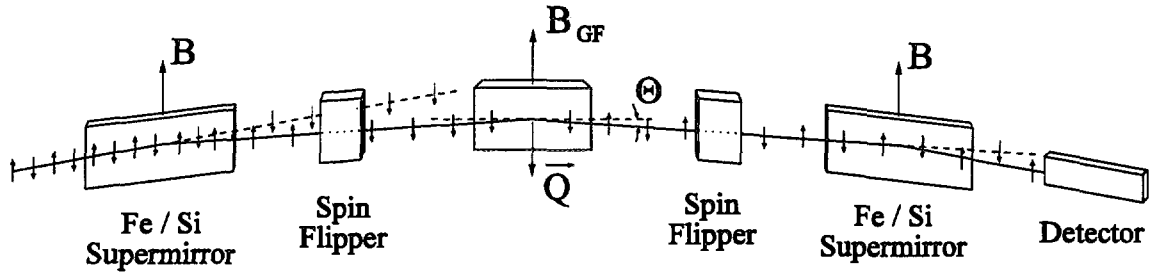


Figure 3: Schematic of a polarized neutron reflectometer showing the elements behind the monochromator. The instrument is shown reflecting the (−−) cross section with both spin flippers on. The small arrows denote the spin state of 'individual' neutrons. The polarizing supermirrors only reflect the (+) spin state.

2. Examples

Polarized neutron reflectivities have been calculated for illustrative purpose as they are frequently encountered in exchange coupled magnetic superlattices. The reflectivities as shown in Fig. 4 are based on a complete dynamical approach of neutron scattering as outlined above. The model superlattice consists of [Fe 40 Å/ Cr 40 Å]x10 double layers where one layer was chosen to be magnetic with nuclear and magnetic scattering length densities corresponding to Fe [$n_A b(Fe) = 8.05 \times 10^6 m^2$, $N_A p(Fe) = 5.09 \times 10^6 m^2$] and the other to be non-magnetic with a nuclear scattering length density corresponding to Cr [$n_A b(Cr) = 2.98 \times 10^6 m^2$]. An interfacial roughness of 4 Å at all interfaces was assumed. In the left column of Fig. 4 the direction of the magnetization vector in each magnetic layer is indicated as used in the model calculations.

Fig. 4(a) reproduces the neutron reflectivities for a ferromagnetically (FM) aligned superlattice with all moments pointing parallel to the Y-direction. In this case the chemical and magnetic periodicities are identical $\Lambda_{mag} = \Lambda_{chem}$. The NSF reflectivities (+, +) and (−, −) are characterized by a first Bragg peak at $Q_z = \sqrt{Q_c^2 + (\frac{2\pi}{\Lambda_{chem}})^2} = 0.8 \text{ nm}^{-1}$ and by N-2 thin film oscillations (Kiessig fringes) between the critical scattering vector Q_c and the first satellite peak, where N is the number of double layers in the superlattice. The strong intensity contrast between the (+, +) and the (−, −) reflectivities is due to the potential difference the up and down neutrons experience in the sample (see Fig. 2, and is a direct indicator of a large M_y component in the sample. Note that this can also be recognized by the different critical scattering vectors Q_c for the (+, +) and (−, −) states. There is no SF scattering since the magnetic moments of all ferromagnetic layers are oriented parallel to the Y-axis.

The second example in Fig. 4(b) considers an antiferromagnetically (AFM) stacked superlattice with a periodicity $\Lambda_{mag} = 2 \times \Lambda_{chem}$. In a weak magnetic field and assuming no magnetic anisotropy in the film plane, the moments will be in the spin flop state, i.e. \mathbf{M} in each Fe layer will be aligned in opposite directions parallel to the X - direction and perpendicular to the applied field parallel to the Y - direction.

This provides a maximum signal in the SF channel and a magnetic satellite peak occurs at $Q_z = \sqrt{Q_c^2 + (\frac{\pi}{\Lambda_{chem}})^2} = 0.4 \text{ nm}^{-1}$, indicating a doubling of the magnetic over the chemical unit cell. There is no corresponding peak in the NSF channel, since the projection of the magnetization parallel to the Y direction is zero. The Bragg peak at $Q_z = 0.8 \text{ nm}^{-1}$ in the NSF channels is of purely nuclear origin. The NSF (+,+) and (-,-) reflectivities are degenerate for all scattering vectors and in particular the NSF reflectivities are not split at Q_c .

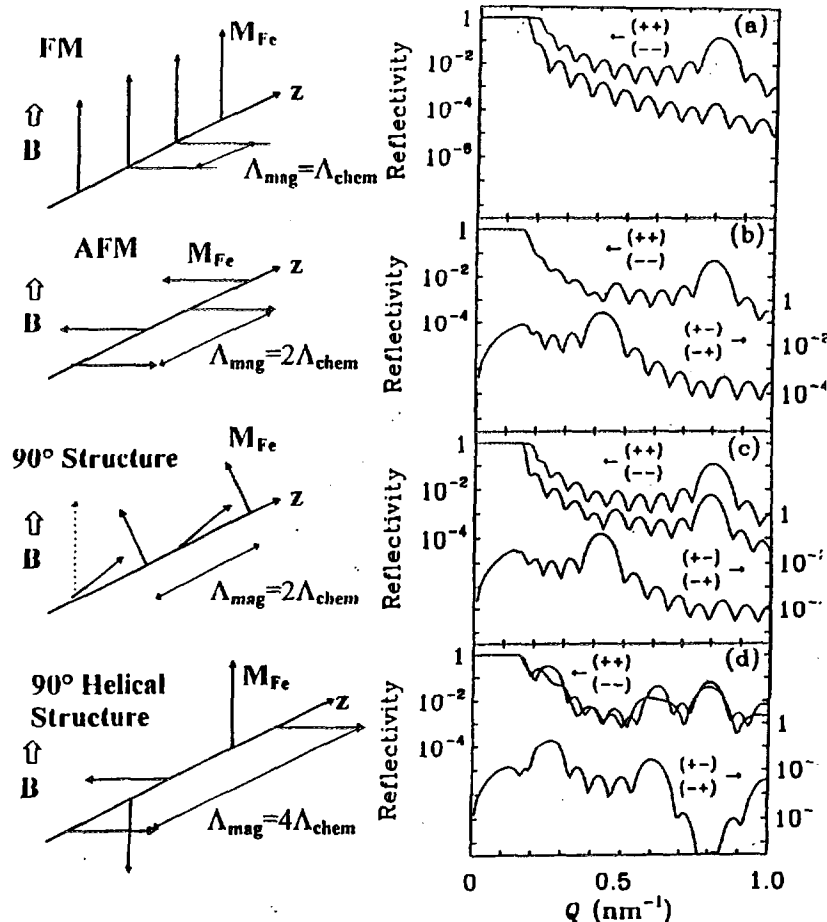


Figure 4: Dynamical calculation of neutron reflectivities for non-spin-flip (NSF) (+,+) and (-,-) and spin-flip (SF) (+,-) and (-,+) cross sections and for model magnetic structures of a 10 period superlattice with a period of $\Lambda = 8 \text{ nm}$. The left panel shows the direction of the magnetization vector in the magnetic sublayers having nuclear and magnetic scattering length densities corresponding to Iron. The non-magnetic spacer is not shown. The external field B designates the orientation of the neutron guiding field along the Y-direction as defined in Fig. 1. In the right panel the calculated reflectivities are reproduced for (a) a superlattice with parallel or FM alignment of M in alternate layers, in (b) for an antiparallel or AFM alignment. The next two examples refer to reflectivities from non-collinear magnetic structures, in (c) to a 90° magnetic structure and in (d) to a helical magnetic structure. The scales for NSF (left) and SF (right) reflectivities are off-set by two orders of magnitude for clarity.

In the next example we consider a 90° magnetic structure, as illustrated in the left panel of Fig. 4(c). This spin structure is representative for non-collinear spin structures which occur as a result of the competition between ferromagnetic and

antiferromagnetic exchange interaction in the presence of layer thickness fluctuations. The reflectivities are calculated assuming that the sample is rotated such that the magnetic moments in alternate layers make angles of $\pm 45^\circ$ against the Y - axis. Therefore, the projection of the magnetization onto the SF axis resembles the AFM case (Fig. 4(b)), whereas the projection along the NSF axis resembles the FM case (Fig. 4(a)). The PNR therefore consists of a reflectivity profile which can be regarded as a superposition of FM and an AFM contributions.

Finally, the reflectivities from a helical spin structure with 90° turn angle are reproduced in Fig. 4(d). In this case the magnetic periodicity is $\Lambda_{mag} = 4 \times \Lambda_{chem}$ and corresponding satellite peaks appear at positions $Q_z = \sqrt{Q_c^2 + (\frac{\pi}{4\Lambda_{chem}})^2}$ and at $Q_z = \sqrt{Q_c^2 + (\frac{3\pi}{4\Lambda_{chem}})^2}$ both in the NSF and SF channels.

3. Exchange Coupling and Non-Collinear Spin Structures

One of the most intriguing results of the research of thin magnetic films was the discovery of an oscillatory exchange coupling between FM layers mediated by paramagnetic spacer layers [6]. For the 3d ferromagnetic transition metals Fe, Co, and Ni the exchange coupling across non-magnetic films, such as Cu, Ag, Au leads to alternate parallel (FM) or anti-parallel (AFM) alignment of the neighboring magnetic layers. It was found that period, phase and amplitude of the oscillations sensitively depend on the Fermi surface of the paramagnetic spacer layer [7]. The exchange coupling through AFM Cr layers is different from the coupling through paramagnetic layers as strong *intra-layer* exchange interactions can interfere with *inter-layer* interactions. This effect is particularly important for the oscillatory exchange interaction with a two monolayer periodicity observed in the [001] direction of Fe/Cr superlattices. Steps and kinks at the interface of monolayer height lead to competing FM and AFM interactions, resulting in non-collinear magnetic structures, similar to those discussed in the previous section.

In Fig. 5 examples are shown of PNR scans from exchange coupled Fe/Cr superlattices. In (a) the reflectivities are reproduced from a FM coupled $[Fe_{52}/Cr_{17}]_5$ superlattice near remanence [8]. The subscripts denote the layer thicknesses in Å and the number of double layers, respectively. A weak guiding field of 17 G was applied parallel to the Y-axis. The splitting of the critical scattering vector and the reflected intensities for the (+,+) and (−,−) channels can clearly be seen. In this case there is no SF scattering since all moments are oriented parallel to the Y-axis.

By changing the Cr thickness, an AFM coupled Fe/Cr superlattices can be fabricated. Fig. 5(b) shows the reflectivities of a $[Fe_{52}/Cr_9]_5$ superlattice[5]. Indeed, the SF reflectivities exhibit a half order peak as expected for an AFM coupled superlattice, and the NSF intensities are degenerate. The weak half order peak in the NSF reflectivity can be modeled assuming only a 10% volume fraction of AFM domains being aligned parallel to the NSF axis, as shown by the fit to the data points plotted as a solid line in Fig. 5(b).

The drastic effect of a change in sample growth temperature on the exchange coupling in Fe/Cr superlattices can be seen by comparing Fig. 5(a) and Fig. 5(c). The data of the latter was taken from a sample of composition $[Fe_{52}/Cr_{17}]_9$ which was grown at an elevated temperature of 250°C.

The striking features of this scan include a splitting of the (+,+) and (−,−) intensities in the NSF channel along with a strong SF scattering and a half order

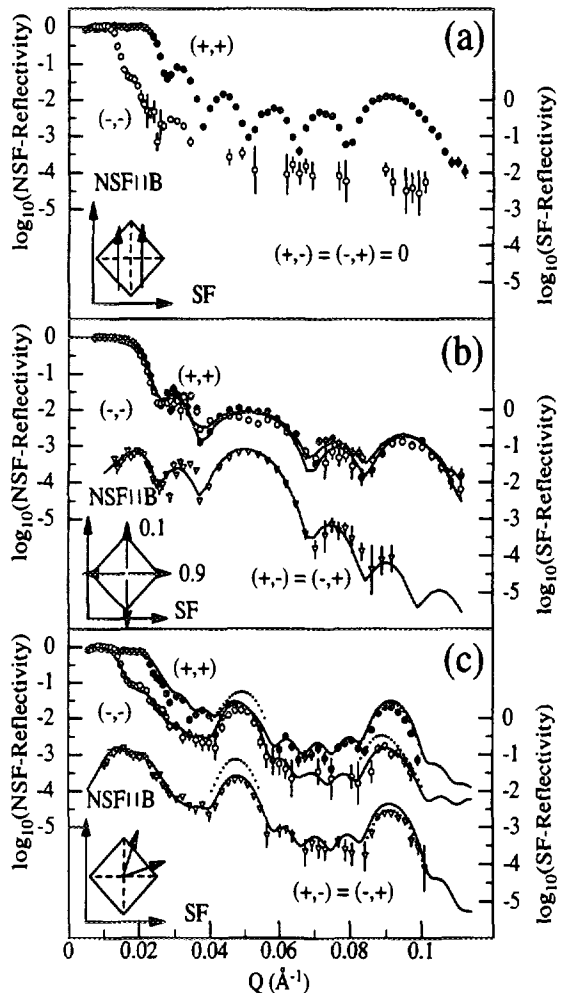


Figure 5: Polarized neutron reflectivity measurements of Fe/Cr superlattices of different composition and growth temperatures (T_G) performed in a neutron guide field of 10 - 20 G after initial saturation along the NSF axis. (a) ferromagnetically ordered superlattice $[Fe_{52}/Cr_{17}]_5$, $T_G = RT$; (b) antiferromagnetically coupled superlattice $[Fe_{52}/Cr_9]_5$, $T_G = RT$; (c) non-collinearly coupled superlattice $[Fe_{52}/Cr_{17}]_9$ ($T_G = 250^\circ C$) with an angle between the magnetic moments in consecutive Fe layers of 50° , as indicated by the inset. For details see text. The insets in the lower left hand corners show the orientation of the samples with respect to SF and NSF axes. The arrows indicate the spin orientations and the dotted lines the easy axes in the Fe(001) plane.

peak in both channels. The NSF intensities signify a resulting component of the magnetic moments projected along the Y-axis. At the same time the SF scattering suggests the presence of magnetic moments projected into the X-axis with an anti-ferromagnetic doubling of the repeat distance, which is also seen in the NSF channel. Taking into account the known magnetocrystalline in-plane anisotropy, the measured reflectivities are inconsistent with superimposed scattering from FM and AFM coupled domains [8]. Careful quantitative analysis of the reflected intensities using the complete quantum mechanical formalism for all reflected and transmitted waves, as sketched in section I.B, revealed a non-collinear spin-structure of the magnetic moments in consecutive Fe layers which make an angle of 50° between them. The solid lines represent best fits to the SF and NSF data points assuming a 50° spin structure as schematically shown in the inset [8]. It should be noted that the non-collinear spin structure in this [Fe/Cr] superlattice is highly coherent as recognized by the width and intensity of the half order peaks. Furthermore, a model assuming a purely bi-quadratic coupling of the Fe-layers with an angle of 90° between consecutive layers can not describe the data well, as shown by the dotted line in Fig. 5(c). Therefore, the reflectivities from this [Fe/Cr] superlattice are indeed due to a non-collinear 50° spin structure. Reviews of recent PNR work can be found e.g. in Refs. [10] and [11].

Non-collinear spin structures arise from competing FM- and AFM exchange interactions in [Fe/Cr] superlattices. This competition, in turn, is due to an uncorrelated interface roughness leading to fluctuating Cr-layer thicknesses on large lateral length scales [8] [9]. Moreover, the Cr layer is expected to have an antiferromagnetic spin structure. Presently there is much interest to illuminate the mutual interdependence between the exchange coupling, the Cr spin structure, and the interfacial roughness. Understanding these correlations is relevant for optimizing the technologically important giant magneto-resistance effect first discovered in [Fe/Cr].

4. .Outlook

We have shown that polarized neutron reflectivity provides quantitative analysis of the vector magnetization in individual magnetic layers of a superlattice. Therefore, precise information on collinear and non-collinear magnetic structures in superlattices as well as on the magnetization vector of individual layers follows from fits to the SF and NSF reflectivities. This information can hardly be obtained by any other method.

As is well recognized for x-ray scattering, the off-specular diffuse intensity contains important information about the correlated and uncorrelated roughnesses of interfaces. PNR offers the unique opportunity to study the magnetic roughness in addition to the structural roughness. In transverse SF scans the diffuse scattering can be analyzed from interfacial magnetic disorder and compared with the structural roughness as observed by transverse scans in the NSF channel. Diffuse magnetic scattering has not been studied extensively in the past. It will, however, increasingly be useful in the future with the advent of new instruments at high flux sources.

Another important direction for future applications of PNR is the combination of high and low angle data. At high angles the magnetic moments are probed on an atomic level, whereas at low angles the average magnetization density within a layer is analyzed. In complex magnetic films and superlattices both structures depend on each other. For instance, the exchange coupling in Fe/Cr superlattices depends on the magnetic state of the Cr sublayers. Their spin structure, however, can only be analyzed in the region of AFM Bragg reflections. Therefore, in the future

neutron reflectivity measurements will have to be extended to higher angles. Due to intensity problems those scans will have to be done with neutron instruments at high flux neutron sources. The new reflectometer/diffractometer "ADAM" is designed for measurements up to high scattering vectors [12]

While PNR is an extremely useful tool for the investigation of spin structures with in-plane magnetization, as exemplified above, it cannot resolve out of plane magnetic moments. Perpendicular magnetization vectors occur in some superlattices and thin magnetic films due to surface anisotropy effects and are of particular interest for technical applications in recording media. The insensitivity of neutrons to the perpendicular orientation is due to the selection rule for magnetic neutron scattering, which requires that the scattering vector $\mathbf{Q}_z \perp \mathbf{M}$. To overcome this problem, a scattering geometry has to be applied with the scattering vector \mathbf{Q} oriented parallel to the sample surface. This scattering geometry is known as surface neutron scattering or grazing angle diffraction (GAD) [13] and is available at the instrument "EVA" at the Institute Laue-Langevin (Grenoble) and the at NG-7 of the NIST research reactor (Gaithersburg). Both, PNR and GAD, will be increasingly important tools for the study of magnetic surfaces and interfaces. In the future neutron scattering, which traditionally has been a bulk method, will contribute more and more to the science and technology of thin magnetic films, surfaces and interfaces.

Acknowledgements

The data shown here have been collected at the instrument BT-7 of the Research Reactor at the National Institute of Science and Technology, Gaithersburg, USA. The authors would like to thank C.F. Majkrzak and J.F. Ankner for a very fruitful collaboration and many discussions. Furthermore we would like to thank M. Schäfer, J.A. Wolf and P. Grünberg for the preparation of the samples. This work was supported by the German BMBF under contract ZA3BOC, the DFG under SFB 166, and by NATO (CRG901064).

- [1] G.P. Felcher et al., *Rev. Sci. Instrum.* **58** (1987) 609.
- [2] C.F. Majkrzak, *Physica B* **156 & 157** (1989) 619.
- [3] C.F. Majkrzak, *Physica B* **173** (1991) 75.
- [4] J.F. Ankner, in *Surface X-Ray and Neutron Scattering*, edited by H. Zabel and I.K. Robinson, *Springer Proceedings in Physics* (Springer, Berlin, 1992), Vol. 61, p. 105.
- [5] A. Schreyer, Ph. D. Thesis, Ruhr-Universität Bochum (1994), in English, available via the WWW at '<http://www.ep4.ruhr-uni-bochum.de/people/as>'.
- [6] see e.g. J.A.C. Bland and B. Heinrich (Eds.), *Ultrathin Magnetic Structures*, (Springer Verlag, Berlin, Heidelberg, 1994), Vols. I and II, or the review of B. Heinrich and J.F. Cochran, *Adv. Phys.* **42** (1993) 523.

- [7] P. Bruno and C. Chappert, *Phys. Rev. Lett.* **67** (1991) 1602, *Phys. Rev. B* **46** (1992) 261.
- [8] A. Schreyer, J.F. Ankner, Th. Zeidler, H. Zabel, M. Schäfer, P. Grünberg, and C.F. Majkrzak, *Phys. Rev. B* **52** (1995) 16 066; *Europhys. Lett.* **32** (1995) 595.
- [9] A. Schreyer, J.F. Ankner, M. Schäfer, H. Zabel, C.F. Majkrzak, and P. Grünberg, *Proceedings of the 4th International Conference on Surface X-ray and Neutron Scattering in Lake Geneva/Wisconsin/USA*, June 26 - 30, 1995, *Physica B* **221** (1996) 366.
- [10] C.F. Majkrzak, *Proceedings of the 4th International Conference on Surface X-ray and Neutron Scattering in Lake Geneva/Wisconsin/USA*, June 26 - 30, 1995, *Physica B* **221** (1996) 342.
- [11] G.P. Felcher, *Proceedings of the Workshop on the Use of Neutrons and X-Rays in the Study of Magnetism* in Grenoble/France, Jan. 21 - 23, 1993, *Physica B* **192** (1993) 137.
- [12] for details see ADAM's home page:
'<http://www.ep4.ruhr-uni-bochum.de/adam.html>'
- [13] H. Dosch, *Neutron News* **6** (1995) 19.

REVIEW ON USE OF NEUTRON RADIOPHOTOGRAPHY AT SACLAY NUCLEAR RESEARCH CENTRE

BAYON Guy
*Saclay Nuclear Research Centre DRE/SRO
91191 Gif sur Yvette, France*

ABSTRACT

The Commissariat à l'Energie Atomique (CEA) operates three research reactors at Saclay. Each of them is equipped with a Neutron Radiology facility. Osiris is involved in studies of nuclear fuel rod behaviour during accidental events. The underwater NR facility allows to obtain images of the rods before and after power ramp. The Orphée installation is devoted to industrial application of NR including non destructive testing and real time imaging. The main activity concerns the examination of the pyrotechnic devices of the Ariane launcher programmes. Other areas of interest are also described.

1. Background

The CEA became deeply interested in neutron radiology in 1966, thirty years ago. Following in the footsteps of our American and British friends, the earliest French installations saw the day at the pool-type reactors of the nuclear research centres in Cadarache, Grenoble, Saclay, and then Fontenay aux Roses. First with immersed devices, and then on beams extracted outside biological shieldings for industrial applications. Some of the early pioneers are well known, including Jean Louis Boutaine, Jean Pierre Perves, Gérard Farny and André Laporte, who all played a major role in the development of this new technique.

A 1972 report [1] lists twelve installations on seven CEA pool-type reactors. Added to these is a liquid reactor operating in pulsed mode, of which three copies were built at the Valduc, Marcoule and Cadarache centres. The CEA even considered selling this installation to industry, but failed in the endeavour. The production of neutrons by nuclear reactions using accelerators was also intensively researched in Grenoble, particularly by the team of Mrs. Breynat. Since then, neutron imaging activities have declined considerably, and the few remaining applications are essentially concentrated in Saclay.

The most important recent steps are indicated below :

- 1973 : commissioning of an installation specialised in the examination of irradiated PWR fuels (Isis reactor).
- 1981 : commissioning of the last immersed device in the pool of the Osiris reactor.
- 1982 : commissioning of the industrial installation associated with the Orphée reactor and final shutdown of the Triton reactor in Fontenay aux Roses.
- 1984 : commissioning of the installation of the Scarabée reactor in Cadarache.
- 1986 : commissioning of the tangential beam on the Isis reactor in Saclay.

1988 : final shutdown of the Mélusine reactor in Grenoble.

Another major deadline has already been set:

1997 : planned final shutdown of the Siloé reactor in Grenoble.

The Saclay installations are mounted on three reactors, Isis, Osiris and Orphée.

2. Nuclear applications of neutron radiography

The CEA conducts research on the physicochemical behaviour of nuclear fuels for pressurised water reactors (PWR). The safety engineers of the installations need to know the extreme conditions liable to cause failure of the zircaloy clads. Destructive tests on fuel rods with various burnups are performed in the hot laboratories for Electricité de France (operator of the French power plants) and Framatome (power plant builder and fuel producer). Major projects today are concerned with MOX (mixed U/Pu oxide) type fuels.

Neutron radiographic inspection is performed when the irradiated fuels arrive at Saclay. The Isis reactor was equipped in 1973 with a highly efficient installation which simultaneously examines five rods 4 m long in an automatic sequence. Thirty-five successive overlapping pictures provide a complete image of the rods, and the whole sequence takes 4 h.

The direct technique combines boron and lithium converters with cellulose nitrate film.

Two major events led us to interrupt the operation of this installation in 1994:

- (1) Decision by the CEA to discontinue examinations of irradiated rods in Saclay, and to transfer them to Cadarache.
- (2) Kodak discontinued the production of very long CN85 film.

This examination prior to destructive tests is now carried out by X-radioscopy in Cadarache.

Osiris is an experimental pool reactor that went critical thirty years ago next October. After the shutdown of the Siloé reactor in Grenoble at the end of 1997, and until the commissioning of the future reactor dedicated to nuclear power research programmes in 2005-2010, Osiris will be the CEA's only material testing reactor. Experiments conducted on Osiris are essentially material irradiations (nuclear fuels, metallic specimens, electrical cables and optical fibres, radioisotopes for medical use, ceramics for fusion, doped silicon etc.).

The neutron radiography device yet described [2] is a pyramidal collimator used as a means of systematic imaging for fuel irradiation programmes and as an analytical means to back up the in-line electrical instrumentation. The behaviour of the fuel rod clad in a transient phase is tested on Osiris by means of power ramps on short 60 cm rods. The

experiments take place in an irradiation loop that reproduces the service temperature and pressure environment. Neutron radiographic examinations of fuel rods before and after the ramp offer an indispensable complement to destructive testing and gamma scanning. The quantification of the residual inter-pellet space helps to estimate the linear power extracted from the rods. The device uses simple and proven techniques:

transfer technique with the use of dysprosium converters,

tightness by the formation of an ice seal in the pool by liquid nitrogen circulation.

Users expressed the need for a real-time radioscopy system, but the construction of a unit is faced with serious difficulties, and the project is currently under examination.

3. Industrial applications

The operation of the installation associated with the Orphée reactor began in 1982, when the Triton reactor was shut down for good. We celebrated the fifteenth anniversary of Orphée's first criticality last December. My predecessor, André Laporte, was solely responsible for designing and supervising the construction of this installation, which is still one of the world's best.

The irradiation cell is installed at the end of the G4 neutron guide [3]. The neutron fluence rate is $9 \times 10^8 \text{ n.cm}^{-2}.\text{s}^{-1}$. The beam has an area of $25 \times 150 \text{ mm}^2$. The spectrum is enriched with cold neutrons by a liquid hydrogen cold source placed in the heavy water tank. The average energy is $7 \times 10^{-3} \text{ eV}$ and the beam contains no gamma pollution. The rooms lying 70 m from the reactor are readily accessible from outside the building.

Orphée runs about 250 days per year. Subtracting weekends and holidays, this leaves nearly 180 days of availability to satisfy our clients. This graph shows the pattern of activity since 1982. A majority of our clients are French. Most of our work is concerned with production controls on pyrotechnic equipment, 70 % of it connected with the European Ariane space programmes.

So far, fifty-nine Ariane 4 launch vehicles (V87) have been launched, with only three failures. This rocket has three superimposed stages, and is equipped with strap-on boosters tailored to match the payload mass. The most powerful version can send 4.8 t into geostationary orbit. The missions of the pyrotechnic devices of this launch vehicle essentially include:

release of the strap-on boosters after combustion,

stage separation,

opening and jettisoning of the payload fairing,

destruction of the launch vehicle in the case of a malfunction.

Depending on the versions, between 400 and 500 parts are inspected by NR in Saclay for each launch vehicle. Launchings range from eight to ten per year. The neutron

radiograms are used by the manufacturers of the objects tested. Their discretion means that we have no information about the scrap rate detected by the examination. Yet it is certain that none of the launching failures can be ascribed to the pyrotechnic device. The steady increase in the mass of the satellites has led to the development of a new European heavy launch vehicle, Ariane 5, to replace Ariane 4 completely by the year 2000.

This new rocket features simpler design, with better overall reliability. Pyrotechnic devices continue to be used, but the total number of elements is smaller. The chief innovation is the generalised adoption of structural separation by sealed expandable tubes instead of traditional explosive cords. The explosive is confined in a flat tube near the structure to be cut, which contains a weaker small-section zone. The pressure generated by detonating the explosive deforms the tube, and the force applied causes the structure to break, tripping the separating devices of the two parts. The tube must remain totally sealed to avoid polluting the surrounding surfaces.

Neutron radiography of all the qualification devices began in 1994 in Saclay. The principle of 100% neutron radiographic inspection was adopted for about 330 different parts. The transmission lines of the explosion logic represent 200 elements for a total length of 400 m. During the qualification phase, neutron radiography and X-ray examination helped to identify nine different types of defect on the ends of the lines, some of which caused operating failures during the working tests.

These defects are listed in the table below, showing those which are detectable by neutrons, by X-rays, and their effect on operation. Note that three critical defects can only be detected by neutron radiography, fully justifying the systematic inspection of these products.

Type of defect	Visible with X-rays	Visible with NR	Potential in-service failure
Mechanical assembling N°1	Yes	No	No
Damage of cord during the welding	Yes	Yes if damage on Hexogen	Yes if damage on Hexogen
Mechanical assembling N°2	Yes	Yes	No
Bad settling of Hexogen in the cone	No	Yes	Yes
Bad settling of Hexogen in the rod	No	Yes	Yes
Alignment of cord	Yes	Yes	No
Two washers instead of one	Yes	Yes	No
Lack of Hexogen in the cord	No	Yes	Yes
Excess of welding flux	No	Yes	No

Ariane 5 solid propellant boosters (273 t each) are composed of three segments assembled together by tenon and mortise. As demonstrated by the terrible accident to the American Challenger shuttle, the tightness of this type of assembly is crucial. The Fig. 1

reproduces the neutron imaging of a flat mock-up of this connection. The material is 30 mm thick steel. The image faithfully reproduces the double O-ring selected by the engineers. The neutrons also help to observe all the artificial defects created specially in this material. Unfortunately, on-site inspection in French Guyana is unfeasible, and only leak tests are performed.

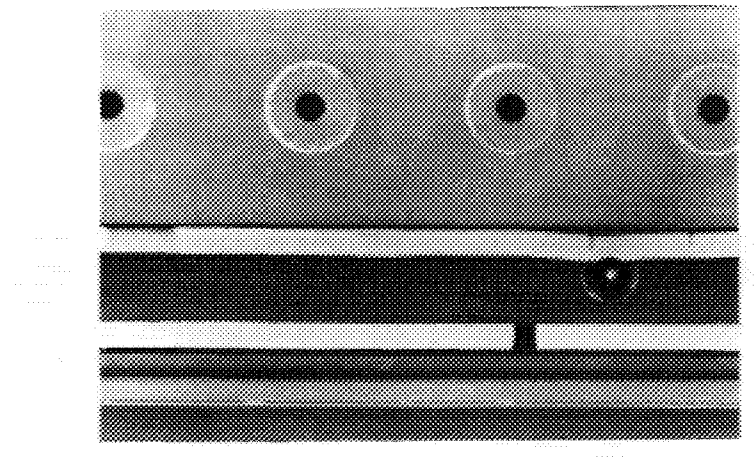


Fig. 1 NR of Ariane 5 booster connection flat mock-up.
Artificial defects in Nitrile O-rings (two parallel lines in white)

4. Metallurgical applications

The production controls regularly performed in Saclay in this area concern the localisation and/or quantification of natural boron dispersed in aluminium alloy plates. These plates are prepared by co-lamination of a composite containing a boron core obtained by powder compression. They serve as edge plates for fuel elements of our research reactors (Siloé, Osiris, Orphée). Boron is used as a burnable poison with reserve reactivity, and to flatten the axial neutron flux distribution.

The Orphée reactor has a very compact and highly reactive core. The safety authorities have imposed a complete quantitative inspection of the boron content of each plate. This quantification is carried out by comparative densitometry with standards of known boron content present in each picture. A special machine was developed, run by a PC. Accuracy of 3 % is obtained for each of the 130 measurement points on the surface of the boron core ($7 \times 60 \text{ cm}^2$).

Samples of welded boron steel sheets have also been tested by neutron radiography. This material is used in storage baskets for irradiated fuel elements and for the manufacture of transport casks.

Examinations have also been performed on samples of aluminium/lithium alloy prepared by microgravity [4].

5. Analytical services

Our services are sometimes enlisted on occasional problems faced by industrial firms. A recent example concerns the automotive industry. A brake hose crimping machine became maladjusted during a production phase. More than twelve thousand suspect parts were scrapped while awaiting a non-destructive testing method that could identify the acceptable parts. The problem was to measure the distance between the end of the flexible hose and the bearing plane of the metal fitting, with a maximum clearance of less than 1 mm. You can see from the Fig.2 that this is a typical case which is ideally resolved by neutron imaging. In the present case, considerable efforts to reduce the cost of the operation have been made and the company is going to convince the final client before testing the whole batch.

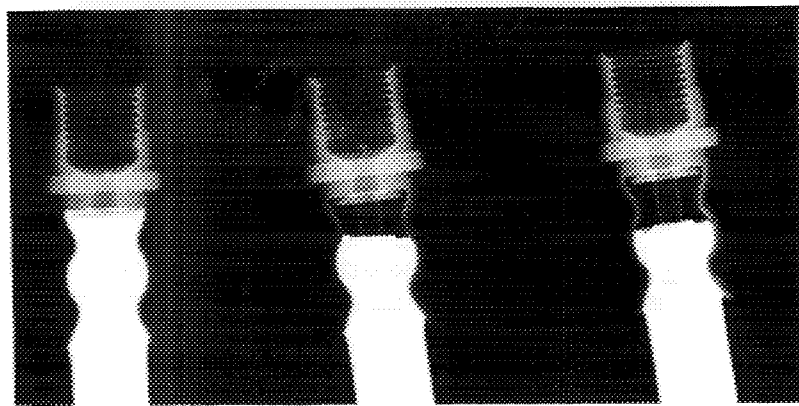


Fig. 2 NR of break hose ends. The hose external diameter is 10 mm.
Correct crimping on the left, two others have to be scrapped

6. Transfer of activity to industry

Our organisation, like many others, is prone to budget cutbacks. The resulting downward spiral in our staff began many years ago. The CEA had a staff of over 23,000 in 1984, and only 17,500 at the end of 1994. This policy has led management to refocus the organisation on its main research functions and to abandon production activities for private companies. On our modest scale, we have asked our industrial clients to test alternative sources to reactors. Sodern was naturally contacted with this aim, to determine the applications that could be satisfied using the demonstrator installed at Limeil Brevannes. Evaluation tests were recently initiated. The CEA will continue, as in the past, to offer neutron radiology services if the private sector fails to meet expectations.

7. Dynamic imaging

The only serious investigation completed in Saclay was presented at the last World Conference in San Francisco by Jacques Du Parquet [5]. The behaviour of the new generation of Freon-free refrigerants was analysed by neutron radioscopy. This project is now nearly finished, and we have had no new applications apart from a few feasibility tests on oil flows in automobile gearbox casings. In actual fact, prospecting is not very intense,

because our beam is now virtually completely occupied in routine production control activities. It would indeed be unfortunate if we were to entice new clients and then make them wait interminably before catering to their needs.

8. Autoradiography on paintings

This activity uses up very little beam time because the irradiations are performed at weekends. After having been dazzled by the work described by Dr. Fischer in our last world conferences, we proposed a joint project with the research laboratory of the Musée du Louvre. The question asked by all the curators was: "How can we be sure that irradiation is not harmful to the picture in the long term?" We nevertheless succeeded in working on a valuable painting in 1995, and the early test results are encouraging. We actually copied the procedures described in the bibliography, sometimes referring to Dr. Fischer for advice. A second and more constructive step is currently under way with the help of a trainee student. A model of samples of different pigments has been made, and will be tested for a closer assessment of the technique potential.

9. Technical developments

The Laboratoire Léon Brillouin (LLB), which finances and uses the Orphée reactor, has a plan for an overall improvement in its experimental facilities. This project, if validated by the Board of Administration, consists in modernising a number of spectrometers and in modifying the neutron guides, of which the passage cross-section will be doubled ($150 \times 50 \text{ mm}^2$ instead of $150 \times 25 \text{ mm}^2$). A new arrangement of the spectrometers would give us a much better flux (plus 40 percent). These major projects are scheduled during a long-term shutdown of about six months, when the zircaloy reactor vessel is replaced in late 1997.

For over fifteen years, the converters used for production control have been massive sheets of natural gadolinium. Since maintenance on these converters is difficult, we asked the CEA metallurgists in Grenoble to prepare vacuum-vapourised deposits coated with an abrasion-resistant layer. Titanium nitride was selected in the form of a $0.3 \mu\text{m}$ layer. We measured a loss of densitometric efficiency of 5 percent, which was deemed acceptable. We had flat converters measuring $150 \times 340 \text{ mm}^2$ and semi-spherical converters prepared to inspect 20 cm diameter coils. Our colleagues in Grenoble, having learned from this experience, are ready to examine any request they receive.

10. International relations

My predecessor André Laporte and I were always convinced of the value of exchanges with our foreign colleagues. The CEA has always been represented at the meetings of the Euratom Group of specialists in neutron radiography of the European Community, since the first meeting in 1979. Joseph Domanus was the chief artisan of the success of these meetings, for which he deserves our thanks. 1993 marked a sweeping change in our habits, because our Group was broadened to include the whole of Europe under the impetus of Joze Rant. The principle of the creation of this new Group was set down in Portoroz in Slovenia at a meeting of the European Nuclear Society. Russian colleagues participated in our meetings for the first time, and we have held a similar meeting every year since then: in Saclay in 1994, followed by Budapest in 1995, where I handed the chairmanship of the Group to Marton Balasko.

11. Conclusions

In conclusion, it is clear that activities around neutron imaging have declined in recent years. At the CEA, we nevertheless consider ourselves as privileged. Although reduced in number, we have succeeded in preserving research reactors and installations. These facilities operate with a high level of safety, and we are envied by many. Moreover, requests for inspections are received steadily from industrial firms, essentially from the aerospace industry. If I credit the declarations of the players in this area, Europe is determined to maintain a major role. Neutron imaging will accompany this development in France, just as it has done for more than twenty-five years.

References

- 1 DESANDRE-NAVARRE C., FARNY G., PERVES J.P. (1972), "La neutronographie sur les réacteurs du CEA", CEA-R-4208 Mars 1972
- 2 BAYON, G., PERSON, J.L. (1986), "Installations et programmes de radiographie aux neutrons auprès des réacteurs de Saclay", in BARTON, J.P. and al. (eds.) Neutron Radiography, proc. of the second world conference, D. Reidel Publishing Company, Dordrecht, 103-107
- 3 ZACCHEO, M., BERTHON, J., UZUREAU, G., and LAPORTE, A. (1981), "Use of a neutron guide in industrial neutron radiography", in BARTON, J.P., and VON DER HARDT, P, (eds.) proc. of the first world conference, D. Reidel Publishing Company, Dordrecht, 99-106
- 4 BAYON, G., DREVET, B., ILIC, R., HUMAR, M., RANT, J., NGUYEN, H. (1996), "Application of Neutron Radiography and Neutron Induced Autoradiography in the Study of Cellular and Dendritic Solidification of Al-Li Alloys" proc. of the fifth world conference(to be published)
- 5 DU PARQUET, J., BAYON, G., (1992), "Contribution of Neutron Radiography to the Conservation of the Environment", in BARTON, J.P., (ed.) proc. of the fourth world conference, Gordon and Breach Science Publishers, p 65

SUMMARY SCIENCE

STEPHEN W. LOVESEY
 Rutherford Appleton Laboratory, U.K.
 and
 EWALD BALCAR
 Atominstitut der Österreichischen Universitäten, Vienna, Austria

Techniques to investigate properties of condensed matter which use beams of neutrons are well established, and are applied to a broad spectrum of topics in condensed matter and materials research. The lectures at the School nicely represented the breadth and depth of current work. Participants were exposed in almost equal amounts to topics in magnetism and other sciences. The topics mentioned included some that are as old as the history of neutron beam research, e.g. the dynamic properties of water, first studied by neutron scattering by Brockhouse in the 50s (one could ponder the consequences on Life if water were a relatively simple molecular fluid which could be well understood after a mere 40 years of effort based on one technique).

Most topics, particularly in magnetism, chosen by lecturers were timely in the development of the subjects on which they spoke. In the past decade, driven to some extent by the discovery of ceramic (high T_c) superconductors, there has been renewed vigour in the discipline of magnetism. Examples which come to mind are the conjecture by Haldane of a pronounced dependence of the spin dynamics in one dimension on the size of the spin (so-called Haldane gap), materials that form spin ladders, giant magnetoresistance, and the static and dynamic properties of spin models on a two-dimensional lattice with spin-spin interactions more complicated than found in the Ising model. In the other sciences fundamental and unresolved problems include the nature of the glass transition, properties of supercooled fluids and turbulence. Techniques using beams of neutrons have had an impact on the first two topics, and a marginal role to date in the latter topic. A challenging field of science not addressed at the School in any depth was biology. However, as mentioned, the spectrum of potential topics for a School is broad and selection is, therefore, necessary (all being well, the Schools will continue and provide a forum to cover biology and other areas, in some depth).

There is no mistaking the strength of the scientific case for a greater supply of neutrons. In conjunction with supply is the pressing need for steady evolution in instrument performance, and methods to increase the flux of useful neutrons at the position of the sample. Various methods have been developed which together lead to increases of an order of magnitude, or more, on instruments fed by beams of neutrons from reactor sources that have not changed in power from the first day of operation, 20 or more years ago. Along with this go big strides in the realization of large efficient detectors. Efforts in these directions must continue, there is no room for complacency, since new sources with higher fluxes are unlikely to be built in the near future and demands placed on the neutron-beam techniques by the difficulty of the scientific questions will continue to grow. In the theme of better use of available neutrons one can renew the plea for better facilities to exploit the use of methods that rely on the states of polarization of the neutrons, in the incident and scattered beams; the presently available facilities are just about tolerable for beams of slow or thermal neutrons.

It is rightly emphasized that techniques which use beams of neutrons produce empirical data that are complementary to data produced with a variety of other techniques, e.g. NMR, light scattering, and Mössbauer spectroscopy. Together, these techniques form a formidable armoury to attack questions in condensed matter and materials research.

On the other hand, the other techniques are also competitors for dwindling funds. This fact is another good reason why users of neutron-beam techniques must not be complacent about the current relatively good position enjoyed in Europe, soon to be bolstered by the operation of SINQ and the accompanying suite of state of the art and innovative instrumentation. Continued effort by the user community is necessary to ensure a bright and healthy future, based on the development of good instruments, methods and sources of neutrons. Of course, the complementary techniques also improve and with this the boundaries of competence between the techniques shift with the passage of time. Perhaps, very few of us, ten years ago, would have correctly predicted the impact on condensed matter and materials research realized with techniques that use X-rays produced by particle accelerators. For the moment, at least, emerging techniques which use beams of X-rays pose a real challenge to those based on the use of beams of neutrons. The challenge to capture and hold the interests of bright young scientists for neutron scattering extends far beyond funding these, as well. (In this respect it seems also necessary to resist growing tendencies to judge applications for research funds on their guaranteed or predictable outcome, and to leave sufficient room and funding for the novel, new, and unpredictable.)

The last point should not need emphasis, other than to note that the quality of the science performed with any facility ultimately depends on the quality of the mind of the investigator. By way of an example, in the field of neutron scattering, of ingenuity making possible the seemingly impossible one can cite the investigation of the dynamical properties of liquid ^3He . The scientific interest in this quantum fluid, composed of equivalent particles that are subject to Fermi statistics, is very large. Set against this is the huge absorption of neutrons by ^3He , so much so, that it is one of the standard materials in the fabrication of neutron detectors. In the mid-70s, scientists at the Argonne National Laboratory brilliantly designed a sample holder which enabled them to measure the dynamical response function of liquid ^3He using an instrument fed with neutrons from a reactor with a modest neutron flux; the rest, as one says, is history, and today our knowledge, at an atomic level of detail, of the properties of ^3He and mixtures of ^3He and ^4He is at an advanced stage.

One of the great strengths of neutron-beam techniques is the well-established dynamic interplay between the flow of experimental data and advances in theoretical physics and chemistry. (The same cannot be said of all work done using beams of X-rays, e.g. resonance-enhanced scattering of X-rays necessarily contains unwelcome information on virtual, intermediate states that carry little useful information about the bulk properties of the sample.) The methods of theoretical physics and chemistry, the computer simulation and ab initio calculations, and the experiments using beams of neutrons are truly complementary. Computer simulations can be extremely valuable in all facets of a neutron scattering experiment. Results from a simulation can help frame good questions to be addressed in an experimental investigation, and simulations can help in the interpretation of data. The same comments apply equally well to theories of condensed matter which are developed using analytic techniques. Simulations and ab initio calculations, analytic theories, and experiments made with beams of neutrons represent a venerable tripos on which rest many key aspects of condensed matter and materials research.



Invited lecturers



..... and participants

*List of Participants, 4th Summer School on Neutron Scattering,**August 18 - 24, 1996, Zuoz, Switzerland*

Mamdouh Adib Reactor & Neutron Physics Dept. Nuclear Research Centre, Atomic Energy Authority P.O. 13758 Cairo, Egypt Tel. ++202 2460924 Fax ++202 354 0982	Mikhail Avdeev Joint Institute for Nuclear Research Frank Laboratory of Neutron Physics 141980 Dubna, Moscow Region Russia Tel. ++709621 63099 Fax ++709621 65882	Ewald Balcar Atominstitut der Österreichischen Universitäten Schüttelstrasse 115 1020 Wien Austria Tel. ++43 1 72 701-235 Fax ++43 1 728 9220
Günter Bauer Paul Scherrer Institut WHGA/252 5232 Villigen PSI Switzerland Tel. ++41 56 310 2524 Fax ++41 56 310 3131	Guy Bayon CEA DRE/SRO Saclay 91191 Gif sur Yvette Cedex France Tel. ++33 169 08 3881 Fax ++33 169 08 7796	Renate Bercher Paul Scherrer Institut WHGA/249 5232 Villigen PSI Switzerland Tel. ++41 56 310 3402 Fax ++41 56 310 3131
Martin Böhm Am Blumenhang 1 8010 Graz Austria Tel. ++43 316 46 69 70 Fax --	Peter Böni Paul Scherrer Institut WHGA/144 5232 Villigen PSI Switzerland Tel. ++41 56 310 2518 Fax ++41 56 310 2849	Oliver Borgmeier Institute für Anorganische Chemie RWTH Aachen Prof. Pirlet Str. 1 52074 Aachen Germany Tel. ++49 241 804665 Fax ++49 241 8888288
Hans-Benjamin Braun Paul Scherrer Institut WHGA/244 5232 Villigen PSI Switzerland Tel. ++41 56 310 4515 Fax ++41 56 310 2646	Jane Brown Institut Laue Langevin BP 156X 38042 Grenoble France Tel. ++33 7620 7040 Fax ++33 7648 3906	Giovanni Bruno Universita Ancona Istituto di Scienze Fisiche Via Ranieri, 65 60131 Ancona Italy Tel. ++39 71 2204607 Fax ++39 71 2204605
Uli Buchenau Forschungszentrum Jülich GmbH Abteilung IFF Postfach 19 13 52425 Jülich Germany Tel. ++49 2641 61 6643 Fax ++49 2641 61 2610	Willi Bührer Paul Scherrer Institut OBBA/1 5232 Villigen PSI Switzerland Tel. ++41 56 310 2086 Fax ++41 56 310 2939	Yiren Chen EPFL CRPP-Technologie de la Fusion OVGA/8 5232 Villigen PSI Switzerland Tel. ++41 56 310 2645 Fax ++41 56 310 2199
Denis Cheptiakov Joint Institute for Nuclear Research Frank Laboratory of Neutron Physics 141980 Dubna, Moscow Region Russia Tel. ++709621 65644 Fax ++709621 65882	Daniel Clemens Paul Scherrer Institut WHGA/142 5232 Villigen PSI Switzerland Tel. ++41 56 310 2925 Fax ++41 56 310 2849	Suzie Coad University of Warwick Physic Dept. CV47AL Coventry UK Tel. ++44 1203 523 2329 Fax ++44 1203 692016
Mireille Crittin University of Fribourg Physics Institute Ch. du Musée 3 1700 Fribourg Switzerland Tel. ++41 37 29 90 80 Fax ++41 37 29 9747	Roland Currat Institute Laue Langevin 156 X 38042 Grenoble France Tel. ++33 7620 7086 Fax ++33 7648 3906	Silvio Decurtins Universität Zürich Anorganisches Chem. Institut Winterthurer Strasse 190 8057 Zürich Switzerland Tel. ++41 1 257 4651 Fax ++41 1 363 86 11

*List of Participants, Summer School on Neutron Scattering,**August 18 - 24, 1996, Zuoz, Switzerland*

Bernard Delley Paul Scherrer Institut Badenerstrasse 569 8048 Zürich Switzerland Tel. ++41 1 492 6350 Fax ++41 1 491 0007	Bruno Dorner Institut Laue Langevin B.P. 156 38042 Grenoble France Tel. ++33 76207293 Fax ++33 76483906	Jürgen Duppich Paul Scherrer Institut WMHA/C9 5232 Villigen PSI Switzerland Tel. ++41 56 310 3320 Fax ++41 56 310 3294
Lixin Fan Frank Laboratory for Neutron JINR 141980 Dubna, Moscow region Russia Tel. ++09621 62674 Fax ++09621 65882	François Fauth Paul Scherrer Institut c/o Institut Laue Langevin B.P. 156 38042 Grenoble France Tel. ++33 7620 7216 Fax ++33 7648 3906	Peter Fischer Paul Scherrer Institut OBBA/9 5232 Villigen PSI Switzerland Tel. ++41 56 310 2094 Fax ++41 56 310 2939
Walter Fischer Paul Scherrer Institut WHGA/250 5232 Villigen PSI Switzerland Tel. ++41 56 310 3412 Fax ++41 56 310 3131	Michael Fricke Hahn-Meitner-Institut Glienicker Strasse 100 14109 Berlin Germany Tel. ++49 30 8062 2804 Fax ++49 30 8062 3172	Oliver Fritz Paul Scherrer Institut c/o Rutherford Appleton Laboratory R3/1-27 Oxfordshire OX11 0QX UK Tel. ++44 1235 44 6652 Fax ++44 1235 44 5642
Albert Furrer Paul Scherrer Institut Labor für Neutronenstreuung OBBA/3 5232 Villigen PSI Switzerland Tel. ++41 56 310 2088 Fax ++41 56 310 2939	Heinz Gäggeler Paul Scherrer Institut OFLA/104 5232 Villigen PSI Switzerland Tel. ++41 45 310 2404 Fax ++41 45 310 4435	Urs Gasser Paul Scherrer Institut Labor für Neutronenstreuung OBBA/4 5232 Villigen PSI Switzerland Tel. ++41 56 310 2089 Fax ++41 56 310 2939
Urs Greuter Paul Scherrer Institut WMHA/C46 5232 Villigen PSI Switzerland Tel. ++41 56 310 3112 Fax ++41 56 310 3717	Hans Grimmer Paul Scherrer Institut WHGA/242 5232 Villigen PSI Switzerland Tel. ++41 56 310 2421 Fax ++41 56 310 2646	Mathias Gutmann Paul Scherrer Institut WHGA/147 5232 Villigen PSI Switzerland Tel. ++41 56 310 2092 Fax ++41 56 310 2939
Patrick Hautle Paul Scherrer Institut WLGA/B25 5232 Villigen PSI Switzerland Tel. ++41 56 310 3210 Fax ++41 56 310 3294	Heinz Heer Paul Scherrer Institut Labor für Neutronenstreuung OBBA/8 5232 Villigen PSI Switzerland Tel. ++41 56 310 2093 Fax ++41 56 310 2935	Wolf-Dietrich Herold Paul Scherrer Institut OLGA/G019 5232 Villigen PSI Switzerland Tel. ++41 56 310 4240 Fax ++41 56 310 2199
Wilfred Hirt Paul Scherrer Institut 5232 Villigen PSI Switzerland Tel. ++41 56 310 2765 Fax ++41 56 310 32 94	Christina Hoffmann Laboratorium für chem. & mineralog. Kristallographie Universität Bern Freie Strasse 3 3012 Bern Switzerland Tel. ++41 31 631 4321 Fax ++41 31 631 3996	Stefan Janssen Paul Scherrer Institut WHGA/150 5232 Villigen PSI Switzerland Tel. ++41 56 310 2875 Fax ++41 56 310 2849

*List of Participants, Summer School on Neutron Scattering,**August 18 - 24, 1996, Zuoz, Switzerland*

Andreas Kahle Mineralogisch-Petrographisches Institut Ohlshausenstrasse 40 24098 Kiel Germany Tel. ++49 431 880 6914 Fax ++49 431 880 4457	Lukas Keller Paul Scherrer Institut OBBA/4 5232 Villigen PSI Switzerland Tel. ++41 56 310 Fax ++41 56 310 2939	Jean Kern Université de Fribourg Physics Department Perolles 1700 Fribourg Switzerland Tel. ++41 37 299 074 Fax ++41 37 299 747
Joachim Kohlbrecher Paul Scherrer Institut WHGA/346 5232 Villigen PSI Switzerland Tel. ++41 56 310 2931 Fax ++41 56 310 2646	Mark Könnecke Paul Scherrer Institut WHGA/247 5232 Villigen PSI Switzerland Tel. ++41 56 310 2512 Fax ++41 56 310 2646	Sonja Kömer Paul Scherrer Institut OBCA 5232 Villigen PSI Switzerland Tel. ++41 56 310 4184 Fax ++41 56 310 2327
Guido Kühne Paul Scherrer Institut WMFA/A14 5232 Villigen PSI Switzerland Tel. ++41 56 310 2924 Fax ++41 56 310 31 32	Eberhard Lehmann Paul Scherrer Institut OSRA/007 5232 Villigen PSI Switzerland Tel. ++41 56 310 2963 Fax ++41 56 310 2327	Jörg Löffler Paul Scherrer Institut WHGA/347 5232 Villigen PSI Switzerland Tel. ++41 56 310 2082 Fax ++41 56 310 2646
Martin Long Birmingham University School of Physics Edgbaston B15 2TT Birmingham Great Britain Tel. ++44 121 414 4663 Fax ++44 121 414 4719	Stephen Lovesey Rutherford Appleton Laboratory Chilton Didcot Oxon OX11 0QX UK Tel. ++44 1235 44 6359 Fax ++44 1235 44 5642	David Maden Paul Scherrer Institut WHGA/247 5232 Villigen PSI Switzerland Tel. ++41 56 310 3616 Fax ++41 56 310 2646
Maria-Luisa Medarde Paul Scherrer Institut OBBA/6 5232 Villigen PSI Switzerland Tel. ++41 56 310 2091 Fax ++41 56 310 2939	Joël Mesot Paul Scherrer Institut WHGA/150 5232 Villigen PSI Switzerland Tel. ++41 56 310 4029 Fax ++41 56 310 2646	Barry Mos Interfaculty Reactor Institute Mekelweg 15 2629 JB Delft The Netherlands Tel. ++31 15 2784533 Fax ++31 15 2786422
Kamelia Naguib Reactor & Neutron Physics Dept. Nuclear Research Centre, Atomic Energy Authority P.O. 13758 Cairo, Egypt Tel. ++202 2010029 Fax ++202 354 0982	Markus Niffenegger Paul Scherrer Institut OVGA/118 5232 Villigen PSI Switzerland Tel. ++41 56 310 2686 Fax ++41 56 310 2199	René Pellaux Universität Zürich Anorg. Chem. Institut Winterthurer Strasse 190 8057 Zürich Switzerland Tel. ++41 1 257 4615 Fax ++41 1 363 86 11
W. Petry TU München Physik Department E13 James-Franck-Strasse 1 85748 Garching Germany Tel. Fax	B.D. Rainford South Hampton University Physics Department SO9 5NH South Hampton UK Tel. Fax	Aldona Rajewska Joint Institute for Nuclear Research Frank Laboratory of Neutron Physics 141980 Dubna, Moscow Region Russia Tel. ++709621 67417 Fax ++709621 65882

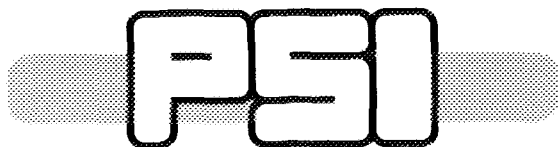
*List of Participants, Summer School on Neutron Scattering,**August 18 - 24, 1996, Zuoz, Switzerland*

Massimo Rogante Università Ancona Istituto di Scienze Fisiche Via Ranieri, 65 60131 Ancona Italy Tel. ++39 71 2204603 Fax ++39 71 2204605	Jürg Schefer Paul Scherrer Institut ODRA/118 5232 Villigen PSI Schweiz Tel. ++41 56 310 4347 Fax ++41 56 310 2646	Nick Schlumpf Paul Scherrer Institut WMHA/C24 5232 Villigen PSI Switzerland Tel. ++41 56 310 3270 Fax ++41 56 310 3717
Helmut Schmalle Universität Zürich Anorganisch-Chemisches Institut Winterthurer Str. 190 8057 Zürich Switzerland Tel. ++41 1 257 4650 Fax ++41 1 363 8611	Peter Schurtenberger ETH Zürich Institut für Polymere 8092 Zürich Switzerland Tel. ++41 1 632 3104 Fax ++41 1 632 1073	Michael Simmonds Paul Scherrer Institut WHGA/350 5232 Villigen PSI Switzerland Tel. ++41 56 310 2931 Fax ++41 56 310 2646
Denis Sobianine Institute of Physics SB RAS 660036 Krasnoyarsk Russia Tel. ++8 3912 494364 Fax ++7 3912 438923	Pierre Stadelmann CIME EPFL Bât. MX-C 1015 Lausanne Switzerland Tel. ++41 21 693 2976 Fax ++41 21 693 4401	M. Stamm Max Planck-Institut für Polymerforschung Postfach 3148 Ackermannweg 10 55021 Mainz Germany Tel. ++49 6131 379 117 Fax ++49 6131 379 100
W. Steurer Labor für Kristallographie und Petrographie ETH Zentrum 8092 Zürich Switzerland Tel. ++41 1 632 6650 Fax ++41 1 632 1133	Uwe Stuhr Paul Scherrer Institut WHGA/344 5232 Villigen PSI Switzerland Tel. ++41 56 310 25 17 Fax ++41 56 310 2646	H. Stuhmann GKSS Forschungszentrum 21502 Geesthacht Germany Tel. ++49 4152 87 1290 Fax ++49 4152 87 1338
Emmanuelle Suard Institut Laue Langevin B.P. 156 38042 Grenoble France Tel. ++33 7620 7164 Fax ++33 7648 3906	Sabine Teichmann Paul Scherrer Institut Inst. for Medical Radiobiology OBUA/2 5232 Villigen PSI Switzerland Tel. ++41 56 310 2966 Fax ++41 56 310 4412	Christophe Terrier Paul Scherrer Institut Labor für Neutronenstreuung WHGA/242 5232 Villigen PSI Switzerland Tel. ++41 56 310 2421 Fax ++41 56 310 2939
Sébastien Tixier Paul Scherrer Institut WHGA/142 5232 Villigen PSI Switzerland Tel. ++41 56 310 4401 Fax ++41 56 310 2849	Helena Van Swygenhoven Paul Scherrer Institut WHGA/350 5232 Villigen PSI Switzerland Tel. ++41 56 310 2931 Fax ++41 56 310 2646	Werner Wagner Paul Scherrer Institut WHGA/348 5232 Villigen PSI Switzerland Tel. ++41 56 310 2517 Fax ++41 56 310 2849
G.A. Webster Department of Mechanical Engineering Imperial College SW7 2BX London UK Tel. ++44 171 594 7080 Fax ++44 171 823 8845	Theo Woike Universität zu Köln Christallographie Zülpicher Str. 49 50674 Köln Germany Tel. ++49 221 470 6355 Fax ++49 221 4704963	Yanping Xu Frank Laboratory for Neutron JINR 141980 Dubna Russia Tel. ++007 09621 65803 Fax ++007 09621 65882

*List of Participants, Summer School on Neutron Scattering,**August 18 - 24, 1996, Zuoz, Switzerland*

H. Zabel Ruhr-Universität Bochum Exp. Physik IV Universitätsstrasse 150 44780 Bochum Germany Tel. ++49 234 700 3649 Fax ++49 234 7094173	Markus Zolliker Paul Scherrer Institut c/o Institut Laue Langevin B.P. 156 38042 Grenoble France Tel. ++33 7620 7348 Fax ++33 7648 3906	
---	--	--

PAUL SCHERRER INSTITUT



Paul Scherrer Institut
CH-5232 Villigen PSI
<http://www.psi.ch>

Phone 056 310 21 11
Fax 056 310 21 99